VELOCITY AND PRESSURE CHARACTERIZATION OF PULSATIONS IN ELEVATED PRESSURE NATURAL GAS AND EFFECTS ON ULTRASONIC FLOW METER ACCURACY

by

CHRISTOPHER L. GRANT, B.S.

THESIS
Presented to the Graduate Faculty of
The University of Texas at San Antonio
in Partial Fulfillment
of the Requirements
for the Degree of

MASTER OF SCIENCE IN MECHANICAL ENGINEERING

COMMITTEE MEMBERS:
Randall D. Manteufel, Ph.D., Chair
Kiran Bhaganagar, Ph.D.
Zhi-Gang Feng, Ph.D.

THE UNIVERSITY OF TEXAS AT SAN ANTONIO
College of Engineering
Department of Mechanical Engineering
May 2017

DEDICATION

This thesis is dedicated to myself, for all my hard work. I'm great. Good job, me.

ACKNOWLEDGEMENTS

I would like to express my sincere gratitude to my advisor, Dr. Randy Manteufel for his guidance and experience. I cannot imagine having a better advisor for my Master's study. I would also like to thank the rest of my thesis committee, Dr. Zhi-gang Feng and Dr. Kiran Bhaganagar.

Special thanks must go to the Metering Research Facility of Southwest Research Institute for the use of specialized equipment, facility use time, and funding. Without the support of John Sullenger, Terry Grimley, and the rest of the Flow Measurement Group, this research would not have been possible. I must also extend my thanks to Terry Schiebel for lending me the use of his piezoelectric transducers and DAQ which I returned in (mostly) good condition.

Although the specific ultrasonic meter manufacturer will be left unnamed, I must thank them for generously allowing the use of their meter in these experiments. I sincerely hope that the data collected here will lead to increased performance of their future products. I would also like to thank the fine engineers at TSI for patiently answering all my questions as I was playing Frankenstein with their products.

I would of course like to thank my parents, Bill and Rosie, for being so supportive in this endeavor specifically, and my academic career generally. All the A's I got were for you two.

And finally, to Kate, thank you. I love you forever.

May 2017

VELOCITY AND PRESSURE CHARACTERIZATION OF PULSATIONS IN ELEVATED PRESSURE NATURAL GAS AND EFFECTS ON ULTRASONIC FLOW METER ACCURACY

Christopher L. Grant, M.S.
The University of Texas at San Antonio, 2017

Supervising Professor: Randall D. Manteufel, Ph.D.

Ultrasonic flow meters (USMs) are common tools in the natural gas industry used to measure gas flow rate with precision. They are highly advanced devices most frequently used in custody transfer, an application in which just a few tenths of a percent error can account for tens of thousands of dollars per day. Because USMs are relative newcomers to the field of natural gas flow measurement, sources of error are still being discovered and studied. One of the most poorly understood sources is pulsation, or a traveling pressure and velocity fluctuation in the flow. In this thesis, a USM was subjected to pulsations at frequencies between 5 Hz and 45 Hz in elevated pressure natural gas flow (*Re* = 470,000 and 1,540,000). A pulsation generator was used to create and control the pulsation frequency and amplitude. The meter error was measured at each frequency for two flow rates. The pulsations themselves were measured directly using high-speed piezoelectric pressure transducers and a traversing hotwire probe that was specially adapted to operate in natural gas. The hot-wire data was used to examine the direct effects of pulsations on flow profile. Due to the pulsations, USM measurement errors exceeding 1% were observed. Results suggest that the error cannot be predicted using maximum pulsation amplitude. The error was found to correlate with pulsation frequency, flow rate, and most significantly the amplitude of pulsation at the meter location. A regression fit using these variables predicts USM measurement error with an R^2 of 95%.

TABLE OF CONTENTS

LIST OF TABLES

LIST OF FIGURES

TERMINOLOGY

Nomenclature

A	King's Law coefficient
A'	modified King's Law coefficient
A''	modified King's Law coefficient
A_p	Power Law coefficient
A_{pp}	pressure pulsation fit amplitude
B	King's Law coefficient
B'	modified King's Law coefficient
B''	modified King's Law coefficient
b_i	pulsation velocity profile fit coefficient
C	King's Law coefficient
c	speed of sound
$\dot{c}$	oscillation normalization coefficient
d	characteristic dimension of object generating a flow disturbance
D	pipe diameter of main branch
D_{branch}	pipe diameter of side branch
D_{bottle}	filter bottle inside diameter
D_{choke}	choke tube inside diameter
E	voltage
f	pulsation frequency
f_c	filter cutoff frequency
f_n	natural resonance frequency
f_{res}	resonance frequency
f_s	vortex shedding frequency
g	insertion point (g=1 is at the pipe wall)
h	heat transfer coefficient
i	square root of -1
I_t	turbulence intensity
j	electrical current
k	thermal conductivity
K	proportionality constant

K_v	coefficient relating rate of change in velocity to differential pressure
L	length of pipe segment producing a standing wave
L_f	acoustic length of filter element
L_u	path length between ultrasonic transducers in an ultrasonic meter
$\mathscr{L}$	distance from upstream pipe elbow to first side branch
N	number of data points used in regression fit
n	integer order of pulsation frequency
nt	index in calculation of turbulent energy
nt_{max}	maximum index in calculation of turbulent energy
P	pressure pulsation wave
P_t	pressure at orifice meter transmitter
P_0	pressure at orifice plate tap or primary element tap
P_1	upstream pressure
ΔP	differential pressure
p	Power Law exponent denominator
p_0	pressure pulsation fit offset
Q_{conv}	convective heat transfer
q	volumetric flow rate
q'	sectional volumetric flow rate
R	pipe radius
r	radial distance from pipe center
r_g	radial distance from pipe wall at point g
$\hat{r}$	xxx
Re	Reynolds number
St	Strouhal number
t	time
T_1	upstream temperature
U	velocity pulsation wave
u	flow velocity
u^*	estimated flow velocity
u'	root mean square of turbulent velocity fluctuations, turbulent energy
u_{avg}	average flow velocity

u_{max}	maximum flow velocity
VMI	Velocity Modulation Index
W_{elec}	electrical work
x	distance from pulsation generator
x_{node}	location of pressure node
x_u	linear distance between ultrasonic transducers in an ultrasonic meter
α	Womersley number
β_i	regression model coefficient
ϵ	estimated turbine meter measurement error
ε	regression model error term
λ	pulsation wavelength
μ	dynamic viscosity
ν	kinematic viscosity
ρ	density
τ	turbine rotor time constant
ω	angular pulsation frequency (rad/s)
$\langle\ \rangle$	operator representing time average of quantity
$\|\ \|$	operator representing absolute value

Abbreviations

acfm	actual cubic feet per minute
AGA	American Gas Association
API	American Petroleum Institute
ASME	American Society of Mechanical Engineers
CCA	constant current anemometer
CTA	constant temperature anemometer
FIP	flow-induced pulsation
ft/s	feet per second
Hz	hertz
kHz	kilohertz (1000 hertz)
ISO	International Organization for Standardization

LAUF	lost-and-unaccounted-for
LOF	likelihood of failure (Energy Institute)
LPL	Low Pressure Loop
MRF	Metering Research Facility
ms	milliseconds
p-p	peak-to-peak
psi	pounds per square inch
psia	absolute pounds per square inch
RMS	root mean square
RMSE	root mean square error
SGA	Southern Gas Association
SNR	signal-to-noise ratio
SRE	square root error
SwRI	Southwest Research Institute
USM(s)	ultrasonic meter(s)

CHAPTER ONE: INTRODUCTION

Ultrasonic flow meters are common tools in the natural gas industry used to measure gas flow rate with precision. They are highly advanced devices most frequently used in custody transfer, or the sale and purchase of a specified volume of natural gas. A single custody transfer can involve millions of dollars' worth of natural gas and a single meter can be responsible for the accurate measurement of hundreds of custody transfers per year. In this application, just a few tenths of a percent error can account for tens of thousands of dollars per day. Because ultrasonic meters are relative newcomers to the field of natural gas flow measurement, sources of error are still being discovered and studied. One of the most poorly understood sources is pulsation, or a traveling pressure and velocity fluctuation in the flow. Pulsations can manifest from a variety of sources commonly present in custody transfer. They can be difficult to detect and mitigate, and the mechanisms by which they affect measurement are still being studied. For the case of ultrasonic meters in natural gas, this is especially true. Very few studies have been done to explore and characterize the effects of pulsations in field condition natural gas applications. Given the monetary losses incurred due to pulsation-induced meter inaccuracy, it is critically important that this phenomenon is better understood.

From the outset, the purpose of this thesis was to eventually benefit the natural gas industry. To this end, all testing was to be done with high precision in a controllable and repeatable facsimile of natural gas field conditions. This meant large diameter pipe in a flow loop with variable flow rate using natural gas as a working fluid. It also required a repeatable pulsation generator and measurement techniques superior to those available commercially. A specialized flow loop was utilized to satisfy these requirements. The research goals of this thesis were twofold. The first was to directly measure the velocity profile shifts in natural gas flow

subjected to pulsations. Historically, pulsations have been quantified using pressure measurements because fast-response pressure transducers are more easily developed and employed in natural gas. However, evidence suggests a relationship between velocity pulsations and meter error exists. In order to achieve this goal and directly measure the changing velocity profiles in pulsating flow natural gas at elevated pressure, a traversing hot-wire anemometer was specially adapted for the experimentation. The hot-wire anemometer was capable of measuring the quickly shifting gas velocities at different points along the flow profile. By combining the hot-wire data collected from a traversal of pulsating flow, an accurate description of the changing flow velocity profile could be generated. The second goal of this thesis was to detect and qualify a relationship between meter error and one or more measureable aspects of pulsation. To this end an ultrasonic meter was subjected to pulsations at frequencies between 5 Hz and 45 Hz in elevated pressure natural gas flow. The meter error was measured at each frequency for two flow rates. In addition to using the hot-wire anemometer, the pulsations themselves were measured using high-speed piezoelectric pressure transducers. These piezoelectric pressure transducers make it possible to map standing pulsation waves in the test section, pinpointing the locations of nodes and antinodes. Combining this knowledge of the pressure waves with the hot-wire velocity measurements can lead to a characterization of the standing velocity pulsation waves generated in the piping. With a sophisticated understanding of the pulsations, the changes in meter error can be correlated to specific pulsation properties. This would lead to a final statistical regression model describing the particular influences of pulsations on meter error.

This thesis is divided into five chapters, of which this introduction is the first. Chapter Two of this thesis offers background information necessary to fully understand this research as

well as the results of a literature review into relevant studies. Flow measurement in natural gas can be unexpectedly complex and the plethora of ways in which pulsations can influence it only adds to that complexity. Because of this, Chapter Two is split into several parts. The first covers the basics of pulsations. Included are descriptions of what pulsations are, how they can be visualized or expressed mathematically, and how they propagate in a fluid like natural gas. The second section provides background information about the natural gas industry and the importance of flow metering. This section provides context and tribal knowledge relating to the measurement of natural gas flow. The structure of custody transfer and common industry practices are illustrated. The third section relates pulsations specifically to natural gas applications. Detailed here are the many sources of pulsation present in the natural gas field. This section will show how common it is to encounter pulsations in flow measurement. The fourth section of Chapter Two describes the operating principles behind ultrasonic flow meters and the effects of pulsations on ultrasonic flow meters based on the literature review for this thesis. This section will highlight the specific vulnerabilities ultrasonic meters have in pulsating flow. The last section provides a summary of the chapter and highlights the gaps in the literature review, which this thesis seeks to help fill.

Chapter Three of this thesis details the experimental approach of the research performed. The goals of the experimentation, as previously stated, were to directly measure the velocity profile shifts in natural gas flow subjected to pulsations and to detect and qualify a relationship between meter error and one or more measureable aspects of pulsation. To achieve these goals, particular capabilities were required of a test facility. These included field-like conditions using natural gas as a working fluid, adequate flow controls, accurate reference metering, and a compatible pulsation generator. The facility used for the experimentation fit these criteria and a

description of its operation and attributes is given in this chapter. Chapter Three also describes the construction of the test section, the transducers employed, and details about the specific ultrasonic meter and hot-wire anemometer used. Finally, the experimental procedure including the test matrix is specified.

Chapter Four of this thesis encapsulates the analysis of the test data and the discussions of results. Due to the reach of the goals of this thesis, this chapter is split into four main sections. The first section of Chapter Four details the development of pressure pulsation standing wave maps using the piezoelectric pressure transducer data. By using the measured pulsation pressure magnitude at several points along the test section, a sinusoidal curve fit was found for each pulsation frequency. The analysis in the chapter's second section uses the hot-wire anemometer data to explore the direct effects pulsations have on velocity profile. Using velocity measurements along a perpendicular traversal of the flow, the flow profile shifts in time were plotted. The third analysis section combines the results of the previous analyses into a coherent understanding of the pulsations in the test section. The velocity pulsation data from the hot-wire anemometer is used to build velocity pulsation maps from the pressure pulsation maps from the third section. In the fourth and final section, these pulsation characteristics are compared to the recorded ultrasonic flow meter data for each pulsation frequency and loop flow rate. By correlating the characteristics of the pulsation waves (both pressure and velocity) with changes in the meter error, a regression was developed to arithmetically relate pulsation to meter error. The last chapter of this thesis summarizes the efforts involved and condenses the findings into cohesive conclusions.

CHAPTER TWO: BACKGROUND AND LITERATURE REVIEW

Pulsations Basics

In the natural gas industry, a "pulsation" refers to a phenomenon observed in piping systems wherein periodic or cyclic fluctuations in local pressure and velocity propagate in the flow. In more general terms, a pulsation is an acoustic wave, or alternating compressions and rarefactions in a fluid. Pulsations occur at set frequencies that vary depending on the pulsation source. In general, the frequency of pulsation does not change as the wave propagates along a conduit unless it encounters a significant flow disturbance. Because of this property, it is common practice to model a pulsation as an acoustic sine wave in units of either pressure or velocity.

Figure 1 depicts the effect of a periodically moving piston on a column of a fluid in straight pipe. The lines represent the positions of fluid molecules in the pipe. When the lines are equidistant, as they are when the piston is in its first stroke position, the fluid is at rest with uniform pressure. When the piston compresses the local fluid in its second stroke position, the lines are shown closer together, symbolizing a localized increase in pressure. In the third stroke position, the piston retracts forming a localized decrease in pressure. In the terms of an acoustic wave, the localized pressure peak is a compression and the localized pressure trough is called a rarefaction. If the piston continues these strokes at a regular frequency, an acoustic wave is formed. An example pressure wave is shown as a sine wave at the bottom of Figure 1. The wavelength λ is measured as the distance from one compression to the next.

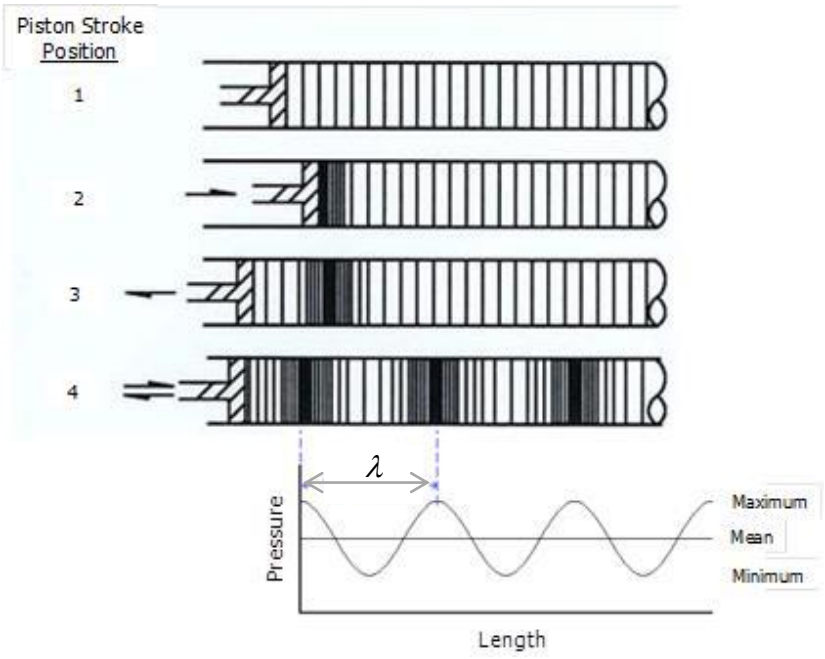

Figure 1. A periodic piston motion creates a traveling acoustic wave (Durke 2012)

As an acoustic wave, a pulsation travels at the speed of sound of the fluid. Using the speed of sound c and the pulsation frequency f, the wavelength of a pulsation wave λ can be easily determined using Equation [1].

$$\lambda = \frac{c}{f} \qquad [1]$$

Although pulsations are easiest to understand when seen as a single wave at a single frequency, most pulsation observed in the natural gas industry is the result of superimposed pulsation waves at different frequencies and with different amplitudes. While these waves typically come from different sources, there are devices and geometries that can generate pulsations as different frequencies simultaneously. At a basic level, whenever pulsation is generated at one frequency, there is a possibility of pulsations at the harmonics of that frequency also coming about. In the most extreme cases, a condition known as "broadband" pulsation

could arise in which pulsations over a sweep of all frequencies in a certain range are produced at once.

These different forms of pulsation affect meters differently and are so varied that the effects of many types are not well understood. Some data exists to suggest that certain meters are affected by specific ranges of frequencies or magnitudes, but a complete picture does not exist. For the purposes of this thesis, only pulsations at singular frequencies are examined. Although this is not the best representation of actual field conditions, generating and controlling pulsations at even a singular frequency is technically difficult and requires specialized equipment. Generating and controlling pulsations at several frequencies simultaneously is nearly impossible. The assumption is that the findings of this research are also valid in field scenarios.

Figure 2 shows how a single acoustic wavefront traveling along a conduit can reflect from a "closed end" or from an "open end." "Closed ends" may be the ends of headers, closed branches, or the ends of gauge or drain lines. "Open ends" may be significant diameter changes, large headers, or locations where a small line connects to pipe of a larger diameter. Although these situations are not truly open pipe ends, their acoustic characteristics resemble each other closely. The distinction between open and closed ends is important because the behavior of the waves will differ depending upon the type of reflection. A pressure maximum that reaches a closed end reflects back as a pressure maximum. In contrast, a pressure maximum that reaches an open end reflects back as a pressure minimum. In this case, the pressure wave will also continue into the open volume.

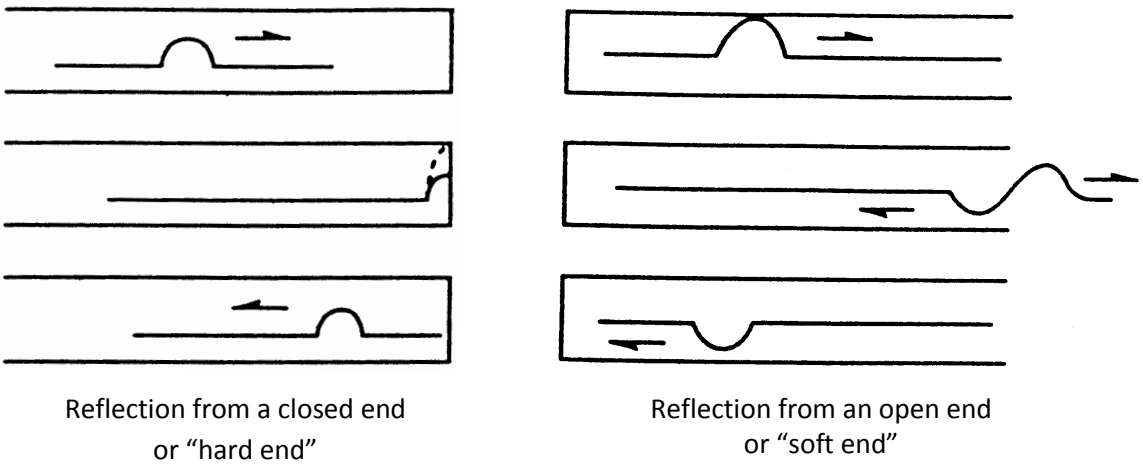

Figure 2. Wave reflections from open and closed ends (McKee 2006)

Like many other types of waves, acoustic pulsation waves can manifest in two main forms. Most commonly, it is a traveling wave, with the wavefronts emanating from the source of the pulsations. In this case, measuring for fluctuations along the length of pipe would give the same pulsation magnitude irrespective of the location of the sensor. However, pulsations can also manifest as standing waves created by a superposition of a traveling wave and its reflection. With the right combination of pulsation frequency and pipe geometry, geometrical features can reflect acoustic waves between them. Through superposition, a traveling wave can reflect and add together with the original wave in such a way that a summation of the two waves' amplitudes form stationary pressure nodes (points of zero pressure oscillation around the average value) and stationary pressure antinodes (points where the pressure oscillates between its maximum and minimum values). Because these nodes and antinodes remain at fixed locations in the pipe, the result is called a "standing wave." The superposition will make the pulsation amplitudes at the antinodes larger than the amplitudes of the original traveling waves. This is known as "acoustic resonance" and depends on the speed of sound in the fluid, the pipe length,

and the natural resonant acoustic frequency of the pipe geometry. Quite different from a traveling wave, there is no guarantee that measurement of the pulsation magnitude at different locations would yield the same value.

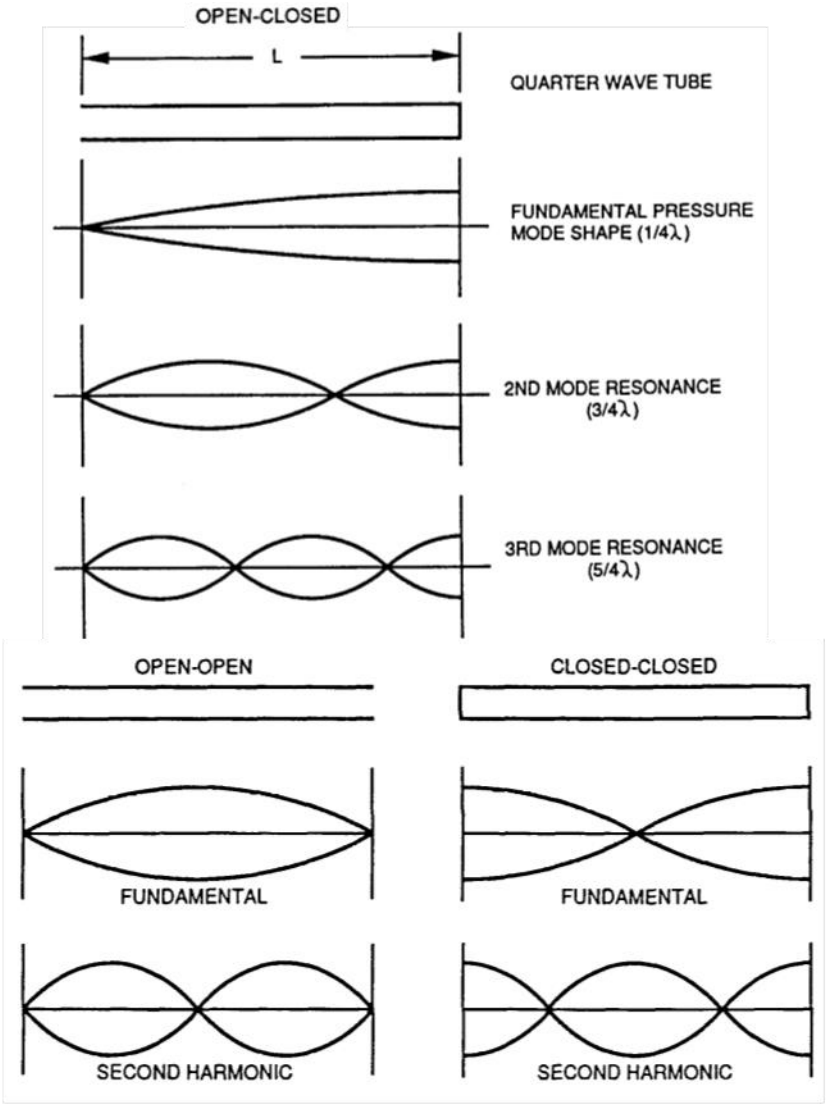

Figure 3. Standing waves and harmonics (McKee 2006)

Examples of standing waves in straight pipes with different combinations of open and closed ends are shown in Figure 3. Also shown is how more than one frequency can produce standing waves in the same length of pipe. The fundamental frequency is the lowest pulsation

frequency that produces a standing wave in the pipe. Higher frequencies that produce resonances in the same length of pipe are called harmonics of this fundamental frequency. For a pipe of length L carrying a fluid in which the speed of sound is c, the resonance frequencies f_{res} can be calculated from Equations [2] and [3]. The integer n in the formulas is known as the order or mode of the resonance frequency. The wavelength decreases as n increases, meaning more nodes and antinodes exist in the same length of pipe at higher order resonance frequencies.

$$f_{res} = \frac{nc}{2L} \text{ (both ends open or closed)} \quad [2]$$

$$f_{res} = \frac{(2n-1)c}{4L} \text{ (one end open, one closed)} \quad [3]$$

Due to the physics of inviscid flow through a pipe, a fluctuation in the local pressure is accompanied by a corresponding fluctuation in local velocity. If pressure variations propagate along a conduit, velocity variations will propagate as well. The frequency of the fluctuations is the same for both pressure and velocity. However, there exists a 90 degree phase shift between the pressure and velocity waves. This can be understood from an intuitive perspective. If acoustic waves can be seen as alternating pockets of compressed and rarefied fluid, it is clear that a pressure "peak" would exist in the center of the compressed fluid pocket and that a pressure "trough" would exist in the center of the rarefied fluid pocket. At these points in the flow, there is no gradient in local velocity. However, between these points exist the fluid particles rushing from a compression pocket to a rarefication pocket. At the center of these areas, the pressure is at a net zero, but the velocity magnitude is greatest. Therefore the velocity peak would be offset from the pressure peak by half the distance between the pressure peak and pressure trough. This corresponds to one quarter of the pulsation wavelength, or a phase shift of 90 degrees. This is illustrated in Figure 4. The importance of this dual nature is in how a pulsation affects a

particular flow meter. Different types of meters can be susceptible to certain aspects of a pulsation and resistant to others. (For the effects on USMs, see the section of this chapter titled "Ultrasonic Flow Meters and the Effects of Pulsation on Meter Accuracy.")

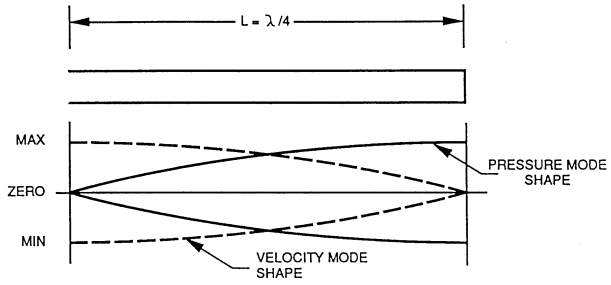

Figure 4. Diagram of pressure and velocity waves existing out of phase (Durke 2012)

This relationship between pressure and velocity pulsations can also be derived analytically starting with the Navier-Stokes equation. When one assumes a very long pipe with a circular-cross section, the Navier-Stokes equation takes the form shown in Equation [4], where x is the direction of flow in the pipe and r is the radial direction from the axis of the pipe. The fluid velocity is expressed as u. The fluid density is expressed as ρ and the dynamic viscosity of the fluid is expressed as μ.

$$\frac{\partial u}{\partial t} = -\frac{1}{\rho}\frac{\partial p}{\partial x} + \frac{\mu}{\rho}\left(\frac{\partial^2 u}{\partial r^2} + \frac{1}{r}\frac{\partial u}{\partial r}\right) \quad [4]$$

The no-slip boundary condition applies such that u=0 at r=R at the pipe wall. Assuming the pressure gradient is periodic, it can be expressed as in Equation [5] where K is a constant, ω is the angular frequency, and t is time. This expression is also shown using complex notation where i is the square root of negative one.

$$-\frac{1}{\rho}\frac{\partial p}{\partial x} = K\ \cos(\omega t) = Ke^{i\omega t} \quad [5]$$

If one assumes the velocity function is of the form in Equation [6], the differential equation [7] arises from applying the simplified Navier-Stokes equation in Equation [4] and the periodic pressure gradient in Equation [5].

$$u(r,t) = g(r)e^{i\omega t} \quad [6]$$

$$g''(r) + \frac{1}{r}g'(r) - \frac{1\omega\rho}{\mu}g(r) = -\frac{K\rho}{\mu} \quad [7]$$

The solution to Equation [7] is given by Equation [8] where J_0 is the Bessel function of the first kind and of zero order.

$$u(r,t) = -i\frac{K}{\omega}e^{i\omega t}\left(1 - \frac{J_0\left(r\sqrt{\frac{-i\omega\rho}{\mu}}\right)}{J_0\left(R\sqrt{\frac{-i\omega\rho}{\mu}}\right)}\right) \quad [8]$$

The Womersley number, given in Equation [9], is used to characterize oscillatory pipe flow and relates the pipe radius, the oscillation frequency, and the fluid viscosity (Evertz 2011). It is closely related to the argument of the Bessel functions in Equation [8].

$$\alpha = R\sqrt{\frac{\omega\rho}{\mu}} \quad [9]$$

For very large values of the Bessel function argument, the asymptotic expansion of the Bessel function [10] can be used. By extension, the asymptotic expansion can be used for large values of the Womersley number.

$$J_0(z) = \sqrt{\frac{2}{\pi z}}e^{i}i^{-1/2} \quad [10]$$

Using the asymptotic expansion yields the velocity function in Equation [11]. For large values of the Womersley number, the second term is quickly damped out as the distance from the pipe wall increases. Therefore the velocity function can be simplified to Equation [12]. (A defense for using this assumption can be found in the "Characterization of Velocity Pulsation Waves Using Pressure Measurements" section of Chapter Four wherein the Womersley numbers for this thesis are calculated using fluid properties recorded during testing.)

$$u(r,t) = \frac{K}{\omega}\left[\sin(\omega t) - \sqrt{\frac{R}{r}}exp\left(-\sqrt{\frac{\omega\rho}{2\mu}}(R-r)\right)\sin\left(\omega t - \sqrt{\frac{\omega\rho}{2\mu}}(R-r)\right)\right] \quad [11]$$

$$u(r,t) \cong \frac{K}{\omega}\sin(\omega t) \quad [12]$$

The velocity function in Equation [12] has a frequency identical to that of the excitation pressure wave in Equation [5]. It is also out of phase with the pressure wave by 90 degrees.

When the value of the Womersley number is set to 5, an intermediate value, the plot in Figure 5 is produced. The figure shows the velocity profile of oscillation at different instants of a single period. As time progresses, the velocity profile of oscillation changes drastically, at some points facing opposite the direction of flow. Also worth noting is that the flow near the wall leads the flow along the axis. Comparing the velocity profiles with a plot of the pressure gradient over time (at the bottom of the figure), the phase difference is apparent.

$$\alpha = R\sqrt{\frac{\omega\rho}{\mu}} = 5$$

$$\dot{c} = \frac{K\alpha^2}{8\omega} = 3.125\frac{K}{\omega}$$

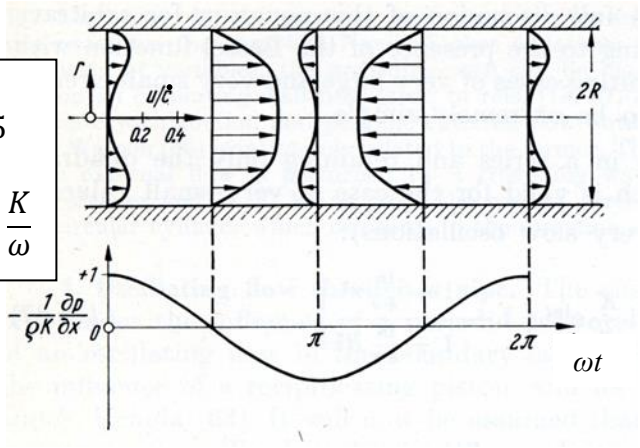

Figure 5. Velocity profile of oscillation shifts (Uchida 1956)

The Natural Gas Industry and Flow Metering

Custody transfer is a central part of the natural gas distribution system but is often not considered by those outside the industry. It refers to the transfer of natural gas from one entity to another. These entities can be separate parts of the same company or completely different companies. The largest custody transfers occur between natural gas producers (companies that extract and process natural gas from underground) and natural gas transmission line owners (companies that own long stretches of the large diameter pipelines that form the backbone of the natural gas transmission network). Because of the sheer quantities of natural gas transferred in these trades, measurement errors that would be negligible in other applications (on the order of 0.5%) could be worth tens of thousands of dollars in lost profits daily. Losses due to custody transfer error are perhaps the most troubling of any monetary losses in the natural gas industry because they are all unnecessary and avoidable.

One might expect the amounts of gas sold would balance with the amounts of gas bought. In the real world, the amounts are rarely exactly equal. When an imbalance in a natural gas transfer is found, the "missing" gas is called "Lost-And-Unaccounted-For" or LAUF. The

sources of LAUF gas are varied. One way there can be an imbalance is due to the meter error. But there are other factors as well. Unlike an incompressible fluid like water, a balance of natural gas is dependent upon pressure and temperature. At different conditions, the same mass of natural gas can occupy a different volume. If these conditions are not well measured and recorded, or are lost due to weather or a power outage, additional errors can arise. Finally, LAUF gas can also come about because the makeup of natural gas is not uniform. Natural gas is a blend of methane, nitrogen, carbon dioxide, ethane, propane, and heavier hydrocarbons. The proportions of the components in natural gas can vary depending upon processing and sourcing. Also, each individual compound reacts differently to changes in pressure and temperature. A heavy hydrocarbon could be gas at one point in the transmission line and liquid at the next. If the meter at the second point ignores the liquid phase, the heavy hydrocarbon could be characterized as LAUF. Each of the potential sources of LAUF gas is preventable and has its own mitigation methods. The focus of this thesis is on reducing the error in the custody meters themselves.

In a custody transfer, a custody meter is used to measure how much gas is being transferred. In the natural gas industry, a custody transfer meter is colloquially called "the cash register." This is because trade deals involving a mass of natural gas changing hands are performed using a custody transfer meter. The particular meter is explicitly identified in a written trade agreement prior to the transfer. Naturally, it is in both entities' best interest for the meter to be as accurate as possible. The larger the meter error (positive or negative), the more one company was shortchanged. Not only is this immediately damaging to profits, it could also degrade future trade agreements. Because of this, natural gas companies invest heavily into employing the most accurate custody transfer meters available. However, regardless of the

purported accuracy of these meters, they can still be susceptible to pulsation related measurement errors.

In practice, custody transfer meters operate as part of a system. Though the meters are by far the most important piece of these systems, their accuracy would be severely impaired without the other components. Generally, these systems are called "meter runs" and consist of the flow meter, pressure and temperature sensors, some form of gas sampling or gas quality determination, and flow conditioning. Although the meters alone can typically infer the flow velocity, the conversion into meaningful quantities of natural gas components requires accurate measurements of temperature and pressure near the meter as well as knowledge of the gas composition. The temperature and pressure of the gas at the meter are typically measured using sensors just up- or downstream of the meter. The gas composition, or gas quality, is determined with the use of a gas chromatograph. In some cases, these are installed near the meter run to provide continuous compositional data. In other cases, samples are manually taken from the gas line and sent to remote analysis groups who may use more sophisticated gas chromatographs.

The last component of a meter run is flow conditioning. In ideal turbulent flow, the flow profile takes on a well-developed "bullet shape" as exemplified in Figure 6. The goal of flow conditioning is to maintain or even recreate this well-developed flow profile in the face of distortions. Several factors present throughout natural gas piping can distort a flow velocity profile. Elbows can skew the flow velocity to one side or induce swirling radial velocity that pushes the flow away from the center (Figure 7). Forcing flow through restrictions can induce so much turbulence that the flow completely loses its "bullet-shape" profile. Pulsations are also theorized to shift velocity profile as in Figure 5, but measurements of velocity profile in field condition natural gas flow are difficult. (See the section titled "Characterization of the Effect of

Pulsations on Velocity Profiles" in Chapter Four for the measurements made during experimentation for this thesis.) Many flow meters will exhibit limited performance if the flow entering the meter has high turbulence, a strong radial velocity component, a skew off center, or is otherwise not "well developed."

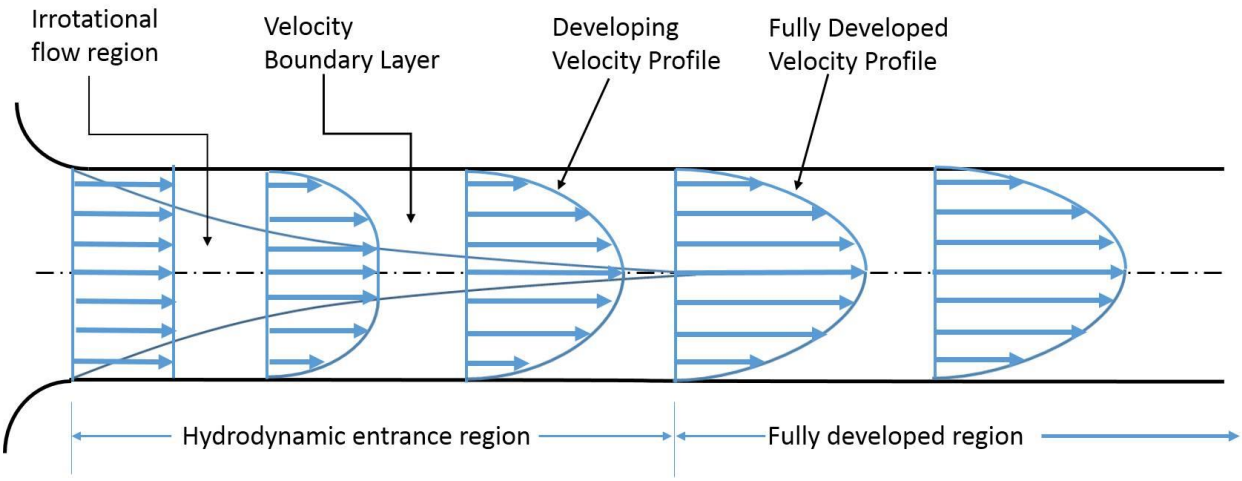

Figure 6. A flow profile develops as the flow move through a straight pipe (Devender 2014)

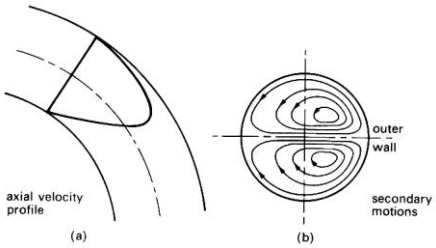

Figure 7. Flow profile distortion due to swirl (Caro 1978)

To aid in the regulation of flow, the American Gas Association recommends the use of long lengths of disturbance free pipe, the use of flow conditioning plates or inserts, and other techniques specific to the type of flow meter being used. An example flow conditioning plate, called a CPA 50E is shown in Figure 8. Flow is redirected through the ports, distributing the flow into a more developed shape. Other flow conditioning methods work in a similar fashion. Combining the meter, the sensors, the gas quality determination, and the flow conditioning

results in the meter run system. Every part must function properly to ensure accurate flow measurement.

Figure 8. Computer generated model of a CPA 50E flow conditioning plate (CPA 2016)

The configurations of meter runs are closely regulated by the American Gas Association to ensure that flow metering is consistent. Configuration requirements can change slightly for different meter types and each set of requirements is captured in a standard released regularly by the AGA. Despite the scale of the natural gas industry in the United States, custody transfer is typically conducted using only three types of flow meters: orifice, turbine, and ultrasonic. (Coriolis and vortex meters can also be used, but are much less common.) For ultrasonic meters, the regulations for a meter run are given in AGA Report No. 9 (AGA 2007). The document outlines the recommended meter run configuration for use with ultrasonic meters, called the AGA-9 default configuration. This configuration is a straight pipe arrangement involving, in order from upstream to downstream, a length of pipe equal to 10 nominal pipe diameters (called 10D in natural gas industry shorthand) after the last upstream flow disturbance, a CPA 50E plate

flow conditioner, a second 10D length of pipe, the ultrasonic meter itself, and 5D of pipe downstream of the meter. The intention of this configuration is provide adequate flow conditioning such that the meter can measure accurately.

Pulsations in Natural Gas Applications

Despite the evidence that exists showing the dangers of pulsation to accurate flow measurement, there are still many in the natural gas industry who do not believe pulsations to be common or who do not believe modern meters are susceptible. The purpose of this section is not to detail every potential source of pulsations in natural gas applications, but instead to give the reader an idea for how prevalent pulsations are. The sources of pulsations are varied. They are so varied that an exhaustive list would likely constitute its own thesis. Pulsation sources include both external sources (such as compressors) as well as internal sources (such as piping geometry, valves, and protrusions into the flow). Figure 9 shows the general relationship between velocity pulsation amplitude and pulsation frequency. It also highlights regions relating to different aspects of natural gas production and transmission. These regions show the expected pulsation frequencies and amplitudes that could be expected from each pulsation source.

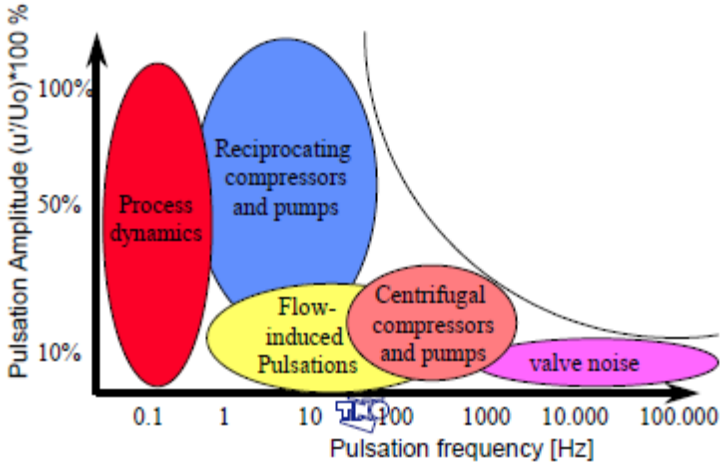

Figure 9. Pulsation amplitude and frequency, with typical sources (van Bokhorst 2002)

The most common sources of pulsations in natural gas applications are detailed in the subsections below. These include reciprocating and centrifugal compressors as well as a variety of static pipe elements that can induce pulsation given the right conditions. The final subsection covers acoustic filters, the most common method for eliminating pulsations, and their weaknesses. In sum, this section is meant to illuminate just how common pulsations are in the natural gas industry and how likely it is that pulsations are affecting custody transfer meters in the field.

Reciprocating Compressors

Reciprocating compressors are a type of positive-displacement compressor that utilizes pistons driven by a crankshaft to pressurize gas. Gas at a low pressure is injected into a piston cylinder, the pressure of the gas is elevated by the piston compressing the gas to a smaller volume, and then the gas is ejected from the cylinder at the higher pressure. Reciprocating compressors are common in the natural gas industry, used to pressurize natural gas either at the beginning of a transmission line or to boost the pressure along the line.

Although this was not always the case, these days reciprocating compressors are notorious for causing pulsations in the discharge line. The cyclic mechanism of the compressor releases periodic pockets of compressed gas. By its nature, this is a pulsation. Typical pulsation frequencies from reciprocating compressors range from 5 Hz to 75 Hz (McKee 2009). Rotary screw and booster compressors produce pulsations in the same frequency range or a slightly higher range as reciprocating compressors. Overall, reciprocating compressors and booster compressors tend to produce pulsations at a single frequency (the frequency of the compressor mechanism) and its harmonics. For this reason, pulsations caused by reciprocating compressors are easily diagnosed. Also, since pulsations are often expected as a result of using a

reciprocating compressor, many are outfitted with tuned acoustic filters which prevent the pulsations from progressing.

Centrifugal Compressors

Centrifugal compressors, also called radial compressors, are a type of turbomachinery used to increase the pressure of a gas in flow. These compressors consist of two main parts: the impeller and the diffuser. The impeller, also called a rotor, is the rotating component of the compressor. Though the design can vary between different compressors, the impeller invariably has guide vanes that direct the flow. It is powered externally and increases the velocity of the gas flow. The diffuser is located just downstream of the impeller. Its purpose is to slow the gas, thereby increasing its pressure. In energy terms, the impeller imparts kinetic energy and the diffuser converts this kinetic energy into potential energy, manifesting as an elevated static pressure. Centrifugal compressors are common in the natural gas industry, most often found in transmission. The compressors are installed at points along a pipeline to overcome the pressure drop of long distance travel.

Although centrifugal compressors do not share the reputation of reciprocating compressors as producers of pulsations, centrifugal compressors can and do generate acoustic disturbances. Pulsations from centrifugal compressors involve complex spectra generated by flow phenomena within the compressor. Pulsations at the higher frequencies produced by these compressors are low-amplitude and are produced by individual blades passing by the discharge point. Pulsations at lower "centrifugal frequencies" are of moderate amplitude and are produced by flow phenomena within the compressor. Pulsations can also be related to centrifugal compressors, but not normally produced by the compressors themselves (McKee 2009). When a compressor is forced into non-standard operating conditions such as stalling or surging,

pulsations at lower than typical frequencies can be generated. Centrifugal compressors can also generate flow energy that can induce vortex shedding at closed side branches or protrusions in the pipe.

Flow-induced Pulsation

Flow-induced pulsation (FIP) is a condition in which an interaction between a gas flow and a geometric feature of a pipe system is the source of pulsation. The behavior of FIP is often governed by the Reynolds number, *Re*, the dimensionless ratio of inertial forces to viscous forces in the flow. At Reynolds numbers greater than $3.5 \cdot 10^6$, the fluid boundary layer along certain geometric features will separate, causing abrupt transitions in the flow path and causing the formation of vortices behind the feature in a phenomenon known as vortex shedding. Although the formation of vortices and the behavior of vortex shedding are complex fields of fluid dynamics, an in-depth understanding is not necessary for this application. In this case, vortices can be simplified as areas of reduced local velocity (the vortices) and amplified local velocity (between the vortices). These vortices are shed at a distinct frequency determined by the geometry and the flow velocity. This property of vortex shedding is why they can be considered pulsations. This behavior is exemplified for a cylindrical feature in Figure 10. As the Reynolds number increases, the downstream flow behavior changes. At Reynolds numbers greater than $3.5 \cdot 10^6$, the cylindrical flow obstruction forms vortices shed at regular intervals.

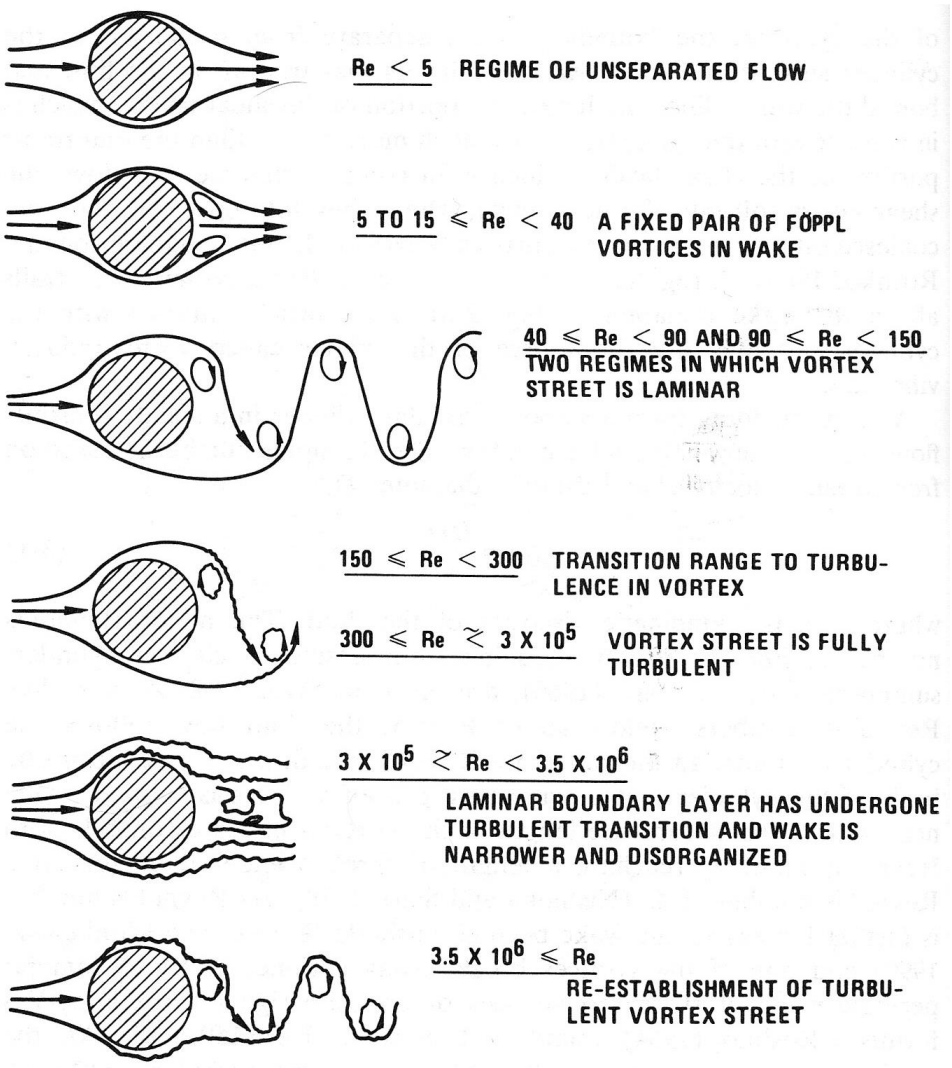

Figure 10. Vortex shedding as a function of Reynolds number (Blevins 1990)

The Strouhal number is typically used to predict the frequencies of pulsations caused by flow-induced vortex shedding. The Strouhal number *St* is a non-dimensional parameter that relates the vortex shedding frequency f_s to the flow velocity u and a characteristic dimension d of the geometric feature producing the vortices. This is shown in Equation [13].

$$St = \frac{f_s d}{u} \qquad [13]$$

An example of the characteristic dimension of an object generating the disturbance would be the diameter of a cylindrical obstruction such as the one pictured in Figure 10. If the range of gas flow velocities over which vortex shedding will occur is unknown for a given flow disturbance, the Strouhal number range that produces shedding can be determined through experimentation. Several published papers and texts provide the Strouhal number as a function of Reynolds number or a variety of common obstruction geometries (Blevins 1990). Once the Strouhal number for a given source of vortex shedding is known, Equation [13] is solved for the vortex shedding frequency, also the frequency of the pulsation.

Broadband Pulsations

The term "broadband pulsations" refers to a condition in which pulsations are present at many frequencies simultaneously, typically within a defined frequency range. Two common sources of broadband pulsations are flow-induced turbulence and high-frequency acoustic excitation. An example of low frequency (<100 Hz), low amplitude (<0.3 psi) broadband pulsations from flow-induced turbulence due to high flow rates around elbows is shown in Figure 11.

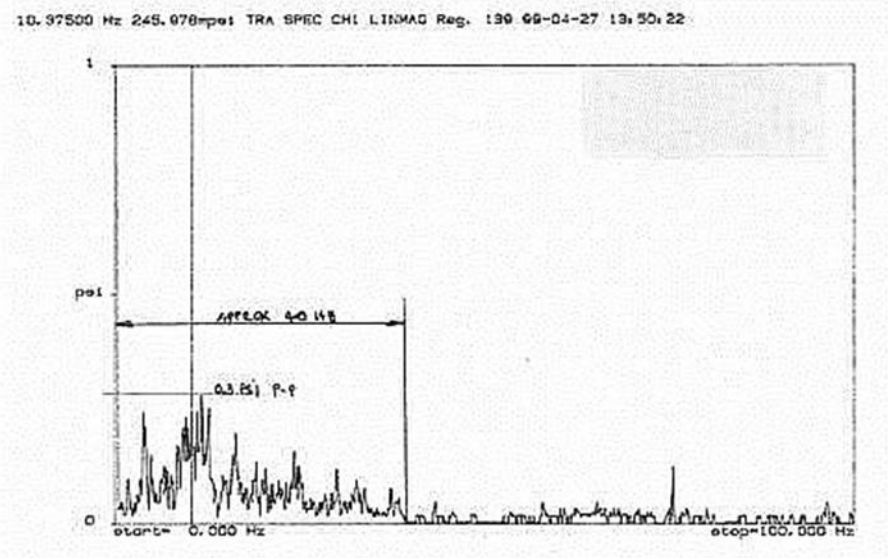

Figure 11. Example of broadband pulsation (Simons 2013)

Flow-induced turbulence is generated naturally by fully-developed turbulent flow (*Re* > 4000), which is typical for all commercial natural gas applications. Turbulence in straight pipe appears as low-amplitude randomly fluctuating pressures on the pipe wall. Such small fluctuations generally cannot develop into broadband pulsation without the influence of another flow disturbance. Partially open valves, elbows, tees, and other pipe fittings can drastically increase the amplitude of the fluctuations. This is the source of flow-induced turbulence broadband pulsation. Energy from flow-induced turbulence is typically concentrated below 100 Hz and may resonate with beam-type bending modes of the piping structure. Thus, high levels of flow-induced turbulence may cause noticeable piping vibration and result in fatigue failures at supports or fittings.

Higher frequency broadband pulsations may be generated across pressure-reducing devices such as valves or orifice plates. Elevated noise levels occur downstream of these devices due to high downstream fluid velocities and turbulence. Additional noise is generated from shock waves if there is choked flow downstream of the device. The noise is broadband and is

typically in the range of 100 – 2500 Hz (Allison 2013). These higher frequency broadband pulsations can resonate with the mechanical shell modes of piping resulting in increased pulsation amplitude at the mechanical natural frequencies of the pipe. For circular cross-sectional pipe, mechanical shell modes mainly involve radial motion of the pipe wall. Figure 12 depicts a number of mode shapes that vary based on the locations of axial and circumferential nodes. The form of these mode shapes is sensitive to pipe diameter and wall thickness as well as the location and type of supports, fittings, and branch piping. Due to the complexity of the calculations and the number of variables involved, these modes are typically found through finite element analysis of a particular piping configuration.

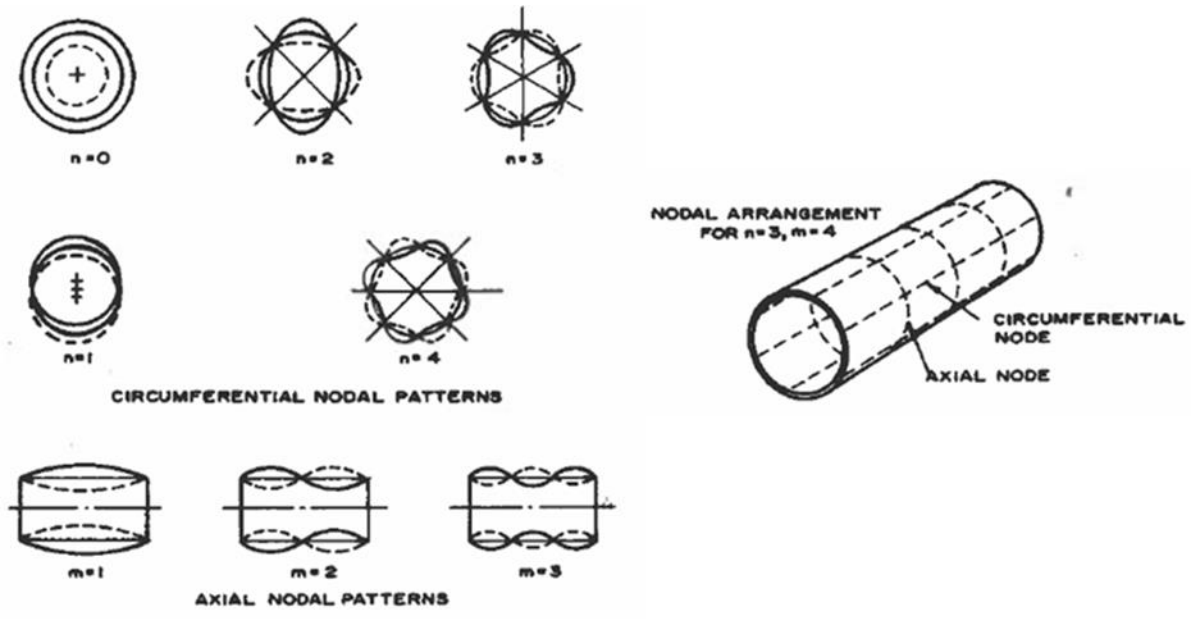

Figure 12. Shell modes of circular cross-sectional piping (Jungbauer 2001)

Under certain conditions, such as when pressure regulating valves or flow control valves search for their optimum setting, valves can produce broadband pulsations over a wide range of frequencies, typically 1000 Hz and higher (van Bokhorst 2002). While these pulsations are lower in amplitude than the low-frequency pulsations generated by compressors, they can excite

acoustic resonances in the geometry of some meter runs and produce much larger pulsations at the natural frequency of the piping system. The resulting background noise in the flow stream can potentially lead to measurement errors by interfering with the acoustic pulses produced by a USM (Durke 2012).

Acoustic Filters

Acoustic filters are the simplest and most common tool used to eliminate pulsations in natural gas flow. As the name would imply, acoustic filters operate as low-pass filters. They allow waves at frequencies under a set design frequency to pass through while attenuating waves of frequencies higher than the design frequency. A basic acoustic filter is comprised of two main parts: the choke tube and the filter volumes. The choke tube is located between the two filter volumes and is sized based on the expected flow rate. The filter volumes are large empty chambers with diameters eight to twelve times larger than the diameter of the choke tube. By choking the flow between the volumes, the pulsations that cannot immediately pass though are forced to dissipate within the volumes. The placements of the inlet and outlet to the acoustic filter also contribute to its capabilities. If the length of a filter volume is described as L_f, the inlet should be located at a distance of $L_f/2$ from the edge of the first volume. The outlet should be located at a distance of $L_f/4$ from the far edge of the second volume. If these locations are not used, it is possible for bandpass frequencies to unintentionally propagate through the filter. Basic schematics for two potential designs are shown in Figures 13 and 14.

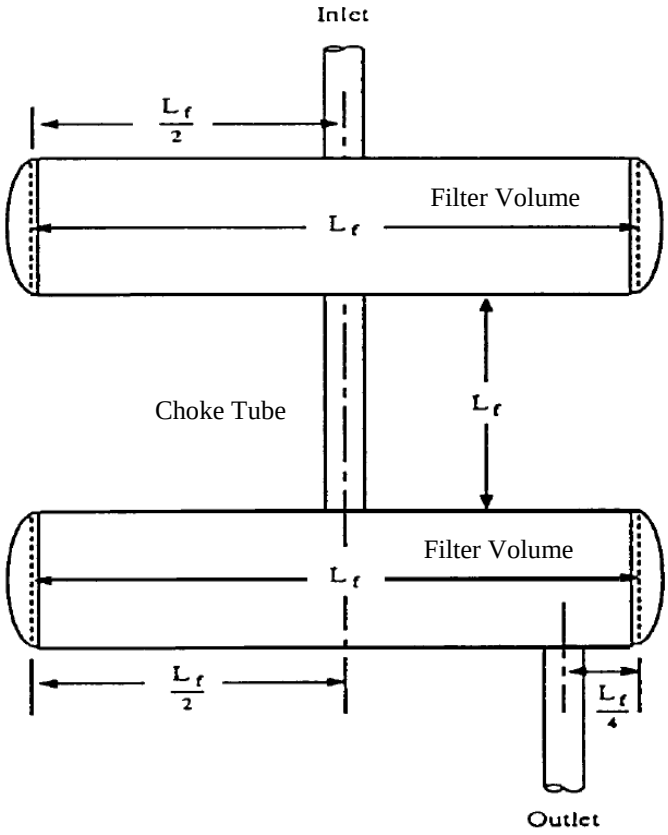

Figure 13. Schematic of two-bottle acoustic filter (McKee 2009)

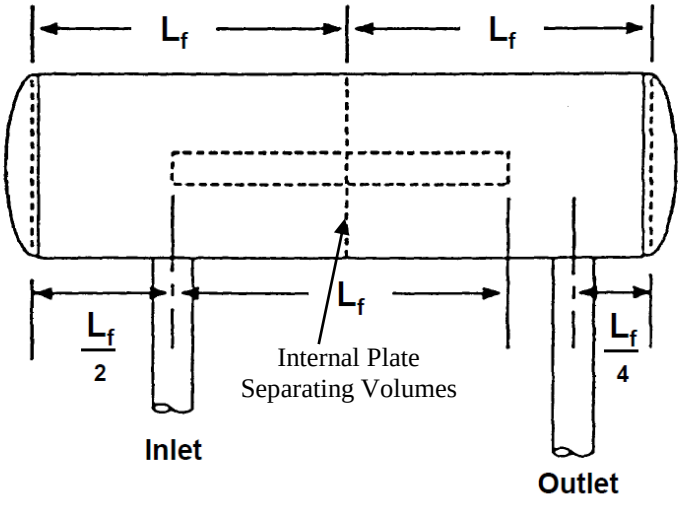

Figure 14. Schematic of single-bottle acoustic filter (McKee 2009)

Despite the effectiveness of acoustic filters, they have several weaknesses. From a practical standpoint, an acoustic filter can be very costly. The lower the cutoff frequency, the larger the filter must be. However, most important to consider is the specificity of a filter design. The calculations that determine the sizes of the choke tube and filter volumes use the expected flow rate and the speed of sound in the gas. These filters are typically designed long before a meter run goes into service. The actual flow rate though the filter could be very different than what had been expected months before. In natural gas, a change in composition can shift the sound speed. A change in either flow rate or sound speed could render the filter useless. In a worst case scenario, such shifts could create a coincidence between pulsation and the natural frequency of the filter. This would result in greatly amplified pulsations. Because acoustic filters consist of only piping components, there is no convenient method for determining how well they are working in practice. It is possible that a meter run equipped with a poorly designed acoustic filter could still suffer from the presence of pulsations. This situation could actually be worse than if the meter run had no acoustic filters. In the least desirable situation, a poorly designed acoustic filter could create a false sense of security while simultaneously amplifying the effects of the pulsations.

A Note on the Prevalence of Pulsations

As this section has shown, the sources of pulsations in natural gas applications are myriad and the pulsations themselves are commonplace. Though in some cases the pulsations may be easily detected and mitigated, there are many situations in which that is not possible. Any one of these situations could be costing a natural gas company tens of thousands of dollars daily.

Ultrasonic Flow Meters and the Effects of Pulsation on Meter Accuracy

Ultrasonic meters (USMs) are the newest and most expensive type of common custody transfer meter. They use high-frequency (>100,000 Hz) acoustic pulses to infer the fluid velocity. Figure 15 shows a longitudinal cross-section of a typical design. The black rectangles represent the ultrasonic transducers that produce the acoustic pulses. The variables x_u and L_u represent the linear distance between transducers and the path distance between transducers. The fluid flow is represented traveling from left to right through the space between the grey pipe walls.

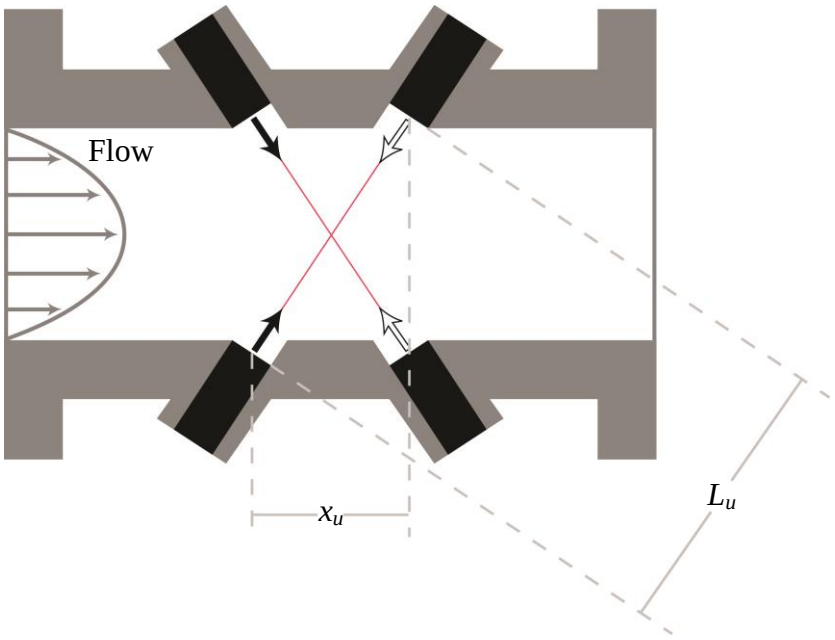

Figure 15. Schematic of USM operation

The acoustic pulses are broadcast from the leftmost transducers in the direction of the black arrows. The pulses travel at an acute angle towards the receiving transducers at the right (downstream) side of the meter. The time taken by the pulse to travel the distance L_u is recorded. Then the rightmost transducers broadcast the acoustic pulses. These pulses travel against the direction of flow and are detected by the leftmost (upstream) transducers. This time is also

recorded. Because the flow impedes counter-directional pulse broadcasts and propels the pulse in the direction of flow, the two times of flight will be different. The differences in these transit times provide an indication of the flow velocity in the pipe, which can be correlated to the volumetric flow rate. The measured times are affected by several factors, including the velocity profile of the gas stream at the measurement point and the acoustic signal characteristics, among others. The ultrasonic pulses are typically sent through the flow stream many times per second. The meter electronics process the measured data and average the results before outputting a flow rate value approximately once to several times per second. Because USMs have no significant protrusions into the flow, they boast extremely low pressure drop. This makes them ideal for transmission pipeline flow measurement. This property, in addition to the high accuracy of the technology, has made USMs extremely desirable as custody transfer meters.

The ultrasonic pulses travel at the speed of sound in the gas medium. For natural gas, this can change significantly depending upon the composition. A mix skewed more towards heavy hydrocarbons would have a slower speed of sound. Natural gas that is nearly pure methane, however, would have a faster than average speed of sound. This is important for ultrasonic meters because they assume the speed of sound to be constant. If the composition changes over time, the meters may exhibit measurement errors.

Each pair of transducers is called a "path." Depending upon the style of the ultrasonic meter, the paths can be straight across the meter body as shown in Figure 19 or they can reflect off of the meter wall once or twice before reaching the receiving transducer. Lengthening these paths can have several advantages. First, longer paths provide better resolution by increasing the differences in time of flight. This can increase the accuracy of the meters. Second, a skewed or

angled reflection path can provide information about radial velocity in the flow or how the velocity is distributed in the flow.

While it is possible to find a one-path or two-path meter for use in natural gas, most high-volume USMs have four to eight paths. In general, the velocities measured by these paths are not simply averaged together. Paths nearer to the pipe wall are downweighted and paths closer to the center of the pipe are upweighted. This is consistent with a fully developed, "bullet-shaped" velocity profile, as shown in Figure 6.

The weighting of these paths is not actively determined as the gas is flowing. Instead, meter manufacturers develop the weightings through experimentation and modeling and code the weights into the flow meter computer. The consequence of this is the inherent reliance of the USM on measuring well-developed flow. If the flow profile is substantially different than what the meter manufacturers anticipated, the weightings will be wrong and the meter will output an incorrect measurement. (See the section titled "The Natural Gas Industry and Flow Metering" earlier in this chapter.) The American Gas Association (AGA) acknowledges this potential shortcoming of USMs and detailed several recommended methods of flow conditioning in AGA Report No. 9 (AGA 2007).

Although custody transfer errors can cost natural gas production and transmission companies incredible sums of money, only a limited amount of publicized research has been performed to characterize and understand sources of error in natural gas flow measurement. This is especially the case with pulsations, a cause of measurement error that has only caught the attention of natural gas companies relatively recently. While the absence of research may seem counter-intuitive, it makes sense when one considers the cost and capital requirements necessary for this kind of experimentation. Natural gas is transmitted at high flow rates and at elevated

pressure in large diameter steel pipe. The meters used to measure flow in the field were bought and are employed by natural gas companies because they are the most accurate on the market. Therefore, in order to perform meaningful research in this field, one would require a controllable natural gas transmission line (at elevated pressure and with a diameter comparable to those in the field) and flow measurement capabilities exceeding those of the best flow meters commercially available. For the case of measuring the effects of pulsations, one would also require a controllable, repeatable method of inducing pulsations into the natural gas flow. Such a setup would be prohibitively expensive to design and procure, even for a series of experiments and despite the possible savings for natural gas companies. These types of experiments could only be reasonably performed in three locations in North America. Not coincidentally, these are the locations at which the natural gas flow meters used across the United States and Canada are calibrated and made ready for use in the field. The experimentation performed for this thesis was conducted at Southwest Research Institute (SwRI), one of these three locations. Also worth considering is the effect of publicized research on the natural gas industry as a whole. Even if a natural gas company funds a research project, when its findings are publicized, all of its competitors also benefit from the research. The original company takes a net loss in this endeavor. Taken together, the cost of experimentation and the lack of incentive due to competition explain the absence of publicized research. This is not to say the research is not being done, simply that it is not publically available. Because of this, the ability to perform an adequate literature review is severely hampered. The available literature is woefully incomplete and has no good common ground in terms of the frequencies and magnitudes of the pulsations used during testing. Nevertheless, some informative research does exist in the public sphere. A

literature review of the available research on the effects of pulsations on natural gas ultrasonic meter error follows.

This section reviews several mechanisms that can cause measurement errors by USMs in pulsating flows. Some are related to fluid phenomena, while others are a function of the meter's data acquisition methods. Because different brands and models of USMs apply different methods to generate and detect acoustic pulses and determine flow rates, errors caused by pulsations are more difficult to predict for USMs than for the other common types of custody transfer flow meters.

Sources of error due to pulsations:

A commonly agreed upon source of error in USMs is aliasing, an artifact of signal processing that can cause a reconstructed signal to differ from the original measured signal. Aliasing occurs when a signal is not sampled at a high enough rate to capture all the signal details, and the samples are characterized using a waveform with different properties (frequency or amplitude) than the original signal. Figure 16 gives an example of a sinusoidal wave that has been aliased by sampling. The original signal in black was sampled at a rate (in samples per second) lower than the signal frequency itself, and the results have been fitted to a waveform in gray that does not reflect the true behavior of the original signal.

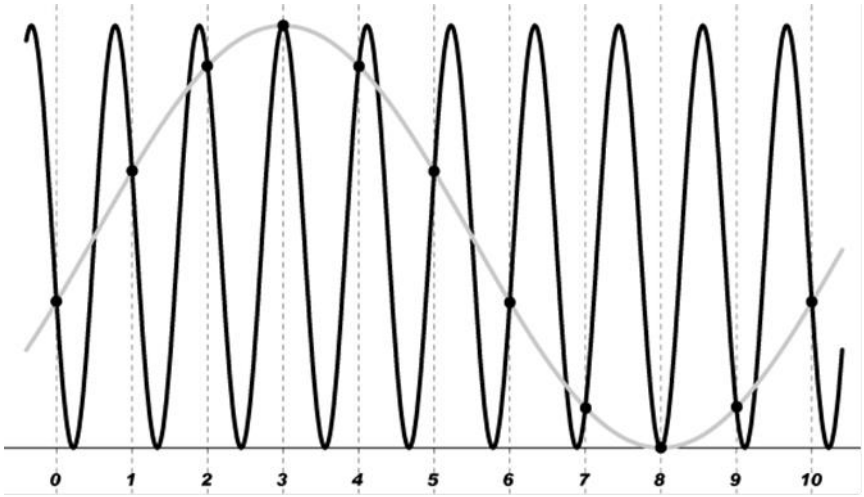

Figure 16. Example of aliased signal

Several references cite waveform aliasing as the primary cause of USM measurement errors in pulsating flows (van Bokhorst 2002, AGA 2007, ISO 1998). In the case of USMs, aliasing can affect measurement in three distinct ways. First, aliasing can occur when the frequency of the meter's sample rate is close to the frequency of the pulsation. A USM's sample rate is determined by how often an ultrasonic pulse is broadcast in a set time period. This is unrelated to the physical acoustic frequency of the pulse itself. Because USMs sample the flow periodically, they may not be able to follow the rapid profile changes that take place during a pulsating flow. This can result in a loss of information after the first stage of processing, hampering or even eliminating the ability of a USM to compensate for pulsating flow. If the frequency of the waveform to be sampled is known beforehand, aliasing can be avoided in theory by sampling at a frequency at least twice that of the original signal (Horowitz 1989). This condition for accurate sampling, known as the Nyquist criterion, may be practical when dealing with low-frequency pulsations from compressors, but may not be practical for regulator and control valve pulsations on the order of 1000 Hz and higher. Additionally, some test results have

shown that higher data sampling rates do not necessarily reduce the magnitude of the measurement error (Durke 2012).

Aliasing can affect USMs a second way by interfering with a meter's reporting rate, or frequency at which a USM actually reports the flow rate being measured. Although USMs send acoustic pulses through the flow many times a second, the meter electronics typically process the measured data before reporting an average flow rate. Time-averaged flow rates and diagnostic data can be reported anywhere from several times per second to once over tens of seconds (McKee 2009, Durke 2012). This differs from the first case in that the aliasing is occurring due to the processing software, and not due to sampling. USM transducers may be capable of sensing the pulsations, but due to the low reporting rate, the information is averaged out. Because of the variation in reporting rates among available USMs, its effect has not been well-documented.

The third and final way in which USMs can suffer from aliasing errors is due to interactions with the acoustic frequencies of the ultrasonic pulses themselves. Ultrasonic pulses are broadcast at different frequencies depending upon the meter style and transducers used, but the frequencies generally exceed 20 kHz. Longitudinal pulsation in the typical sense is unsustainable at such high frequencies in natural gas applications. However, broadband pulsation at the high frequencies produced by regulators and control valves can change the characteristics of the acoustic pulses induced by USMs, causing errors in the measured transit times used to compute flow rates (McKee 2009). A study observed a similar pulse distortion in flows at Reynolds numbers above 11,000, and attributed this to large amplitude, high frequency turbulence intensities in the experimental flow conditions (Håkansson 1994).

Apart from aliasing, measured transit times can be influenced by other factors, including the velocity profile of the gas stream at the measurement point. Commercial USMs often apply corrections for expected changes in velocity profiles with changes in the Reynolds number. However, pulsation also changes the shape of the velocity profile across a pipe, and USMs are known to be sensitive to such changes (Durke 2012). This effect on velocity profiles was explored in the first section of this chapter (Figure 5). The profile shown in the figure is for pulsations in laminar pipe flow, but periodic velocity gradients similarly distort the profile of a turbulent flow. Pulsations can distort velocity profiles by inducing periodic shifts, an effect that is difficult for a USM to counter. Measurements of pulsating turbulent flows have found that the instantaneous velocity profile is flatter during the accelerated part of the pulsation cycle and more peaked during the decelerated part of the cycle (Mizushina 1973). This is generally consistent with the theoretical profile fluctuations shown in the figure.

As mentioned in the description of USMs in the previous section, USM path weighting is developed and programmed by meter manufacturers. Typically these cannot change substantially in real time to adjust for changing flow conditions. Evidence suggests that meters that can be adjusted to correct measurements for these expected changes in pulsating velocity profiles, but can then no longer be considered accurate in steady flow after the adjustment (McKee 2009).

For standing waves, the location of a meter relative to velocity nodes will affect USM errors, since meter error depends on the amplitude of the local velocity modulations. If a USM is located at the velocity antinode, the point where the oscillations are largest, it will suffer from larger measurement errors than it would experience at a velocity node, the point where fluctuations are small or nonexistent (Durke 2012).

Previous studies of USMs and pulsations:

Researchers Håkansson and Delsing studied errors of ultrasonic meters in pulsating flows from both the analytical and the experimental perspectives. They began by deriving theoretical formulas to predict USM errors from flow properties, pulsation properties, and the pulsation sampling frequency of the ultrasonic transducers. Overall meter error was taken as the sum of three contributions: aliasing error due to pulsation E_p, noise error caused by flow turbulence E_n, and the error of the USM related to the signal-to-noise ratio (SNR). Håkansson and Delsing derived a key theoretical relationship between E_p, the root-mean-square amplitude of the velocity pulsations u_{rms}, the pulsation frequency f in Hz, and the integration time t_i for one sample by the meter. If the pulsation is assumed to be sinusoidal, and the meter measures flow velocity at some instant t_m in the cycle, the error due to aliasing can be described by Equation [14]. The maximum possible error due to aliasing was then given as Equation [15] (Håkansson 1994).

$$E_p = \frac{u_{rms}}{\sqrt{2}\pi f t_i}\{\cos[2\pi f_p t_m] - \cos[2\pi f(t_m + t_i)]\} \times 100\% \quad [14]$$

$$|E_p| \leq \frac{\sqrt{2}u_{rms}}{\pi f t_i} \times 100\% \quad [15]$$

Note from these relationships that pulsation error increases with increasing velocity pulsation amplitude and decreases with increasing frequency and longer sample integration times. Similarly, the maximum possible error caused by flow turbulence was derived as Equation [16]. In this formula, a_n is the amplitude of the turbulent velocity noise, D is the pipe diameter, and u is the flow velocity. This term is only significant for high turbulence intensities and can be neglected for laminar flows.

$$|E_n| \leq \frac{\sqrt{2}a_n D}{\pi t_i u} \times 100\% \qquad [16]$$

Håkansson and Delsing also tested a single-path ultrasonic meter in an air flow subjected to pulsations from a piston pulsator (Håkansson 1994). The meter was mounted on a 0.8-inch pipe 100 pipe diameters (100D) downstream of the pulsation source. During the tests, pulsation amplitude was varied from zero to 70% rms of the mean flow rate, and pulsation frequencies of 2 Hz, 5 Hz, 10 Hz, and 20 Hz were imposed on the flow. Flow velocities ranged from 3.9 ft/s to 31.5 ft/s, corresponding to Reynolds numbers from 1,700 (laminar flow) to 13,600 (fully turbulent flow). Pulsation amplitude, pulsation frequency, and flow rate were changed independently to study their individual effects on meter performance. The single-path meter design allowed effects of test variables to be examined in detail. A hot-wire anemometer was used to directly quantify velocity pulsations in the air flow at atmospheric pressure. While the meter and test conditions do not represent current USM designs in natural gas service, the results are relevant to this research.

In tests on laminar flows (*Re* ≈ 1,700), flow measurement biases by the single-path meter ranged from approximately zero to -12%. Biases generally became more negative with increasing pulsation amplitude, but were not a clear function of pulsation frequency. By comparison, in a turbulent flow test (*Re* ≈ 8,400), all biases were within ±0.5%. The authors associated the larger biases in the laminar flow with flow profile changes caused by pulsation. The hot-wire anemometer data indicated that pulsations in laminar or transitional pipe flows changed the flow profile to resemble that of a higher Reynolds number. This finding is consistent with the theoretical behavior described by Uchida (Figure 5) and in two earlier studies cited by the authors (Uchida 1956). However, pulsation effects on turbulent flow profiles were

found to be negligible. The authors stated that in theory, flow profile shifts from pulsations could produce either positive or negative measurement biases (Håkansson 1994).

Of particular interest is that Håkansson and Delsing traced the unpredictability of measurement errors in laminar flow test results to aliasing effects. Using a variation of [14], the authors calculated the contribution of aliasing and subtracted it from the overall measurement error. Figure 17 demonstrates that once the measurements were corrected for aliasing, the remaining biases were better correlated to pulsation amplitude. This suggests that it is possible to predict and correct aliasing errors by USMs that are not a simple function of pulsation characteristics.

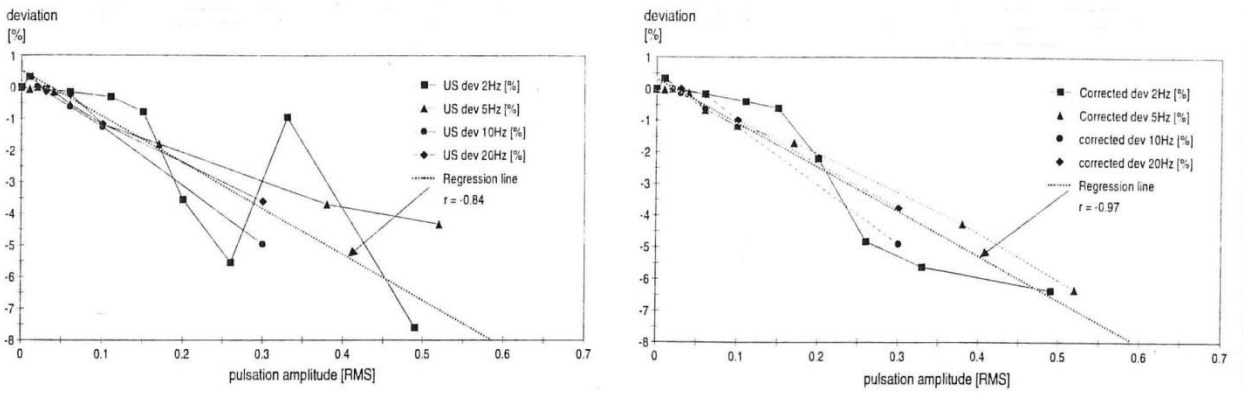

Figure 17. Effect of subtracting aliasing error from meter error (Håkansson 1994)

There is a limited amount of test data on the effects of pulsations on the accuracy of USMs for natural gas custody transfer. One study agrees with Håkansson and Delsing that USM error does not correlate well to the amplitude of pressure pulsations, but depends on the amplitude of velocity pulsations (Durke 2012). The effect of pulsations on velocity profiles discussed above may explain this dependence. McKee and Durke both cite a NOVA study in the public domain showing USMs in natural gas flows can experience errors of 4% to 7% or more from pulsations (McKee 2009, Durke 2012, Karnik 1998). Figure 18, taken from the NOVA

study, compares measurement errors by an orifice meter and an ultrasonic meter in the same pulsating flows. Note that Meter A1 (the ultrasonic meter) displayed different measurement errors for pulsations at different frequencies and even responded differently to pulsations of different amplitudes at the same frequency. At the worst test condition of pulsations at 22 Hz, the meter error ranged from -2.2% to +4% of the meter reading. Meters can over-register or under-register the true flow rate in the presence of pulsations, as the figure shows.

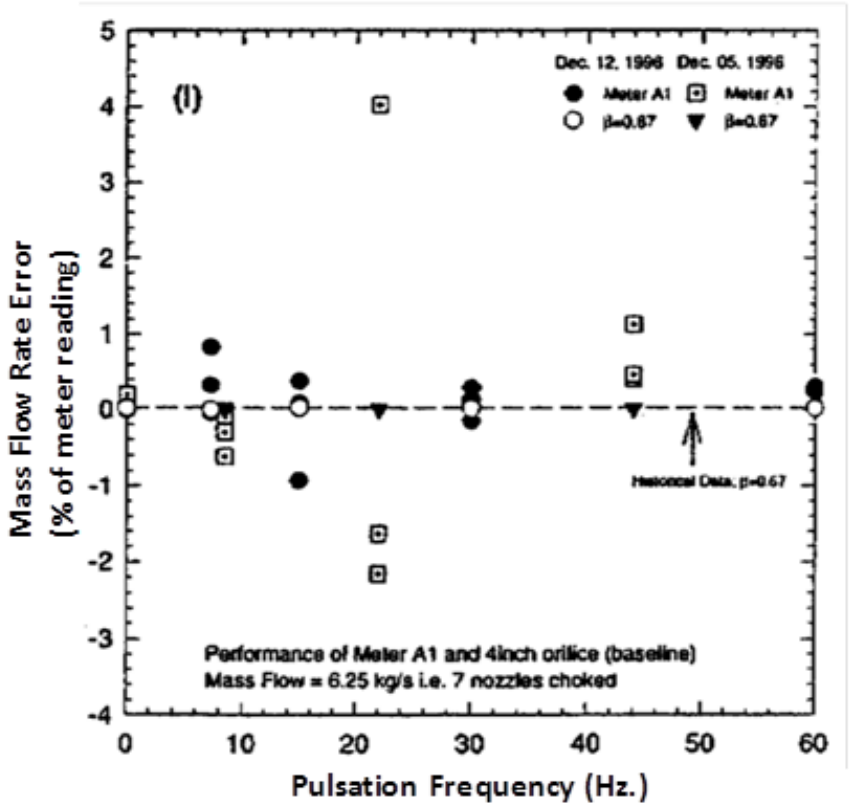

Figure 18. Test data from study of USMs in pulsation natural gas flow (Karnik 1998)

From 2000 to 2002, NOVA METCON funded a series of tests to study pulsation effects on ultrasonic meters in use at the time (Karnik 2000, Karnik 2001, Studzinki 2002). NOVA used their pulsation generator to test a variety of eight-inch (200-mm) diameter meters and assess pulsation-related errors. Similar tests were performed by NOVA on a *Sick Maihak*

FLOWSIC600 4+1 meter, a more recent design that combines a four-path meter and a single-path meter having separate measurement electronics (Lansing 2011). The tests of the *Sick* meter were not sponsored by METCON, and the results were published separately, but because the tests were performed at the same facility under similar conditions, it is worth discussing the results of these studies together.

Table 1. USMs and pulsating flow conditions in tests at NOVA (Karnik 2000, Karnik 2001, Studzinki 2002, Lansing 2011)

Meter manufacturer	Year tested	Path arrangement	Meter samples per second	Line pressures	Flow velocities	Pulsation frequencies	Pulsation amplitudes at meter	
							Velocity	Pressure
Daniel	2000	Multipath	4	667 psi (46 bar) to 725 psi (50 bar)	15 ft/s (4.7 m/s) and 26 ft/s (8 m/s)	7 Hz to 32 Hz	0.3 ft/s (0.1 m/s) to 15 ft/s (4.5 m/s)	0.15 psi (1 kPa) to 5.4 psi (37 kPa)
Instromet	2000	Multipath	15	667 psi (46 bar) to 725 psi (50 bar)	15 ft/s (4.7 m/s) and 26 ft/s (8 m/s)	7 Hz to 32 Hz	0.3 ft/s (0.1 m/s) to 10 ft/s (3.0 m/s)	0.15 psi (1 kPa) to 5.4 psi (37 kPa)
Daniel	2001	Single path	5, 50	667 psi (46 bar) to 900 psi (62 bar)	13 ft/s (4.1 m/s)	7 Hz to 31 Hz	7 ft/s (2 m/s)	
Daniel	2002	Single path	5, 50	700 psi (48 bar)	15 ft/s (4.5 m/s) and 25 ft/s (7.5 m/s)	7 Hz to 31 Hz	2 amplitudes, max 7 ft/s (2 m/s)	
Instromet	2002	Single path	5, 50	700 psi (48 bar)	16 ft/s (5 m/s) and 28 ft/s (8.5 m/s)	7 Hz to 31 Hz	2 amplitudes, max 7 ft/s (2 m/s)	
FMC Kongsberg	2002	Multipath	1	800 psi (55 bar)	16 ft/s (4.8 m/s) and 27 ft/s (8.2 m/s)	7 Hz to 31 Hz	2 amplitudes, max 7 ft/s (2 m/s)	
Sick Maihak	2007	4+1 multipath	10, 15, and 20 (four-path unit), 75 (single path unit)	Not listed	15 ft/s (4.6 m/s) and 28 ft/s (8.5 m/s)	8 Hz to 23 Hz		0.73 psi (5 kPa) to 4.35 psi (30 kPa)

Table 1 describes the meters tested by NOVA and the range of flow conditions and pulsation conditions under which each meter was tested. Note that the meters were tested under similar, but not identical, conditions. All the meters tested had eight inch nominal diameters. Once each meter was installed in the meter run, it was not moved during the tests. As a result, each meter was subjected to either traveling waves or a particular location relative to a standing wave velocity node, depending on the pulsation frequency. Pulsations were generated using the NOVA high-pressure pulsation generator, a porous paddle located in a pipe cross and driven by a hydraulic motor that controls the pulsation frequency by varying the paddle speed. Pulsation amplitude was controlled by varying the flow through a bypass around the paddle housing (Lansing 2011). It is important to note that the NOVA facility reference had accuracies on the order of the meters being tested. As a result of this, overall errors less than ±0.5% cannot be considered significant.

NOVA concurred with Håkansson and Delsing that aliasing, changes in the flow profile with pulsation, and "non-linear" effects resulting from very large instantaneous velocity amplitudes were the sources of the observed measurement errors (Karnik 2001). Larger errors were observed when each meter was at or near a velocity antinode, the location in the wave where velocity fluctuations (not pressure fluctuations) were largest. Errors were also found to increase as the amplitudes of the velocity pulsations increased. A typical threshold for measurement errors to remain within ±0.5% was that the velocity pulsation amplitude must remain under 2.3 ft/s to 3.0 ft/s. However, errors varied with the meter make and design, flow velocity, pulsation frequency, and pulsation magnitude. Among the meters tested from 2000 through 2002, the worst performer presented errors in pulsating flows from +10% to 100% (failure to register) (Studzinki 2002). For the newer *Sick* 4+1 meter, measurement errors from

the four-path unit were within ±2% in pulsating flows. Interestingly, the single path unit of the meter performed better than the four-path unit, exhibiting measurement errors from -1% to +0.5% under the same conditions (Lansing 2011).

Studies of the effects of meter sampling rate on measurement error were conflicting. In the 2001 tests of the Daniel single-path meter, meter errors were within ±0.4% when the sampling rate was at least twice the pulsation frequency, but errors exceeded 1% at lower sampling rates. Based on the 2000 and 2001 test results, NOVA recommended a Nyquist criterion of 2.5 for use in the 2002 testing; that is, the USM sampling frequency should be at least 2.5 times the pulsation frequency to avoid aliasing errors. Results from the 2002 study with the Daniel and Instromet single-path meters partly supported the conclusion that higher sampling frequencies would reduce measurement errors. For the Daniel single-path meter at velocity pulsation amplitudes above 3.0 ft/s, errors within 0.5% could not be attained even at 50 samples per second. Under certain test conditions, the Instromet single-path meter experienced larger errors when sampling at 5 samples per second than at 50 samples per second. Thus, the Instromet results supported the recommendation for higher sampling rates in pulsating flows, while the Daniel results did not (or at least indicated that a higher Nyquist criterion was needed).

Lansing published an analysis of the test results from the *Sick* 4+1 meter (Lansing 2011). This meter was installed in an AGA-9 default configuration (see the previous section titled "The Natural Gas Industry and Flow Metering" for a detailed description). The CPA 50E plate flow conditioner used in the AGA-9 default configuration was not used in the earlier NOVA tests, so the use of the plate in these tests may have altered the pulsation environment from that of the Daniel, Instromet, and FMC tests. The single-path unit was operated at a rate of 75 samples per

second, while the sample rate of the four-path unit was varied from 10 samples per second to 20 samples per second to determine if there was a benefit to sampling at different rates.

At the lower flow velocity of 15 ft/s, measurement errors greater than 0.5% were only observed from the four-path meter under high-amplitude pulsations at 23 Hz. All other test conditions produced measurement errors within ±0.5%. Notably, the four-path sampling rates during these tests were all slower than the pulsation frequency. At the higher flow rate of 28 ft/s, errors exceeding 0.5% were observed from the four-path unit when the sampling rate was set to 15 samples per second and the pulsation frequency was 15 Hz, suggesting that aliasing was occurring. Surprisingly, the four-path unit performed best when the meter was sampling at its lowest rate of 10 samples per second, which runs counter to the expectation that higher sampling rates should prevent measurement errors in pulsating flows. Also, the single-path unit showed a greater deviation from the reference flow rate than the four-path meter under some test conditions. The measurement errors by the separate single-path unit were attributed to deviations in the velocity profile caused by the pulsations. As noted above, the CPA flow conditioner may have altered the pulsation conditions from those in the other NOVA tests, so direct comparison of the *Sick* results to those of the other meters may not be valid.

Finally, several meter diagnostics from the *Sick* meter, primarily the turbulence value, the profile factor, and the symmetry factor, showed significant deviations under pulsating flows from baseline conditions without pulsations. Path velocities were shown to track the flow velocity pulsation patterns in one extreme case. Lansing noted the potential to use these diagnostics to identify the presence of measurement errors caused by pulsations, though their capability to estimate measurement errors was not discussed (Lansing 2011).

Conclusions of USM literature review:

In available literature, ultrasonic flow meter error does not appear to closely correlate to the amplitude of the pressure pulsation or the frequency of the pulsation. The flow rate measurement generally depends on the pulsation velocity amplitude, and errors as great as several percent of the meter reading have been reported in the open literature. As shown in Figure 4, for standing waves, velocity amplitudes are highest at points of lowest pressure amplitude. This means that if a standing pulsation wave is present, severe pulsation may be undetectable using pressure transducers. Additionally, this means that meter error is a function of meter location relative to areas of high amplitude velocity pulsation. Errors of over-registration relative to the 'actual' or 'true' flow rate, as well as errors of under-registration, have been reported. Some meter error has been attributed to aliasing of the measured flow values due to inadequate flow data sampling frequency by the meter. However, at least some test results have shown that higher data sampling rates do not necessarily reduce the magnitude of the measurement error. Although multipath ultrasonic meters can accommodate certain levels of flow distortion, they provide more accurate measurement when presented with a fully developed flow profile. The average flow profiles were observed to "flatten" in the presence of pulsations, essentially appearing more turbulent.

Overall, much of the available literature studying the effects of pulsation on USMs did not employ conditions consistent with natural gas custody transfer. Many used other flow media, such as air, or natural gas at a low pressure. Others used far smaller line sizes than would ever be encountered in natural gas transmission. The NOVA tests were the closest to field conditions, using natural gas at elevated pressure and using eight inch line sizes, consistent with small custody transfer. However, the flow rates for the NOVA tests were very low for use in custody

transfer, making the results more difficult to apply to real world applications. Additionally, the reference for the NOVA tests was not particularly robust, which resulted in preventing meter errors less than ±0.5% from being counted as significant. In an application where 0.1% error can still lead to substantial losses, more resolution would be required to adequately describe the effects of pulsations. Finally, although the meters used in the NOVA studies were well sized for natural gas applications, the meters do not represent the capabilities of modern day ultrasonic metering technology. Ten years ago, multipath meters were new. Four- or five-path meters were on the cutting edge. Now, eight-path meters with complex path geometries and advanced diagnostics are not uncommon. For the past several years, research relating to these new meters has been kept from public access, leading many in the natural gas industry to erroneously believe that modern USMs are unaffected by pulsations. In all, the collection of relevant literature has more gaps than applicable data. Most significantly, studies of modern USMs in pulsating flow under controlled field conditions were not found.

The Importance of Pulsation Research

This chapter has illustrated the prevalence of pulsations in the natural gas industry and their potentially disastrous effects on accurate flow measurement. The success of the natural gas industry relies upon the accurate measurement of natural gas custody transfer, which in turn relies upon the custody transfer flow meters being free of errors. The presence of pulsations in natural gas flow endangers this system. Even more dangerous is how the relative absence of publically available research on the effects of pulsations on USMs has resulted in a misconception that pervades the industry: that modern USMs are not as susceptible to pulsation related errors. The best way to eliminate this misconception is to research the effects of pulsations on modern USMs until these effects are clearly understood.

CHAPTER THREE: EXPERIMENTAL APPROACH

As stated in Chapter One, the goals for this thesis were to directly measure the velocity profile shifts in natural gas flow subjected to pulsations and to detect and qualify a relationship between meter error and one or more measureable aspects of pulsation. To achieve these goals, a series of experiments was developed, involving subjecting a USM to pulsating flow while simultaneously measuring the behavior of the pulsating flow. This chapter details the planning and set up of the experiments. Where appropriate, assumptions that influenced the experimental design process are called out.

In total, this chapter is comprised of six sections. Together, the information in this chapter should completely describe the experimental approach for these tests. The first section of this chapter introduces the Metering Research Facility, the testing facility where the experiments were performed. The second section outlines the general test plan for the experiments and explains how the relevant behaviors were measured. The next three sections describe the measurement devices introduced in the test plan with more specificity. Finally, the sixth section shows how the piece parts of the testing setup fit together. This section includes the test matrices, complete with average Reynolds numbers, pressure and temperature set points, and sampling rates of the measurement tools.

The SwRI Metering Research Facility

Testing of this nature requires high precision in a controllable and repeatable facsimile of natural gas field conditions, including large diameter pipe, adjustable flow rate, the use of natural gas as a working fluid, and a repeatable, compatible pulsation generator. Most importantly, the testing needs reference measurement techniques superior to those available commercially in order to accurately isolate the effects of pulsations. As mentioned in the literature review,

natural gas flow research of this nature is only economically feasible in three locations in North America. The experimentation for this thesis was performed at one of these locations: Southwest Research Institute (SwRI) in San Antonio, Texas. More specifically, the experiments took place at the SwRI Metering Research Facility (MRF). The MRF is known throughout the natural gas industry as a center for meter development, calibration, and testing in a facsimile of actual field operational conditions. It consists broadly of two controllable, recirculating, closed flow loops that use processed natural gas from the local distributor as the working fluid. The pressures, temperatures, and flow rates of the natural gas in these flow loops can be controlled by the MRF operators.

One of the MRF's central capabilities is the calibration of natural gas flow meters to be used in the field. As a calibration facility, the MRF is required to have flow measurement that is substantially more accurate than the commercially available flow meters being calibrated. More than that, the calibrations need to be traceable to the United States National Institute of Standards and Technology (NIST) standards for mass and time. Volumetric flow rates in both test loops are determined using critical flow Venturi sonic nozzles. Choking the flow through a Venturi sonic nozzle fixes the flow rate to a set value, determined by the nozzle dimensions. For both loops, the nozzles are installed in "nozzle banks," parallel lines with nozzles of different sizes. By choking the flow across the nozzles, the flow rate in a flow loop can be tuned, albeit in discrete increments. Opening and closing the lines in the nozzle bank adjust the throughput flow rate. Because the systems are flow loops, with no gas added or subtracted at any point, the flow rate through the nozzle bank is the flow rate of the loop. Both loops also utilize specialized check turbine meters used as secondary references.

The experiments were performed in the MRF's Low Pressure Loop (LPL), of the two recirculating test loops used to simulate flowing conditions in transmission pipelines using processed natural gas as the flowing medium. The LPL also includes elements critical to the study of meter performance in pulsating flows, including a pulsation generator and acoustic filters to eliminate pulsation effects on the critical flow sonic nozzles and reference check turbine meter. Flow in the LPL is driven by a reciprocating compressor (LPL blower), with typical flow rates ranging from 100 acfm to 700 acfm at line pressures of 200 psia and below. Although these conditions are not average for a field conditions, the highest pressure and highest flow rate achievable by the LPL is well within the range of pipeline conditions for natural gas applications. For this experiment, the flow rates 200 acfm and 700 acfm were chosen. These correspond to approximate Reynolds numbers of 470,000 and 1,540,000 respectively.

The sonic nozzles and check turbine meter are calibrated using a gravimetric flow standard called a Weigh Tank system. At its core, the Weigh Tank system is a highly accurate version of a very basic measurement technique, the "bucket and stopwatch" method of average flow rate calculation. For a flow rate assumed to be constant, the flow is allowed to empty into an empty volume, the "bucket," for a set period of time, the "stopwatch." The average mass flow rate is then calculated as the total mass collected divided by the time of the collection. In the case of the Weigh Tank system, the "bucket" is a large steel pressure vessel designed to store elevated pressure natural gas. The vessel sits atop a gyroscopic scale capable of extreme accuracy, as shown in the LPL Weigh Tank gravimetric flow standard specifications in Figure 19. The LPL Weigh Tank system is traceable to NIST.

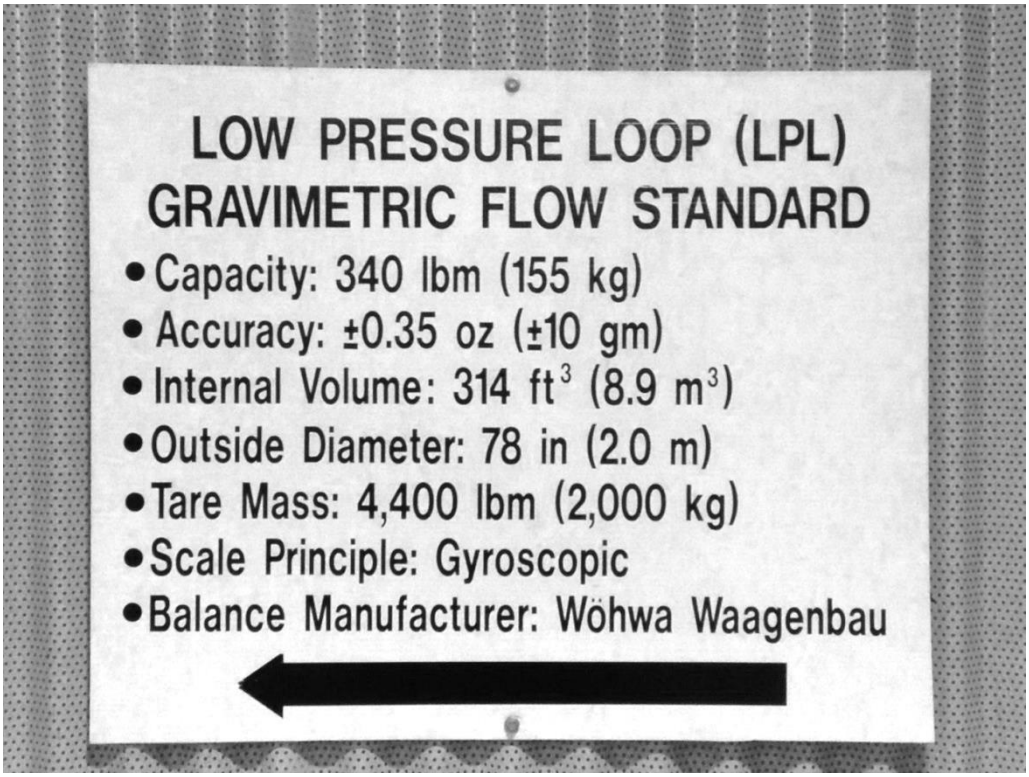

Figure 19. LPL Weigh Tank system specifications, located next to the system

A basic schematic of the LPL is shown in Figure 20. Downstream of the LPL blower discharge is an acoustic filter that was especially designed to dissipate the pulsations produced by the reciprocating compressor. Past the filter, no pulsations generated by the compressor are observed.

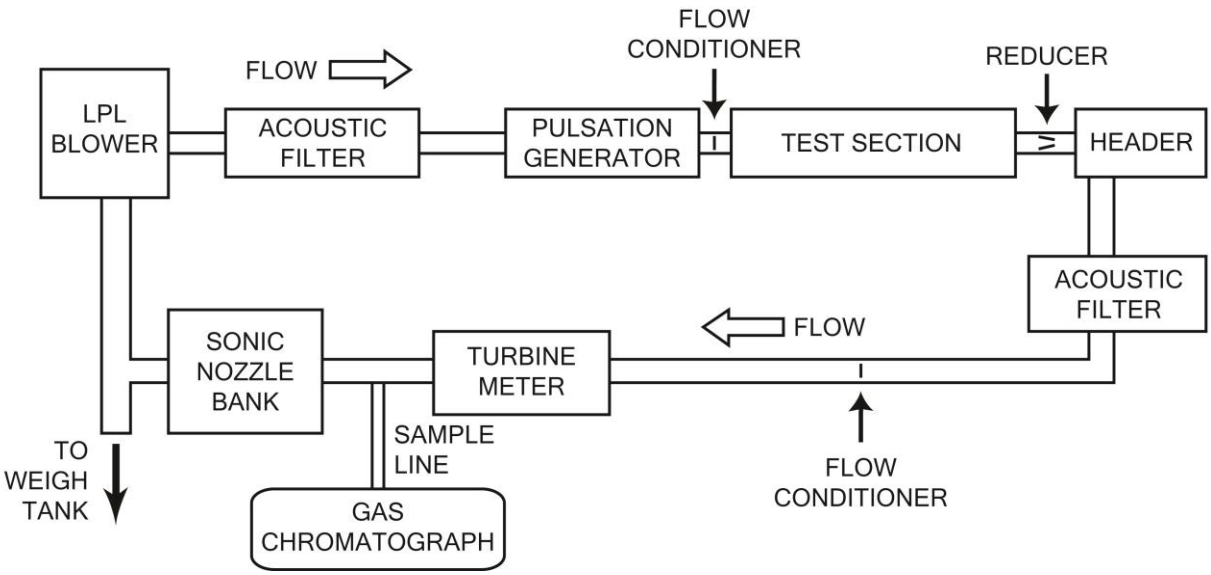

Figure 20. LPL schematic

Continuing in the direction of flow is the LPL pulsation generator. The pulsation generator, shown in Figure 21, consists of a 12-inch pipe segment with two circular slotted plates installed on a common central shaft coaxial with the center axis of the pipe segment. One plate is stationary, while the other plate (the rotor) rotates on the central shaft. As the rotor spins, it causes the slots on the plates to align and misalign, creating pulsations in the flow (Figure 22). The rotor is driven by an externally mounted AC motor, also shown in Figure 21. A variable frequency drive controls the rotational speed of the motor, which in turn controls the rotor speed and the flow pulsation frequency. The pulsation generator also includes a mechanism that controls the spacing between the static plate and the rotor. The plate spacing can be adjusted to control the amplitude of the flow pulsations. Moving the rotor and stator closer together will result in higher pulsation amplitudes, although the exact amplitude depends on other factors in the flow, such as flow velocity. The pulsation generator is capable of producing pulsations at frequencies between 0.1 Hz and 45.8 Hz.

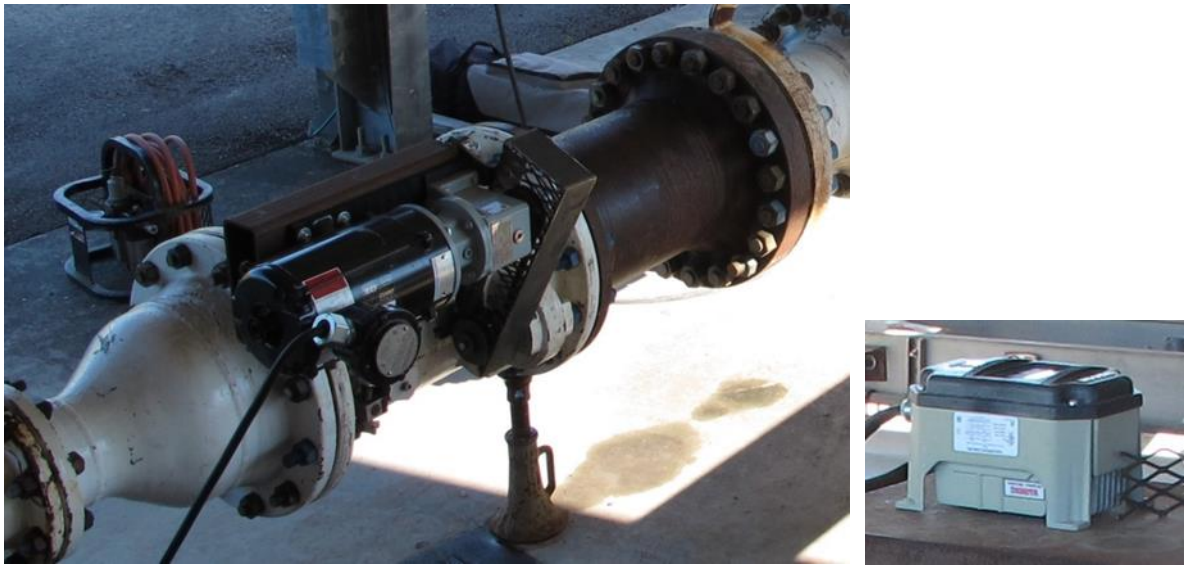

Figure 21. The LPL pulsation generator (left) and AC motor (right)

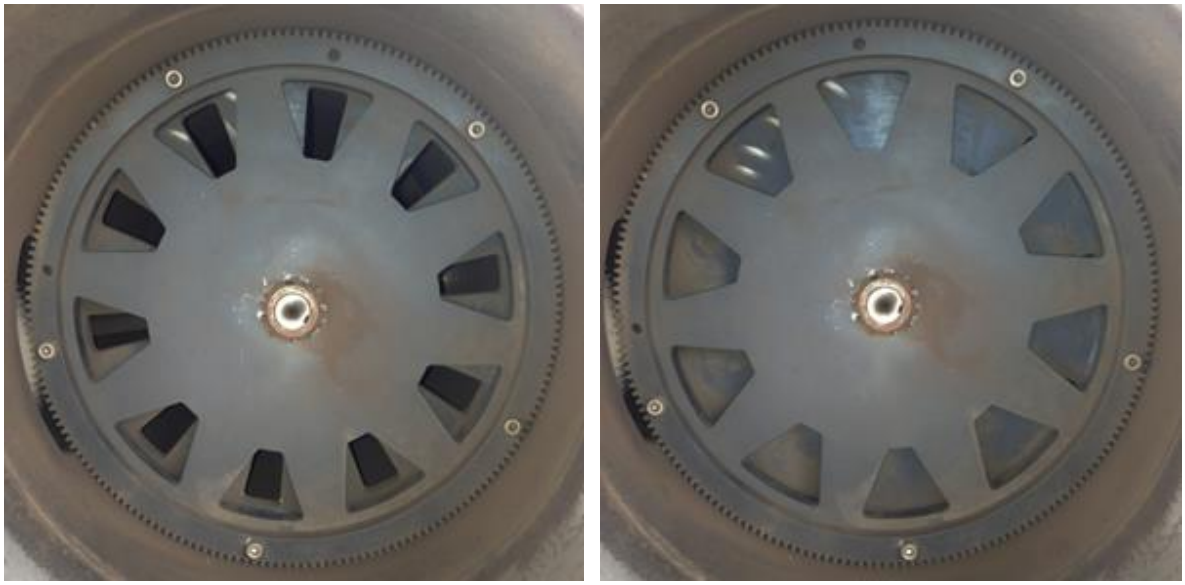

Figure 22. The pulsation generator rotor and stator plates showing open and closed

Downstream of the pulsation generator is the LPL test section in which the test setup for this thesis was installed. Immediately after the test section is another set of acoustic filters. These acoustic filters are much larger than the filter installed near the LPL blower and are capable of attenuating the pulsations generated by the pulsation generator. After the second

acoustic filter is the return and LPL reference section, which includes a flow conditioner, the reference turbine meter, and the sonic nozzle bank. Also in this section is a tubing line to the on-site gas chromatograph and a line to the LPL Weigh Tank system. During testing, the gas chromatograph was sampling the gas in the LPL at a rate of once per 12 minutes. Throughout the entirety of the testing, no significant changes in gas composition were detected. This was expected; the LPL is a closed loop. For the duration of testing, the line to the LPL Weigh Tank was kept closed. Downstream of the LPL sonic nozzle bank is the LPL blower suction intake, after which the loop restarts.

Flow temperature was measured with Rosemount 3144 Temperature Transmitters. One was installed just downstream of the test section. A second one was installed downstream of the check turbine meter. Static and differential pressures were measured with Rosemount 3051 Pressure Transmitters. These were located at several points in the flow loop including at the suction and discharge of the LPL blower, at the test section, at the check turbine meter, and across each sonic nozzle. The specifications for these transmitters are shown in Table 2.

Table 2. Transmitter specifications (Rosemount Aug 2016, Rosemount Sep 2016)

Sensor Type	Model	Range	Accuracy
Temperature	Rosemount 3144	-328 to 1022 °F	±0.18 °F
Static and Differential Pressure	Rosemount 3051	0 to 800 psia	±0.04% of span (±0.32 psi)

Data from the transmitters were collected using the MRF data acquisition system (DAQ). The DAQ also collected flow rate data from the test section meter and the check turbine meter. Gas composition data was also recorded from the gas chromatograph. Using a unified DAQ for these systems allowed the data to be organized in time sequence. With every sensor synchronized, there is far less risk of faulty data.

Overall, the LPL satisfied every requirement necessary to meaningfully study pulsations and their effects on ultrasonic flow meter measurement. The flow controls allowed for full adjustment of the flow rate. Static pressure, temperature, and flow composition were kept constant. The piping used was consistent with sizes used in the field. A compatible pulsation generator allowed control of the frequencies and magnitudes of the induced pulsations. Perhaps most importantly, the LPL had a measurement reference far more accurate than the meter being studied. Taken as a whole, the LPL was an ideal system in which to perform this type of experiment.

The Test Setup

As stated previously, the goals for this thesis were to directly measure the velocity profile shifts in natural gas flow subjected to pulsations and to detect and qualify a relationship between ultrasonic flow meter error and one or more measureable aspects of pulsation. A single test configuration was used in the pursuit of both of these goals. At a basic level, the test setup involved the LPL pulsation generator and sensors of three types: an ultrasonic meter, a hot-wire anemometer, and several high-speed piezoelectric pressure transducers. The hot-wire anemometer was a fast-response velocimetry tool needed to measure the velocity component of the pulsations. It was capable of traversing the pipe diameter in order to capture the flow profile shifts due to pulsation, the first goal of this thesis. The USM, of course, was necessary for observing the effects of pulsations on measurement error. The piezoelectric pressure transducers were needed to measure the pressure component of the pulsations. Using the piezoelectric transducers in conjunction with the hot-wire anemometer allowed for the full characterization of the pulsations. With these three sensor types, it was possible to relate the USM error to pulsation attributes, the second goal of this thesis.

The core intent of the test setup was to induce pulsations using the pulsation generator and observe changes in the USM measurement accuracy as compared to the LPL flow standards. Simultaneously, the hot-wire anemometer and piezoelectric pressure transducers would be used to jointly characterize the velocity and pressure components of the pulsation waves. Using the information collected from these two sides, the effects of pulsations on the USM could be related to pulsation characteristics.

A general schematic of the test setup is shown in Figure 23. Figure 23 shows the rough positions of the hot-wire anemometer as well as the USM in relation to the LPL pulsation generator. Though not shown in the figure, the piezoelectric pressure transducers were installed along the test section to properly model the pulsation waves. In the figure, the pipe segment lengths are described in industry shorthand using a capital "D" representing the nominal pipe diameter following a number. The length of the pipe segment described in this manner is equal to the product of the number and the nominal pipe diameter. For example, an 8"-diameter pipe segment that is described as "10D" is ten pipe diameters long, or 80". (Two pipe segments are left unlabeled in Figure 23. These lengths were determined in the acoustic sizing of the test section, explained in the last section of this chapter, "The Final Test Setup and Experimental Procedure." They are not necessary to understanding the core goals of the test setup, so were left out for simplicity. The fully specified test section is given at the end of this chapter in Figure 31.)

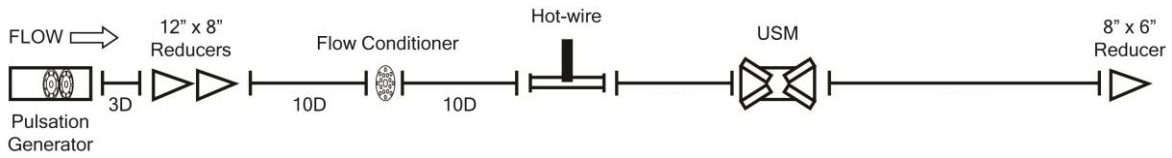

Figure 23. Basic schematic of test setup

In the field, USMs are typically installed in the AGA-9 default recommended meter run configuration (AGA 2007). This configuration is a straight pipe arrangement involving, in order from upstream to downstream, a 10D length of pipe after the last upstream flow disturbance, a CPA 50E plate flow conditioner, a second 10D length of pipe, the ultrasonic meter itself, and 5D of pipe downstream of the meter. The lengths for the pipe segments involved are minimum lengths. Longer pipe lengths can only aid in the development of the flow profile. In order to ensure that the findings of these experiments are valid for real-world applications, a variant of the AGA-9 default configuration was employed for this setup. Consistent with the AGA-9 default configuration, a CPA 50E plate flow conditioner (Figure 8) was located between the two 10D pipe segments upstream of the hot-wire anemometer and USM. This model of flow conditioner has previously been found to have no effect on pulsations (Durke 2012). This means it was safe to use the flow conditioner without the risk of influencing the pulsations being induced. Instead of installing the USM directly after this pipe segment, however, the hot-wire anemometer was installed here. The USM was placed further downstream, separated by another pipe segment from the anemometer. Based on the assumptions made by the American Gas Association, the hot-wire anemometer and the USM would encounter equally developed flow at these points (AGA 2007). Downstream of the USM, a pipe segment longer than 5D was installed prior to the reducer.

Directly upstream of the pulsation generator was a 12" header. Upstream of the header was the LPL blower, which provided the natural gas flow to the test section (Figure 20). Downstream of the reducer at the end of the test section was another 12" header, followed by a plug valve and a set of acoustic filters designed to eliminate the pulsations from the pulsation

generator. The flow reference nozzle bank and check turbine meter were located downstream of the filters.

The Piezoelectric Pressure Transducers

High-speed piezoelectric pressure sensors are standard tools for detecting pulsations in natural gas flows. These are most commonly used to diagnose compressor-generated pulsations, but are capable of detecting pulsations up to 5000 Hz. The piezoelectric transducers used in the tests were Model 112M66 dynamic pressure sensors made by PCB Piezotronics. These transducers measure near-static and dynamic pressures over a range of 0 to 3,000 psi. For the experiments, the transducers were connected to threadolets along the test section, allowing the active piezoelectric components of the sensors to interface directly with the flow. A coaxial cable carried the signal from each transducer to a PCB Piezotronics Model 422E52 in-line charge amplifier. Each amplifier converted the high-impedance charge signal from the transducer to a low-impedance voltage signal (PCB Piezotronics 2005). These voltage signals were then recorded by a laptop computer using a National Instruments® DAQ. The DAQ was configured to record readings from the transducers at a frequency of 200 Hz. This frequency was well above the highest pulsation frequency (45 Hz) and its Nyquist sampling limit. Pressure data were collected in two-second samples, with samples collected over a window of approximately one minute. Each two-second sample was analyzed by the software for frequency content, and the resulting spectrum from each transducer was immediately displayed by the data acquisition laptop so that resonant frequencies in the test section could quickly be confirmed.

Eight piezoelectric transducers were placed along the test section such that standing pressure pulsation waves formed in the test section could be mapped (roughly shown in Figure 24). As an example, a hypothesized 43Hz standing wave is shown below the test section piping.

The piezoelectric pressure transducers are used to measure the peak-to-peak (p-p) magnitude of a standing pressure wave at eight points, allowing the standing wave to be reconstructed analytically. For traveling waves, the eight transducers would all give the same measurements.

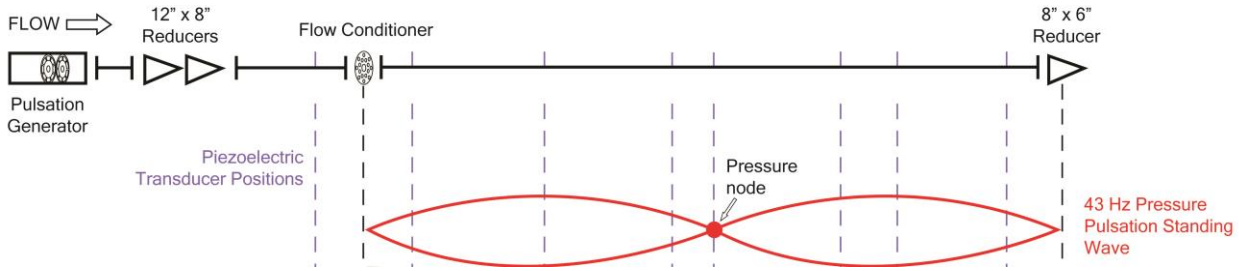

Figure 24. Piezoelectric pressure transducer approximate positions

A ninth piezoelectric pressure transducer (not pictured) was installed downstream of the acoustic filter, upstream of the flow references. The purpose of this transducer was to verify that the acoustic filter was appropriately attenuating the pulsations being generated. If pulsations were progressing past the filter, the control measurements of flow rate (the sonic nozzles and reference turbine meter) might have been unreliable. In this case, the meter error comparison component of the analysis would have had to be abandoned. As part of the testing procedure, the reading from this transducer was checked before recording meter data for each frequency. Fortunately, this transducer showed no sign of pulsations downstream of the filter during the entire run of testing. No meter error records were deemed invalid.

The Hot-wire Anemometer

In order to characterize the velocity component of pulsation waves, a highly dynamic velocimeter was needed. For this experiment, a hot-wire anemometer was chosen. A hot-wire anemometer is a point velocity measurement tool capable of dynamic response (>10 kHz) (Bruun 1995). They are traditionally used in air at atmospheric pressures (scale tests of aeronautics, for example), capable of detecting very small shifts in with high accuracy. Hot-wire

anemometers utilize heat transfer to infer the flow of a fluid. A hot-wire tip consists of two major components: the wire and the prongs. In Figure 25, the wire is depicted as a white cylinder supported on either end by the grey prongs. The fluid flow is shown as black arrows passing over the wire.

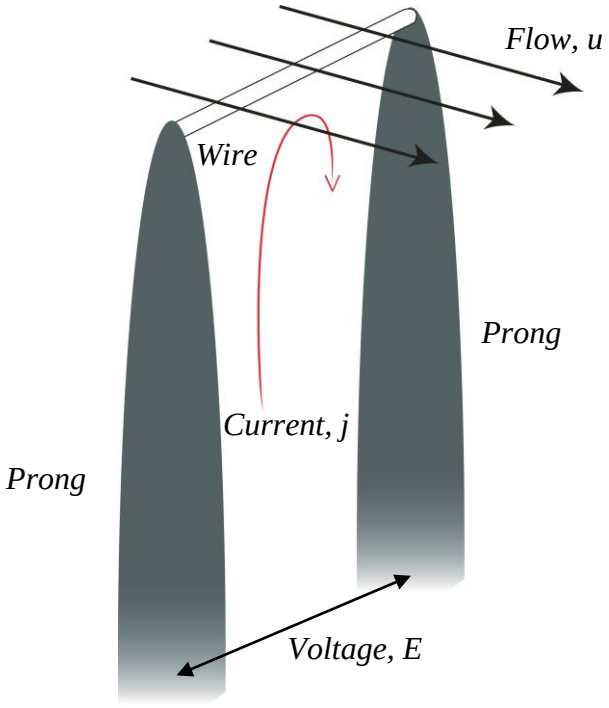

Figure 25. Hot-wire tip schematic

The wire is a thin sliver of metal on the order of 1 micron thick and 1 mm long with a low thermal mass. It can be constructed of different metals for different applications, but is most commonly made of tungsten, platinum, or nickel. The prongs are lengths of rigid steel or nickel of a similar size to a needle that suspend the wire between them. The prongs are electrified, forcing current through the thin wire. As electricity flows through the system, the wire increases in temperature due to material resistance. When the wire is introduced to fluid flow, convective heat transfer takes place between the wire and the fluid. (Due to the disparity in thermal mass,

the prongs are assumed to be not included in the heat transfer.) The heat transfer can be related to fluid flow rate using a calibration, allowing the hot-wire anemometer to be an effective measurement tool.

Hot-wire anemometers come in two varieties, constant temperature anemometers (CTA) and constant current anemometers (CCA). For the purposes of this thesis, CCAs are ignored; the anemometer used was a CTA. A CTA is designed such that the current through the prongs is adjusted using a control circuit and the temperature of the wire remains constant. In this case, the wire is incorporated into a bridge circuit and the wire temperature is maintained by servo amplifier (Kurtulu 2010). The governing equation relating fluid flow and prong voltage for a CTA is commonly presented as Equation [17] where E is the prong voltage, u is the fluid velocity, and A, B, and C are constants (Bruun 1995).

$$E^2 = A + B \cdot u^C \quad [17]$$

This relationship can be derived from conservation of energy, as given in Equation [18] where W_{elec} is electrical work that heats the wire and Q_{conv} is heat transfer between the fluid and the wire. Steady-state is assumed.

$$W_{elec} = Q_{conv} \quad [18]$$

Because the work is electrical and the heat transfer is convective, Equation [18] can be expanded to Equation [19] where j is the electrical current, R_w is the resistance of the wire, T_w is the temperature of the wire, T_f is the temperature of the fluid, A_w is the projected area of the wire, and h is the heat transfer coefficient.

$$j^2 R_w = h A_w (T_w - T_f) \quad [19]$$

The resistance of the wire is typically a function of the temperature of the wire. However, because the wire in a CTA is kept constant, R_w is considered constant. Ohm's Law can be used to rewrite Equation [19] in terms of voltage E, shown in Equation [20].

$$\frac{E^2}{R_w} = hA_w(T_w - T_f) \quad [20]$$

King's Law for heat transfer from an infinite cylinder to fluid flow is given as Equation [21] where k is the thermal conductivity of the fluid, L_w is the length of the wire in the direction of flow, d_w is the wire diameter, and A and B are constants (Bruun 1995).

$$\frac{hL_w}{k} = A + BRe^{0.5} = A + B\left(\frac{\rho d_w u}{\mu}\right)^{0.5} \quad [21]$$

By assuming k, L_w, ρ, μ, and d_w are constant, [21] can be simplified to [22] where A' and B' are constants.

$$h = A' + B'u^{0.5} \quad [22]$$

Substituting Equation [22] into Equation [21] gives Equation [23].

$$\frac{E^2}{R_w} = \left(A' + B'u^{0.5}\right)A_w(T_w - T_f) \quad [23]$$

Wire area, temperature, and resistance are constants. If fluid temperature is also assumed to be constant (a safe assumption for this controlled system), Equation [23] can be simplified further to Equation [24] where A" and B" are constants.

$$E^2 = A'' + B''u^{0.5} \quad [24]$$

Equation [24] is equivalent to the commonly accepted relationship in Equation [17] if C is close to 0.5. When calibrating a hot-wire anemometer, this can be used to check the validity of the fit.

Hot-wire anemometers have a number of advantages over other velocimeters for this application. First, they have high frequency response, greater than 10 kHz and sometimes up to 1 MHz (Bruun 1995). This is ideal for measuring pulsations. Second, they are capable of measuring wide ranges of velocities. This allows for the ability to test at different flow rates with the same setup. Third, they have low signal to noise ratios; a resolution of 1:10000 is achievable (Kurtulu 2010). The measurements are reliable even in rapidly shifting flow. However, hot-wire anemometers can have several drawbacks. First, the wires are fragile. It is not uncommon to suffer breakage in high velocity flows or flow with entrained particulates. Second, the measurements are insensitive to direction. If the flow reverses direction, the hot-wire reading will remain the same. Third, they are point measurements by design. A single hot-wire cannot measure a flow field from a single location. For this experiment, these weaknesses are mitigated. The natural gas flow in the LPL is looped and is not exposed to a normal level of entrained contaminants as would commonly be found in the field. The pulsation amplitudes are smaller than the fluid flow rates; it is not expected that the flow should reverse. The hot-wire anemometer used in this experiment was installed on a traversing mechanism, allowing it to measure velocities at different points along the pipe diameter. For this experiment, the advantages of a hot-wire anemometer were exploited to the utmost while its disadvantages were mitigated.

Hot-wire anemometers are traditionally not used in natural gas applications, especially at elevated pressures and large pipe diameters. Due to the fragility of hot-wire tips, they break swiftly in normal natural gas flow. Also, a hot-wire is quite literally an electrified wire, a spark source. Because natural gas is explosive in the correct mixture with oxygen, hot-wire anemometers can be incredibly hazardous to employ outside of lab conditions. For the case of

the experiments performed for this thesis, a nitrogen purge procedure was used to ensure that the powered hot-wire tip was never in the presence of an air-fuel mixture.

Because hot-wire anemometers are so rarely used in natural gas applications, one was not readily available for use in testing. Instead, an existing commercially available hot-wire anemometer system was modified for use in natural gas. The system was obtained from TSI, Inc. and included a bridge circuit, several hot-wire tips, and a tip mount. The bridge circuit was a model 1750 Constant Temperature Anemometer Module (Figure 26). It was a basic bridge circuit that output the hot-wire voltage between 0 and 10 V. The rated frequency response for this model was 100 kHz (TSI 2016). Used with the bridge circuit were a precision 47Ω resistor (model 1304) and a 15V AC/DC power supply (model 1751). The hot-wire tips were of the model type 1201, measuring about 2.5 inches long (Figure 27). The wires on these tips were made of tungsten (TSI 2016). The mount to hold the tips was of model type 1150-36. This piece was significantly modified in the construction of the natural gas compatible hot-wire tool.

Figure 26. Hot-wire anemometer bridge circuit (Model 1750 - TSI, Inc.)

Figure 27. Hot-wire anemometer tip (Model 1201 - TSI, Inc.)

The hot-wire anemometer was installed in a traversing mechanism to allow the measurement of several points along the flow profile. The traversing mechanism was adapted from wedge pitot probe flow measurement tool. In its original incarnation, the traversing mechanism employed a ¼" pitot probe that passed through an active seal that resisted the internal pressure. Using external controls, the pitot probe could be inserted or retracted from the pipe while the elevated pressure natural gas was flowing. The probe itself was mounted perpendicular to the pipe such that it could take measurements at different points along the flow profile. A custom 8" diameter pipe segment was used to mount the traversing mechanism. By using this system, the hot-wire anemometer was improved from a point velocimeter to a profile velocimeter.

Starting with the base components from TSI, the hot-wire tip mount needed to be modified to be compatible with the traversing mechanism. A three foot length of straight stainless steel ¼" tubing (tube wall 0.049") was lapped to be compatible with the traversing mechanism. This tubing was counterbored on one end to accommodate the width of the tip mount (0.18"). The tip mount was cut to one inch length and rewired gauge 18 wire. Feeding the wire through the tubing, the tip mount was fitted into the counterbore. On both ends of the tubing, 3M Scotchcast epoxy was used to seal against the pressure of natural gas in the test section. The 3M Scotchcast epoxy resists organic compounds, insulates against electricity, and

is often used in sub-sea applications where pressures exceeding 100,000 psi are not uncommon. The epoxy was allowed 36 hours to cure and adequately seal the tubing.

Using 10-minute epoxy, the tubing was fitted with a chock designed to fit into the traversing mechanism. The ends of the wire were soldered to a male BNC connector. A removable hot-wire anemometer tip was installed in the tip mount before the mount itself was installed in the traversing mechanism. At this point, the hot-wire anemometer setup was no different than it would have been without the traversing mechanism. The BNC connector of the hot-wire mount was connected to the bridge using a coaxial cable. The 47Ω resistor was installed on the bridge and the 15V power supply was also connected. The output of the bridge was connected to the DAQ. After the traversing hot-wire anemometer was assembled, it was not disassembled for the duration of testing. The chock on the tubing had a right angle cut-out into which fit a component of the traversing mechanism. By keeping the chock locked in place, the hot-wire tip orientation was maintained at a perpendicular angle to the direction of flow.

A photo of the complete build installed in the test section can be seen in Figure 28.

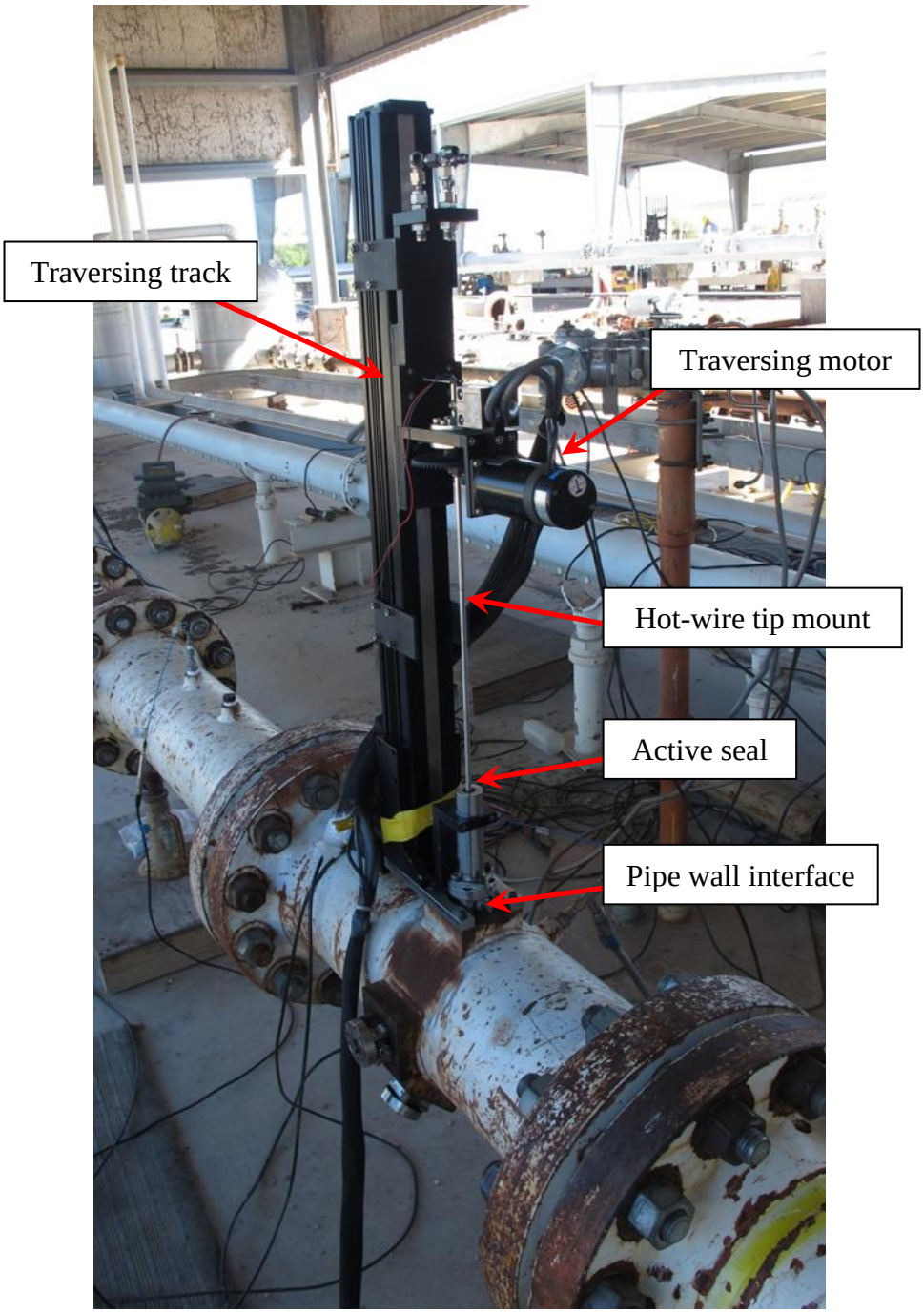

Figure 28. Assembled traversing hot-wire anemometer installed in test section

The DAQ used for the hot-wire anemometer was custom built in LabView and was temporarily integrated into the native DAQ at the MRF. This allowed the MRF operator to control the position of the hot-wire tip from the MRF control room. The voltage readings from

the hot-wire tool were recorded at a frequency of 1 kHz with the use of an A/D converter. Because the DAQ was integrated, the meter readings, hot-wire readings, and hot-wire positions were all recorded together in the same log files. This ensured that the results would be synchronized throughout the analysis process.

The hot-wire anemometer was calibrated in place using the LPL flow references. As there was no calibration tool for the newly built device, the calibration process was complex. It involved two main steps. First, raw voltage data was collected in pulsation-free flow and correlated to flow velocity using the LPL flow references. Second, this correlation was verified by applying it to Power Law fits of expected velocity profiles. These two steps are explained in greater detail in the following.

Before the hot-wire anemometer was calibrated, it was introduced into natural gas flow at the test pressure at a flow rate of 200 acfm. As the tip was traversed across the pipe diameter, the raw voltage output readings from the anemometer were collected. Each sample was comprised of a five second recording. The data were collected at 21 locations spread evenly between the pipe wall and the center of the pipe. This was repeated twice for flow at 700 acfm. For every hot-wire reading, data was also collected simultaneously from the LPL flow references. These raw data were used to calibrate the hot-wire anemometer.

Plugging the voltage readings into the hot-wire anemometer governing equation in Equation [17] (with guesses for A, B, and C) allowed estimates of flow velocity at each point. In this thesis, this will be called the "King's Law Velocity Correlation." For each flow velocity, the sectional volumetric flow rate q' can be found using the integral in Equation [25], where u^* is the estimated flow velocity and r_g is the distance from the pipe center at insertion point g. The

variable g is an integer index between 1 and 21 inclusive and begins at the pipe wall position (r_1 = 3.9905").

$$q' = \int_{r_{g+1}}^{r_g} 2\,\pi\,u^* r_g'\,dr_g' = \pi\,u^*\left(r_g{}^2 - r_{g+1}{}^2\right) \qquad [25]$$

The total volumetric flow rate q is the sum of the sectional volumetric flow rates, shown in Equation [26].

$$q = \sum_{g=1}^{21} q' \qquad [26]$$

The estimated average velocity u^*_{avg} can be found from the volumetric flow rate as in Equation [27]. Here, r_1 is the pipe radius, 3.9905".

$$u^*_{avg} = \frac{q}{\pi r_1{}^2} \qquad [27]$$

The actual average flow velocity was calculated by the LPL DAQ using the flow references. By comparing the two values for average flow velocity and iterating over the constants in Equation [17] (*A*, *B*, and *C*), the best fit can be found by reducing the squared error between the two measures (least-squares method). Using this technique, the constants *A*, *B*, and *C* were found to be 2.66, 0.623, and 0.474 respectively. The value for *C* is consistent with the analytical solution in Equation [24] where *C* was found to be 0.5. This concluded the calibration of the hot-wire anemometer. A plot of the calculated flow velocities at each insertion point for both flow rates and the continuous King's Law Velocity Correlation is given in Figure 29.

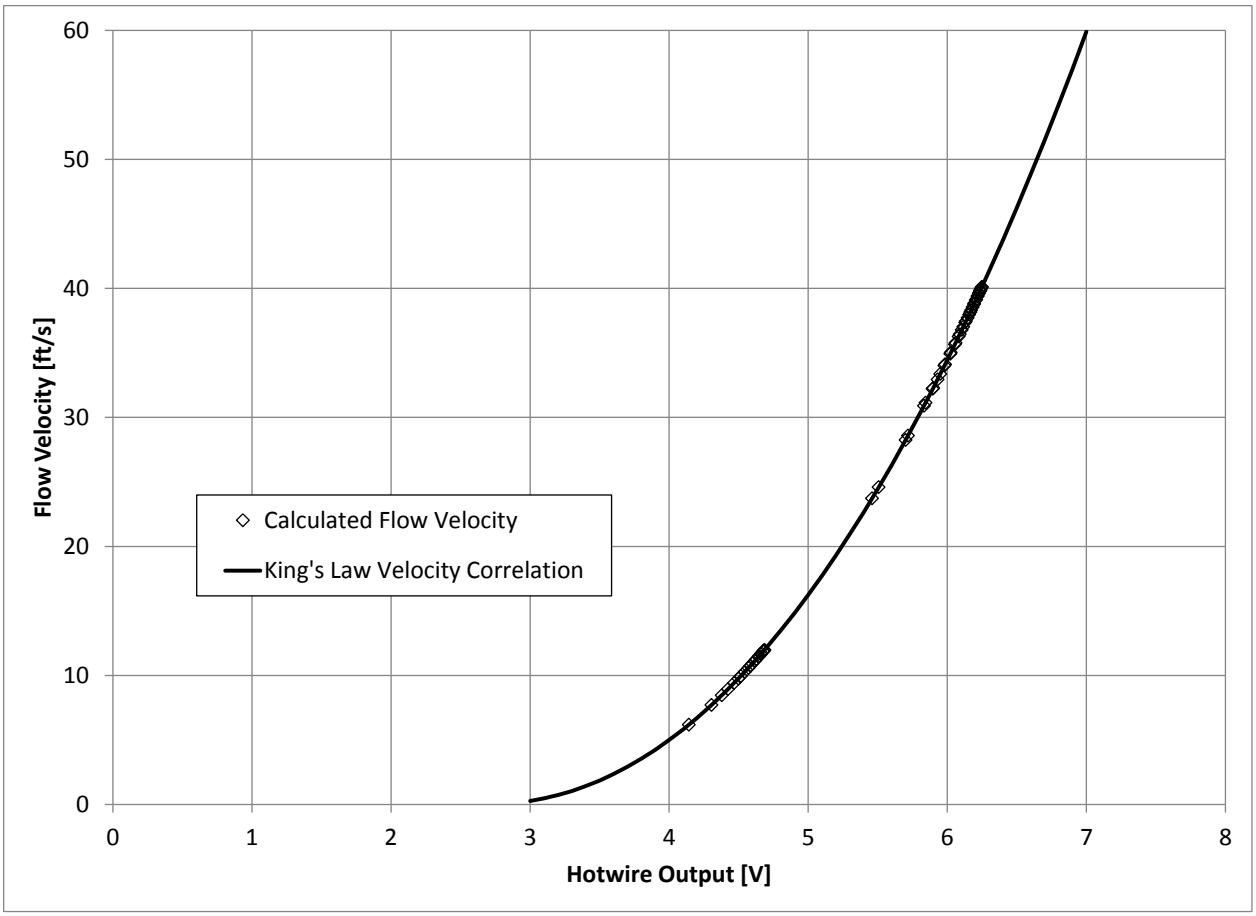

Figure 29. Hot-wire anemometer calibration using King's Law

To verify the hot-wire anemometer calibration, the calculated flow velocities were compared to theorized flow velocities assuming a turbulent flow velocity profile. For turbulent flows, the shape of the flow profile can be described by the Power Law as in Equation [28] (Schlichting 1968). Here, p is the denominator of the Power Law exponent and A_p is a constant. For turbulent flows, p is typically between 5 and 10, though larger values are possible. More turbulent flows are described with greater values of p than less turbulent flows. The variable r is the radial distance from the pipe wall (as opposed to the radial distance from the pipe center r_g).

$$u = A_p \cdot r^{\frac{1}{p}} \qquad [28]$$

Again comparing the flow velocities and iterating over the constants in [28] to minimize the squared error, the Power Law fits were found for 700 acfm and 200 acfm. For 700 acfm, A_p and p were 34.3 (ft/s) and 8.23 respectively. For 200 acfm, A_p and p were 9.78 (ft/s) and 6.44 respectively. These values are in the expected range for turbulent flow at the Reynolds numbers observed and demonstrate the suitability of the calibration approach. A plot of the calculated flow velocities and the Power Law fits for both flow rates is shown in Figure 30. Power Law fit for hot-wire anemometer calibration verification.

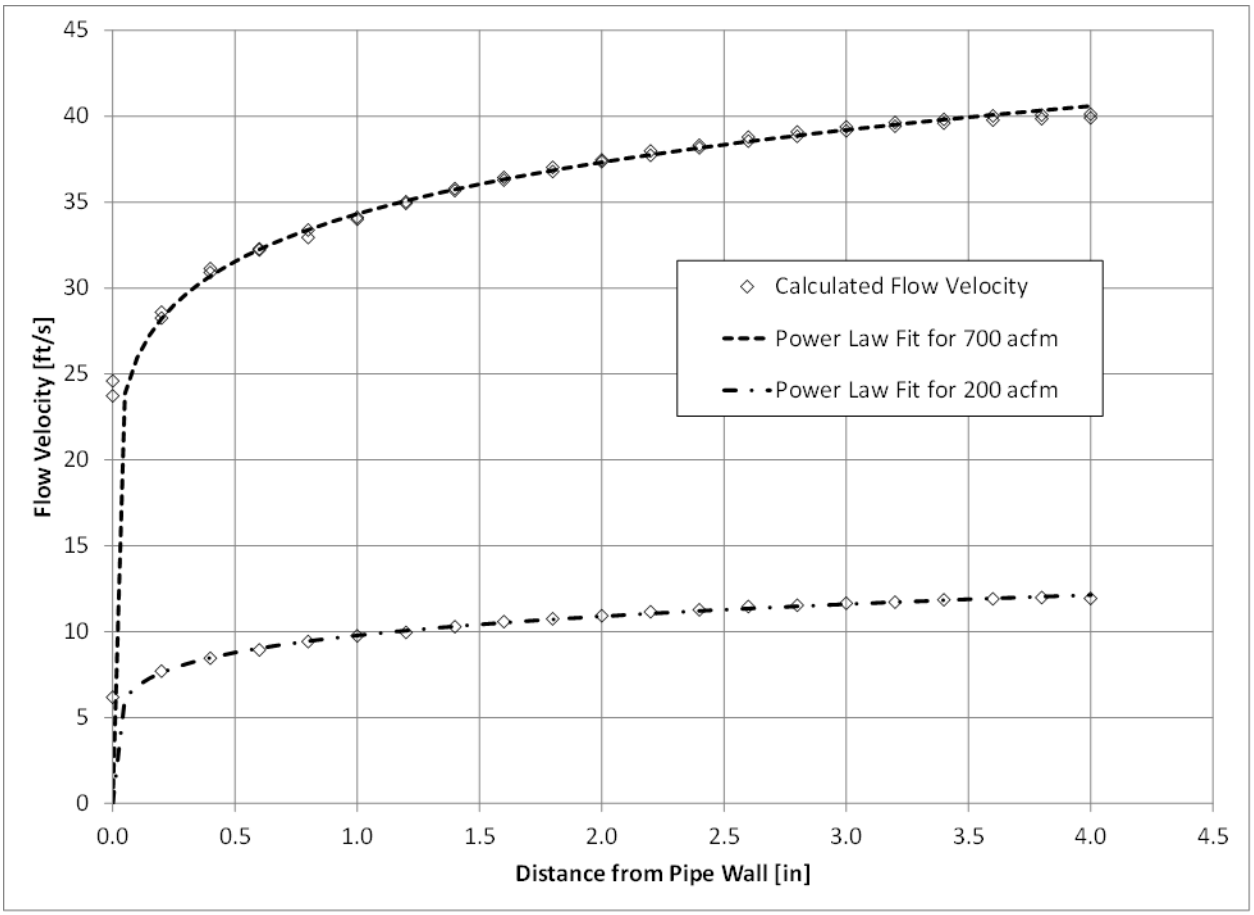

Figure 30. Power Law fit for hot-wire anemometer calibration verification

Despite the expected fragility of the hot-wire anemometer tip, the one first installed survived the entire testing regimen. By inspection after the testing was concluded, the hot-wire anemometer tip was determined to have not sustained any damage from the testing. It was indistinguishable from an unused tip.

As shown in Chapter Two, protrusions into gas flow like the hot-wire anemometer can potentially cause FIP. These can be predicted using Equation [13] and an analytically determined relationship between Reynolds number and Strouhal number. For this experiment, the approximate Reynolds numbers at the two flow rates were 470,000 and 1,540,000 based on the pipe diameter. To determine which relationship between Reynolds number and Strouhal number to use, the Reynolds numbers must be recalculated for the characteristic length of the hot-wire anemometer tip, ¼". Using this dimension, the Reynolds numbers for the hot-wire anemometer tip were 6530 and 21,400. For Reynolds numbers between 250 and $2 \cdot 10^5$, the relationship in Equation [29] can be used (Blevins 1990).

$$St = \frac{f\,d}{u} = 0.198\left(1 - \frac{19.7}{Re_d}\right) \qquad [29]$$

Be rearranging Equation [29], the expected Strouhal frequencies can be determined using known quantities, as shown in Equation [30].

$$f = 0.198\frac{u}{d}\left(1 - \frac{19.7}{Re_d}\right) \qquad [30]$$

Using Equation [30] with the two calculated Reynolds numbers yields the following Strouhal frequencies: 113.5 Hz and 380.9 Hz. These frequencies are above the maximum generated pulsation frequency (45 Hz). During testing, no significant pulsations were detected at either frequency. It is likely that the test results were not influenced by FIP from the hot-wire anemometer tip.

The Ultrasonic Meter

A major focus of this research is the effects of pulsations on the accuracy of ultrasonic meters. The USM used in the testing was donated by a meter manufacturer in exchange for detailed diagnostic analysis. However, because the diagnostic analysis could be used to identify the meter used, it cannot be presented here. Although the USM model and the proprietary diagnostic analysis cannot be shared, several aspects of the USM can be revealed for the sake of this study. The meter used was an eight-path model. Some of the paths used were straight paths and some were bounce paths intended to measure flow swirl (radial velocity). The bore diameter of the meter was eight inches. Each ultrasonic transducer in the meter sent out a 200 kHz pulse at a rate of one per 1.667 msec, or at a frequency of 600 Hz. At 200 kHz, the pulses themselves were unaffected by the induced pulsations, which had a maximum frequency of 45 Hz. The meter was configured such that each measurement update cycle (each reported averaged flow rate value) consisted of 75 samples. For eight transducers with 75 samples each, each measurement update was the average of 600 individual samples (8 transducers × 75 samples). Each measurement cycle was one second in duration, or the duration of 600 pulses (600 pulses × 1.667 msec = 1 sec). The measurement frequency is equal to the frequency at which the complete set of transducers was sampled. In this case, that frequency is 75 Hz (600 Hz / 8 transducers). Note that this is below the Nyquist sampling frequency for the pulsation frequencies induced. Using a Nyquist factor of 2, the desired minimum sample rate to avoid aliasing for all pulsation frequencies induced is 90 Hz (2 × 45 Hz). By the same logic, aliasing could be assumed to be a factor for pulsation frequencies greater than 37.5 Hz (75 Hz / 2).

Prior to the start of testing, the USM was calibrated in pulsation-free flow using the LPL flow references. This was necessary to be able to isolate the effects of the pulsations. The USM

calibration was performed in an AGA-9 default recommended configuration. At each of seven different flow rates, the meter readings were taken for six sequential 90-second runs. The averages of these readings were used to configure the meter with a multi-point linearization such that the meter readings agreed with the flow references. After the calibration, confirmation runs at two flow rates were taken to verify the calibration had succeeded. This calibration process was typical for USMs being calibrated at the MRF. The great majority of meter calibrations are performed in this way. After the calibration and verification, the meter uncertainty was ±0.1%.

During testing, the USM was connected to the LPL DAQ along with the hot-wire anemometer. This ensured that the hot-wire anemometer readings, the USM readings, and the LPL settings were synchronized and recorded together in the same log files.

The Final Test Setup and Experimental Procedure

In an effort to ensure the production of at least one standing wave, the test section was acoustically designed. The known dimensions of the LPL test area and the distances to the acoustic filter were used as a starting point to specify the dimensions of the test section. As described in "Pulsations Basics" in Chapter Two, common flow elements can reflect pulsations to aid in the formation of a standing wave. The reflection points can be either open ends or closed ends. For this test setup, the CPA 50E flow conditioner was assumed to operate as a closed end. The sudden expansion of the reducer at the end of the test section was assumed to act as an open end. Between these points, a standing wave could form with n wavelengths where n is a positive integer.

Using the wavelength formula in Equation [1] and the speed of sound in the LPL natural gas as calculated by the gas chromatograph (c = 1,395 ft/s), the wavelength could be found for any frequency pulsation wave. The maximum distance available between the CPA plate and the

end of the reducer was 389 inches, or 32.4 feet. Using the formula in Equation [1], this is approximately one full wavelength of a 43 Hz pulsation wave, as shown in [31]. Because the LPL pulsation generator only produces pulsations up to 45.8 Hz, 43 Hz was the only possible frequency that could produce a whole number wavelength between the CPA plate and the reducer. In order to guarantee the formation of at least one standing wave, the test section was acoustically designed around a 43 Hz wave.

$$\lambda = \frac{c}{f}\ ; 32.4\ ft \approx \frac{1395\ ft/s}{43\ Hz} \qquad [31]$$

From the literature review, some evidence exists that USMs are most susceptible to strong velocity pulsations. Because of this, the USM in the test section was located at a pressure node (a velocity antinode) for 43 Hz as shown in Figure 31. The hot-wire anemometer was installed at the end of the 10D-flow conditioner-10D section at the start of the test section. This roughly coincided with a velocity node for 43 Hz. A 8.3D pipe segment was used as a spacer between the anemometer and the USM. Downstream of the USM, several pipe segments totaling a length of 21.5D were installed to make up the remainder of the LPL test area available length.

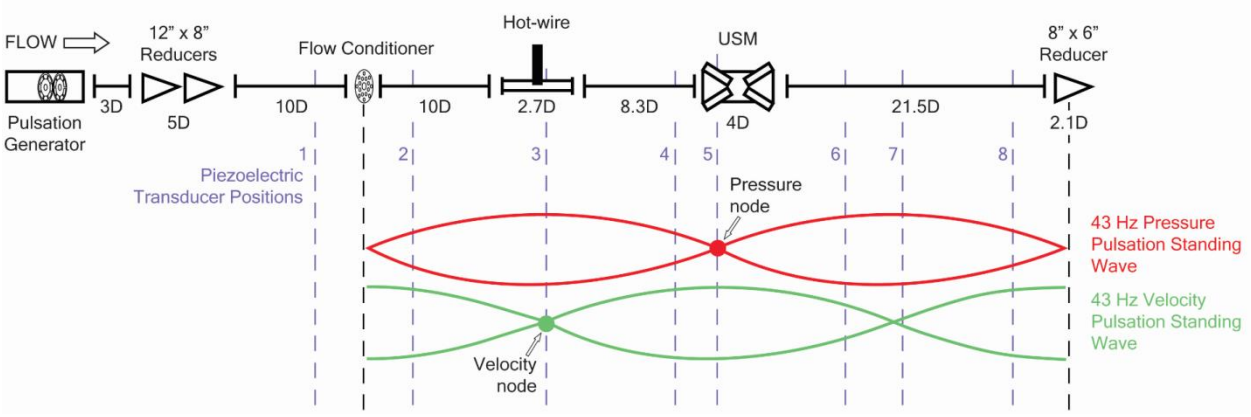

Figure 31. Schematic of test setup

Figure 31 also shows the installation locations of the piezoelectric pressure transducers in relation to the other features of the test setup. Table 3 specifies the exact locations of each of the eight test section transducers.

Table 3. Piezoelectric pressure transducer positions and relation to setup features

Transducer	Distance downstream of pulsation generator	Distance from other features
1	119.75 inches	24.25 inches upstream of CPA plate
2	168.5 inches	24.5 inches downstream of CPA plate
3	235 inches	At hot-wire anemometer
4	299.125 inches	13.38 inches upstream of USM inlet
5	328.5 inches	At USM
6	424 inches	79.5 inches downstream of USM outlet
7	464.75 inches	51.5 inches upstream of 8x6 reducer
8	490.25 inches	26 inches upstream of 8x6 reducer

The LPL pulsation generator was limited to producing pulsations at frequencies between 0.1 Hz and 45.8 Hz. No literature was found that suggested USMs were susceptible to the effects of pulsations of frequencies less than 5 Hz, so 5 Hz was used as a lower limit of pulsations tested. For ease of understanding, the upper limit of the pulsation frequencies tested was 45 Hz. These frequencies are consistent with pulsations generated by reciprocating compressors, some centrifugal compressors, and some FIP. To ensure that the frequency resolution was sufficient to observe a relationship between pulsation frequency and meter error, a frequency step of 2 Hz was used. Because findings from the literature review suggested that high amplitude pulsations affected USMs more than low amplitude pulsations, the pulsation generator was set to its maximum amplitude throughout the testing. In order to determine the effect of flow rate on USM error, the testing was conducted at two flow rates: 200 acfm and 700 acfm (corresponding to approximate Reynolds numbers of 470,000 and 1,500,000 respectively). The entire testing procedure was split over five days and is shown in the test matrix in Table 4.

Table 4. Test matrix

<table>
<tr><th>Day 1</th><th colspan="2">Day 2</th><th colspan="2">Day 3</th><th colspan="2">Day 4</th><th>Day 5</th></tr>
<tr><td>-</td><td>Flow rate [acfm]</td><td>Frequency [Hz]</td><td>Flow rate [acfm]</td><td>Frequency [Hz]</td><td>Flow rate [acfm]</td><td>Frequency [Hz]</td><td>-</td></tr>
<tr><td rowspan="12">Installation</td><td rowspan="24">200</td><td>Baseline</td><td rowspan="25">700</td><td>Baseline</td><td rowspan="12">700</td><td>Baseline</td><td rowspan="25">Breakdown</td></tr>
<tr><td>15</td><td>15</td><td>11</td></tr>
<tr><td>17</td><td>17</td><td>9</td></tr>
<tr><td>19</td><td>19</td><td>7</td></tr>
<tr><td>21</td><td>21</td><td>5</td></tr>
<tr><td>23</td><td>23</td><td>Baseline</td></tr>
<tr><td>25</td><td>25</td><td rowspan="12">200</td><td>Baseline</td></tr>
<tr><td>27</td><td>27</td><td>13</td></tr>
<tr><td>29</td><td>29</td><td>11</td></tr>
<tr><td rowspan="13">Shakedown</td><td>31</td><td>31</td><td>9</td></tr>
<tr><td>33</td><td>33</td><td>7</td></tr>
<tr><td>35</td><td>35</td><td>5</td></tr>
<tr><td>37</td><td>37</td><td>Baseline</td></tr>
<tr><td>39</td><td>39</td><td colspan="2" rowspan="13"></td></tr>
<tr><td>41</td><td>41</td></tr>
<tr><td>43</td><td>43</td></tr>
<tr><td>45</td><td>45</td></tr>
<tr><td>Baseline</td><td>13</td></tr>
<tr><td colspan="2"></td><td>Baseline</td></tr>
</table>

The first day was dedicated to installation and shakedown. Days two through four were testing days. The term “baseline” in Table 4 refers to a test with no pulsations. Baseline tests were run at the beginning and end of each testing day to ensure the USM was not drifting. No USM drift was detected. The fifth day was intended as a contingency day, but was used instead for breakdown. Testing took place during the week of November 16th, 2015.

Using the LPL controls, the gas conditions were kept constant. The temperature was set to 70°F. The loop pressure was set to 180 psia. These settings (along with the selected flow rates) are consistent with a minor to moderate custody transfer meter run in the field.

The testing procedure was as follows. Each day of testing would begin and end with a baseline run with no pulsation. On day four, when two flow rates were tested, a baseline run was taken for the start and end of each flow rate. The piezoelectric transducer DAQ and the LPL DAQ (which controlled the loop conditions and recorded the USM and hot-wire anemometer data) were synchronized every day before first baseline run. For all three testing days, a test at a specific pulsation frequency consisted of setting the pulsation generator to the desired frequency and recording data using the LPL DAQ. Each test involved a five second hot-wire anemometer voltage output recording at 1,000 Hz at each of 21 distances from the pipe wall. The hot-wire tool would penetrate into the pipe a fixed distance, record for five seconds, and then traverse further into the pipe. Traversal would begin at the pipe wall and end at the pipe center. For each hot-wire tip position, the reading from the USM were also recorded for five seconds. The 21 five-second USM readings for each frequency were averaged to a single meter error result for the purposes of the analysis. Piezoelectric pressure transducer data were collected continuously over the course of each test day and were related to the test stage using a timestamp.

A photo of the final complete installed test setup is shown in Figure 32.

Figure 32. Panoramic photo of final test setup installed at the MRF LPL

CHAPTER FOUR: RESULTS AND DISCUSSION

This chapter exhibits the results of the experiments described in Chapter Three. It is split into four sections, one for each of the major analyses performed using the data from the experiments. The first section focuses on the data from the piezoelectric pressure transmitters. Using the data and a sinusoidal fit, the pressure standing wave for each pulsation frequency is mapped in the geometry of the test section. The second section studies the shifts in velocity profiles due to pulsations. Using the data collected using the hot-wire anemometer, the changes in velocity profile are plotted over time for pulsations of different frequencies. The third section incorporates elements from the piezoelectric pressure transducers and the hot-wire anemometer to characterize the velocity pulsation waves. These are plotted in the geometry of the test section similar to the pressure pulsation waves. The final section of this chapter takes the characterized pulsation waves and correlates their properties with the ultrasonic meter error. A statistical regression analysis is performed to determine which aspects of pulsations can be used as predictors of meter inaccuracy.

Characterization of Pressure Pulsation Standing Waves

As explored in Chapter Two, pressure pulsation waves can be described as sinusoidal acoustic waves. The data from the piezoelectric pressure transducers were used to create sinusoidal maps of standing pulsation waves. These maps show the locations of pressure nodes and antinodes for the different pulsation frequencies generated. Surprisingly, the data for the great majority of pulsation frequencies showed evidence of standing waves. To create the maps, the magnitudes of peak-to-peak pressure fluctuations logged by each piezoelectric transducer were plotted versus transducer position in the test section. The magnitudes for each test were

then fit to Equation [32] using the least-squares method. In Equation [32], P represents the sinusoidal pressure pulsation wave, A_{pp} represents the amplitude of the wave, x is the distance from the pulsation generator in the direction of flow, and p_0 is a pressure offset. A non-zero value for p_0 suggests the presence of a traveling wave. The wavelength λ was input as a known value obtained by applying Equation [1] to the speed of sound in the natural gas and the frequency of the pulsation induced in the flow. The piezoelectric pressure transducers output the magnitudes of the pressure fluctuations at specific frequencies rather than the instantaneous deviation from average pressure. Equation [32] involves an absolute value operator because the peak-to-peak pressure pulsation measurements are never negative.

$$P = A_{pp}\left|\sin\left(\frac{2\pi}{\lambda}x\right)\right| + p_0 \qquad [32]$$

The results of fitting to Equation [32] were unsatisfactory, however. For several cases, the maps did not appear to converge to a meaningful representation of the pulsation wave that was measured. The problem with the fits was determined to be the locations of the pressure nodes. Contrary to the expected locations of the pressure nodes used in the acoustic design process in Chapter Three, the pressure nodes did not appear to form at the flow conditioner and/or the reducer at the end of the test section. Rather than these locations, the pressure nodes appeared to form at pipe features further downstream, including the plug valve (645 inches downstream of the pulsation generator) and the acoustic filter (800 inches downstream of the pulsation generator). To account for this, Equation [32] was modified to use the known location of a pressure node as a variable in the fit. The modified fit is given as [33] where x_{node} is the known location of a pressure node.

$$P = A_{pp}\left|\sin\left(\frac{2\pi}{\lambda}(x_{node} - x)\right)\right| + p_0 \qquad [33]$$

For most frequencies, the node location was either the plug valve or the acoustic filter. For the 19 Hz pulsation waves, the node appeared to be located at the reducer. For the 17 Hz pulsations, no pipe features coincided with a node location. Instead, an antinode appeared at the flow conditioner. For 17 Hz alone, the pulsation wave map was fit using a cosine instead of a sine to account for the known location of the antinode. For each frequency, the node locations are shown in Table 5. Between flow rates, there was no difference in standing wave structure; the node location depended solely upon pulsation frequency.

Table 5. Node locations by pulsation frequency

Pulsation Frequency (Hz)	Node Location (inches downstream of pulsation generator)	Corresponding Pipe Feature
5	800	Acoustic Filter
7		
9		
11		
13		
15		
17	144 (antinode)	Flow Conditioner
19	533	Reducer
21	645	Plug Valve
23		
25		
27		
29		
31		
33		
35		
37		
39		
41		
43		
45		

An example pressure pulsation map for a 27 Hz pulsation (with 700 acfm flow) is shown in Figure 33. On the x-axis is the distance downstream of the pulsation generator. It begins at 0 inches, the location of the rotor plate, and ends at 800 inches, the location of the LPL acoustic filter. The y-axis shows the peak-to-peak pressure magnitude in psi. The line represents the fit; the markers are the average peak-to-peak pressure magnitudes measured by the piezoelectric transducers.

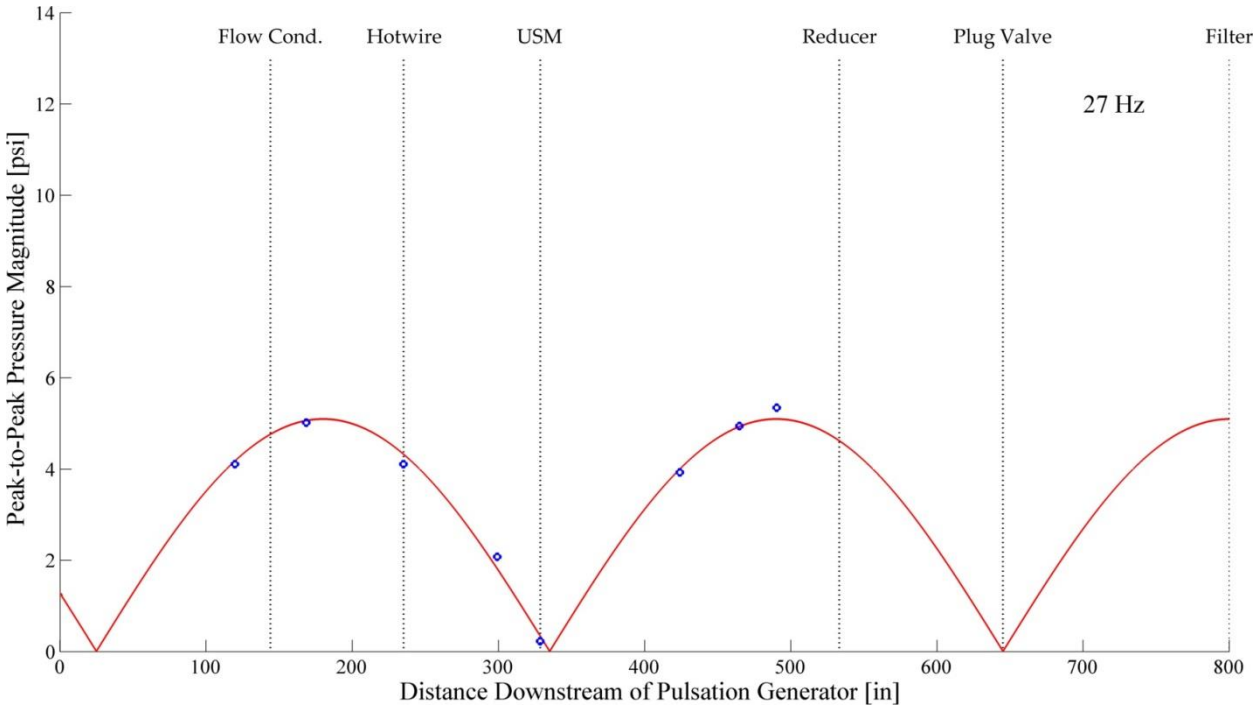

Figure 33. Pressure pulsation map for a 27 Hz pulsation

The fit for the 27 Hz pulsation wave had a zero offset, meaning that there is no evidence of a traveling wave. The average peak-to-peak pressure magnitudes did not change while the pulsation generator was creating the 27 Hz wave. Also, the measurements are clearly different values, indicative of a standing wave. In this case, a pressure node appears near the USM and at the plug valve. The pressure antinodes can be seen just downstream of the flow conditioner and just upstream of the reducer.

The 700 acfm pressure pulsation map for the 19 Hz pulsation is shown in Figure 34. The scale is unchanged from Figure 33. Even though a fit was resolvable for this frequency, there is evidence that this wave is possibly a traveling wave. First, the fit has a non-zero offset, meaning there is a constant fluctuation throughout the length of the test section. This occurs when there are no distinct nodes that reduce the local fluctuations to zero. Second, the piezoelectric transducer readings are very low in magnitude. As explained in Chapter Two, standing waves

have amplified magnitudes due to superposition. It would make sense that a travelling wave would have a reduced amplitude compared to a standing wave. Third, the readings do not change by a large amount between transducer locations. Although this could be a result of the overall low amplitude of the wave, a constant reading irrespective of location is indicative of a travelling wave.

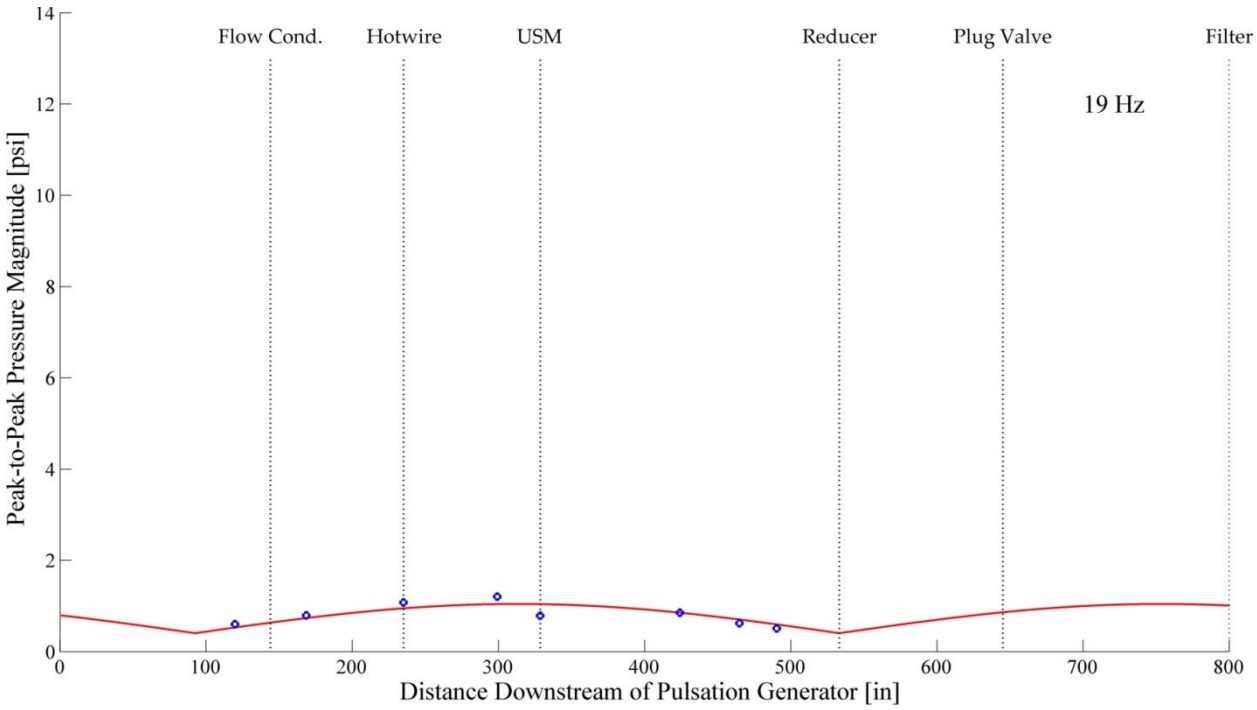

Figure 34. Pressure pulsation map for a 19 Hz pulsation

The pressure pulsation maps for all tested frequencies in 700 acfm flow are shown in Figures 35, 36, and 37. The frequencies are split between the figures for clarity. Similarly, the pressure pulsation maps for all tested frequencies in 200 acfm flow are shown in Figures 38, 39, and 40. The scale is kept constant between figures, though the y-axis differs between flow rates. All individual pressure pulsation maps are included in Appendix A.

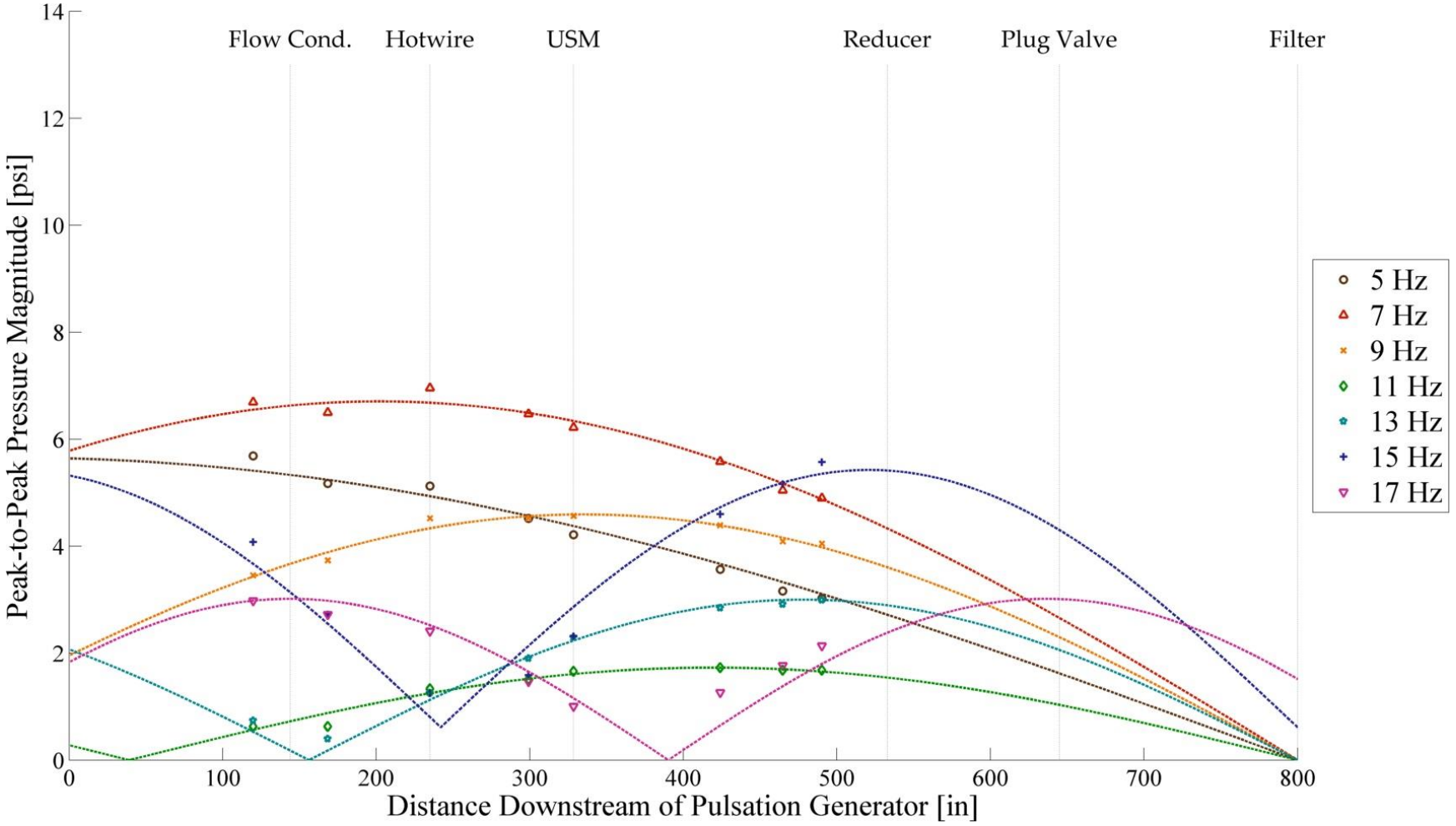

Figure 35. Pressure pulsation maps for frequencies between 5 Hz and 17 Hz in 700 acfm flow

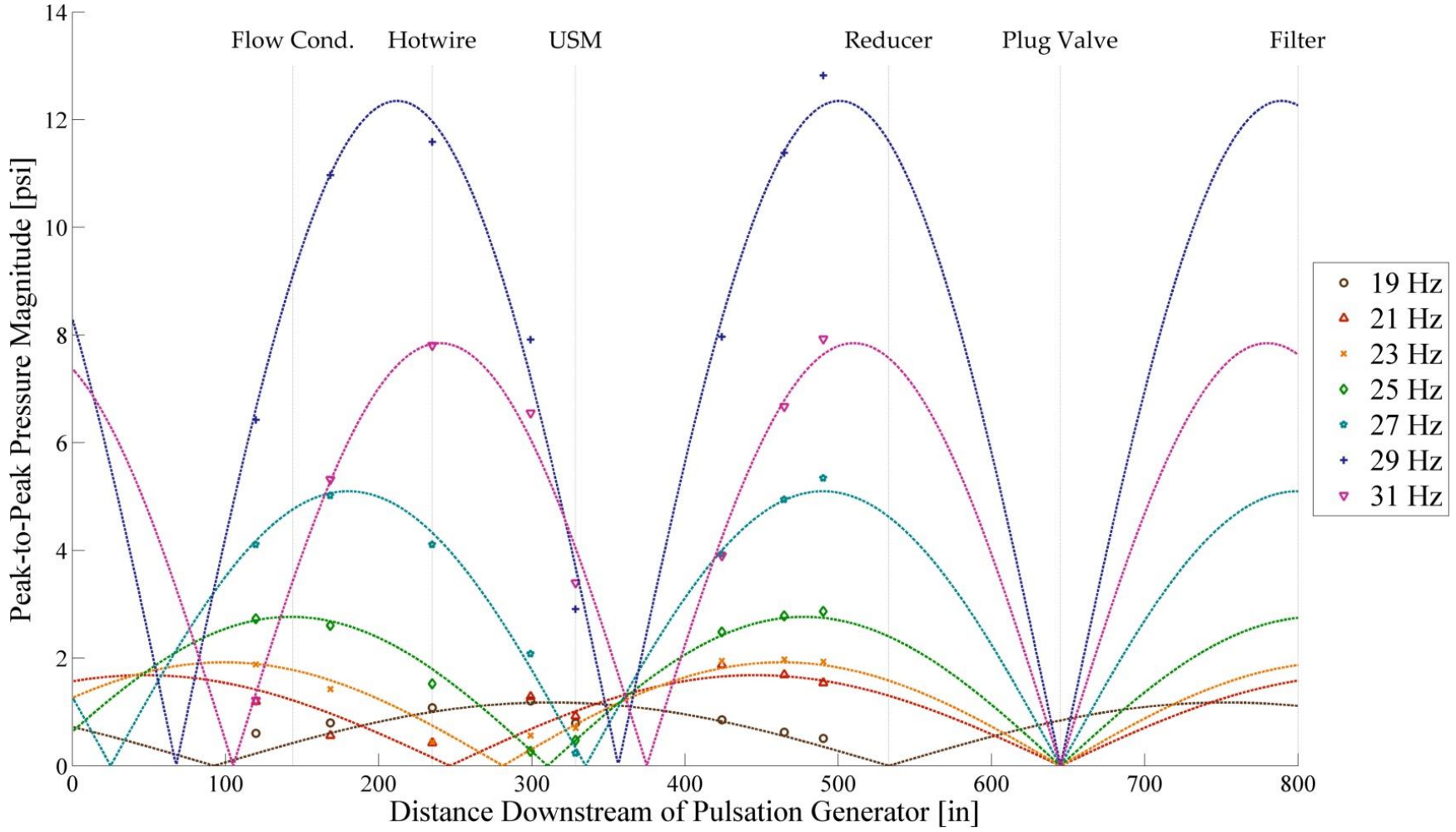

Figure 36. Pressure pulsation maps for frequencies between 19 Hz and 31 Hz in 700 acfm flow

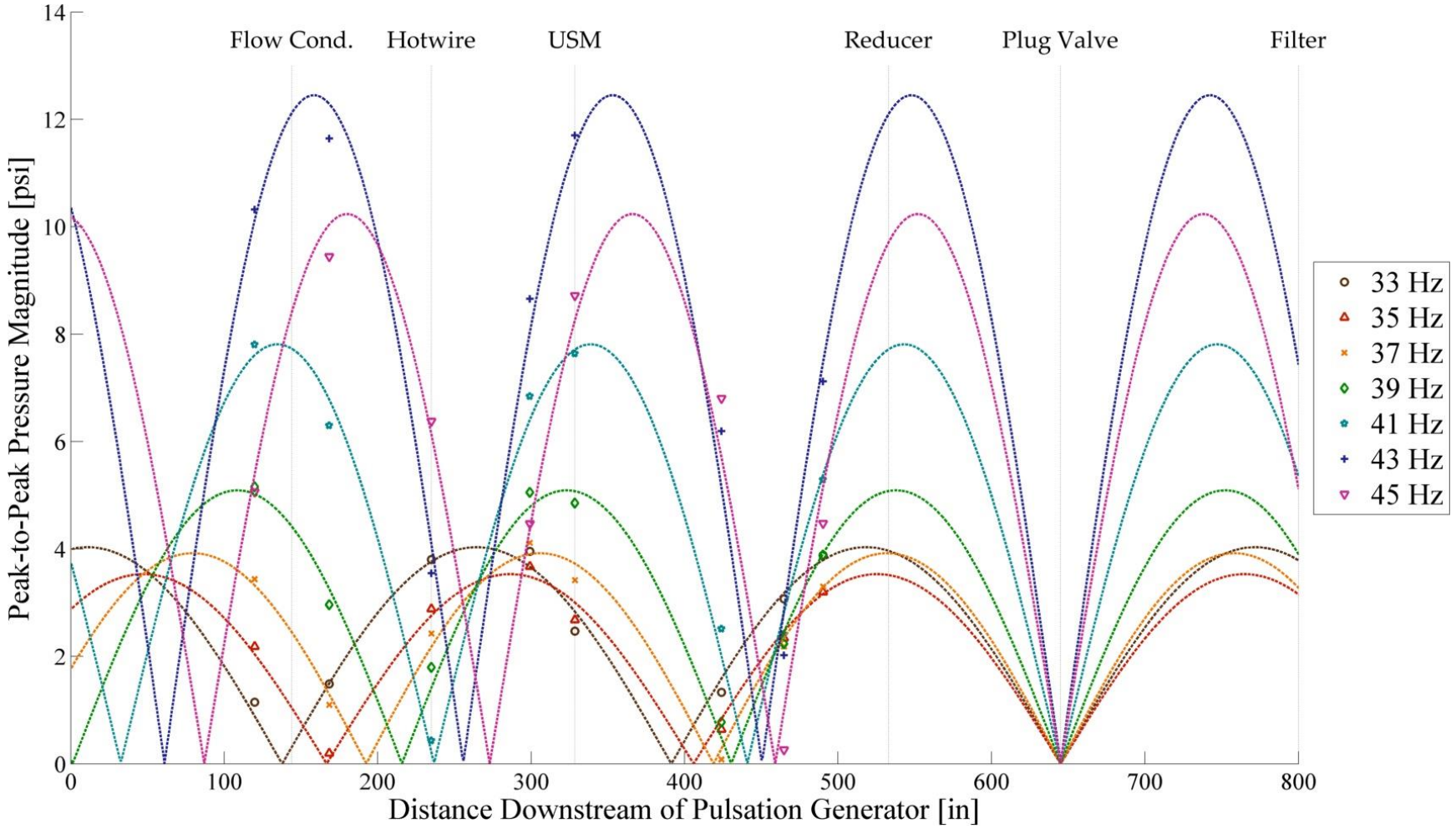

Figure 37. Pressure pulsation maps for frequencies between 33 Hz and 45 Hz in 700 acfm flow

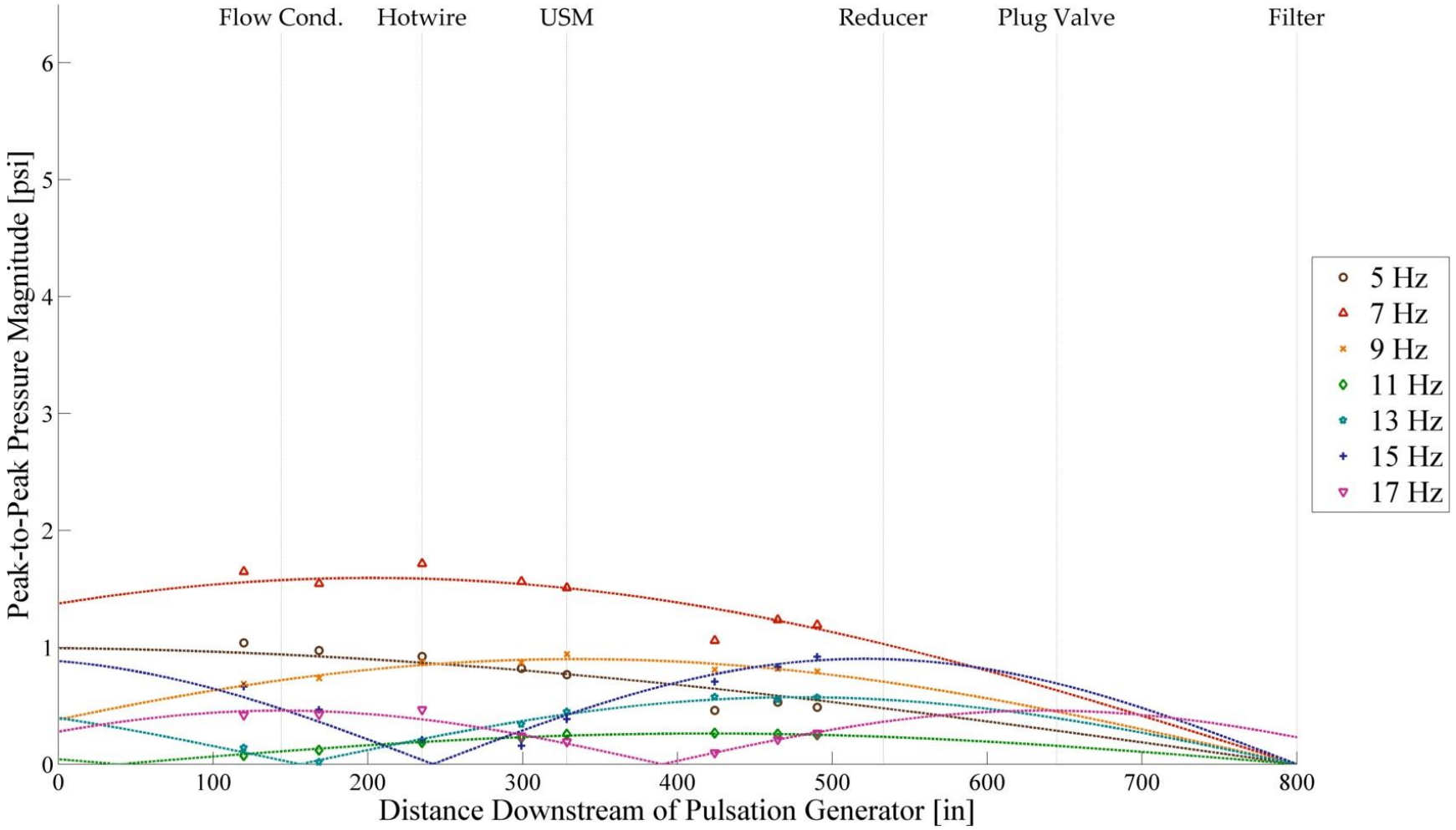

Figure 38. Pressure pulsation maps for frequencies between 5 Hz and 17 Hz in 200 acfm flow

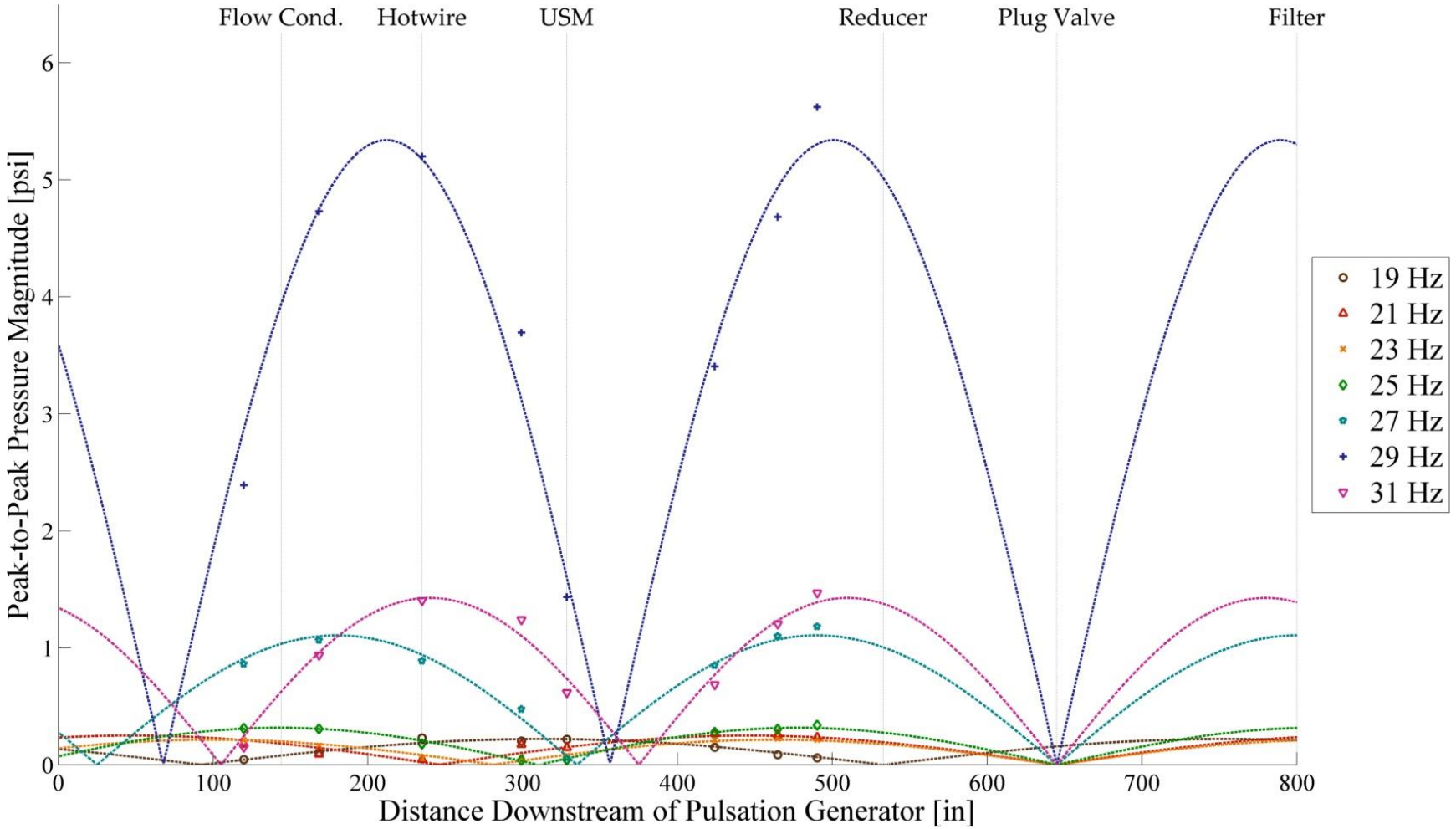

Figure 39. Pressure pulsation maps for frequencies between 19 Hz and 31 Hz in 200 acfm flow

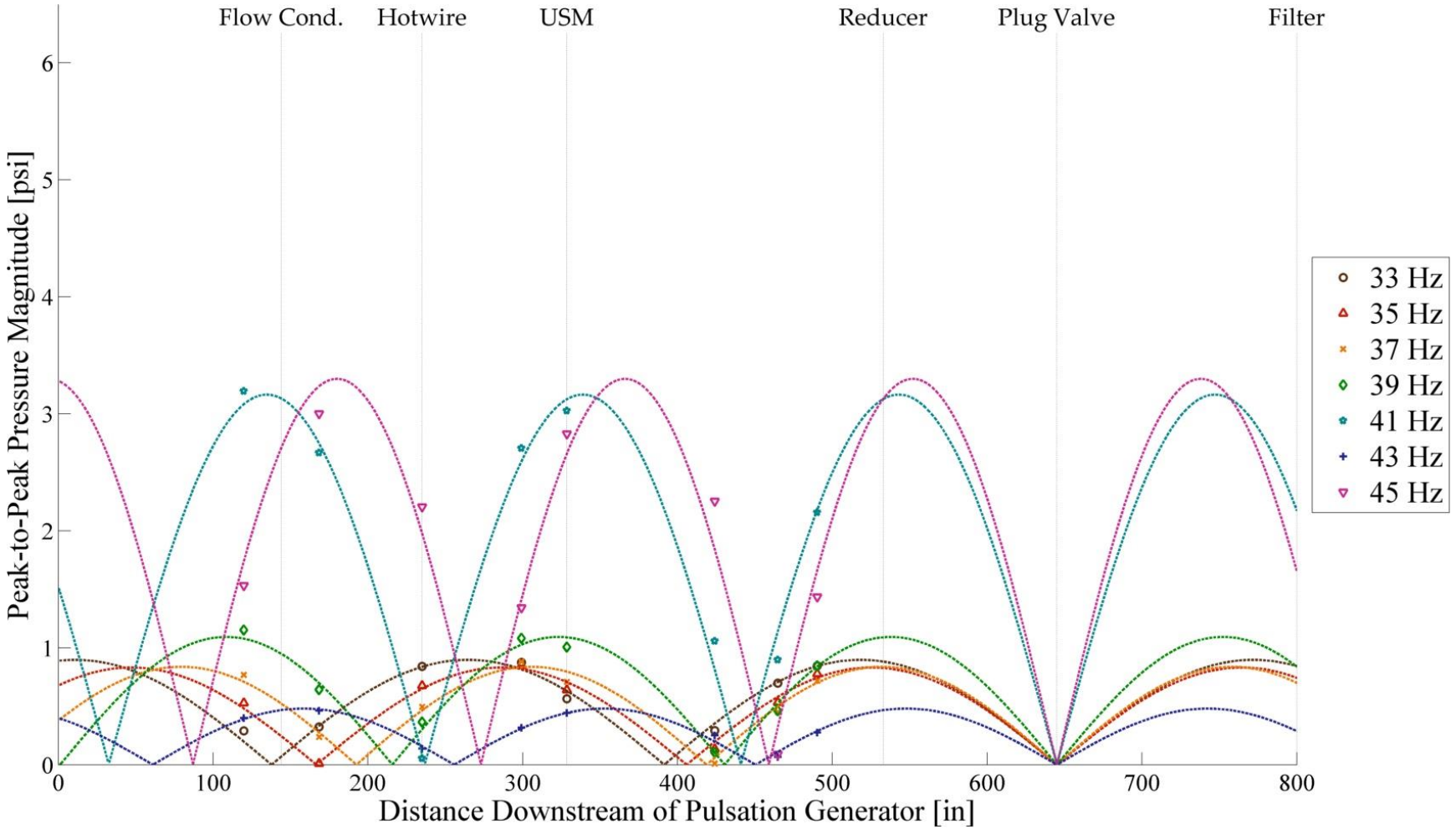

Figure 40. Pressure pulsation maps for frequencies between 33 Hz and 45 Hz in 200 acfm flow

Although these fits are non-linear, it is still possible to obtain some statistical measure for goodness of fit. The most commonly accepted goodness of fit measure for non-linear regressions is root mean squared error (*RMSE*). *RMSE* is a measure of sample standard deviation among residuals, the differences between the measured values and the modeled (fitted) values. As a measure of standard deviation, the smaller the value for *RMSE*, the better the fit. There is no upper limit on *RMSE* and it is scale-dependent. Still, it is in the units of the pressure pulsations and can be used to estimate the expected uncertainty. The definition of *RMSE* is given in Equation [34], where $\hat{y}_z$ is a fitted value, y_z is a measured value, N is the total number of data points that contributed to the regression, and z is an index (Montgomery 2012).

$$RMSE = \sqrt{\frac{\sum_{z=1}^{N}(\hat{y}_z - y_z)^2}{N}} \quad [34]$$

The *RMSE* values calculated from the 700 acfm data are shown in Figure 41 as a function of pulsation frequency.

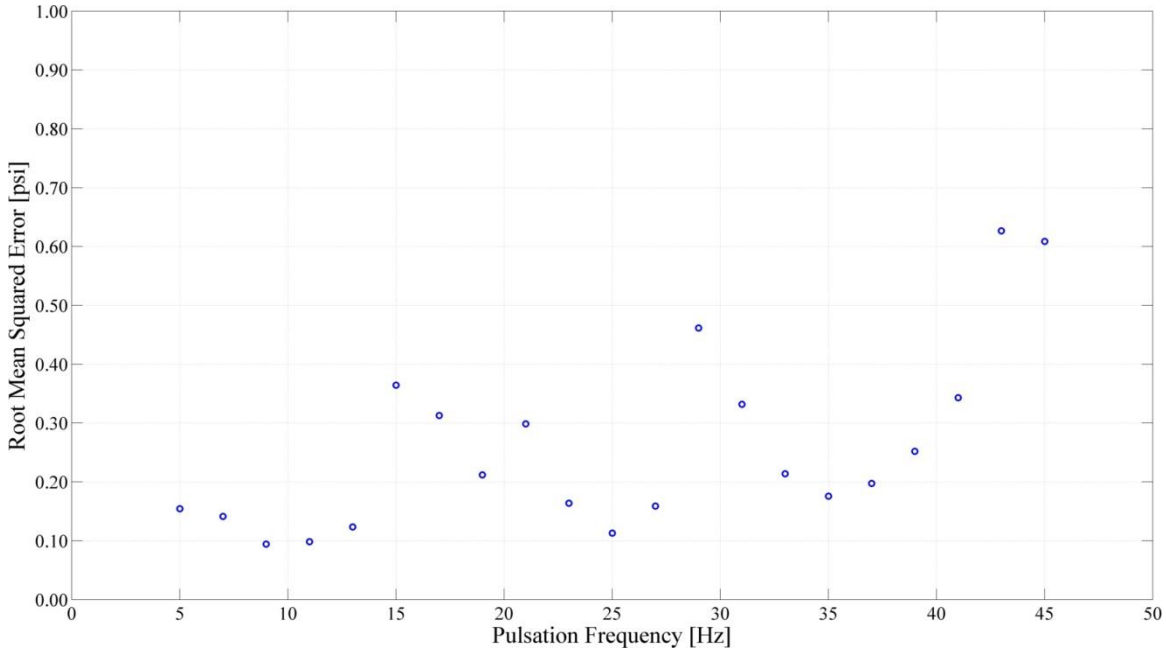

Figure 41. RMSE vs. frequency for the 700 acfm pressure pulsation maps

As previously stated, *RMSE* is scale-dependent. Without context it can be difficult to see how the fits compare. Figure 41 would seem to imply that the fits at 43 Hz and 45 Hz were the worst as they have the largest values of *RMSE*. This is misleading, however, as the pulsation waves varied greatly in amplitude. For example, the scale of the pulsations at 45 Hz were very different from the scale of pulsations occurring at 33 Hz. A *RMSE* of 0.60 may be large for the 33 Hz wave, but small for the 45 Hz wave. It is clear that the *RMSE* values correlate with the maximum pulsation amplitudes, as shown in Figure 42.

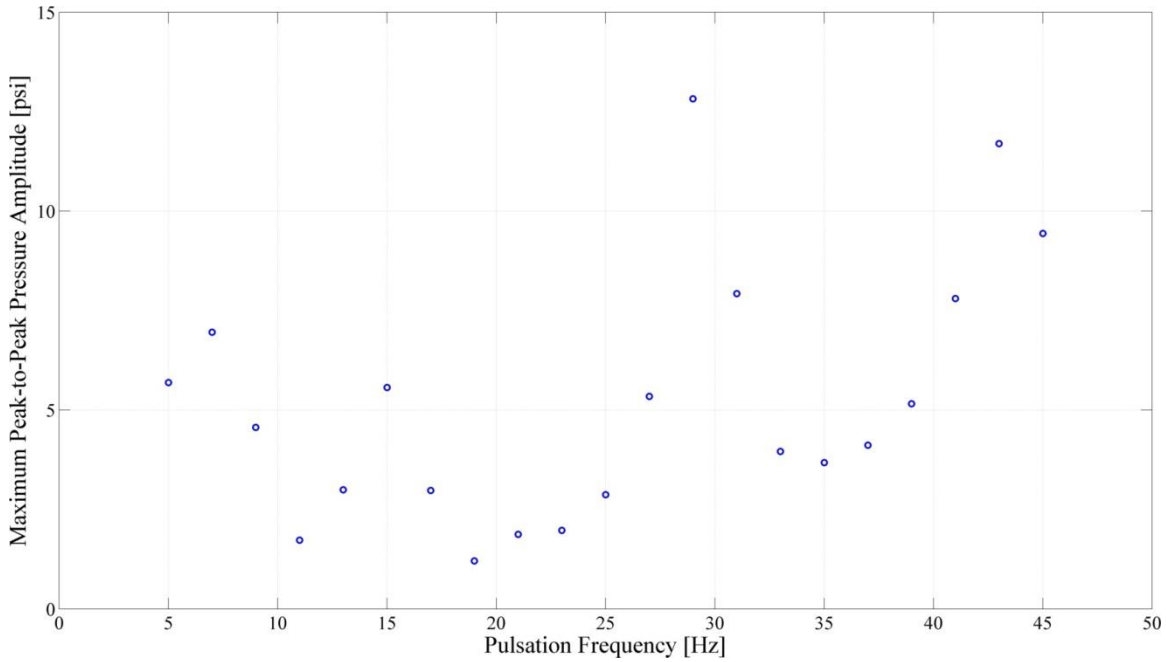

Figure 42. Maximum pulsation amplitude vs. frequency for the 700 acfm pressure pulsation maps

By dividing each *RMSE* value by the corresponding maximum pulsation amplitude for that frequency, a "normalized" *RMSE* value can be found for each. These values are plotted in Figure 43.

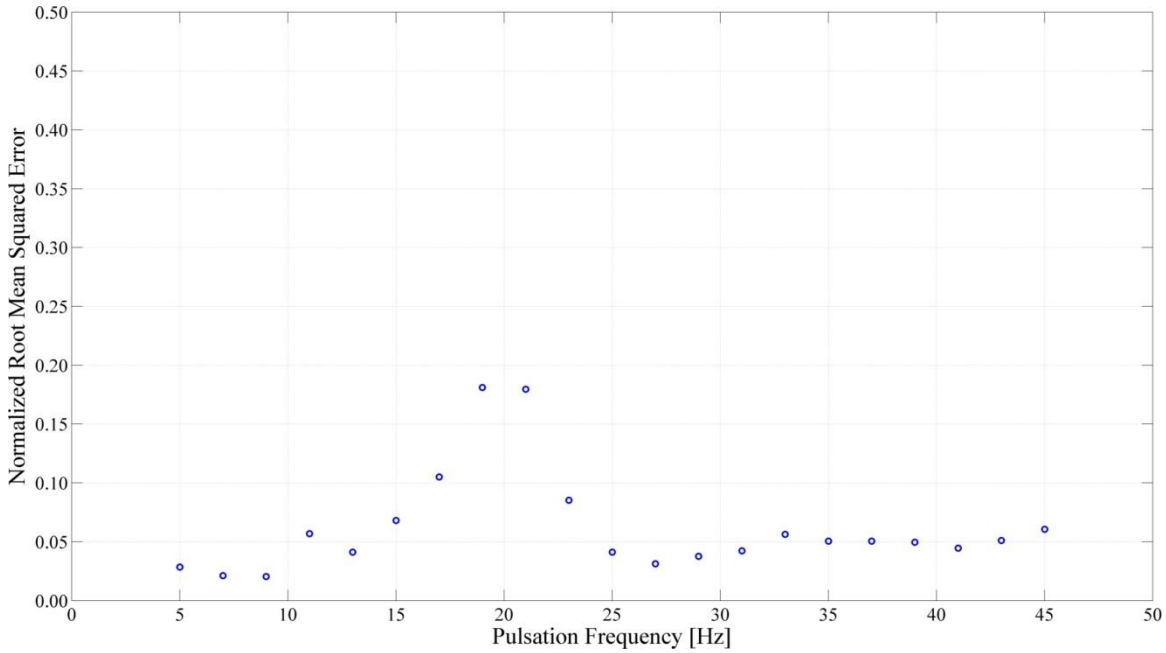

Figure 43. Normalized RMSE vs. frequency for the 700 acfm pressure pulsation maps

From this plot, it is clear that the apparently large *RMSE* values for the 43 Hz and 45 Hz pulsation maps were not large when compared to the pulsation amplitudes at those frequencies. For all but three frequencies, the *RMSE* value was less than 10% of the pulsation amplitude. The majority of fits had *RMSE* values at or under 5% of the pulsation amplitude. What are significant are the elevated *RMSE* values for the pulsation maps at 17 Hz, 19 Hz, and 21 Hz. These correspond to the low-amplitude maps that could indicate traveling waves. It is expected that these fits would be less descriptive of the pulsation behavior and thus would produce larger values of *RMSE*. Nevertheless, even the highest *RMSE* value does not exceed 20% of the maximum pulsation amplitude. That is not enough to dismiss the sinusoidal fits at 17 Hz, 19 Hz, and 21 Hz.

This structure is consistent with the *RMSE* values calculated from the 200 acfm data. The raw *RMSE* values are shown in Figure 44.

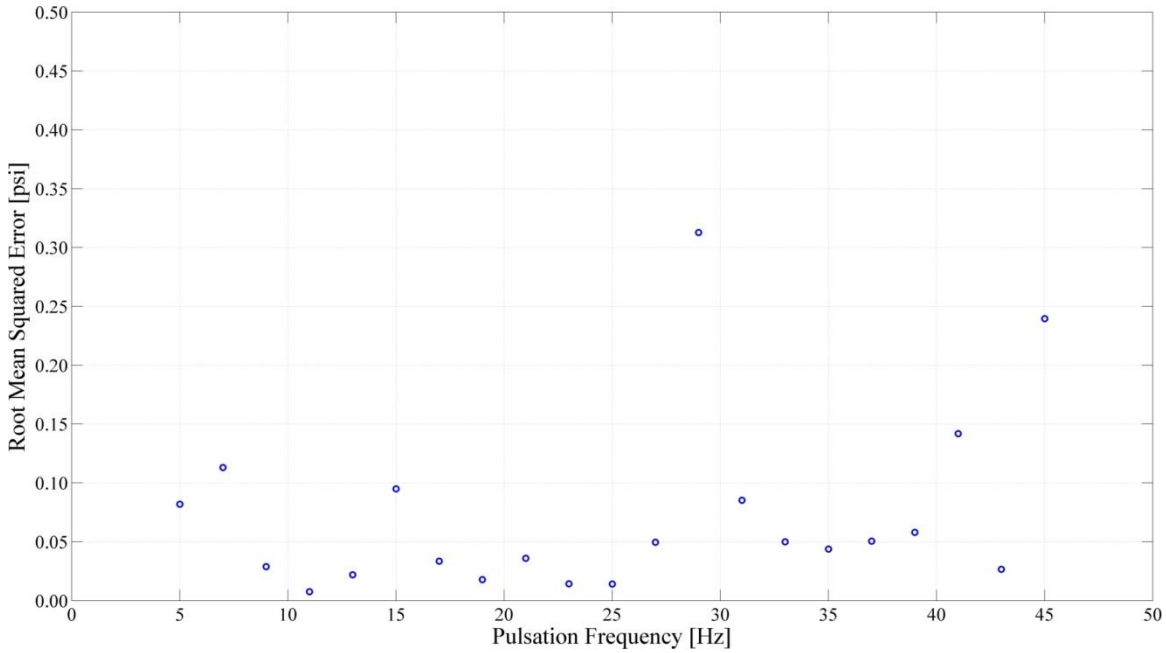

Figure 44. RMSE vs. frequency for the 200 acfm pressure pulsation maps

These *RMSE* values correlate with the maximum pulsation amplitude for each frequency, as shown in Figure 45.

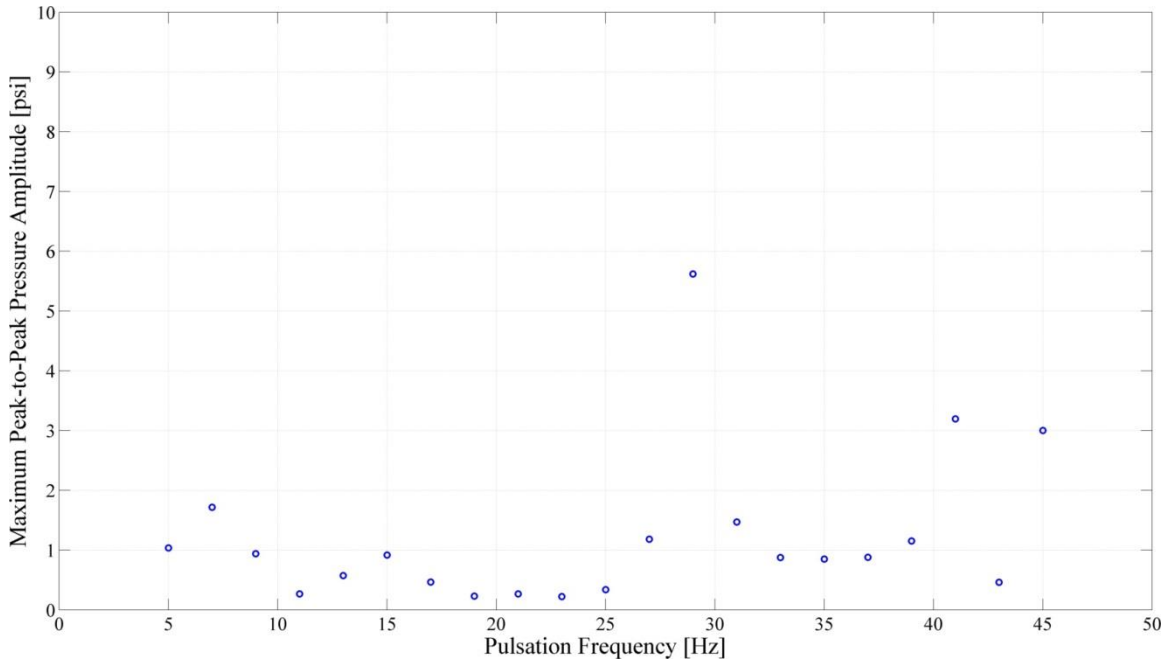

Figure 45. Maximum pulsation amplitude vs. frequency for the 200 acfm pressure pulsation maps

Similar to the 700 acfm data set, the 200 acfm *RMSE* values can also be normalized by dividing by the maximum pulsation amplitudes. These normalized values are shown in Figure 46.

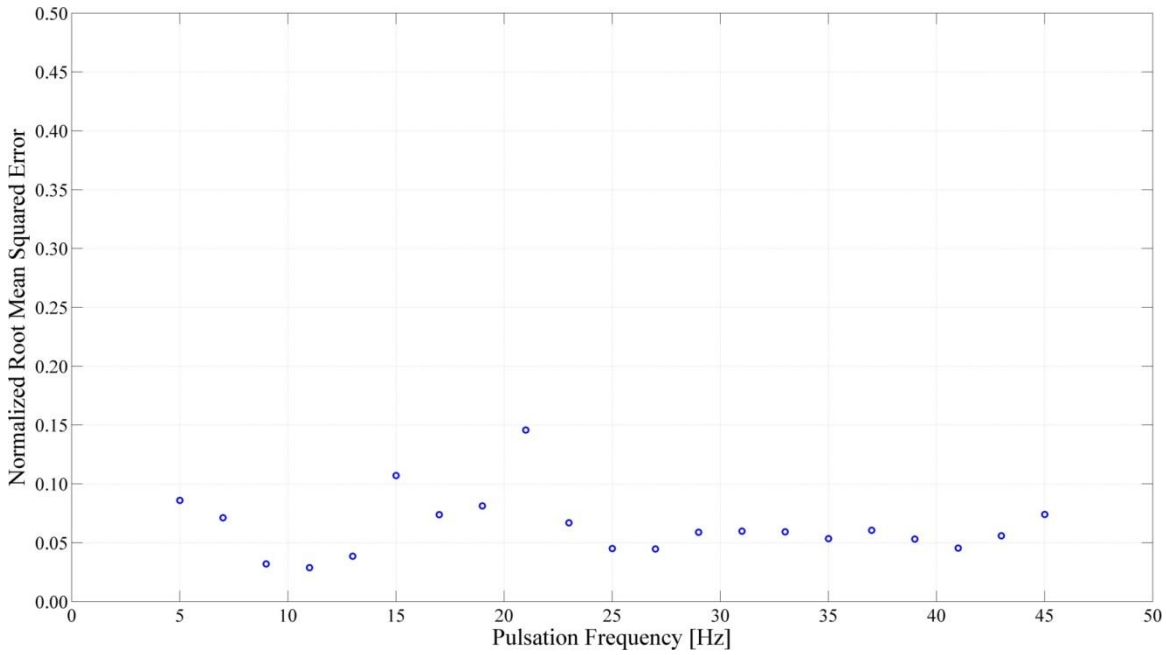

Figure 46. Normalized RMSE vs. frequency for the 200 acfm pressure pulsation maps

Once again, the fit for the 21 Hz pulsation displays an elevated *RMSE* but does not exceed 15% of the maximum pulsation amplitude. Other elevated *RMSE* values can also be observed for pulsation maps at 5 Hz and 15 Hz, though none are as great as the 21 Hz *RMSE*. None of the *RMSE* values from the 200 acfm data suggest that the fits were invalid.

In addition to finding an *RMSE* value for each test, it was possible to examine the residuals directly. For a good fit, residuals are small, random, and independent of the variables involved in the fit. A graphical residual analysis for the 27 Hz fit shown in Figure 49 is given in Figure 47.

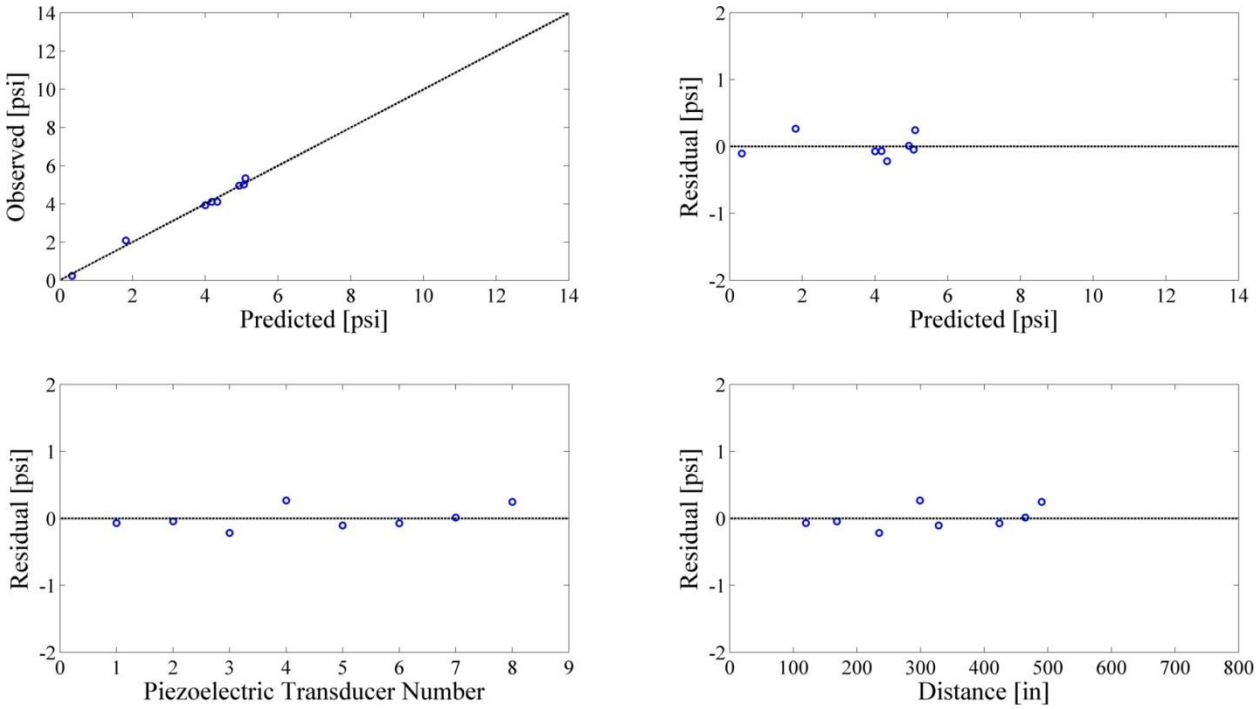

Figure 47. Residual analysis of pressure pulsation map regression, 27 Hz at 700 acfm

In the top left, the observed (measured) pressure readings are plotted against the predicted (fitted) pressure readings. For a perfect fit, the plotted markers would lie on top of the black dotted line. Clearly, for this fit, the markers are not far off from the dotted line. The other three graphs show residuals plotted against the predicted values (top right), the transducer number (bottom left), and the distance from the pulsation generator (bottom right). In none of these plots are the residuals clearly correlated with any of the variables, showing randomness and independence. There were no fits that stood out in the residual analysis; every fit showed the same residual patterns. The graphical residual analyses of the fits for all frequencies and both flow rates can be found in Appendix C.

As shown in this section, the pulsations produced varied widely in amplitude and node location. The particular traits of these pulsation waves in relation to USM error is discussed in the final section of this chapter. From a qualitative standpoint, however, it was unexpected to be able to generate so many standing waves in a single pipe geometry. Nearly all frequencies tested formed standing waves, including all frequencies 27 Hz and above. Some frequencies, such as the 19 Hz wave shown in Figure 34, are suspected to be travelling waves, but sinusoidal fits were resolvable for all frequencies. While the number of standing waves is fortuitous from a data analysis standpoint (providing higher amplitude pulsations and varying node positions for greater range in regression modeling), this situation poses grave implications for field applications. These findings suggest standing pulsation waves may be far more common than previously thought. Exact geometrical conditions do not seem to be necessary. If the pipe geometry is "close enough," it appears as though a standing wave will naturally develop.

This problem is compounded when considering real-world applications, in which a meter run could be subjected to pulsations from a number of sources (at several different frequencies) simultaneously. The superimposed standing wave could be complex to the point where it would be difficult to model, even with a large number of measurement points, which most meter runs lack. If measurements are performed on a field meter run to detect pulsations, the readings would vary substantially depending upon the location of the measurement relative to the standing wave. In a worst case scenario, locations close to pressure nodes could be the only ones available for measurement. This would result in the test engineer to conclude that pulsations are not significant, despite the possibility of high amplitude pulsations occurring elsewhere. That these findings show a high likelihood of standing wave formation for a variety of frequencies

indicates that this worst case scenario could be happening much more frequently than most industry professionals believe.

Characterization of the Effect of Pulsations on Velocity Profiles

Using the traversing capability of the hot-wire anemometer, it was possible to measure the flow velocity at different points along the flow profile. The end goal of this segment of the analysis was to graphically model the changes in flow velocity profile due to pulsations. As a first step, the average flow velocities for the different probe insertion locations were calculated. This was done for the baseline conditions and for each pulsation frequency for both flow rates.

When the individual average point velocity measurements are plotted together, the average flow velocity profiles can be seen. A plot of the average flow velocity profiles for the baseline and all pulsation conditions for 700 acfm flow is shown in Figure 48. A similar plot, showing the average flow velocity profiles for the baseline and all pulsation conditions for 200 acfm flow, is shown in Figure 49.

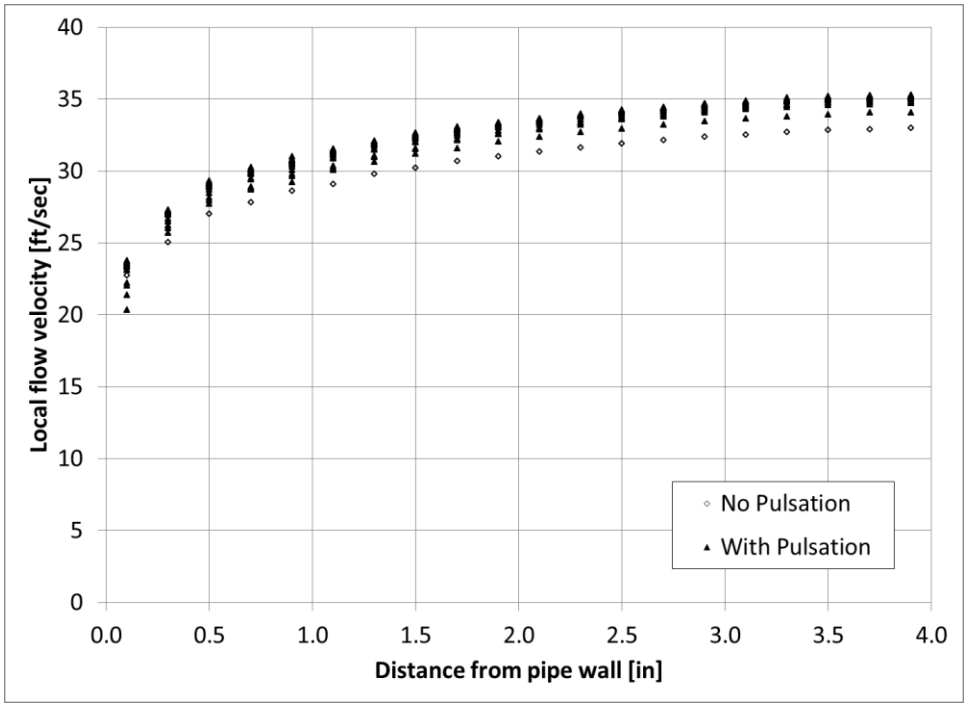

Figure 48. Average flow velocity measurements for 700 acfm flow

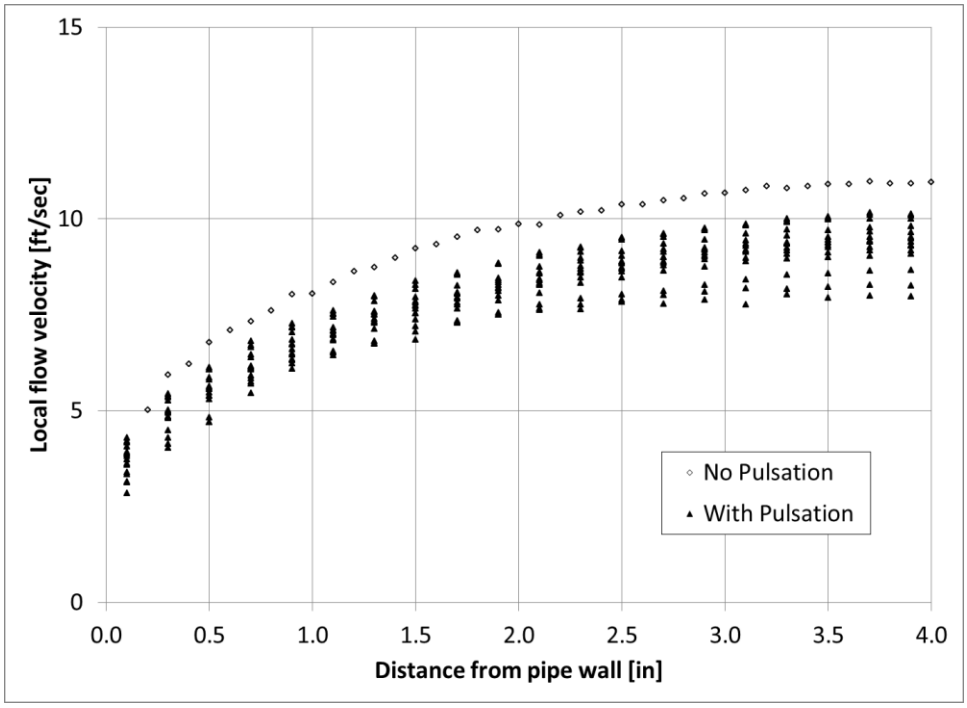

Figure 49. Average flow velocity measurements for 200 acfm flow

Although these plots reveal little insight into how specific pulsation frequencies are affecting the flow velocity profile, several pertinent observations can be made. First, one effect of pulsation is the change in average flow velocity profile. This is true for every pulsation tested. Regardless of any other effects, this alone would cause USM error. A USM is configured to expect a specific flow profile. A deviation from this, as shown in Figures 48 and 49, would induce a bias into the flow measurement. Another observation is the directional effect of the pulsations. For the measurements taken in 700 acfm flow, pulsations appear to draw out the flow profile in the center, making it more bullet-shaped. For 200 acfm flow, the pulsations appear to do the opposite. The average velocity profiles in the presence of pulsations appear flatter than the baseline profile. This conflicts with previous theories about the modeling of pulsations which suggested that pulsations could be simplified as an additional source of turbulence (Mizushina 1973). This theory would imply that a flow profile in pulsating flow would appear flatter than the flow profile in steady flow. This effect was clearly not observed in the average flow velocity profiles in Figures 48 and 49. It is probable that the effects of pulsations on flow profile cannot be simplified to generic turbulence. A final observation, the profile shifts appeared to be a function of pulsation frequency. The most bullet-shaped profile was observed in 45 Hz pulsation. The flattest profile was observed in 5 Hz pulsation. The profiles in between cascaded sequentially from 45 Hz to 5 Hz. This was consistent for both flow rates and did not appear to relate to the baseline flow profile. The reason for this is not clear. Because the hot-wire data were being collected at 1 kHz, aliasing is unlikely. It may be a direction for future research.

In order to model the behavior of pulsations on instantaneous flow velocity profile, several assumptions must be made. The readings from the hot-wire anemometer only showed

the velocity shifts at one point for a duration of time. The points were measured sequentially and no phase data was captured. Linking these disparate measurements together into a cohesive flow profile requires the assumption that the pulsation's effects on the flow profile are cyclic. If this is true, then the measurements can be joined by finding local maximum in the readings and shifting each data set such that the time series for each begins at a maximum. The assumption of cyclic behavior in pulsations is supported by previous studies. For single frequency standing waves, the amplitudes are not observed to change over time. In this case specifically, the pulsations were caused by a controlled pulsation generator which kept the frequency and amplitude constant.

Another assumption that must be made is the nature of the flow profile under the influence of a pulsation. In other words, the mathematical description used in fitting the flow profile must be assumed. For this application, a simple equation with three terms was used for the regression fits. Equation [35] combines the Power Law description of a turbulent flow profile from Equation [31] with a sinusoidal component to describe the pulsation. Here, a cosine is used instead of a sine because the pulsations are suspected to have their greatest effects near the centerline of the pipe. An additional constant term was added to account for centerline velocity shifts exaggerated by the cosine. In Equation [35], $\bar{u}$ represents a normalized flow profile (defined in Equation [36] where u_{max} is the maximum flow velocity), $\hat{r}$ represents a normalized radius (defined in Equation [37] where R is the pipe radius), and b_i are fit coefficients.

$$\bar{u} = A_{pp}(1 - \hat{r})^{\frac{1}{p}} + b_1 + b_2 \cos(\hat{r}) \quad [35]$$

$$\bar{u} = \frac{u}{u_{max}} \quad [36]$$

$$\hat{r} = \frac{r}{R} \quad [37]$$

Using Equation [35], regression fits were calculated for the average flow profile and maximum flow profile for the 45 Hz pulsation at 700 acfm. These are shown together in Figure 50. The y-axis shows the vertical position into the 8-inch pipe. The x-axis shows the flow velocity normalized with respect to the average flow velocity (for 700 acfm, this was 32.2. ft/s). The red line shows the average flow profile. The blue data markers are the velocity readings from the hot-wire anemometer. The blue line is the regression fit for those markers. The points at the pipe wall were set to zero in accordance with the no-slip boundary condition.

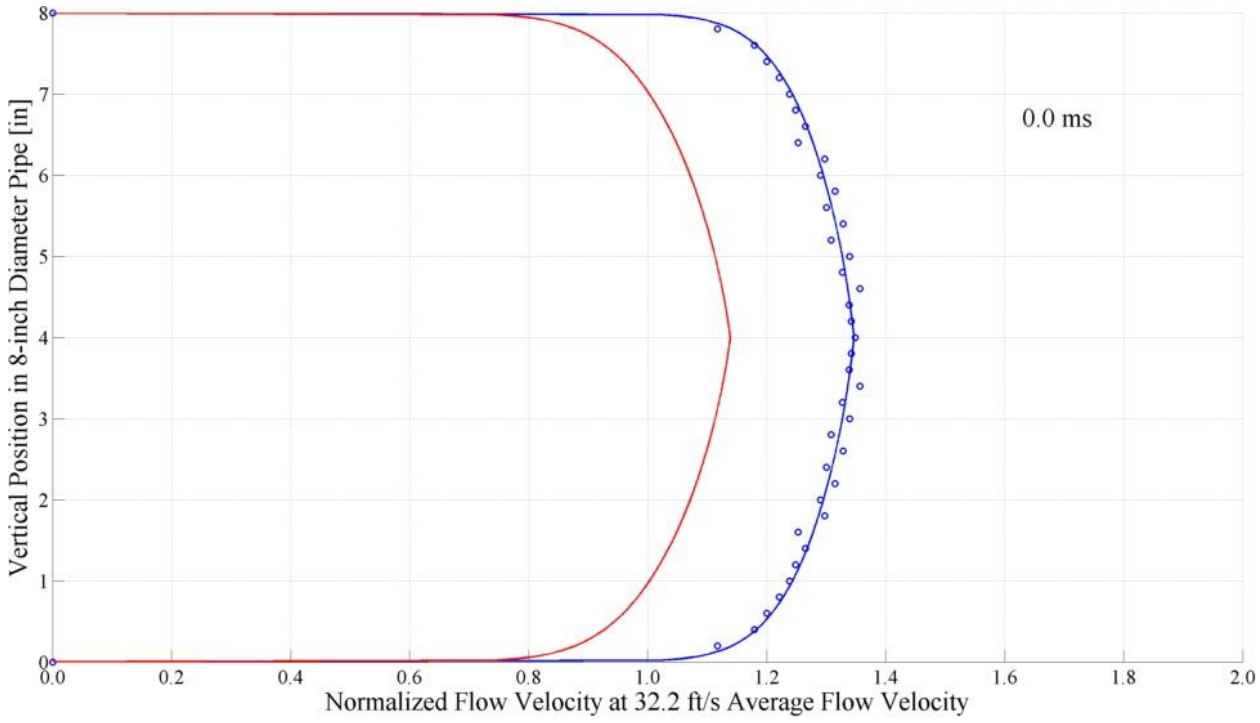

Figure 50. Average and maximum normalized flow velocity profiles for 45 Hz pulsation at 700 acfm

In Figure 50, the half profile measured with the hot-wire anemometer (as the probe tip only extended to the center of the flow) was doubled and flipped to aid in visualizing the full flow profile. This assumes that the effects of the pulsation do not differ across angular positions in the flow, a safe assumption considering the radial symmetry of the piping and the pulsation generator.

Finding the local maximum of the time series in order to create the plot in Figure 50 involved fitting the raw data with a sinusoidal fit at the known pulsation frequency. This can be seen in Figure 51 for an example 45 Hz time series. The raw measurements, shown in blue data markers, were fit with a simple sinusoidal fit, shown as the red line. A script was written to procedurally detect the first and subsequent maxima of the time series using the sinusoidal fit. Once this was complete for all insertion points, the time series were shifted such that the first maxima of each coincided with each other. Because the pulsation frequency did not change, the subsequent maxima for each time series also coincided with each other. The first maxima for 45 Hz at 700 acfm is the plot shown in Figure 50. Example sinusoidal plots like the one in Figure 51 for every frequency at both flow rates can be found in Appendix D.

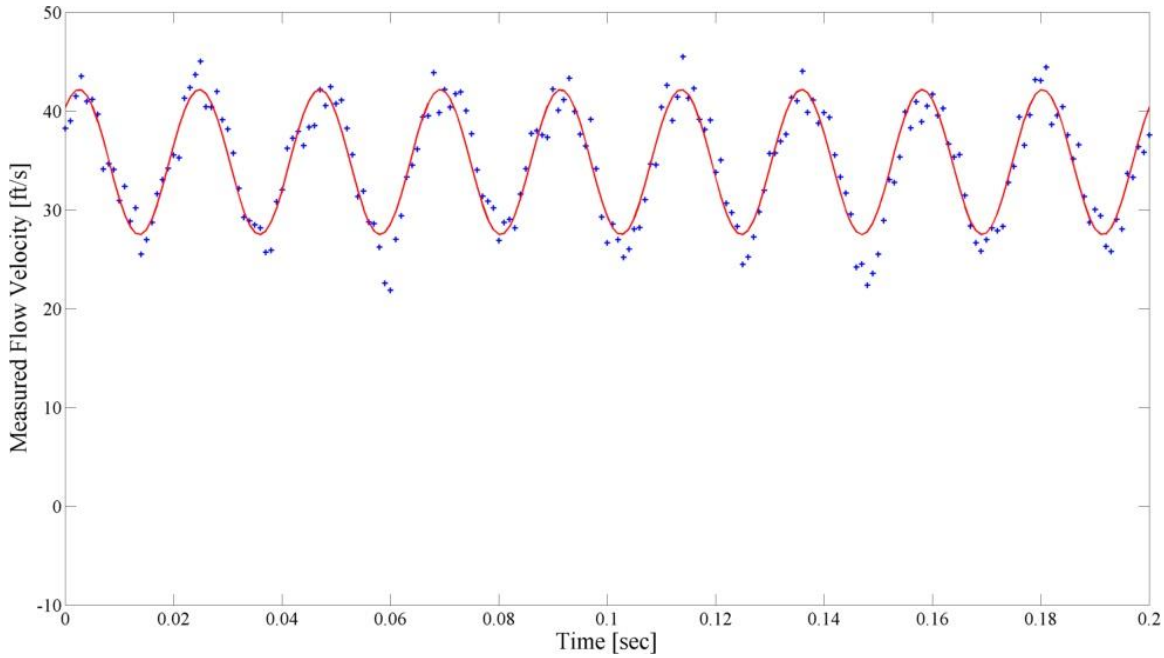

Figure 51. Sinusoidal fit to hot-wire anemometer output time series

By plotting the velocity time series for each insertion point at different time steps, the profile shifts over time can be observed. For the 45 Hz pulsation at 700 acfm, this can be seen in Figure 52.

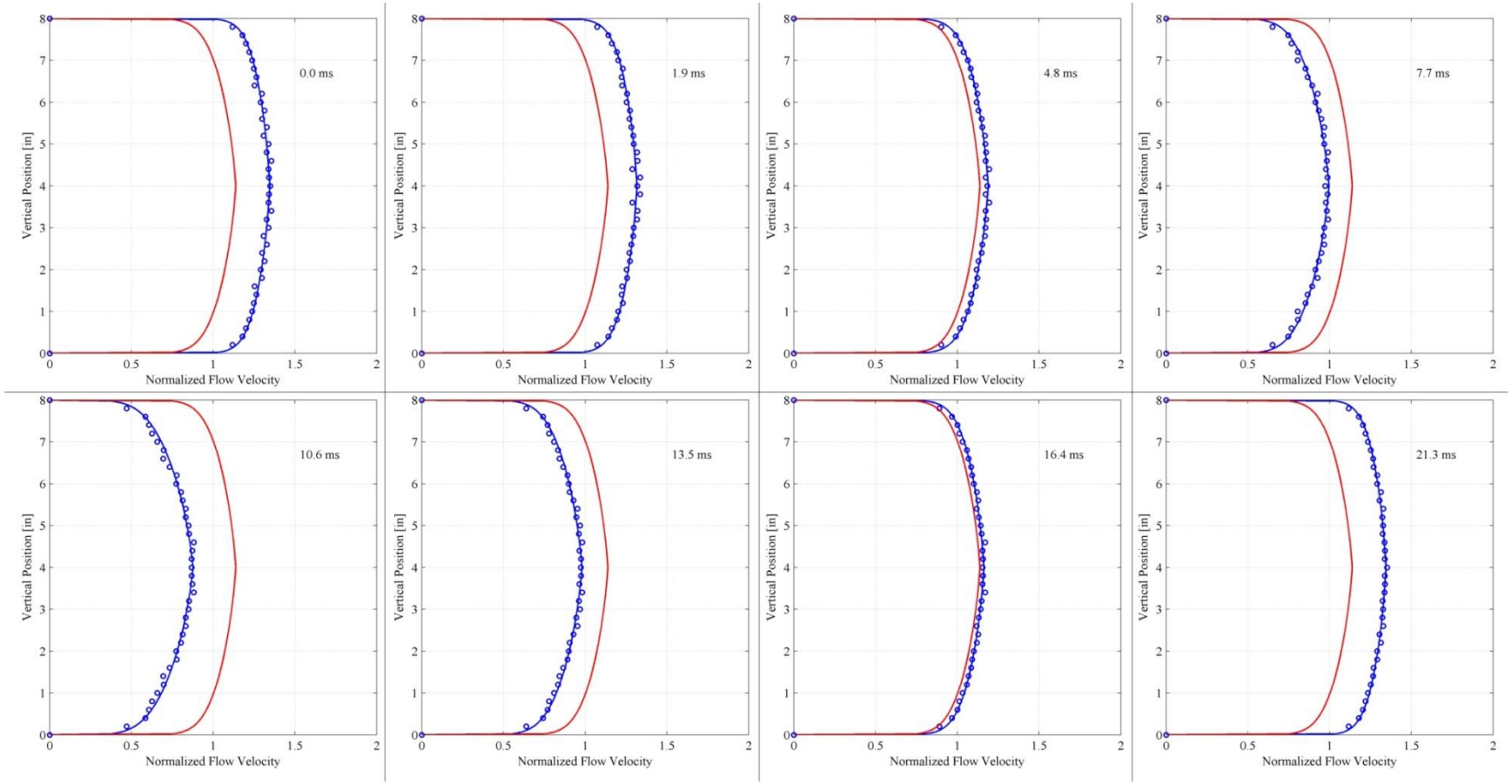

Figure 52. Velocity profile shifts over time for 45 Hz pulsation at 700 acfm

The plot in the top left of Figure 52 is the plot from Figure 50, the maximum flow profile for the 45 Hz pulsation. Each of the plots have a time in milliseconds (ms) denoted in the top right corner. This represents the time from the start of the cycle when the flow profile looks as depicted. The start of the cycle is denoted as 0.0 ms. The sequence in Figure 68 represents a complete cycle. At 22.2 ms after the start, the flow profile looks identical to the flow profile at 0.0 ms. This is expected as the period of a 45 Hz wave is approximately 22.2 ms.

As Figure 52 shows, the flow profile changed greatly over time when subjected to a 45 Hz pulsation wave. These findings show that the flow profile shifted as much as 30% from the average. It is also worth noting that this was occurring at the frequency of the pulsation. The flow profile was shifting from 20% greater than the average to 30% below the average in just over 10 ms. This was happening continuously, 45 times per second. This type of profile change explains the large errors observed in USMs subjected to pulsating flow. Not only are the shifts large in magnitude, they are occurring at rates faster than the meter is able to process them. Granted, the 45 Hz wave at 700 acfm was one of the strongest waves observed. Other pulsation waves did not induce the same levels of profile shift. However, the results remain that the flow profile shifted as much as 50% of the average (p-p) at a frequency of 45 times per second.

The magnitudes of the profile shifts varied greatly between pulsation frequencies and flow rates. Complete time studies of profile changes for each frequency and both flow rates (similar to Figure 52) can be found in Appendix E. These time studies were procedurally generated directly from the hot-wire anemometer output data using a script written for this purpose. The effects of these shifts on USM measurement error are explored in the final section of this chapter.

As before, it is worth examining the statistical goodness of fit for the regressions applied in this section. Also as before, the fit in Equation [35] was non-linear, so *RMSE* remains the best method for evaluating the regression fits. (Refer to the previous section for a full description of *RMSE*.) While calculating the *RMSE* for each fit is possible, the first step was calculating *RMSE* for only the regressions on the average flow profiles. When calculated for each pulsation frequency, the values of *RMSE* are given in Figure 53 for flow at 700 acfm and in Figure 54 for flow at 200 acfm.

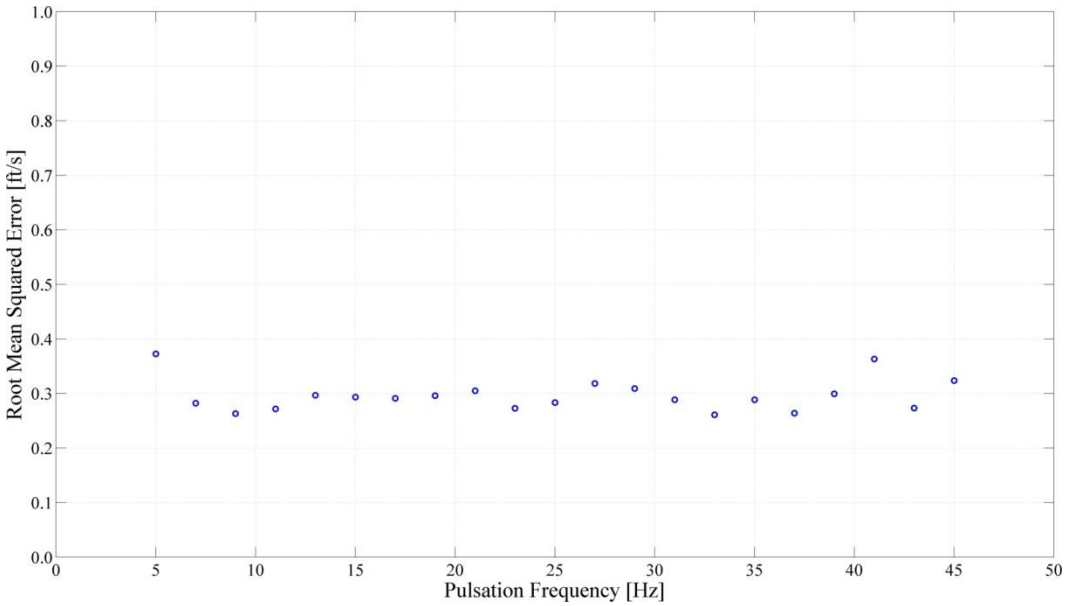

Figure 53. RMSE vs. frequency for the 700 acfm average velocity profiles

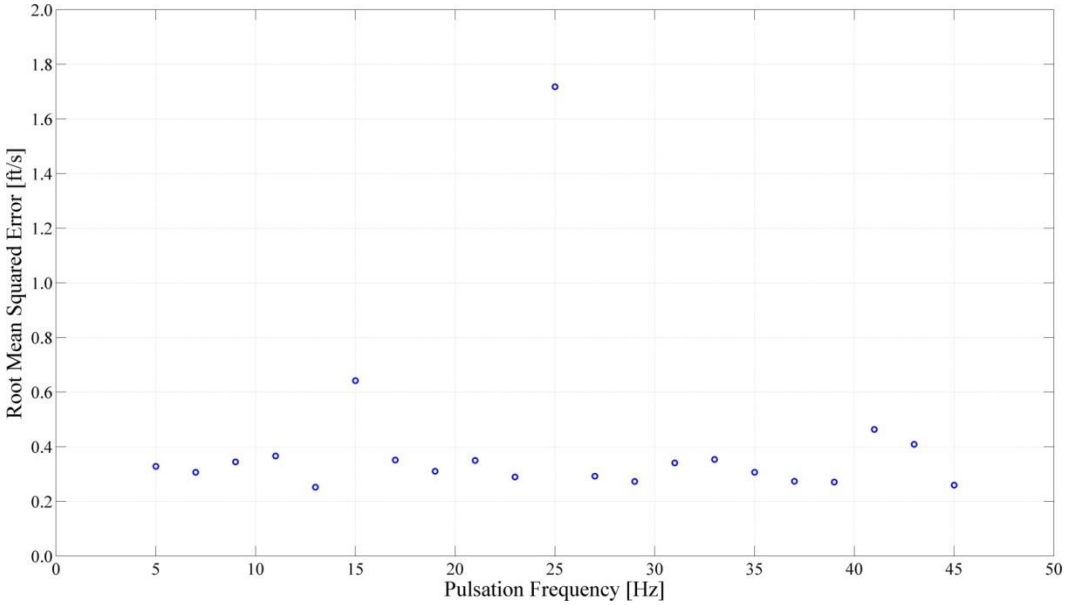

Figure 54. RMSE vs. frequency for the 200 acfm average velocity profiles

When these *RMSE* values are normalized by dividing by the maximum velocity amplitude shift, the plots in Figure 55 and Figure 56 are created.

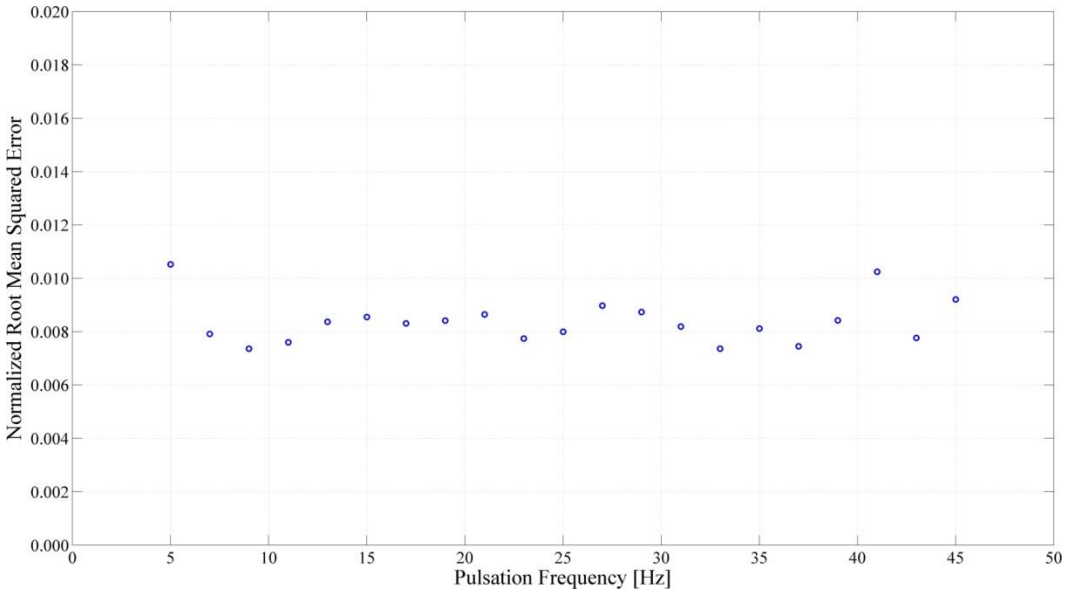

Figure 55. Normalized RMSE vs. frequency for the 700 acfm average velocity profiles

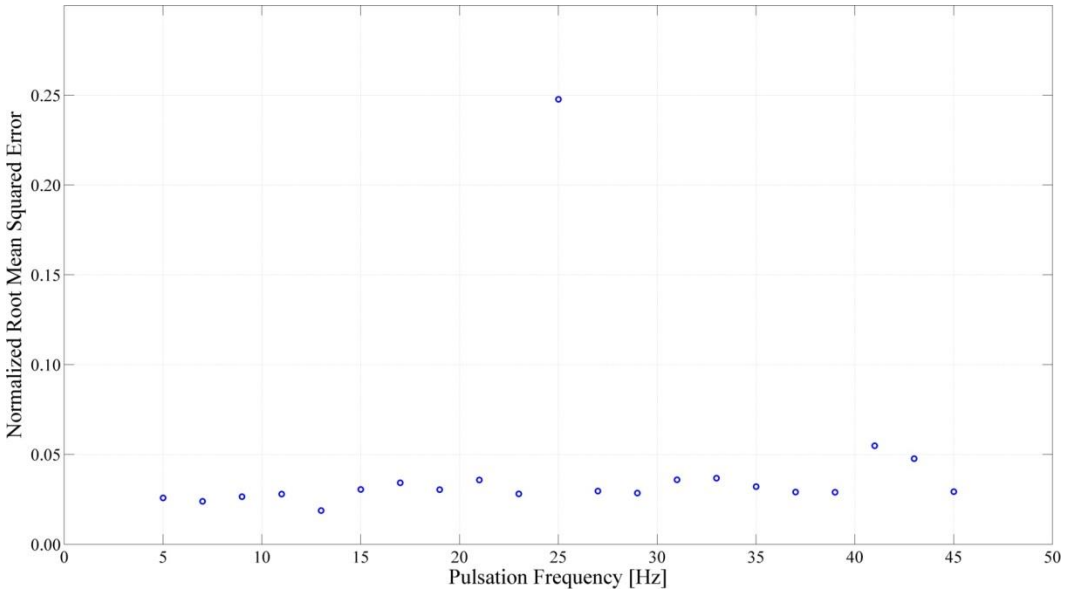

Figure 56. Normalized RMSE vs. frequency for the 200 acfm average velocity profiles

As shown in Figure 55 and Figure 56, the fits were adequate for all but one test condition: the 25 Hz pulsation at 200 acfm. To uncover the issue with this particular test condition, the individual residual analyses can be examined. An example of the residual analysis of a good fit, the 45 Hz pulsation at 700 acfm average flow velocity profile, is given in Figure 57.

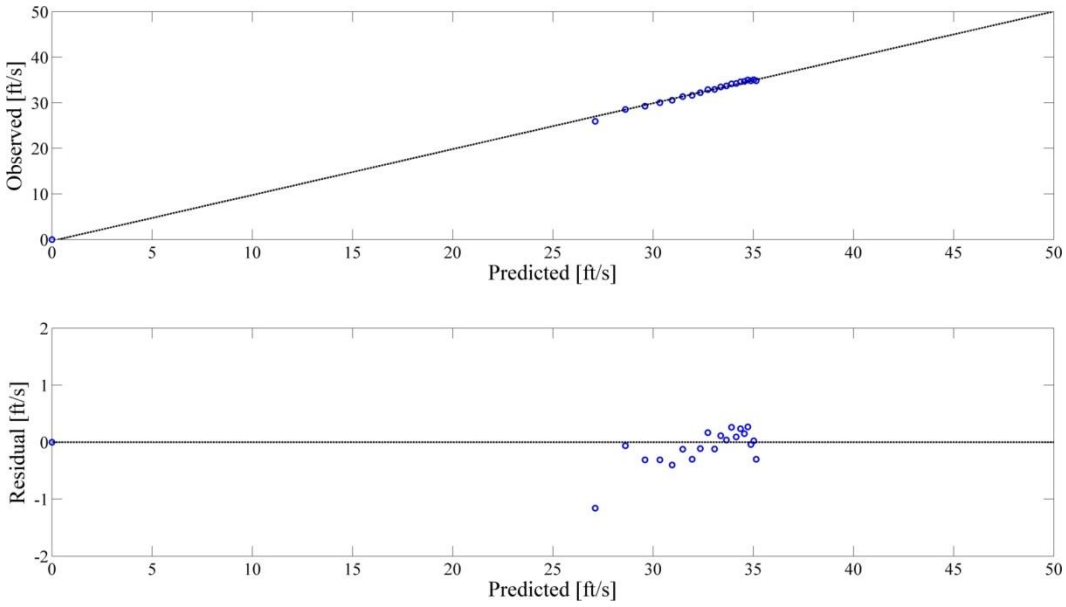

Figure 57. Residual analysis of average profile regression, 45 Hz at 700 acfm

The plot on the top of Figure 57 shows the observed (measured) velocity readings plotted against the predicted (fitted) velocity readings. For a perfect fit, the plotted markers would lie on top of the black dotted line. For this fit, the markers do not deviate greatly from the dotted line, indicating that the fit is reasonable. The bottom plot shows residuals plotted against the predicted velocity values. Here, a good fit shows roughly even vertical distribution and random placing. Although the residuals in this fit do appear to have a slight correlation with the expected value, the nature of the relationship is not strong or obvious (such as a linear or quadratic relationship). While it is not ideal, the regression fit for the 45 Hz average flow profile at 700 acfm is acceptable.

The residual analysis for the 25 Hz average flow profile fit at 200 acfm is given in Figure 58.

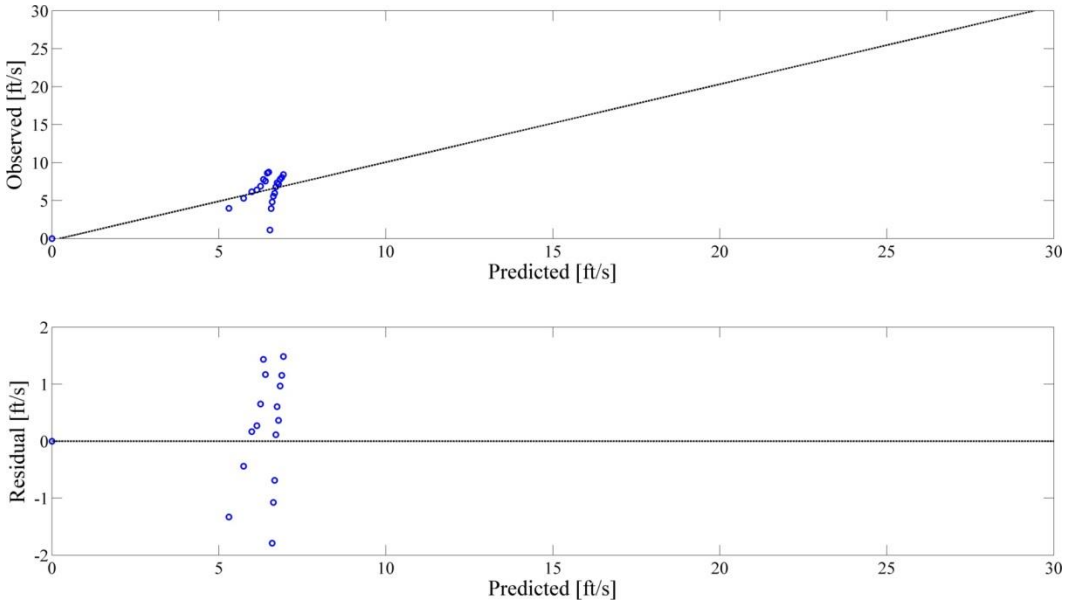

Figure 58. Residual analysis of average profile regression, 25 Hz at 200 acfm

Here, there is clear deviation from the dotted black line in the top plot, suggesting large differences between the observed and predicted values. The residuals in the bottom plot appear

to be centered at two predicted values, branching off into two almost perpendicular lines. This regression fit is clearly unsatisfactory. The reason why lies in the use of sinusoidal fits to determine the start of the pulsation cycles (Figure 51). An example sinusoidal fit for this test condition is shown in Figure 59.

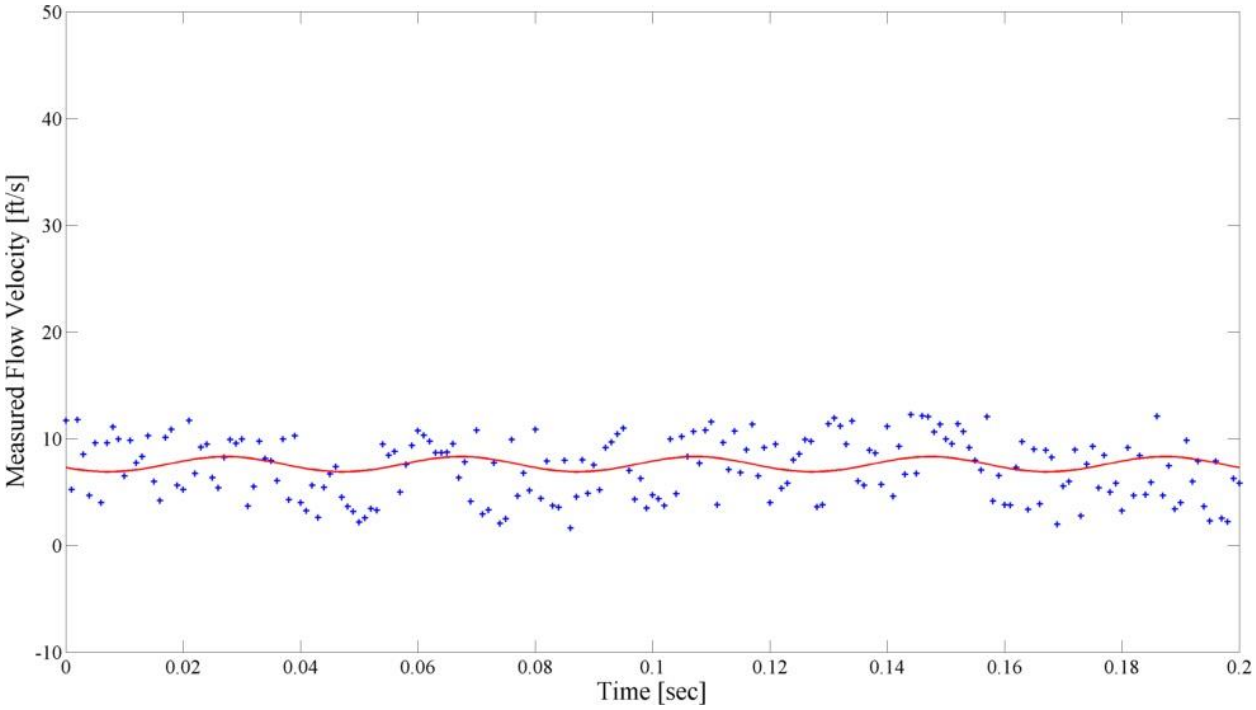

Figure 59. Sinusoidal fit to hot-wire anemometer output time series for 25 Hz, 200 acfm

By observation, the hot-wire anemometer time series is noisy for this frequency. A proper determination of the cycle start was not possible. This led to a poor velocity profile fit. The hot-wire anemometer did not appear to detect the 25 Hz pulsation wave. Examining Figure 39, this is understandable. The 25 Hz wave at 200 acfm had a relatively low pressure amplitude compared to the other waves. Based on the analysis that led to the relationship between pressure and velocity pulsations in Equation [12], it is reasonable to conclude that the low pressure magnitude correlated to a low velocity magnitude. The velocity magnitude for this wave was clearly too small for the hot-wire anemometer to resolve. The residual analyses for all average

flow profile regressions are provided in Appendix F. These reveal that the only unacceptable fit was for the 25 Hz, 200 acfm test condition.

By using the hot-wire anemometer data to construct time studies of profile changes, the first goal of this thesis, directly measuring the velocity profile shifts in natural gas flow subjected to pulsations, was achieved. These fits were generally validated by the statistical evaluations. This type of direct flow profile visualization was absent from the literature relevant to this field. The expected shifts in incompressible, laminar flow were modeled by Uchida in 1956, but the effects in compressible, turbulent flow were never analytically determined (Uchida 1956). Without the visual representation of the profile shifts, many members of the natural gas industry struggle to understand the effects pulsations have on flow and, by extension, flow measurement. Now, with the visualizations in Appendix E, it is possible to show the directly measured flow profile shifts in pulsating, elevated pressure natural gas flow.

Characterization of Velocity Pulsation Waves Using Pressure Measurements

In order to fully characterize the pulsation waves generated in the testing, the velocity pulsation maps must be determined in the same fashion as the pressure pulsation maps. This will allow the velocity nodes and antinodes to be located in relation to the test section features. The literature review found evidence that USMs are particularly susceptible to fluctuations in velocity. This implies that without the velocity component of the pulsation waves, the USM measurement error cannot be well correlated to the characteristics of the pulsation waves.

If the pressure pulsations are described as in Equation [5], mapping the velocity pulsation waves requires an important assumption made in simplifying Equation [11] to develop the velocity pulsation description in Equation [12] to hold true for the testing conditions. The simplest method of verifying this assumption is to calculate the Womersley number described in

Equation [9]. If it is large, the assumption is valid. For the experiments performed in this thesis, the natural gas fluid properties such as density and viscosity remained virtually constant and were recorded during testing. The average values for density and viscosity were 8.81 kg-m^{-3} and $5.92 \cdot 10^{-6}$ Pa-s respectively. Density was observed to vary less than 1.5% over the course of testing. Viscosity was calculated to vary less than 5% over the course of testing. The diameter of the piping was 8 in, meaning R = 0.1016 m. Because the dimensionless constant is positively correlated with frequency, the smallest value for the constant would appear at 5 Hz. Using these values, the dimensionless constant can be calculated to equal approximately 695, rounded down. Because this is large, it is safe to assume the velocity pulsation waves take the form of Equation [12]. (Equations [5], [9], [11], and [12] are reproduced below.)

$$-\frac{1}{\rho}\frac{\partial p}{\partial x} = K\ \cos(\omega t) = Ke^{i\omega t} \qquad [5]$$

$$\alpha = R\sqrt{\frac{\omega\rho}{\mu}} \qquad [9]$$

$$u(r,t) = \frac{K}{\omega}\left[\sin(\omega t) - \sqrt{\frac{R}{r}}exp\left(-\sqrt{\frac{\omega\rho}{2\mu}}(R-r)\right)\sin\left(\omega t - \sqrt{\frac{\omega\rho}{2\mu}}(R-r)\right)\right] \qquad [11]$$

$$u(r,t) \cong \frac{K}{\omega}\sin(\omega t) \qquad [12]$$

These equations were originally used by Uchida to plot the profile shifts shown in Figure 5 using a Womersley number of 5 (Uchida 1956). This describes a scenario very different from the pulsations generated in the course of this thesis. However, it is still meaningful to graphically compare the two profile shifts.

Uchida used Equation [38] to normalize the profiles and expressed the profile shifts in terms of $\frac{u}{\dot{c}}$ where $\dot{c}$ is a normalization factor in units of velocity. In Equation [38], *K* represents a constant and is related to the amplitude of the pressure wave in Equation [5]. The Womersley number is expressed as α and ω represents the pulsation frequency in rad/sec. For the analytical solution plotted in Figure 5, Uchida dropped *K* and ω, choosing to describe the profile shifts when the Womersley number was 5.

$$\dot{c} = \frac{K\alpha^2}{8\omega} = 3.125\frac{K}{\omega} \qquad [38]$$

For this experiment, the Womersley numbers were much greater, at a minimum of 695 as shown previously. At a pulsation frequency of 45 Hz and a flow rate of 700 acfm, the Womersley number is calculated to be 4172. Based on the piezoelectric pressure transmitter data, the magnitude of the pressure pulsations at the hot-wire location is known. In the case of the 45 Hz test condition at 700 acfm, the pulsation magnitude was 9.44 psi peak-to-peak. The value of *K* in this case would be equal to half that value, or 4.70 psi. Using that value, the Womersley number, and the known pulsation frequency (converted to rad/sec), the value of $\dot{c}$ is calculated to be $3.54 \cdot 10^7$ ft/sec.

By normalizing the profile shifts in Figure 52 with $\dot{c}$ and plotting them against a time series of the piezoelectric pressure transducer data, a plot similar to Figure 5 can be constructed for the pulsations measured in this experiment. Such a plot for the 45 Hz, 700 acfm test condition is shown in Figure 60. The pressure pulsation time series is shown in the lower plot. The profile shifts over time are shown in the top plot. The shaded area represents the flow profile. The dashed line is the time averaged flow profile.

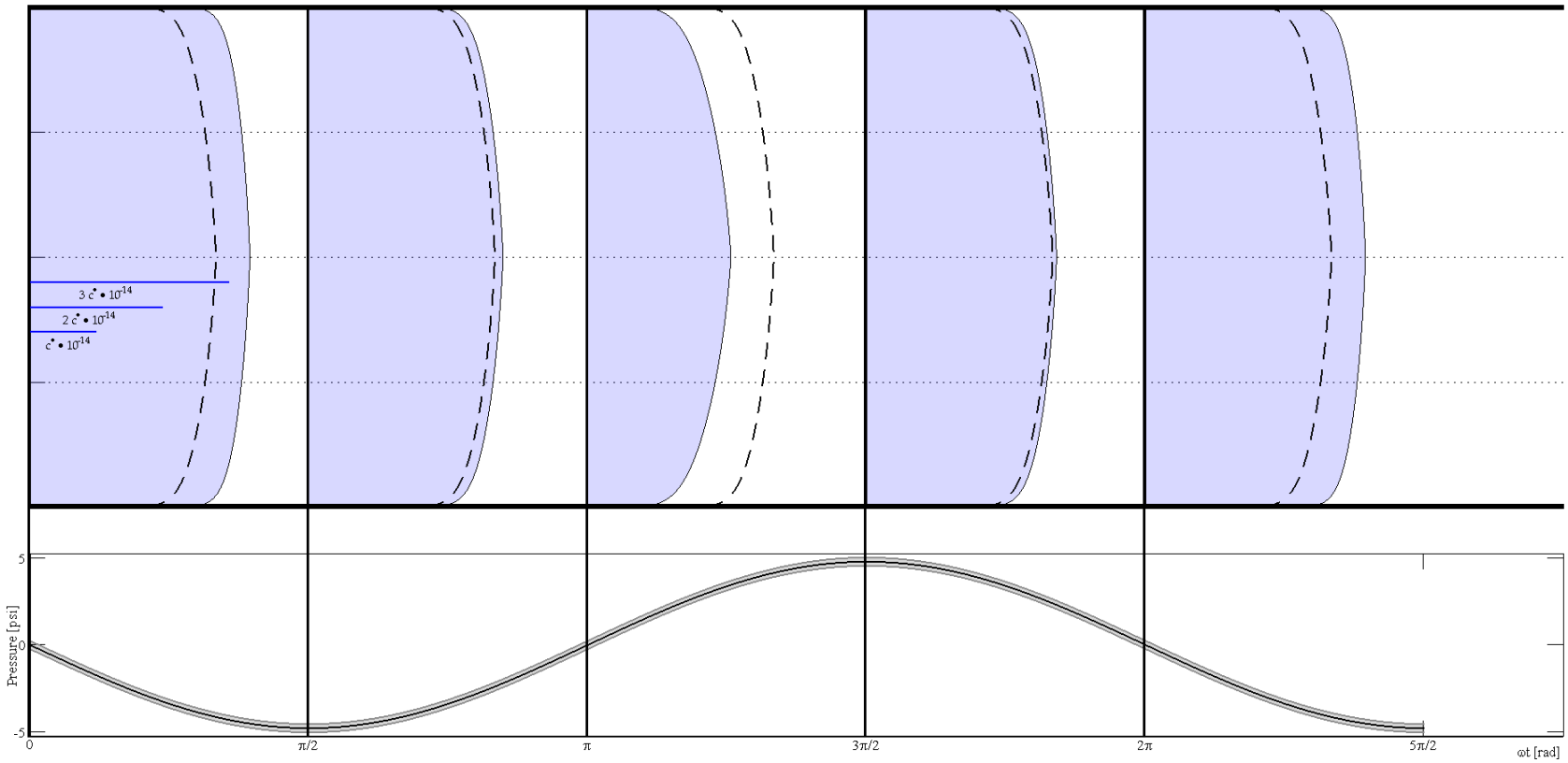

Figure 60. Profile Shifts and Pressure Pulsations: 45 Hz, 700 acfm

There are clear differences between Figure 5 and Figure 60. Most glaringly, the overall shape of the flow profiles do not change as drastically in Figure 60. Flow is always moving with positive velocity. Figure 5 shows complete inflection of the flow. This difference is also shown when observing the proportion of $\frac{u}{\dot{c}}$ in both plots. In Figure 5, the oscillations are on the order of 0.4 $\dot{c}$. In contrast, the oscillations in Figure 60 are on the order of 10^{-14} $\dot{c}$. Clearly for higher Womersley numbers (such as those for natural gas applications), the magnitude of the oscillations are smaller and do not cause flow inflections. Nevertheless, the 45 Hz, 700 acfm test condition still cause significant measurement error in the USM.

Using the description of the velocity pulsations in Equation [12], the pressure wave maps found earlier in this chapter ("Characterization of Pressure Pulsation Standing Waves") could be transformed by shifting the pulsation maps by 90 degrees. Although this would allow the velocity nodes and antinodes to be located, the actual velocity magnitudes cannot be determined using this method. Instead, normalized velocity maps can be created by dividing the magnitudes of the waves by the maximum overall pressure reading observed. As shown in [12] and as suggested by the hot-wire anemometer findings, the magnitude of a velocity pulsation are related to the magnitude of its pressure pulsation counterpart. By normalizing using the largest pressure reading, the velocity wave maps can be compared on a relative basis.

The normalized velocity pulsation maps for all tested frequencies in 700 acfm flow are shown in Figures 61, 62, and 63. The frequencies are split between the figures for clarity. Similarly, the velocity pulsation maps for all tested frequencies in 200 acfm flow are shown in Figures 64, 65, and 66. For these plots, the scale on the y-axis spans 0 to 1, with 1 signifying the highest measured magnitude. Each flow rate is normalized separately. This was done because

the pressure pulsation magnitudes observed in 200 acfm flow were considerably less the pressure pulsation magnitudes observed in 700 acfm flow. Normalizing the maps for both flow rates using the highest overall pressure magnitude would have resulted in the 200 acfm velocity pulsation maps being unreadable.

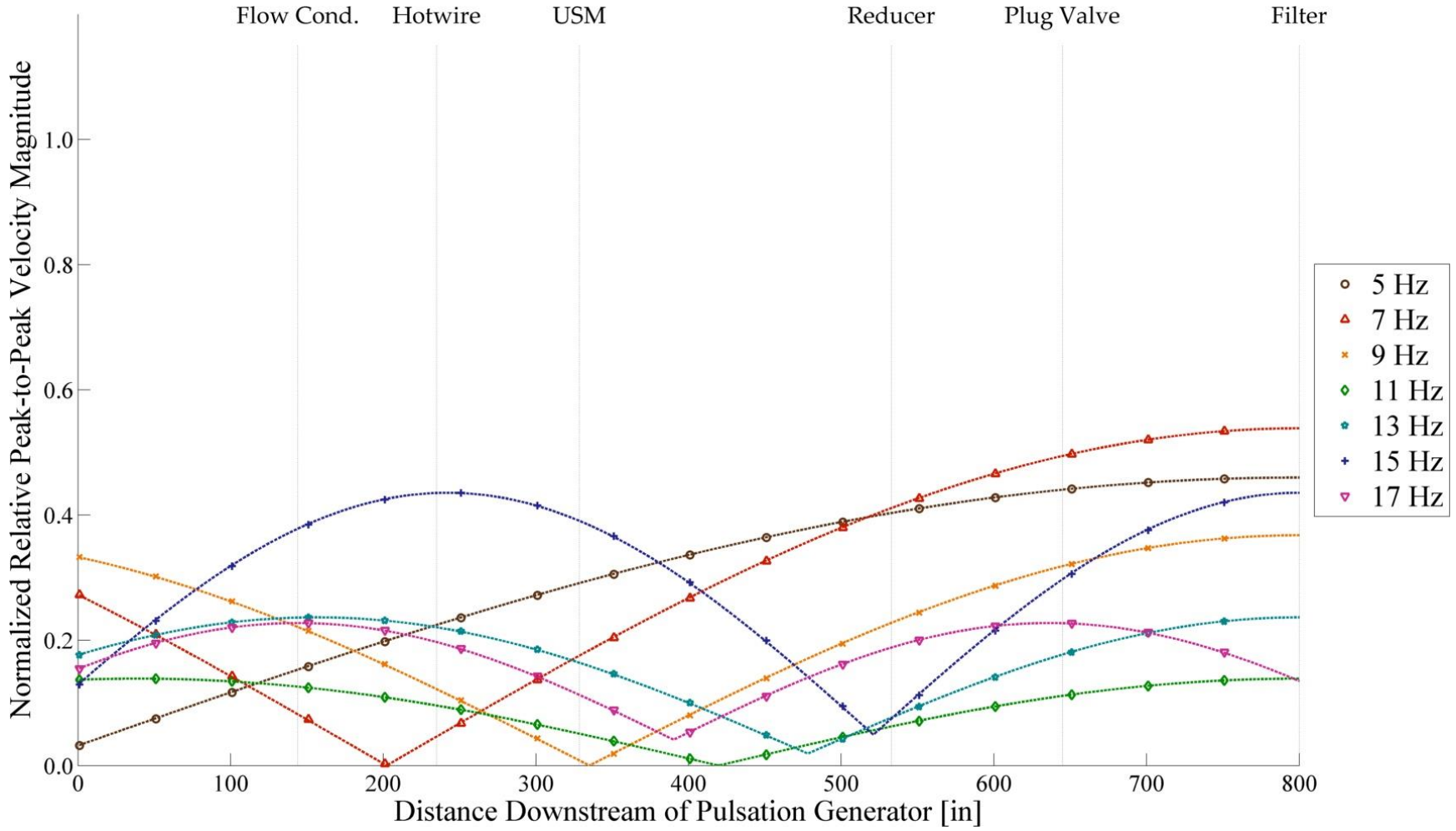

Figure 61. Normalized relative velocity pulsation maps for frequencies between 5 Hz and 17 Hz in 700 acfm flow

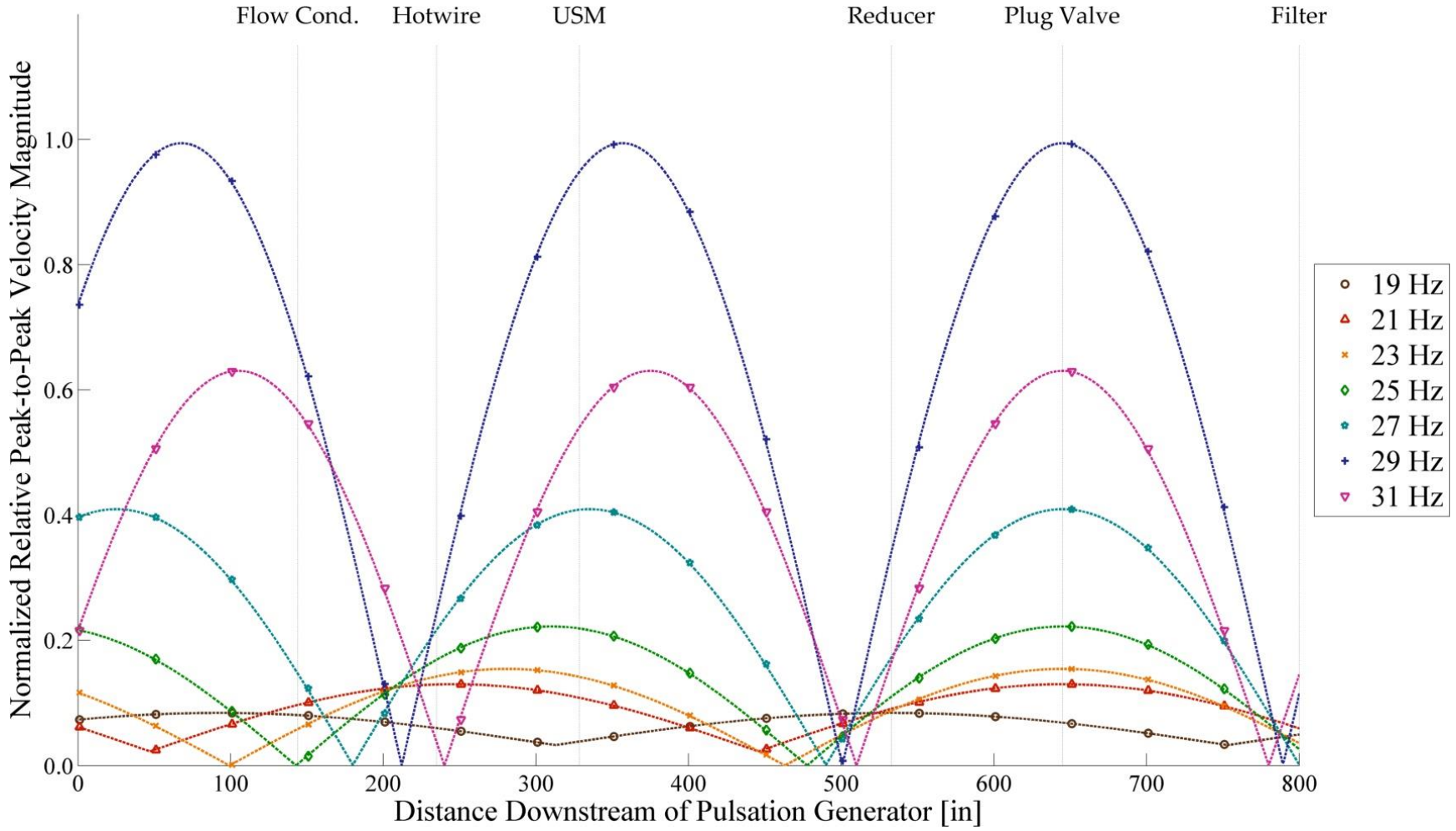

Figure 62. Normalized relative velocity pulsation maps for frequencies between 19 Hz and 31 Hz in 700 acfm flow

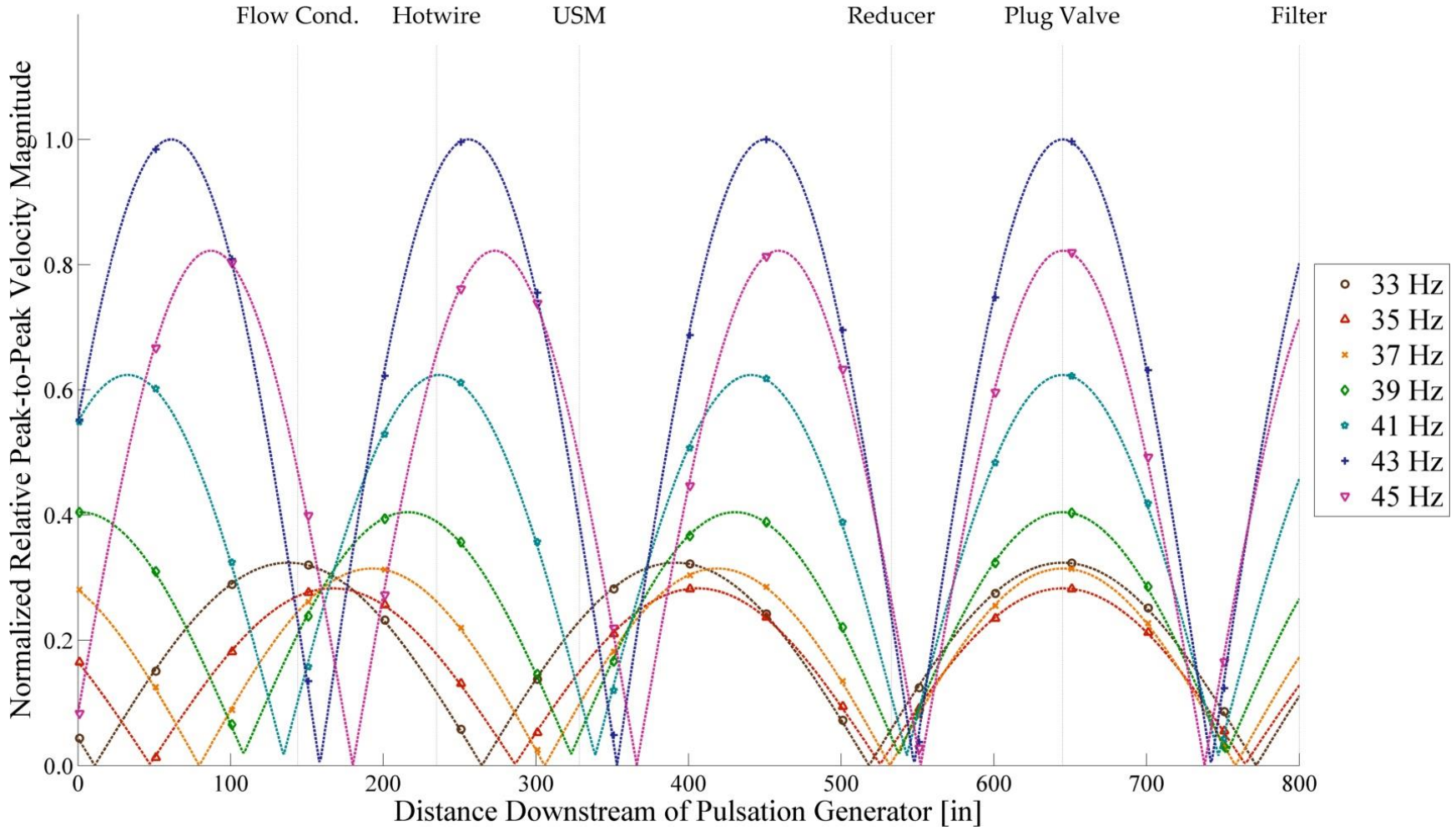

Figure 63. Normalized relative velocity pulsation maps for frequencies between 33 Hz and 45 Hz in 700 acfm flow

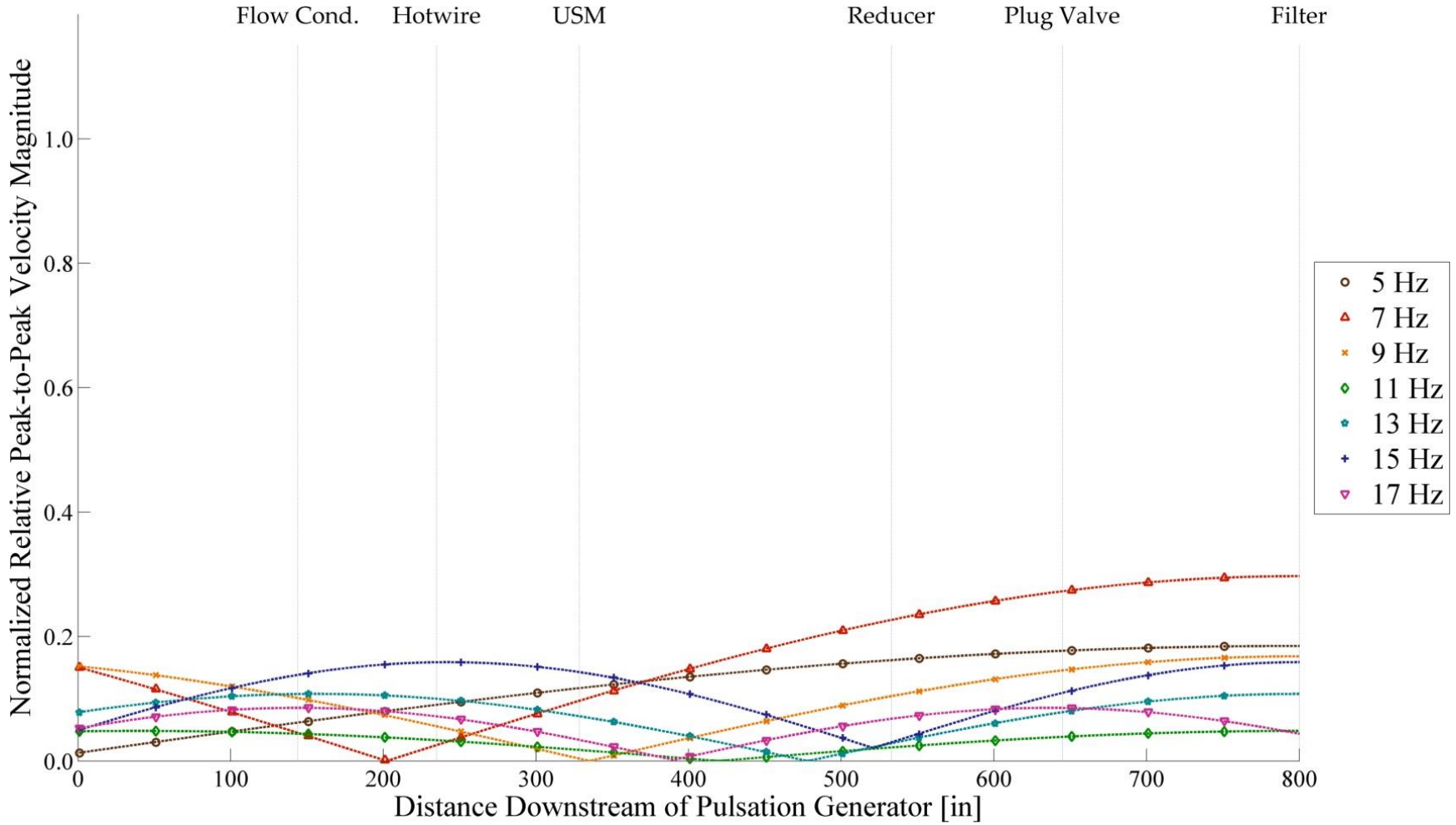

Figure 64. Normalized relative velocity pulsation maps for frequencies between 5 Hz and 17 Hz in 200 acfm flow

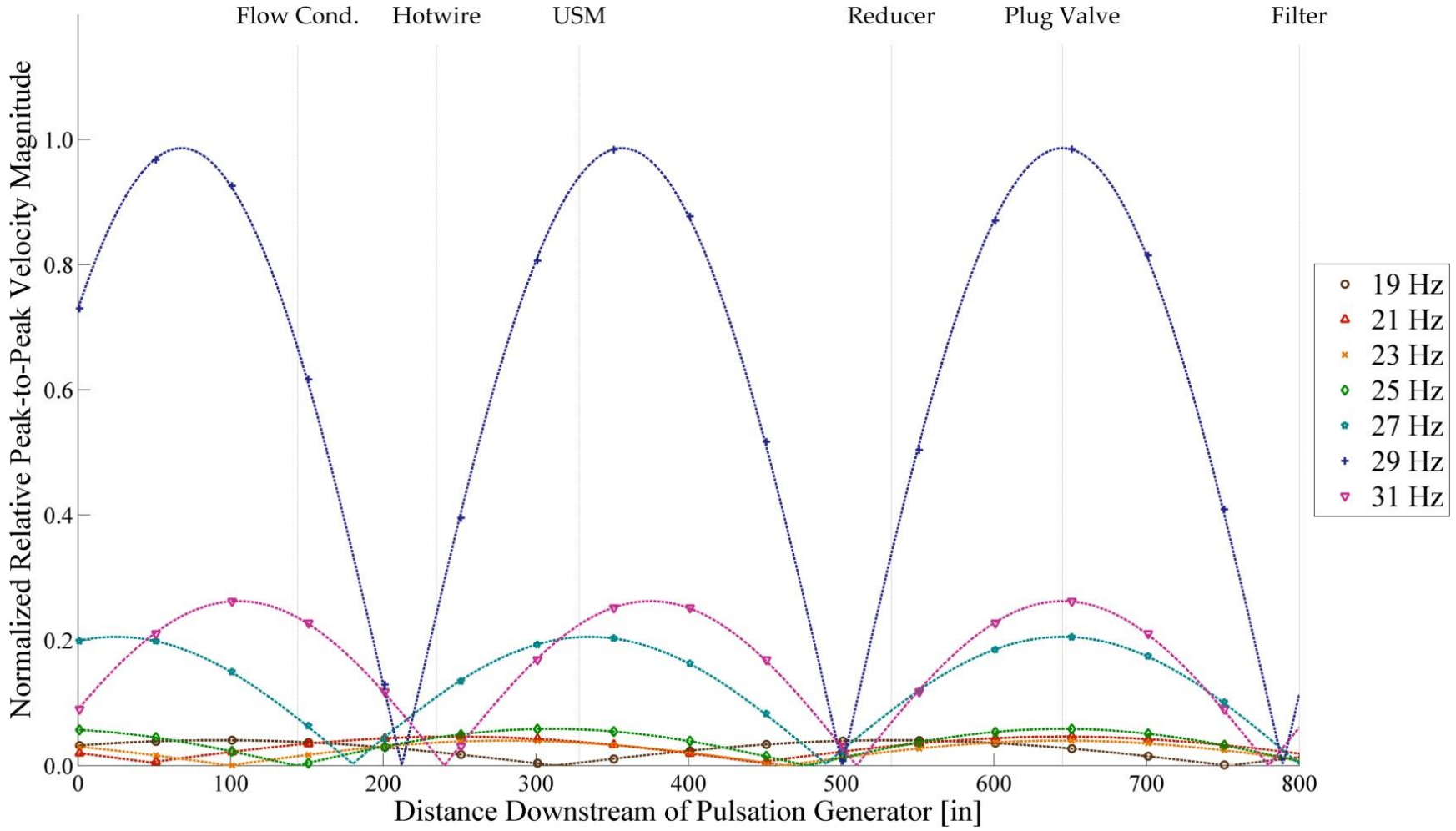

Figure 65. Normalized relative velocity pulsation maps for frequencies between 19 Hz and 31 Hz in 200 acfm flow

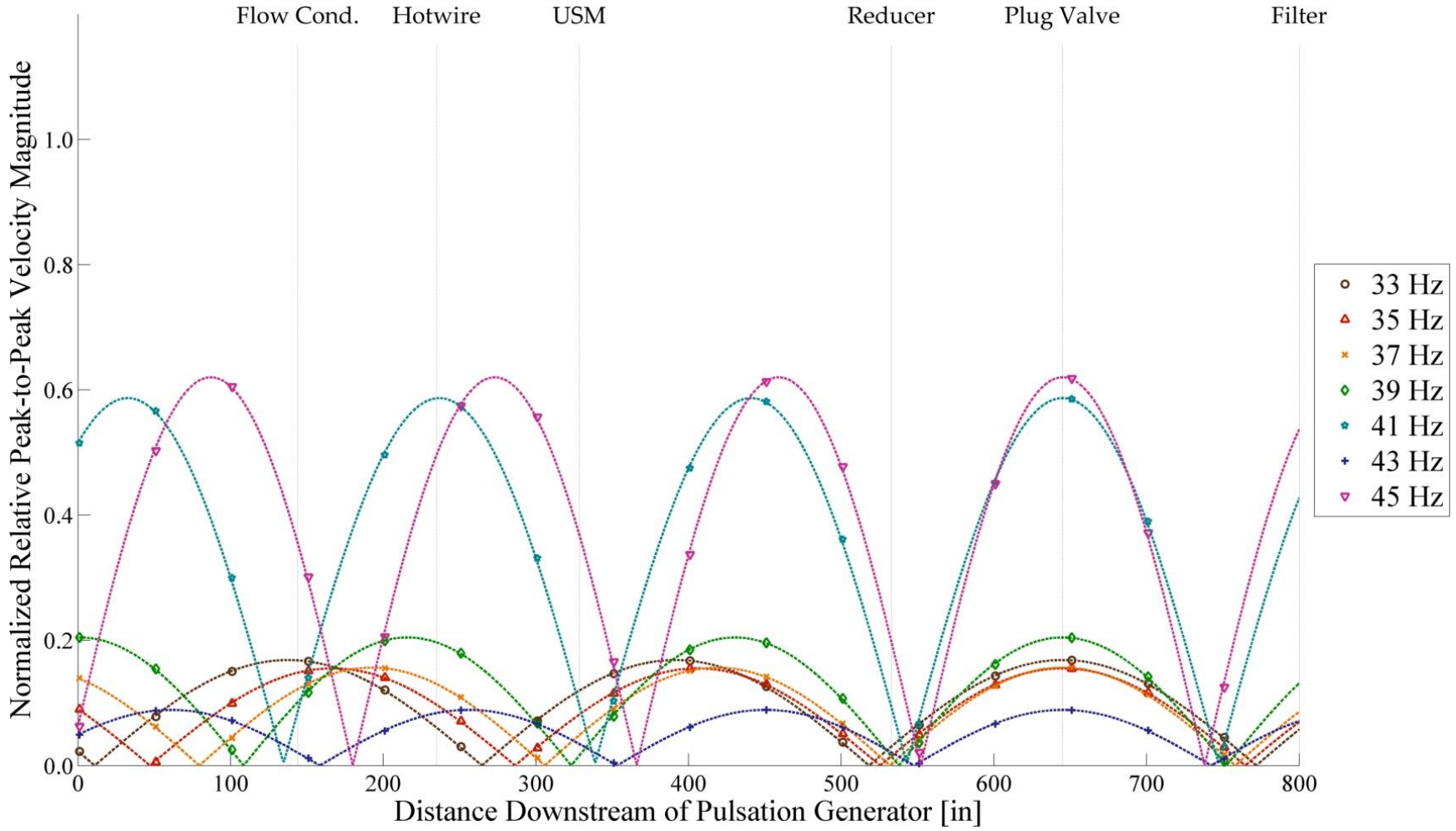

Figure 66. Normalized relative velocity pulsation maps for frequencies between 33 Hz and 45 Hz in 200 acfm flow

A cursory examination of the relative normalized velocity maps reveals the locations of the velocity antinodes that would threaten a USM measurement. For both flow rates, high amplitude peak-to-peak velocity fluctuations are present near the USM location for 27 Hz, 29 Hz, and 31 Hz frequencies. For these frequencies, this is due to the presence of a velocity antinode at or near the meter. High amplitude velocity fluctuations at the meter are also seen for 45 Hz and (for 700 acfm) 43 Hz frequencies. Conversely, a velocity node is located at or near the meter for 39 Hz and 41 Hz frequencies. In the meter error analysis in the final section of this chapter, a high error would be expected for the velocity antinode frequencies while low error would be expected for the velocity node frequencies.

As previously stated, the normalized velocity maps are unsatisfactory for fully characterizing the velocity component of the pulsation waves. Fortunately, the hot-wire anemometer data can be used to provide the missing velocity measurements. By using the peak-to peak velocity pulsation magnitudes measured by the hot-wire anemometer, the velocity maps can be scaled to the actual velocity magnitudes of the pulsation waves. In this process, each of the maps is normalized separately, dividing by the maximum pressure magnitude in the individual pressure pulsation map. The correctly scaled velocity pulsation map can be calculated by multiplying the normalized wave by the maximum peak-to-peak velocity pulsation magnitude measured at the hot-wire anemometer and dividing by the proportion at the hot-wire anemometer location.

The estimated velocity pulsation maps for all tested frequencies in 700 acfm flow are shown in Figures 67, 68, and 69. The frequencies are split between the figures for clarity. Similarly, the estimated velocity pulsation maps for all tested frequencies in 200 acfm flow are shown in Figures 70, 71, and 72.

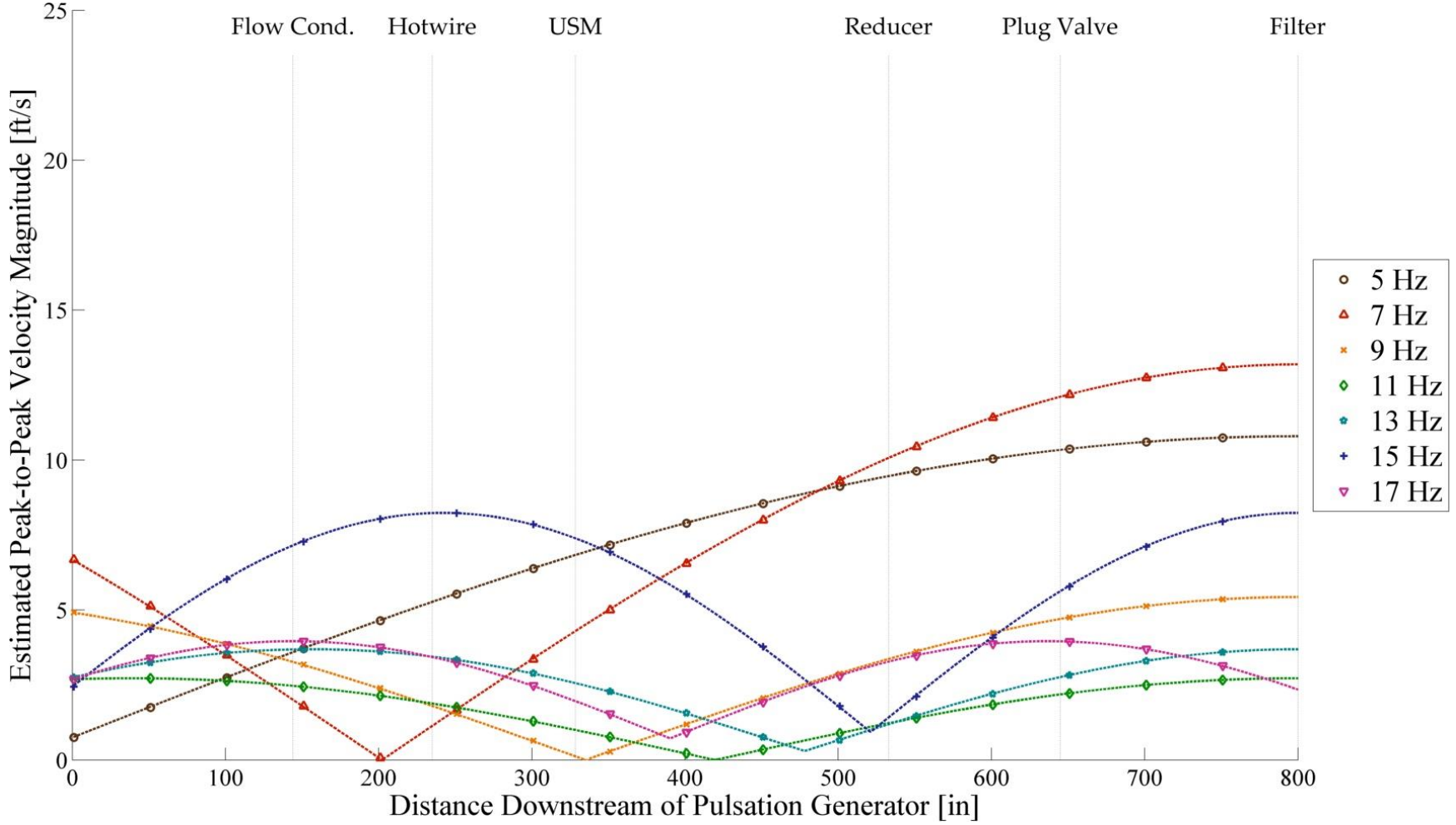

Figure 67. Velocity pulsation maps for frequencies between 5 Hz and 17 Hz in 700 acfm flow

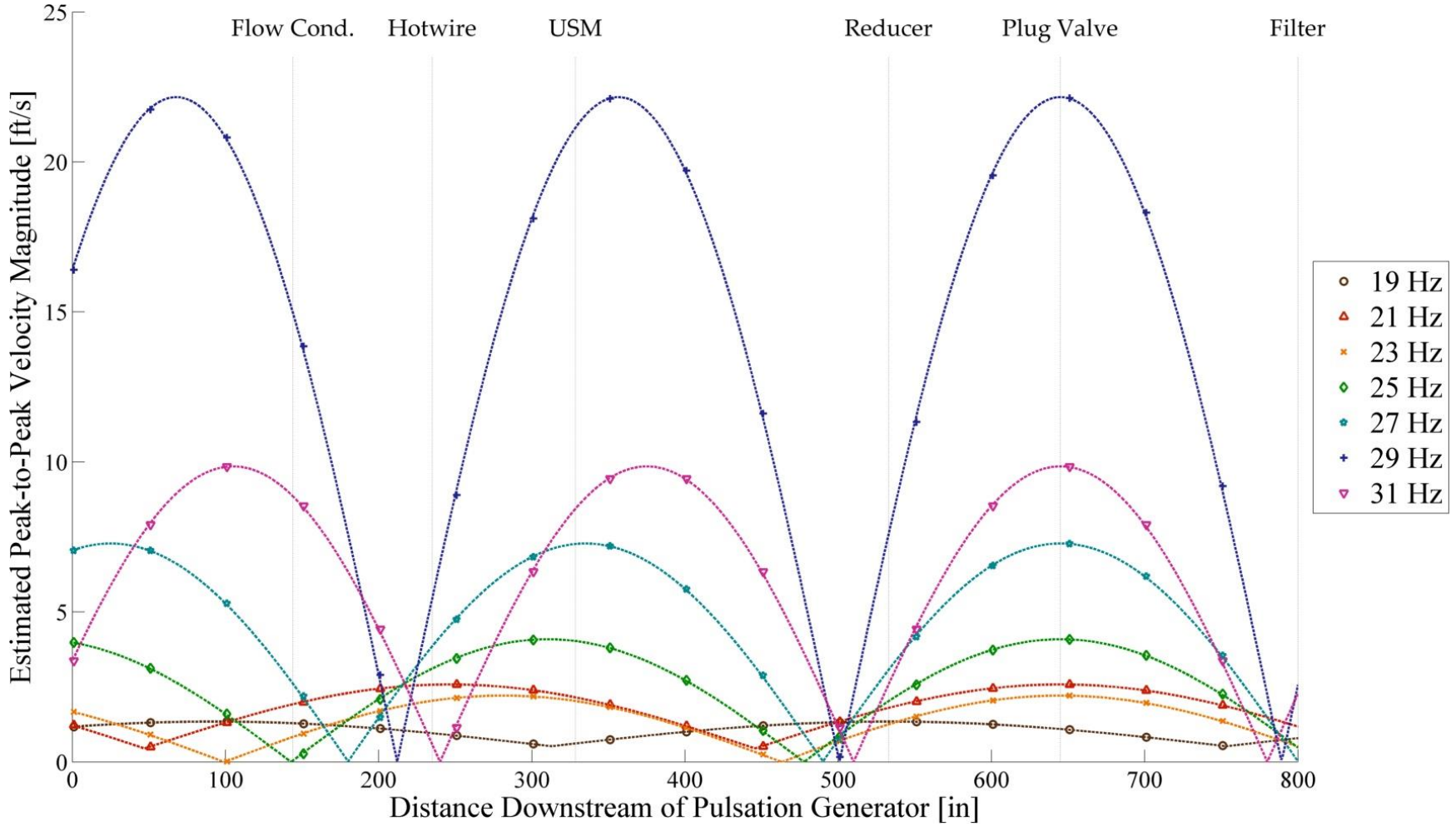

Figure 68. Velocity pulsation maps for frequencies between 19 Hz and 31 Hz in 700 acfm flow

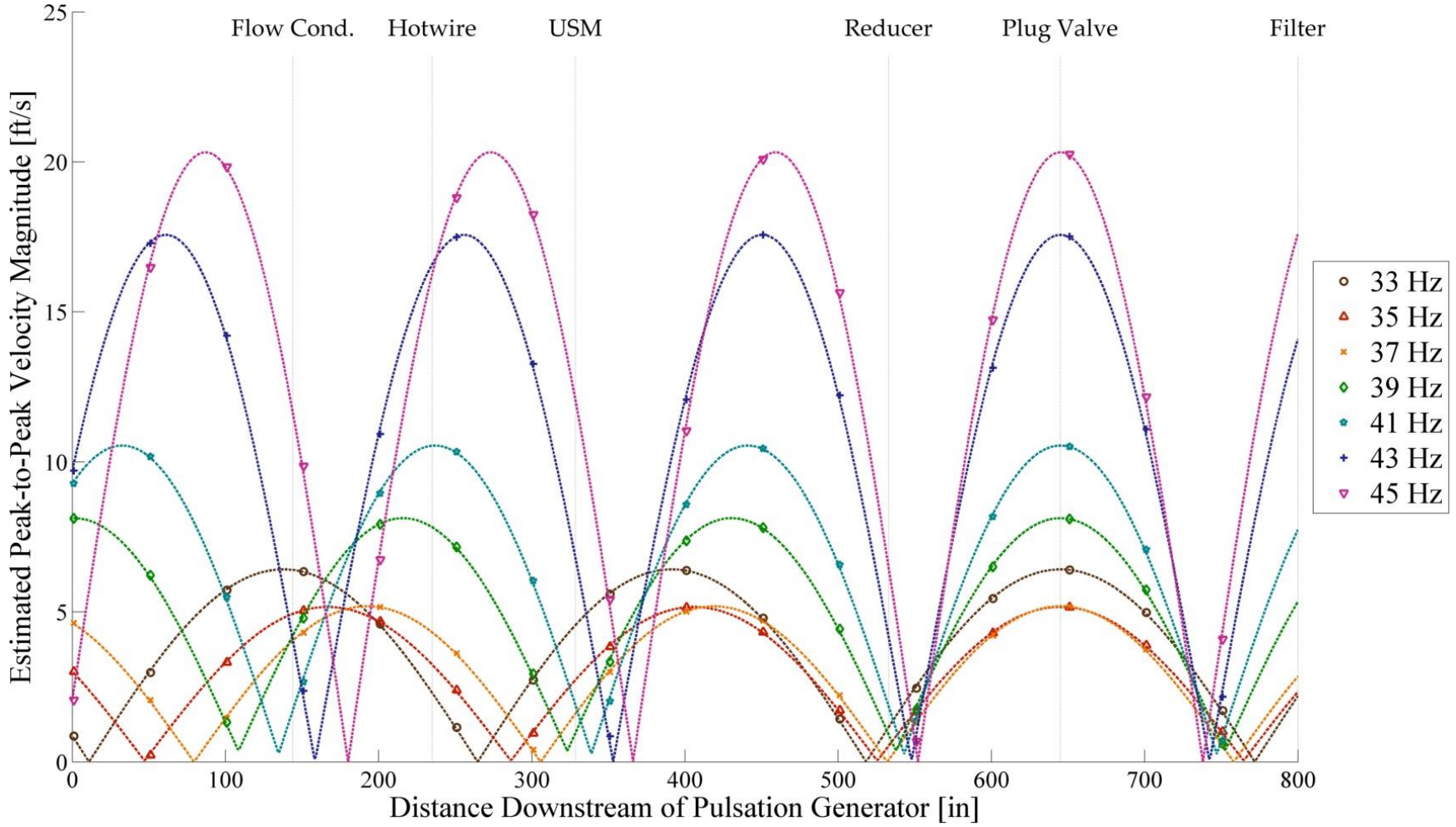

Figure 69. Velocity pulsation maps for frequencies between 33 Hz and 45 Hz in 700 acfm flow

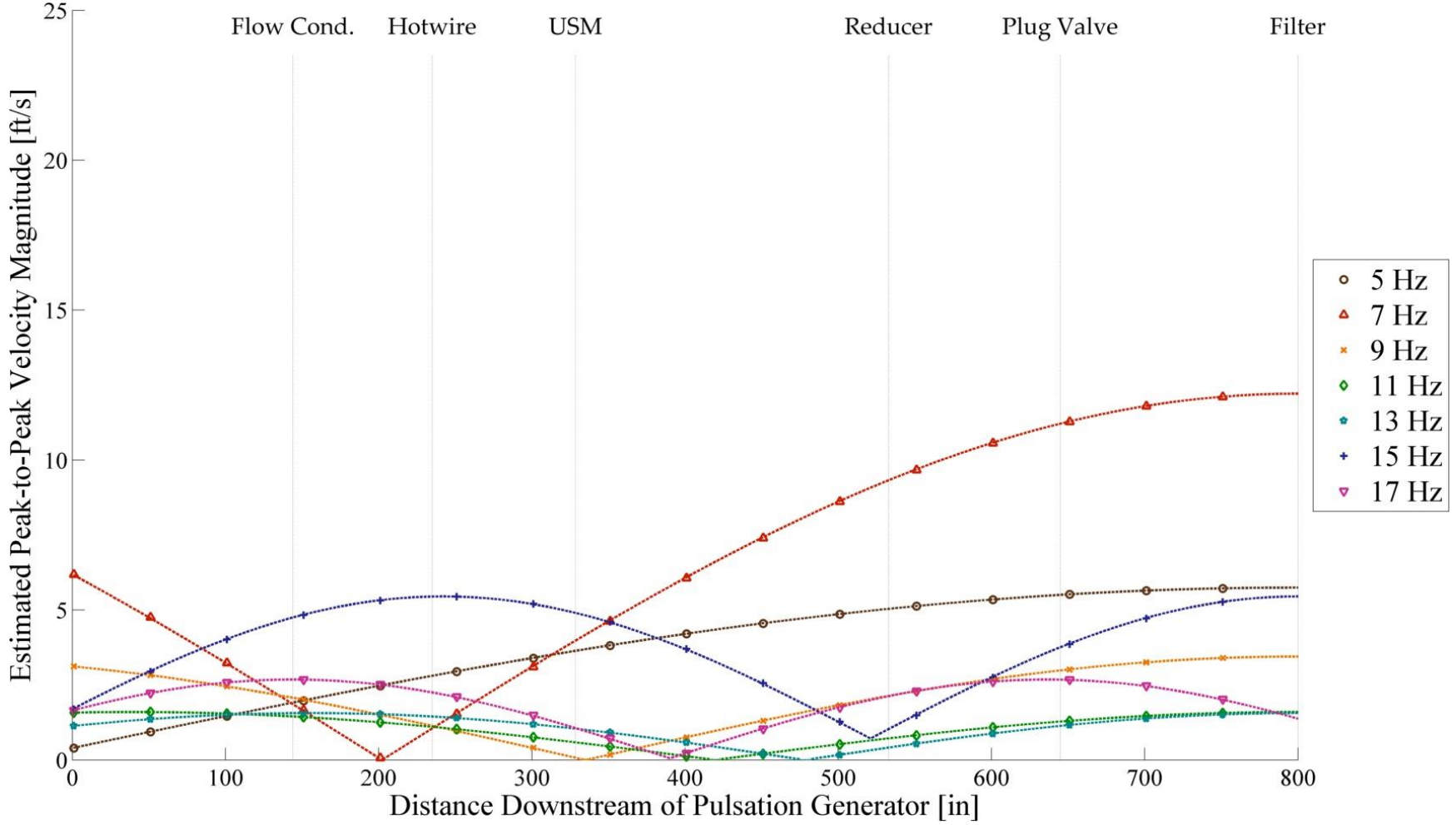

Figure 70. Velocity pulsation maps for frequencies between 5 Hz and 17 Hz in 200 acfm flow

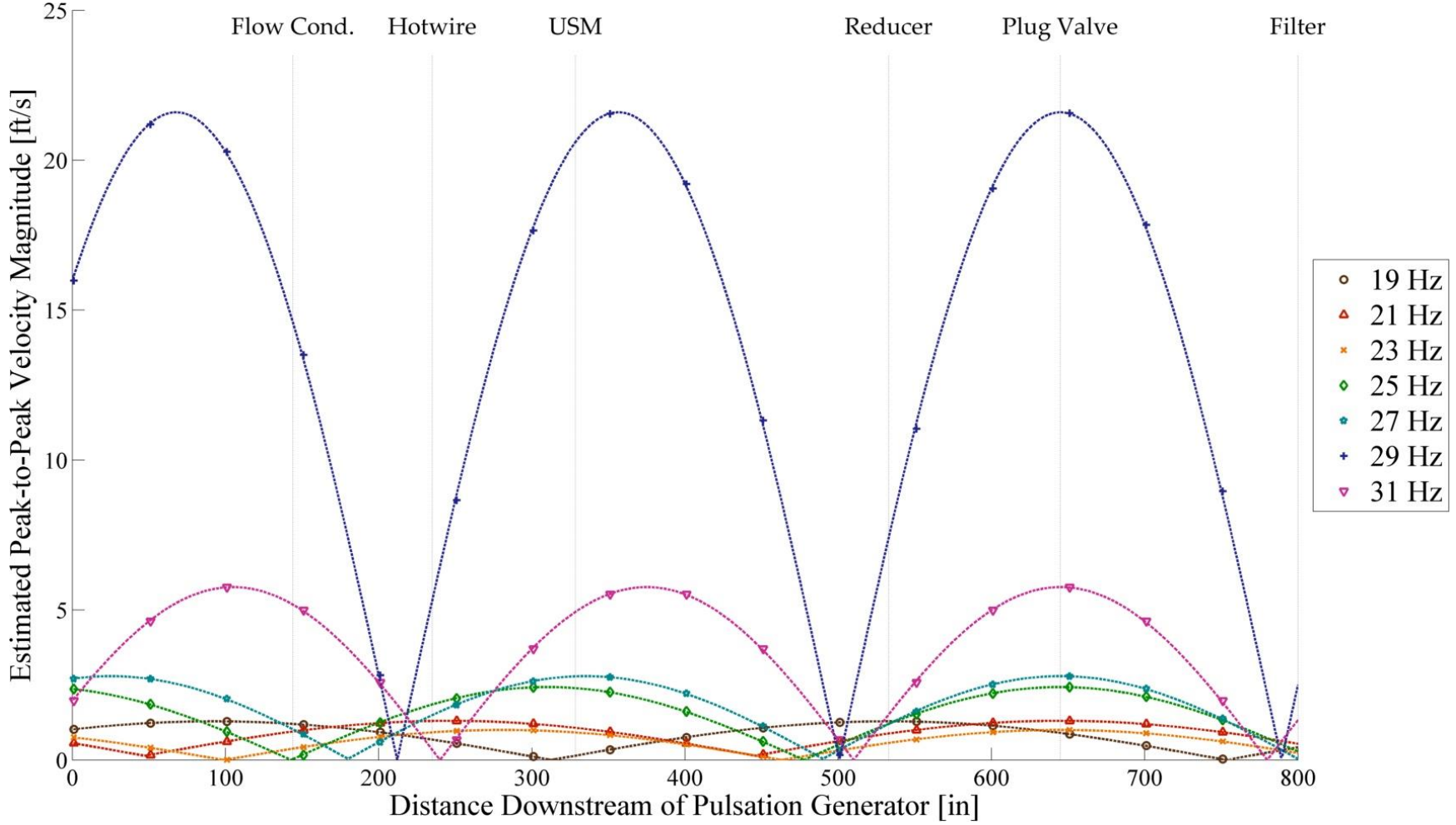

Figure 71. Velocity pulsation maps for frequencies between 19 Hz and 31 Hz in 200 acfm flow

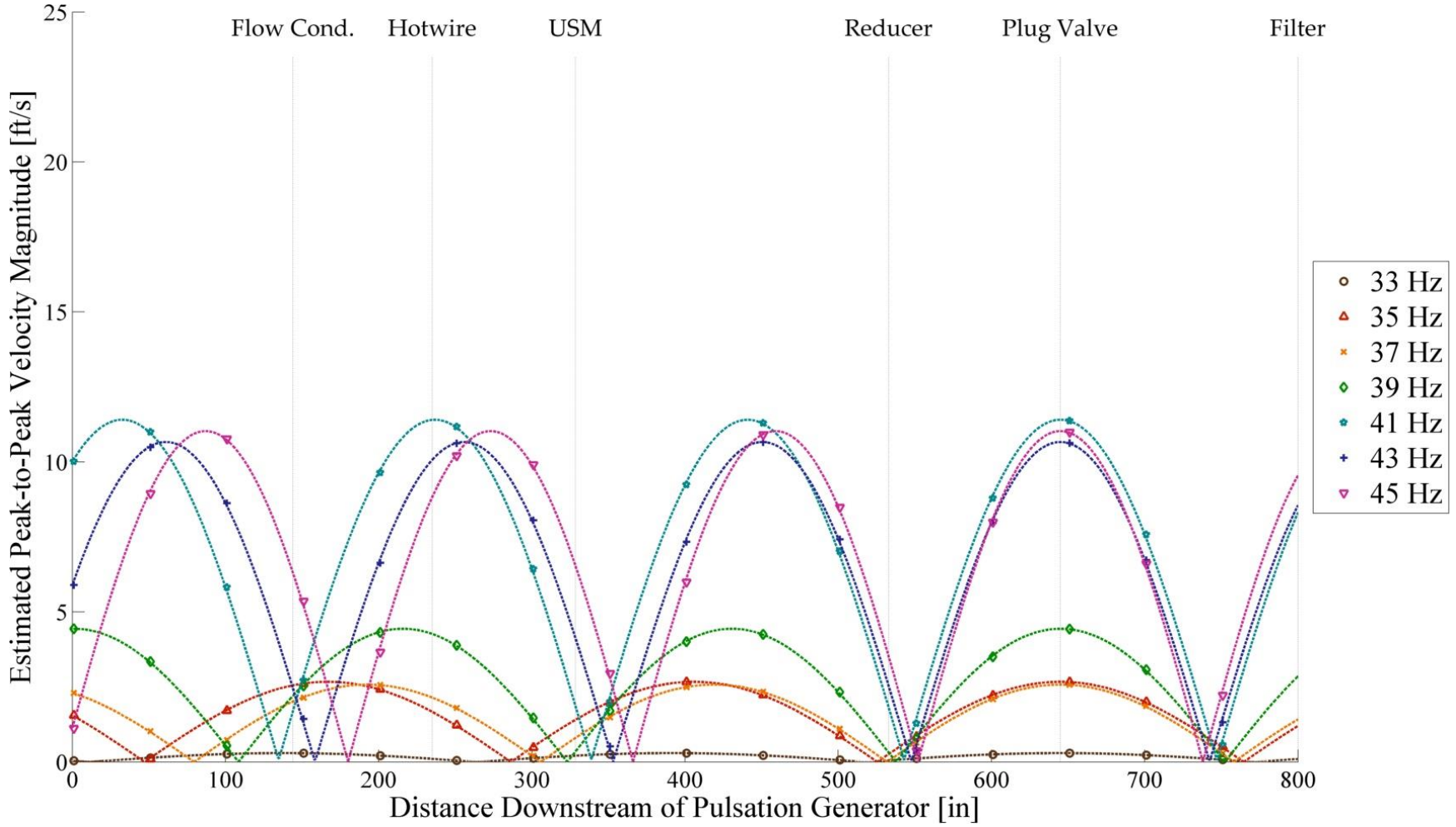

Figure 72. Velocity pulsation maps for frequencies between 33 Hz and 45 Hz in 200 acfm flow

The peak-to-peak velocity pulsation magnitude at the hot-wire anemometer was calculated as the average difference between maximum and minimum flow profiles across all hot-wire tip insertion positions, excepting the points at the pipe walls which were set to zero. Only the data were used; the profile fits were not considered in this calculation. The measure of the peak-to-peak velocity pulsation magnitude as an average across the profile was chosen because the differences between maximum and minimum flow velocity profiles differed by location relative to the pipe wall. Using a centerline peak-to-peak measure would not have been representative.

As an example of how this method works, suppose a normalized velocity wave shows that the peak-to-peak amplitude at the hot-wire anemometer is 0.5 of the maximum amplitude. Also, suppose the hot-wire anemometer measured a maximum peak-to-peak velocity pulsation magnitude of 5 ft/s. The correctly scaled velocity pulsation map is calculated by multiplying the normalized wave (scaled 0 to 1) by the maximum peak-to-peak velocity pulsation magnitude (5 ft/s) and dividing by the proportion at the hot-wire anemometer (0.5). In this example, the maximum peak-to-peak velocity pulsation would be equal to 10 ft/s (5 ft/s / 0.5).

For these plots, the units on the y-axis are ft/s, the units of the flow velocity and represent the peak-to-peak velocity pulsation magnitude along the standing waves mapped. It is worth noting here that the average flow velocities of 700 acfm and 200 acfm flows are 32.2 ft/s and 9.8 ft/s respectively. For pulsations of several frequencies at 200 acfm, the maximum peak-to-peak velocity magnitude exceeded the average flow velocity. Because these plots show peak-to-peak velocity magnitudes, this does not mean the flow was reversing direction. The amount by which the velocities were influenced in the positive and negative directions was half of the peak-to-peak magnitude.

The only test condition where the peak-to-peak velocity magnitude exceeded twice the average flow velocity was for the pulsation at 29 Hz in 200 acfm flow. The maximum peak-to-peak velocity magnitude in this test condition was approximately 22 ft/s, meaning the velocity was being modulated by approximately ±11 ft/s. For flow with an average velocity of 9.8 ft/s, this shows that the flow was potentially reversing direction at the velocity antinodes. The pulsation frequency of 29 Hz is especially significant as the velocity antinode is very near to the USM for both flow rates. Also, the 29 Hz pulsations had unusually high amplitudes, as shown by the pressure pulsation maps and corroborated by the velocity pulsation maps. Significant meter error would be expected for the 29 Hz pulsations.

With the creation of the velocity pulsation maps in Figures 67 through 72, the pulsations generated in the experiments are fully characterized. Both the pressure and velocity components of each wave are fully described for all pulsation frequencies and both flow rates. What remains is to relate these characterizations with the recorded USM measurement error.

Analysis of Ultrasonic Meter Measurement Error

Using the characterizations created in the previous section, the individual pulsation traits for each wave can be found. By comparing these traits to the observed USM measurement error, an algebraic relationship can be determined. This regression fit would relate measureable pulsation wave characteristics to meter error, allowing an end user to predict measurement error by measuring a pulsation wave. The regression fit would also provide a comprehensive method for determining which pulsation traits affect a USM and which do not. The goal of this is analysis is to move forward the public body of pulsation research such that USMs and USM meter runs can be improved with higher resistance to pulsation related measurement errors.

From the pulsation wave characterization, six candidate variables were identified or calculated for each test condition. These variables would then be included in the regression fit of USM measurement error. They included: the flow rate, the pulsation frequency, the maximum measured peak-to-peak pressure pulsation magnitude, the maximum measured peak-to-peak velocity pulsation magnitude, the measured peak-to-peak pressure pulsation magnitude at the USM location, and the estimated peak-to-peak velocity pulsation magnitude at the USM location. For each test condition, the values for the six variables are listed in Tables 6 and 7.

Table 6. Pulsation wave characterization and USM error, 700 acfm

Flow Rate (acfm)	Freq. (Hz)	Meter Error (%)	Maximum Pressure P-P Pulsation Amplitude (psi)	Maximum Velocity P-P Pulsation Amplitude (ft/s)	Pressure P-P Pulsation Amplitude at Meter (psi)	Estimated P-P Velocity Amplitude at Meter (ft/s)
700	5	0.11	5.69	5.27	4.37	6.84
	7	0.18	6.95	2.27	6.34	4.30
	9	0.02	4.56	1.80	4.59	0.12
	11	0.04	1.73	1.88	1.61	1.00
	13	0.13	2.99	3.44	2.24	2.56
	15	0.67	5.57	8.23	2.86	7.39
	17	0.07	2.98	3.43	1.16	1.96
	19	0.01	1.21	0.96	1.17	0.62
	21	0.18	1.87	2.58	1.01	2.15
	23	0.17	1.97	2.04	0.76	2.03
	25	0.40	2.87	3.11	0.47	4.03
	27	0.76	5.34	3.86	0.34	7.27
	29	1.58	12.82	5.47	3.69	21.15
	31	1.13	7.92	0.57	4.04	8.44
	33	0.63	3.96	2.30	2.83	4.57
	35	0.57	3.68	3.24	3.00	2.74
	37	0.37	4.11	4.31	3.73	1.62
	39	0.37	5.16	7.82	5.08	0.97
	41	0.47	7.81	10.54	7.71	1.88
	43	1.06	11.70	16.60	11.49	6.77
	45	2.16	9.44	16.28	8.25	12.03

Table 7. Pulsation wave characterization and USM error, 200 acfm

Flow Rate (acfm)	Freq. (Hz)	Meter Error (%)	Maximum Pressure P-P Pulsation Amplitude (psi)	Maximum Velocity P-P Pulsation Amplitude (ft/s)	Pressure P-P Pulsation Amplitude at Meter (psi)	Estimated P-P Velocity Amplitude at Meter (ft/s)
200	5	0.02	1.04	2.81	0.77	3.64
	7	0.04	1.71	1.05	1.51	3.98
	9	0.00	0.94	1.14	0.90	0.08
	11	0.01	0.27	1.10	0.24	0.59
	13	0.07	0.57	1.45	0.43	1.04
	15	0.27	0.92	5.45	0.42	4.90
	17	0.04	0.46	2.25	0.18	1.06
	19	0.01	0.23	0.68	0.22	0.14
	21	0.07	0.27	1.30	0.15	1.07
	23	0.07	0.22	0.92	0.09	0.92
	25	0.15	0.34	1.85	0.05	2.40
	27	0.28	1.18	1.50	0.07	2.79
	29	0.97	5.62	5.33	1.60	20.61
	31	0.42	1.47	0.34	0.73	4.94
	33	0.26	0.87	0.11	0.63	0.21
	35	0.26	0.85	1.67	0.71	1.41
	37	0.23	0.88	2.14	0.80	0.80
	39	0.28	1.15	4.27	1.09	0.35
	41	0.36	3.20	11.40	3.12	1.84
	43	0.57	0.46	10.07	0.44	4.11
	45	0.93	3.00	8.83	2.66	6.53

(Turbulence intensity was also analyzed, but was not included in the regression analysis. See Appendix H.)

Figure 73 shows a plot of the measured meter error against the gas flow rate. Although the range of errors observed is greater for the higher flow rate, no clear trends are present.

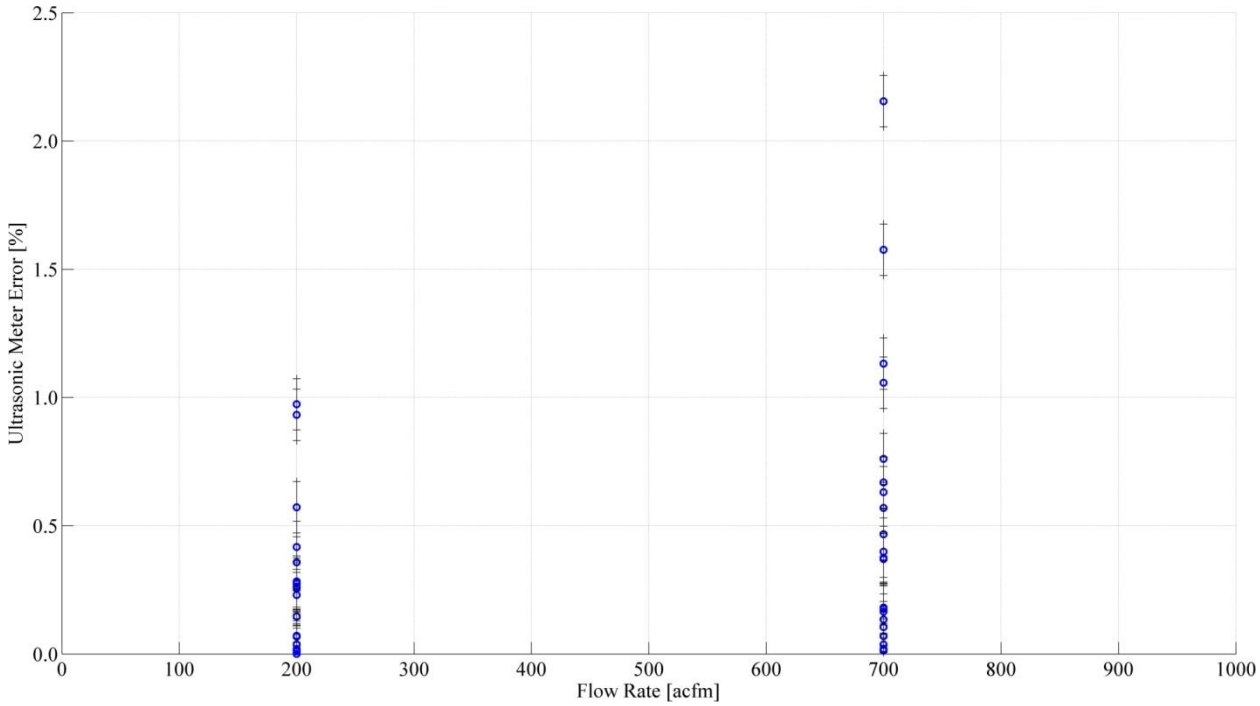

Figure 73. Flow rate vs. meter error

Figure 74 shows a plot of the measured meter error against the pulsation frequency. In general, the error seems to be positively correlated with pulsation frequency. However, another behavior can be seen in the plot. Peaks of higher error can be seen at 15 Hz, 29 Hz, and 45 Hz. These peaks do not agree with a linear or quadratic fit.

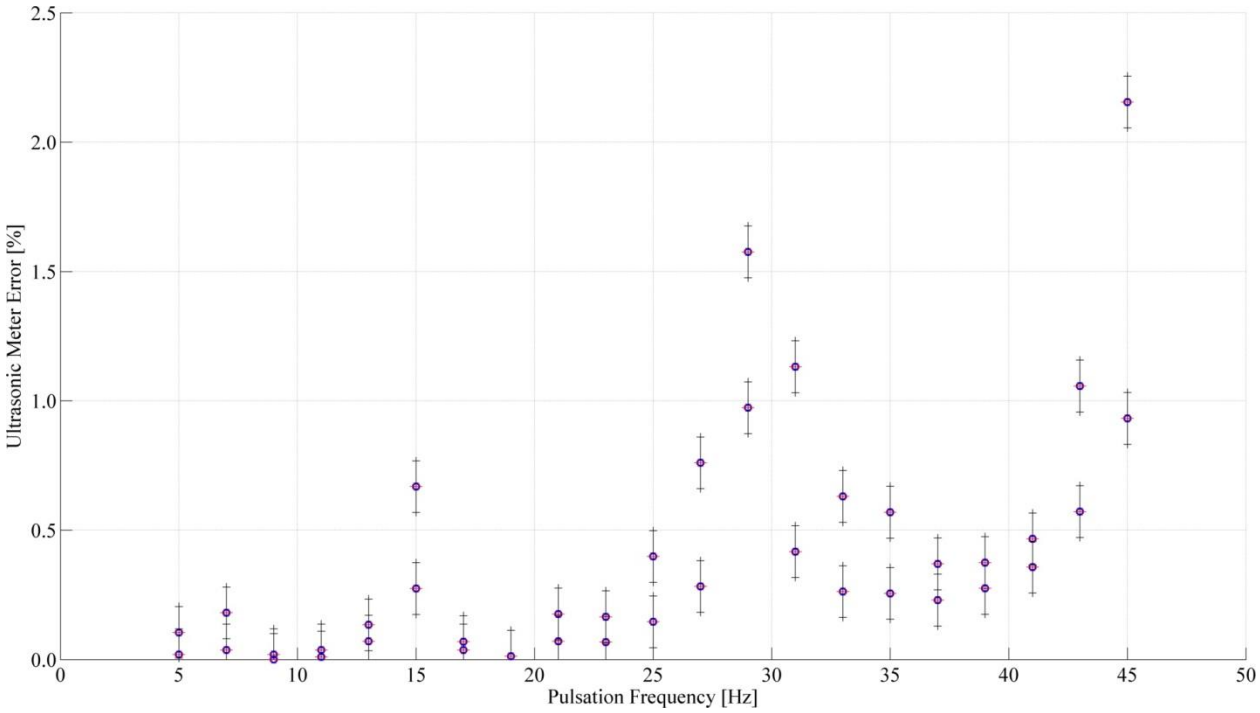

Figure 74. Pulsation frequency vs. meter error

Figure 75 shows a plot of the measured meter error against the maximum observed peak-to-peak pressure pulsation amplitude. The error generally correlates with the pressure pulsation amplitude, but there are clear deviations from an ideal fit. There are incidences of low observed error for amplitudes up to 7 psi. The highest error was observed at only the third greatest amplitude measurement.

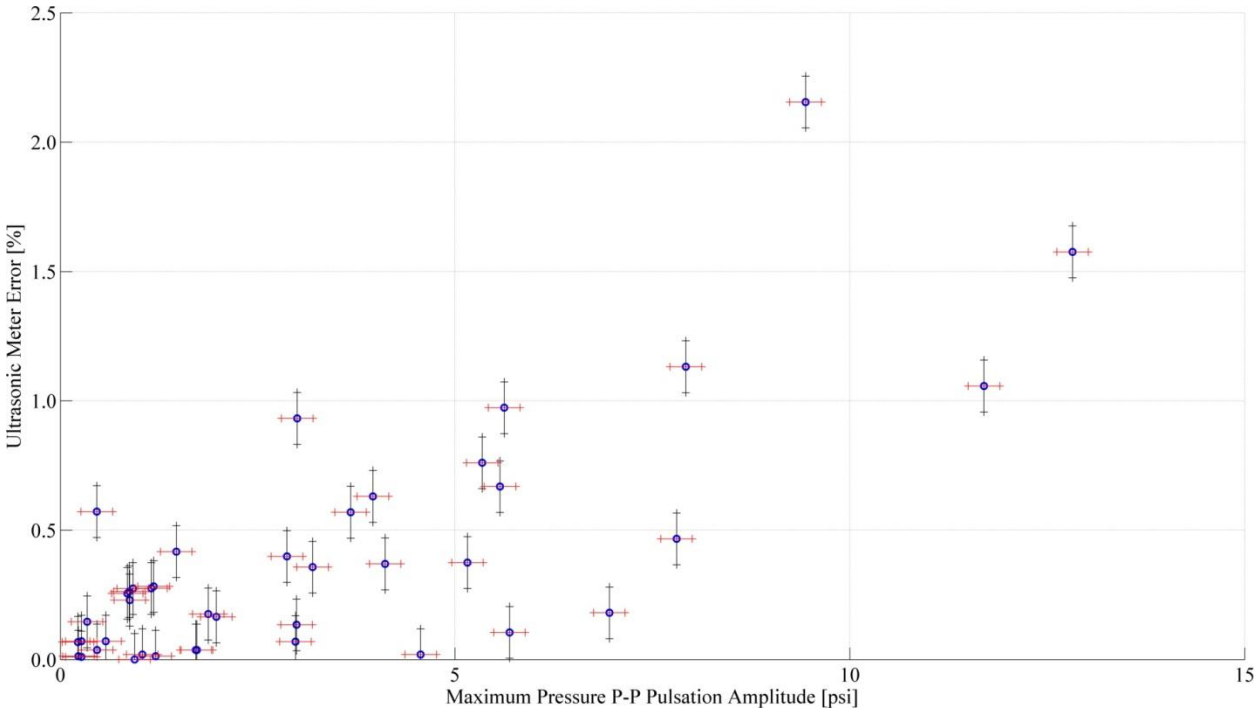

Figure 75. Maximum observed peak-to-peak pressure pulsation amplitude vs. meter error

Figure 76 shows a plot of the measured meter error against the maximum observed peak-to-peak velocity pulsation amplitude using the hot-wire anemometer. Again, there is a general positive correlation, but several deviations exist. The third greatest pulsation amplitude was observed for a test condition that resulted in an error of less than 0.5%. There are two incidences of error greater than 1% in the lower half of the amplitude range.

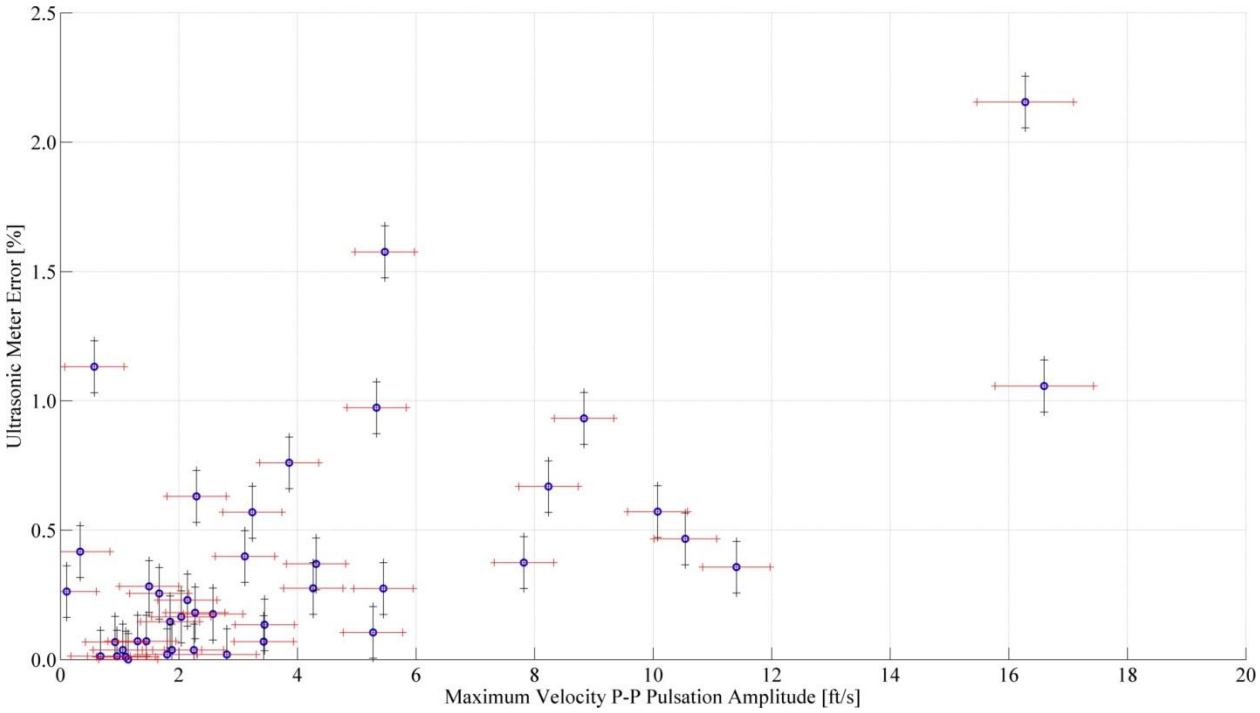

Figure 76. Maximum observed peak-to-peak velocity pulsation amplitude vs. meter error

Figure 77 shows a plot of the measured meter error against the average observed peak-to-peak pressure pulsation amplitude at the USM location. Consistent with the other variables, the pressure pulsation amplitude at the meter correlates positively with error. However, this variable provides the least convincing fit. It is more likely that the error is related to another factor that is similarly related to pressure pulsation at the meter. The maximum observed peak-to-peak pressure pulsation amplitude in Figure 75 provided a better correlation.

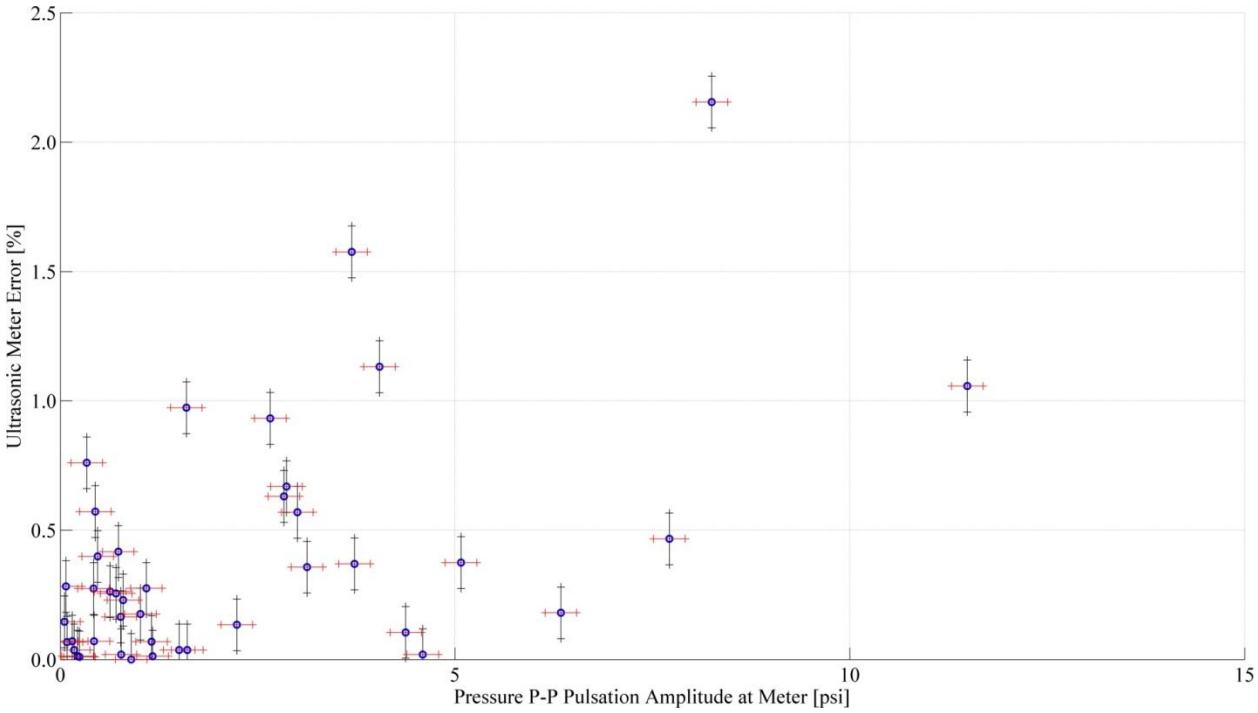

Figure 77. Average observed peak-to-peak pressure pulsation amplitude at the USM location vs. meter error

Figure 78 shows a plot of the measured meter error against the estimated peak-to-peak velocity pulsation amplitude at the USM location. These values were found as a product of the analysis in the previous section. Of all the six variables, this appears to correlate most closely with error. Finding that the velocity pulsations at the meter affect meter error is consistent with the prevailing knowledge of USMs. A strong change in the flow velocity profile is expected to lead to high meter inaccuracy.

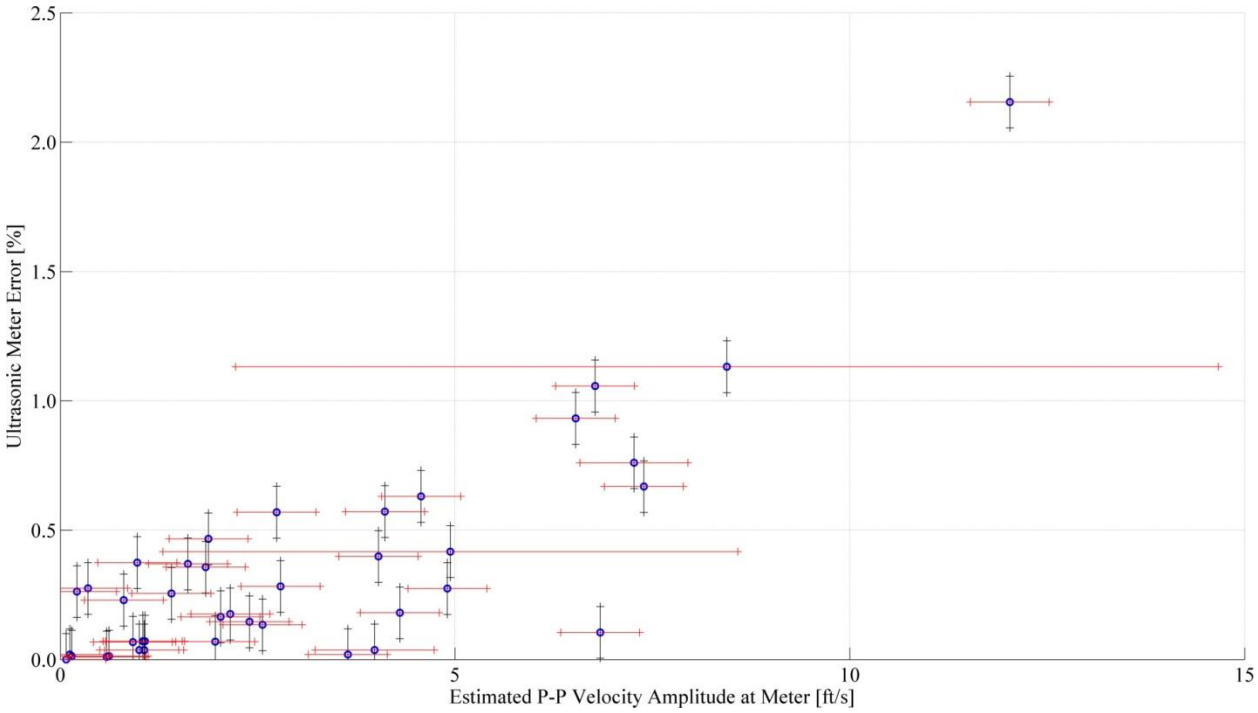

Figure 78. Estimated peak-to-peak velocity pulsation amplitude at the USM location vs. meter error

Clearly, no individual variable is capable of describing the relationship between a pulsation and the induced meter error. This is consistent with previous studies which predominantly explored fewer variables (refer to the Chapter 2 section titled "Ultrasonic Flow Meters and the Effects of Pulsation on Meter Accuracy"). Many previous studies were also unable to directly measure velocity pulsations in natural gas. These limitations led to inconclusive results that failed to predict meter error due to pulsating flow.

To find a more sophisticated relationship between the variables in Tables 6 and 7 and the measured meter error, a regression analysis was used. The REG procedure in SAS was employed to perform the regression analysis (the complete commented SAS code is provided in Appendix G). All of the 42 data points from Tables 6 and 7 were included in the analysis. (For the sake of the analysis, the uncertainties are ignored.) Equation [39] shows the regression model used, where *error* represents the measured meter error (the dependent variable in

question) and ε represents the model error. The regressors included in the model are *flowrate* (flow rate in acfm), *freq* (pulsation frequency in Hz), *maxpp* (maximum pressure peak-to-peak pulsation amplitude in psi), *maxvp* (maximum velocity peak-to-peak pulsation amplitude in ft/s), *meterpp* (the pressure peak-to-peak pulsation amplitude located at the meter in psi), and *metervp* (the estimated peak-to-peak velocity amplitude located at the meter in ft/s). The intercept of the regression model is denoted with θ_0. The regressor coefficients (parameters) are denoted with θ_i for *i* between 1 and 6 and correspond to the regressor variables in the order described above.

$$error = \beta_0 + \beta_1 flowrate + \beta_2 freq + \beta_3 maxpp + \beta_4 maxvp + \beta_5 meterpp + \beta_6 metervp + \varepsilon \quad [39]$$

The results of the regression analysis using the model in Equation [39] are given in the ANOVA and parameter estimates in Table 8.

Table 8. ANOVA and parameter estimates from regression analysis

Analysis of Variance					
Source	DF	Sum of Squares	Mean Square	F Value	Pr > F
Model	6	7.39643	1.23274	36.36	<.0001
Error	35	1.18660	0.03390		
Corrected Total	41	8.58303			

Root MSE	0.18413	R-Square	0.8618
Dependent Mean	0.38965	Adj R-Sq	0.8381
Coeff Var	47.25430		

Parameter Estimates					
Variable	DF	Parameter Estimate	Standard Error	t Value	Pr > |t|
Intercept	1	-0.35065	0.09793	-3.58	0.0010
flowrate	1	0.00010034	0.00018338	0.55	0.5877
freq	1	0.01425	0.00292	4.88	<.0001
maxpp	1	0.02902	0.03950	0.73	0.4673
maxvp	1	0.01269	0.01267	1.00	0.3233
meterpp	1	-0.00260	0.03636	-0.07	0.9435
metervp	1	0.05097	0.01446	3.52	0.0012

At a 0.05 (95%) significance level, the ANOVA p-value in Table 8 (presented as <.0001) reveals that at least one of the regressors in the model significantly affects the meter error. The results also show a promising R^2 of 86.18%. Other aspects suggest an unsuitable fit, however. Looking at the parameter estimates, the p-values for many regressors exceed 0.05 meaning that the model contains unneeded regressor variables. The coefficient of variation (Coeff Var) is 47.25, high enough to signify collinearity between the regressor variables (Montgomery 2012). The collinearity can be explored further by examining the collinearity diagnostics in Table 9.

Table 9. Collinearity diagnostics from regression analysis

Collinearity Diagnostics (intercept adjusted)								
			Proportion of Variation					
Number	Eigenvalue	Condition Index	flowrate	freq	maxpp	maxvp	meterpp	metervp
1	3.30228	1.00000	0.01343	0.01379	0.00433	0.01864	0.00698	0.00610
2	1.16484	1.68374	0.10552	0.27260	0.00189	0.03769	0.00047445	0.00029750
3	0.85178	1.96899	0.05180	0.01439	0.00148	0.00676	0.01124	0.15316
4	0.43712	2.74858	0.22152	0.57911	0.00006567	0.15993	0.02793	0.00345
5	0.21349	3.93293	0.31330	0.06727	0.02691	0.62009	0.12049	0.01065
6	0.03050	10.40577	0.29442	0.05285	0.96533	0.15689	0.83289	0.82634

The only eigenvector of concern is number six, with a condition index of 10.4. The next highest condition index is 3.93, not indicative of collinearity (Montgomery 2012). Eigenvector six shows that there exists a collinearity between *maxpp*, *meterpp*, and *metervp*. The final regression fit should not contain all three of these regressor variables.

Table 10 shows a normality analysis of the residuals of the regression fit. Using the Shapiro-Wilk test at a 0.05 significance level, a p-value of <.0001 shows that the residuals are not normally distributed. For a regression fit to be considered valid, the residuals must be normally distributed (Montgomery 2012).

Table 10. Normality analysis of regression fit

Tests for Normality				
Test	Statistic		p Value	
Shapiro-Wilk	W	0.664529	Pr < W	<0.0001
Kolmogorov-Smirnov	D	0.248489	Pr > D	<0.0100
Cramer-von Mises	W-Sq	0.680938	Pr > W-Sq	<0.0050
Anderson-Darling	A-Sq	3.833677	Pr > A-Sq	<0.0050

Figure 79 shows a plot of the Studentized residuals from the regression analysis plotted against the predicted meter value error. For a valid regression fit, the residuals should show no relationship to the predicted value. The variance should be constant with respect to the predicted value. In this case, the residuals fan outwards as the predicted value increases. Additionally, the plot highlights three potential outliers in points 14, 21, and 34. These correspond to the following test conditions respectively: 700 acfm with 29 Hz pulsations, 700 acfm with 45 Hz pulsations, and 200 acfm with 29 Hz pulsations.

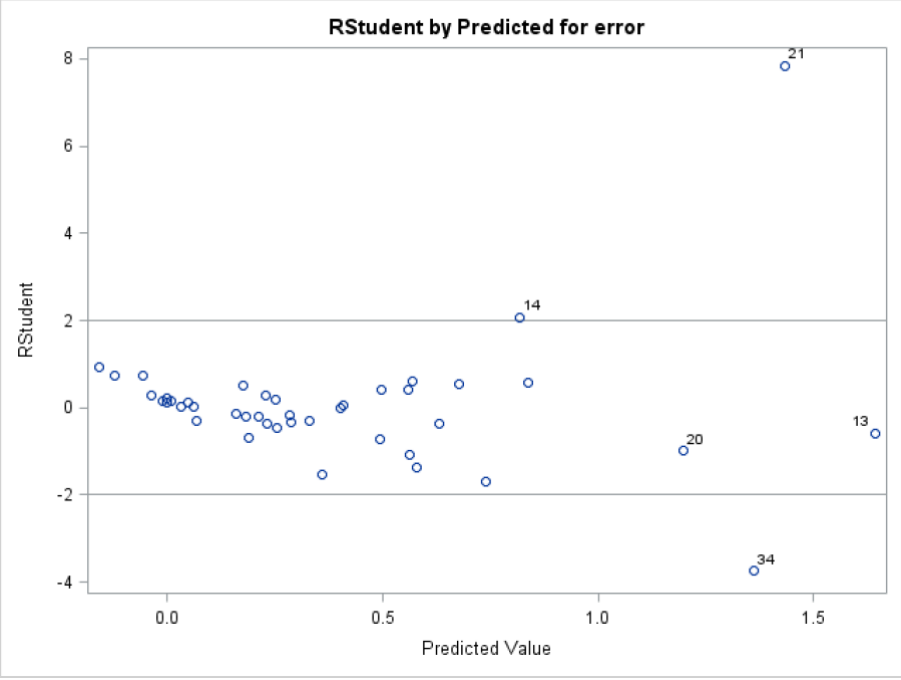

Figure 79. Studentized residuals vs. predicted values from regression analysis

In order to rectify these issues with the regression fit, several steps were taken. First, two outliers were removed. Reviewing the 29 Hz pulsation data, the velocity node was found to be

located very close to the hot-wire anemometer. This led to the comparatively large uncertainty in the velocity pulsation amplitude estimation at the meter, located close to a velocity anti-node. As this was the case for both flow rates and because the meter velocity pulsation magnitude was suggested by the literature to be an important factor, these points were removed from the subsequent regression analysis. No similar issues were observed when reviewing the 45 Hz pulsation data, so data point 21 was left in the analysis. Second, to counter the relationship between predicted value and variance, the dependent variable was transformed. Instead of attempting to model meter error directly, the new regression model would attempt to model the square root of meter error. Third, a stepwise variable selection method was used to eliminate extraneous regressor variables from the model. At a 0.05 significance level, the three regressor variables found to be significant were pulsation frequency, flow rate, and the magnitude of the velocity pulsations at the meter location. By extension, reducing the number of regressor variables in the model also removed the collinearity. The new model is given in Equation [40].

$$\sqrt{error} = \beta_0 + \beta_1 flowrate + \beta_2 freq + \beta_3 metervp + \varepsilon \quad [40]$$

Table 11 shows the ANOVA table and parameter estimates from the regression analysis using the new model in Equation [40]. As before, at a 0.05 significance level, a p-value of <.0001 shows that at least one of the regressors in the new model significantly affects the meter error. The new model regression also has a much higher R^2, capable of describing 95.62% of the variation in meter error. Looking at the parameter estimates, the three remaining regressor variables are all significant at a 0.05 significance level. Based on the data in Table 11 alone, the revised regression model is superior to the original.

Table 11. ANOVA and parameter estimates from revised regression analysis

Analysis of Variance					
Source	DF	Sum of Squares	Mean Square	F Value	Pr > F
Model	3	3.67866	1.22622	261.66	<.0001
Error	36	0.16871	0.00469		
Corrected Total	39	3.84737			

Root MSE	0.06846	R-Square	0.9562
Dependent Mean	0.49922	Adj R-Sq	0.9525
Coeff Var	13.71282		

Parameter Estimates								
Variable	DF	Parameter Estimate	Standard Error	t Value	Pr > |t|	Variance Inflation	95% Confidence Limits	
Intercept	1	-0.15755	0.03112	-5.06	<.0001	0	-0.22067	-0.09443
flowrate	1	0.00014789	0.00004609	3.21	0.0028	1.13345	0.00005440	0.00024137
freq	1	0.01529	0.00089691	17.05	<.0001	1.05166	0.01347	0.01711
metervp	1	0.06911	0.00434	15.94	<.0001	1.18511	0.06032	0.07790

As explored earlier, a valid regression model must satisfy three main assumptions: no collinearity, constant variance, and normally distributed residuals. Compared to the previous fit, the new regression fit has a lower coefficient of variation at 13.7. This shows that the collinearity in the first model has been eliminated by removing extraneous regressor variables. This is also supported by the three regressor variance inflation factors in Table 11. As none exceed 1.2, there is negligible collinearity (Montgomery 2012).

The variance can be examined by plotting residuals against predicted value as in Figure 80. Because of the transformation, the fan shape observed in Figure 79 is no longer present. The variance is generally constant with respect to predicted value.

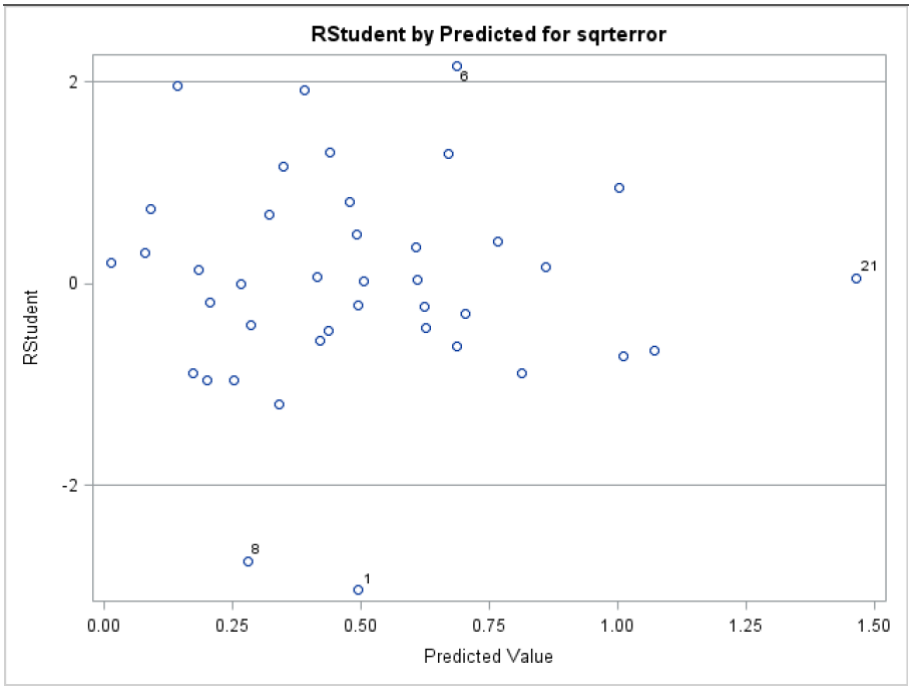

Figure 80. Studentized residuals vs. predicted values from revised regression analysis

The normality of the residual distribution is again tested using Shapiro-Wilk. The results of the test are shown in Table 12. At a 0.05 significance level, the Shapiro-Wilk test shows the residual distribution is not significantly non-normal.

Table 12. Normality analysis of revised regression fit

Tests for Normality				
Test	Statistic		p Value	
Shapiro-Wilk	W	0.950897	Pr < W	0.0814
Kolmogorov-Smirnov	D	0.1109	Pr > D	>0.1500
Cramer-von Mises	W-Sq	0.071551	Pr > W-Sq	>0.2500
Anderson-Darling	A-Sq	0.564919	Pr > A-Sq	0.1391

With these three assumptions proven, the revised regression fit is sound from a statistical perspective. However, as mentioned in Chapter 2, a primary cause of ultrasonic meter error in pulsating flow is aliasing. Because the frequencies of the pulsations generated for the experiment were low compared to the ultrasonic pulse frequency (200 kHz) and the pulse rate frequency (600 Hz) for the USM used in testing, aliasing could only affect the measurement

update frequency (75 Hz). Clearly 75 Hz does not exceed the Nyquist limit for the pulsations generated for the test (maximum 45 Hz). Using a Nyquist factor of 2, any results from test conditions with a pulsation frequency greater than 37.5 Hz (75 Hz / 2) could be subject to aliasing errors. In terms of the regression model, this would be expressed as greater meter errors for higher pulsation frequencies. Because there exists a strong positive correlation between pulsation frequency and meter error, the possible influence of aliasing could not be dismissed out of hand.

To test for the influence of aliasing on the revised regression model, the regression analysis was repeated with all test conditions with pulsation frequencies greater than 37.5 Hz removed from the data set. Repeating the variable selection procedure on the abbreviated data set resulted in a slightly different model. Instead of flow rate, the maximum pressure pulsation amplitude was included as a significant regressor. This is shown in the ANOVA table and parameter estimates for the alias testing regression fit shown in Table 13.

Table 13. ANOVA and parameter estimates from alias testing regression analysis

Analysis of Variance					
Source	DF	Sum of Squares	Mean Square	F Value	Pr > F
Model	3	1.93236	0.64412	130.78	<.0001
Error	28	0.13791	0.00493		
Corrected Total	31	2.07027			

Root MSE	0.07018	R-Square	0.9334
Dependent Mean	0.41666	Adj R-Sq	0.9262
Coeff Var	16.84343		

Parameter Estimates							
Variable	DF	Parameter Estimate	Standard Error	t Value	Pr > |t|	95% Confidence Limits	
Intercept	1	-0.15041	0.03255	-4.62	<.0001	-0.21708	-0.08374
freq	1	0.01656	0.00126	13.19	<.0001	0.01399	0.01913
maxpp	1	0.02507	0.00836	3.00	0.0056	0.00795	0.04219
metervp	1	0.06146	0.00762	8.07	<.0001	0.04585	0.07707

If aliasing was the primary cause for the correlation of pulsation frequency and meter error, frequency would not have been found to be significant with the abbreviated data set. On the contrary, pulsation frequency was found to be comparably significant with p-values less than 0.0001 in both analyses, showing that the correlation exists even for lower frequencies. With this additional analysis, the former regression fit should be considered valid.

The final regression equation for predicting the effects of pulsation on meter error is given in Equation [41]. The numbers in brackets represent 95% confidence bounds on the regression parameters. As previously shown, this model has an R^2 value of 95.62%.

$$\sqrt{error} = -0.16[\pm 0.06] + 0.00015[\pm 0.00009]flowrate + 0.015[\pm 0.002]freq + 0.069[\pm 0.009]metervp \quad [41]$$

This model agrees with previous research and theory, but presents a much simpler picture of how pulsations affect USMs. It is not surprising that flow rate significantly affects meter error because flow at different Reynolds numbers have different flow velocity profiles and a single USM is only calibrated to expect a specific well-developed profile. Were the USM used in the experiment calibrated at each flow rate prior to pulsation testing, the flow rate dependency might have been eliminated. Consistent with previous research, the magnitude of velocity pulsations at the meter location significantly affected the meter error. Velocity pulsations distort the flow profile at the same frequency as the pulsations themselves. An average USM simply cannot process and report flow measurements at a rate fast enough to capture the dynamic changes in flow profile. It follows that greater velocity pulsation amplitude would more severely distort the flow profile, which in turn would increase the measurement error. As shown, the frequency dependency cannot be attributed to aliasing alone. Although the exact mechanism by which pulsation frequency affects the meter error is not clear, it may be as simple as the fact that

standing waves of higher frequencies have more velocity antinodes. If there are more velocity antinodes in the same length of pipe, the overall likelihood of a meter being subjected to moderate to severe velocity pulsation increases. It is worth noting that the regression analysis did not find pressure pulsation amplitude to be significant, especially considering piezoelectric pressure transducers are commonly used in field studies to diagnose pulsation-related meter error. While high pressure pulsation amplitude is linked to high velocity pulsation amplitude, the location dependency of the relationship between error and pressure node undercuts the value of measuring the pressure pulsations. It is conceivable that by measuring at a pressure node, one could conclude a false negative. Although there is no available velocity measurement tool for natural gas applications at the moment, this research shows the importance of the development and use of such a tool.

CHAPTER FIVE: CONCLUSIONS

Pulsations, acoustic waves in natural gas pipelines, are common, poorly understood, difficult to characterize, and detrimental to accurate flow measurement. All custody transfer meter runs are at risk of pulsation related errors. In particular, the effects of pulsations on ultrasonic meter measurement are both inadequately understood and strongly negative. These measurement errors can be higher than 1%, significant for meters in the natural gas industry where tenths of a percent in error can have substantial financial impact.

The focus of this thesis was to better understand the links between pulsations and USM measurement error and the effects pulsations have on pipeline-applicable natural gas flow velocity profiles. To this end, two goals were set. The first was to directly measure the velocity profile shifts in natural gas flow subjected to pulsations. Historically, pulsations have been quantified using pressure measurements because fast-response pressure transducers are more easily developed for and employed in natural gas. In order to directly measure the changing velocity profiles in pulsating flow natural gas at elevated pressure, a highly dynamic velocity measurement tool was needed. A traversing hot-wire anemometer was specially adapted for the experimentation. The hot-wire anemometer was capable of measuring the quickly shifting gas velocities at different points along the flow profile. By combining the hot-wire data collected from traversals of pulsating flow, accurate descriptions of the changing flow velocity profiles were generated. The second goal of this thesis was to detect and qualify a relationship between meter error and one or more measureable aspects of pulsation. This required subjecting an ultrasonic meter to controlled pulsative flow and comparing the meter readings to a flow standard. In addition, the pressure pulsation waves needed to be mapped using high-speed piezoelectric pressure transducers. Combining this knowledge of the pressure waves with the

hot-wire velocity measurements led to a complete characterization of the velocity pulsation waves generated in the piping. With the sophisticated understanding of the pulsations that full characterization provides, the changes in meter error were correlated to specific pulsation properties. This led to a final statistical regression model describing the particular influences of pulsations on meter error.

To achieve these goals, a series of experiments was developed, using a USM in pulsating flow while simultaneously measuring the behavior of the pulsating flow. The testing was performed in the LPL at the MRF of Southwest Research Institute, a flow lab specializing in natural gas meter calibration. This afforded the use of a pulsation generator capable of controlling the frequencies of the pulsations in the flow. The LPL also had reliable flow standards in the form of sonic nozzles. An 8-inch 8-path USM was installed in the LPL in AGA-9 default meter run configuration, similar to a field installation. The pulsation generator was located upstream of the meter run. Nine piezoelectric pressure transducers were installed to measure the pressure pulsations. The hot-wire tool was installed upstream of the USM in the meter run. Pressurized natural gas was used as the flow fluid (180 psia, 70°F). Testing was performed at two flow rates: 200 acfm and 700 acfm (corresponding to approximate Reynolds numbers of 470,000 and 1,500,000 respectively). The pulsation frequencies generated were between 5 Hz and 45 Hz in 2 Hz increments. This frequency spread covered frequencies commonly generated by reciprocating compressors, FIP, and some centrifugal compressors.

By using the hot-wire anemometer data to construct time studies of profile changes, the first goal of this thesis, directly measuring the velocity profile shifts in natural gas flow subjected to pulsations, was achieved. These fits were generally validated by the statistical evaluations. This type of direct flow profile visualization was absent from the literature relevant to this field.

The expected shifts in incompressible, laminar flow were modeled by Uchida in 1956, but the effects in compressible, turbulent flow were never analytically determined. Without the visual representation of the profile shifts, many members of the natural gas industry struggle to understand the effects pulsations have on flow and, by extension, flow measurement. Now it is possible to show the directly measured flow profile shifts in pulsating, elevated pressure natural gas flow. In particular, the flow profile changed greatly over time when subjected to a 45 Hz pulsation wave. These findings show that the flow profile shifted as much as 30% from the average. It is also worth noting that this was occurring at the frequency of the pulsation. The flow profile was shifting from 20% greater than the average to 30% below the average in just over 10 ms. This was happening continuously, 45 times per second. This type of profile change explains the large errors observed in USMs subjected to pulsating flow. Not only are the shifts large in magnitude, they are occurring at rates faster than the meter is able to process them. Granted, the 45 Hz wave at 700 acfm was one of the strongest waves observed. Other pulsation waves did not induce the same levels of profile shift. However, the results remain that the flow profile shifted as much as 50% of the average (p-p) at a frequency of 45 times per second.

The pulsation waves measured in this experiment were fully characterized using a combination of the piezoelectric pressure transducer data and the hot-wire anemometer data. From the pulsation wave characterization, six candidate variables were identified or calculated for each test condition. They included: the flow rate, the pulsation frequency, the maximum measured peak-to-peak pressure pulsation magnitude, the maximum measured peak-to-peak velocity pulsation magnitude, the measured peak-to-peak pressure pulsation magnitude at the USM location, and the estimated peak-to-peak velocity pulsation magnitude at the USM location. These variables were included in the regression fit of USM measurement error.

The final regression equation for predicting the effects of pulsation on meter error is given in the last section of Chapter Four. This model has an R2 value of 95.62%. It agrees with previous research and theory, but presents a much simpler picture of how pulsations affect USMs. It is not surprising that flow rate significantly affects meter error because flow at different Reynolds numbers have different flow velocity profiles and a single USM is only calibrated to expect a specific well-developed profile. The magnitude of velocity pulsations at the meter location significantly affected the meter error. Velocity pulsations distort the flow profile at the same frequency as the pulsations themselves. An average USM simply cannot process and report flow measurements at a rate fast enough to capture the dynamic changes in flow profile. It follows that greater velocity pulsation amplitude would more severely distort the flow profile, which in turn would increase the measurement error. As shown, the frequency dependency cannot be attributed to aliasing alone. Although the exact mechanism by which pulsation frequency affects the meter error is not clear, it may be as simple as the fact that standing waves of higher frequencies have more velocity antinodes. If there are more velocity antinodes in the same length of pipe, the overall likelihood of a meter being subjected to moderate to severe velocity pulsation increases.

It is worth noting that the regression analysis did not find pressure pulsation amplitude to be significant, especially considering piezoelectric pressure transducers are commonly used in field studies to diagnose pulsation-related meter error. While high pressure pulsation amplitude is linked to high velocity pulsation amplitude, the location dependency of the relationship between error and pressure node undercuts the value of measuring the pressure pulsations. It is conceivable that by measuring at a pressure node, one could conclude a false negative. Although

there is no available velocity measurement tool for natural gas applications at the moment, this research shows the importance of the development and use of such a tool.

APPENDIX A: SUPPLEMENTARY BACKGROUND INFORMATION

Orifice and Turbine Flow Meters

Orifice Meters

A differential pressure meter uses Bernoulli's principle to relate fluid velocity to a change in pressure. Differential pressure meters use flow restrictions that cause fluid pressure to fall as it passes through. This decrease in pressure is called a "pressure drop." As the flow rate increases, the pressure drop grows larger. By relating the two, the velocity of a fluid can be determined by measuring the differential pressure. Any differential pressure meter consists of two parts: the flow restriction and the differential pressure transducer. Respectively, these parts are called the "primary element" and the "secondary element." The flow restriction is typically a solid, geometrically constrained article that is installed in the pipe such that it creates a repeatable pressure drop. The differential pressure transducer can take many forms, but at its core it measures and records the difference between the fluid pressures up- and downstream of the flow restriction. This can either be two separate pressure indicators situated ahead and after the flow restriction, or much more commonly, a single pressure transmitter that reads the pressure at both locations and outputs the differential pressure.

An orifice meter is a type of differential pressure meter that uses a circular plate perpendicular to the direction of flow with a centered bore to create the pressure drop. The plates, called orifice plates, are machined precisely as small changes in the plate geometry can lead to significant errors in flow measurement. These meters are very common in the natural gas industry. Compared to other meter types, they tend to be inexpensive and easy to maintain. They are also some of the oldest flow measurement technology that is accurate enough to survive in the modern day. Many technicians and engineers continue to use orifice meters simply

because they are most comfortable with a measurement technique that has a long history. However, of the three most common natural gas flow meter types, orifice meters tend to be the least accurate. The plates are susceptible to wear and contamination over time. These meters also lack range. Generally, a plate is designed for use with flows of a specific velocity range. Going outside this range is likely to cause inconsistent or difficult to measure pressure drops. Finally, but their very nature orifice meters cause significant pressure drops. These can increase transmission costs by forcing the use of more compressors to maintain pipeline pressure.

The AGA standard for measuring flow using orifice meters, AGA Report No. 3 addresses the effect of pulsation on orifice meter accuracy. The standard states that for accurate measurement using an orifice meter, the maximum allowable pulsation level is 10% root mean square (RMS) variation in ΔP (RMS is a statistical measure of the magnitude of the variation in ΔP) (AGA, 2000). Though pulsation-related errors can only be estimated, their sources are well-known. Pulsations can affect both the primary element and the secondary element in orifice meters. The sources of error related to the differential pressure (ΔP) across the primary element include SRE, inertial error, and discharge coefficient shift (Viana 2012).

SRE:

Square Root Error (SRE) is the most basic and well-known source of orifice meter error. It stems from the fact that the orifice flow rate is proportional to the square root of ΔP, not to ΔP itself. For accurate flow rate determination, the square root of the instantaneous ΔP values should be determined and, if necessary, averaged over time. However, typical industrial-grade pressure transducers do not accurately track the rapid changes in ΔP in a pulsating flow. Instead, the resulting measurement process captures an averaged ΔP before the

square root of the ΔP value is taken to determine flow rate. This means that SRE is often inherent in the measurement process (Durke 2012).

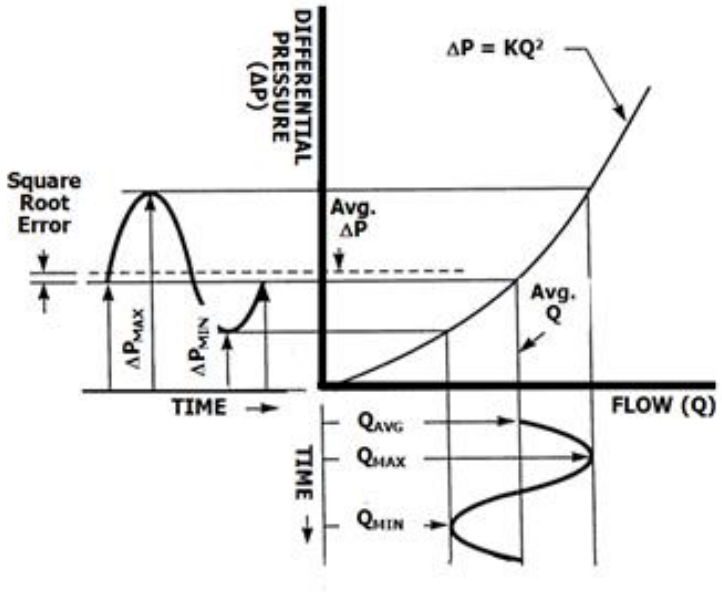

Figure 81. SRE in orifice meters (Durke 2012)

Figure 19 shows how pulsations in flow velocity and volumetric flow rate affect the oscillation in ΔP across an orifice plate. If ΔP measurements are averaged over long periods of time, and the square root of the average ΔP is used to compute the orifice flow rate, the result will be incorrect. Because of the square-law relationship between flow rate and ΔP the square root of the average ΔP value is slightly higher than the average of the square roots of the instantaneous ΔP values. As shown in the figure, it is the latter value that corresponds to the average flow rate. Thus, SRE is always a positive error and increases with increasing pulsation amplitude. Mathematically, using the brackets $\langle x \rangle$ to represent the time average of x, the SRE is given by [14].

$$SRE\ (\%) = \frac{\sqrt{\langle \Delta P \rangle} - \langle \sqrt{\Delta P} \rangle}{\langle \sqrt{\Delta P} \rangle} \times 100\%. \qquad [14]$$

To avoid SRE, the ΔP across the orifice plate must be sampled at a rate that is sufficient to avoid aliasing at the pulsation frequency. (See the subsection Ultrasonic Meters for a more thorough exploration of aliasing.) The square root of each ΔP must be calculated separately, and the average of the calculated √ΔP values over several cycles must be determined. Finally, ⟨√ΔP⟩ must be used to calculate the orifice flow rate. Alternatively, SRE can be measured using fast-response transducers and correct data processing methods so that it can be used to correct errors in flow rates computed using √(⟨ΔP⟩).

To correctly measure gas pressure in pulsating flow, a pressure transmitter must be capable of accurately sampling and recording the pressure signal at a frequency of at least twice the highest pulsation frequency present in the flow. Sampling and recording a transmitter output at a frequency slower than at least two times the maximum pulsation frequency will cause data describing actual flow changes to be lost and flow measurement error will result. It is important to note that industrial-grade analog and digital pressure transmitters used today by the natural gas pipeline industry are not capable of sampling at a high enough frequency to precisely follow the typical variation in pressure caused by pulsations. This point is illustrated in Figure 20, which demonstrates the response of industrial-grade transmitters, typical of those used at meter runs, to a sudden change in pressure. The time required for the actual pressure to drop to its minimum value was less than 0.1 second. The outputs of some of the transmitters took well over one second to reach the minimum test pressure. Pressure transmitters of this type are not able to accurately measure pressure fluctuations occurring at frequencies of one cycle per second and higher.

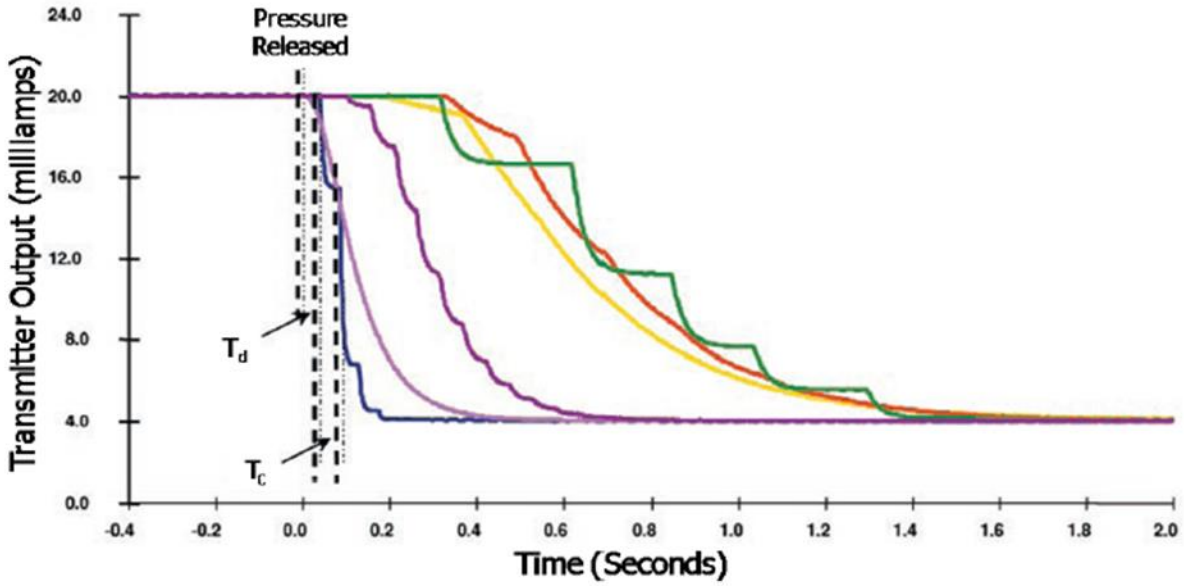

Figure 82. Pressure transmitter performance comparison (Durke 2012)

If a pressure transmitter is used with a frequency response range high enough to accurately measure the differential pressure across an orifice plate experiencing pulsating flow, the mathematical relationship shown in [14] can be utilized to determine the magnitude of the SRE. Figure 21 illustrates how well SRE measurements can account for pulsation effects at a variety of pulsation frequencies using this method.

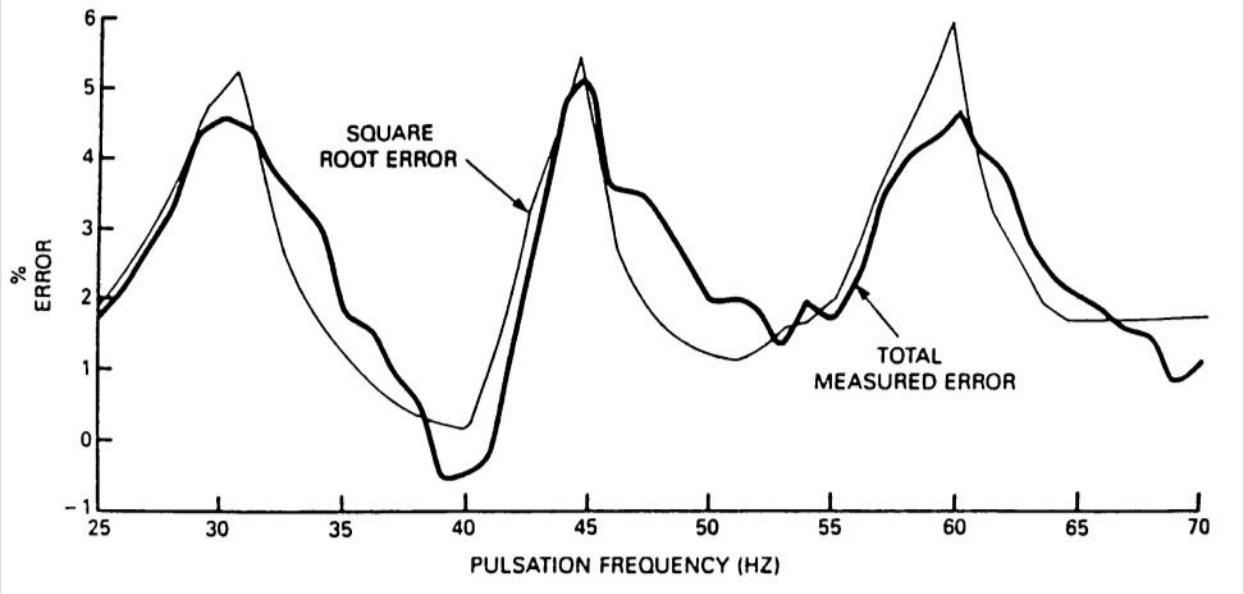

Figure 83. Comparison of SRE to total measurement error (McKee 2006)

It is important to note that the measured amount of SRE cannot be used to perfectly correct for orifice measurement error associated with flow pulsation, but SRE can be used to indicate if pulsation is causing a significant problem at an orifice flow meter. As previously stated, the maximum allowable pulsation level specified in AGA Report No. 3 is 10% RMS variation in ΔP (AGA 2012). This level of pulsation corresponds to an SRE value of approximately 0.125%. Any SRE above this threshold indicates that the pulsation is adversely affecting the orifice meter accuracy. For custody transfers with extremely high volumetric flow rates, 0.125% error may be intolerably large and efforts to reduce the error may be worthwhile. Section 2.6.4 of the standard states: "Currently, no satisfactory theoretical or empirical adjustment for orifice measurement in pulsation flow applications exists that, when applied to custody transfer measurement, will remain the measurement accuracy predicted by this standard. Arbitrary application of any correcting formula may even increase the flow measurement error

under pulsating flow conditions. The user should make every practical effort to eliminate pulsations at the source to avoid increased uncertainty in measurements" (AGA 2012).

Inertial error:

SRE usually accounts for most, but not all, of the pulsation-induced error associated with an orifice flow meter. Inertial effects can also contribute to measurement error. Inertial effects do not become problematic unless relatively high-amplitude pulsations occur at relatively high frequencies. Because SRE usually develops well before inertial effects become significant, inertial effects are generally ignored when estimating the adverse effects of pulsation.

Error due to inertial effects can be derived from the one-dimensional momentum equation for steady flow through an orifice. The momentum equation for unsteady flow may also be used to develop the orifice flow equation, but a time rate of change term must be included also. In [15] below, the term to the right represents the fluid inertia term, which includes the derivative of the fluid velocity with respect to time and accounts for the extra differential pressure needed to accelerate or decelerate the gas as it flows through the orifice. One feature of the inertial effect is that when it is averaged over time, the average is zero. However, if the square root of the instantaneous differential pressure, ΔP, across the orifice is recorded correctly to eliminate SRE, then the inertial effect is not zero.

$$\Delta P = K \cdot u(t)^2 + \lambda \frac{du(t)}{dt} \qquad [14]$$

Here, ΔP is the differential pressure across the orifice plate, u is the gas velocity, λ is the pulsation wavelength, K is a proportionality constant, and t is time.

Just as a solid object tends to stay in motion due to inertia, when gas is in motion through an orifice and the differential pressure changes (decreases), the gas tends to remain in motion due to its inertia. As a result, flow velocity changes lag behind differential pressure changes, and the

relationship between ΔP and flow rate is altered. On the orifice relationship plot, as flow changes, the differential pressure is not always on the square law curve, but may fall on the oval shown in Figure 22.

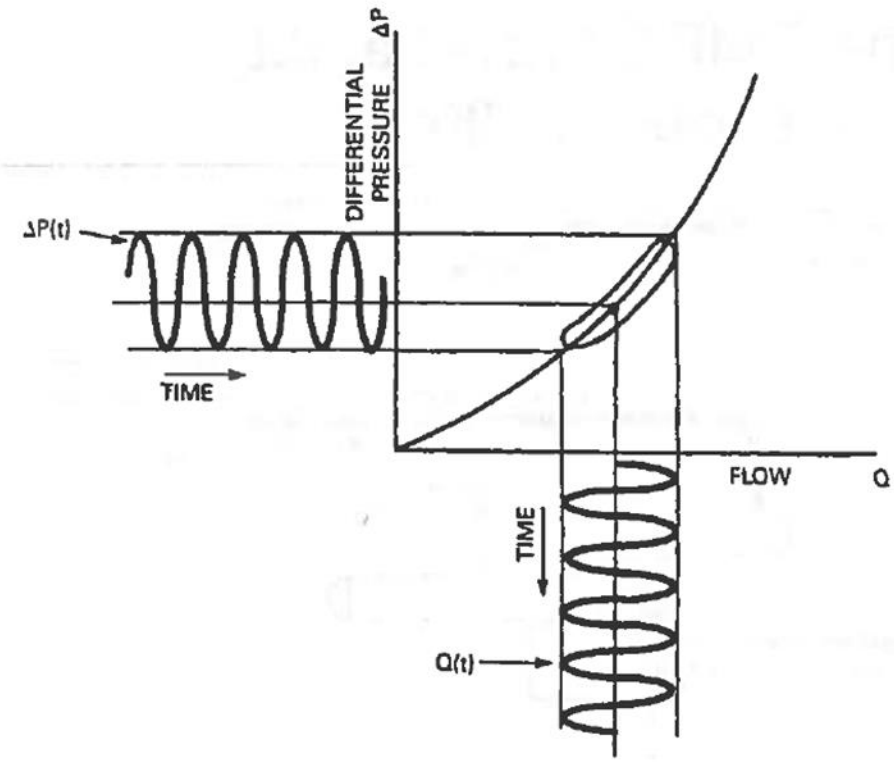

Figure 84. Inertial effect on orifice coefficient (McKee 1994)

Unfortunately, SRE and inertial errors cannot be corrected simultaneously. If the ΔP is averaged to eliminate the inertial error, SRE is introduced. If square roots of the instantaneous ΔPs are taken to eliminate SRE, the inertial error remains because it produces a change in the time-varying differential pressure. Fortunately, inertial effects are insignificant unless the pulsations are fairly large in amplitude and at a relatively high frequency. Still, it is because of inertial errors that SRE measurements should not be used to correct measured flows, but only to determine if pulsations are adversely affecting an orifice installation.

The results from a large number of tests are plotted in Figure 23. The plot shows the residual error versus the differential pressure modulation, which is defined as the zero to peak variation in differential pressure divided by the average differential pressure. Residual error is defined as actual measured error in flow minus the SRE. If SRE were the only error in orifice measurement, then the residual error would be zero.

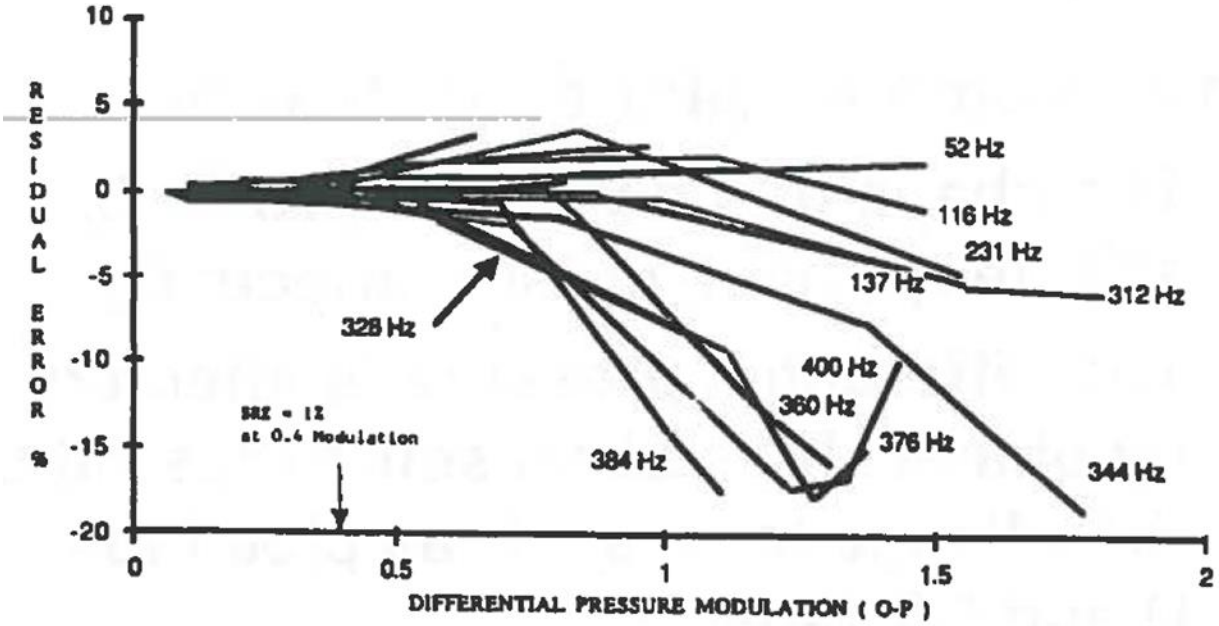

Figure 85. Contribution of inertial error to overall error (McKee 1994)

In Figure 23, the residual error is near zero in the region where the differential pressure modulation is below 40 percent. At modulations above 40 percent, Figure 23 demonstrates that residual error becomes negative as a result of the inertial effect. Figure 23 also shows that for pulsation frequencies below 100 Hz, the inertial effect is generally small. Thus, inertial effects are important if the pulsations are above 40 percent ΔP modulation, and the frequency is above approximately 100 Hz. When inertia of the flow through an orifice does become significant, the differential pressure for a given flow is reduced. Thus, significant inertial errors will cause undermeasurement, while SRE will cause overmeasurement.

Inertial errors generally occur at high frequency or high amplitude and are generally smaller than SRE. At most metering installations, inertial effects will not cause significant errors, but when they do, the measurement errors become less positive and more negative.

Coefficient shift:

The final error related to pulsations and the primary element of the orifice meter is called coefficient shift. In the previous discussions of SRE and inertial error, it was assumed that the orifice flow coefficient is constant. However, under some conditions, a change in the orifice coefficient is possible. Swirl and flow profile distortions are known to cause discharge coefficient variations up to several percent (Viada 2012). Pulsations are also known to cause distortion of average velocity profiles, so these can also be expected to cause shifts in the discharge coefficient.

Gauge line errors:

Pulsation may also adversely affect the secondary element of an orifice meter which include the gauge lines connecting the pressure transmitters to the meter fitting and the pressure transmitters themselves. The gauge lines that connect the pressure transmitters to an orifice plate installation can amplify or attenuate the pulsations that exist across the orifice plate and, in the process, change the measured ΔP value. When gauge line amplification occurs, as shown in Figure 24, the actual pulsation amplitude in the pipe and the true SRE at the orifice meter might be small, and the effect of pulsation on the correct orifice flow measurement should be low. However, because of the amplification, pulsations at the differential pressure transmitter would appear high, and if SRE were occurring at the end of the gauge lines, a significant pulsation error would result.

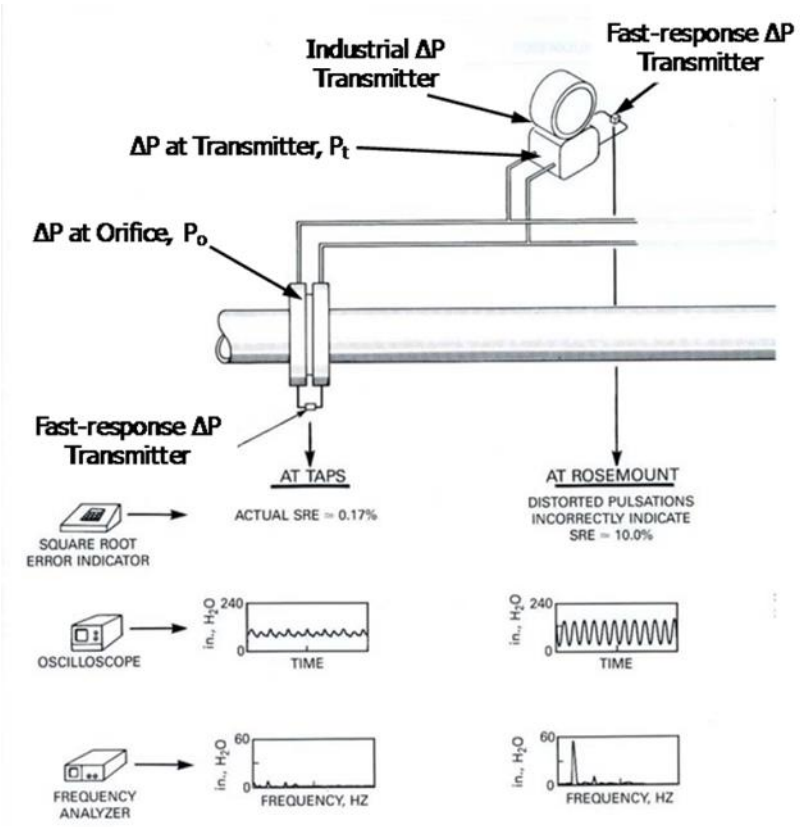

Figure 86. Gauge line amplification of pulsations (McKee 1994)

Gauge line amplification is usually a result of a gauge line being excited by pulsation at its fundamental acoustic resonance frequency or one of its higher order harmonics. Figure 25 illustrates the frequency response characteristics of an example gauge line with a resonance at 100 Hz. As the figure illustrates, a gauge line can cause both pressure amplification and attenuation, depending on its resonance frequency. It is desirable for the pressure measured at the transmitter, P_t, to be exactly equal to the pressure at the orifice, P_o (or that $P_t/P_o = 1.0$, as shown in the figure).

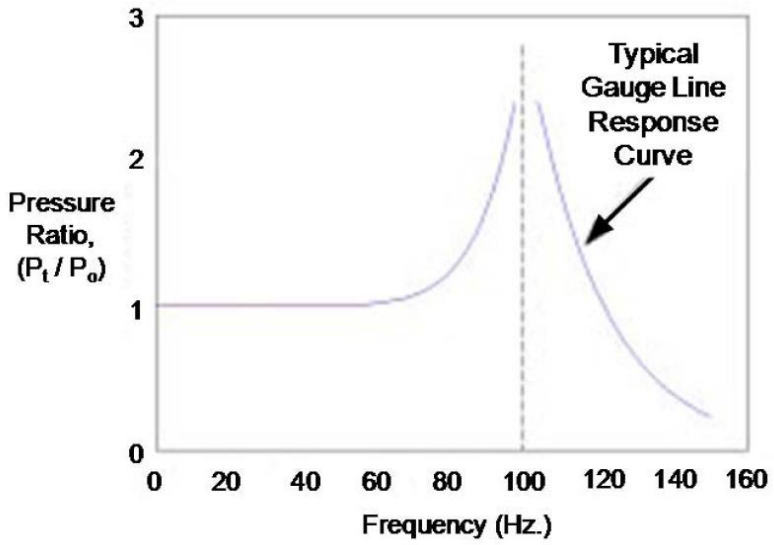

Figure 87. Example gauge line frequency response (Durke 2012)

Gauge line attenuation, which can occur when gauge lines are not responsive to the pulsation frequency, has the opposite effect as gauge line amplification. When attenuation occurs, there can be large pulsation amplitudes at the orifice meter, but little or no indication of pulsation at the ends of the gauge lines connected to the differential pressure transmitter. If attenuation is present and SRE is being measured at the end of the gauge line, then a pulsation error can be missed.

Gauge line shift is a change in ΔP along the length of a gauge line and is a result of phenomena associated with the gas alternately flowing into and out of a gauge line. A plot pressure changes along a gauge line with pulsations present is shown in Figure 26. There is a change in the pressure at the entrance to the gauge line and there is a pressure gradient along the gauge line. These changes in gauge line pressure under dynamic conditions can occur when the resistance to flow into the gauge line is different than the resistance to flow out of the gauge line. Frequency-dependent influences can also contribute to gauge line shifts. Research has shown that the amplitude of a gauge line shift is typically on the order of a few inches of water column

differential pressure (Durke 2012). Gauge line shift does not usually make a significant difference in static pipeline pressure measurements. However, a few inches of water column difference out of perhaps 30 to 50 inches of water column total differential pressure across an orifice plate can result in a relatively large flow measurement error.

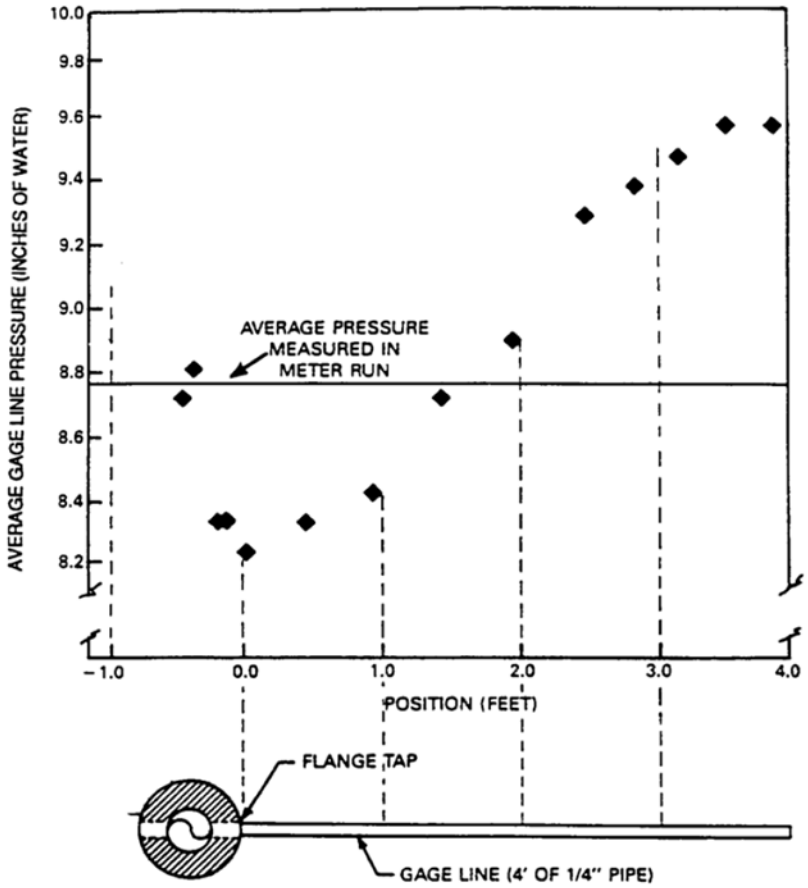

Figure 88. An example of gauge line shift (Durke 2012)

Turbine Meters

Turbine meters measure flow by detecting the speed at which a rotor spins when acted upon by the moving fluid. The rotor, able to spin freely on a spindle, has guiding vanes or blades that translate fluid velocity into rotational movement. Separate from the rotor, a magnetic pickup detects the passing of each vane as the rotor spins. The detections are transmitted as voltage

pulses. As fluid velocity increases, the rotor spins faster. As the rotor spins faster, the pickup produces more pulses. Using this relationship, the pulse rate from a turbine meter can correlate to an inference of flow rate. Turbine meters excel in measuring the flow of clean fluids, including most processed natural gas. This made them popular choices for custody transfer meters. However, turbine meters do have some weaknesses. Because the meters contain moving parts, the bearings can wear over time, requiring replacement. If the blades are damaged, the performance of the meter will suffer. Also, the rotor always causes some form of pressure drop, making these meters less desirable in a transmission pipeline application.

In steady-state flow conditions, the flow velocity and the turbine rotor's tangential velocity are proportional to one another, producing accurate measurements. Pulsations take the system out of steady-state, however, creating fluctuations in flow velocity that are faster than the turbine meter can adjust to. Because of the turbine rotor's inertia, rapid velocity changes cannot be observed, and the accuracy of turbine meters can be diminished by flow pulsations.

Turbine flow meters can be adversely affected by pulsation, which can cause flow rate measurement errors as large as 50% of meter reading, depending on many factors, including the pulsation velocity amplitude at the meter, flow rate, gas density, and both meter and pulsation properties. The effects of pulsation on turbine meters are complex but when an error exists, it usually results in an over-registration, compared to the actual or 'true' flow rate due to the rotor's inertia. In recognition, AGA Report No. 7, the U.S. natural gas industry recommended practice for turbine flow meters, notes that pulsation causes a positive error in turbine meter output that is dependent upon the factors listed above, but no arithmetic relationship has been clearly determined (AGA 2009).

Pulsation-induced measurement errors in turbine meters are challenging to predict. Published tests have shown that such errors do not correlate with pulsation frequency, flow rate, or pulsation amplitude (George, 2005). In Figure 27 below, it can be seen that the turbine meter measurements are in error in the presence of 25 Hz pulsations, but at 44 Hz, the meter demonstrates nearly no deviation from calibration values.

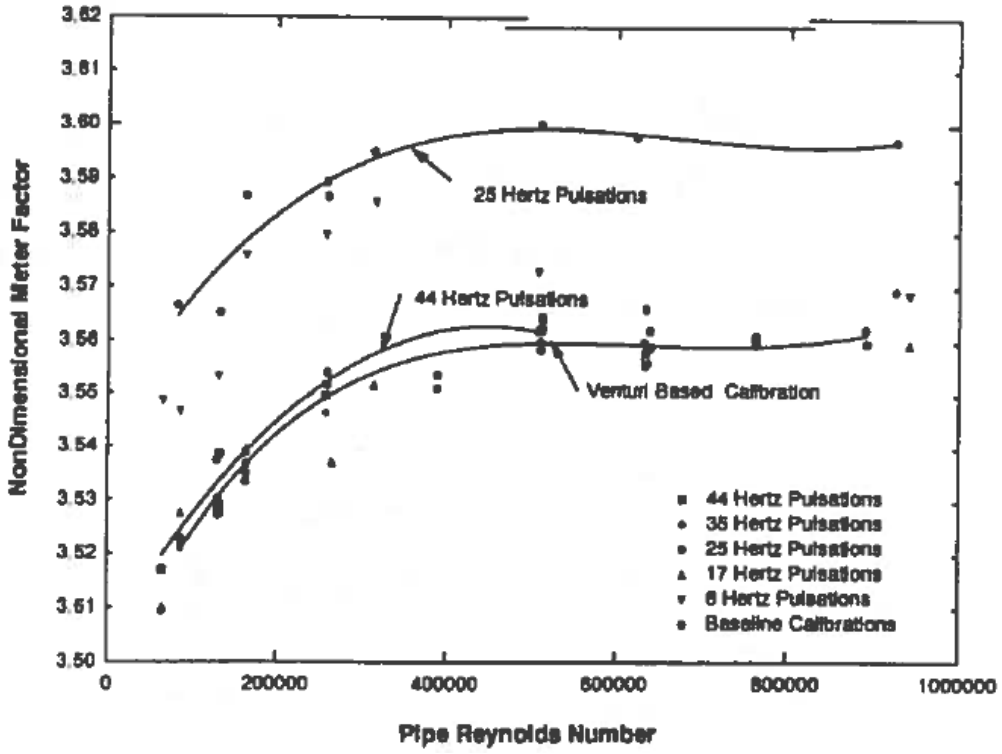

Figure 89. Effects of changing pulsation frequency on turbine meter error (George 2005)

In Figure 28, the results of other pulsation tests are presented, again showing an absence of error correlation with flow rate, frequency, and amplitude (George, 2005). The largest error, in excess of 20%, is observed at a flow rate of about 150 acfm. However, the next largest error is seen at a flow rate of about 20 acfm with nearly the same pulsation amplitude. Additionally, errors of less than 1% are observed for several flow rates, but at different frequencies. As in Figure 27 the error does not exhibit an arithmetic relationship with the pulsation frequency.

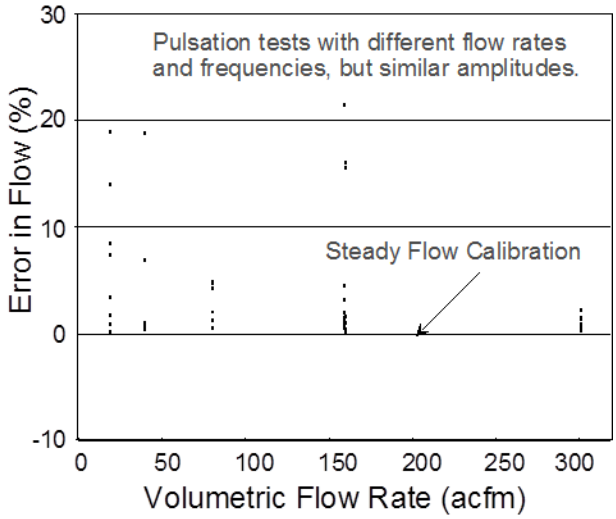

Figure 90. Turbine meter error at different flow rates and frequencies (Durke 2012)

Fluctuations in flow velocity caused by pulsations have been found to affect turbine meters much more strongly than pressure perturbations (Bronner 1991). These velocity fluctuations are typically quantified using the dimensionless Velocity Modulation Index (VMI) shown in [15].

$$VMI = \frac{u_{max} - u_{min}}{u_{avg}} \quad [15]$$

Here, u_{max} is the maximum instantaneous flow velocity, u_{min} is the minimum instantaneous flow velocity, and u_{avg} is the average flow velocity. Unlike frequency, flow rate, and amplitude, the Velocity Modulation Index does correlate with measurement error.

Using VMI, an estimate of the magnitude of the measurement error can be made as [16] where τ is the rotor time constant and ω is the pulsation frequency in rad/s.

$$\epsilon = \frac{VMI^2}{2}\left[\frac{\omega\tau^2}{1 + \omega\tau^2 - \frac{VMI^2}{2}}\right] \quad [16]$$

As shown in Figure 29, this formula can predict an upper limit on turbine meter error. However, because the VMI is challenging to accurately measure outside of laboratory conditions, turbine meter measurement errors continue to be difficult to estimate in the field.

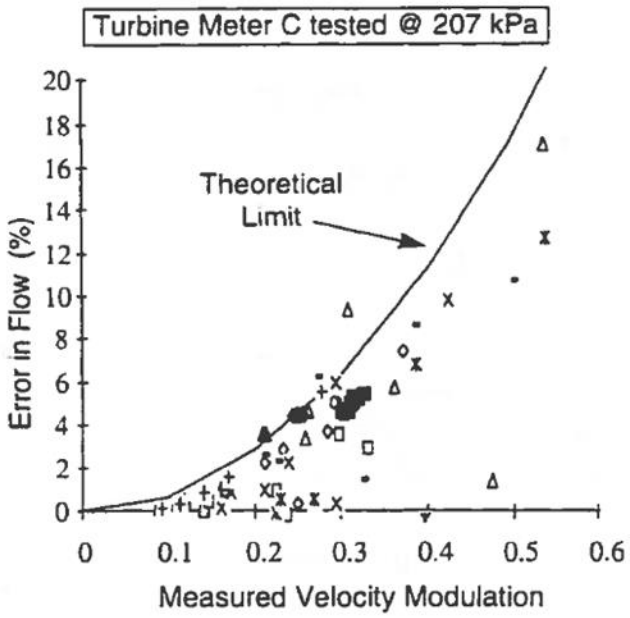

Figure 91. VMI-based predicted error limit with data (McKee 1994)

The normalized pulsation frequency, expressed as $\omega\tau$ in [16], can also be used as a predictive tool (Pish 1991). For $\omega\tau<0.1$, the pulsation-induced error is negligible. For $0.1<\omega\tau<10$, the error will depend on the pulsation frequency and Velocity Modulation Index. For $\omega\tau>10$, the error is maximized and only depends upon the Velocity Modulation Index. These relationships can be seen in Figure 30.

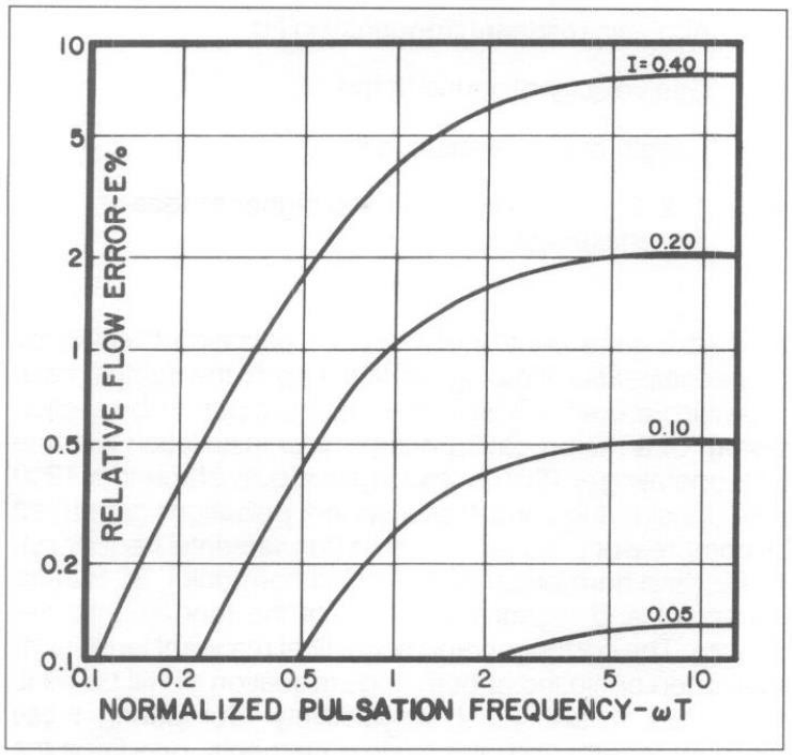

Figure 92. Turbine measurement error and normalized pulsation frequency (Pish 1991)

Flow-induced Pulsation

While the following should not be considered an exhaustive exploration of the potential sources of FIP, it is intended to provide the reader with an understanding of the more prevalent FIP sources in the natural gas industry. The most common sources of FIP are protrusions, flow restrictions, and piping arrangements. In natural gas applications, these are typically exemplified by specific features that are not universal to all applications of fluid dynamics. Where appropriate, these features are described and explained.

FIP: Protrusions

The most common protrusions in natural gas applications are thermowells and sample probes. Thermowells are long, typically cylindrical protrusions into a pipe that encapsulate resistance temperature detectors (RTDs) or other types of temperature sensor. Thermowells

shield the sensors from the flow pressure. Heat is conducted through the thermowell to the temperature sensor. By using a thermowell, the temperature of a flow can be accurately measured without direct contact between the fluid and the sensor. Because the temperature of the natural gas flow is necessary in compressible flow calculations, it would be highly unusual to find a natural gas meter run without at least one thermowell. The other common protrusion in natural gas, sample probes are hollow cylinders through which small quantities of the flow are extracted. These extractions are then sent to a local gas chromatograph or are stored in a sample bottle for later analysis at a remote location. Since the composition of natural gas is extremely important in determining its market value, taking regular gas samples is an integral part of custody transfer. Because of this, it would be unusual to encounter a meter run with no sample probe. Thermowells and sample probes share the same geometrical characteristics that can cause flow-induced pulsation. Both are long cylinders extending perpendicularly from the pipe wall into the flow.

For thermowells and sample probes, the Strouhal number for vortex shedding is usually considered 0.2 (API 2006). However, for Reynolds numbers on the order of 10^6 or higher, the Strouhal number has been experimentally determined to be as high as 0.45 (Brock 1974). The characteristic dimension used for the Strouhal number is the tip diameter of the thermowell or sample probe. Separate from the formation of pulsations, if the vortex shedding frequency happens to coincide with the cantilever mechanical modes of thermowell or sample probe, significant vibrations could be caused. In some cases this can lead to fatigue failure of the protrusion. ASME Performance Test Code 19.3 TW-2010 (ASME 2010) is an industry standard for thermowells and sample probes that includes design information to avoid a resonance condition between the natural mechanical frequency of the thermowell or sample probe and the

excitation frequency for vortex shedding. Although this type of design consideration is entirely necessary for safe operations of natural gas meter runs, it has bred a culture of complacency in terms of pulsation generation. Many technicians and engineers in the natural gas industry possess the mindset that avoiding resonance also prevents pulsations, not realizing that these are separate mechanisms. Even if a thermowell or sample probe is designed such that no resonance is possible, high-amplitude FIP may still be present.

FIP: Flow Restrictions

Flow restrictions common in the natural gas industry such as valves and orifice plates can also produce FIP. In the natural gas industry, both valves and orifice plates are used to regulate flow rate and control downstream pressure. Regulating valves in particular are ubiquitous for meter runs nationwide.

FIP from valves begins with the boundary layer of the flow separating from the sharp edge of the valve body and forming vortices (Figure 11). In addition to forming pulsations downstream, the vortices can also collide with an edge of the valve internals and travel back upstream to amplify new vortices forming in the boundary layer (Ziada 1989). This creates sustainable pressure fluctuations in the flow which can then resonate with the acoustic modes of the valve. Once a resonance occurs, high-amplitude pulsations, significant audible noise, and structural damage can occur. Case studies and experimentation have correlated a Strouhal number of 0.2 to the onset of resonance in a control valve (Ziada 1989).

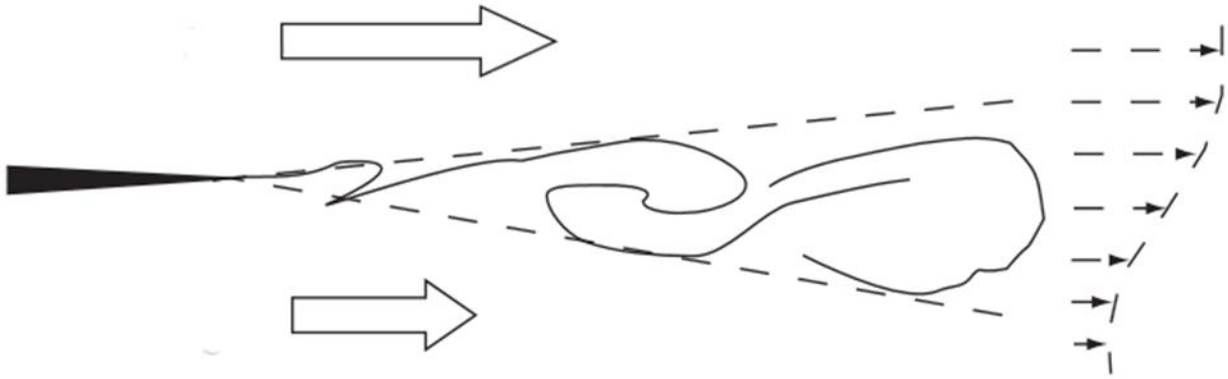

Figure 93. A vortex being formed downstream of a sharp edge (Jiménez 2004)

Orifice plates are also potential sources of USM due to flow restriction. At certain Reynolds numbers, single-hole orifices can generate high-frequency noise and vibrations (Lacombe 2011). A resonance can arise between the frequency of the vortex shedding and the three dimensional acoustic natural frequencies of the pipe structure. This can produce pulsations at that frequency. For sharp-edged orifice plates, the commonly accepted Strouhal number of resonance for pulsations is 0.2-0.35, primarily depending on the orifice plate thickness and orifice flow velocity (Blevins 1990).

FIP: Piping Arrangements

The structure of the piping itself can also be the cause of FIP. In the most common instances, FIP will occur due to the presence of smaller diameter piping branching off from a main line, called "side-branches." These side-branches can be of a simple perpendicular configuration, as shown in Figure 12, or they can be more complex, involving angles, reducers, etc. From left to right, the simple configurations depicted in Figure 12 are called "single" (a), "tandem" (b), and "coaxial" (c).

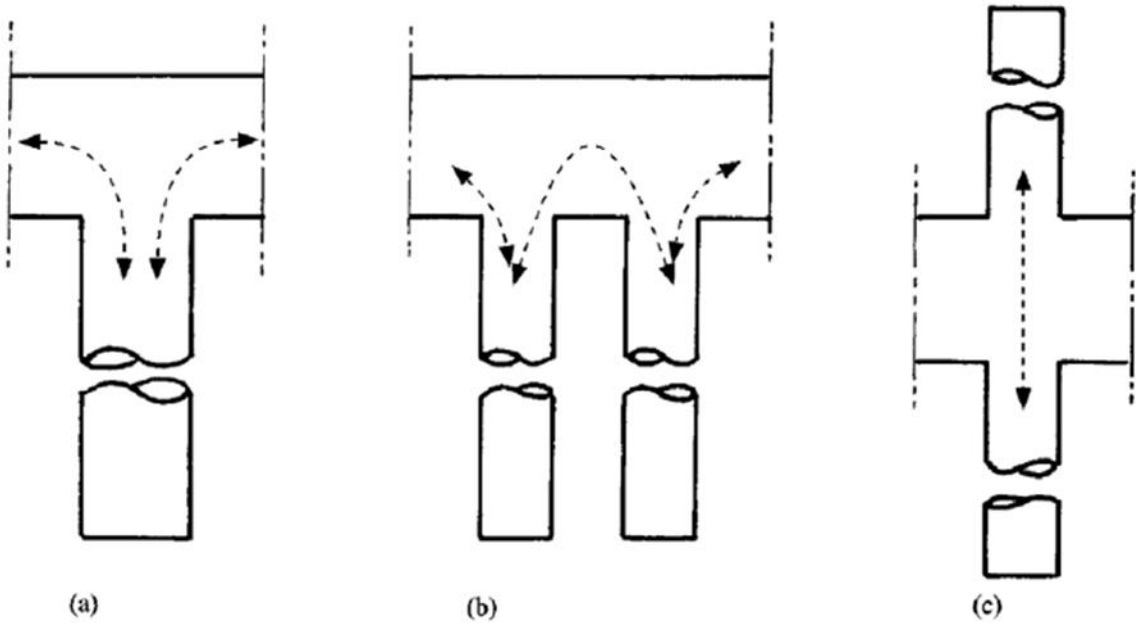

Figure 94. Simple side-branch configurations (Ziada 1999)

Single side-branches are the most common source of low frequency FIP in the natural gas industry. Single side-branches produce the lowest pulsation amplitudes, and any pulsations they produce tend to be damped by friction, heat conduction, and radiation losses before they can travel far into the piping system. However, it has been observed that high vibration and pulsation levels can occur even in cases where the coincidence is associated with a single side-branch (Broerman 2010). Tandem branches are side-branches that are located on the same side of a main pipe in close proximity. In the case of resonant tandem side-branches, increasing the distance between the branches, the pulsation amplitudes were reduced (Ziada 2002). The same effect was seen when the tandem side-branches had significantly different lengths. Tandem side-branches tend to generate substantially higher pulsation amplitudes than single side-branches under otherwise similar conditions. Coaxial branches are defined as side-branches that are diametrically opposed on a main pipe. When the branches are of equal or near equal length, the

strength of the excitation doubles, resulting in a significantly higher pulsation amplitude that can extend into the main piping system (Graf 1992). Of the three simple side-branch configurations, coaxial side-branches were found to generate the strongest pulsation amplitudes (Ziada 2002).

When resonance occurs in a side-branch, the frequency of vortex shedding in the gas flow can excite an acoustic standing wave in the side-branch resulting in significant pulsation amplitudes. The standing wave produced by a closed side-branch is a quarter wave response whose frequency can be calculated using [3], with L equal to the length of the side-branch. The order of the pulsation frequency, n, can be 1, 2, 3, or a higher order. This approach can only be used for simple side-branch geometries and cannot be applied to side branches containing reducers, piping branches connected to the side branch, or other complex configurations. An acoustic simulation tool would be necessary to calculate the acoustic natural frequencies of complex side branch configurations.

A 1999 study of the three types of simple side-branch configurations experimentally determined the Strouhal numbers associated with resonant behavior. Figure 13 illustrates the findings.

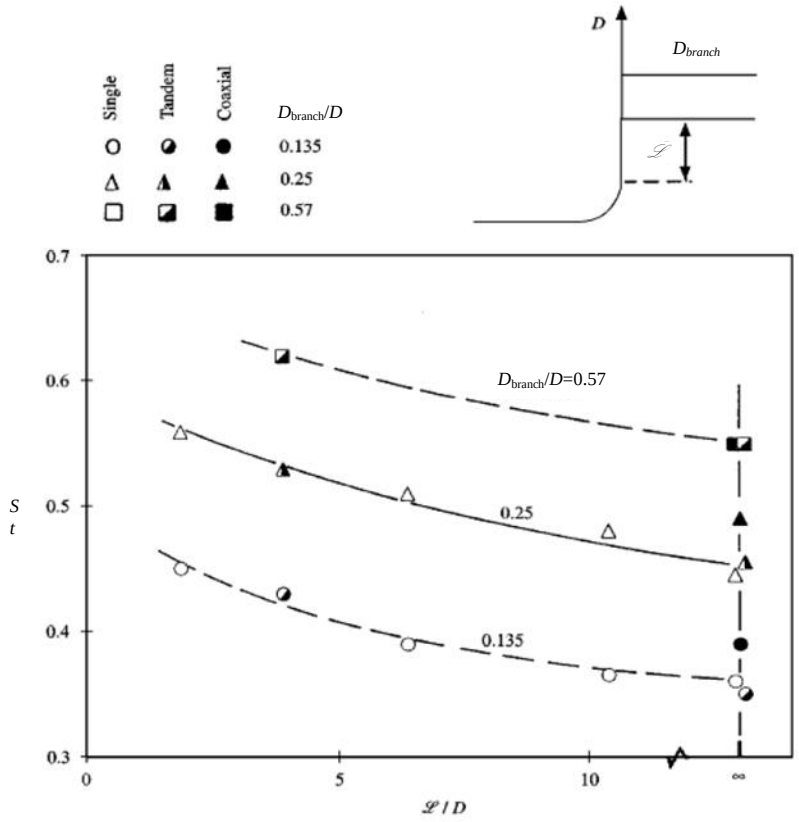

Figure 95. Strouhal numbers associated with side-branch resonance (Ziada 1999)

For this application, characteristic length in the Strouhal number is the diameter of the side-branch, D_{branch}. In Figure 13, $\mathscr{L}$ is the distance along the main pipe from an upstream elbow to the first side-branch and D is the pipe diameter of the main pipe. The resonant Strouhal number varies mainly with the ratio D_{branch}/D, and is only significantly affected by flow from the elbow when $\mathscr{L}/D$ is less than 10. From the study, the values of Strouhal numbers most commonly associated with the onset of resonance for various types of side branch configurations vary from 0.35 to 0.62 (Ziada 1999). These results agree with an older study of field experimentation that showed the onset of vibration in side-branch configurations occurs at a Strouhal number of approximately 0.5 (Sparks 1982).

The Energy Institute provides a screening analysis to determine the likelihood of pulsation problems for each side-branch connecting to main gas piping called the Likelihood of Failure or LOF (Energy Institute 2008). It applies to simple side-branch geometries only. Two calculations are given for the Strouhal number based on the Reynolds number of the gas flow. To reduce the LOF, the Energy Institute guideline requires the acoustic natural frequency of the side-branch to be higher than the vortex shedding frequency of the main gas flow. Evidence from field studies cited in the guideline shows that a coincidence of the side branch acoustic natural frequency and the vortex shedding frequency when the frequencies are at or below 10 Hz does not cause pulsation issues in low gas flow rates (Jungbauer 1997). The Energy Institute uses this finding to defend its 10 Hz limit in determining the LOF. This requirement makes the screening analysis very conservative and results in most relatively long side-branch geometries failing the screening even if the vortex-shedding frequencies are near or below 10 Hz.

APPENDIX B: PRESSURE PULSATION STANDING WAVE MAPS

Individual, 700 acfm:

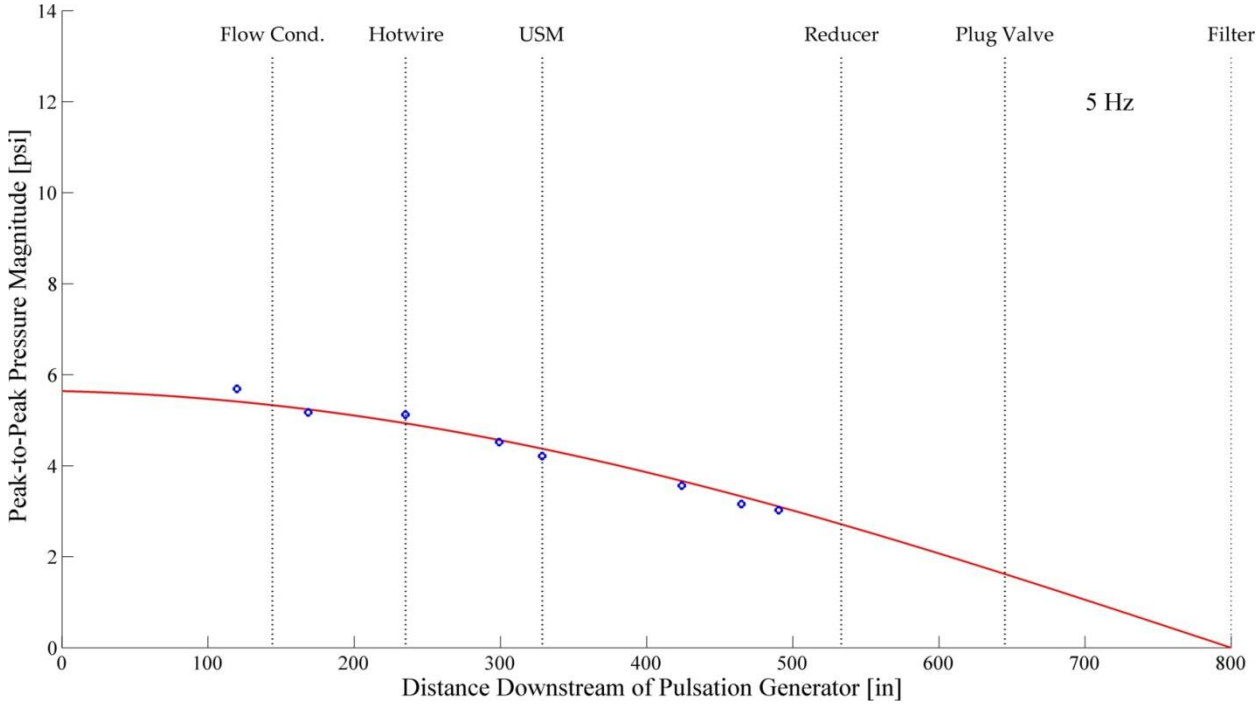

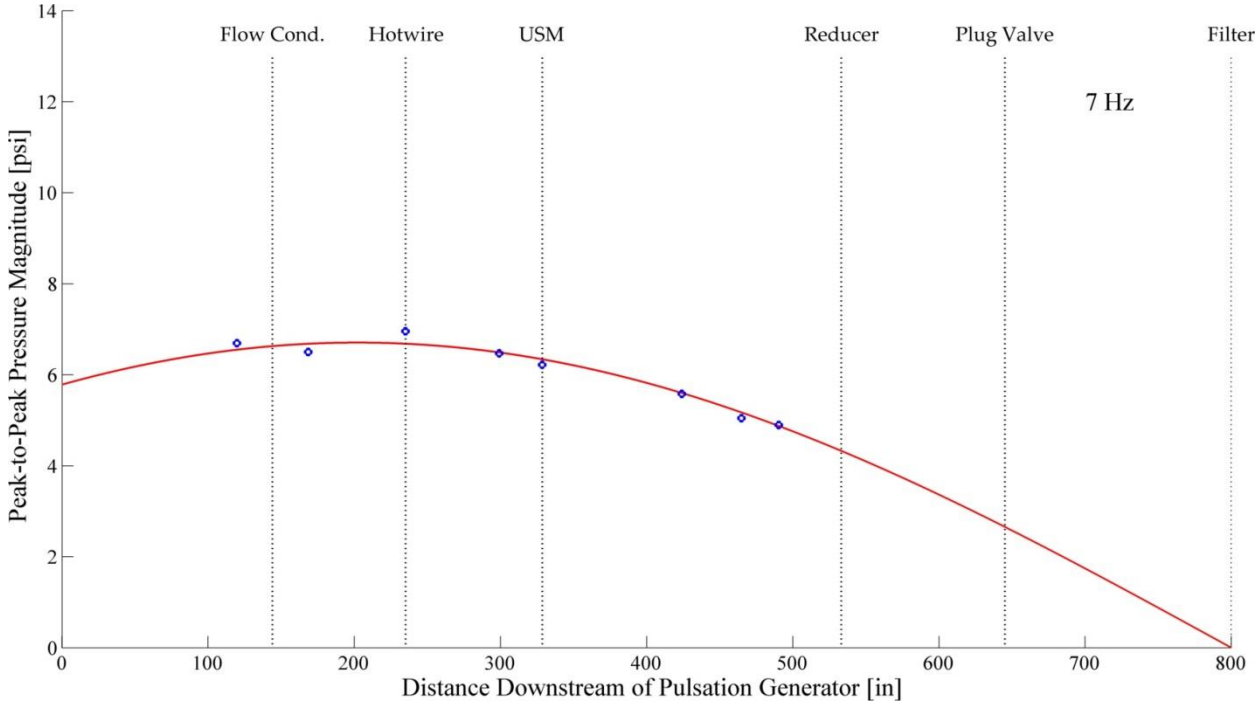

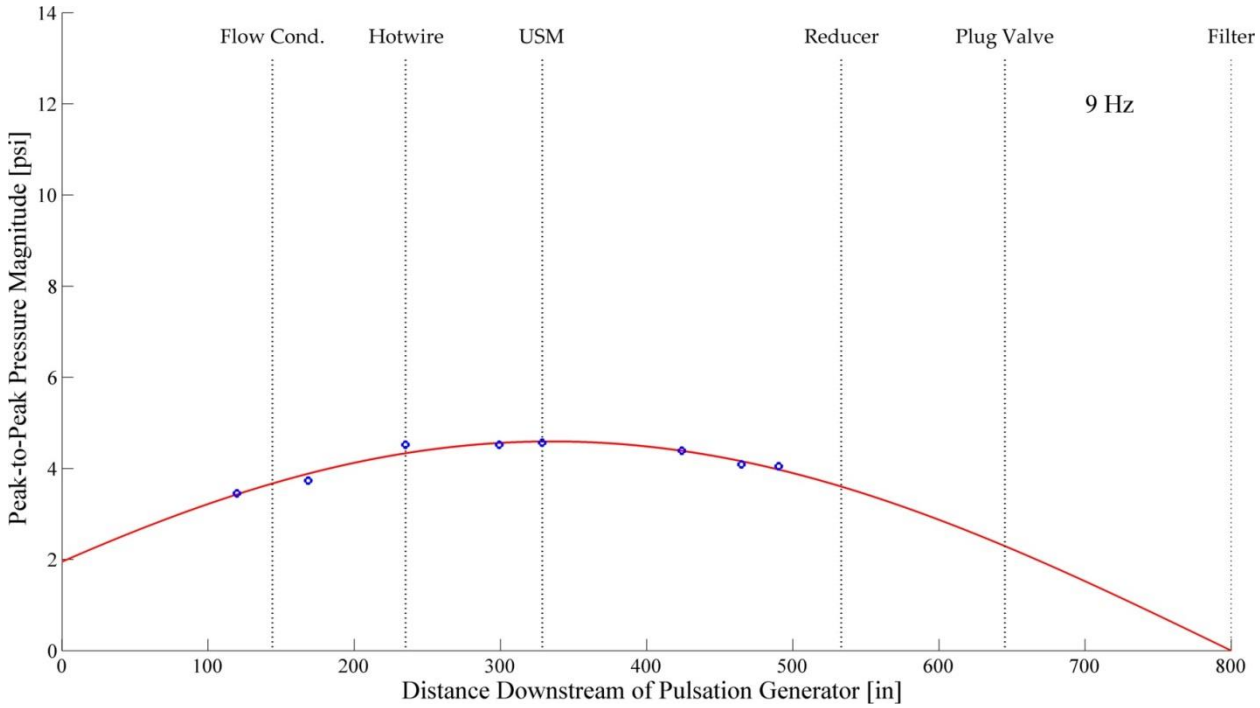

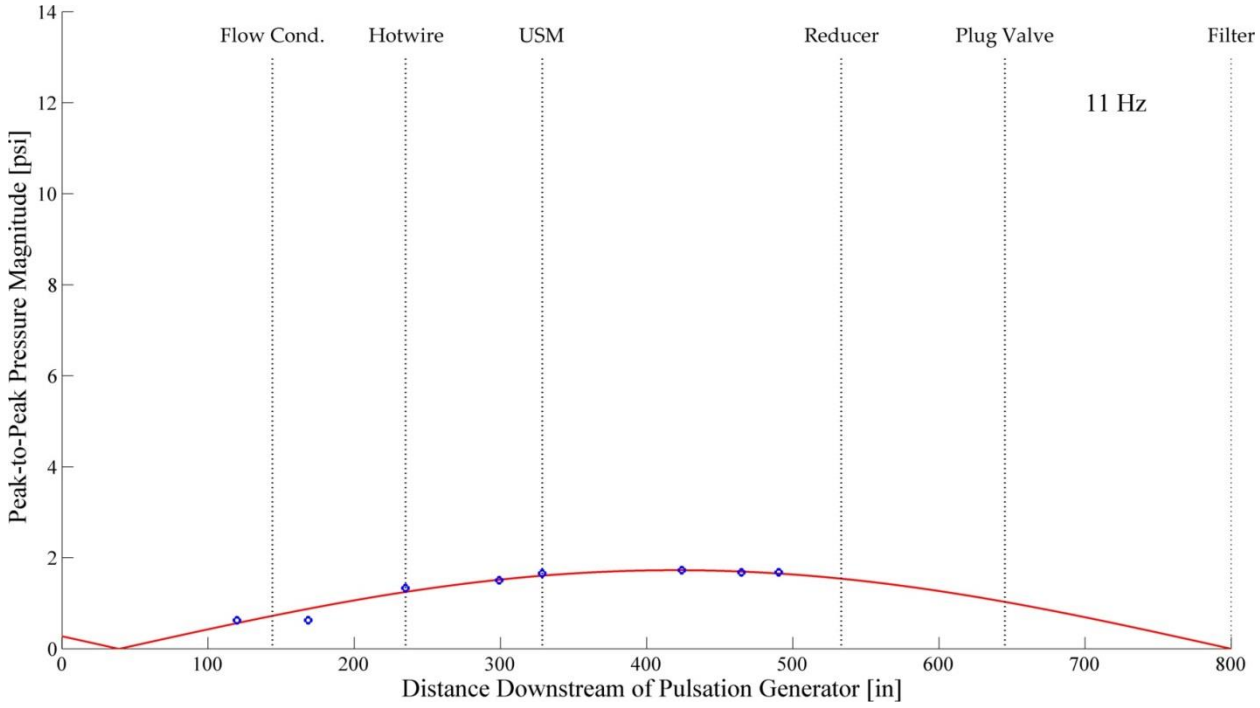

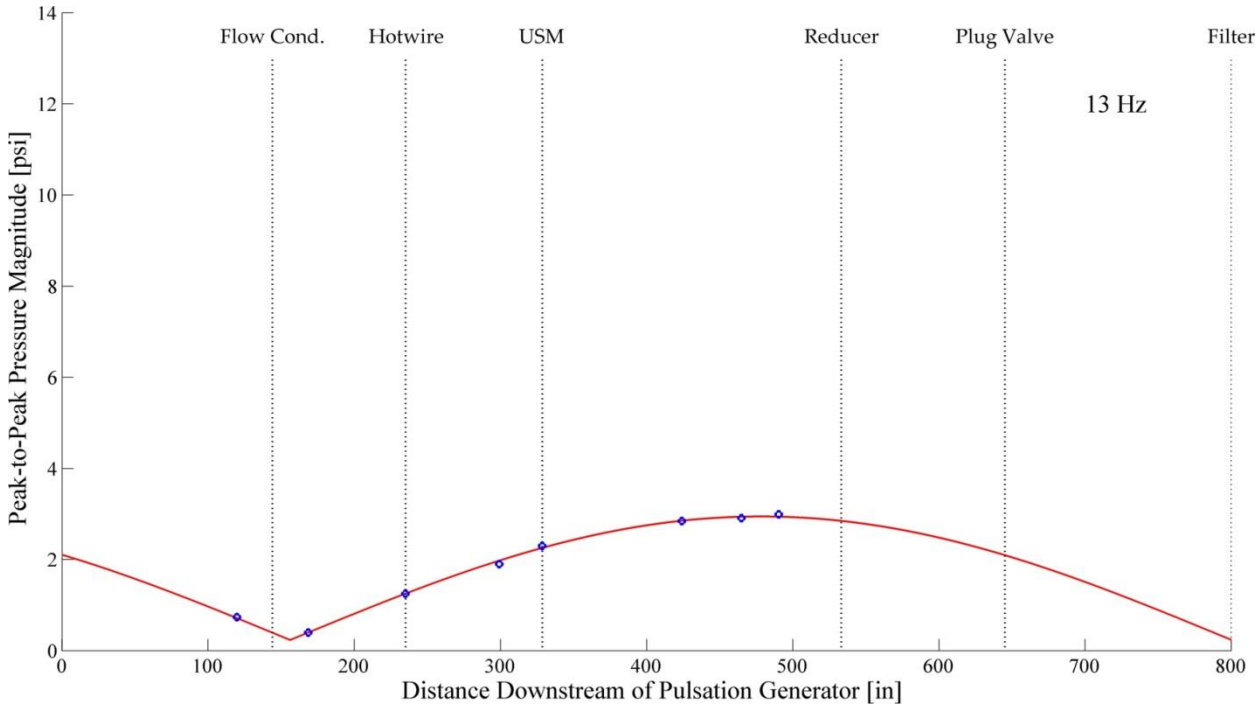

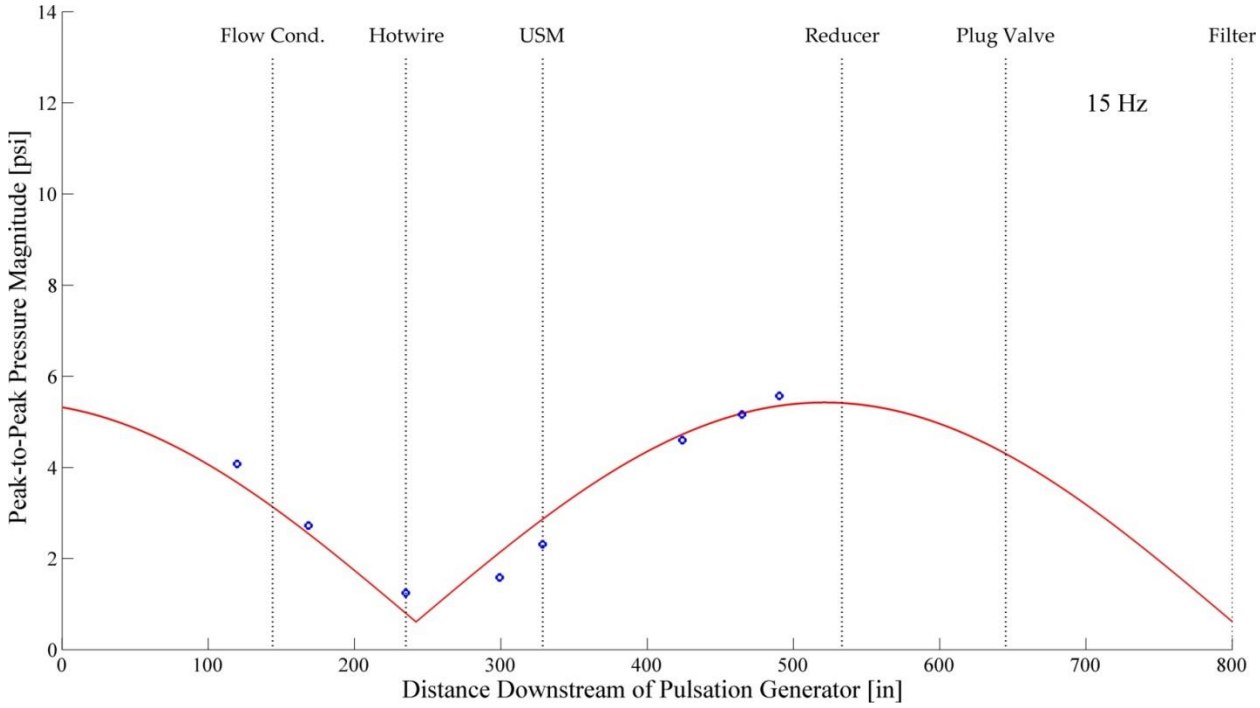

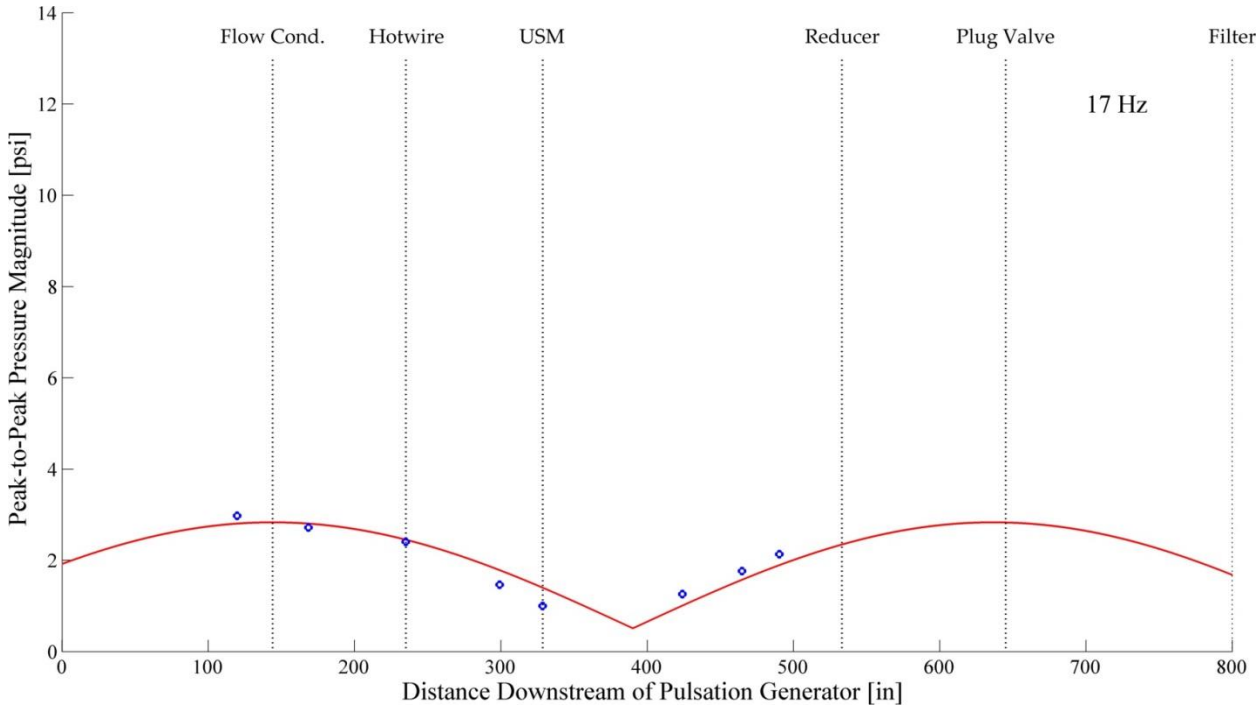

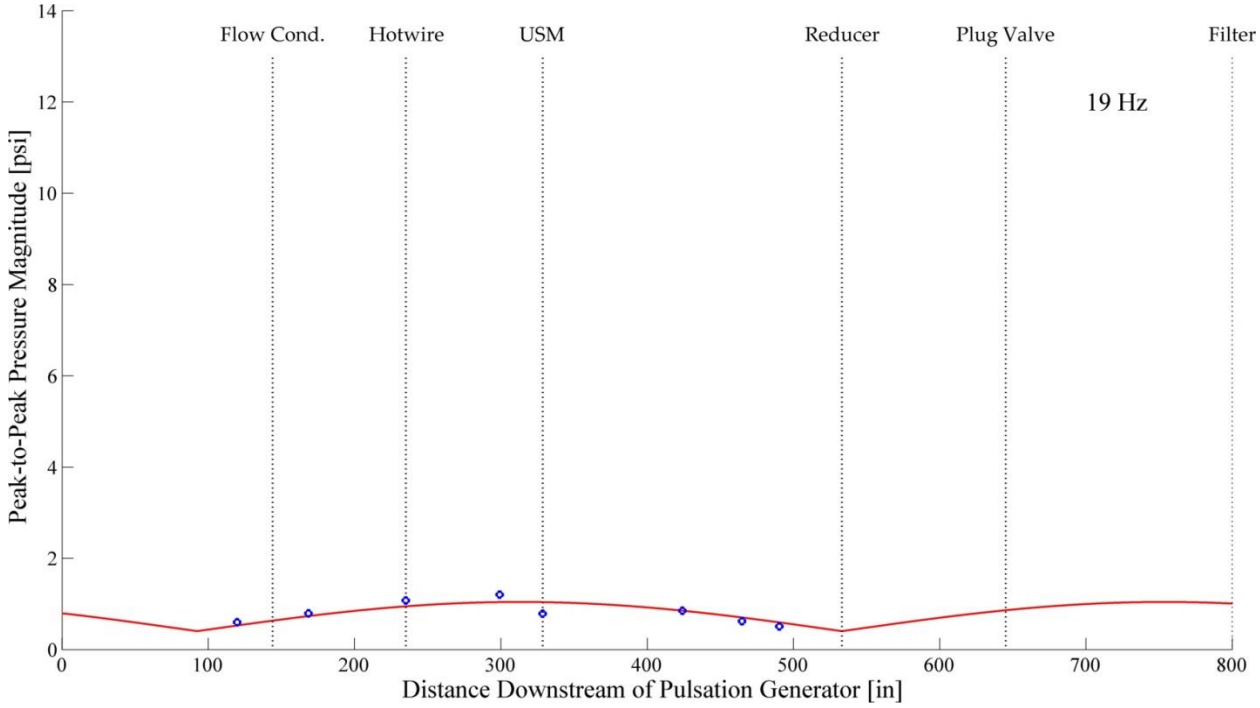

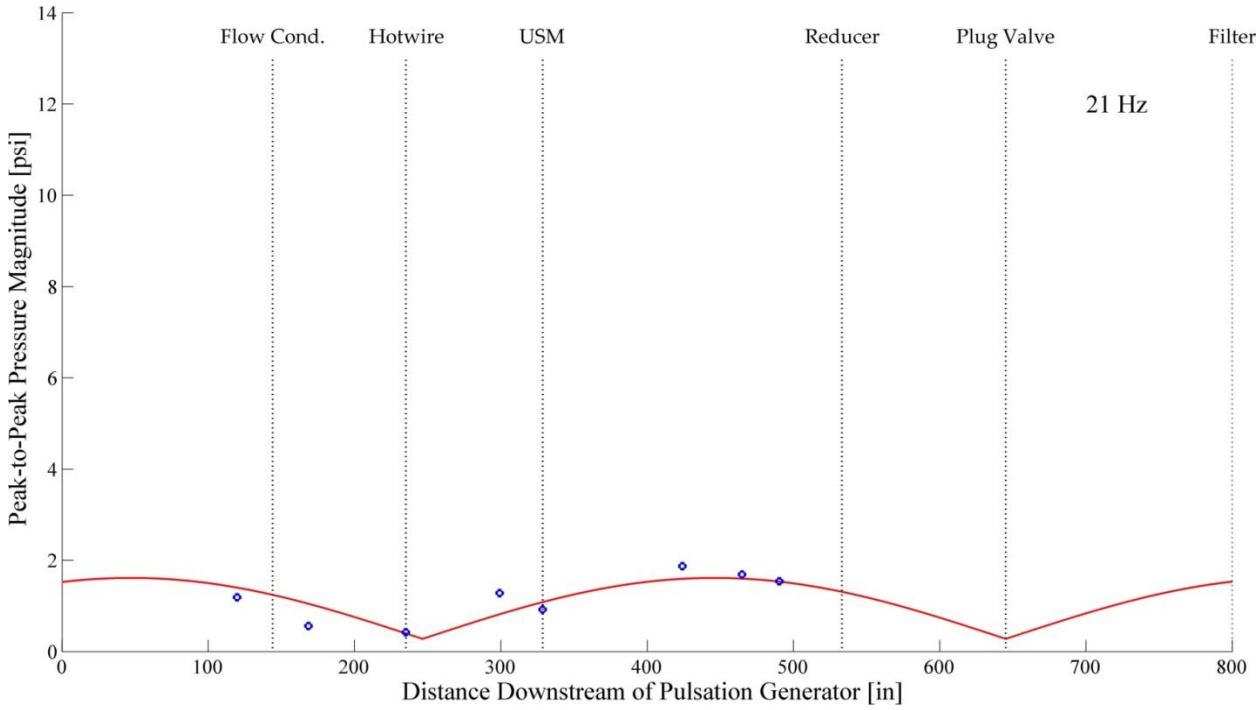

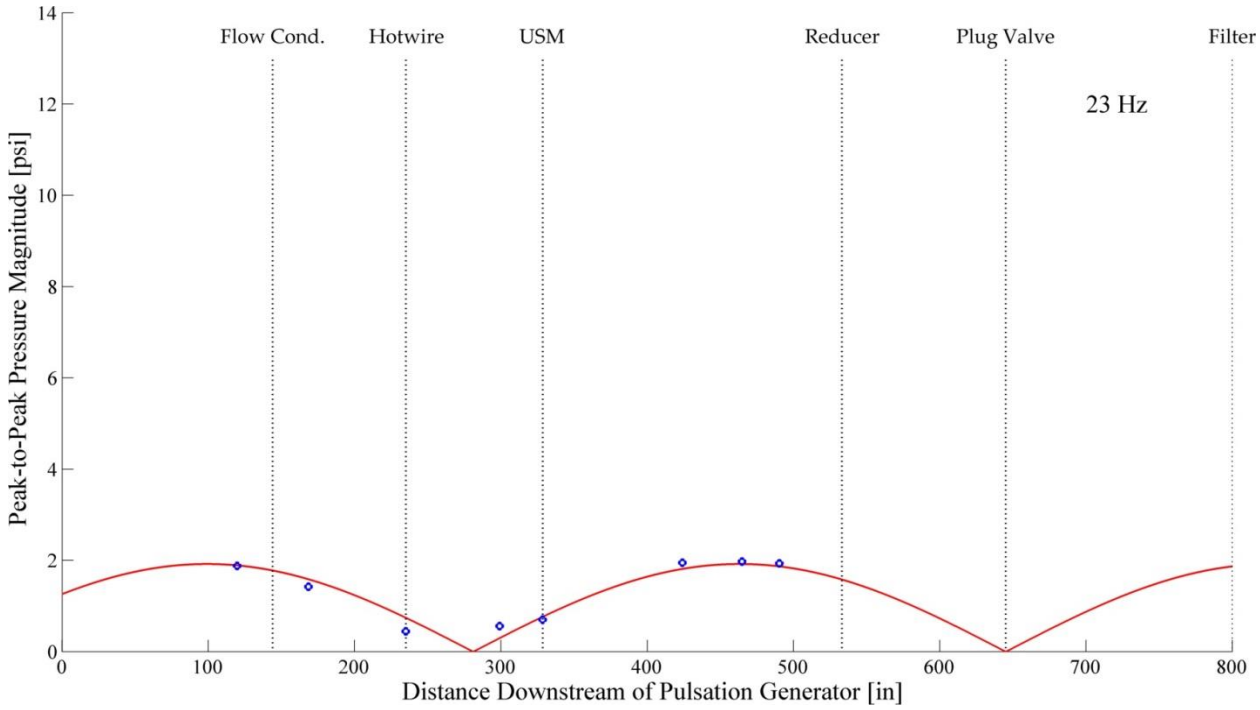

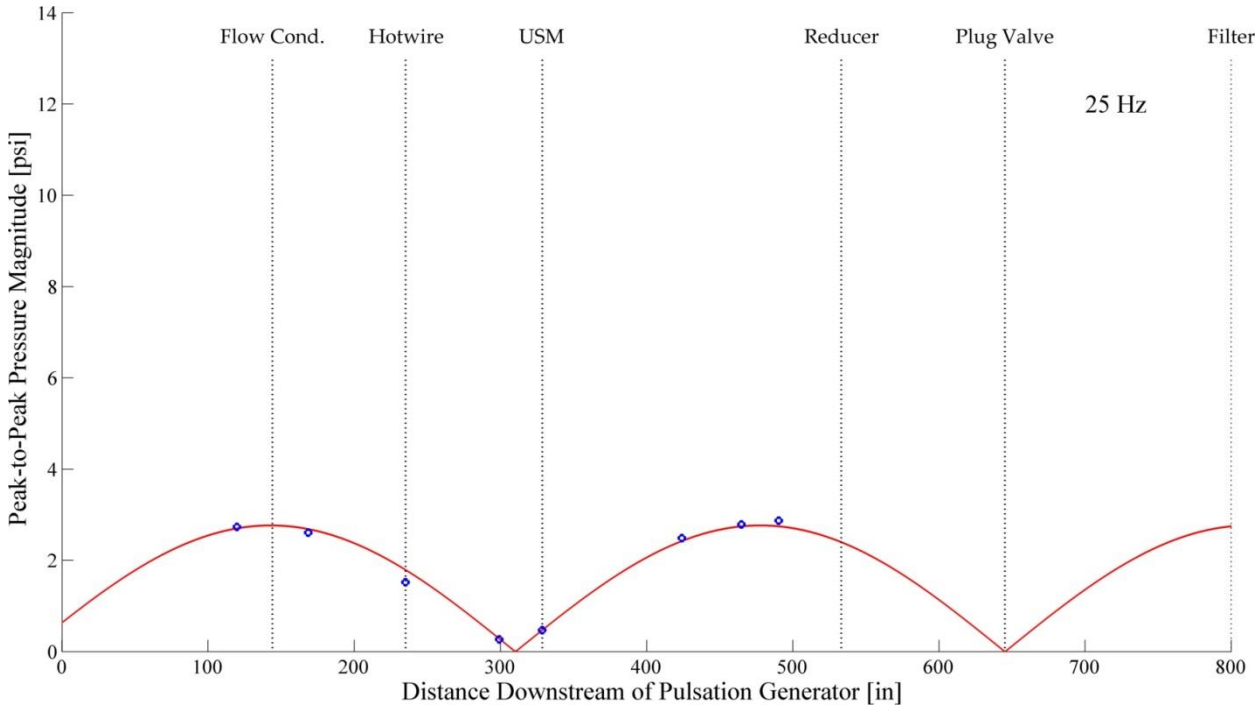

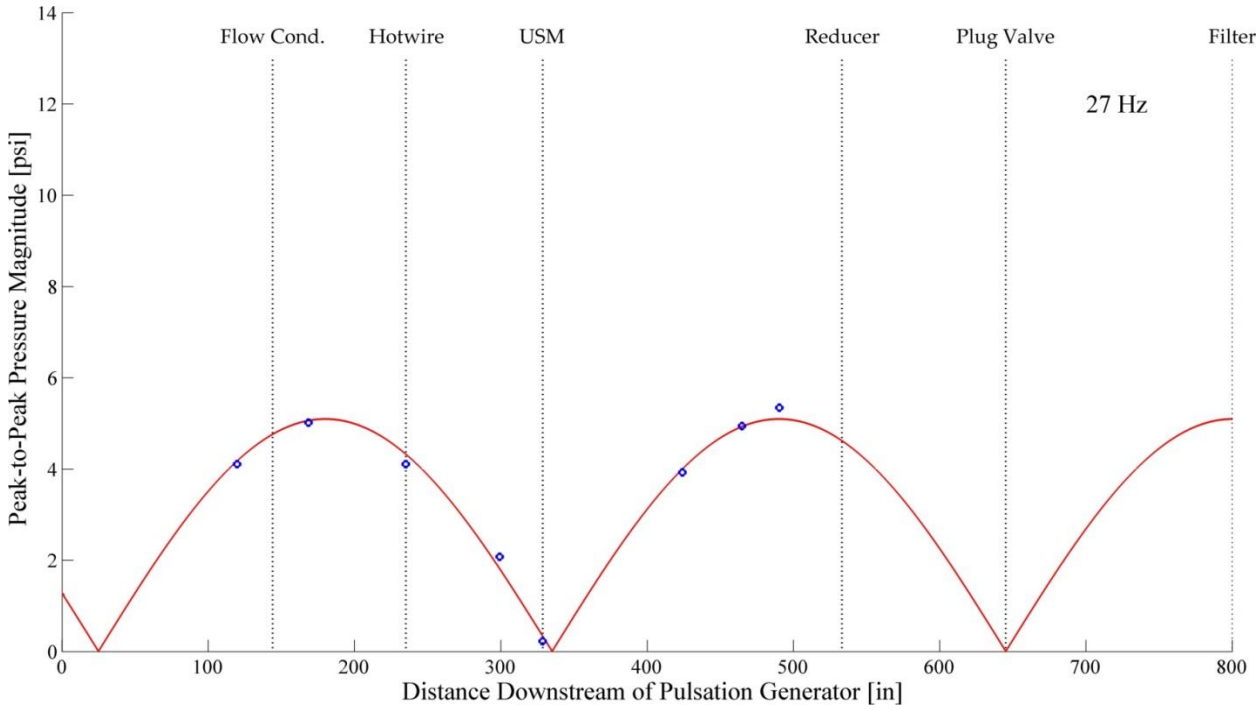

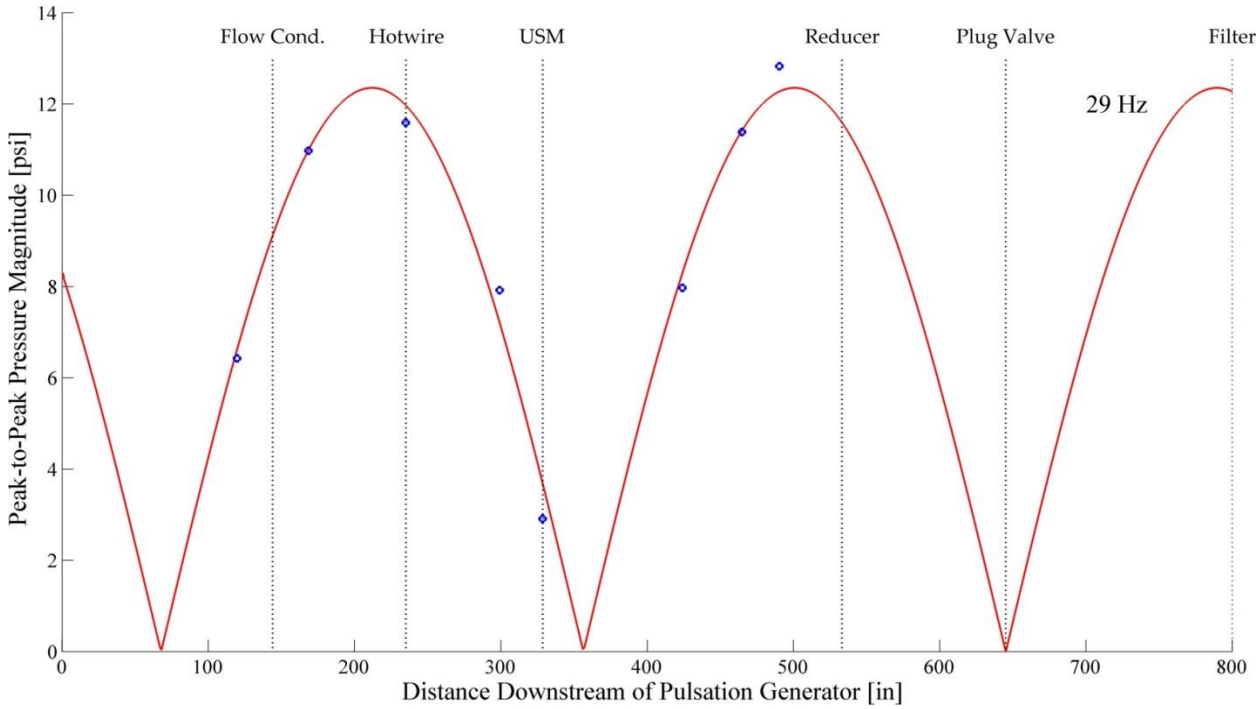

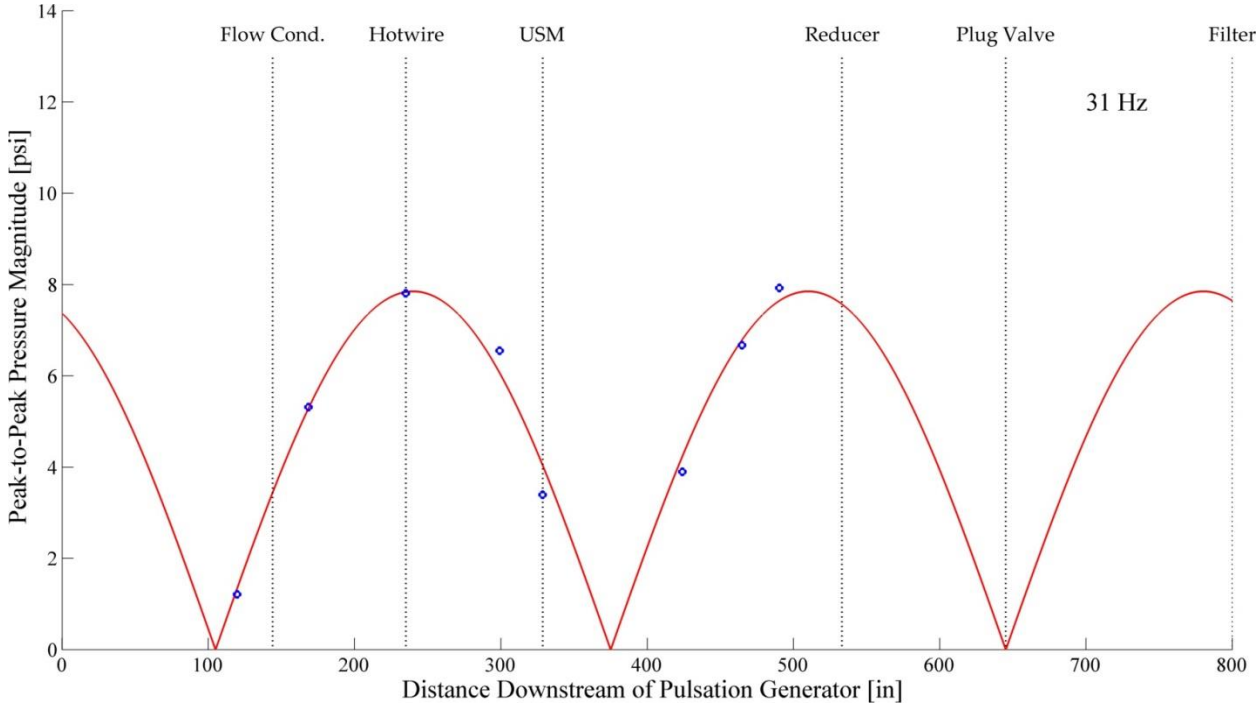

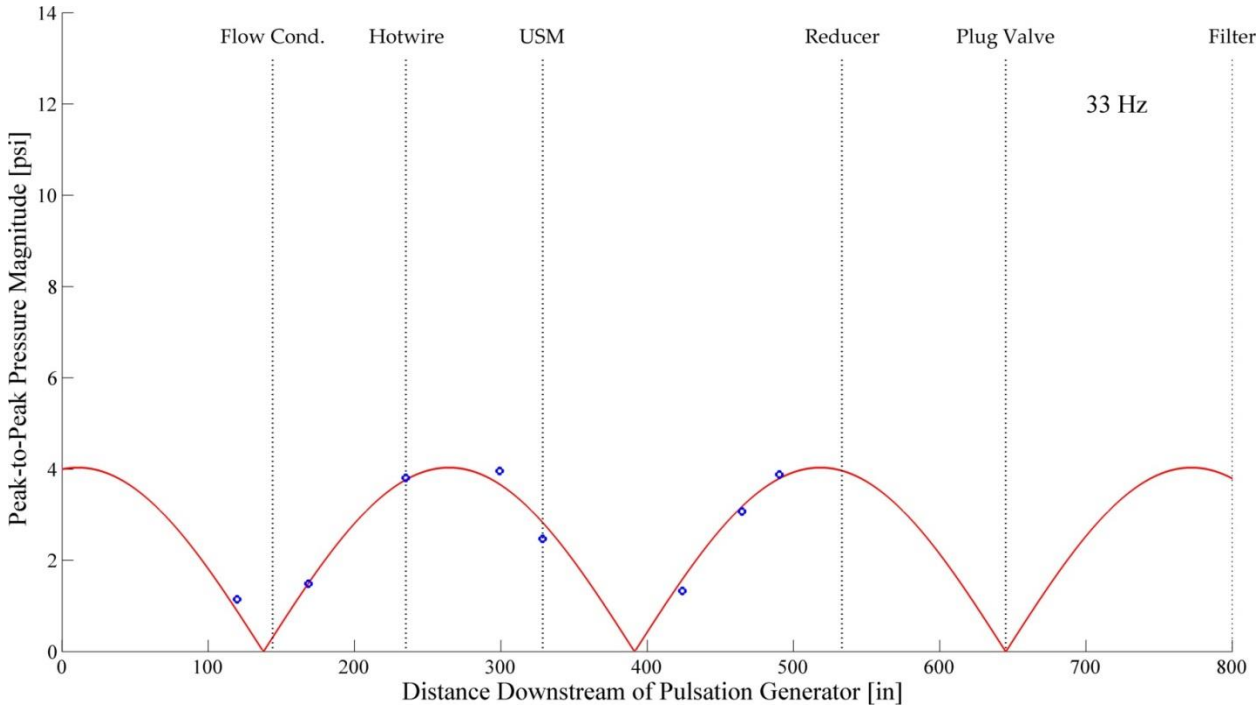

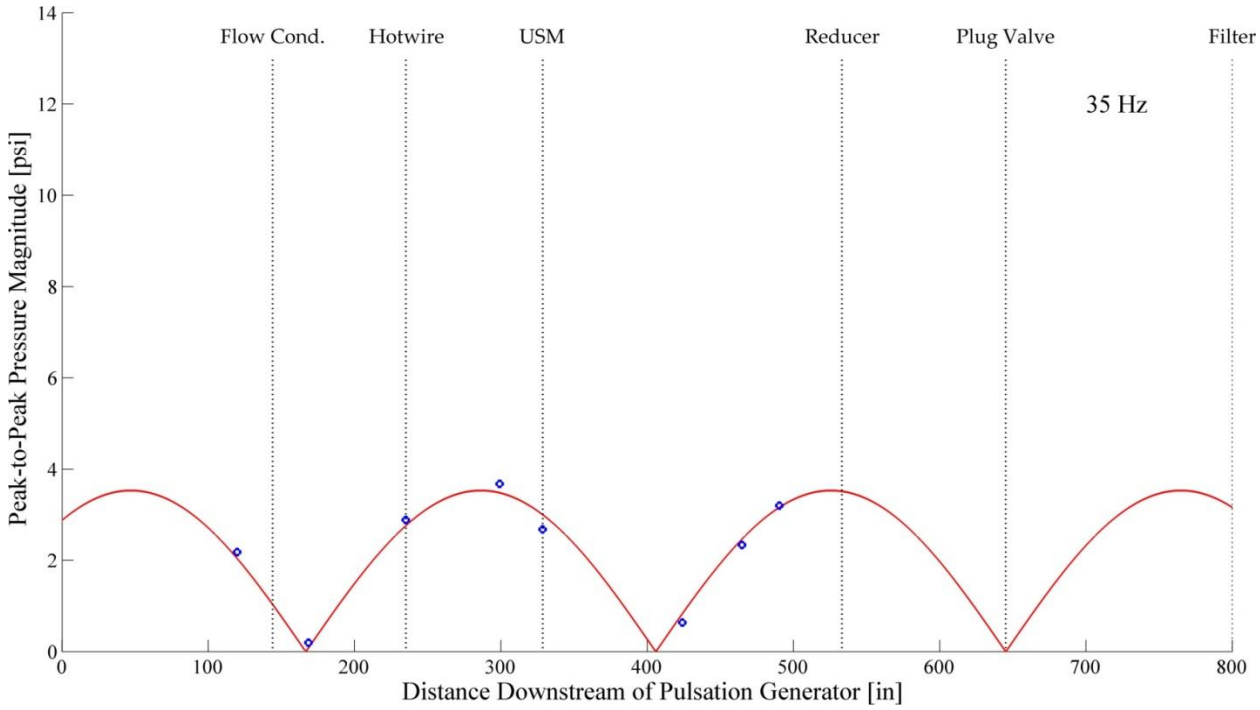

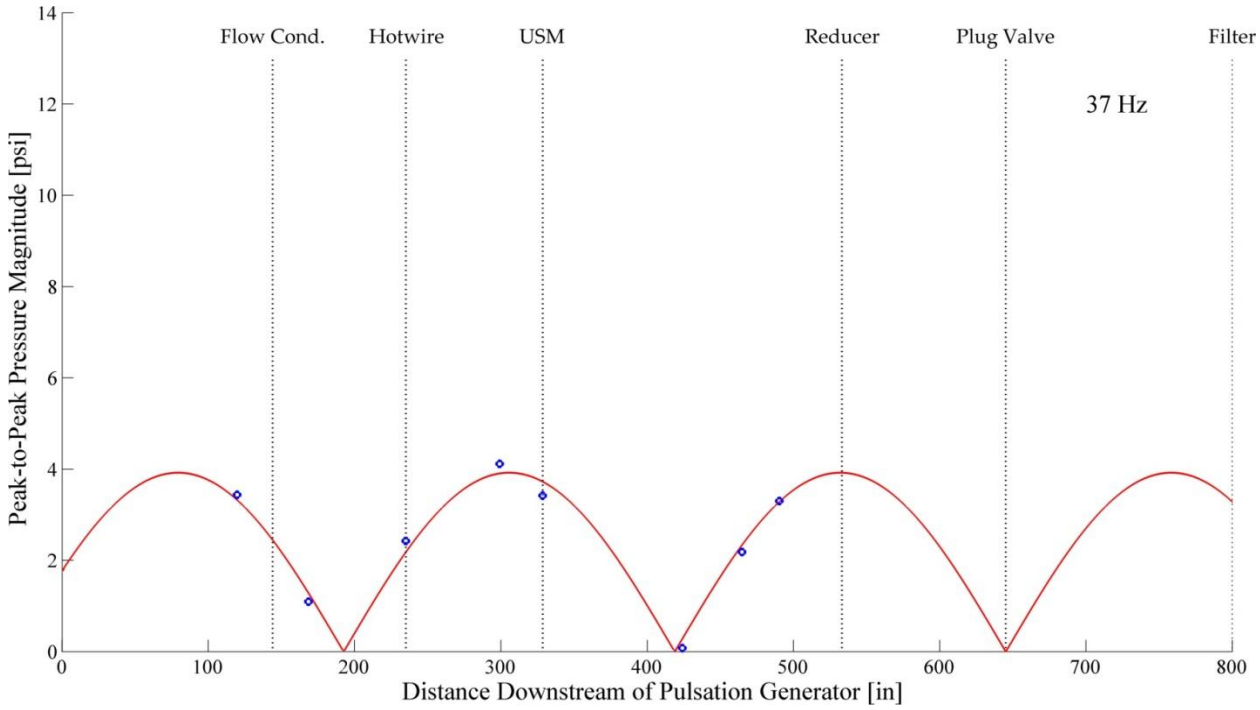

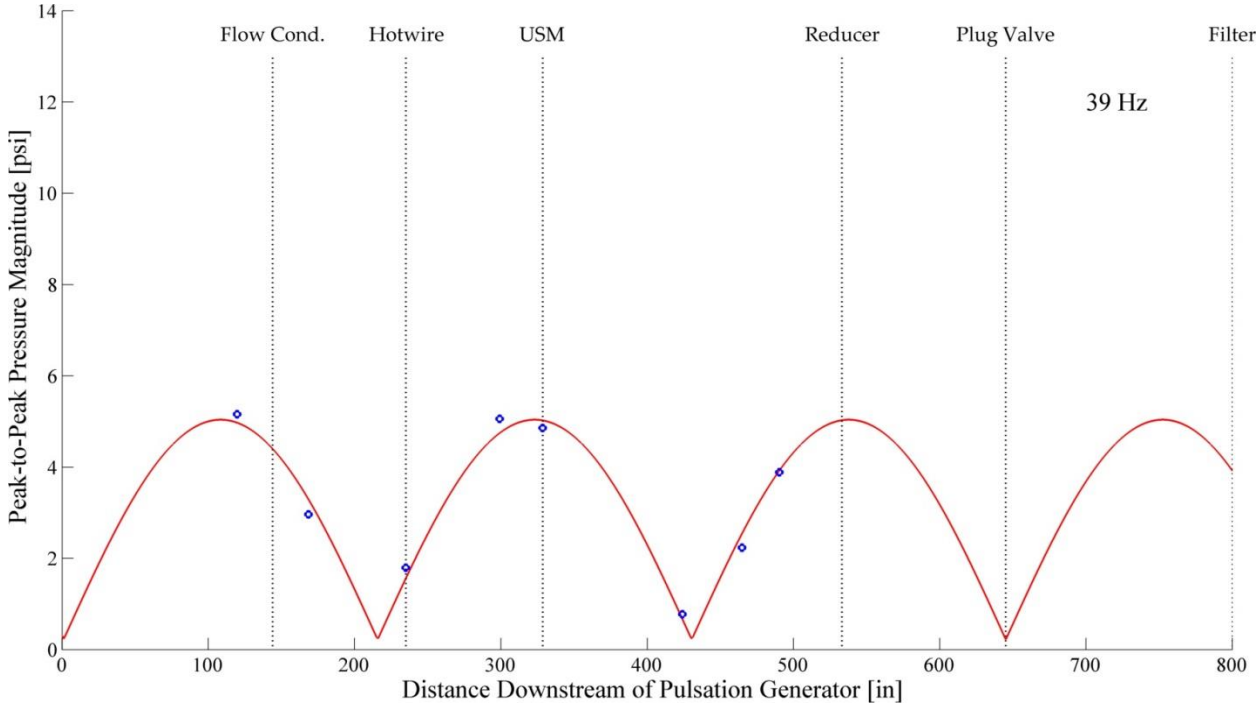

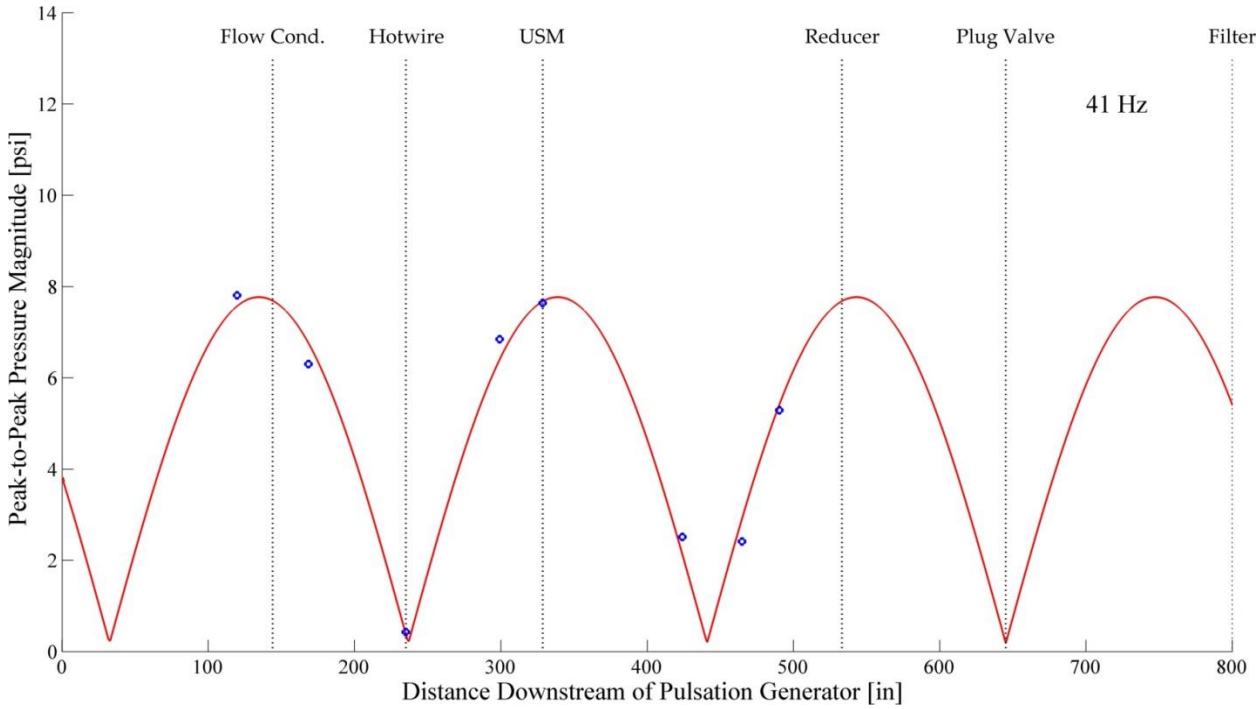

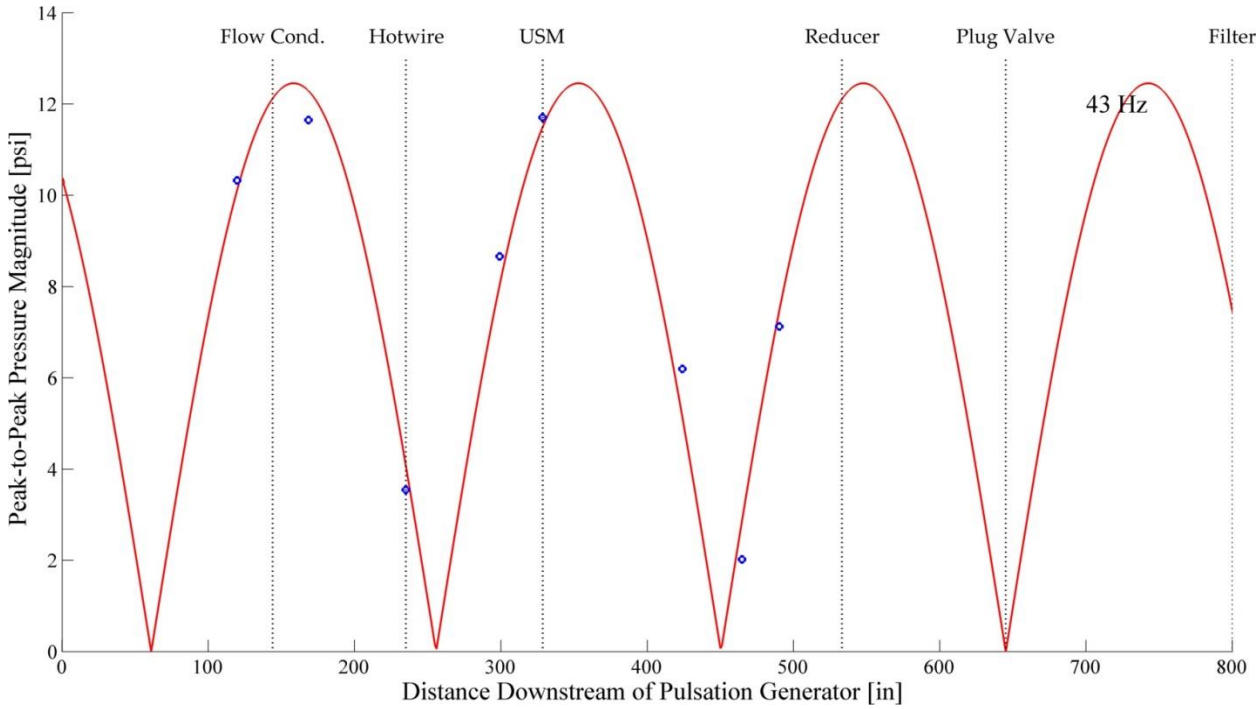

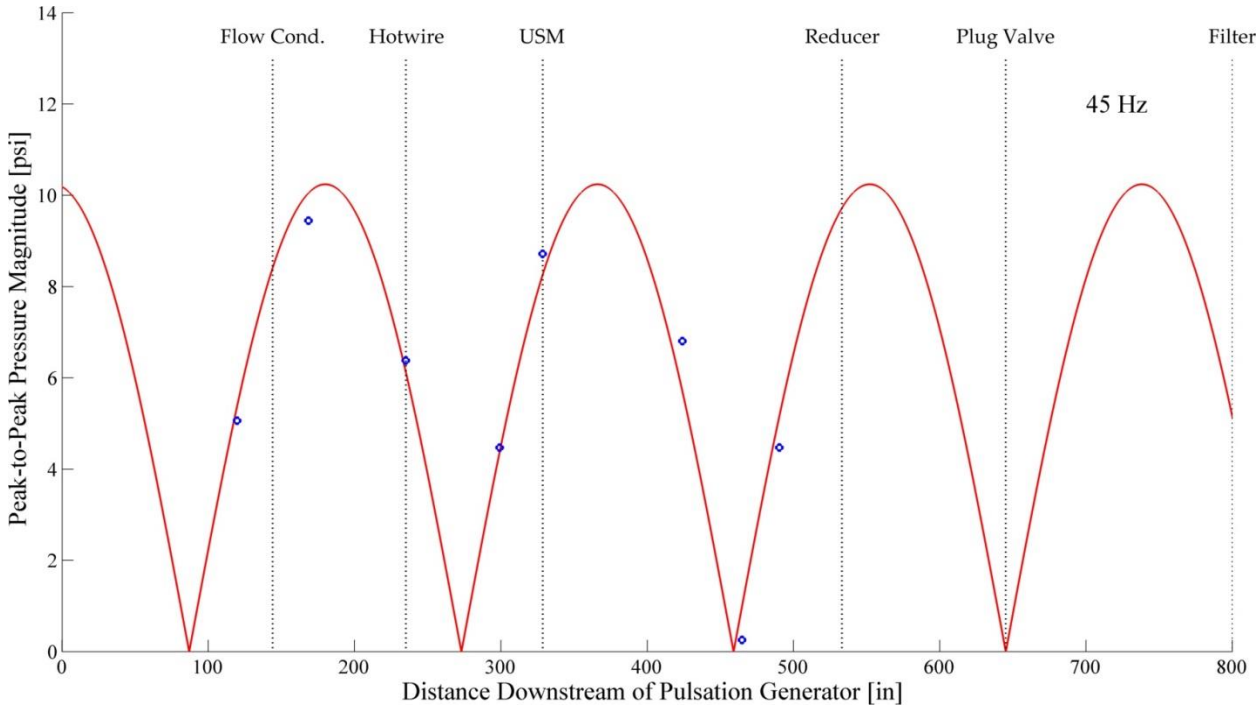

Grouped, 700 acfm:

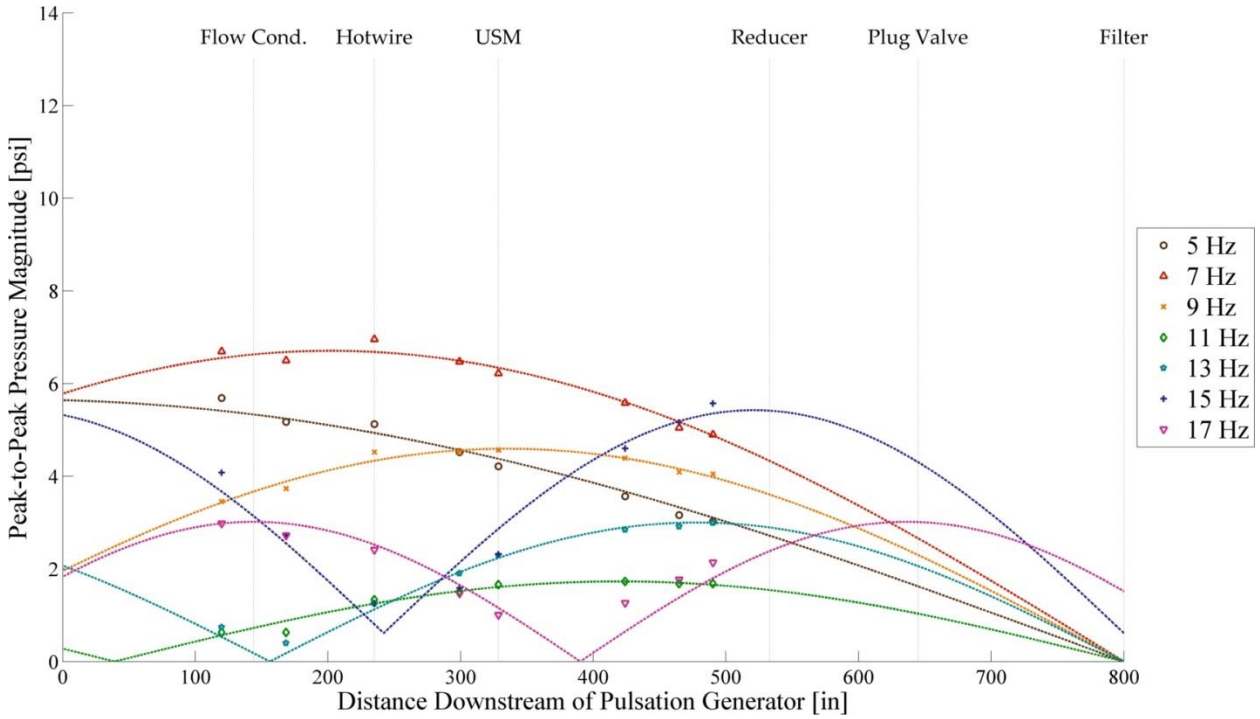

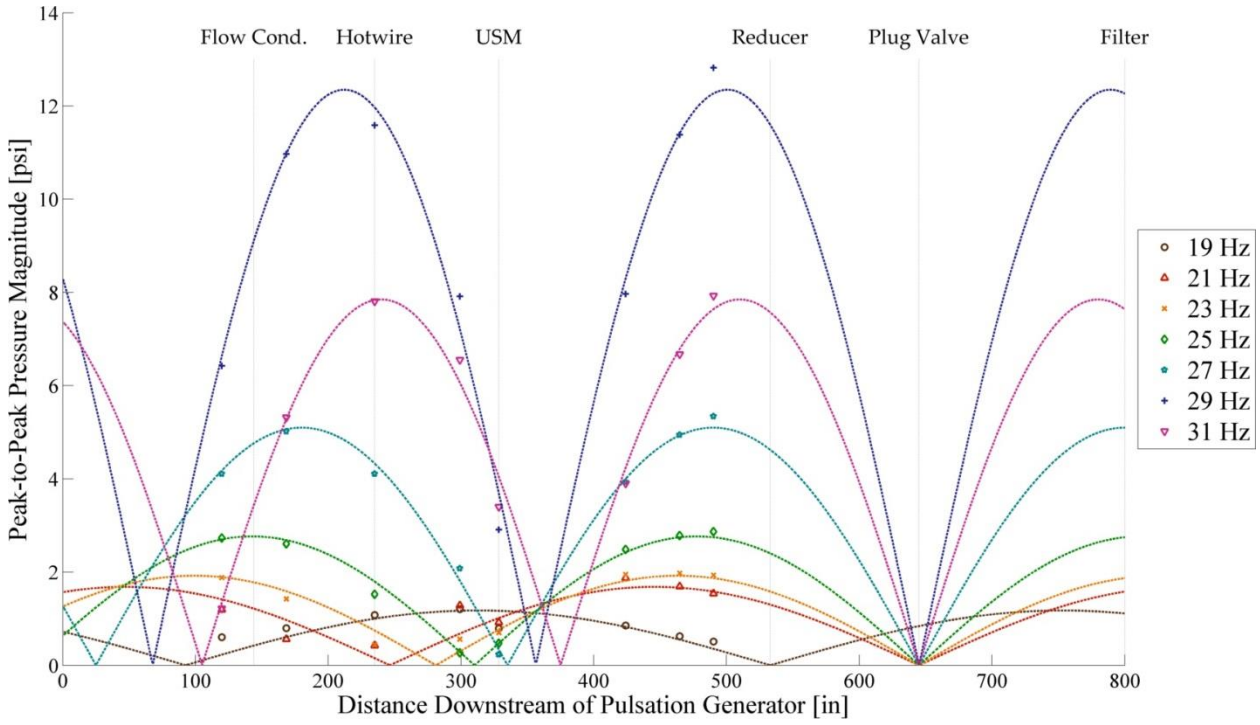

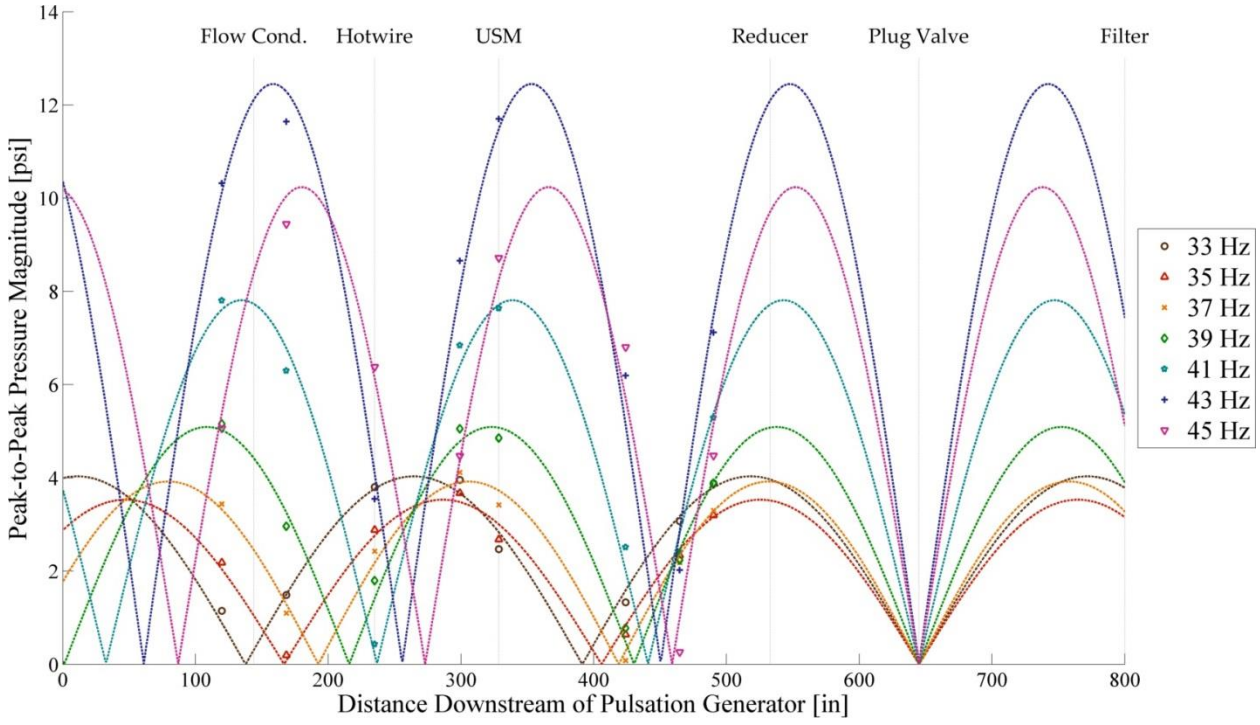

Individual, 200 acfm:

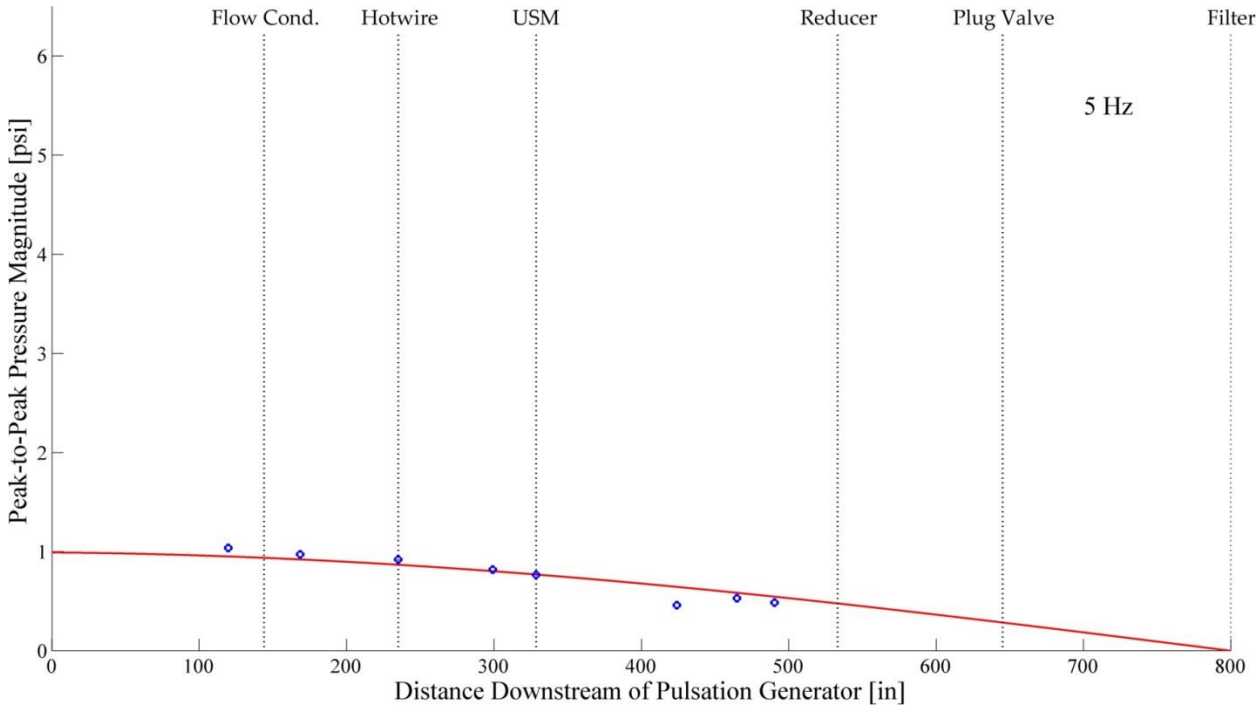

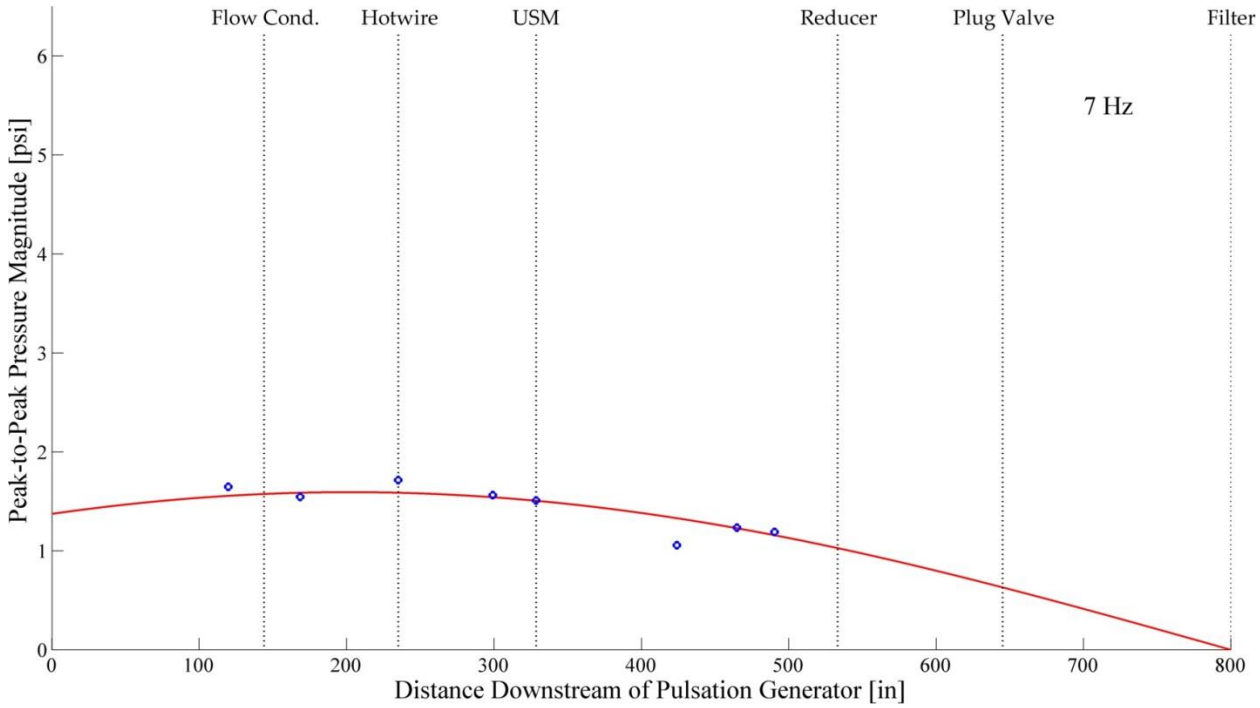

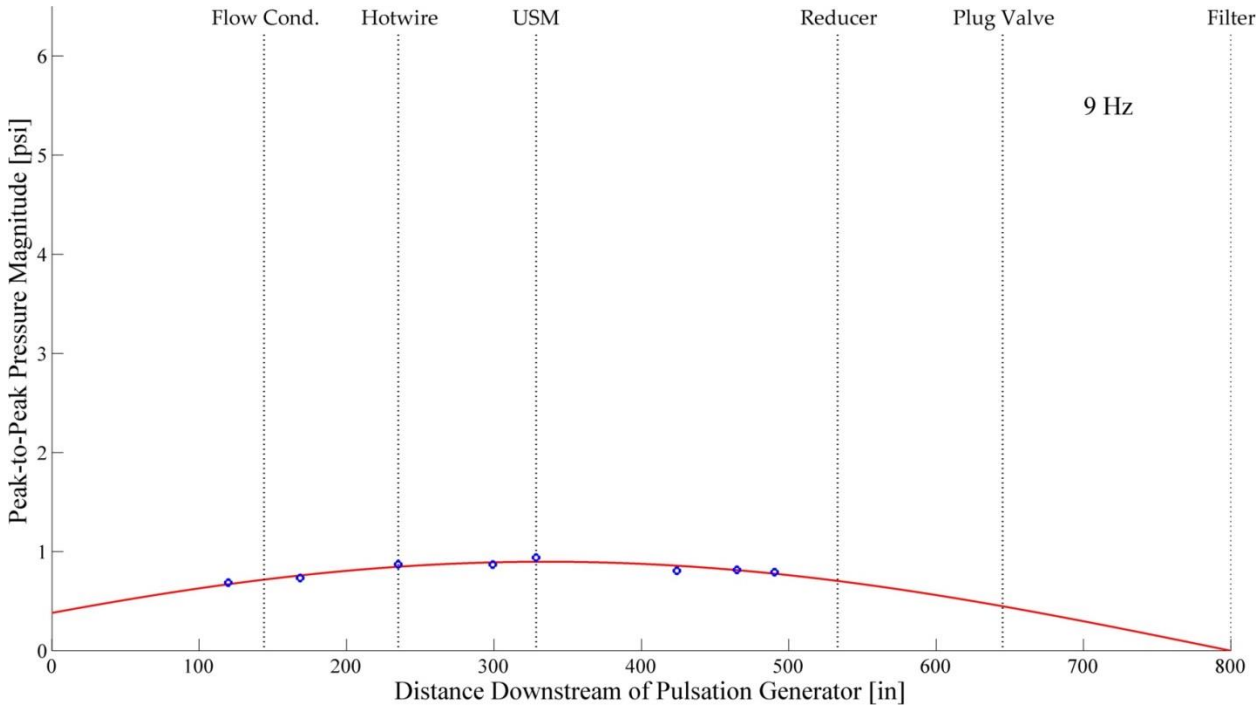

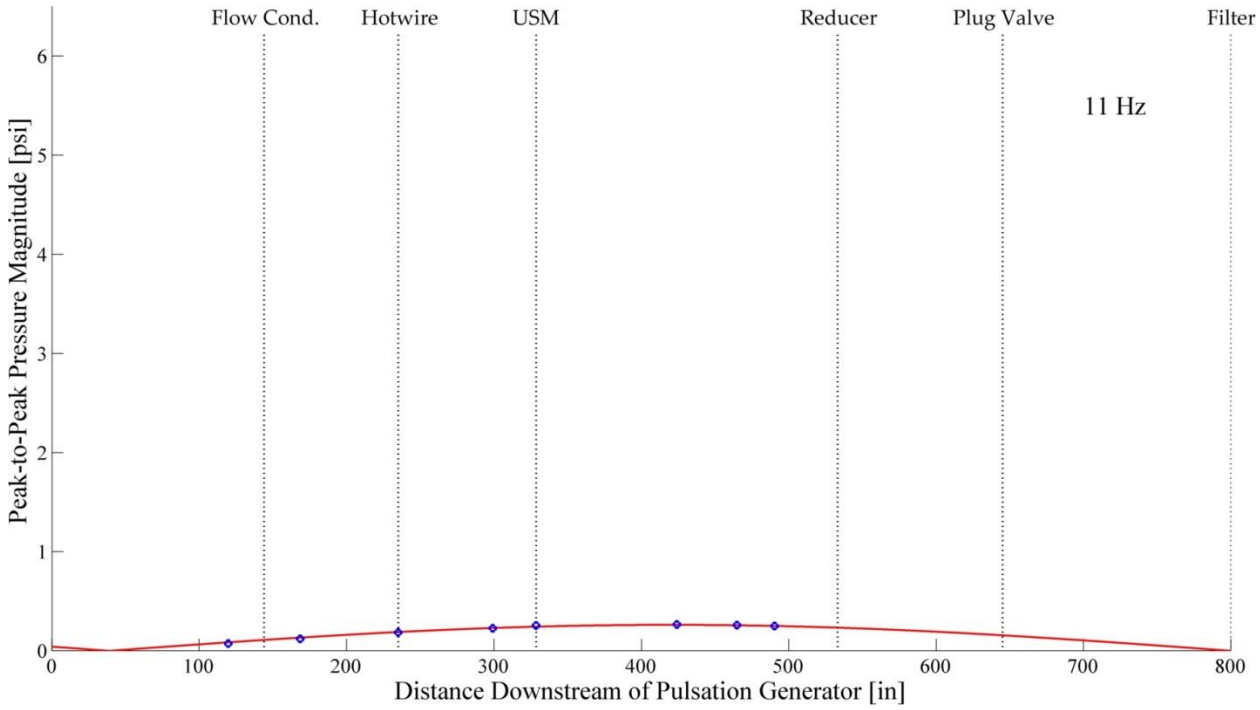

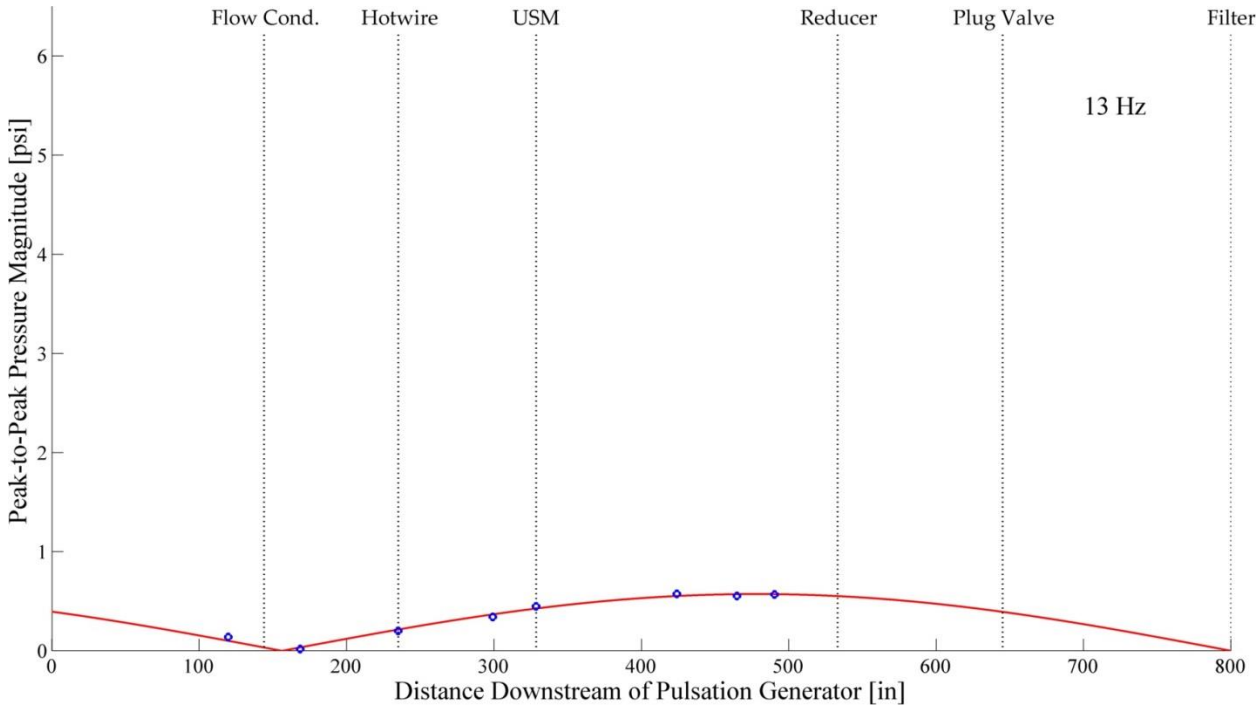

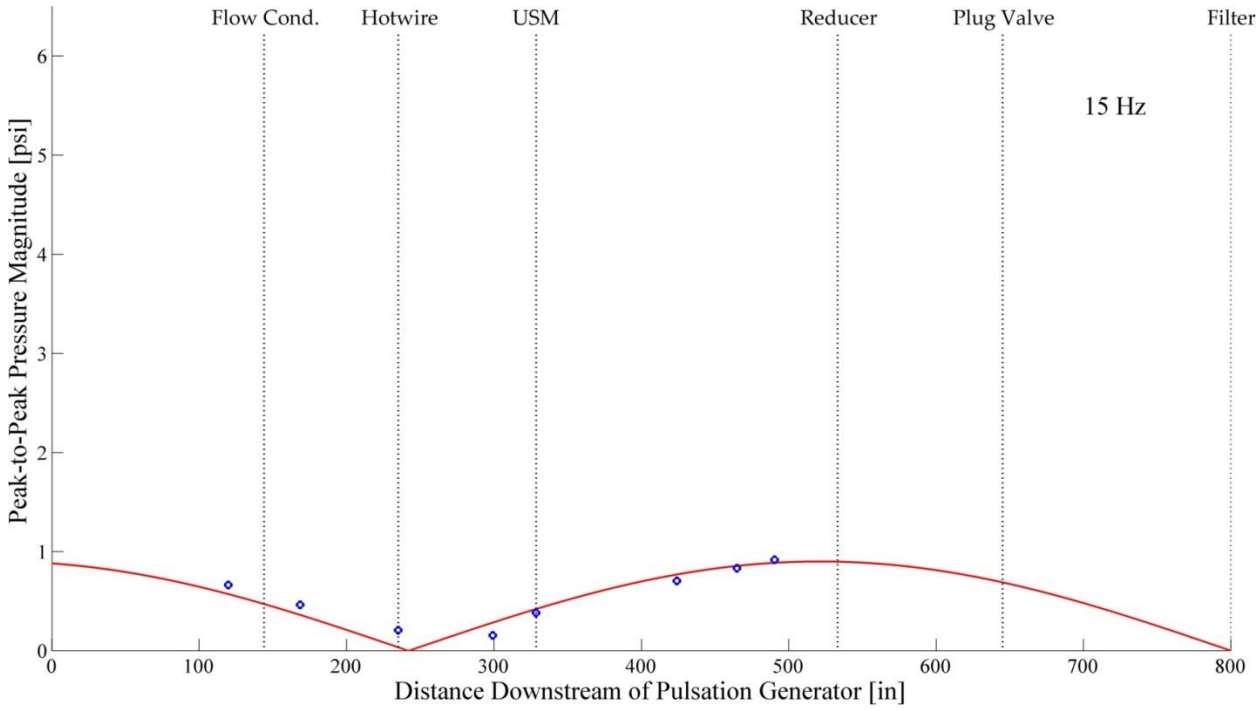

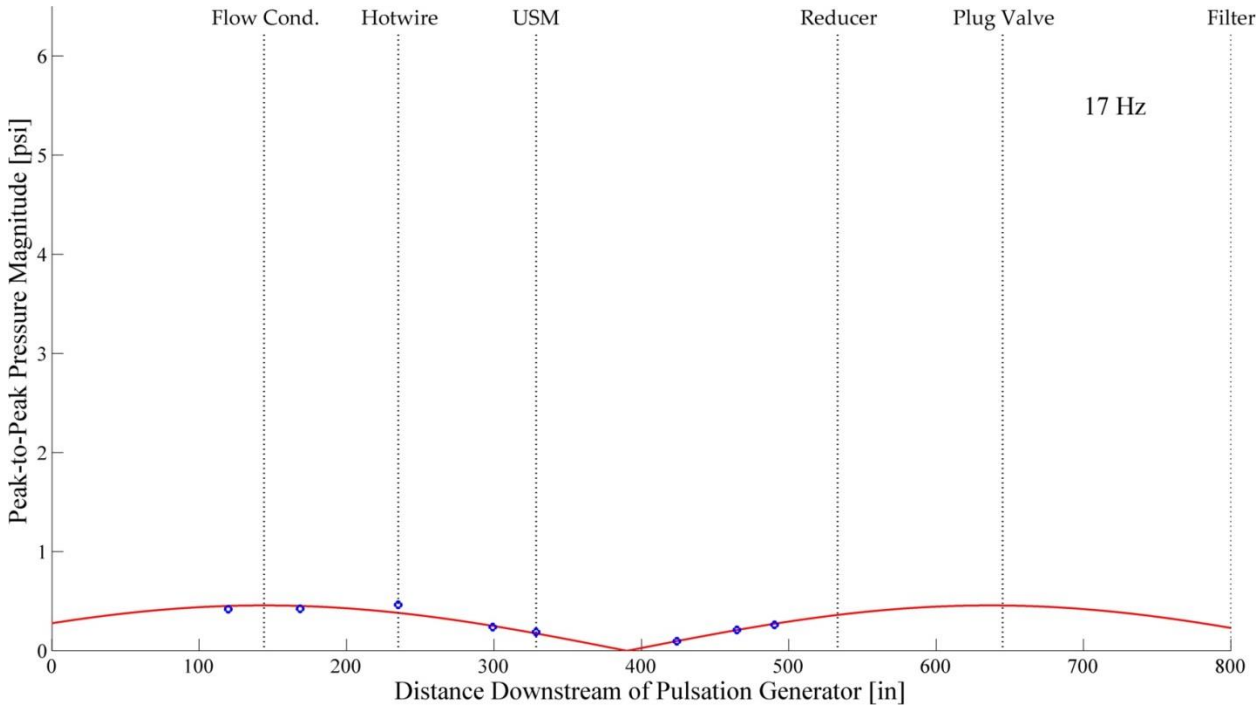

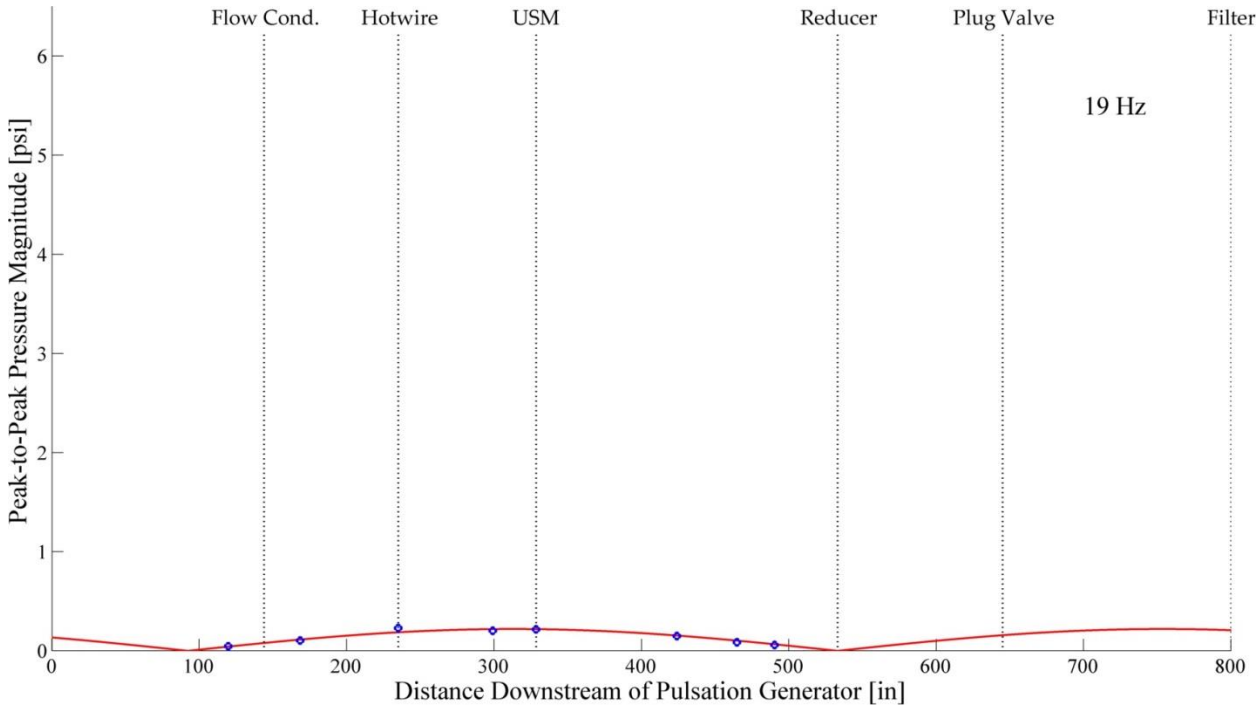

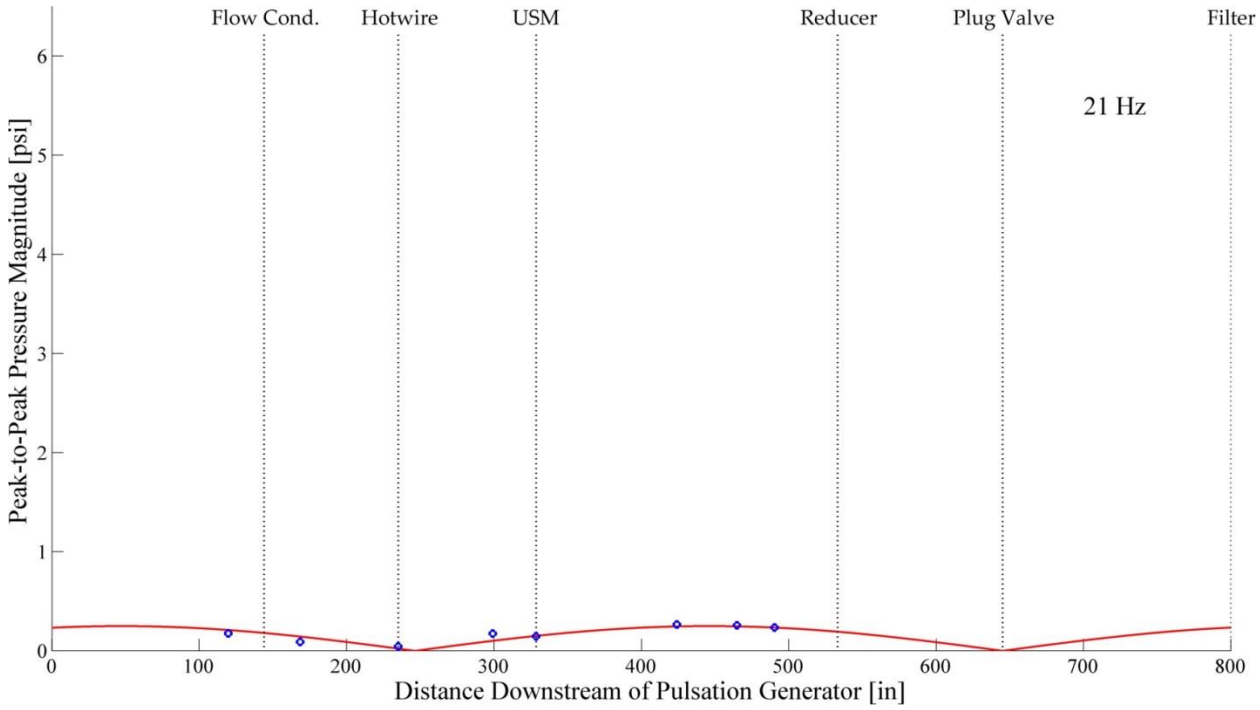

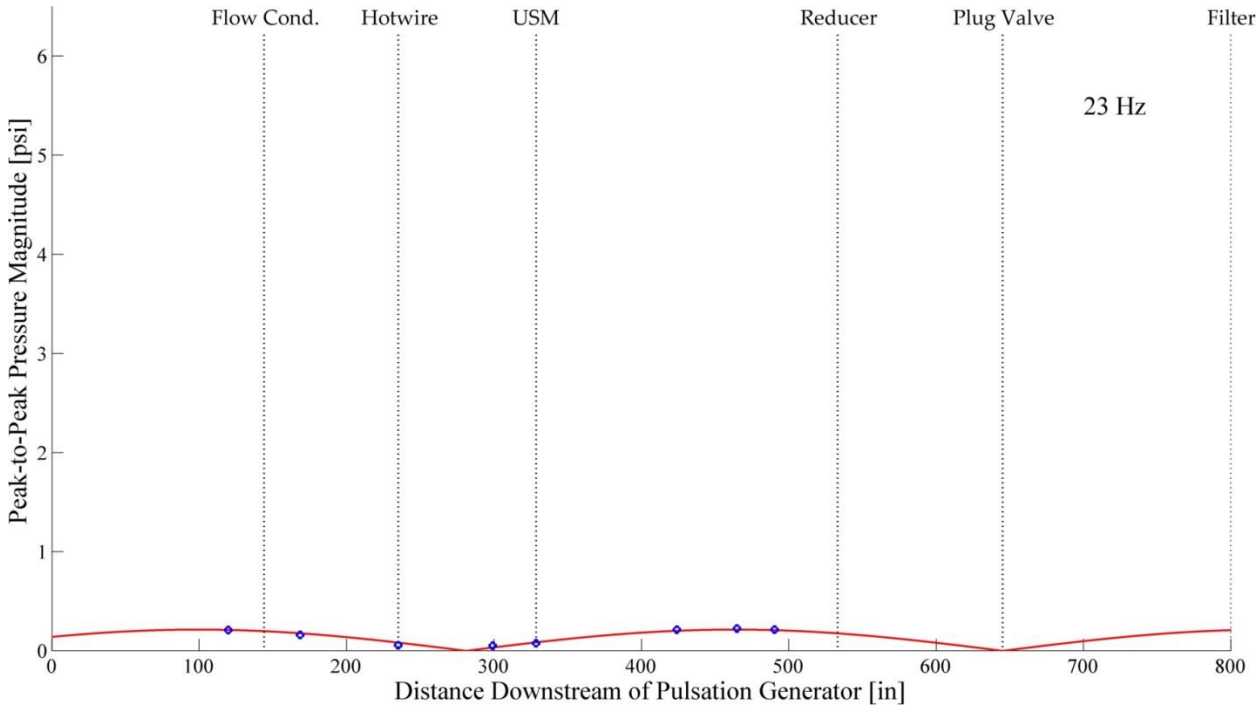

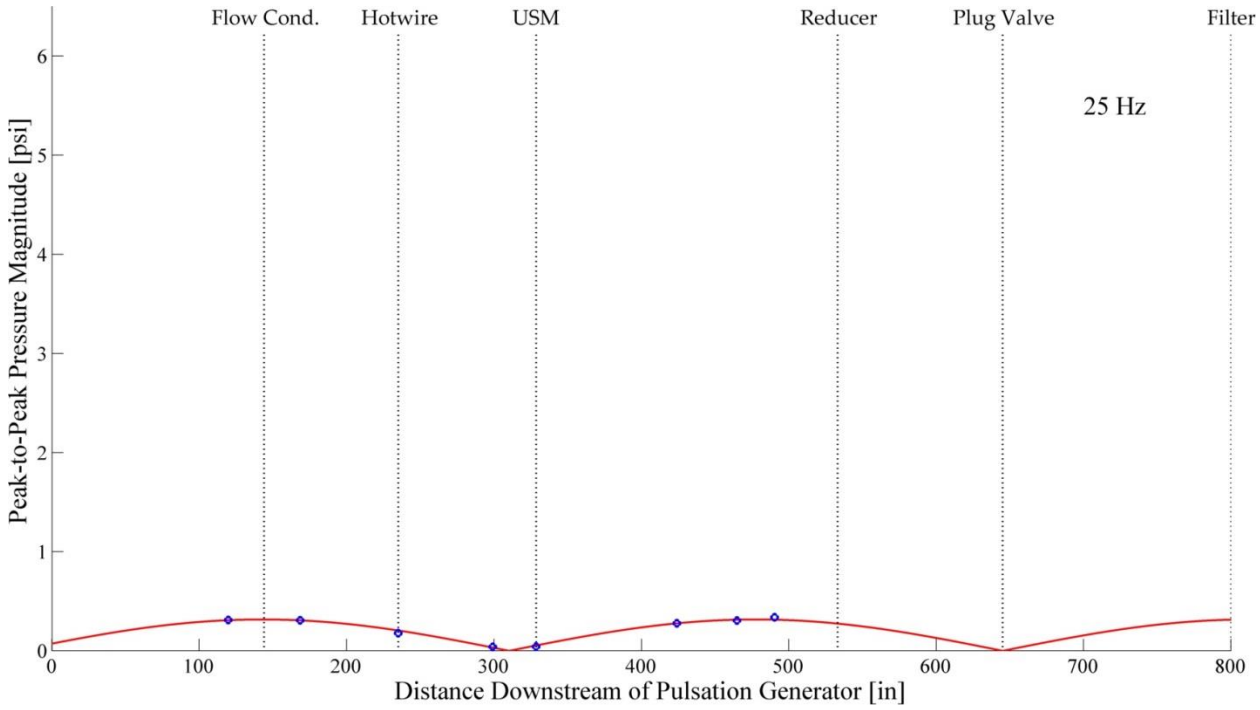

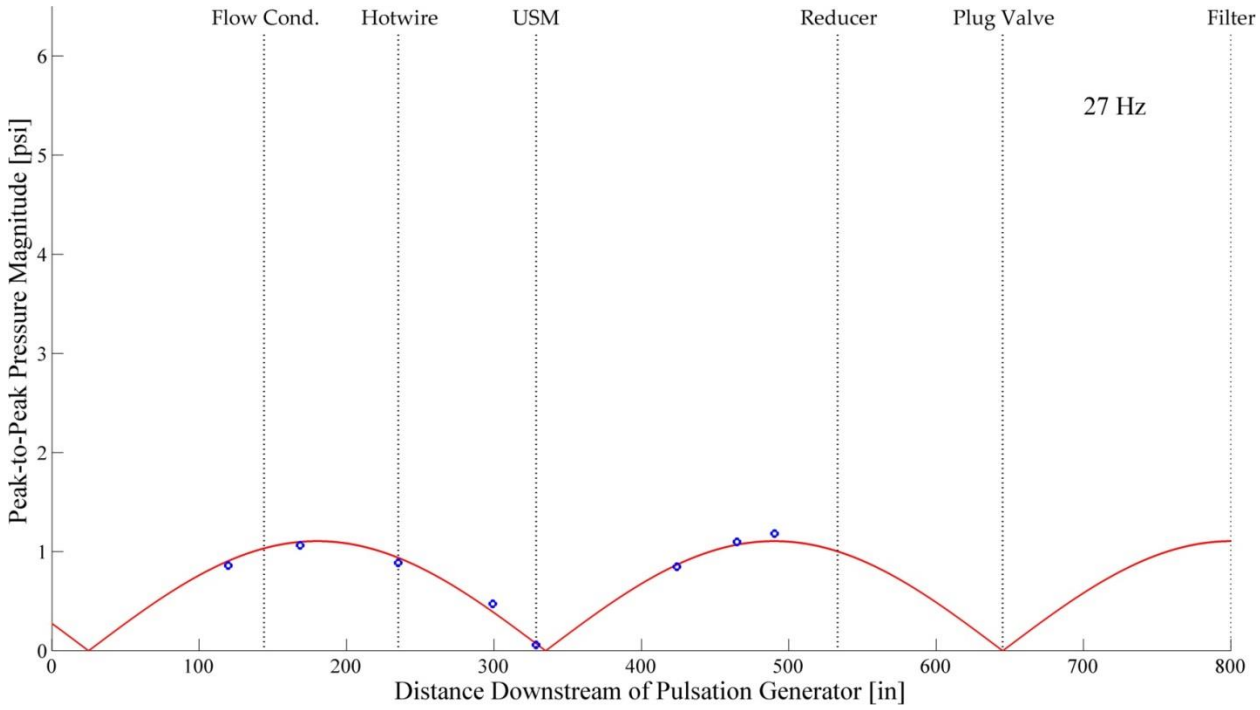

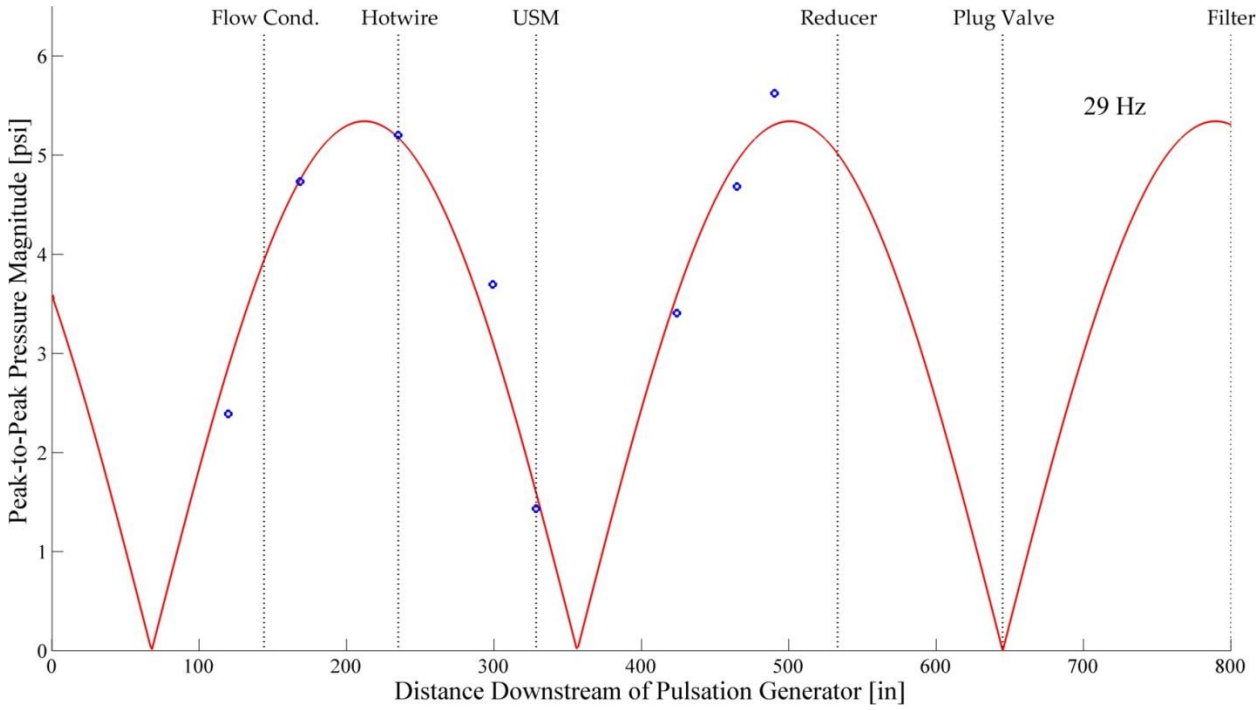

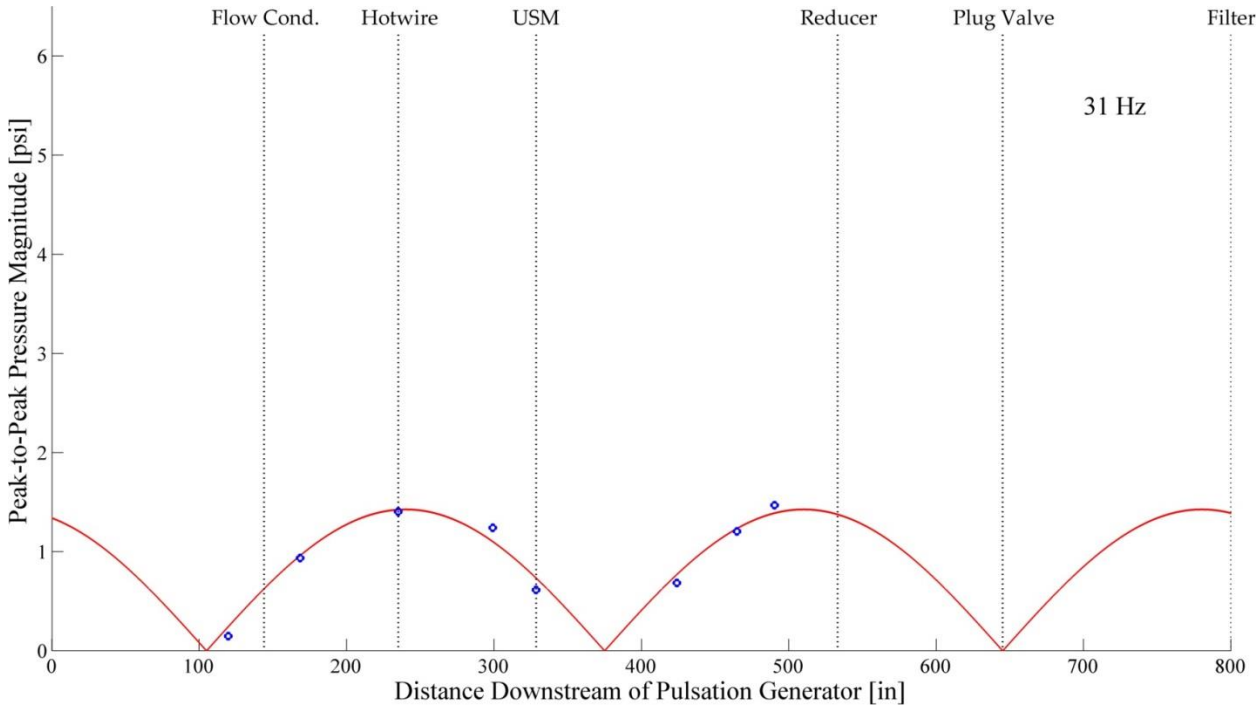

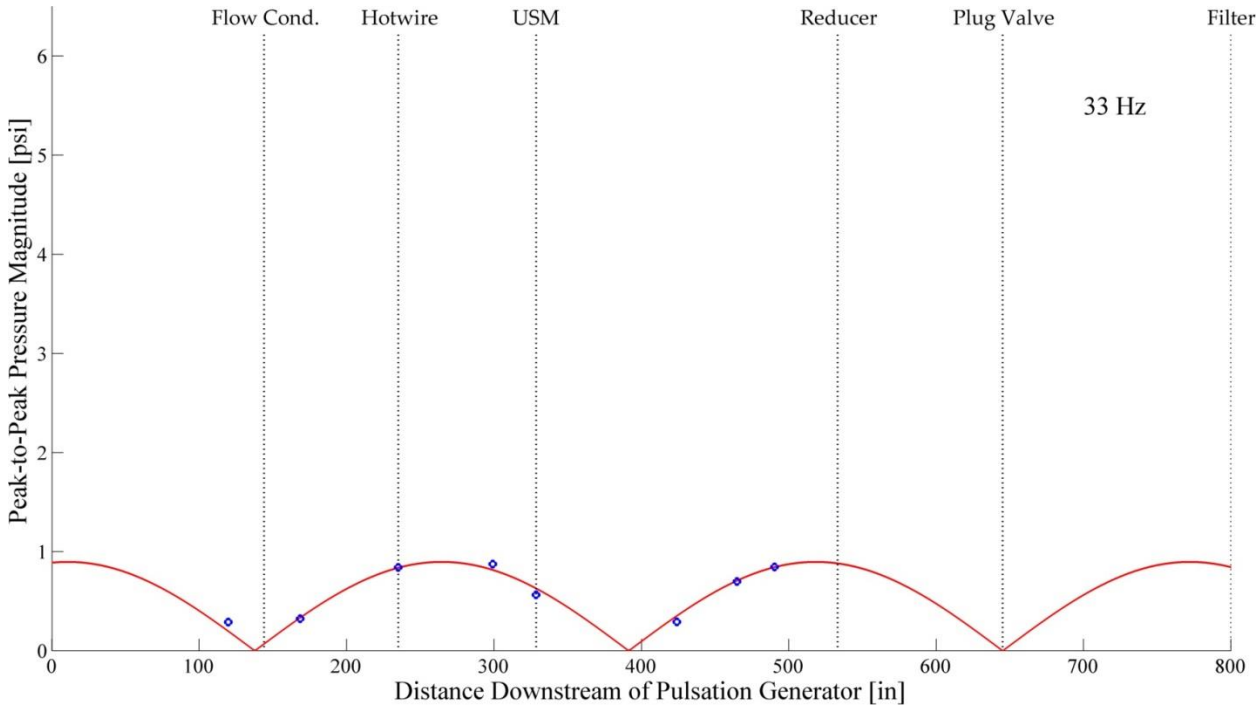

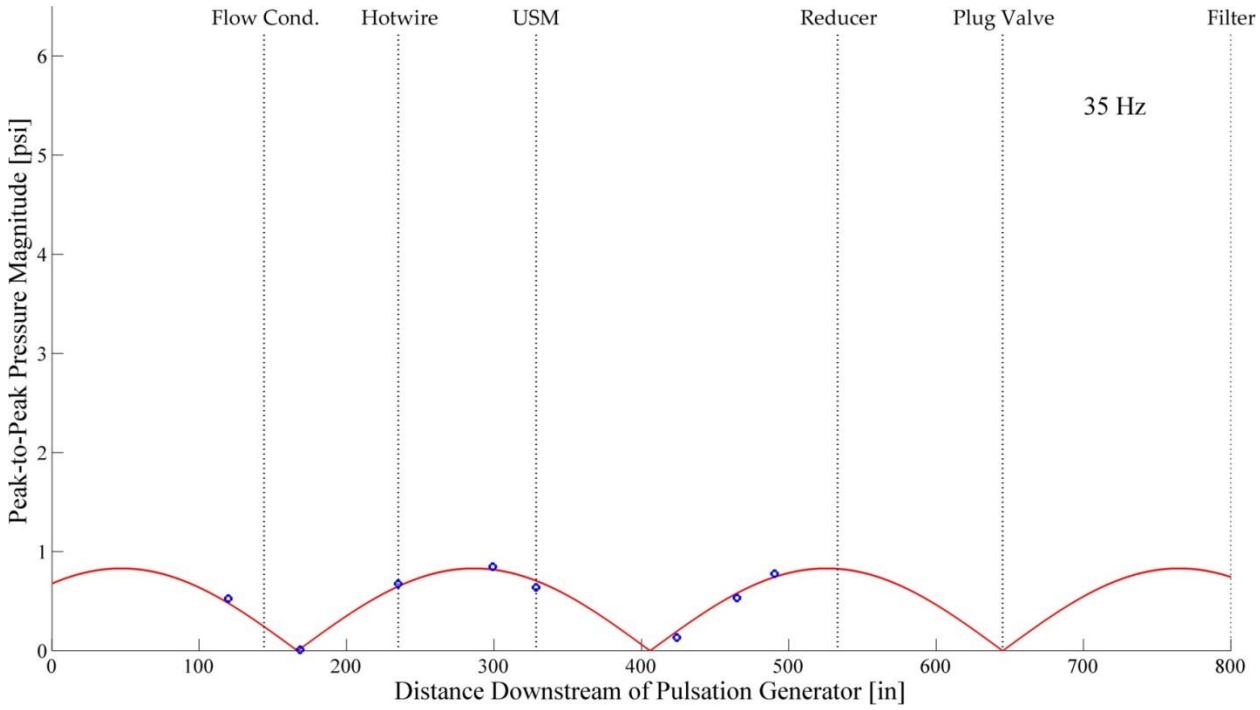

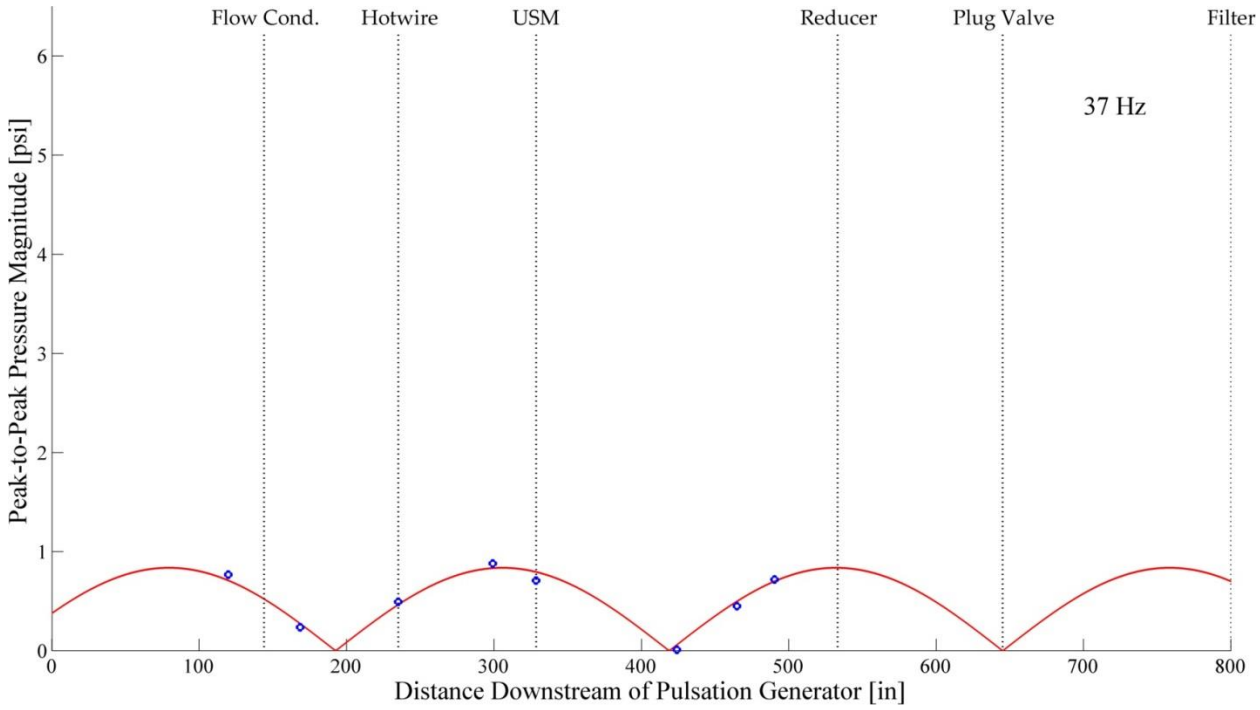

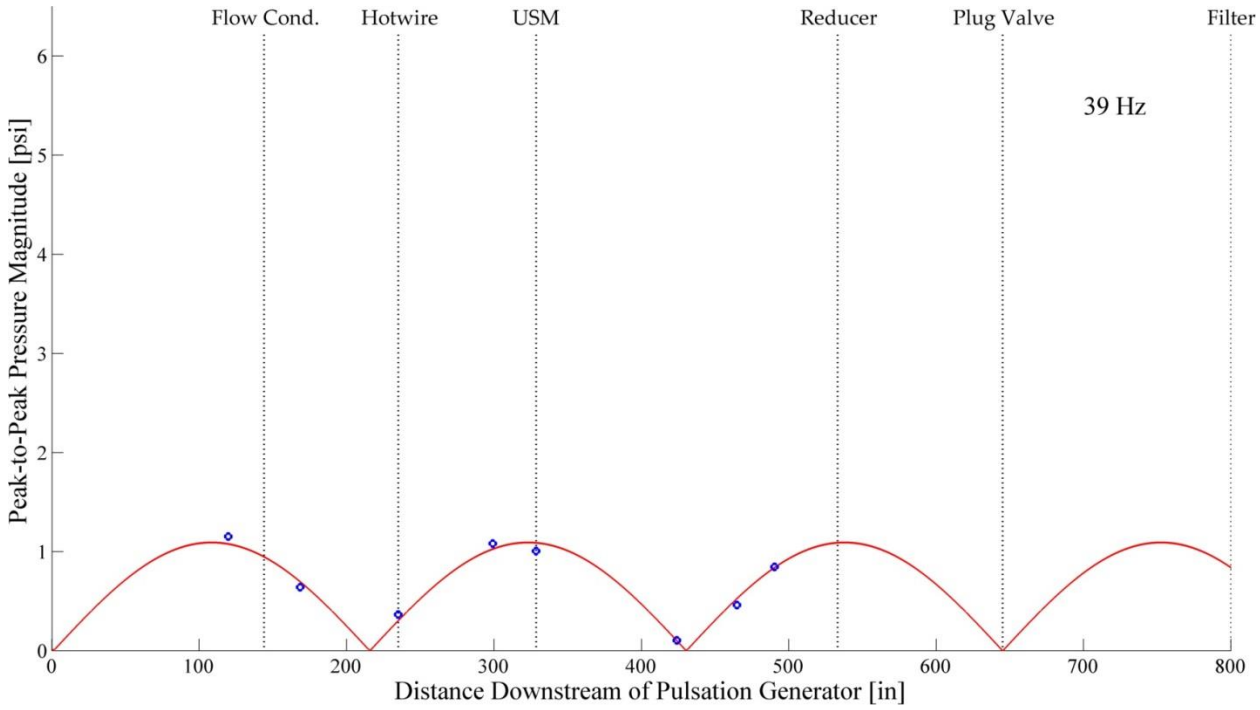

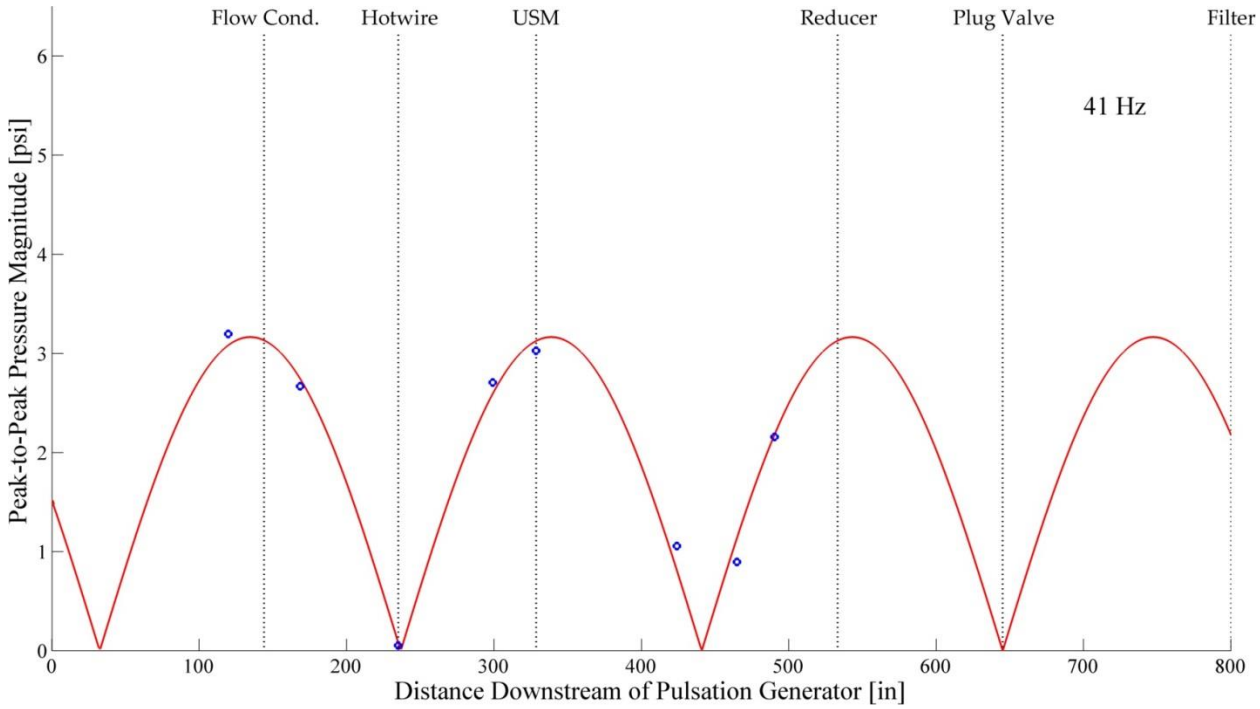

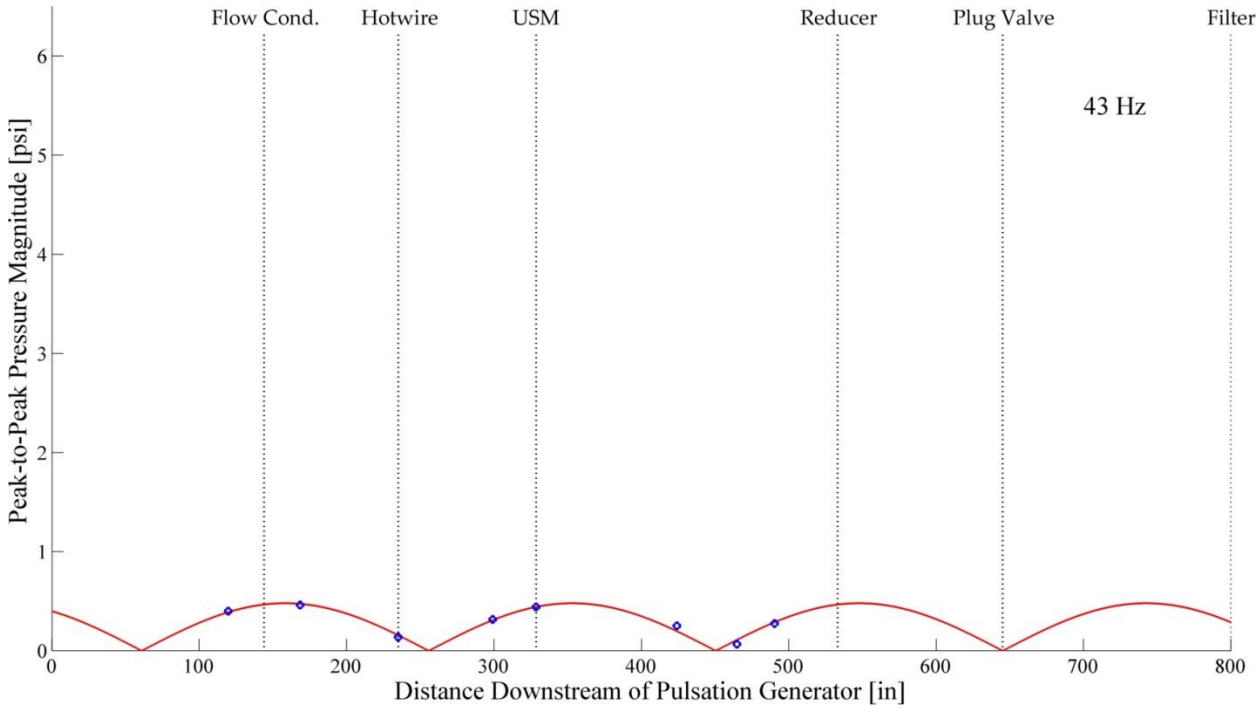

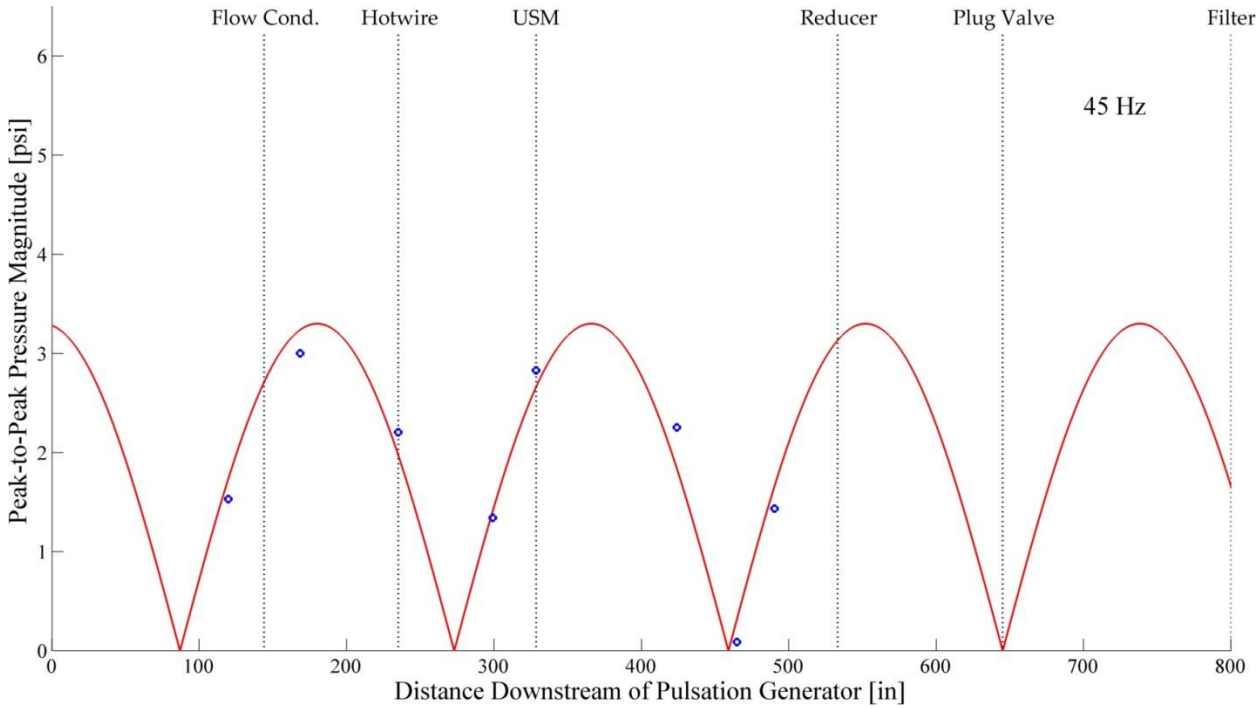

Grouped, 200 acfm:

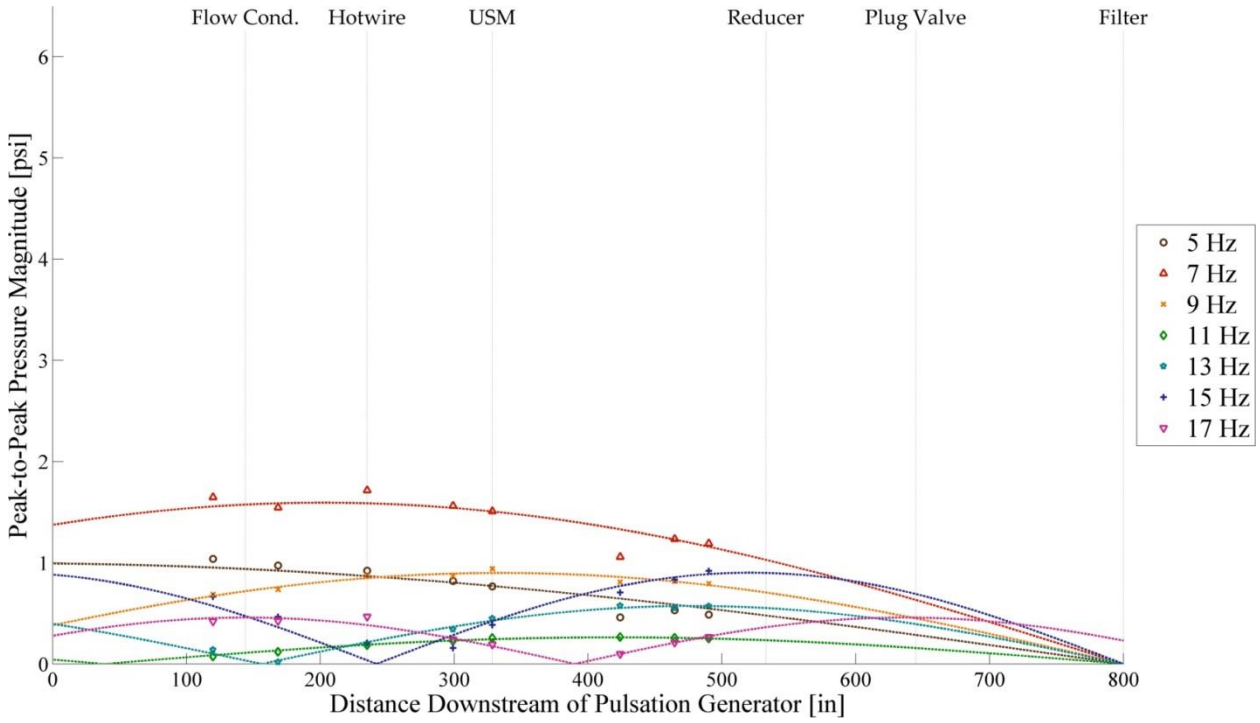

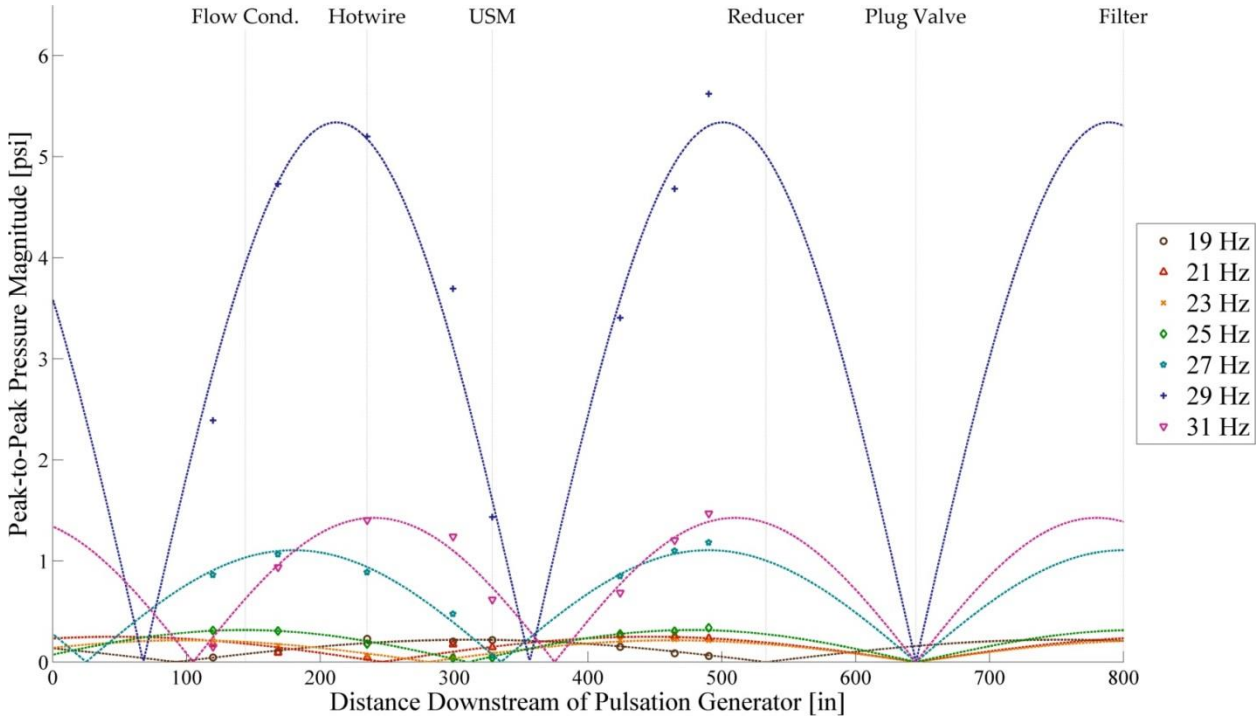

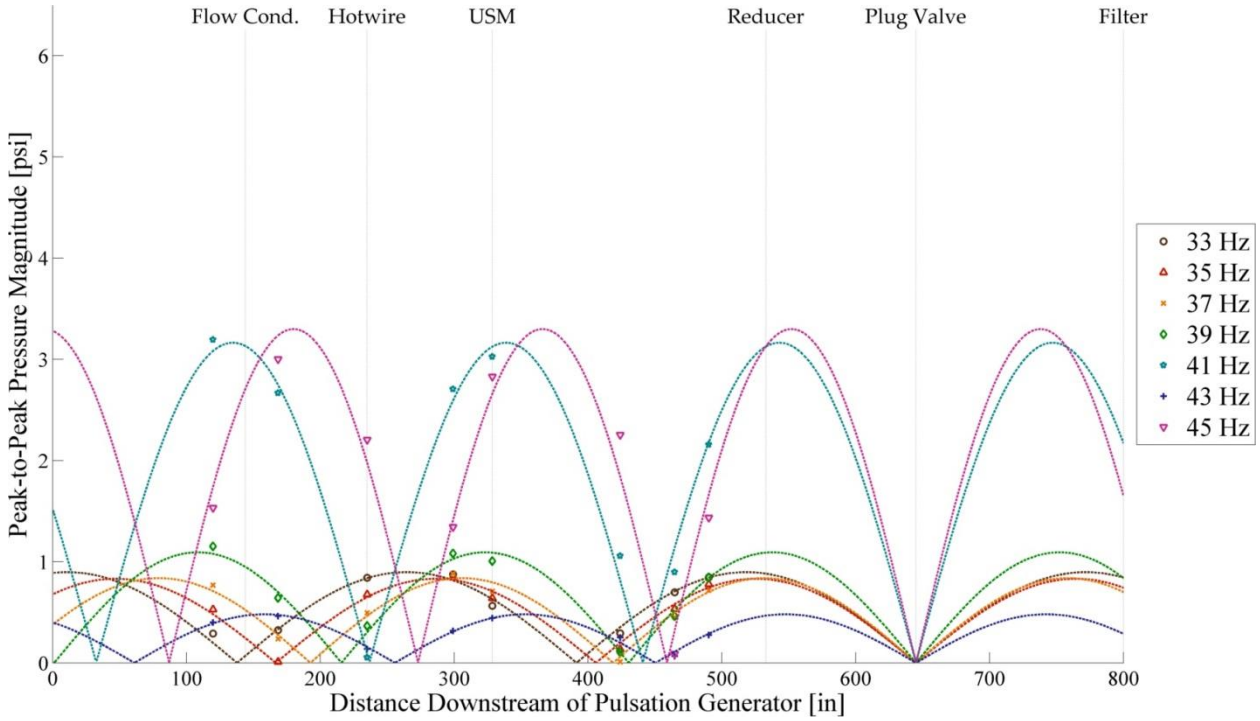

APPENDIX C: PRESSURE PULSATION STANDING WAVE STATISTICS

700 acfm:

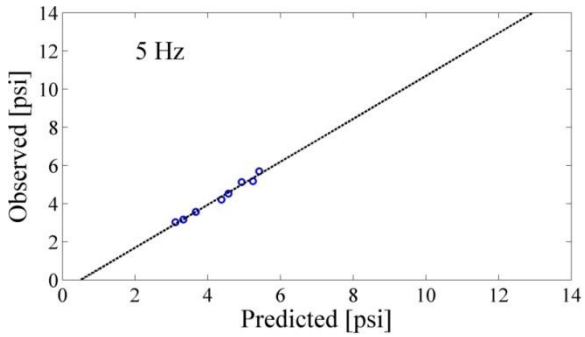

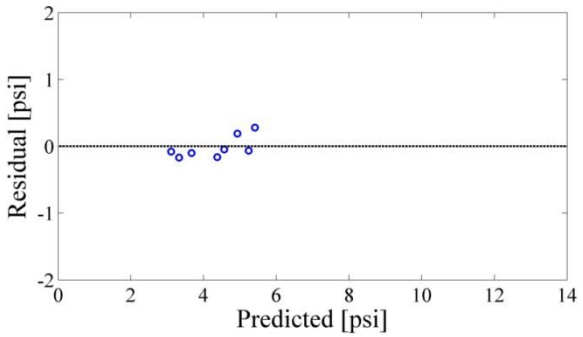

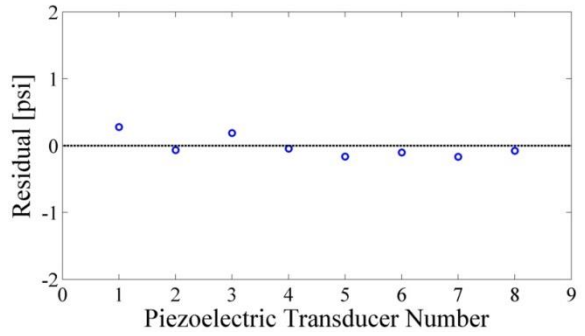

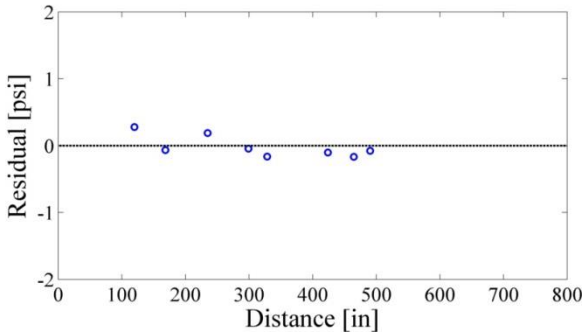

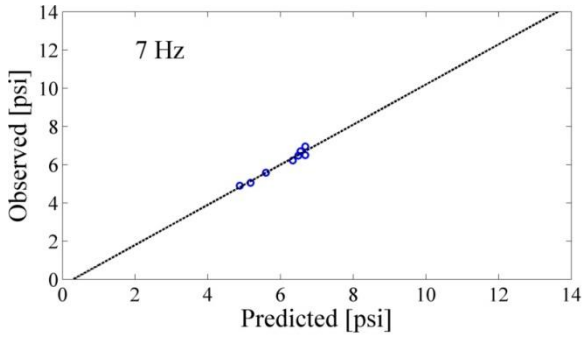

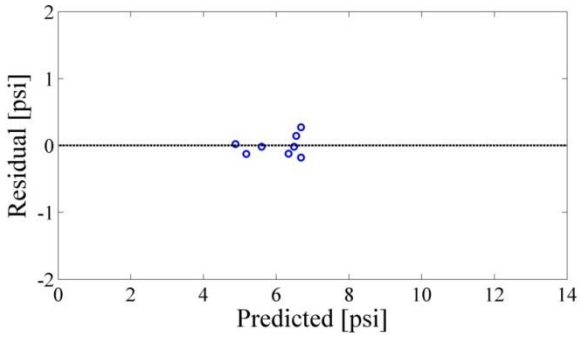

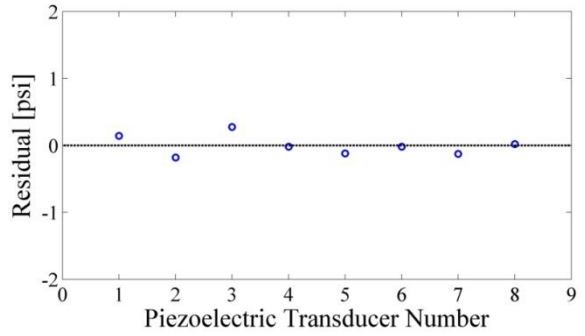

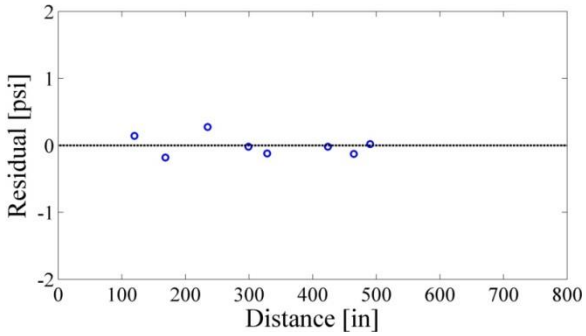

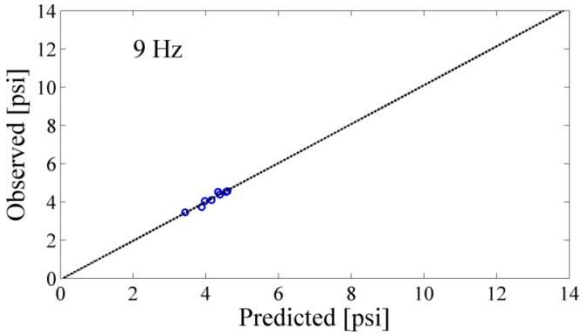

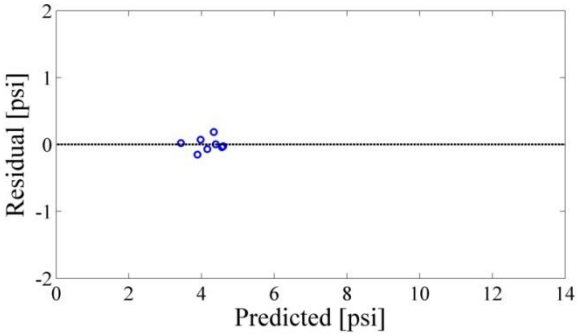

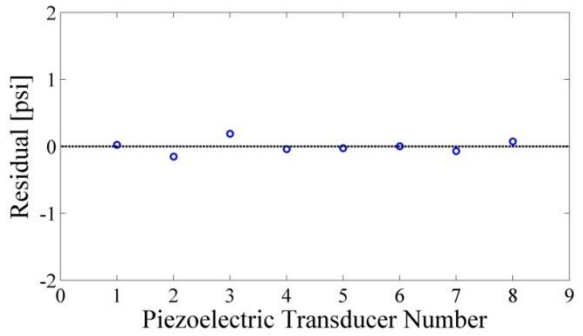

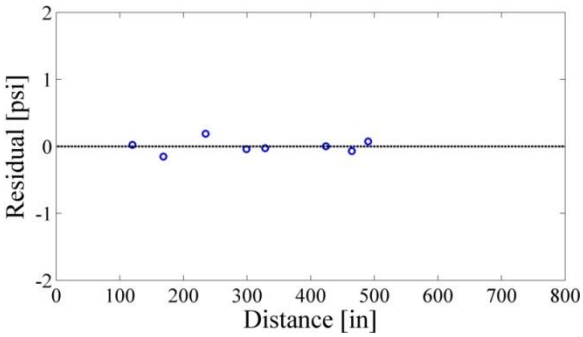

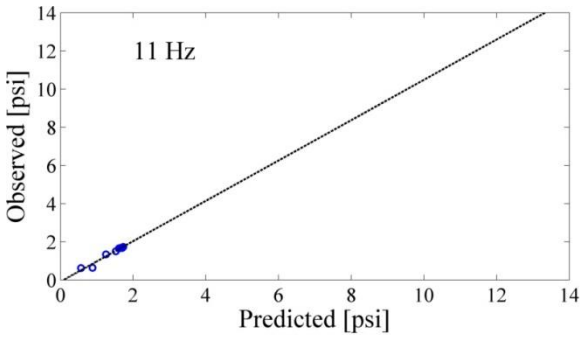

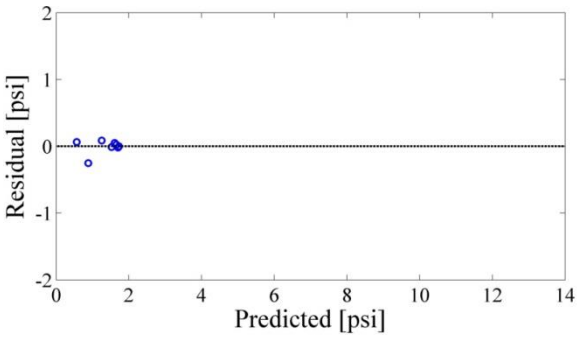

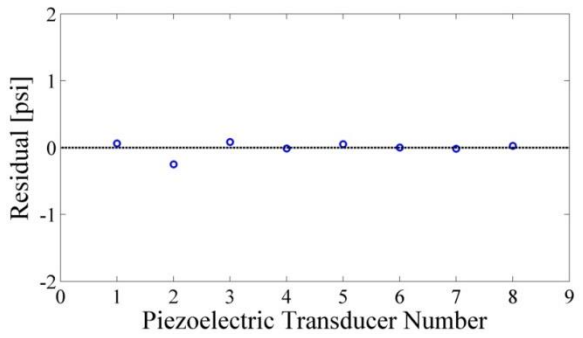

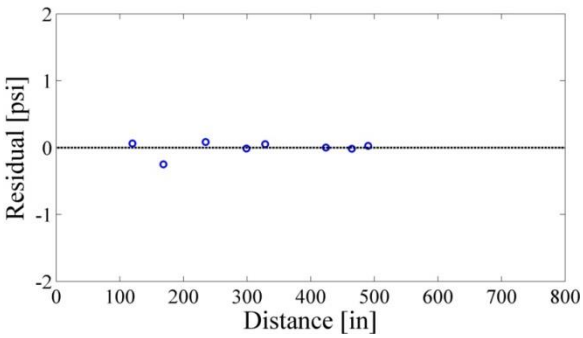

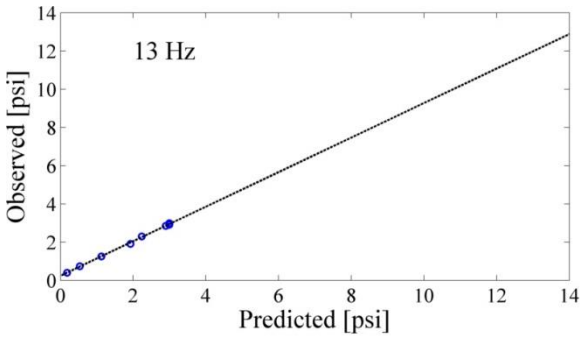

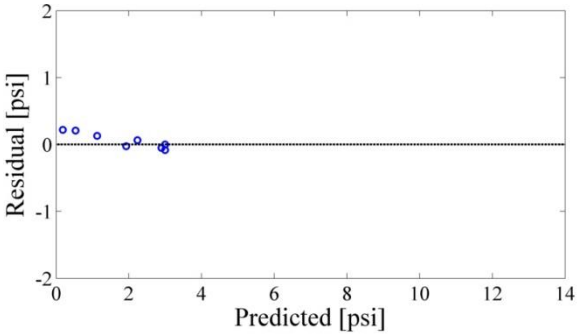

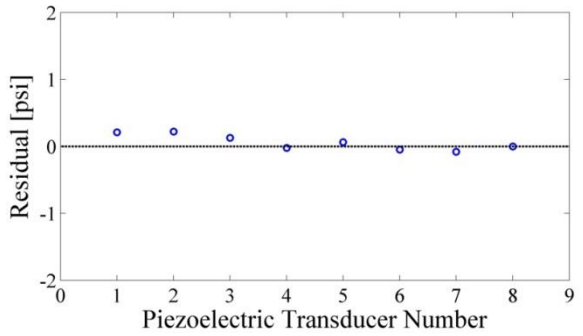

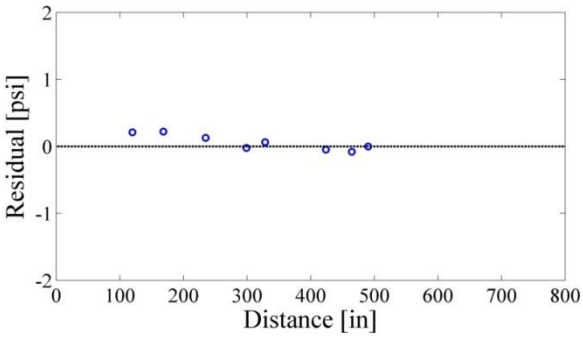

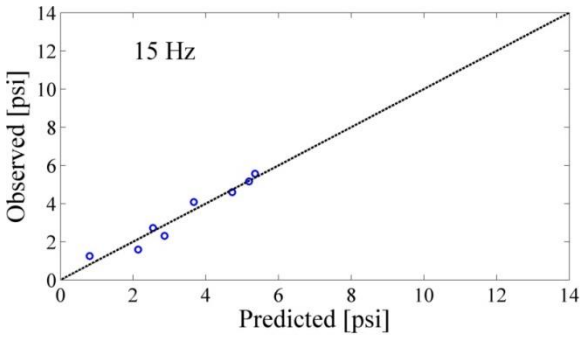

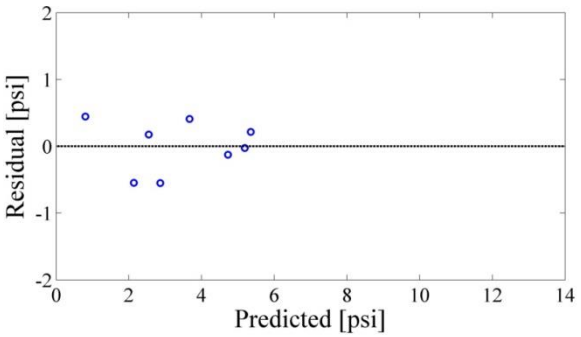

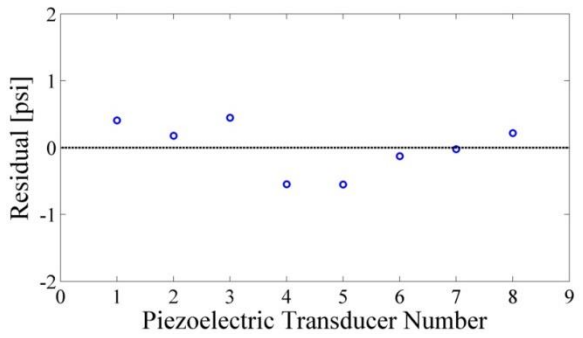

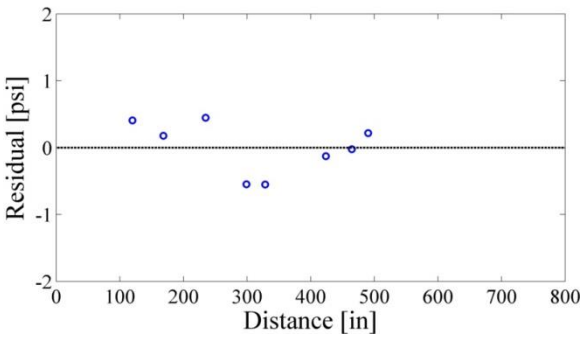

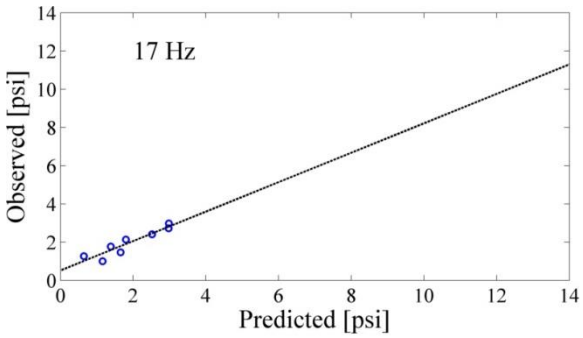

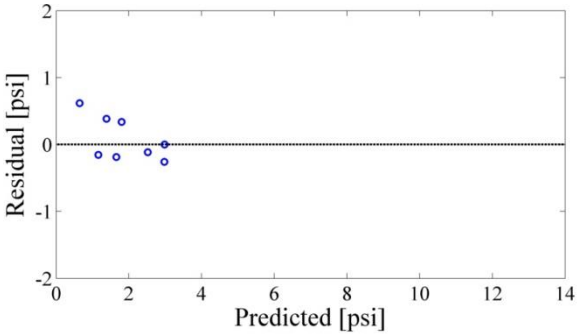

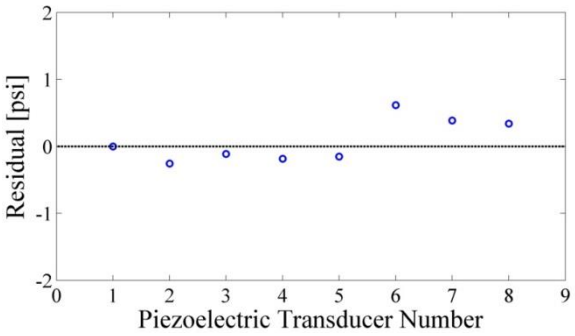

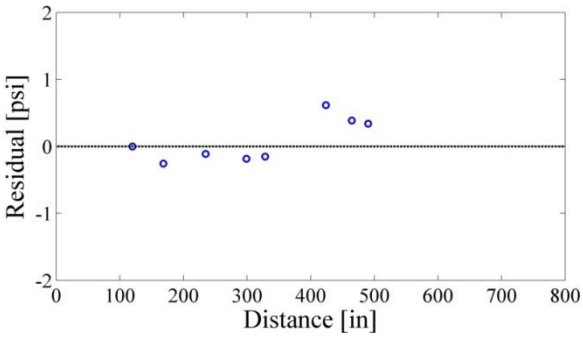

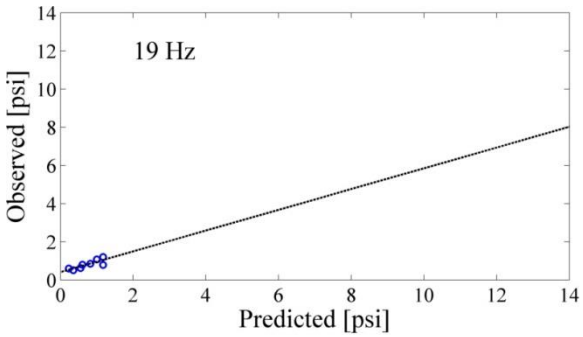

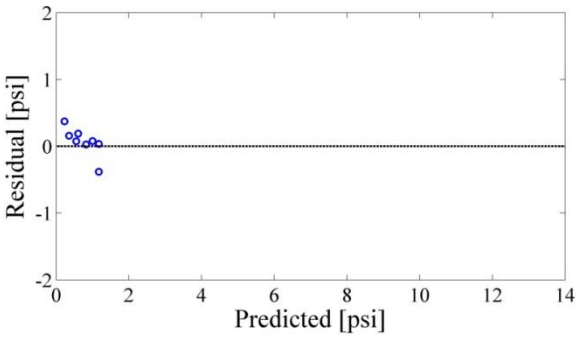

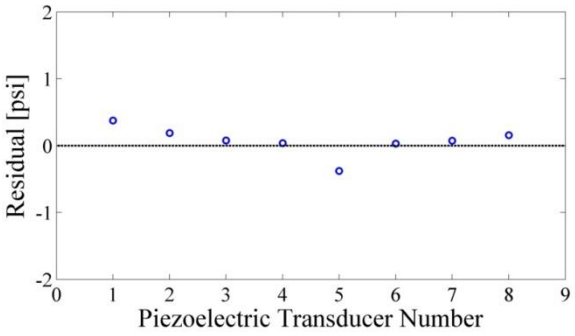

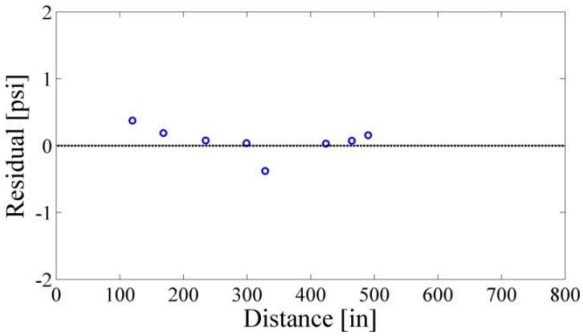

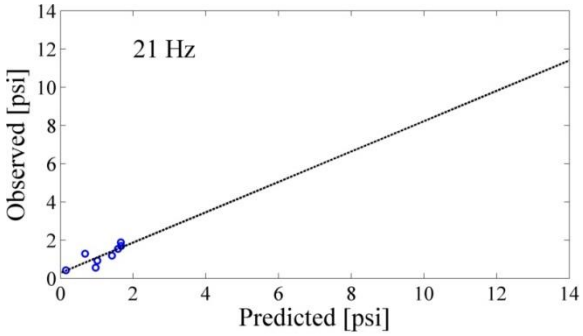

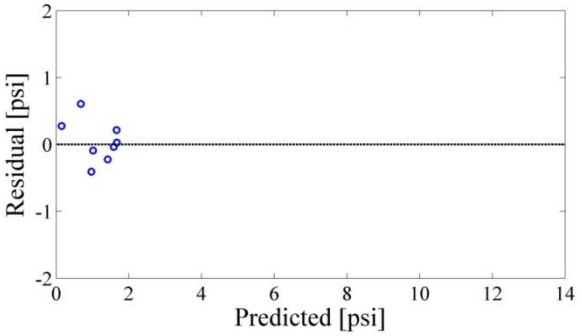

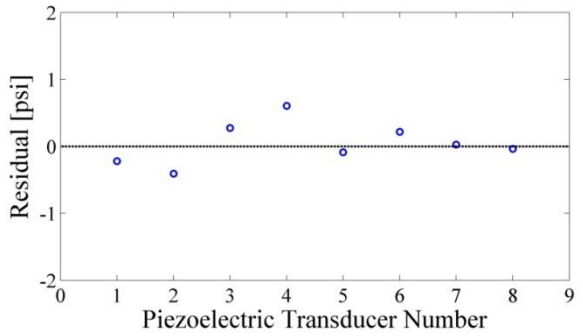

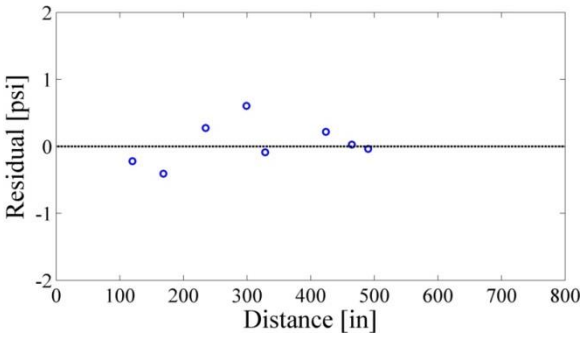

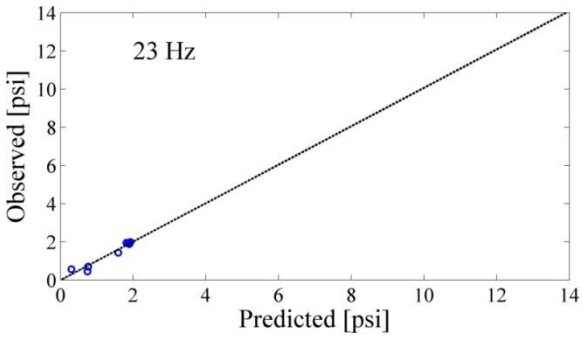

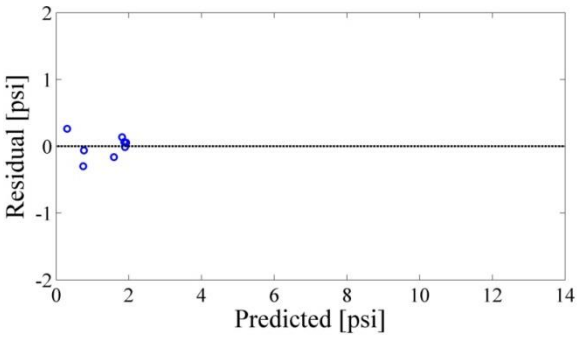

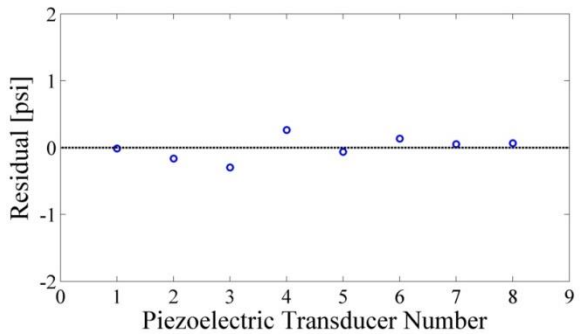

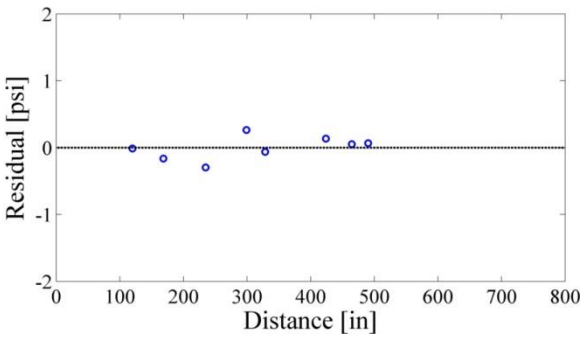

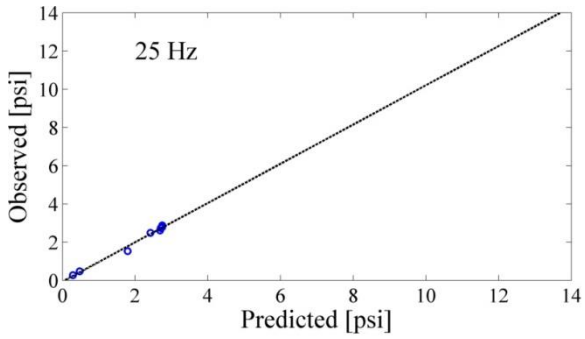

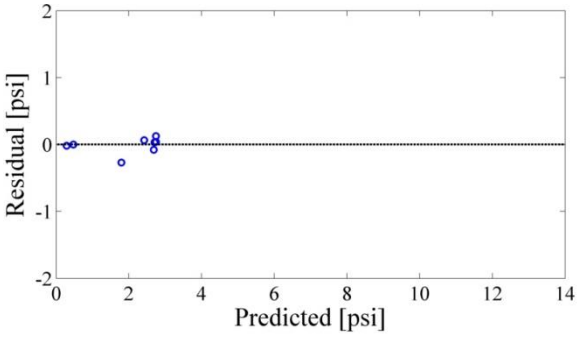

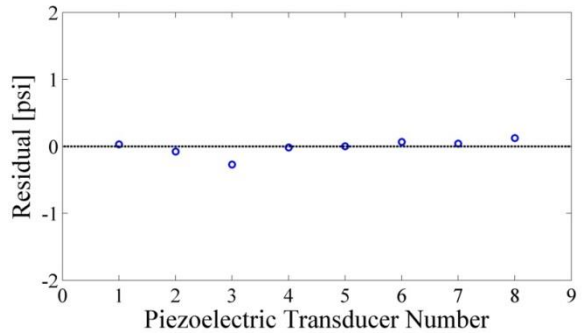

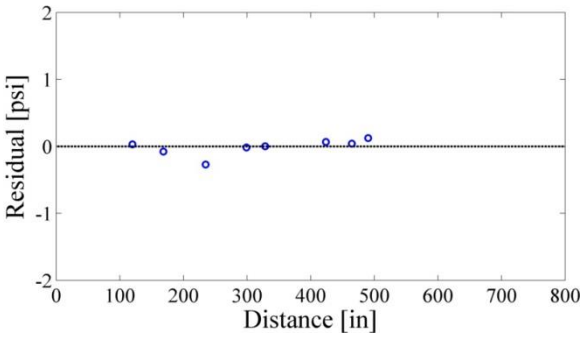

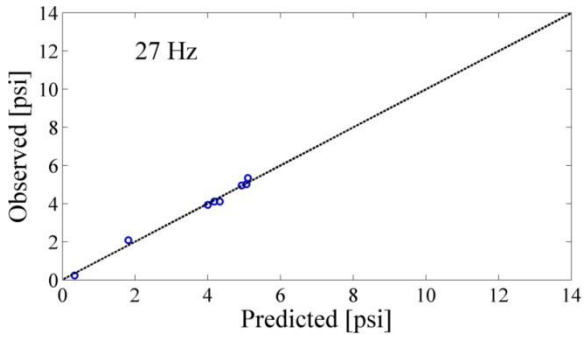

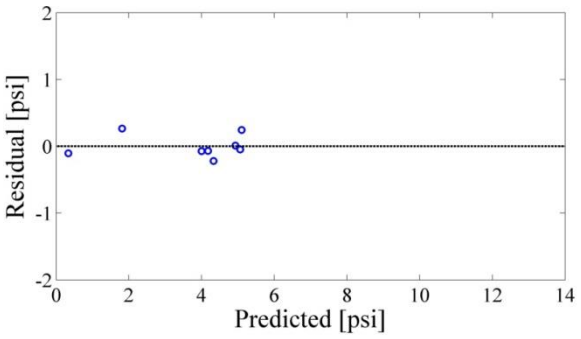

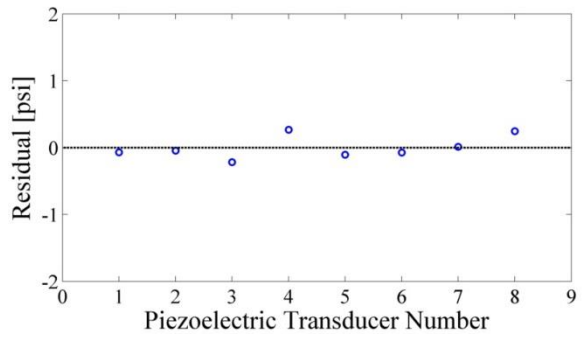

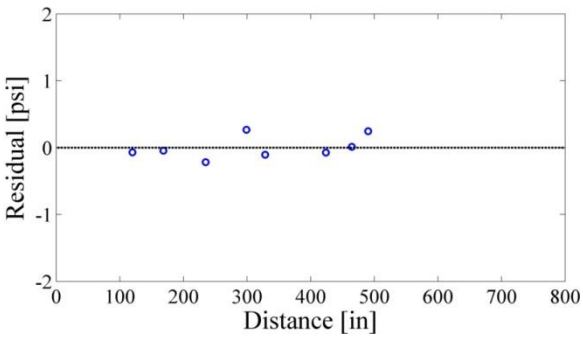

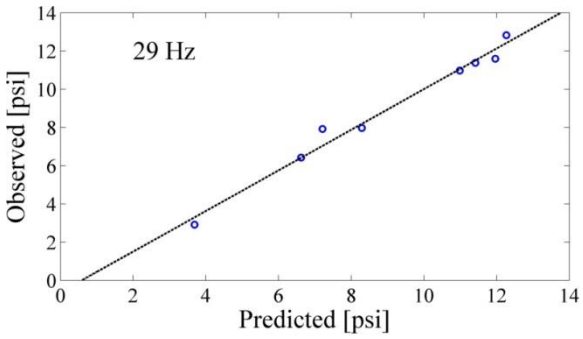

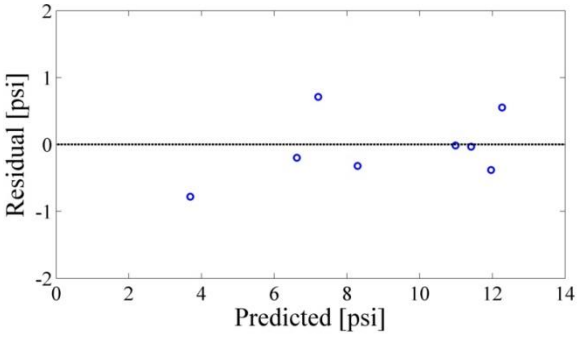

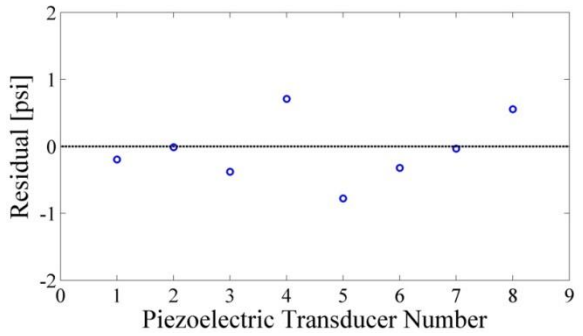

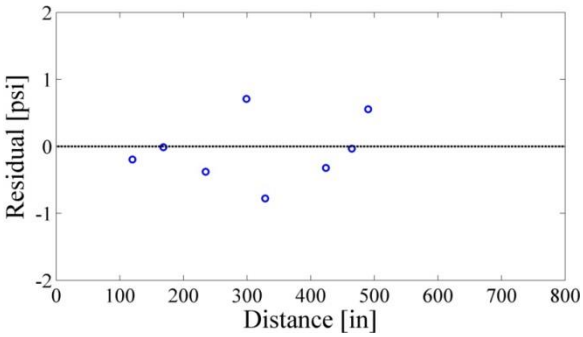

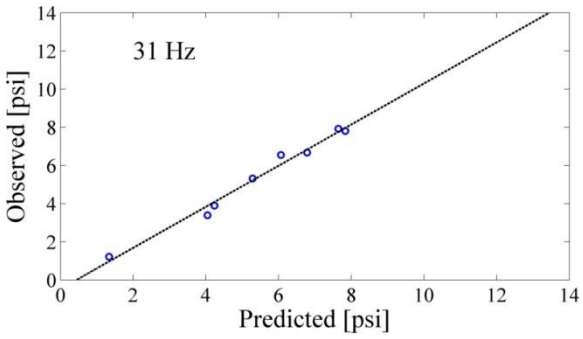

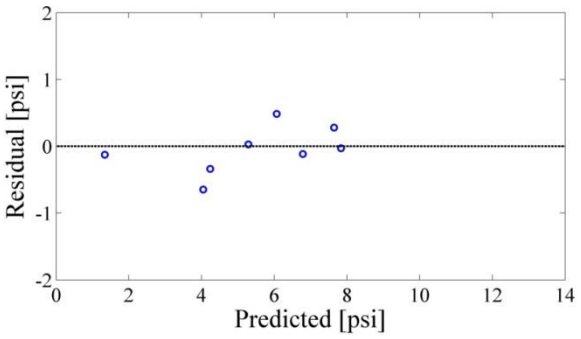

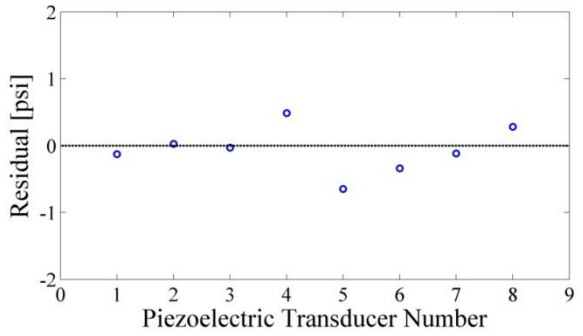

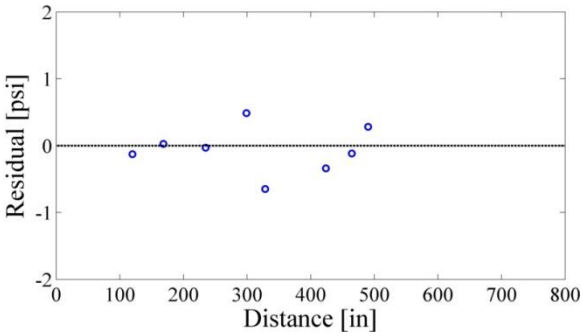

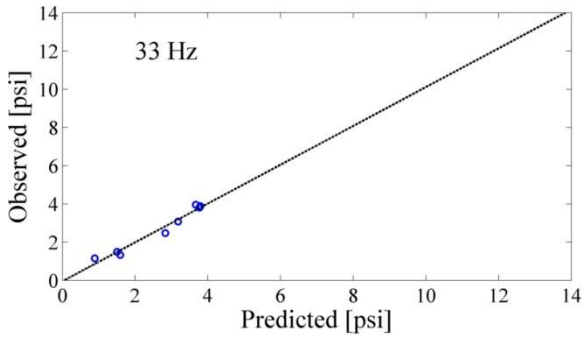

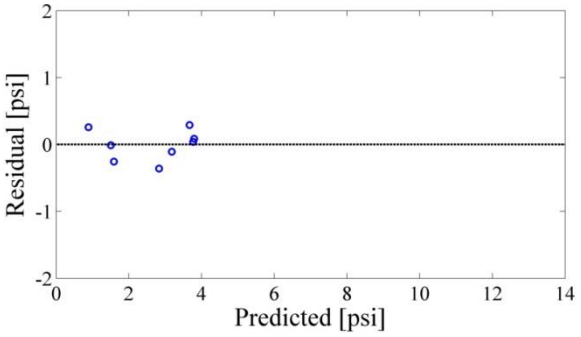

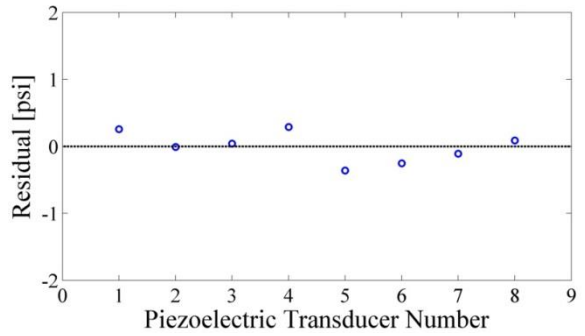

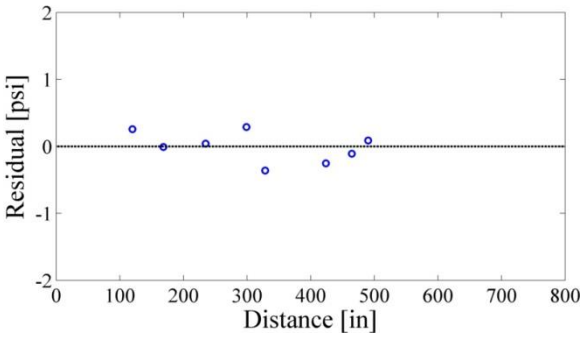

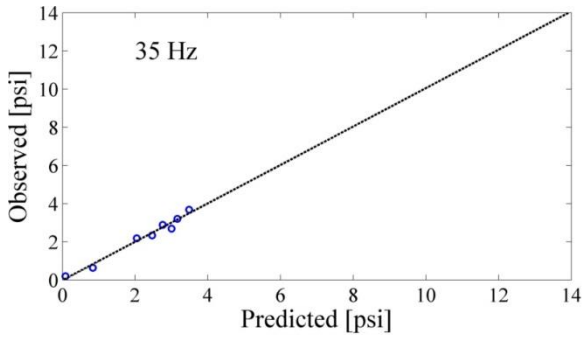

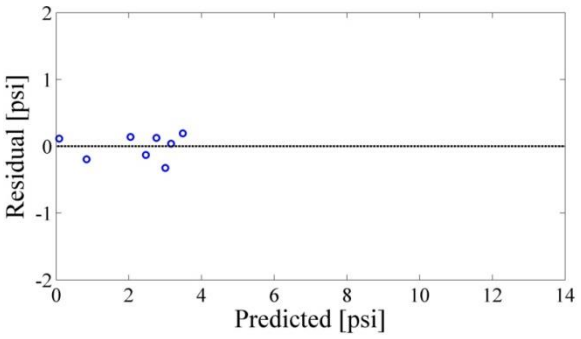

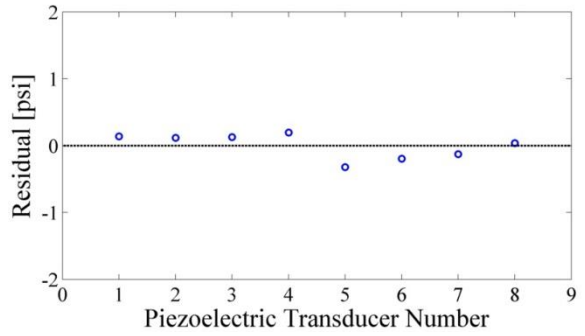

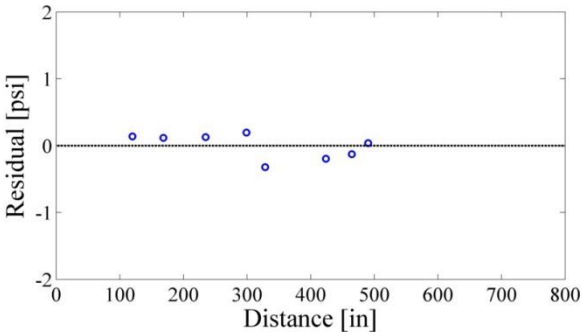

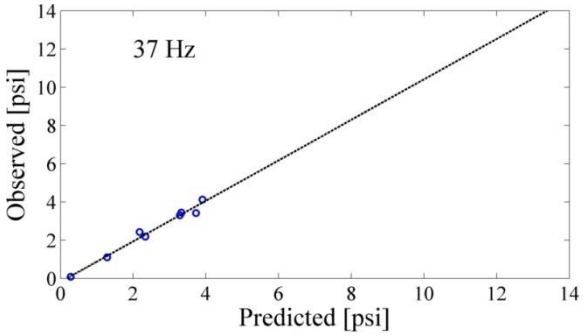

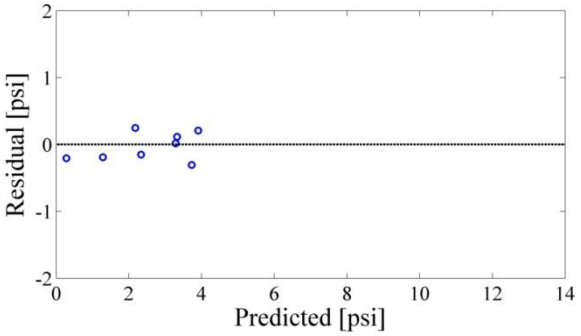

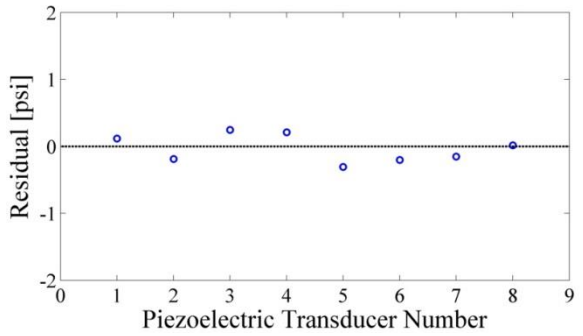

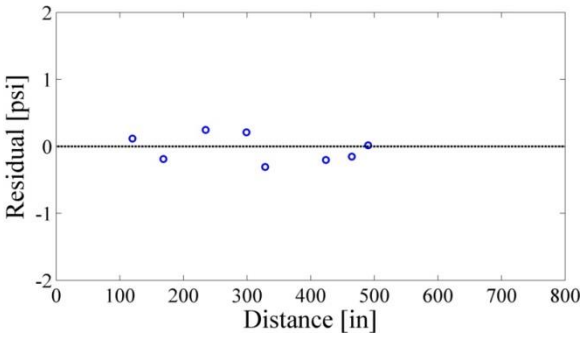

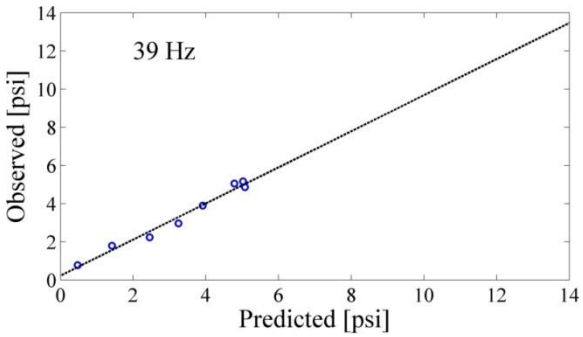

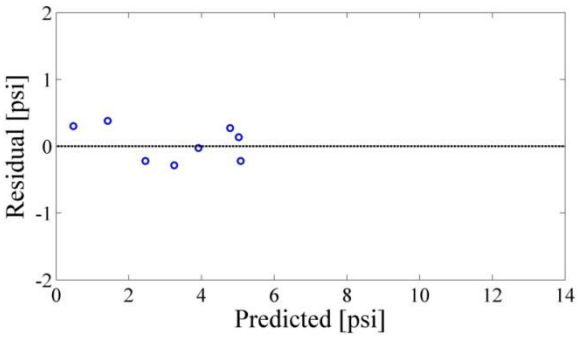

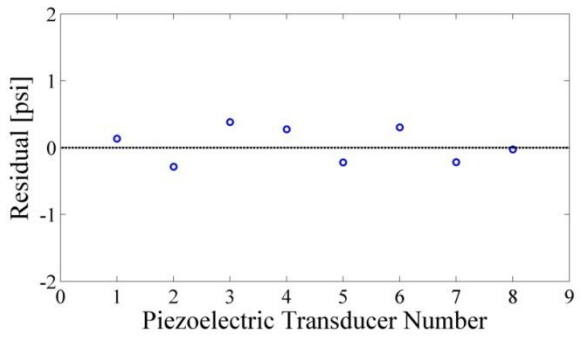

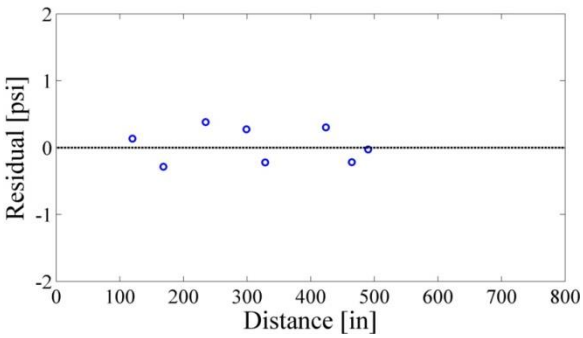

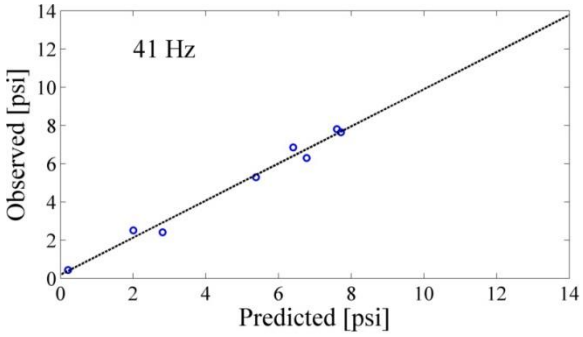

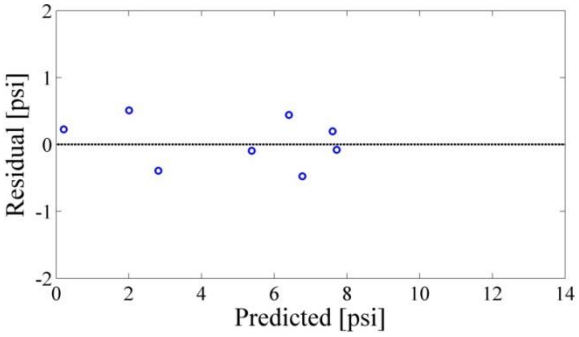

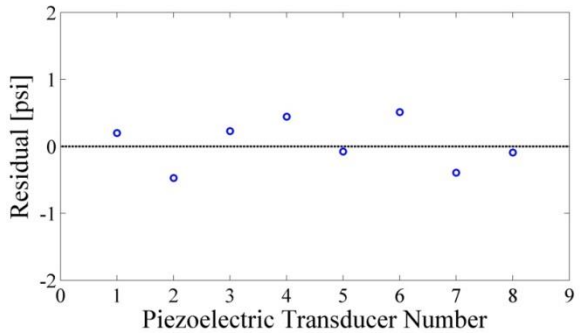

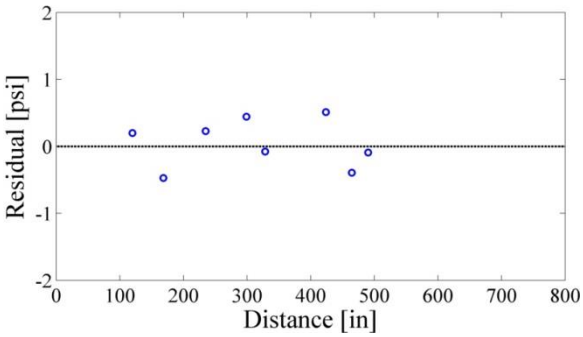

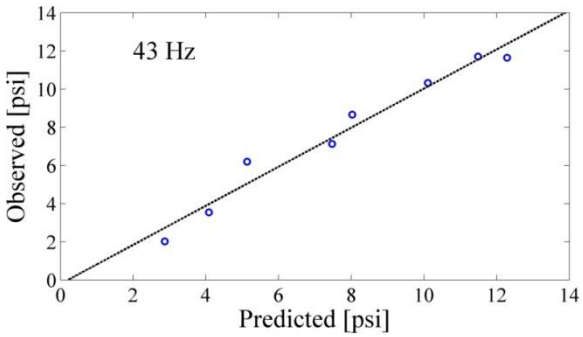

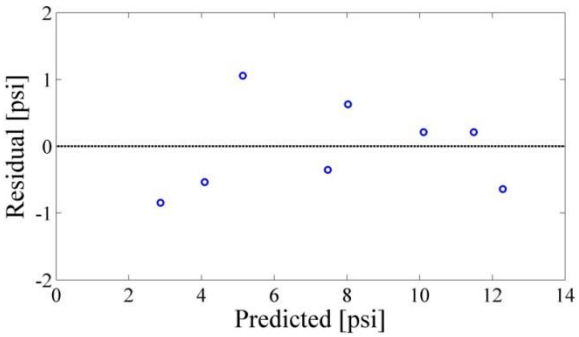

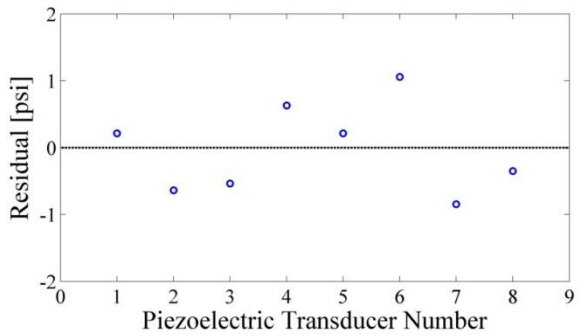

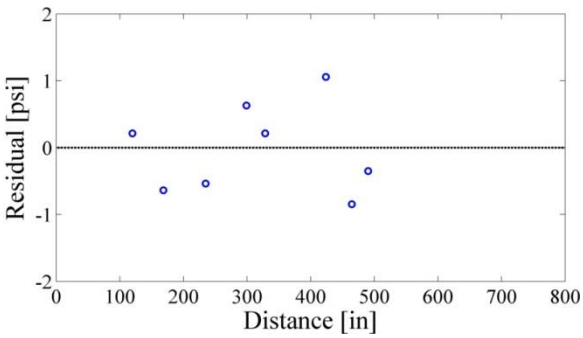

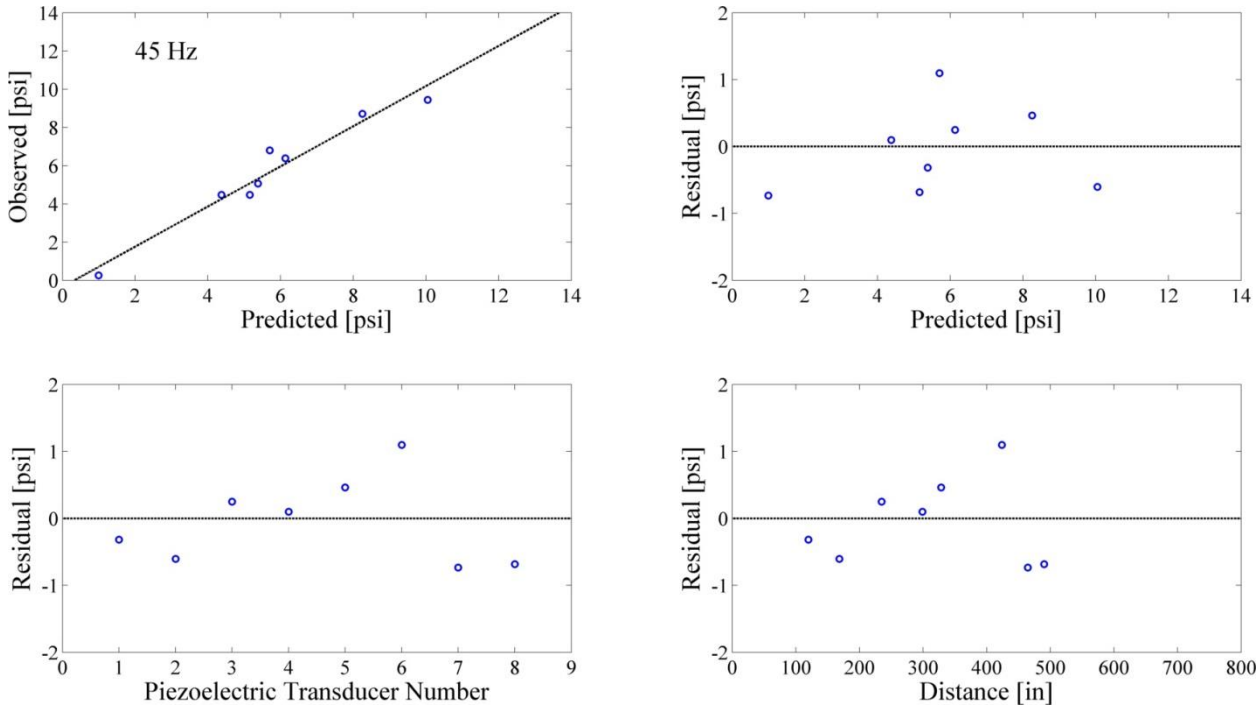

200 acfm:

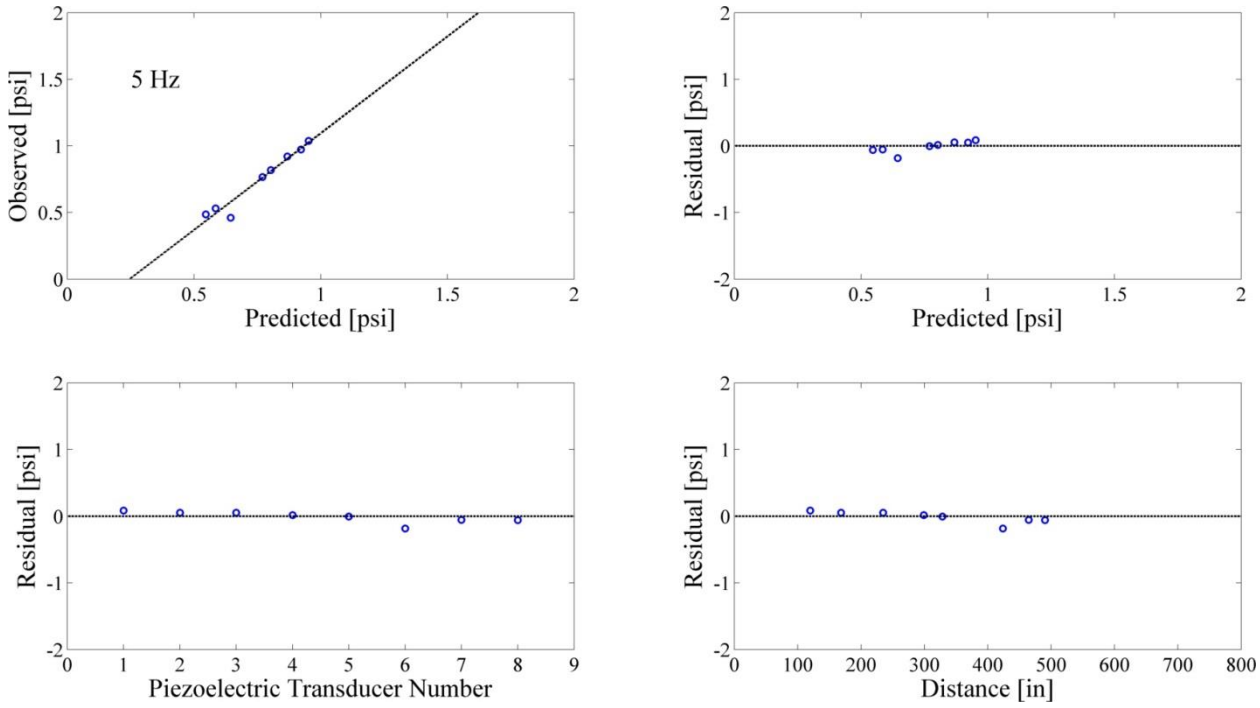

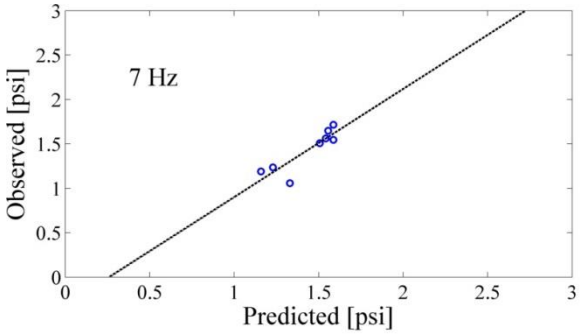

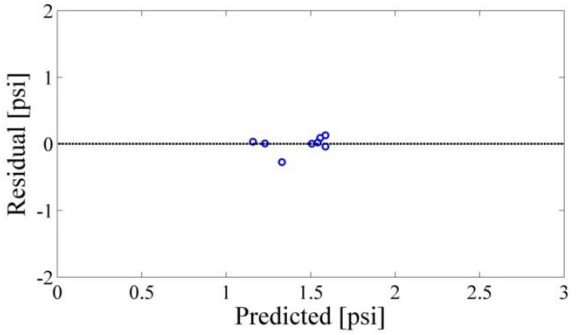

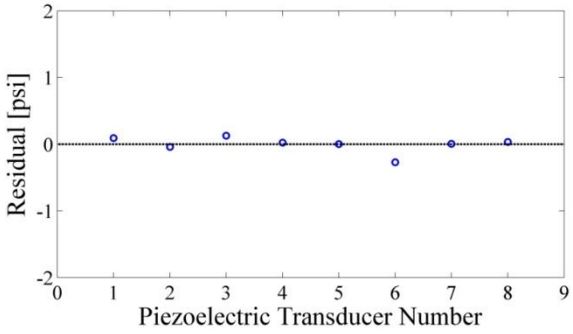

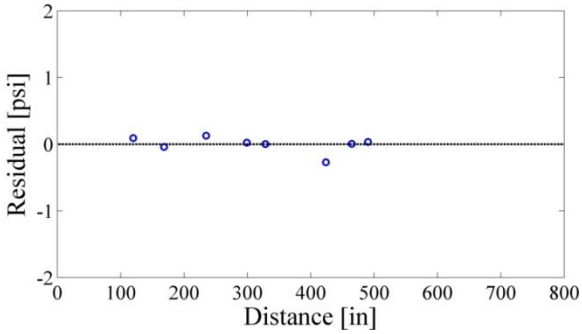

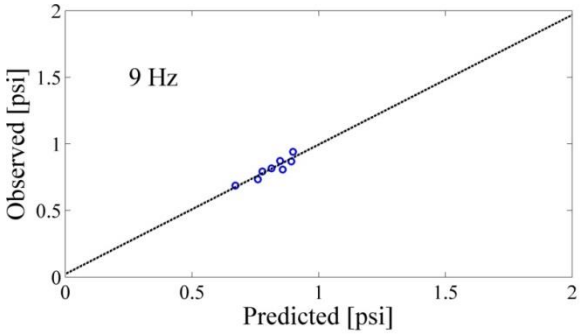

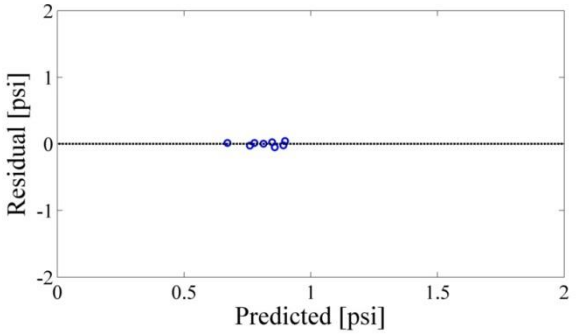

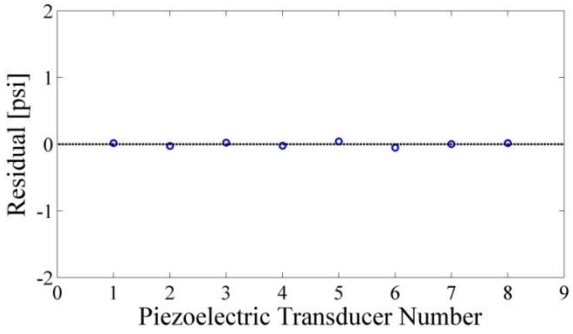

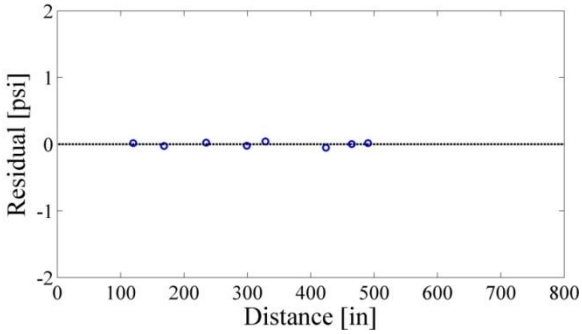

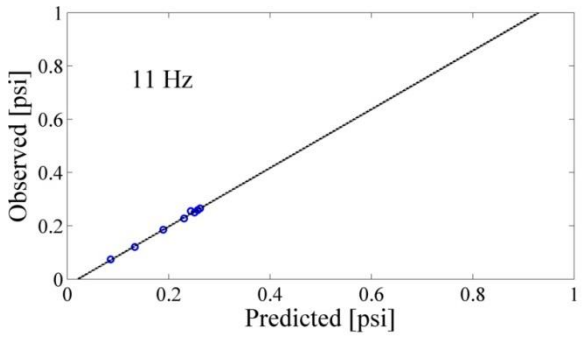

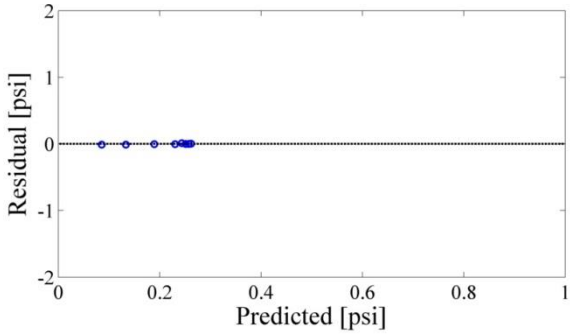

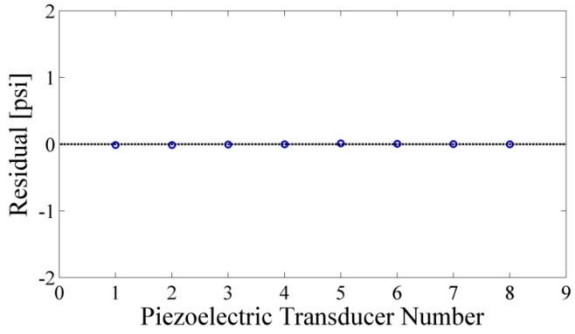

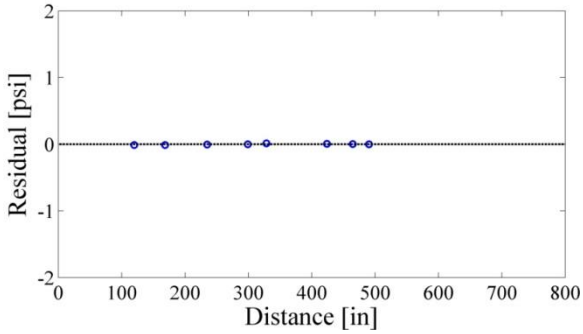

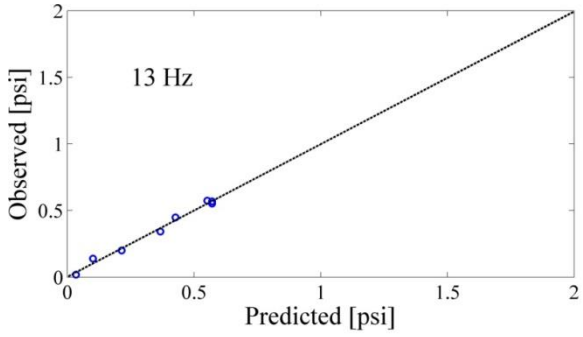

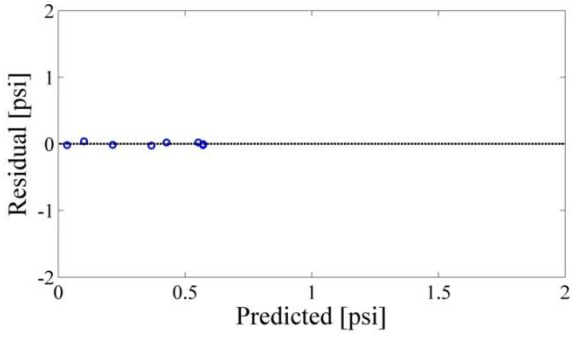

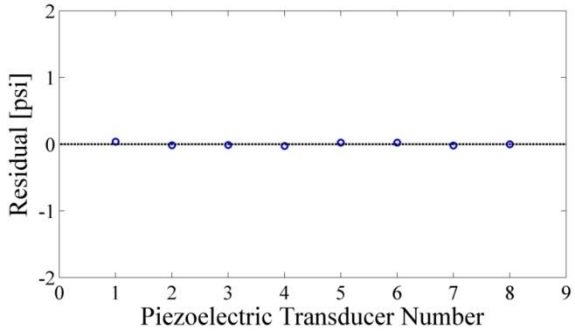

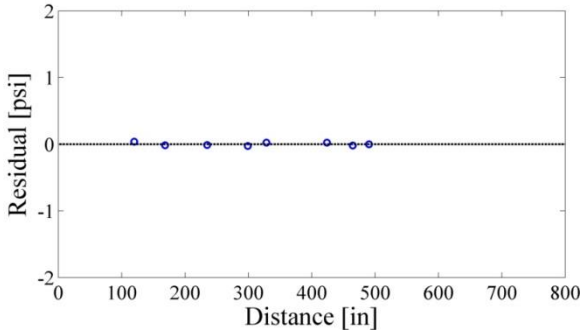

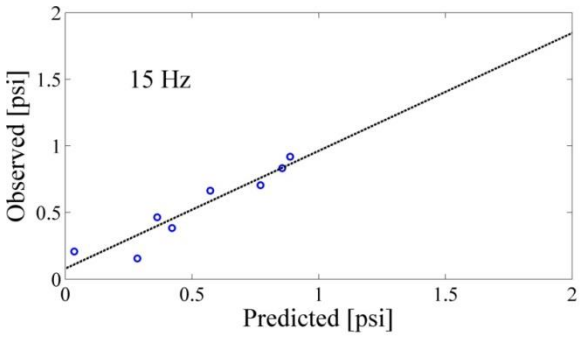

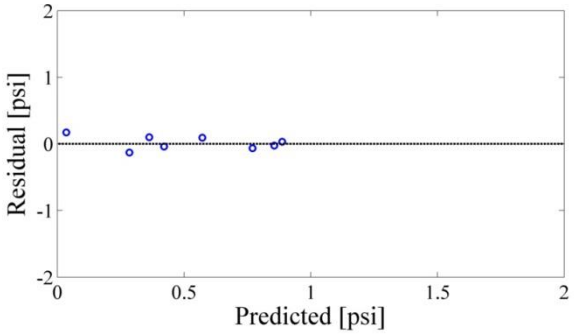

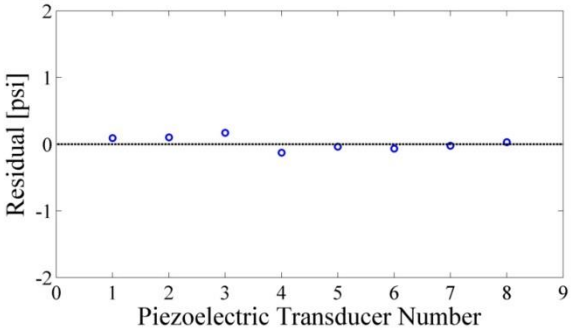

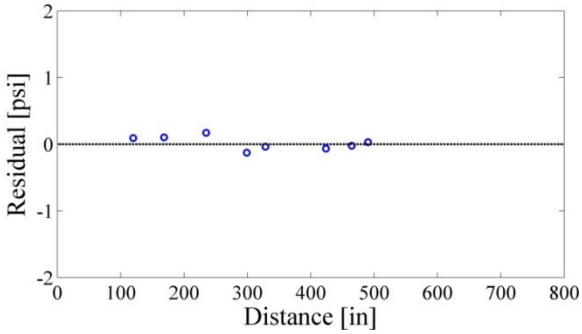

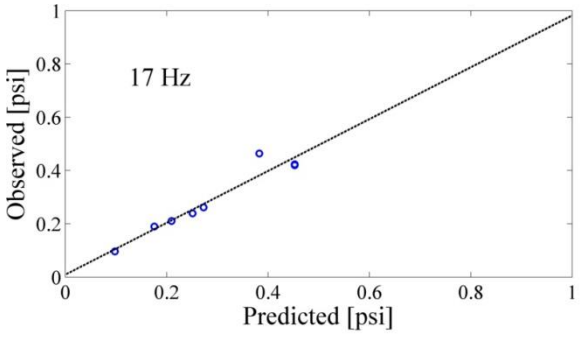

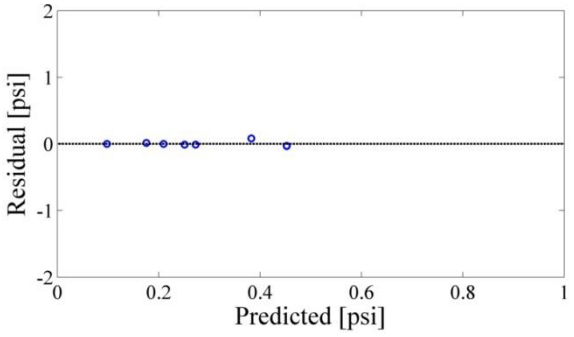

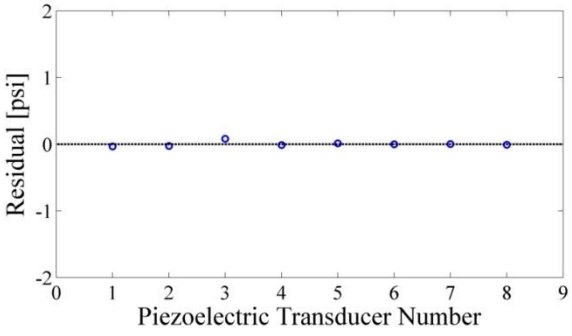

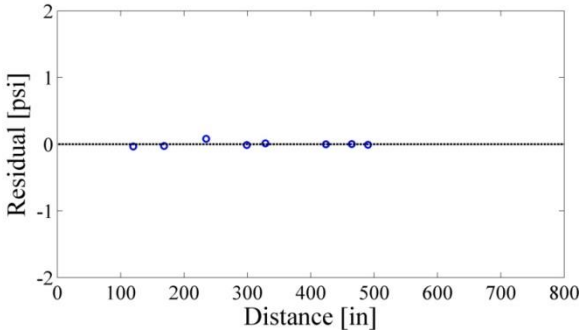

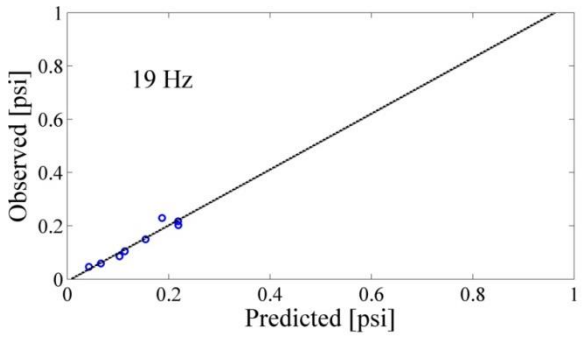

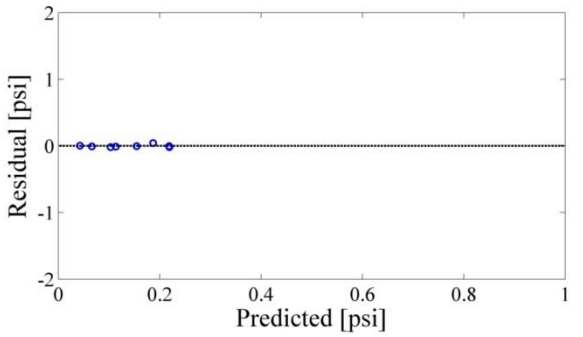

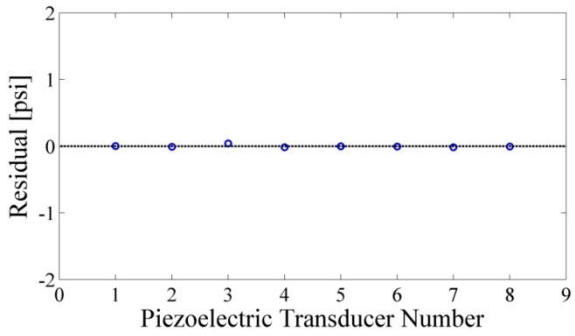

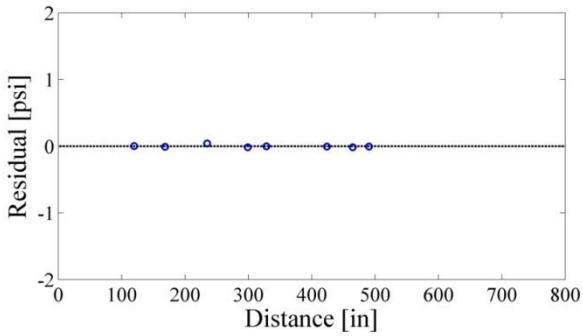

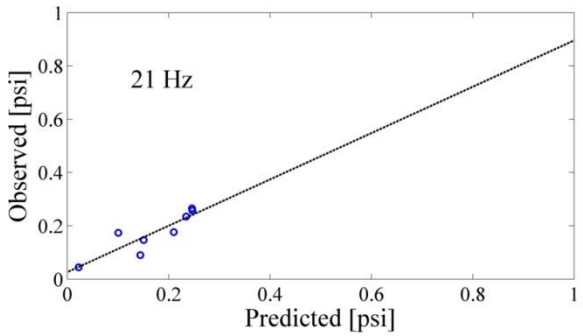

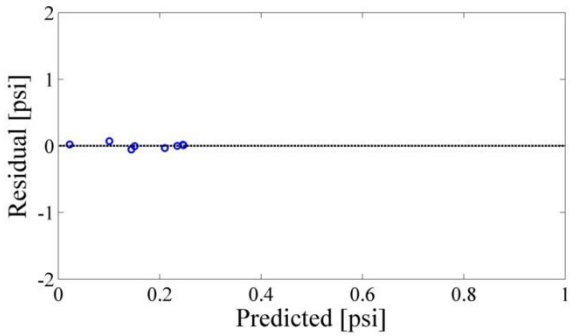

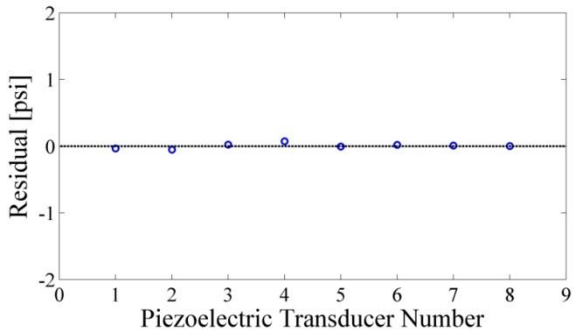

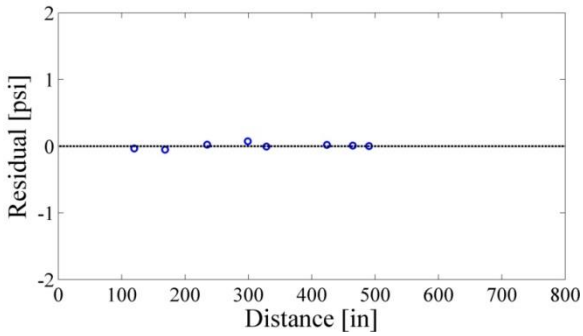

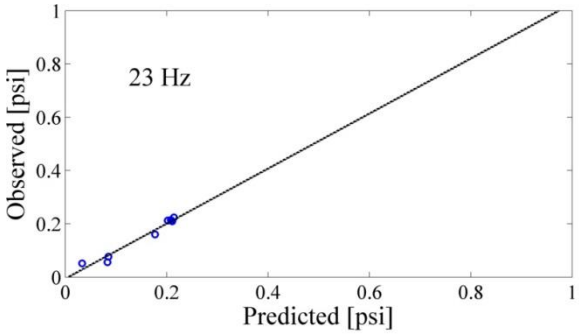

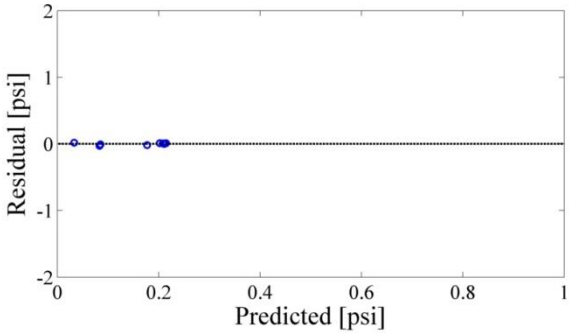

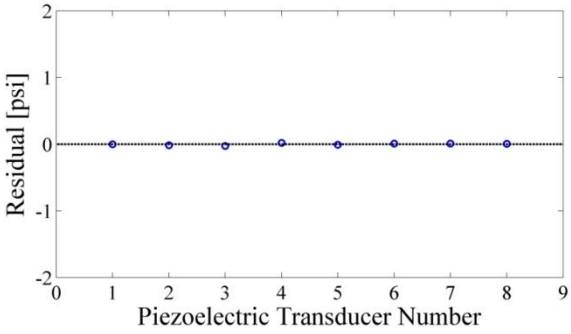

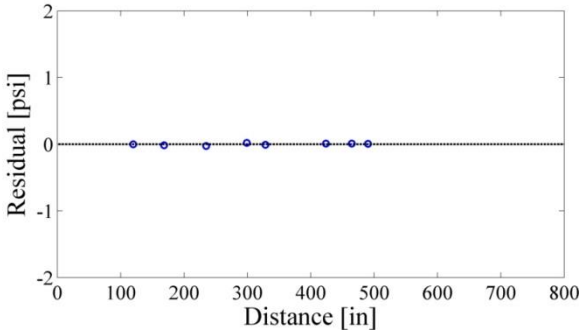

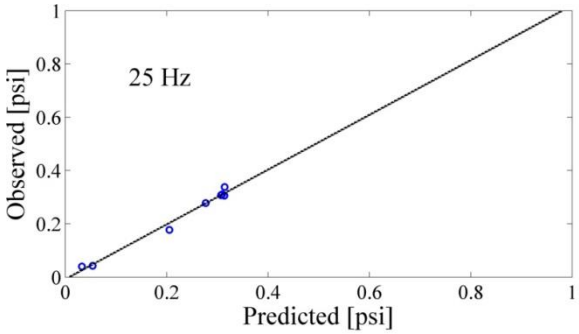

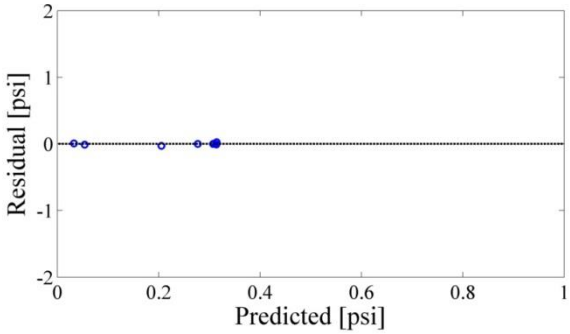

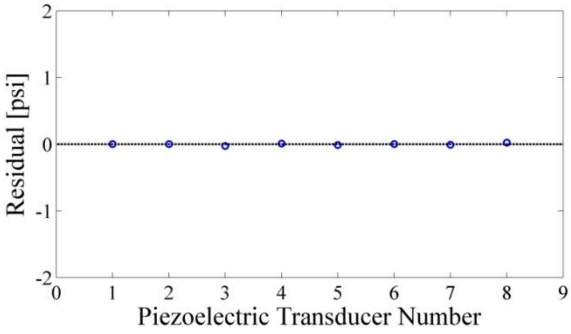

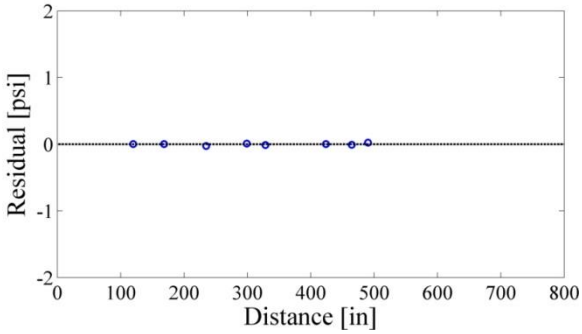

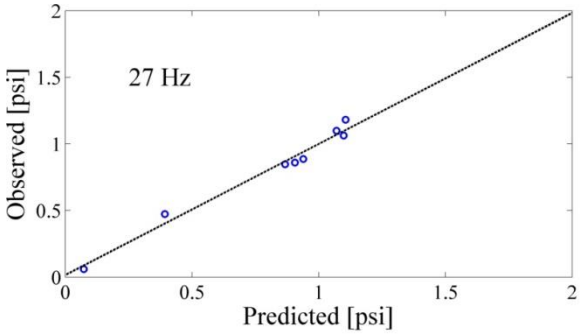

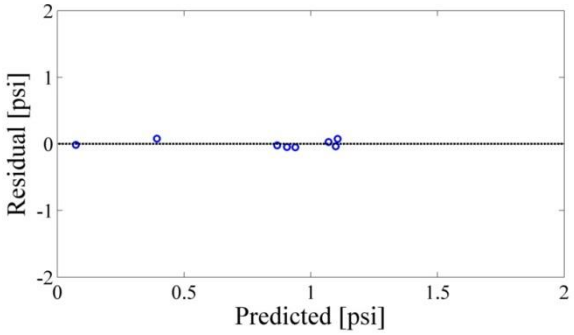

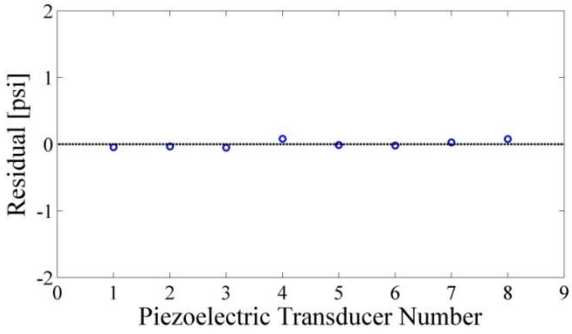

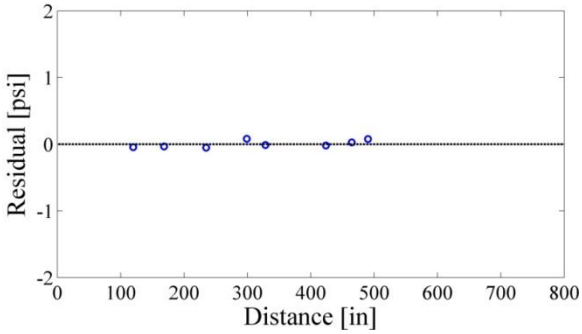

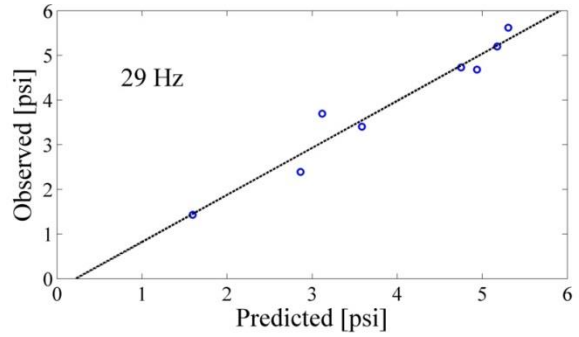

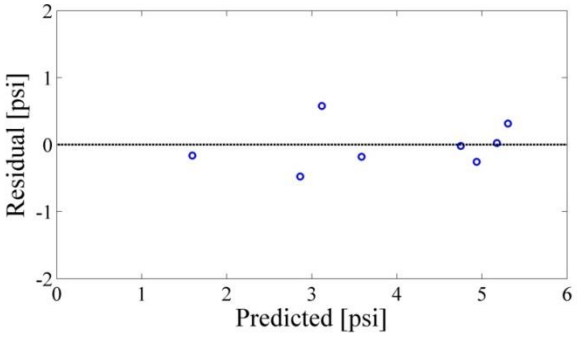

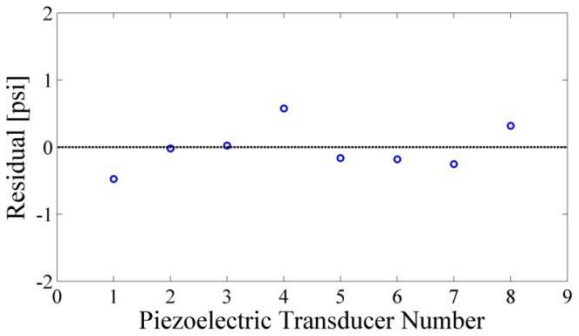

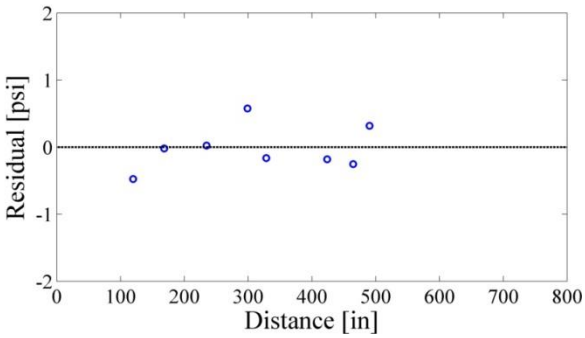

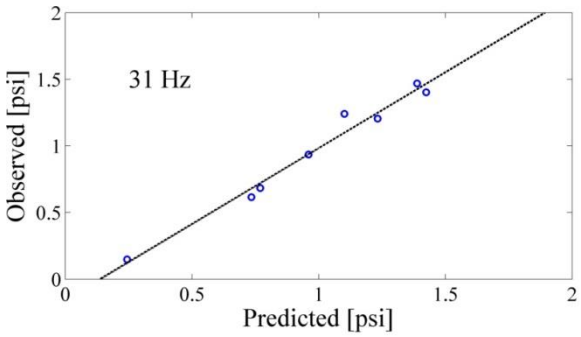

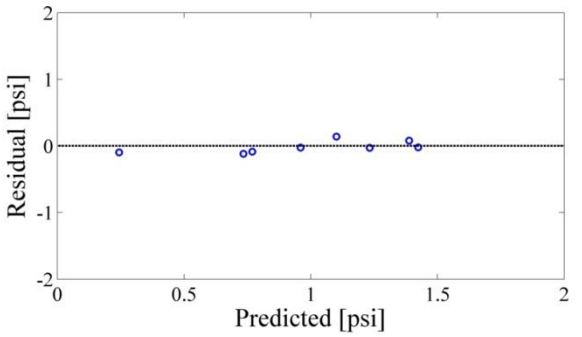

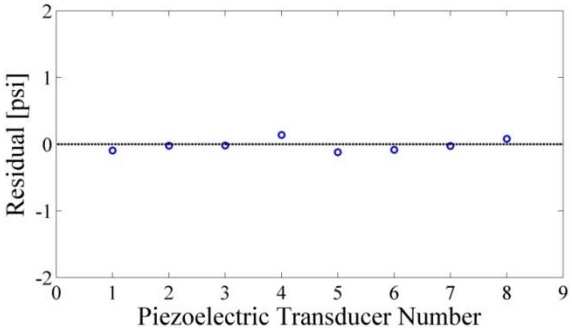

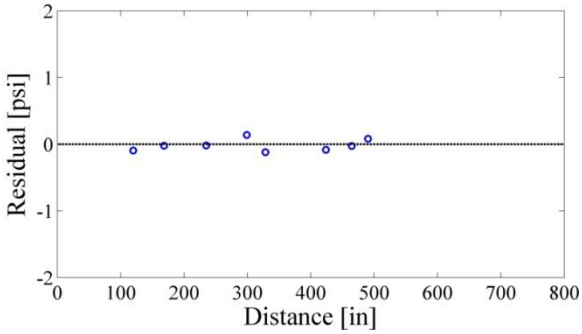

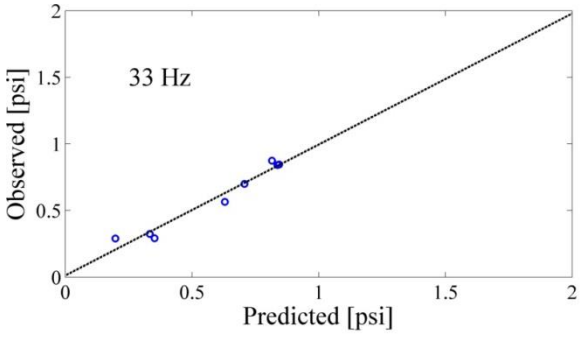

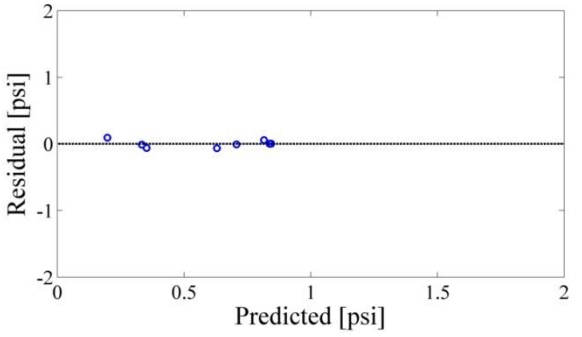

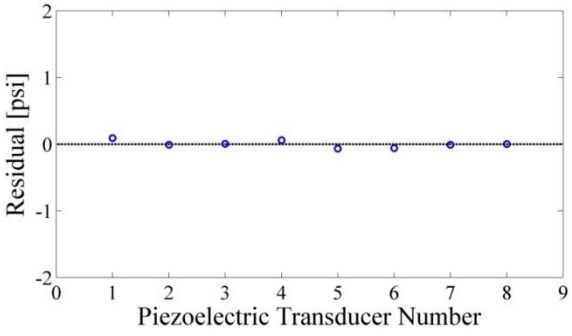

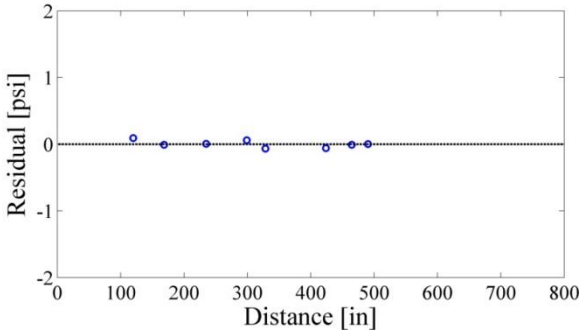

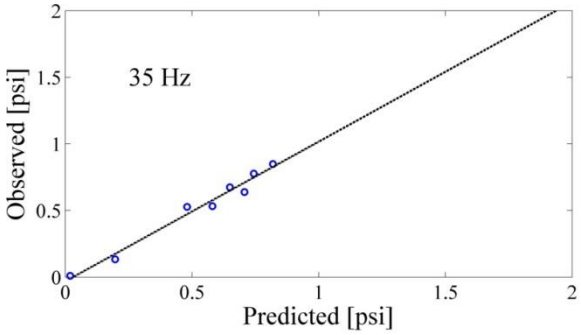

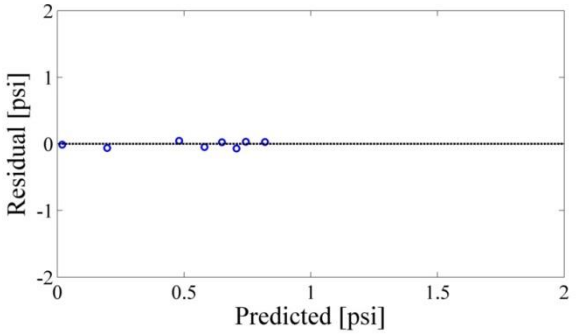

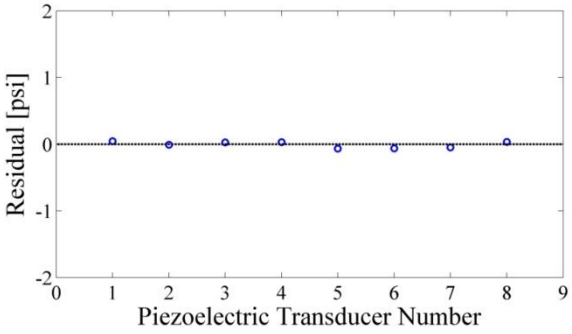

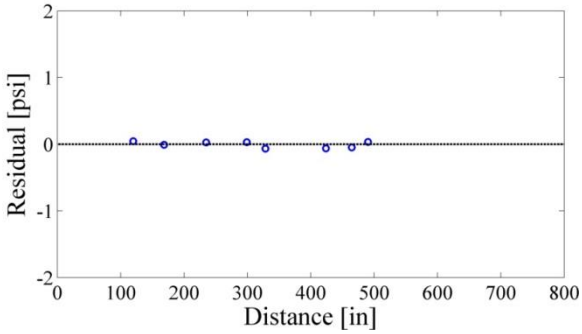

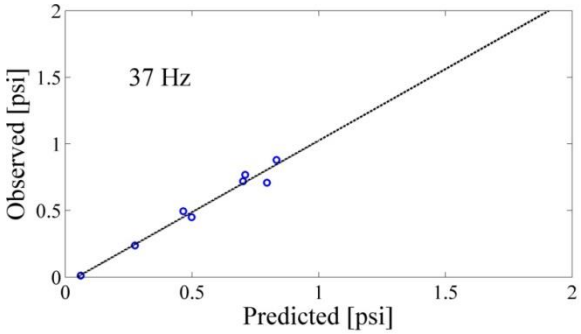

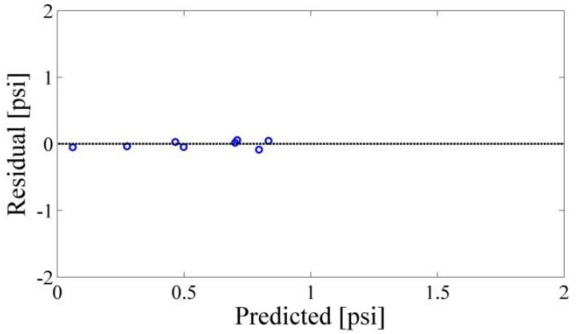

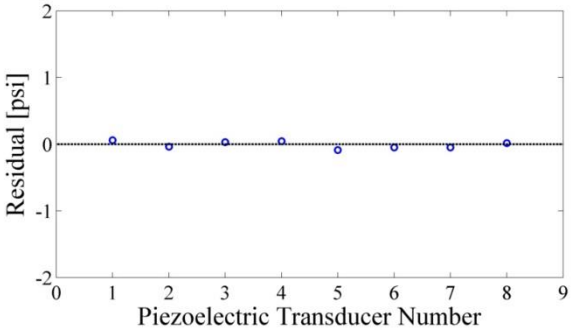

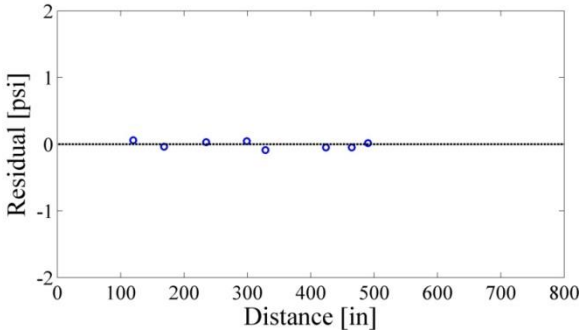

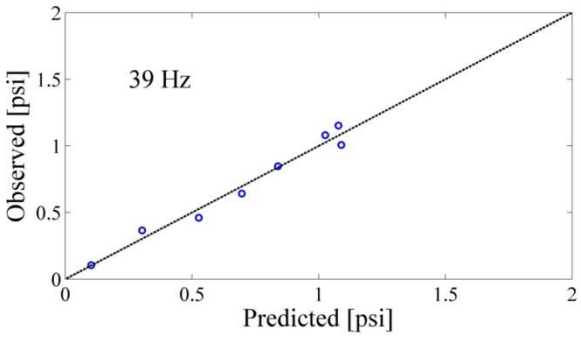

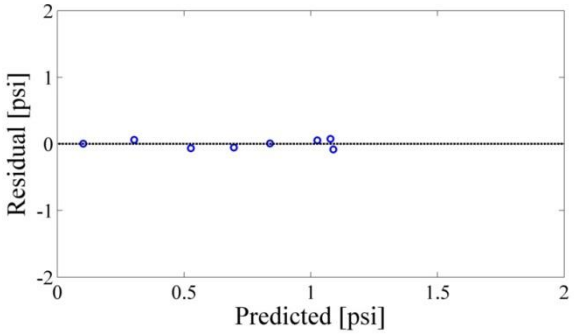

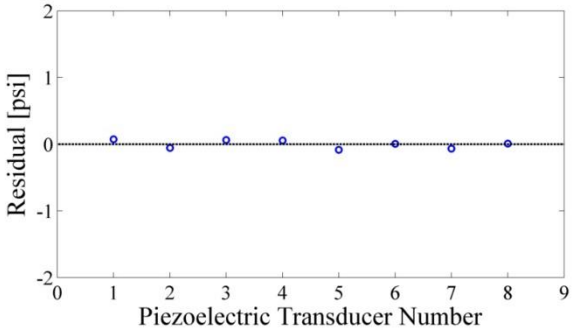

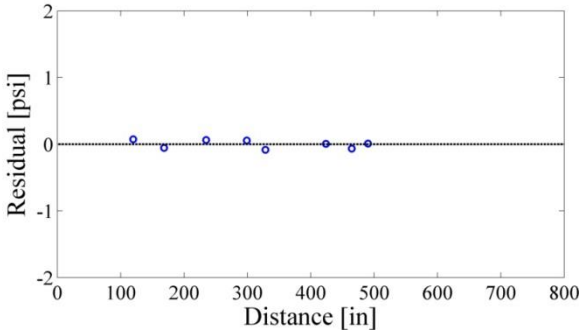

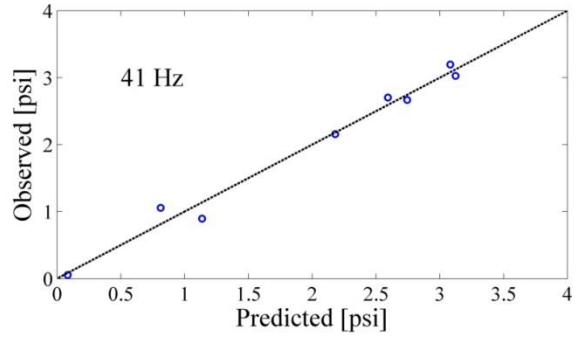

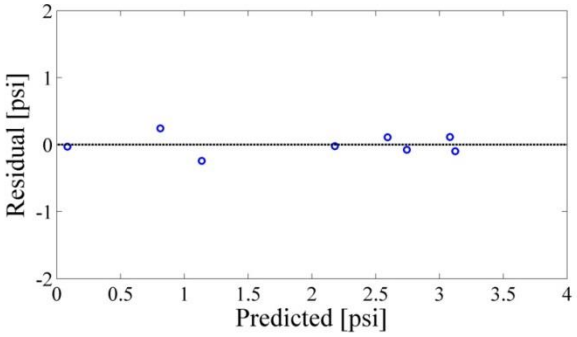

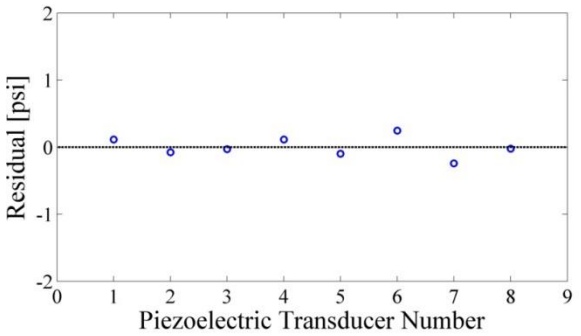

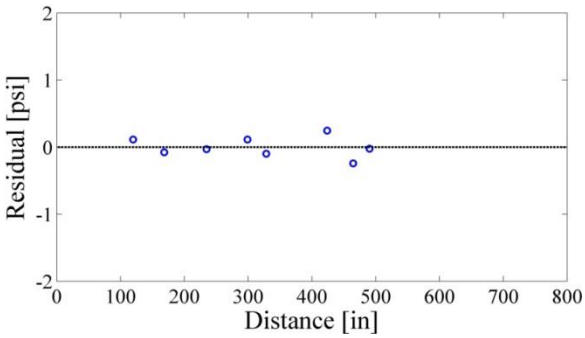

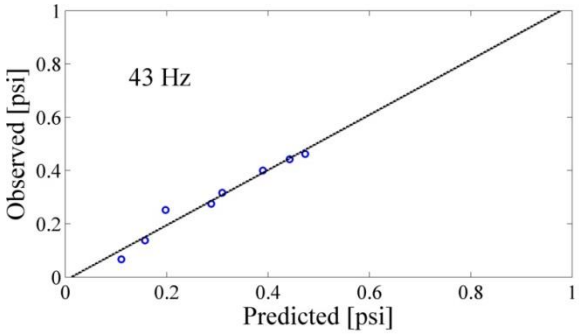

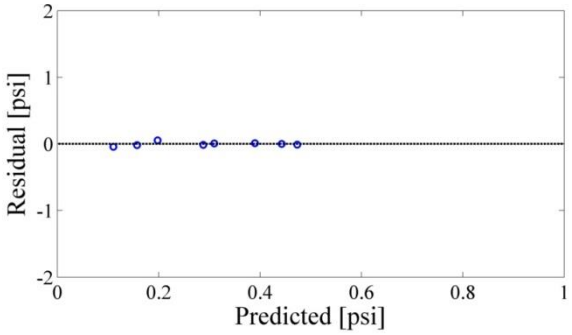

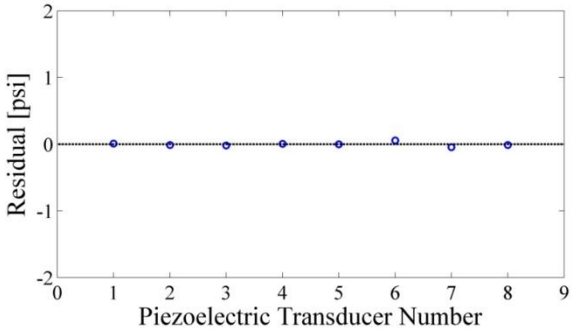

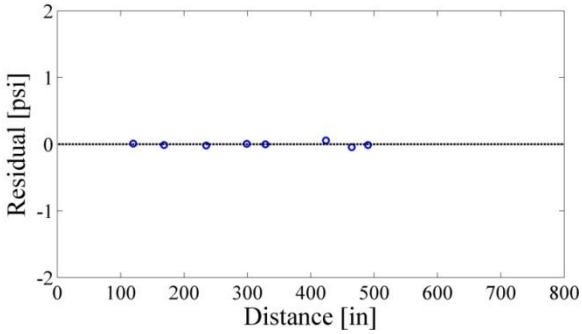

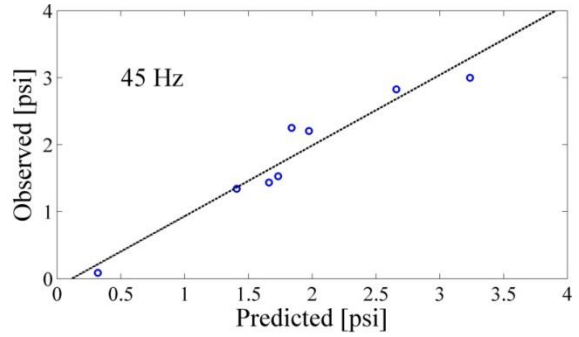

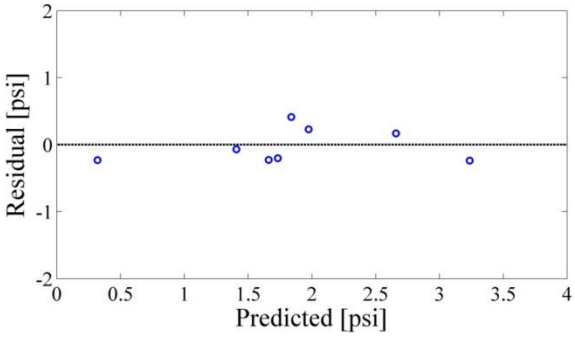

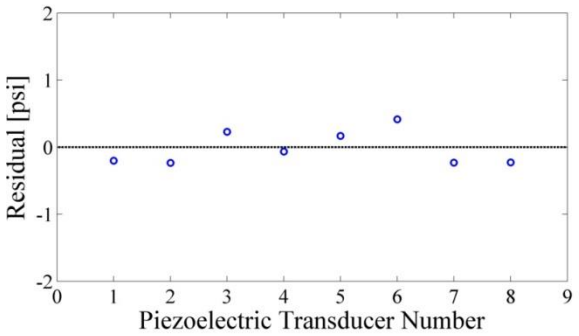

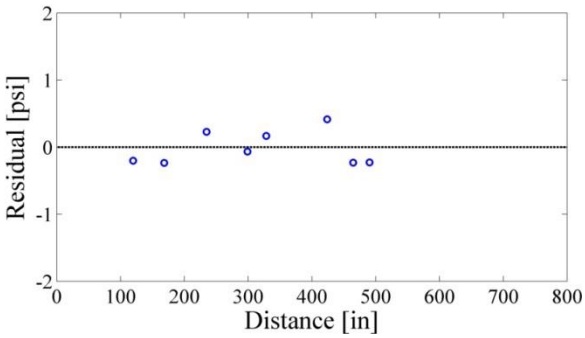

APPENDIX D: HOT-WIRE OUTPUT DATA SINE WAVE FITS

700 acfm:

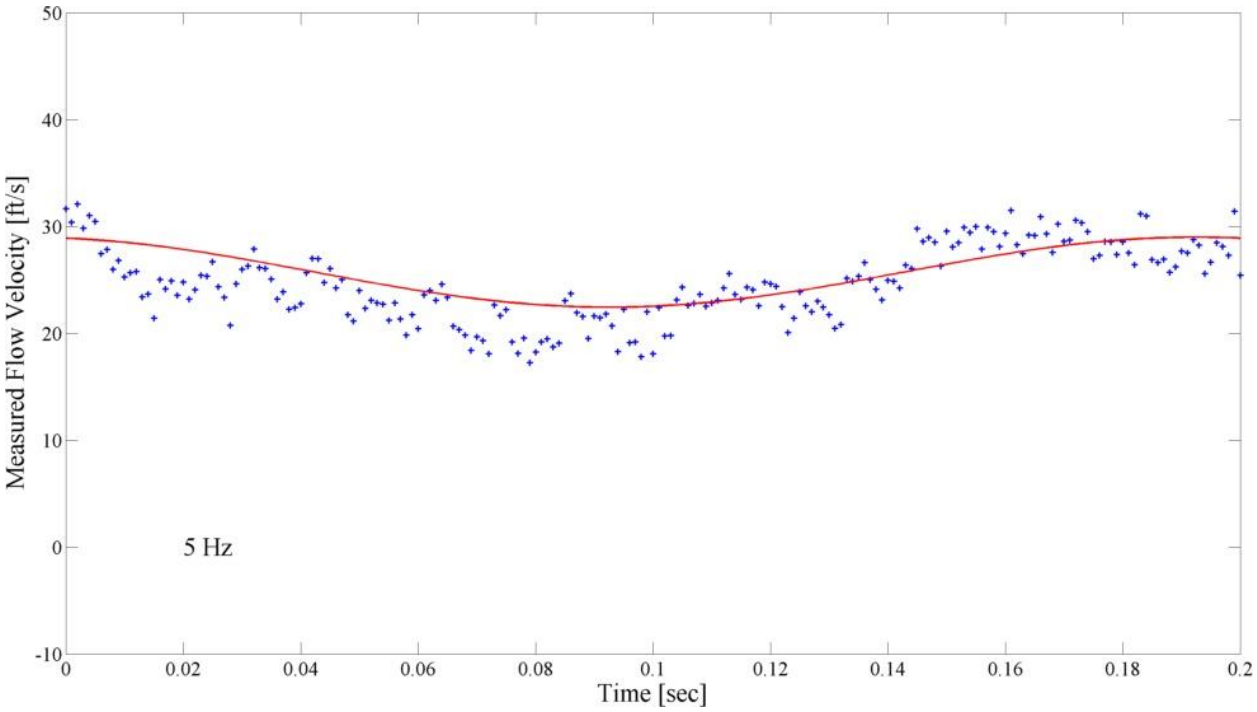

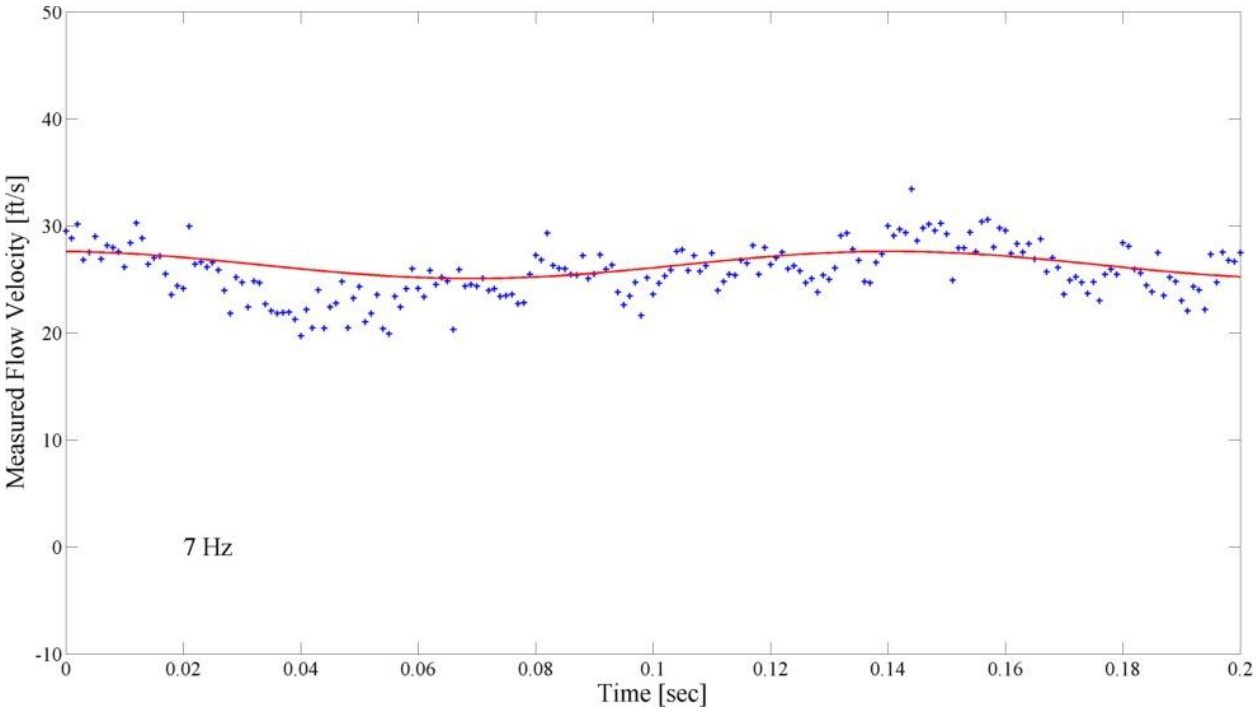

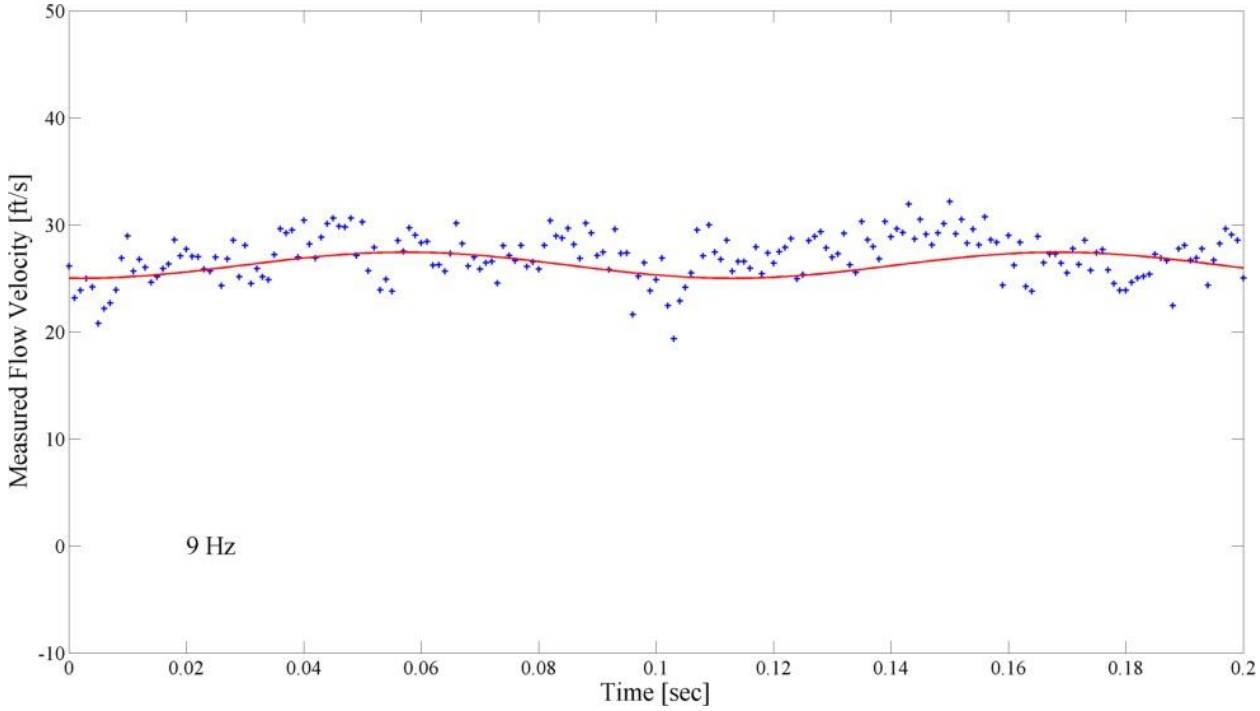

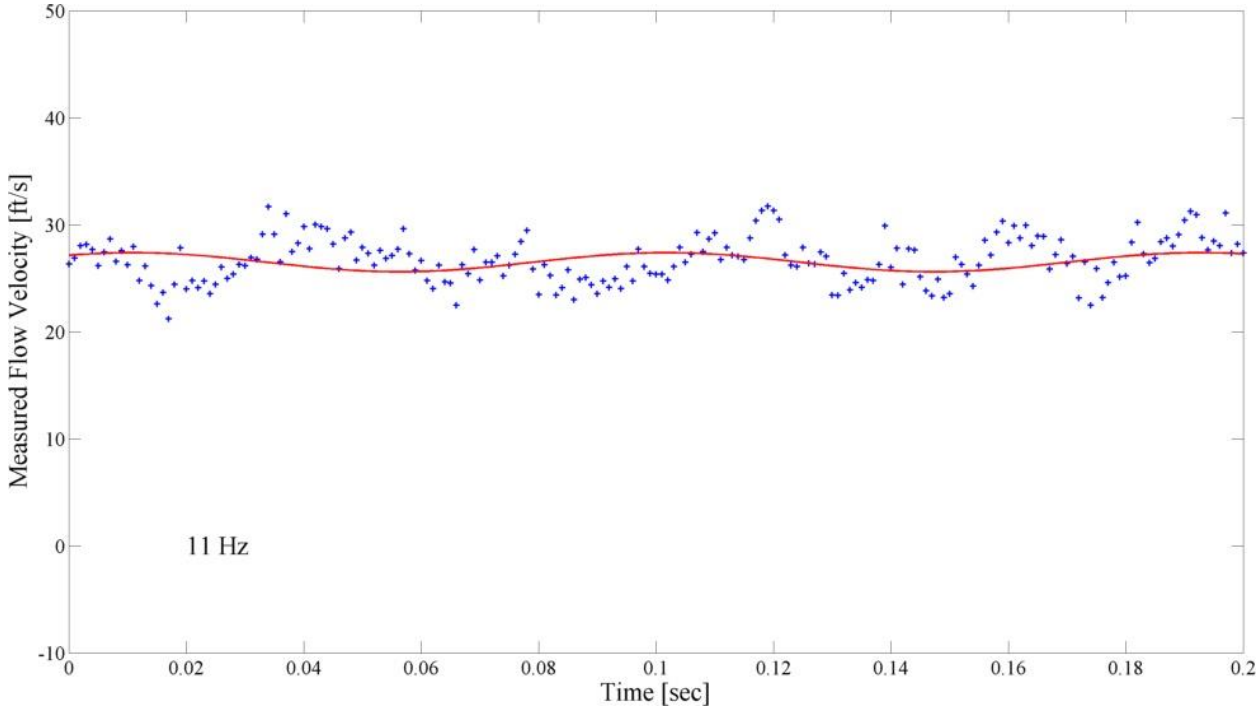

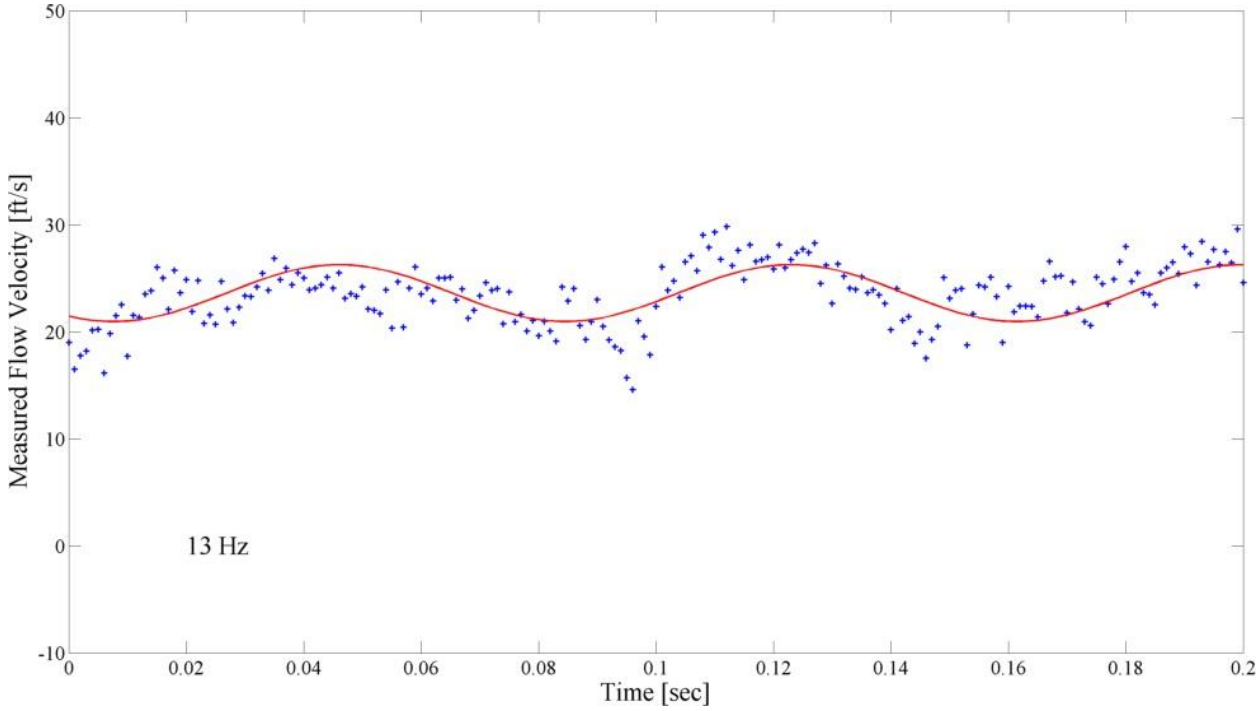

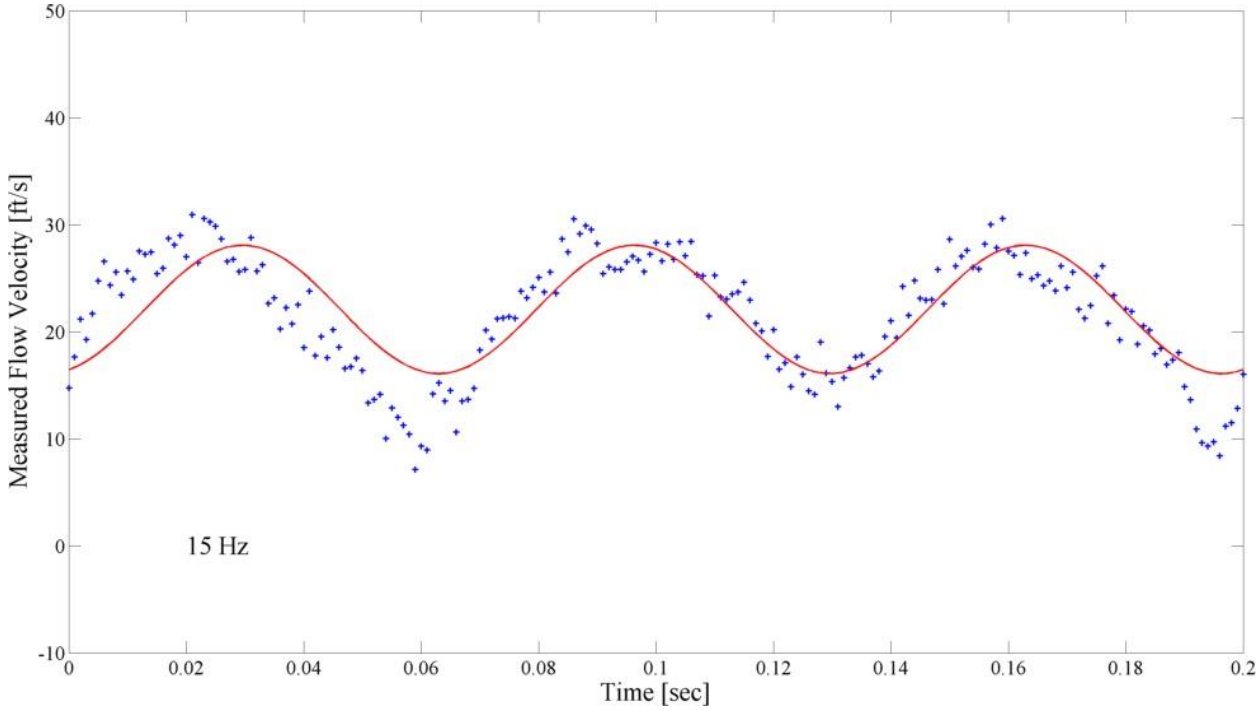

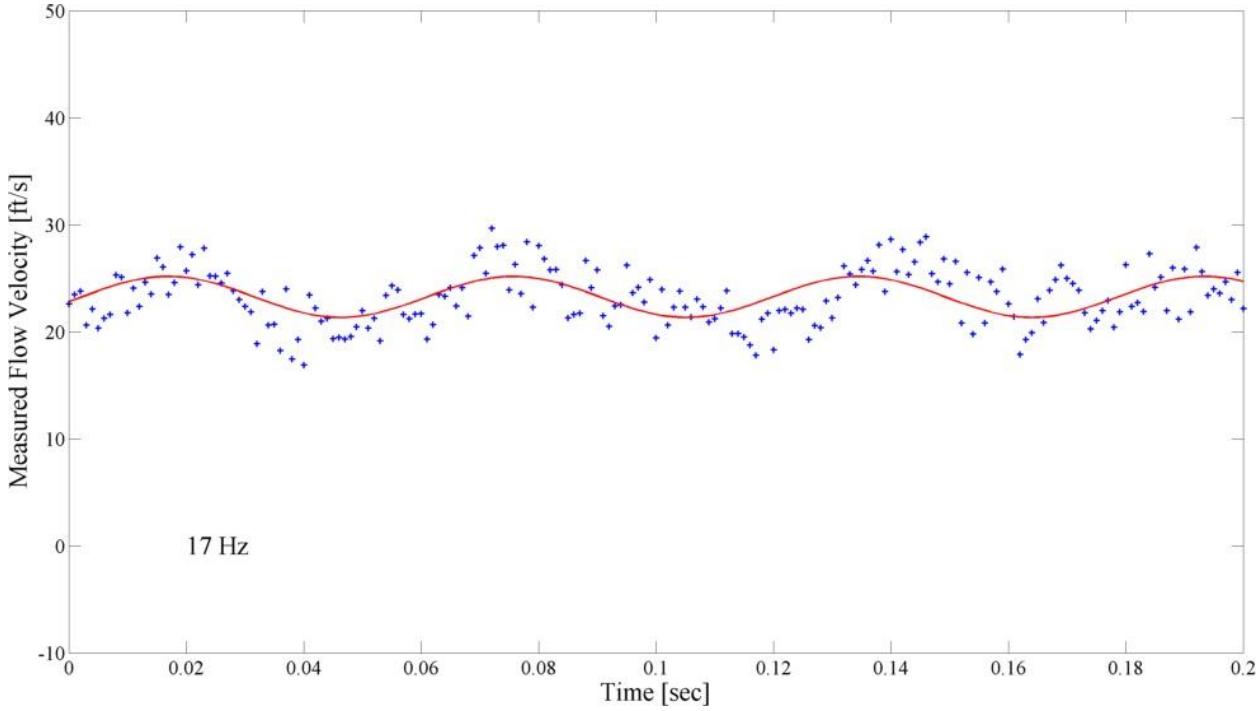

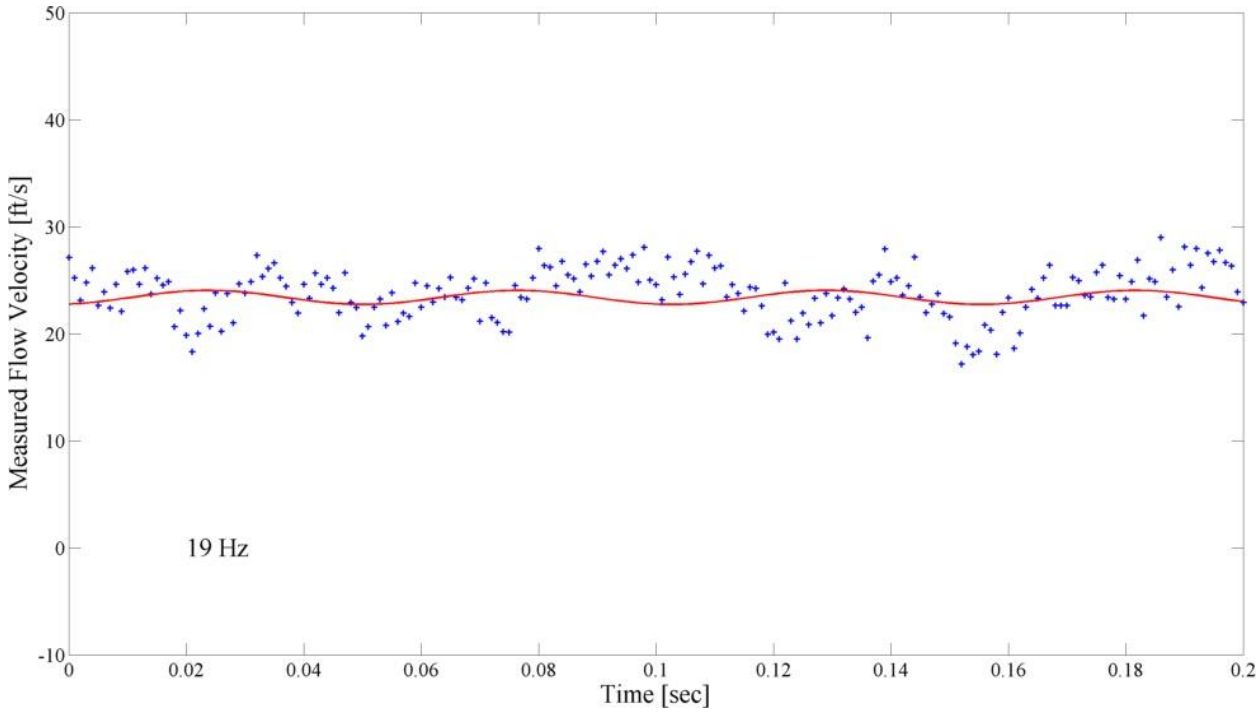

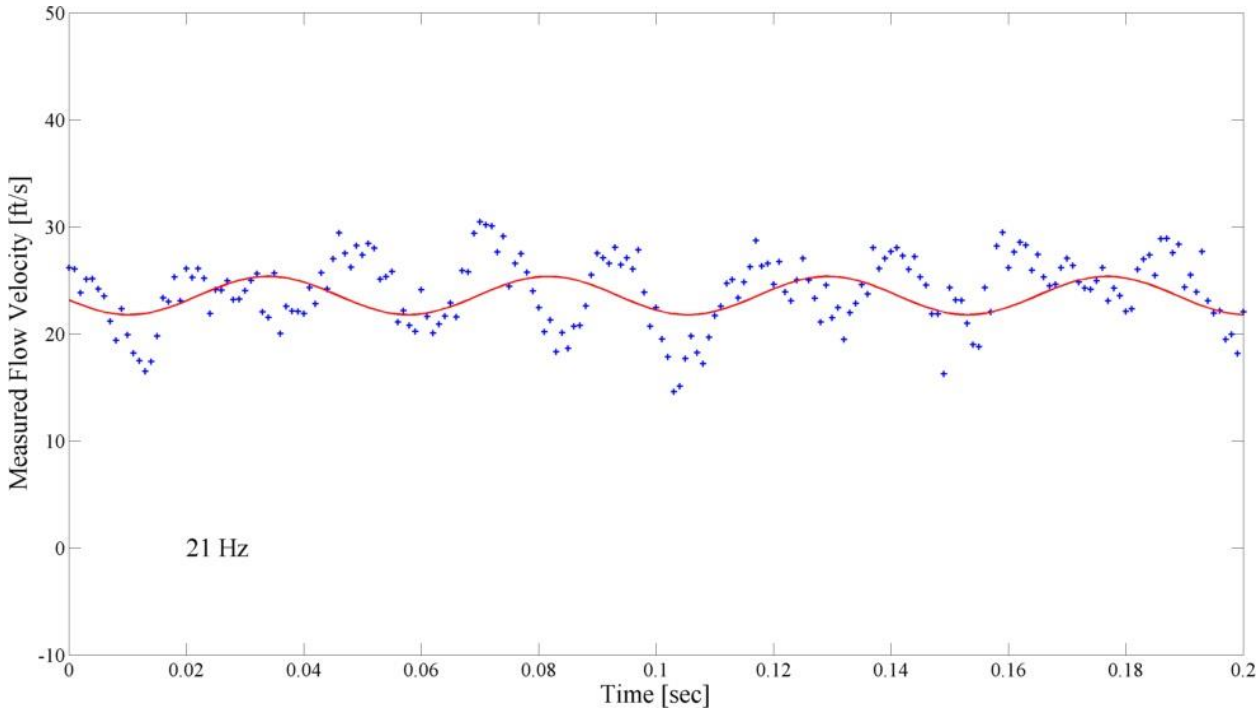

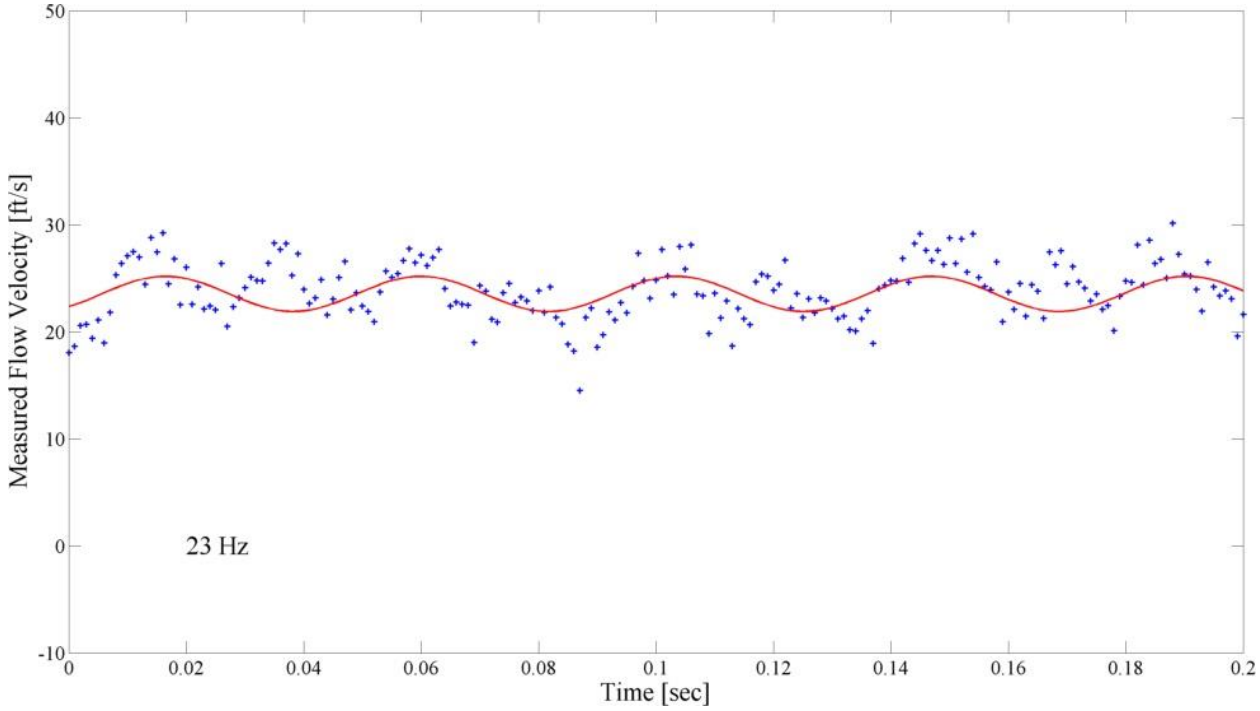

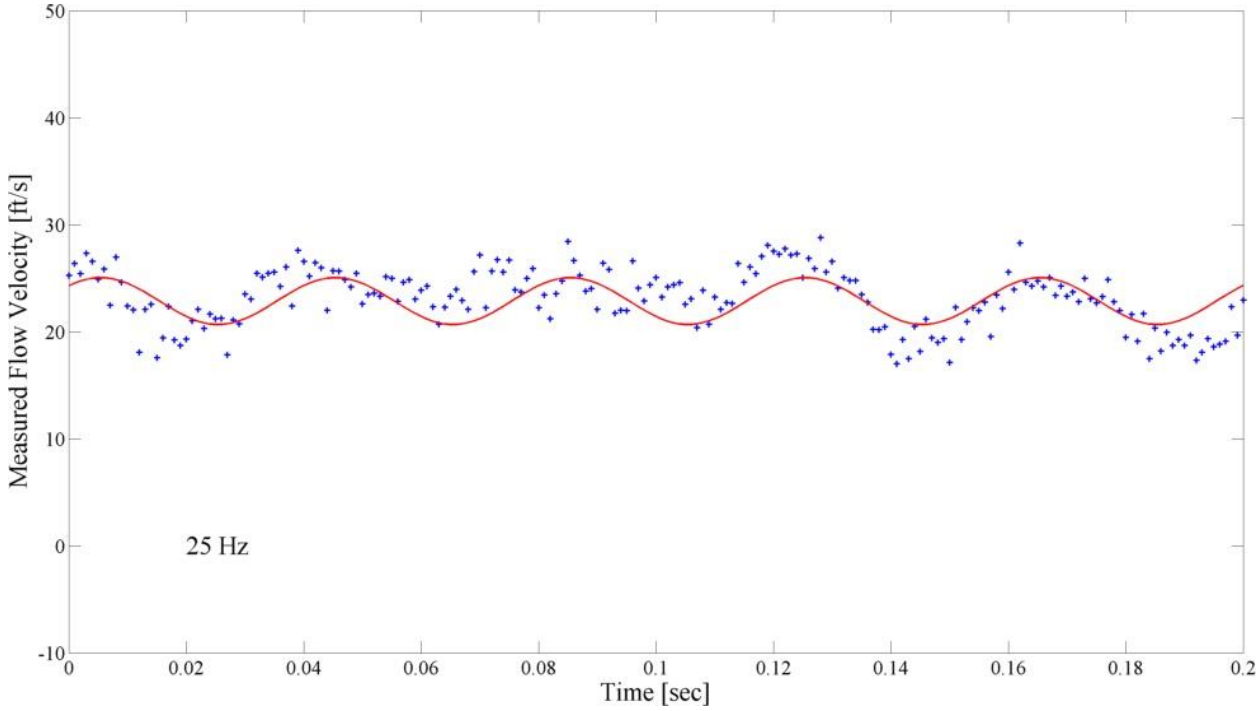

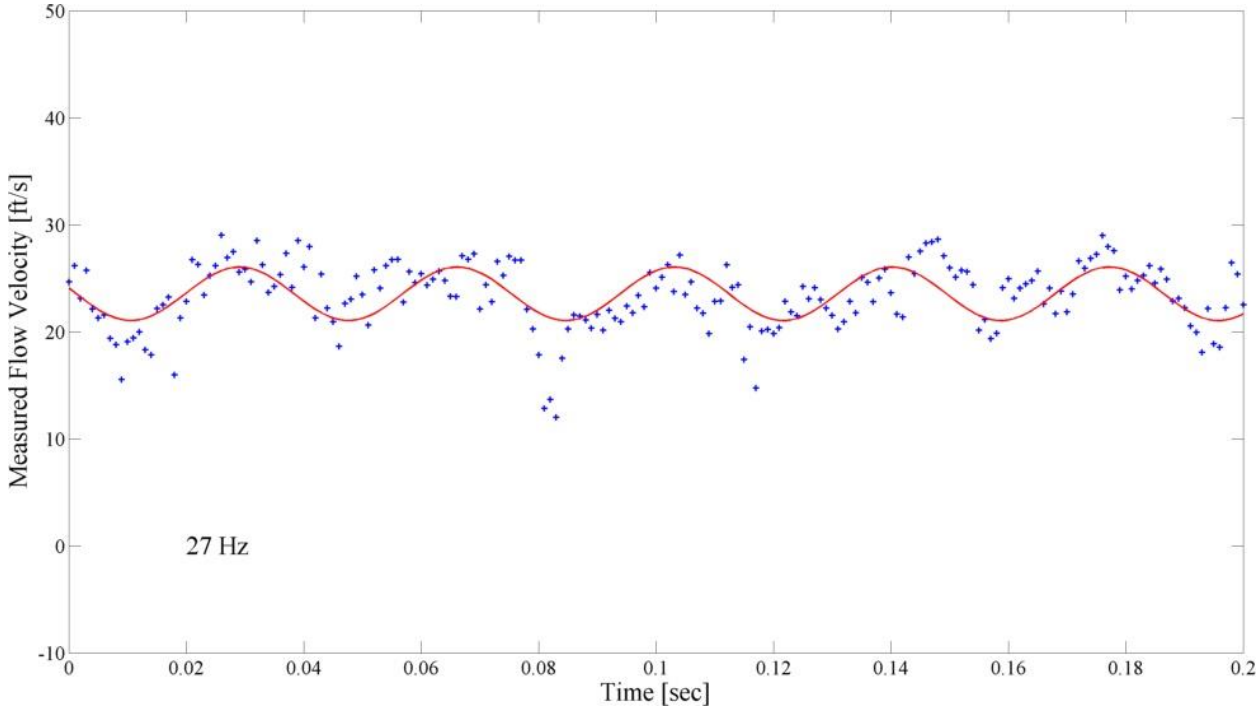

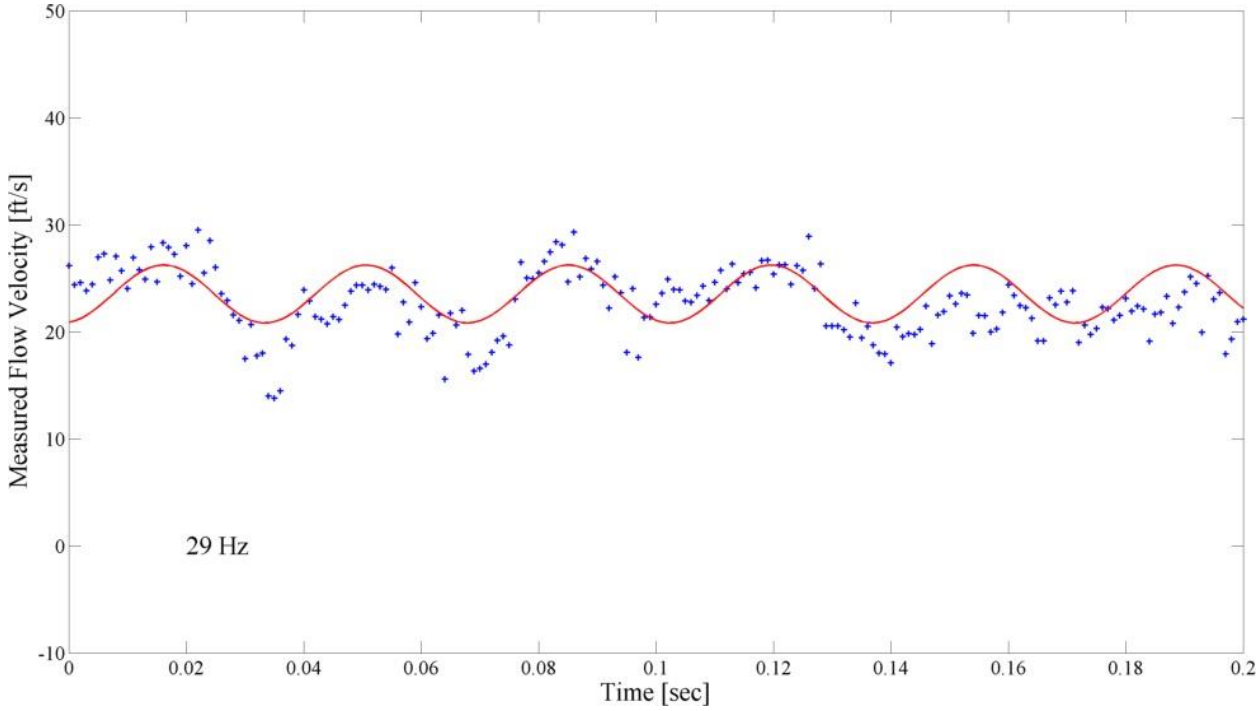

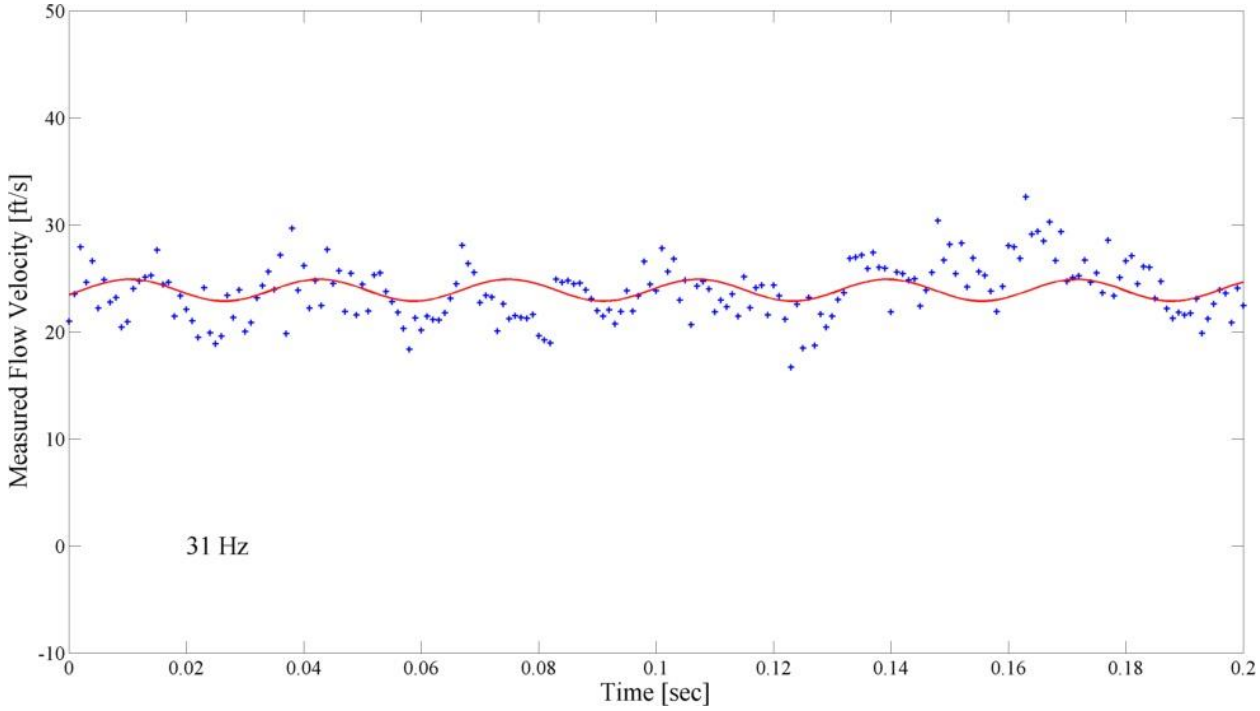

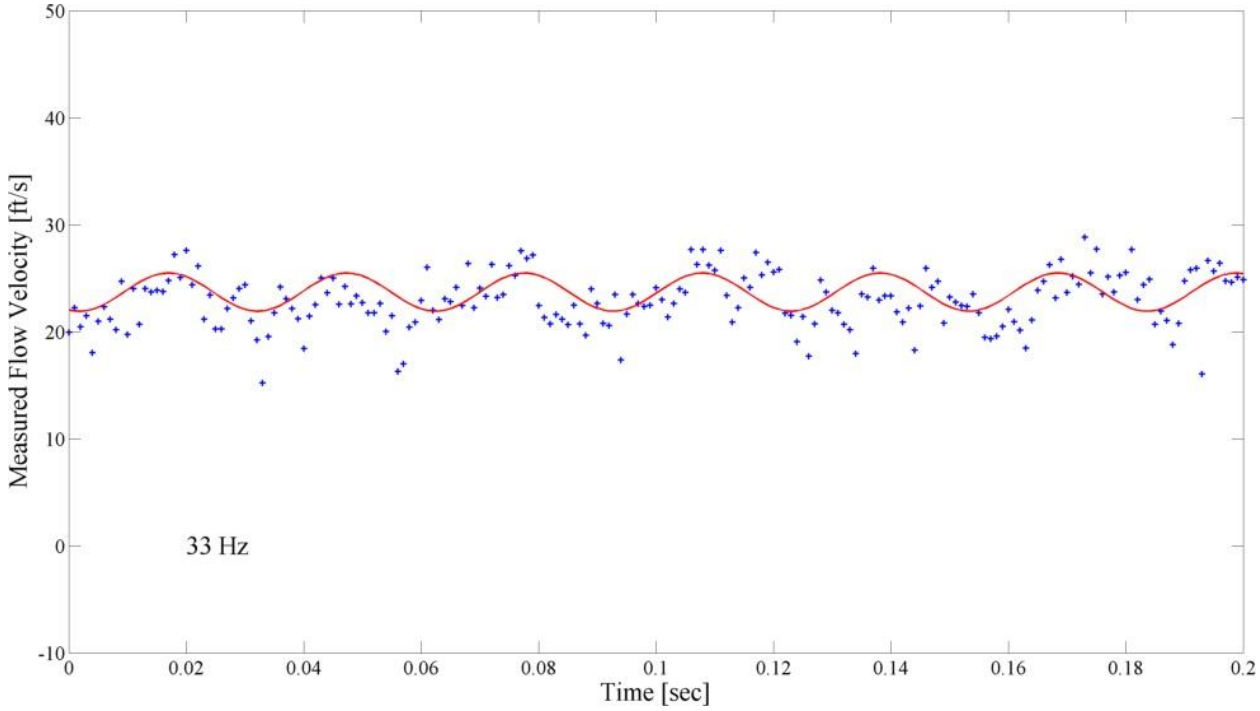

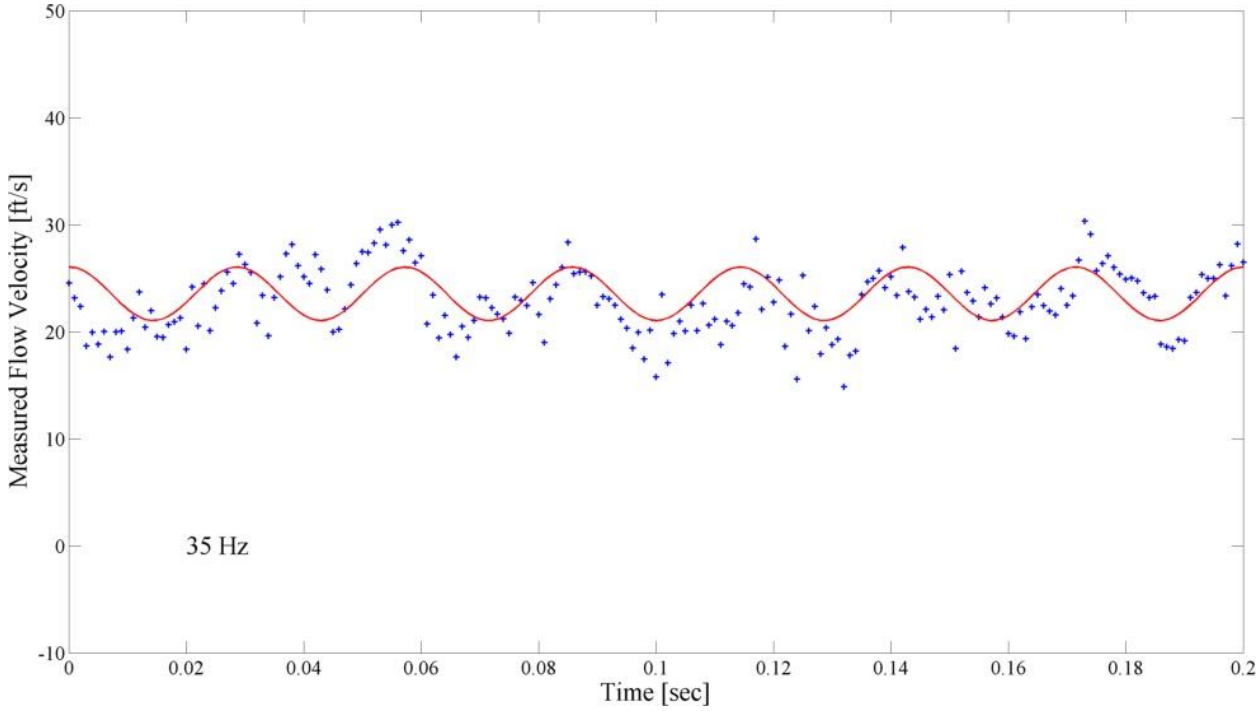

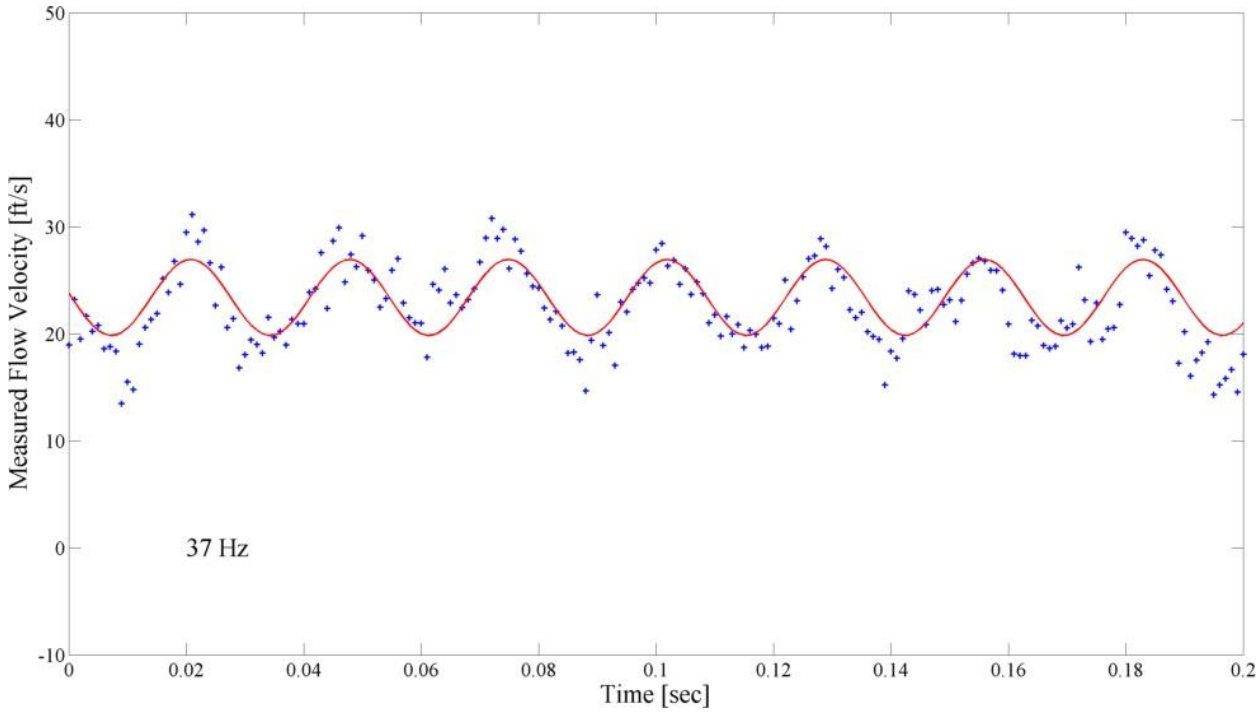

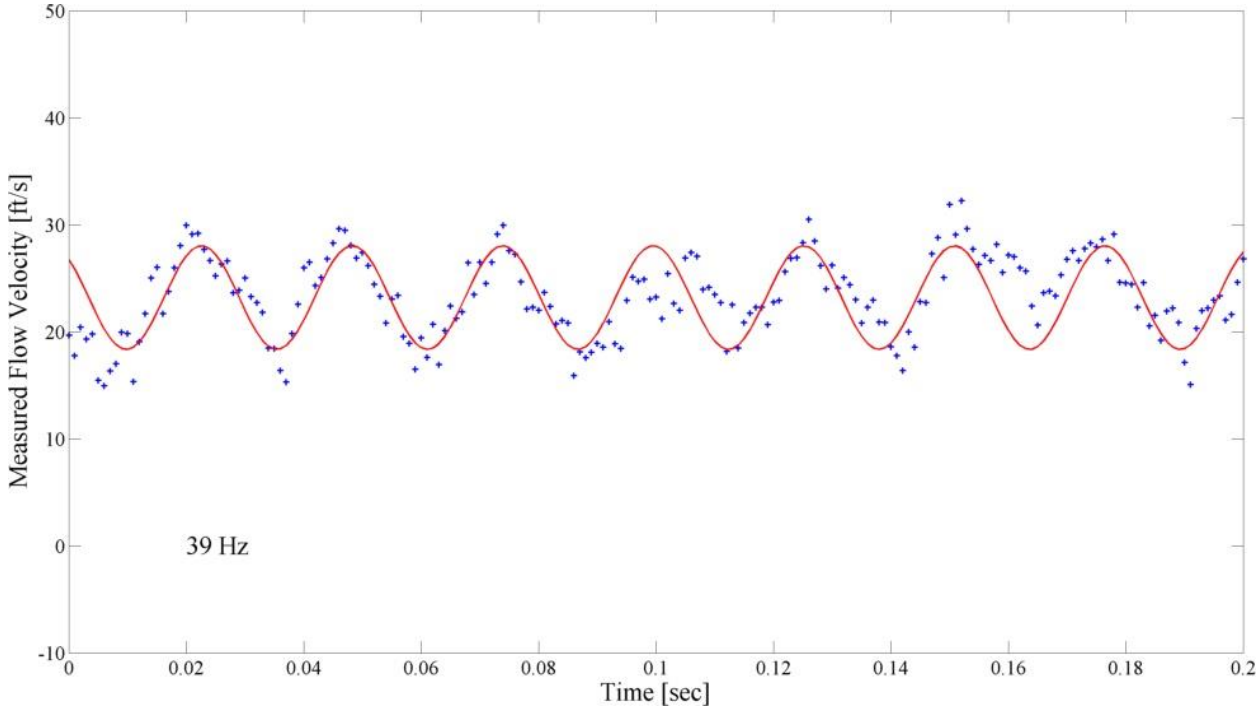

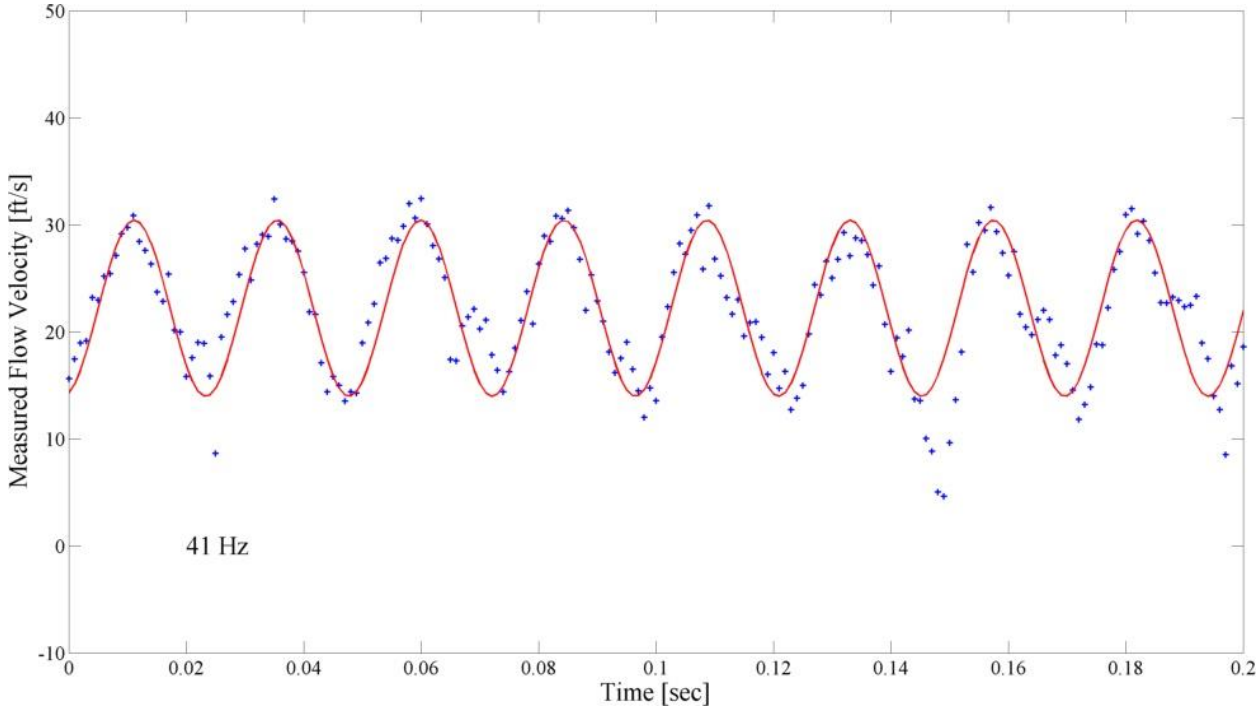

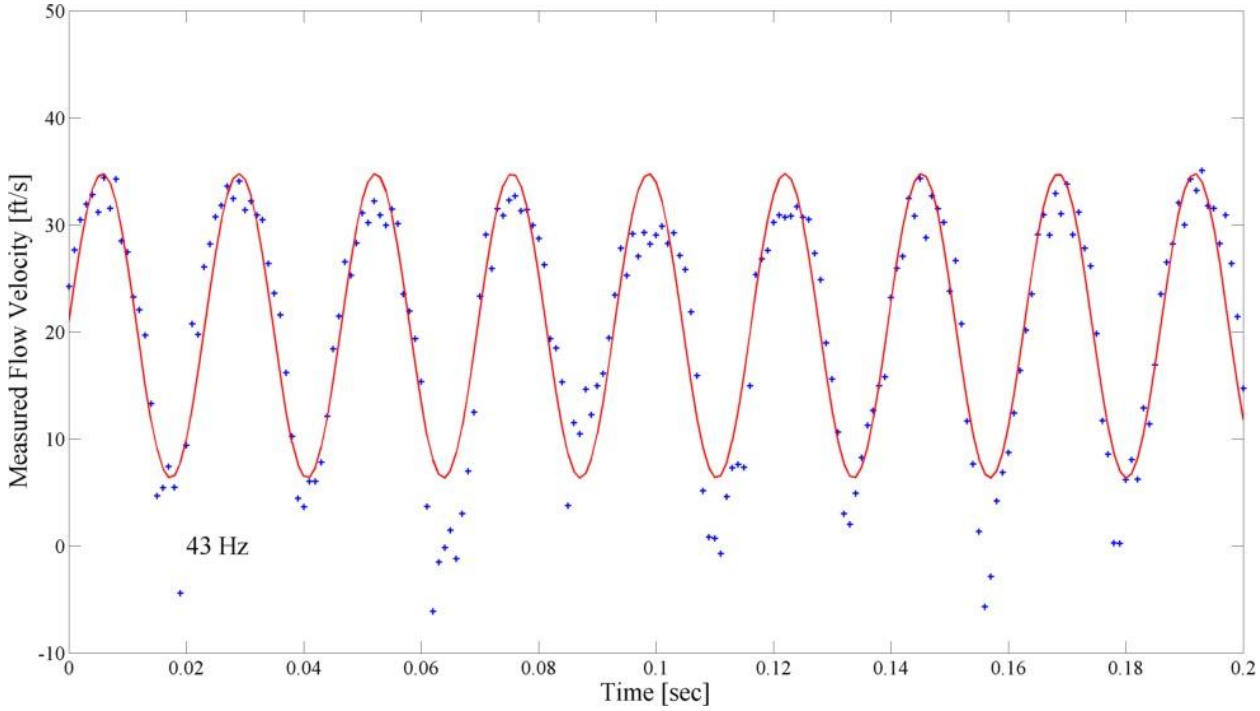

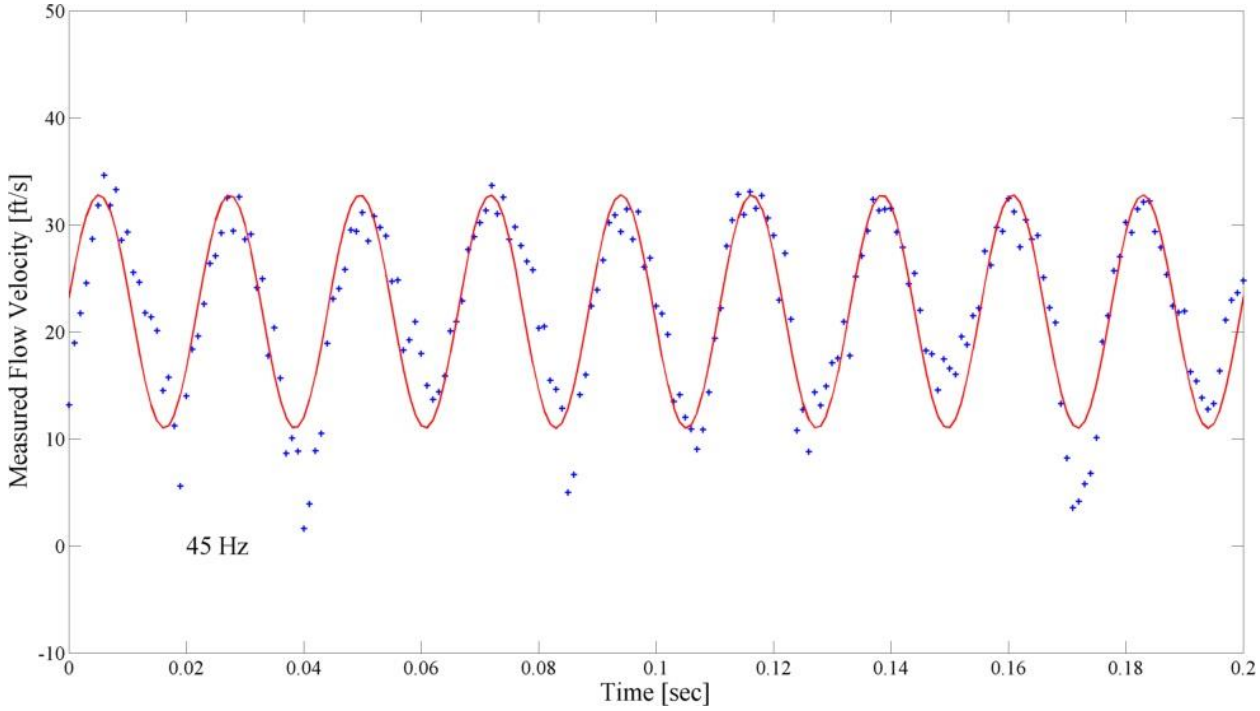

200 acfm:

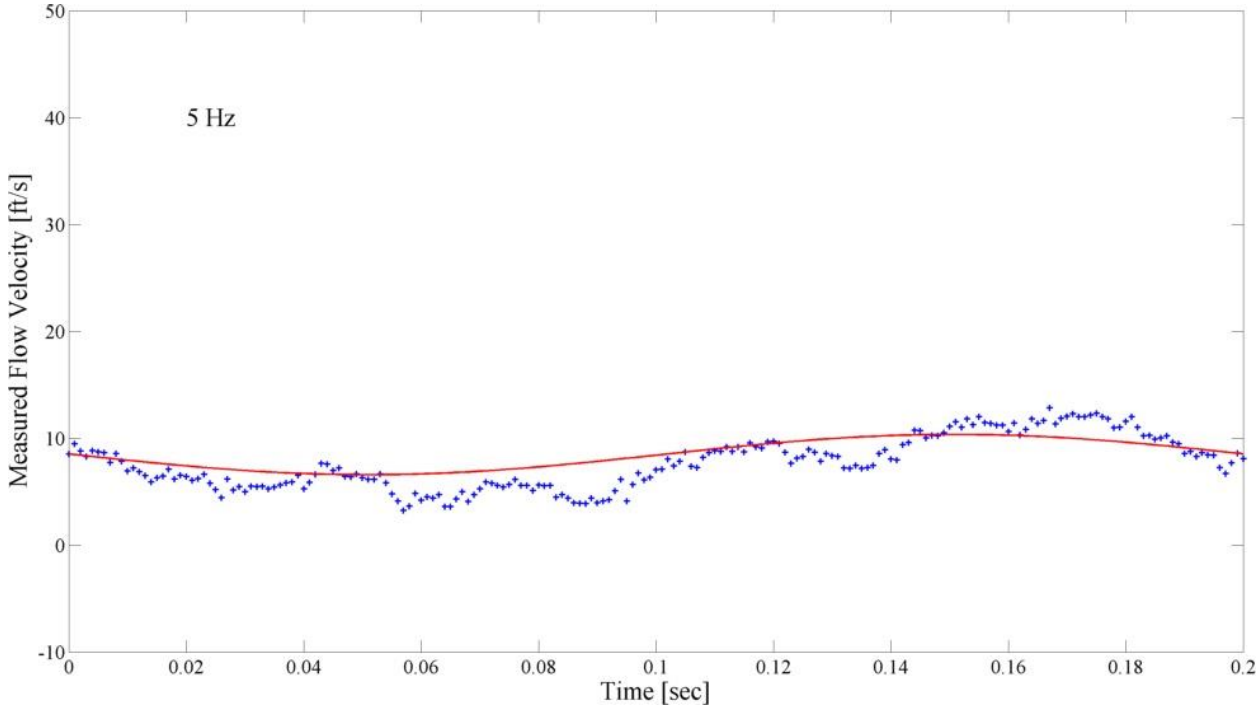

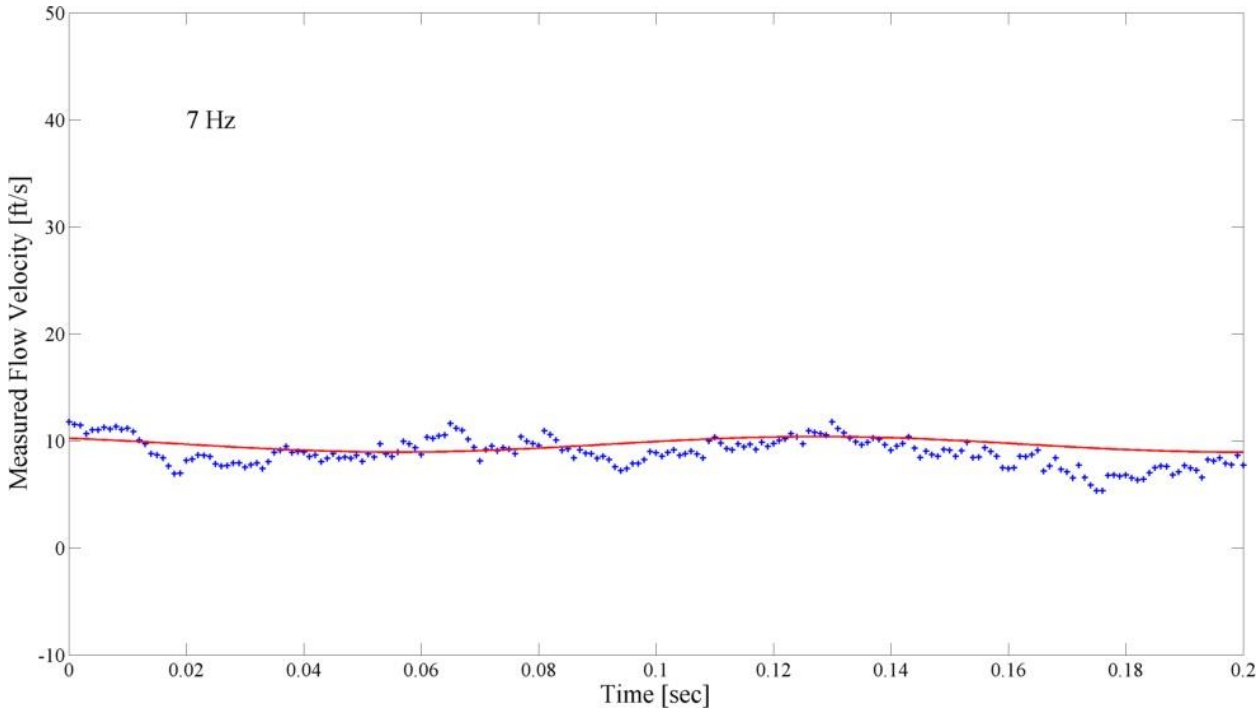

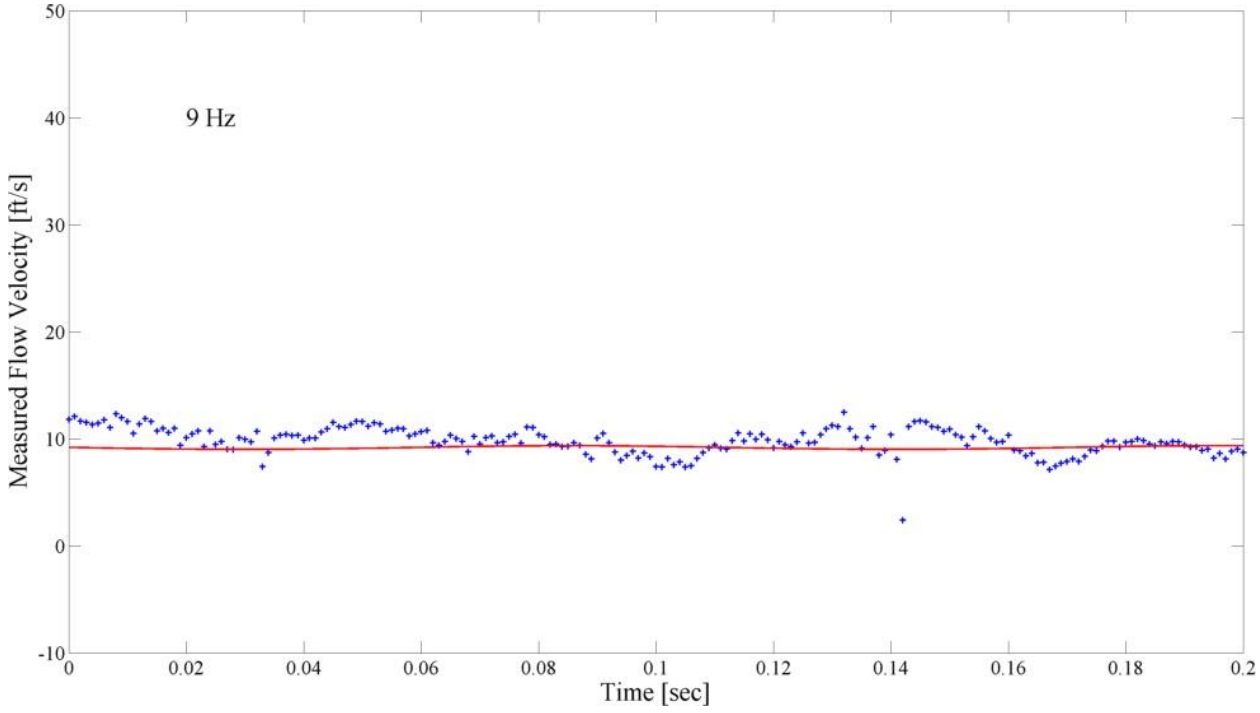

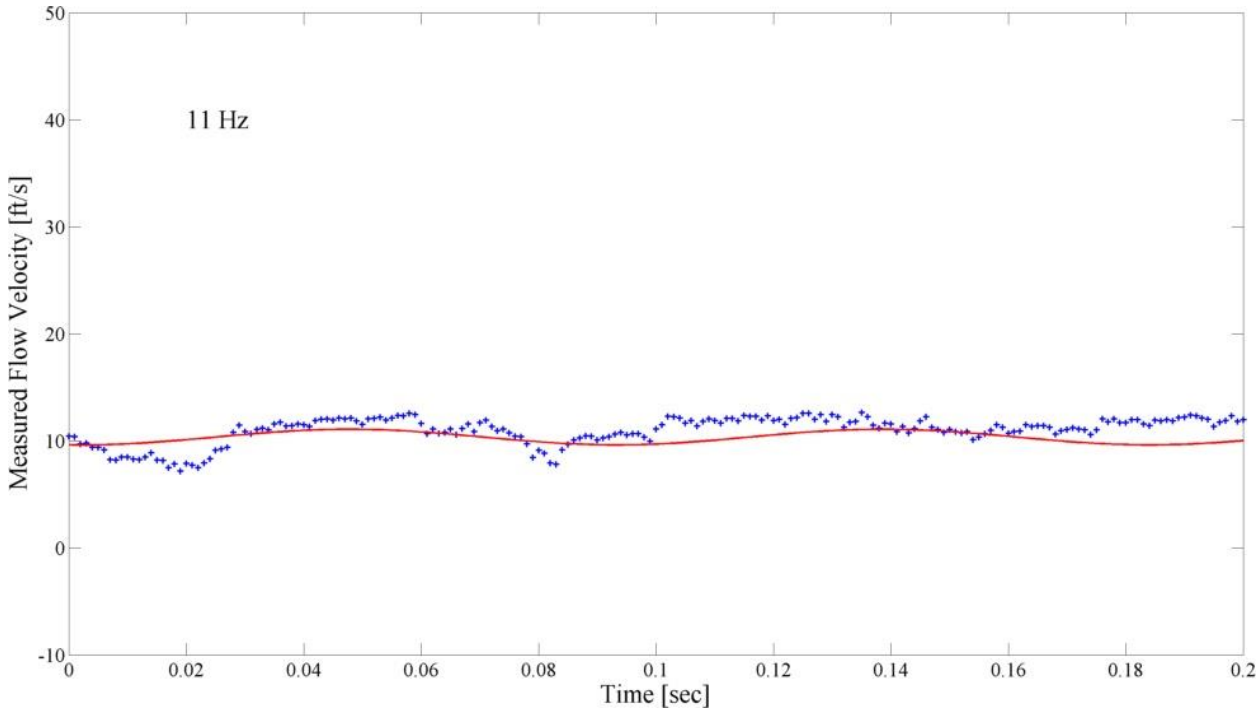

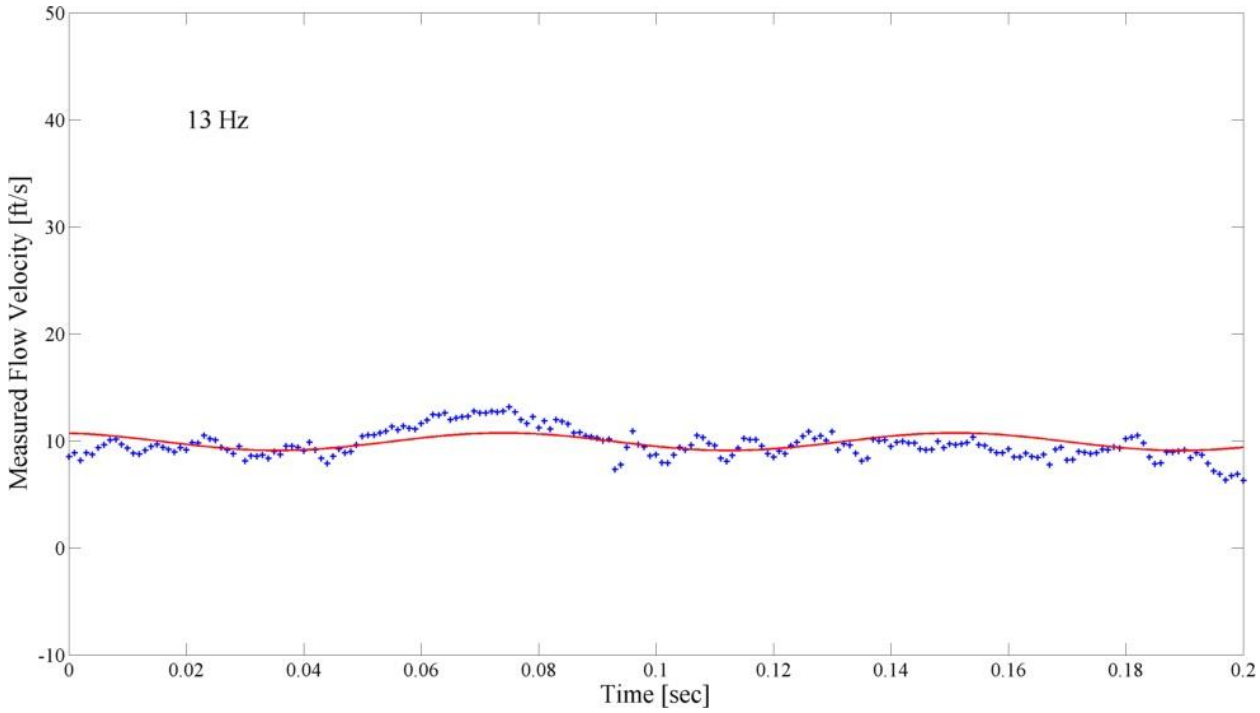

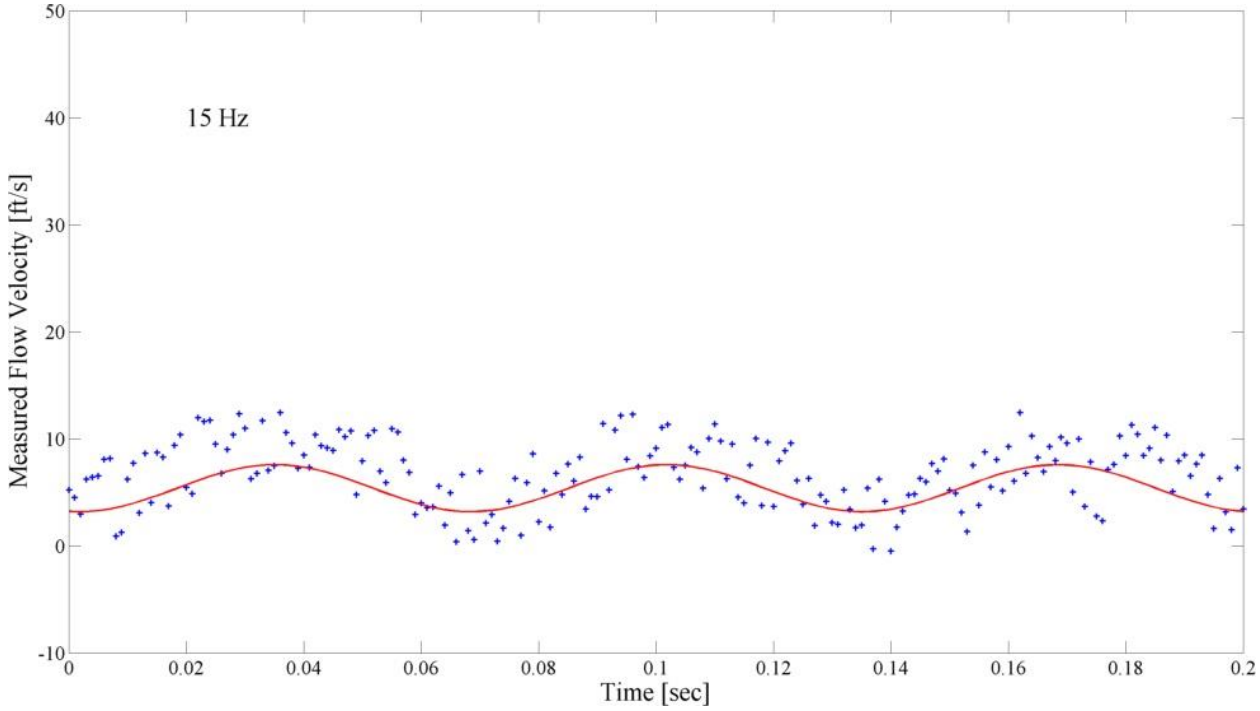

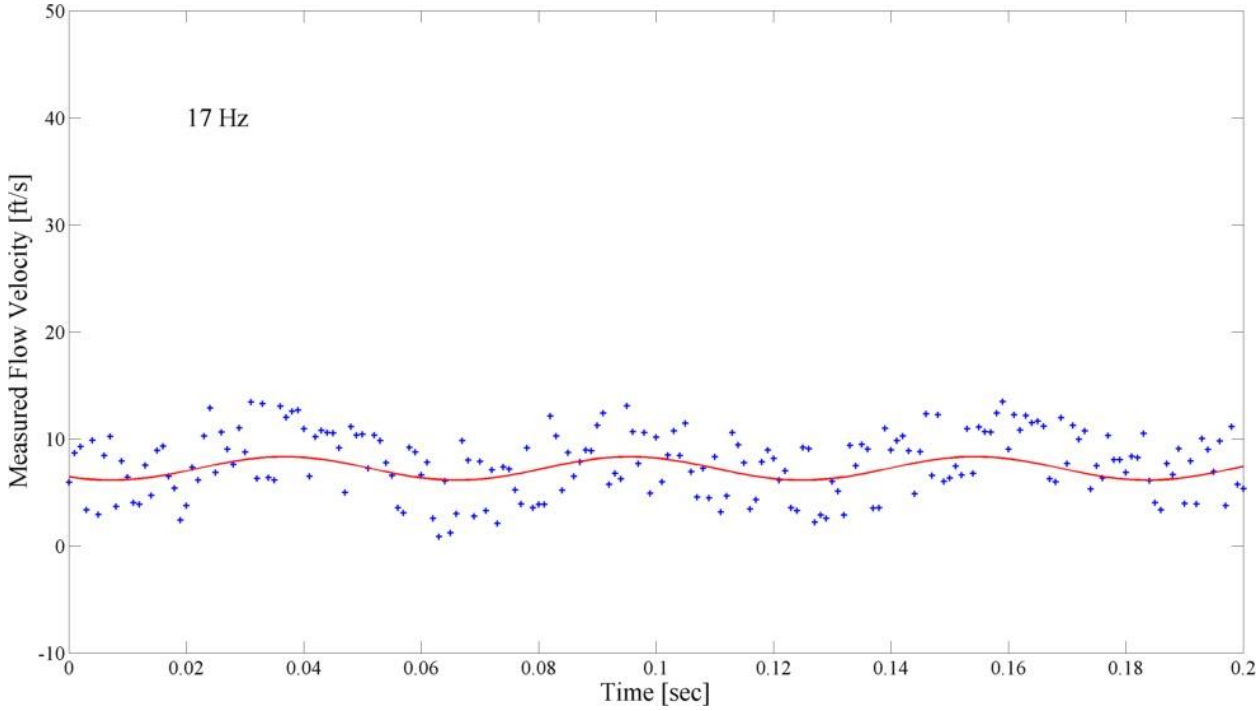

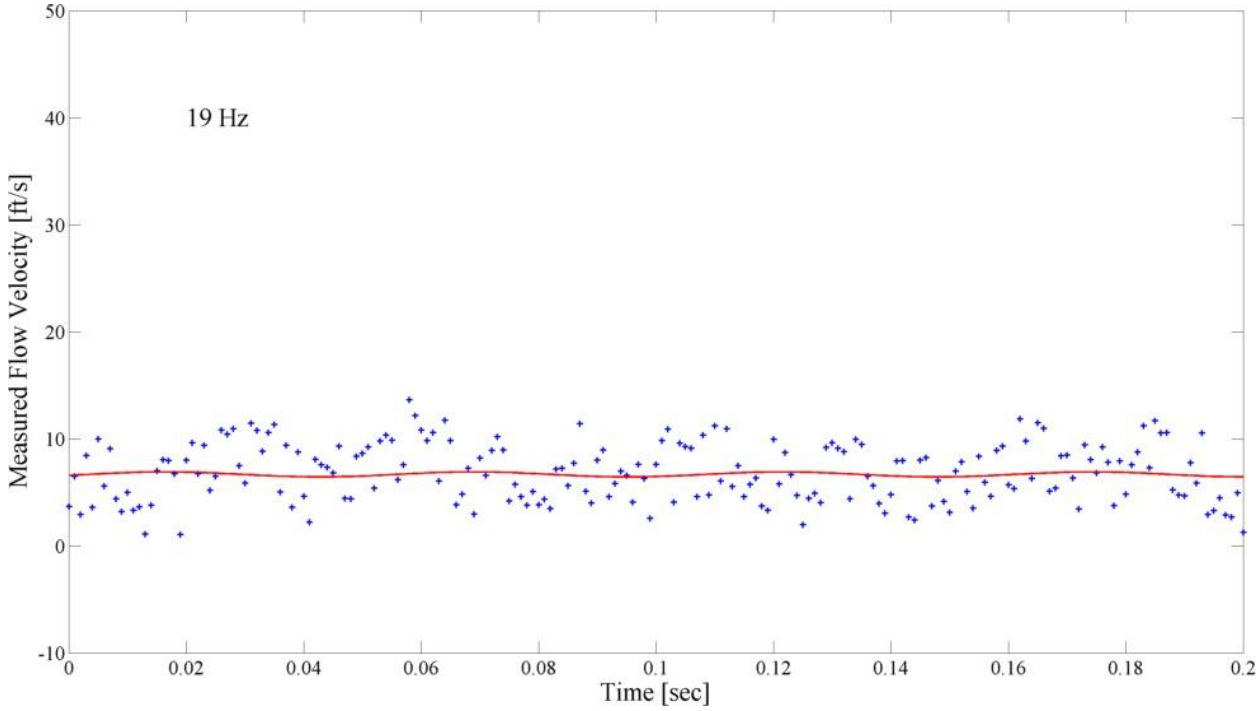

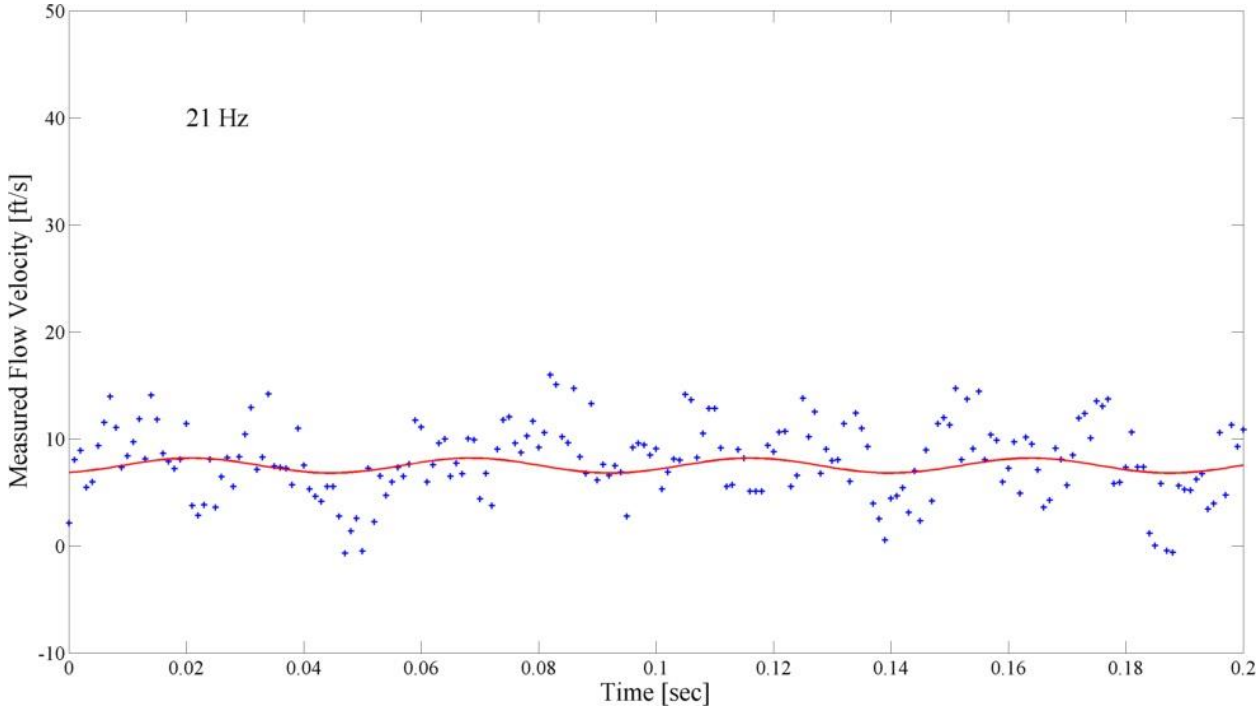

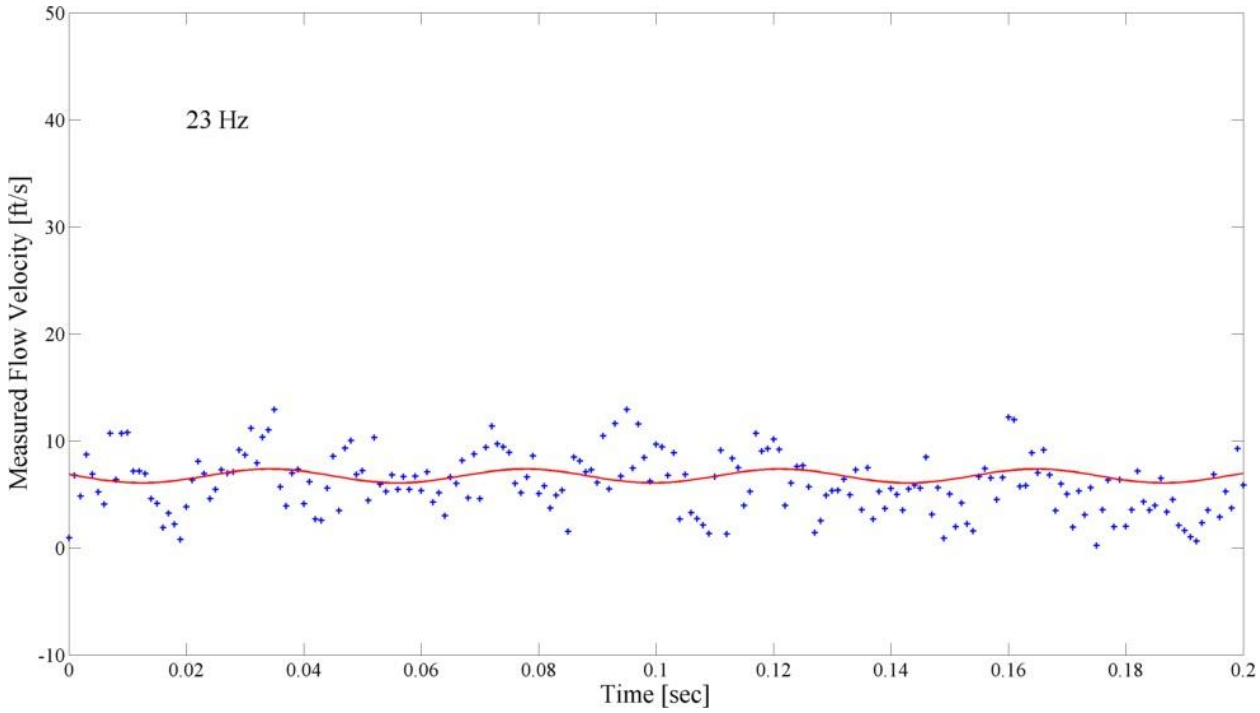

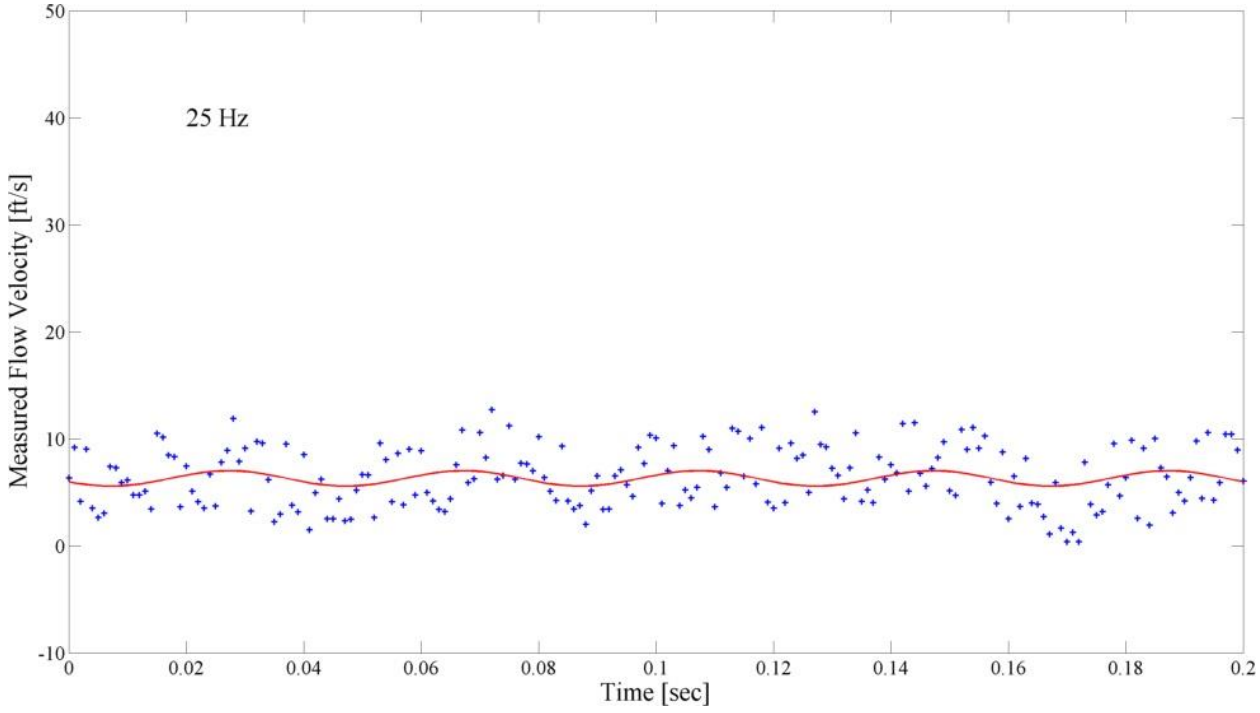

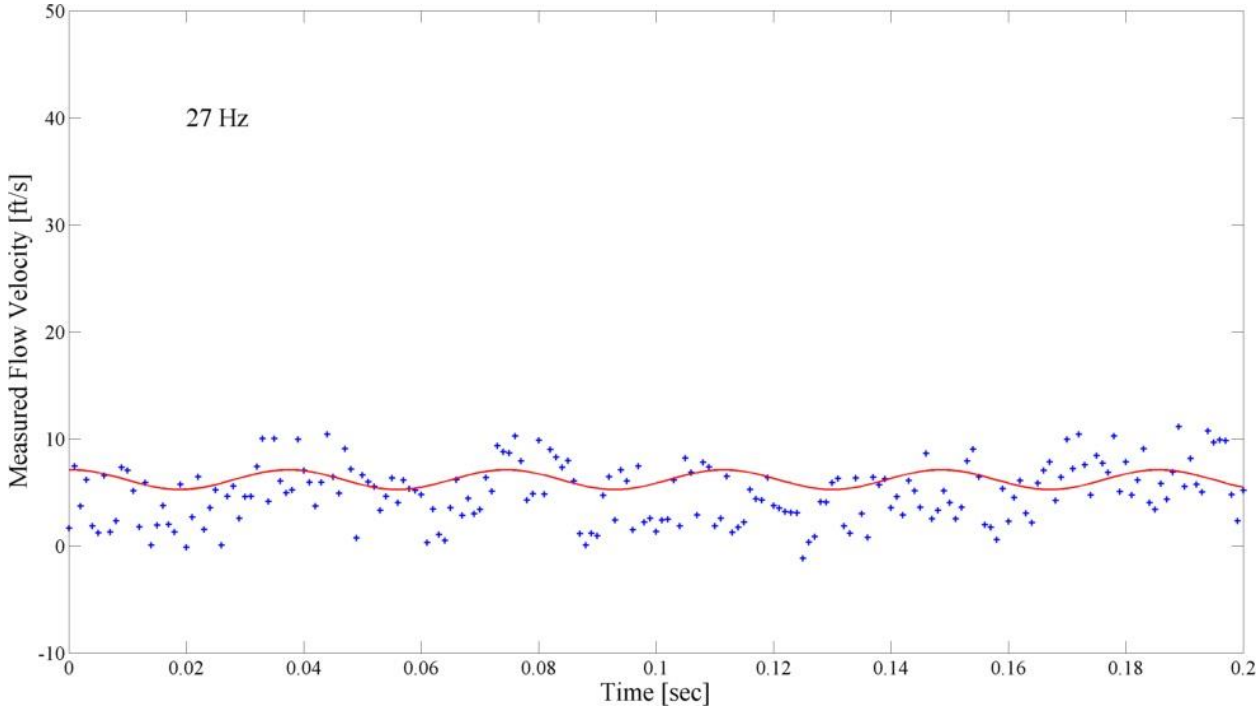

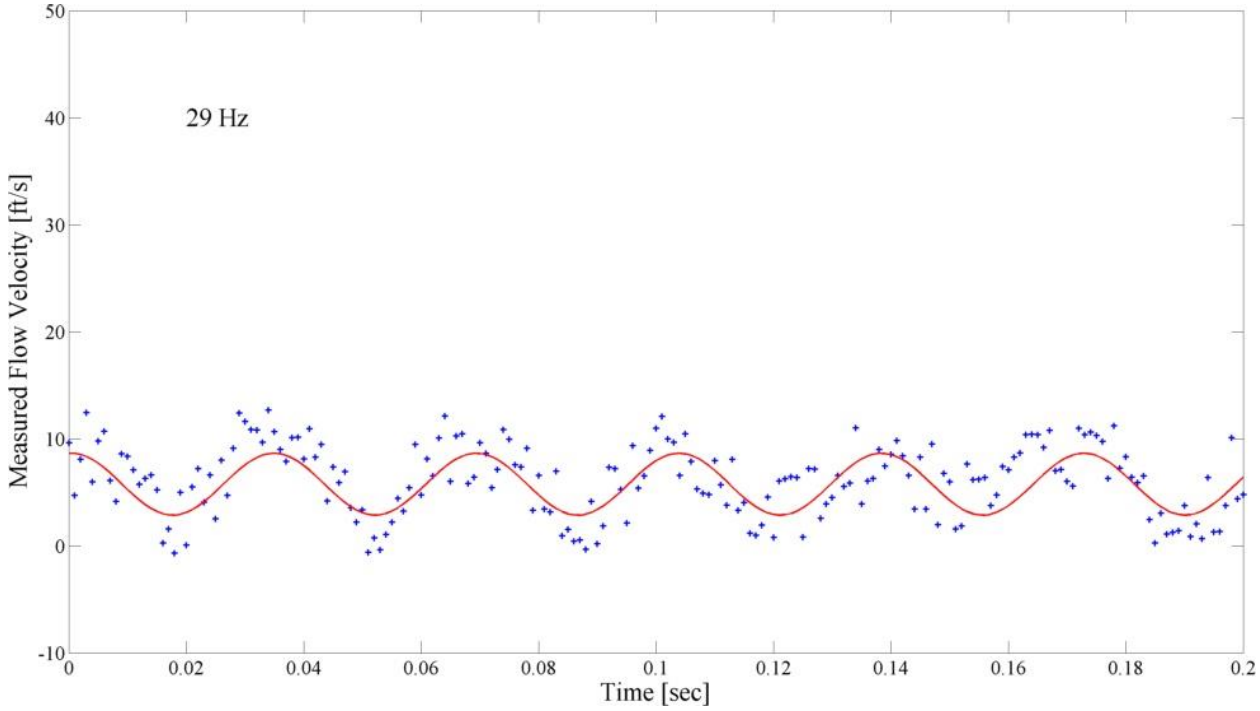

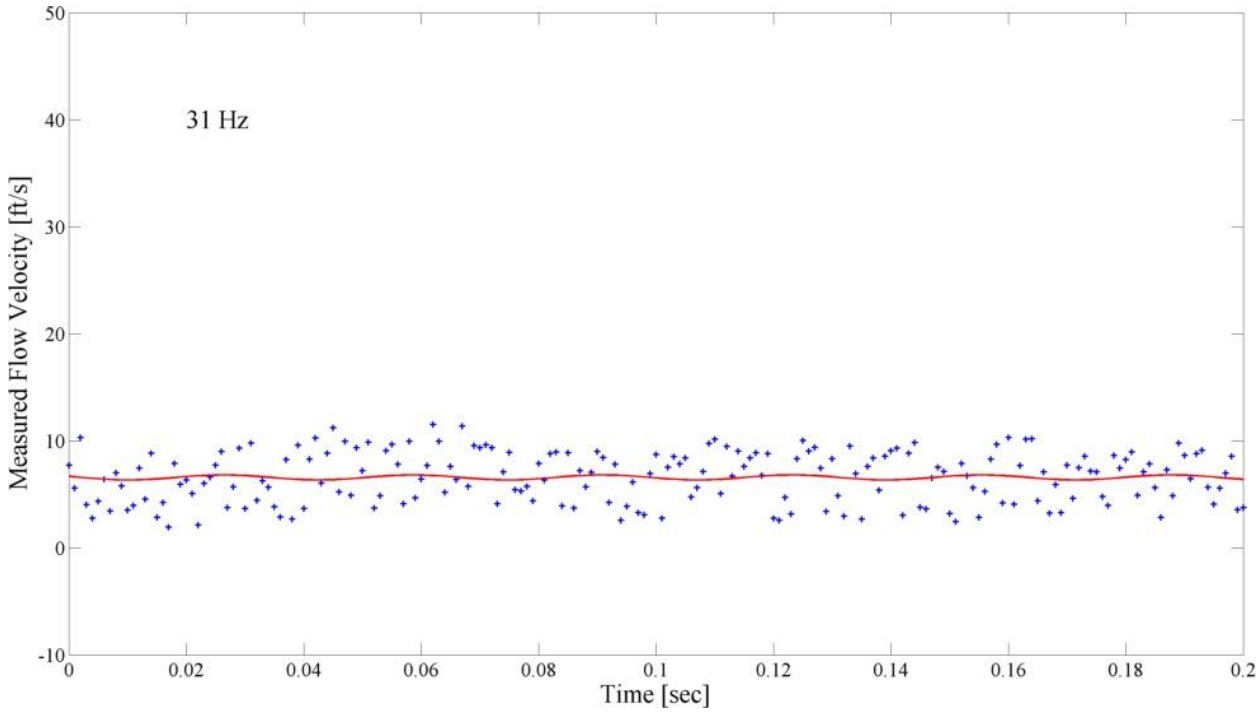

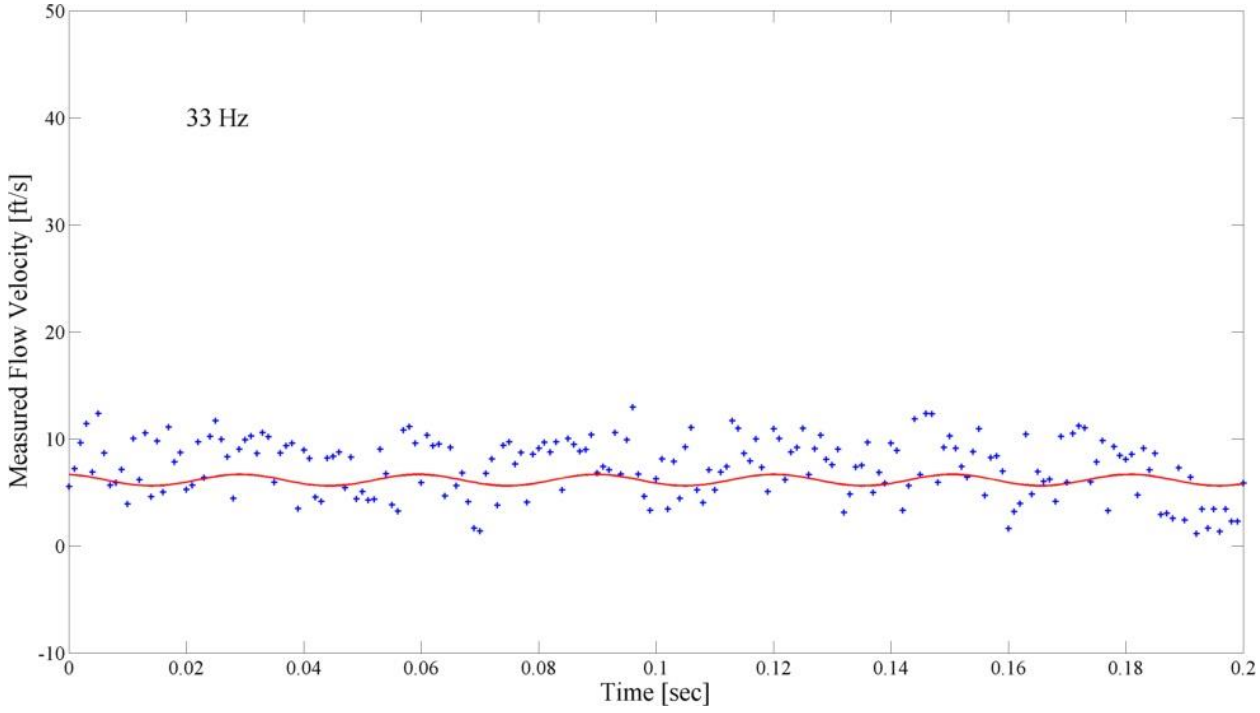

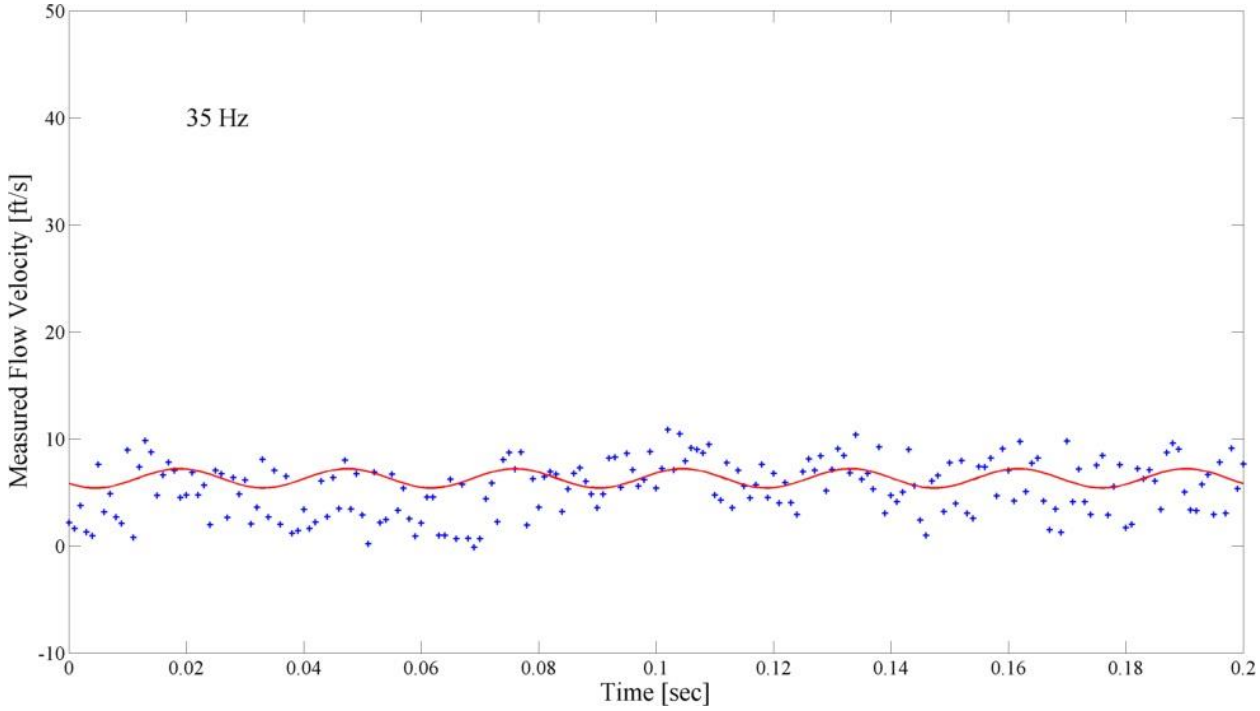

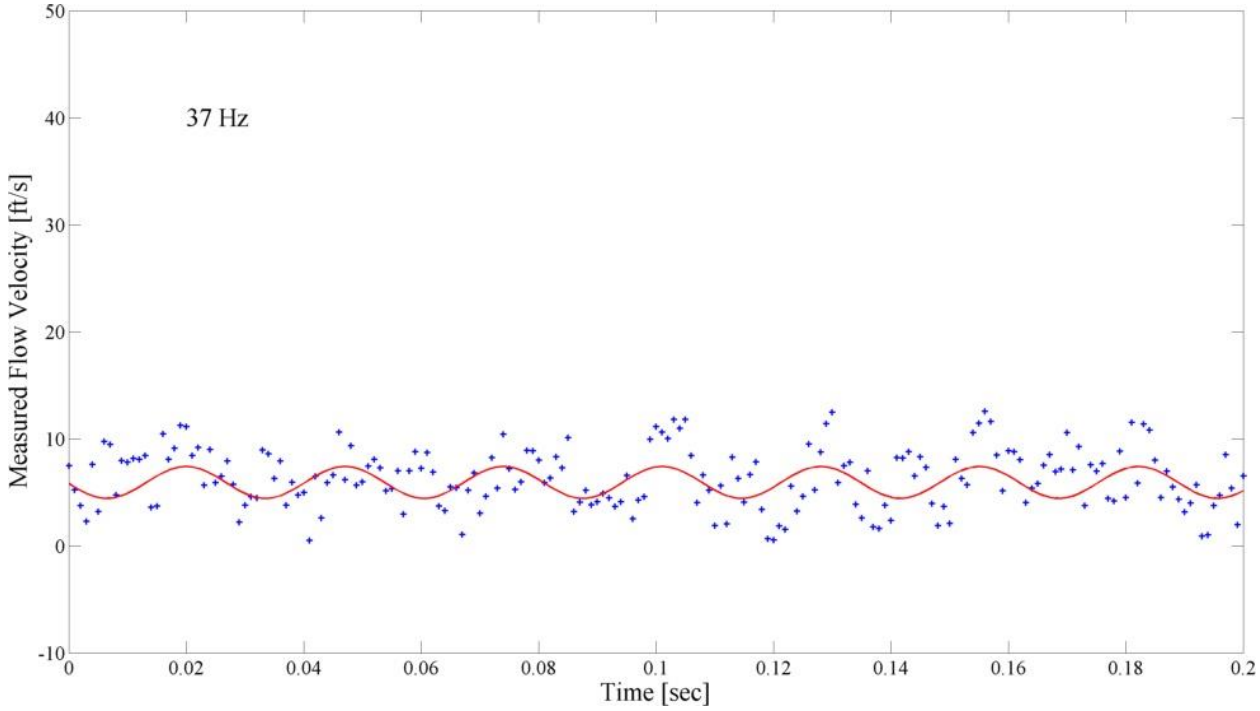

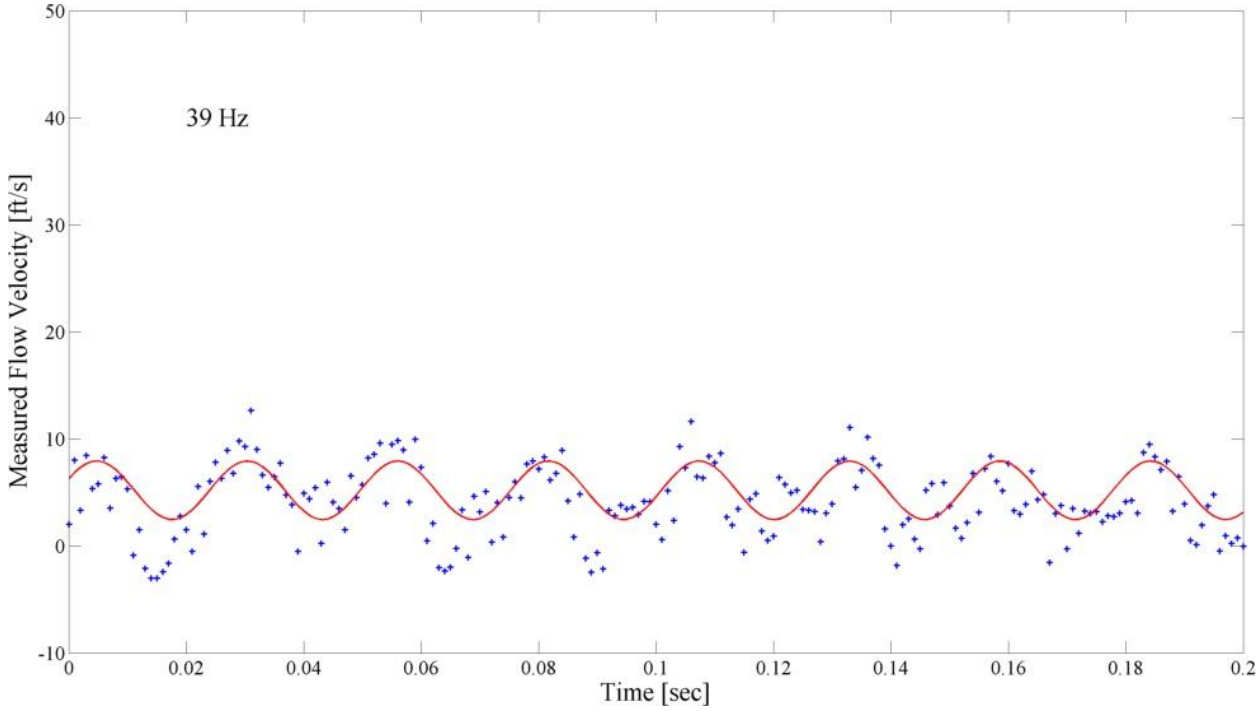

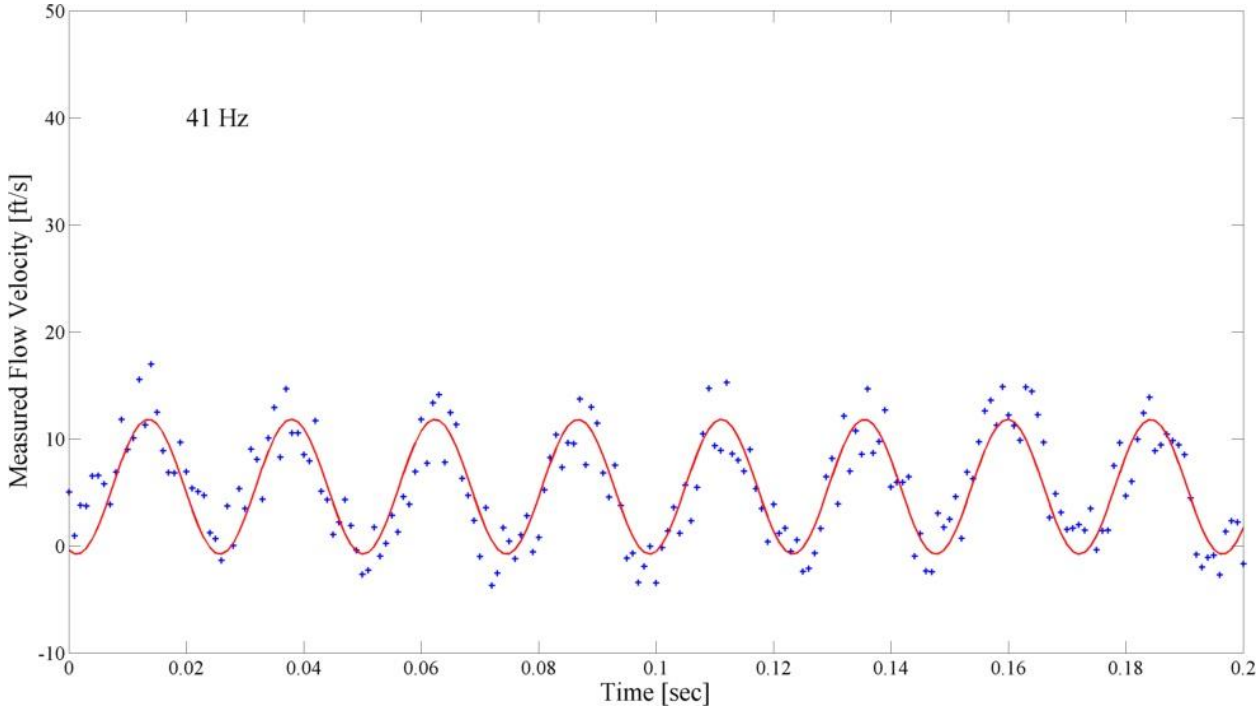

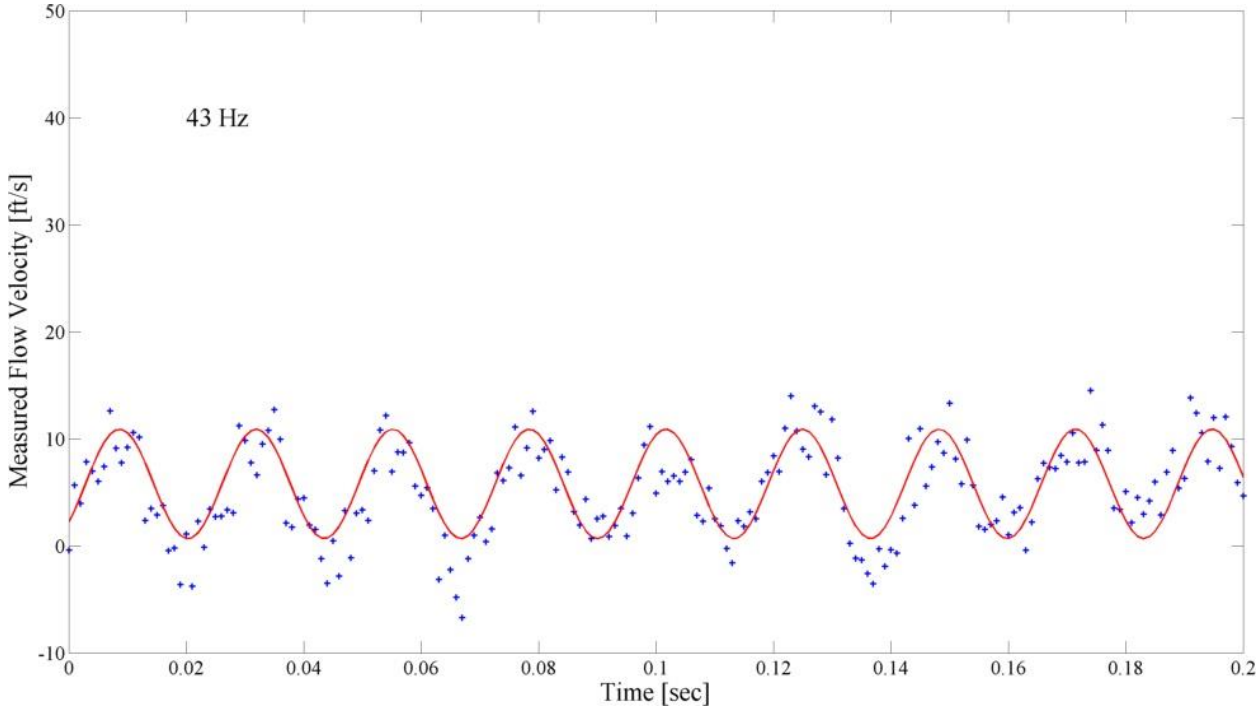

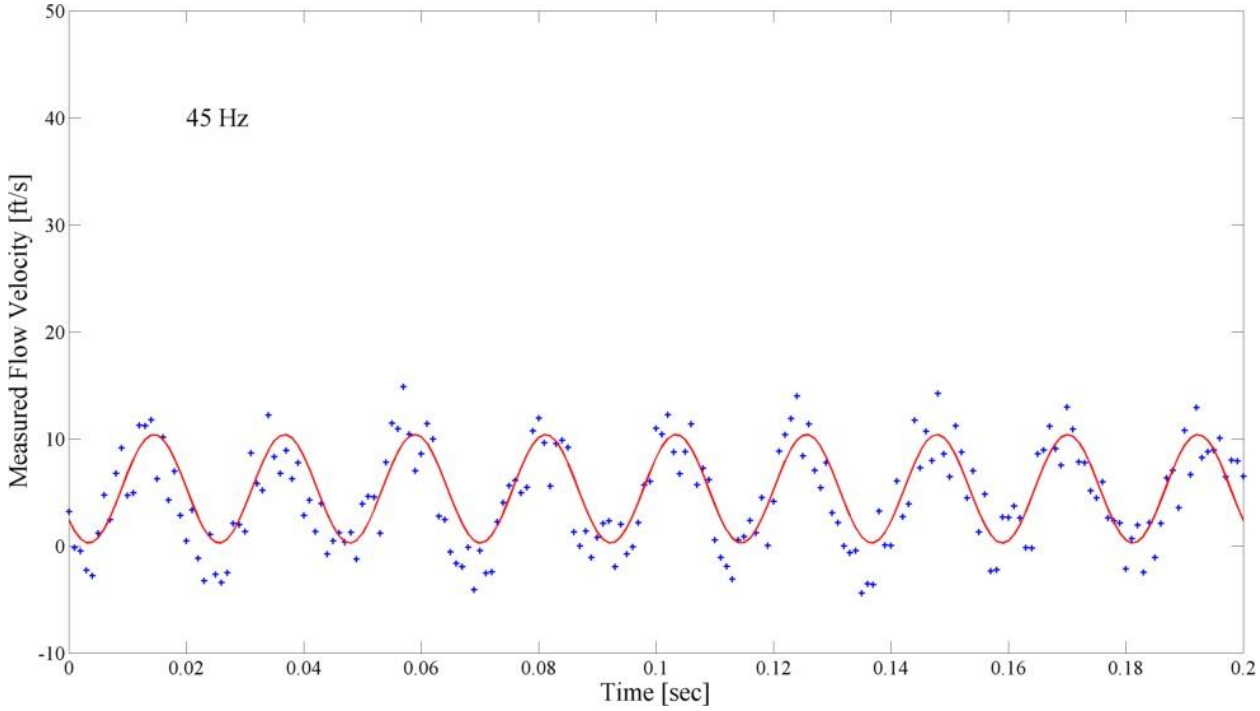

APPENDIX E: VELOCITY PROFILE SHIFTS DUE TO PULSATION

700 acfm:

5 Hz

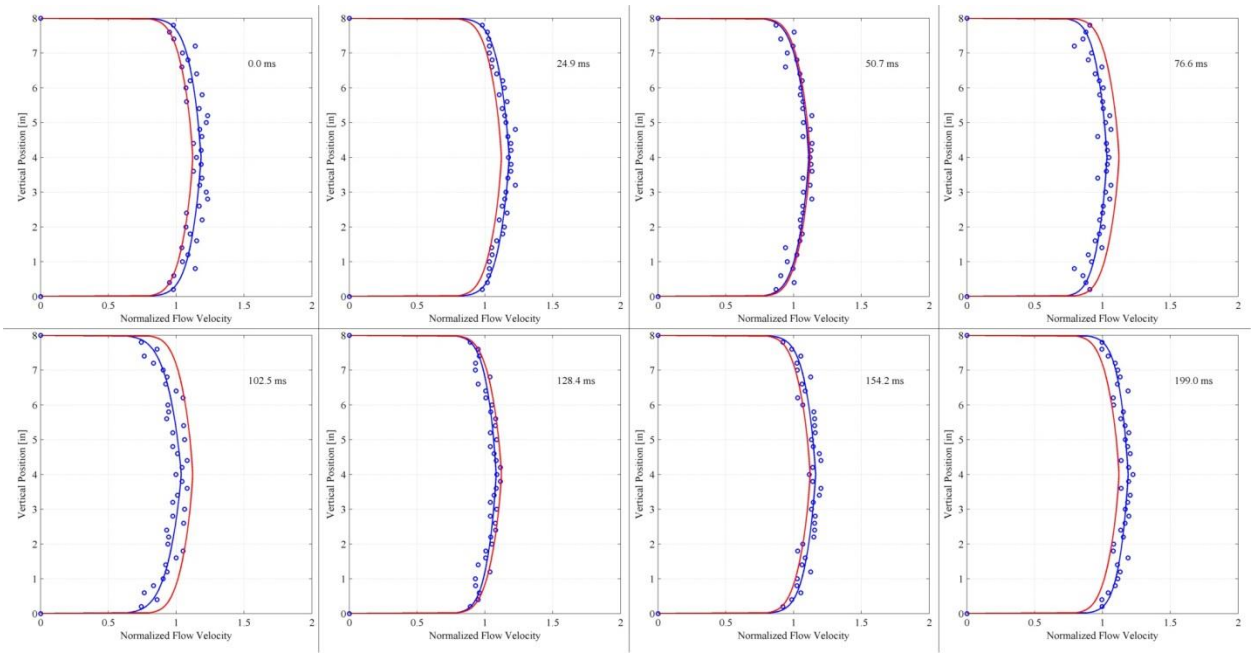

7 Hz

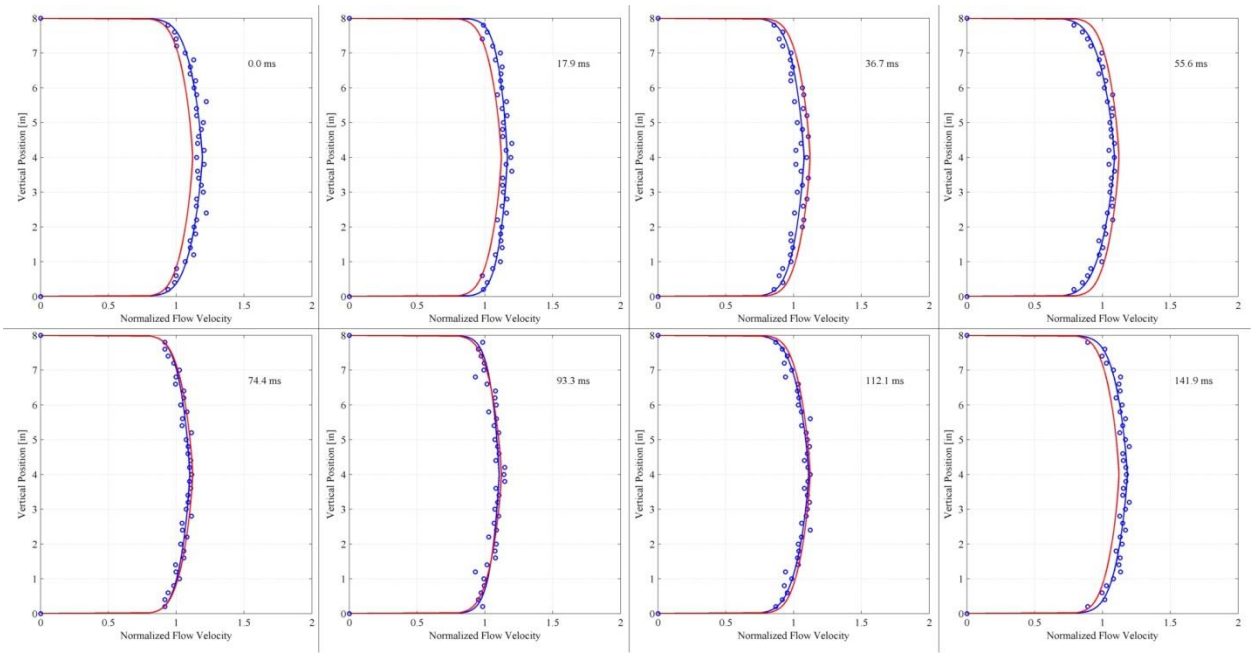

9 Hz

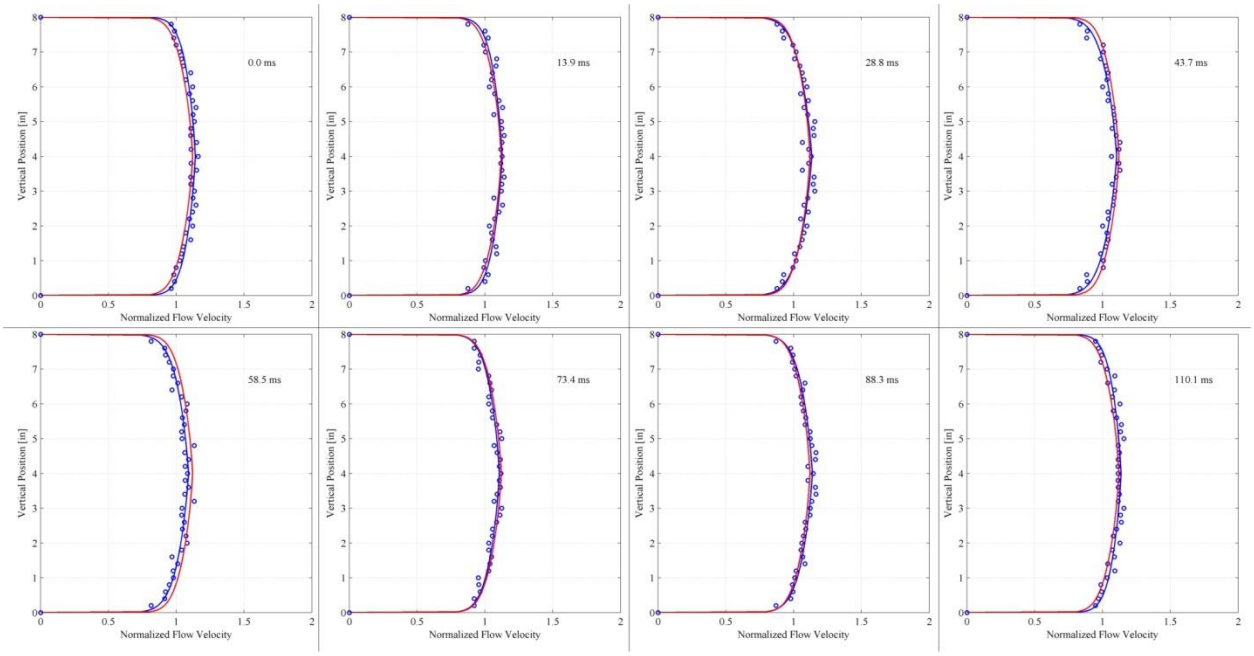

11 Hz

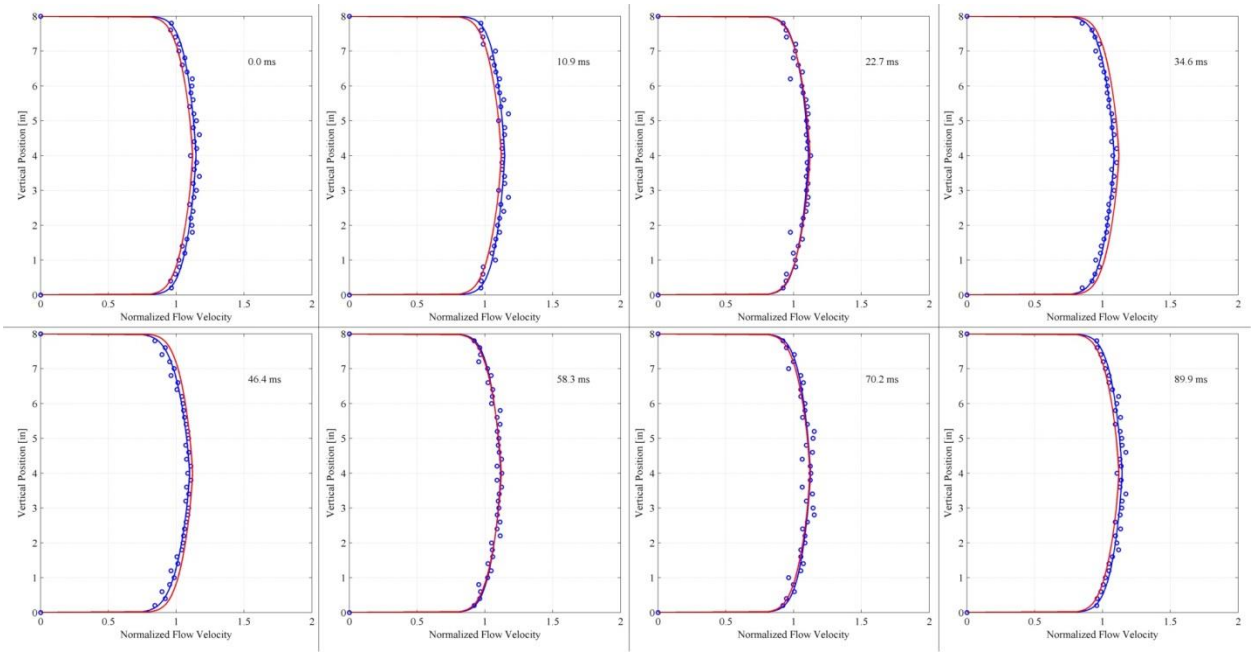

13 Hz

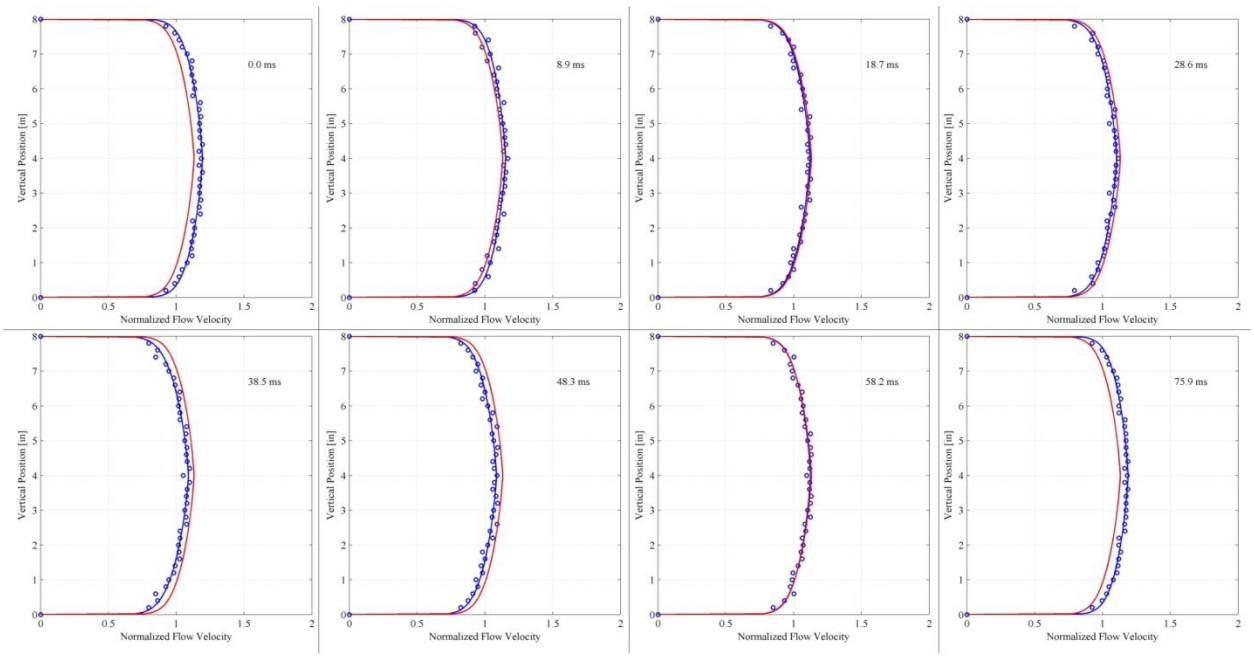

15 Hz

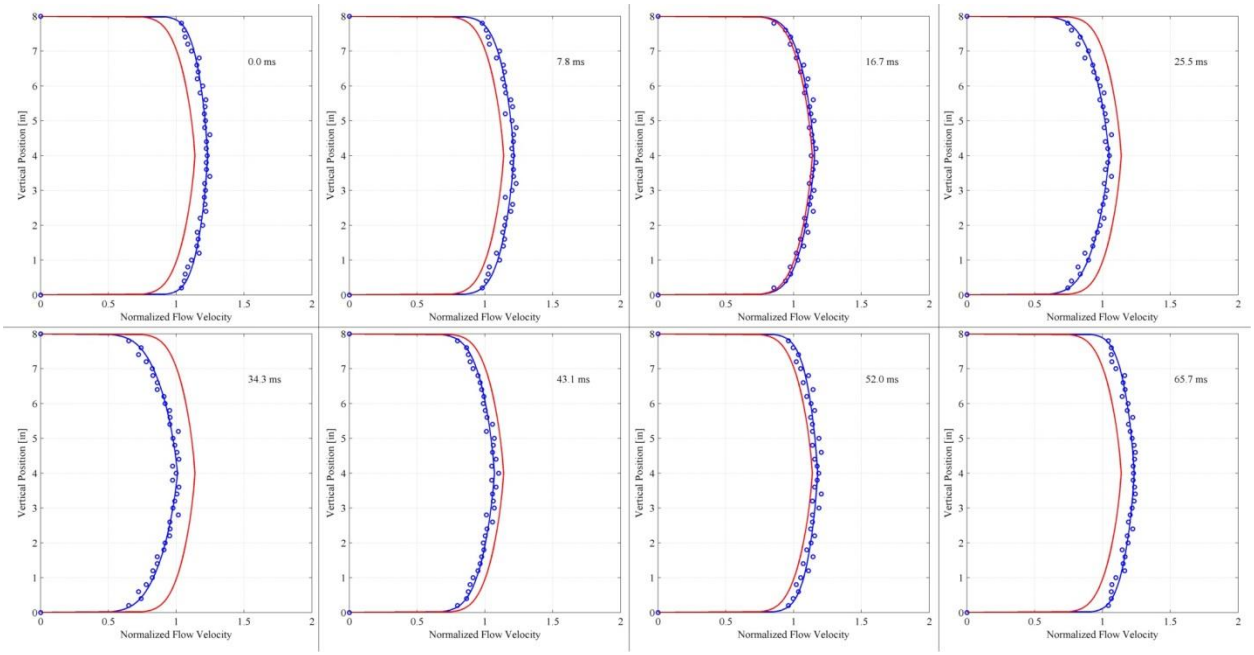

17 Hz

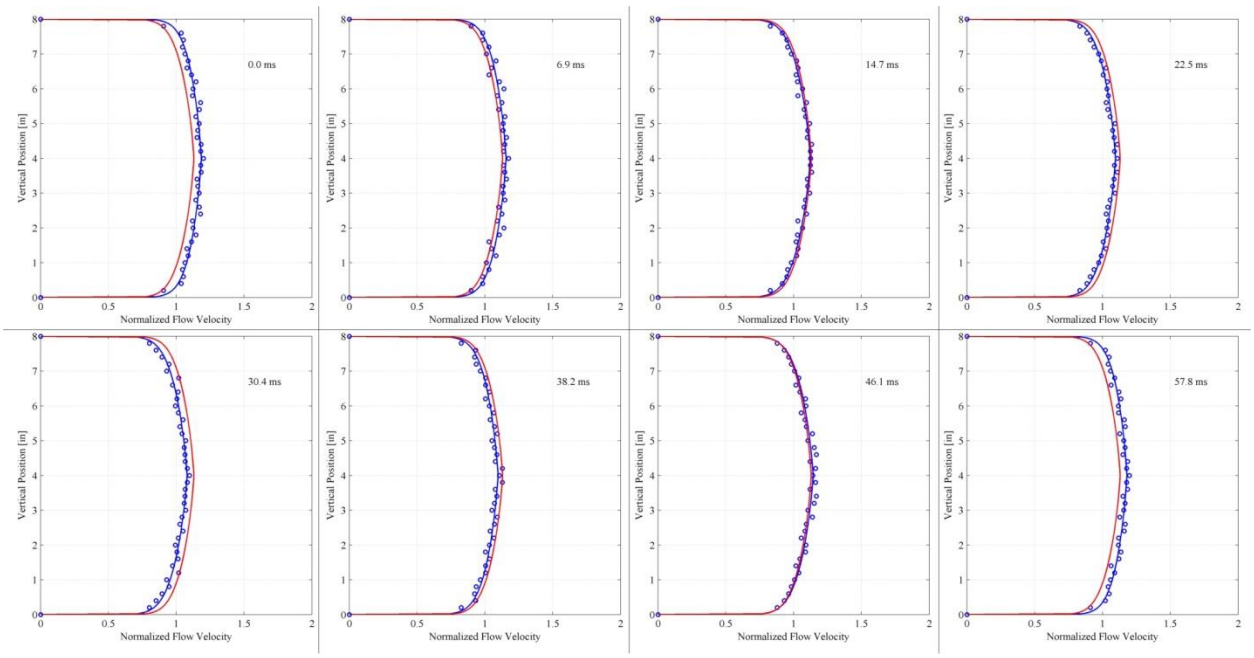

19 Hz

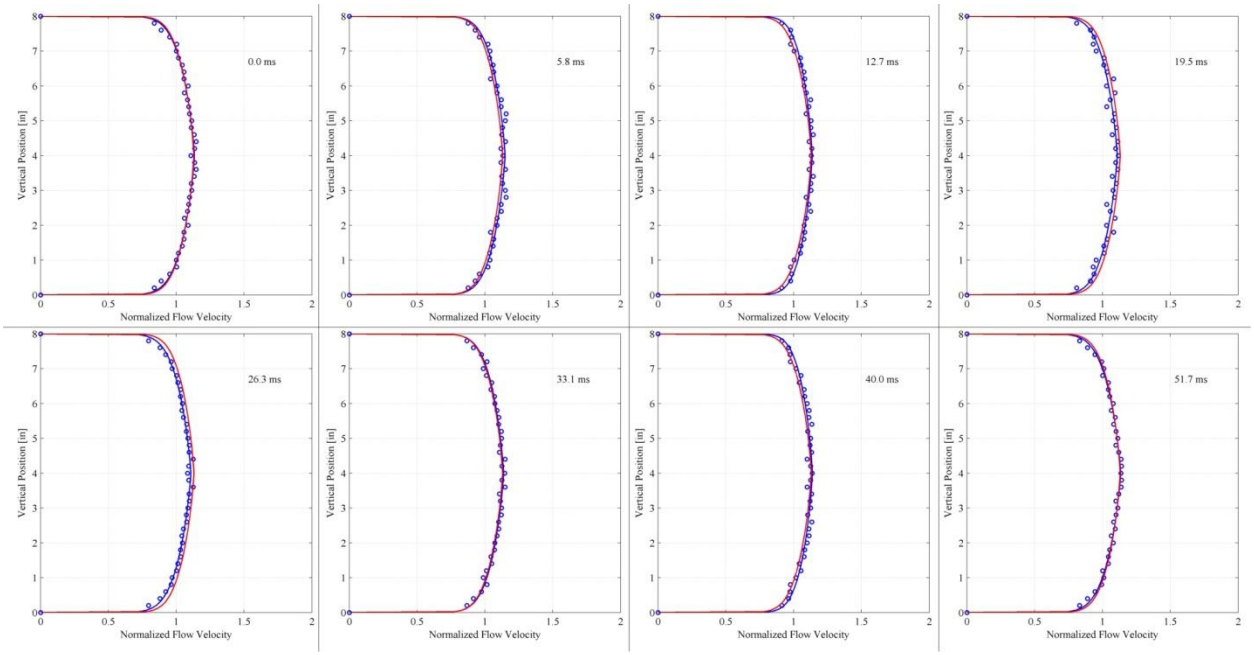

21 Hz

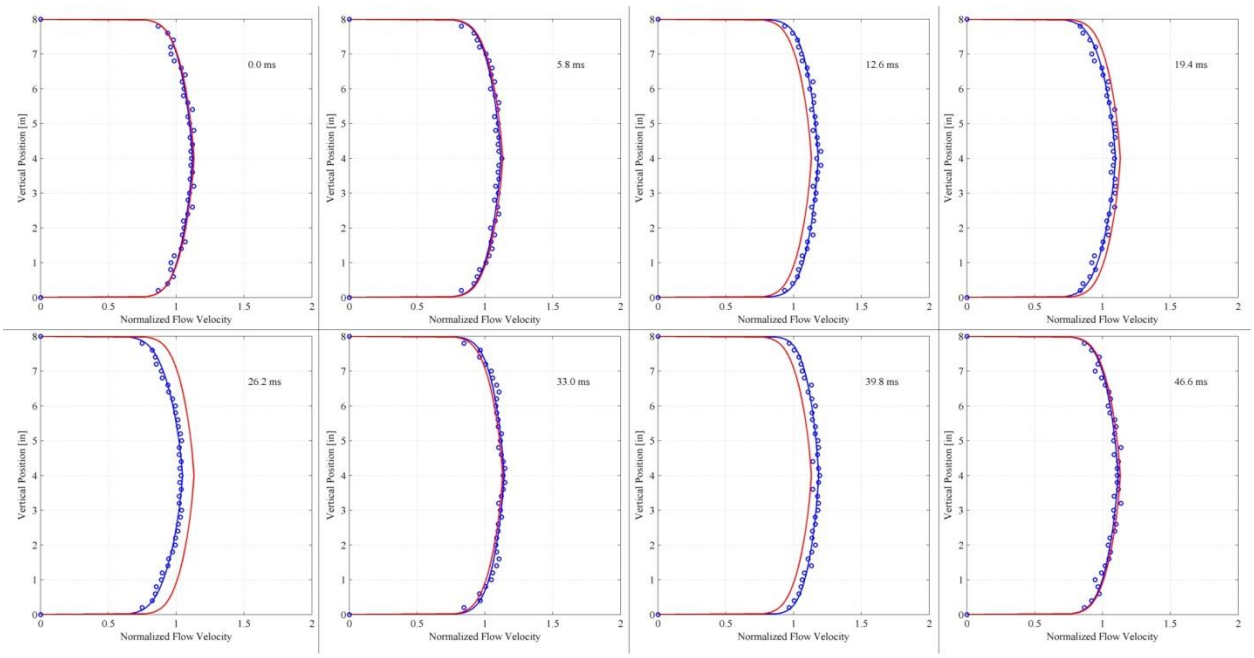

23 Hz

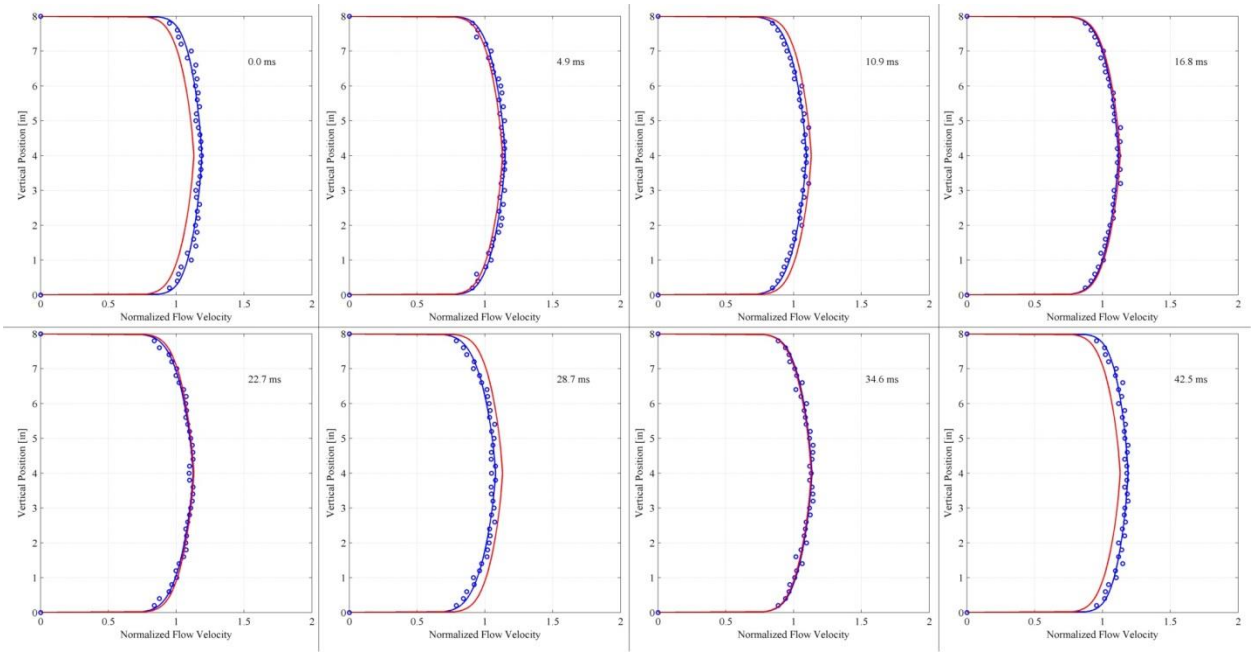

25 Hz

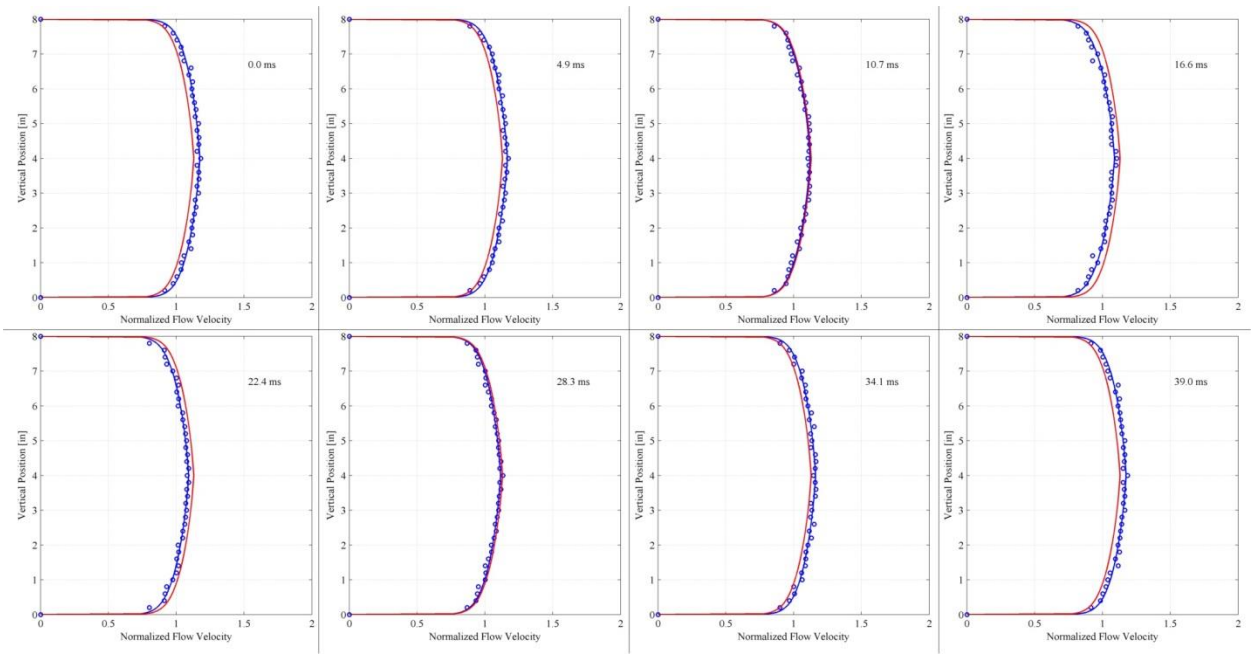

27 Hz

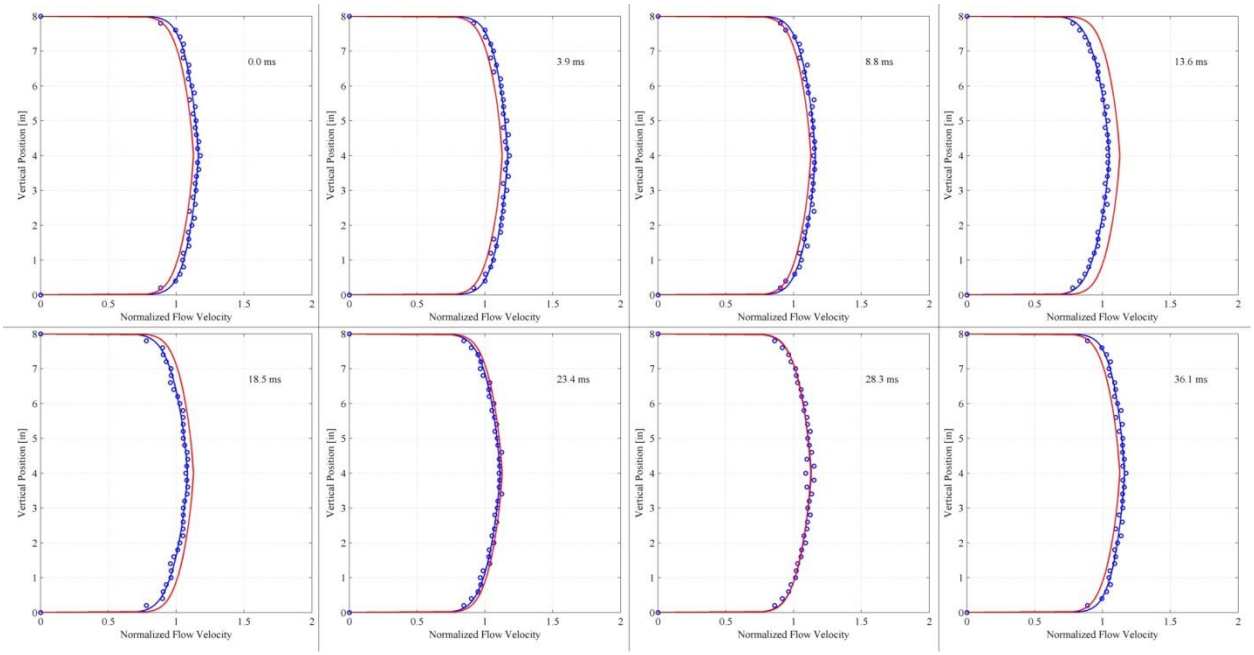

29 Hz

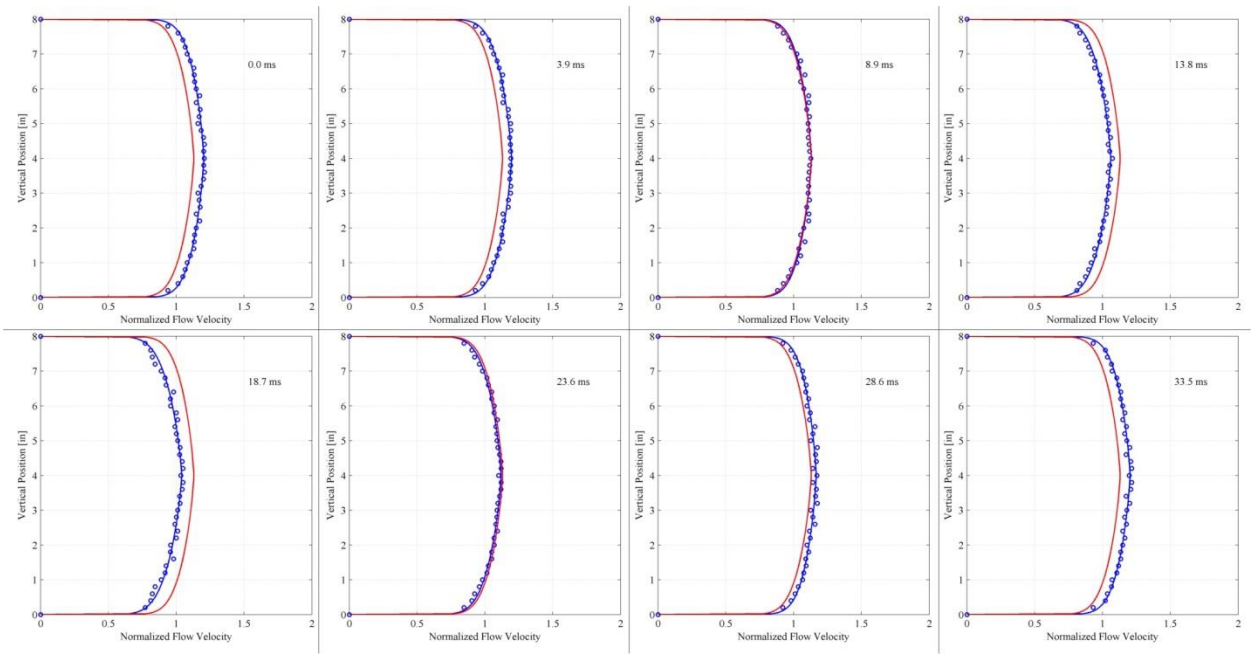

31 Hz

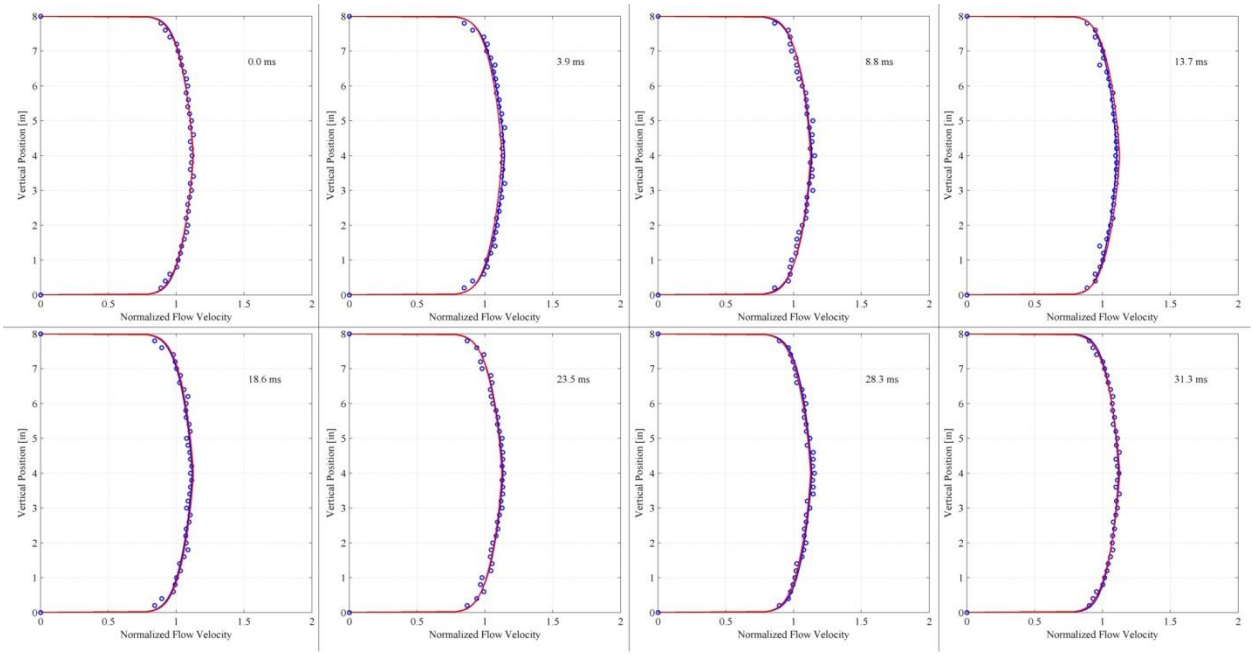

33 Hz

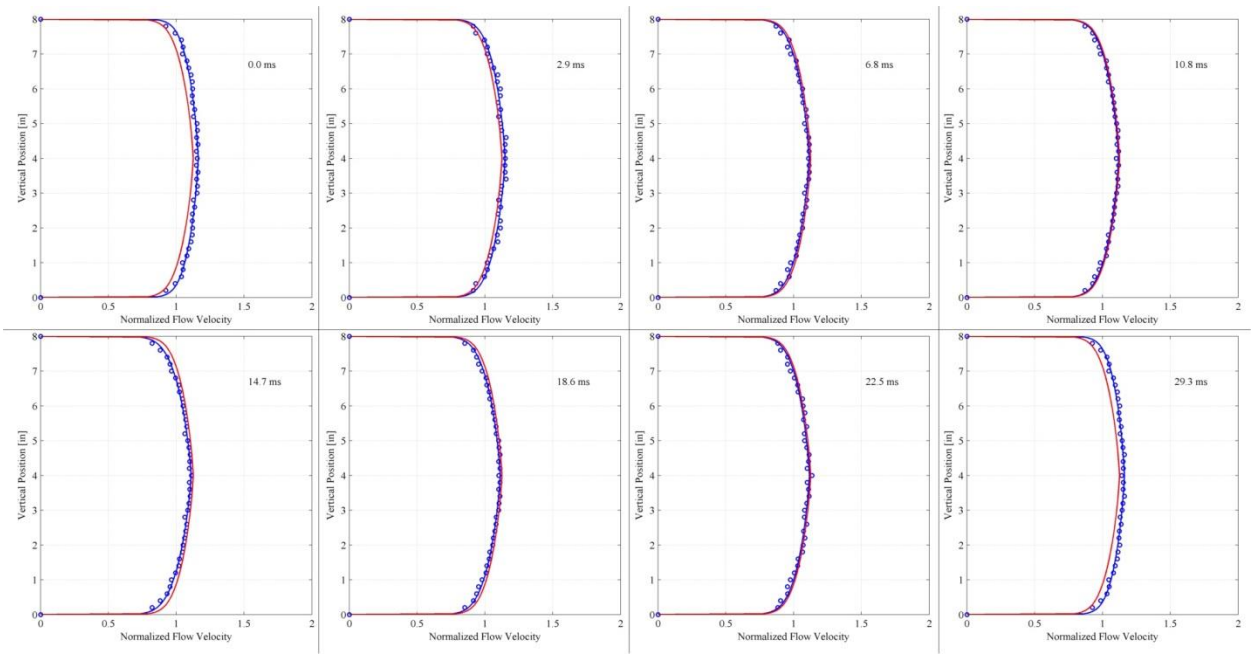

35 Hz

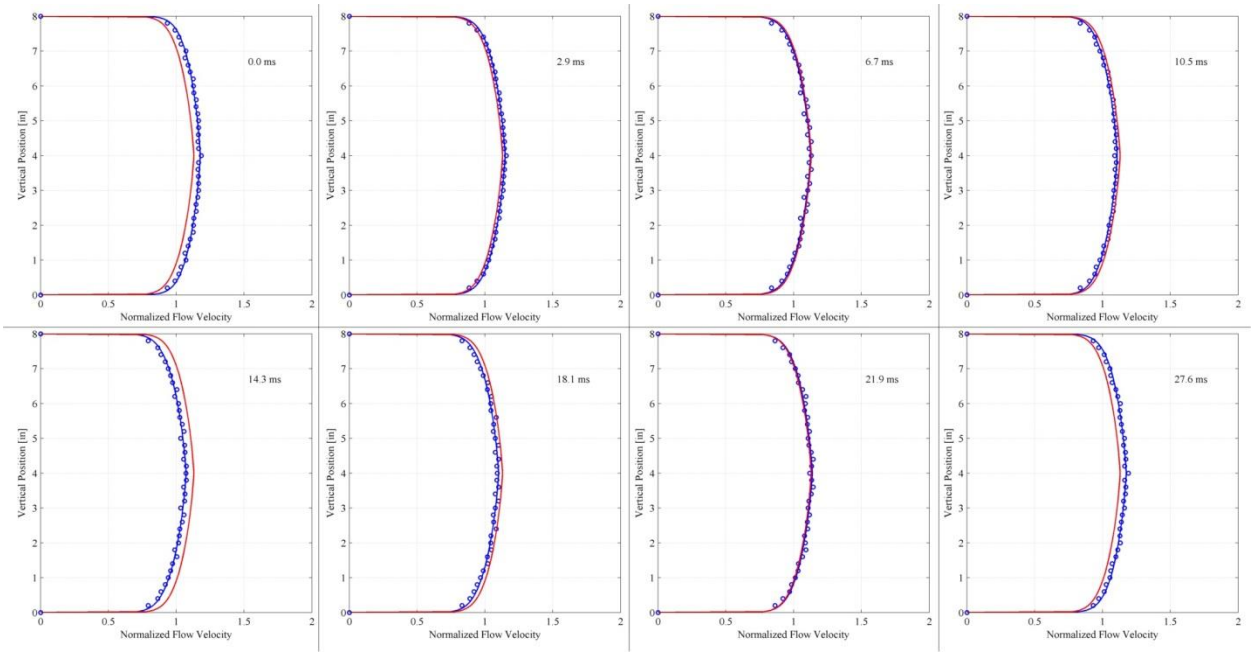

37 Hz

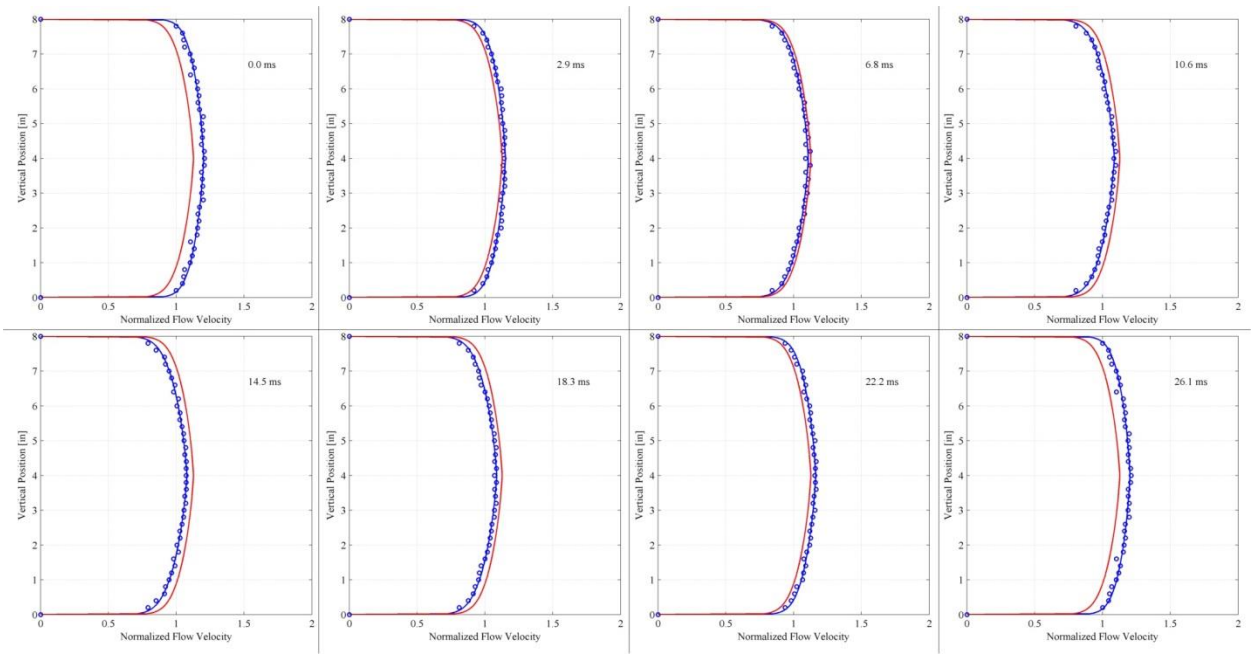

39 Hz

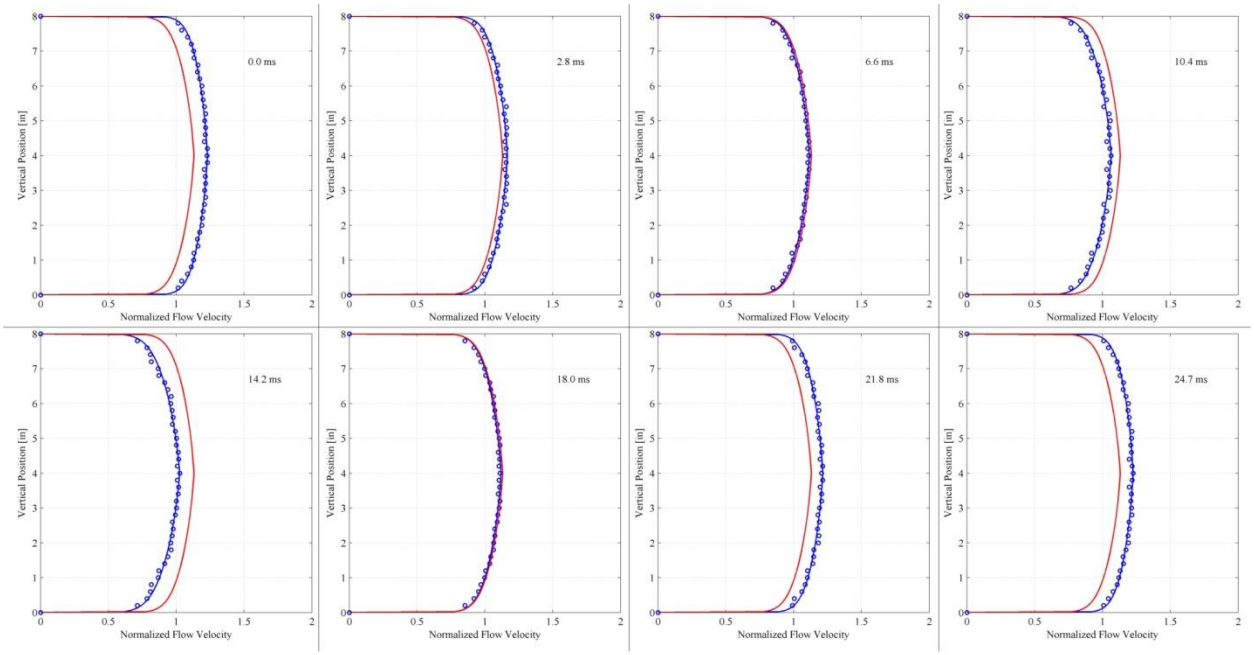

41 Hz

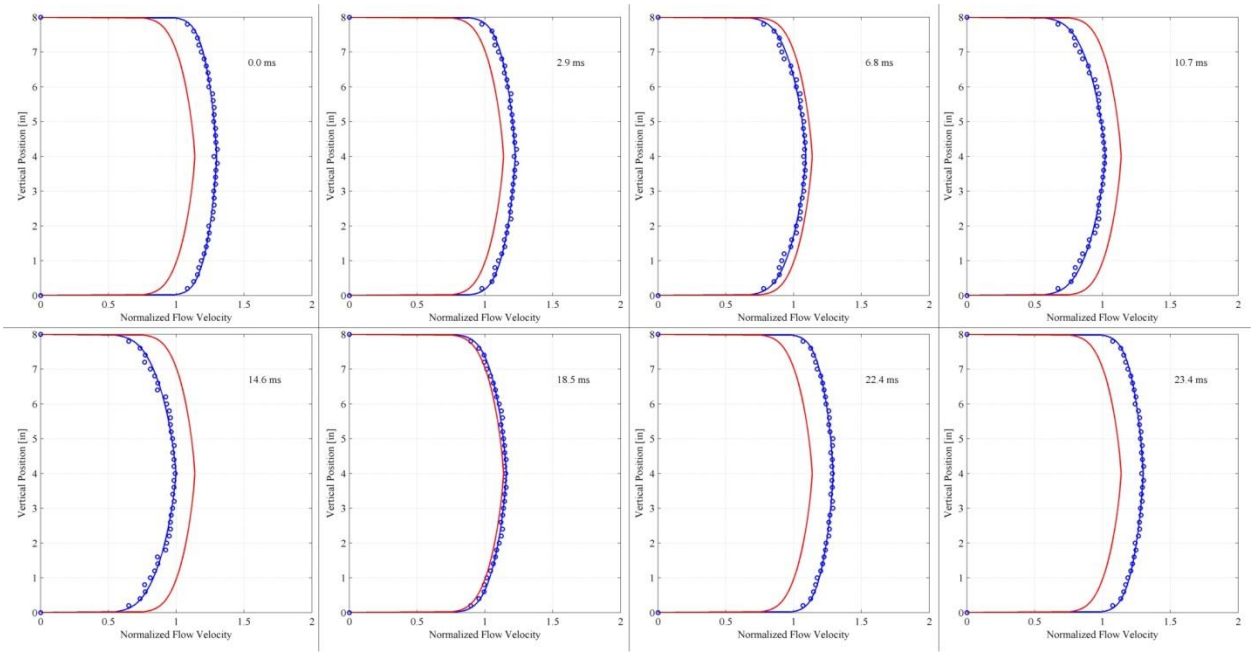

43 Hz

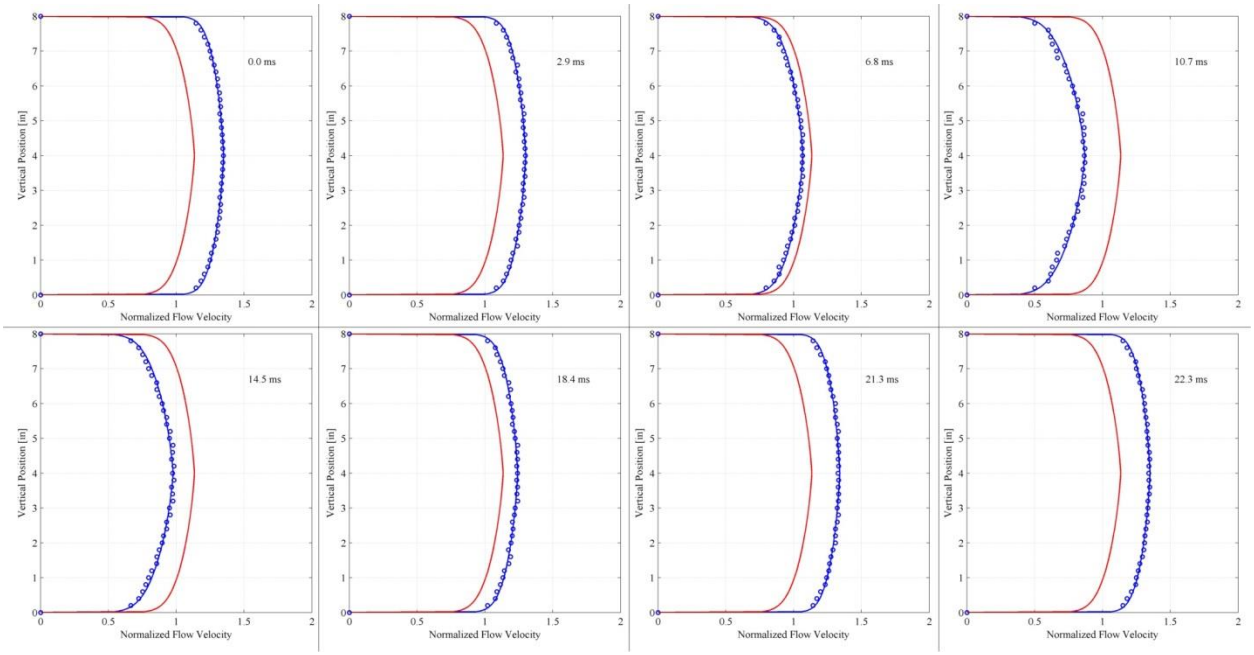

45 Hz

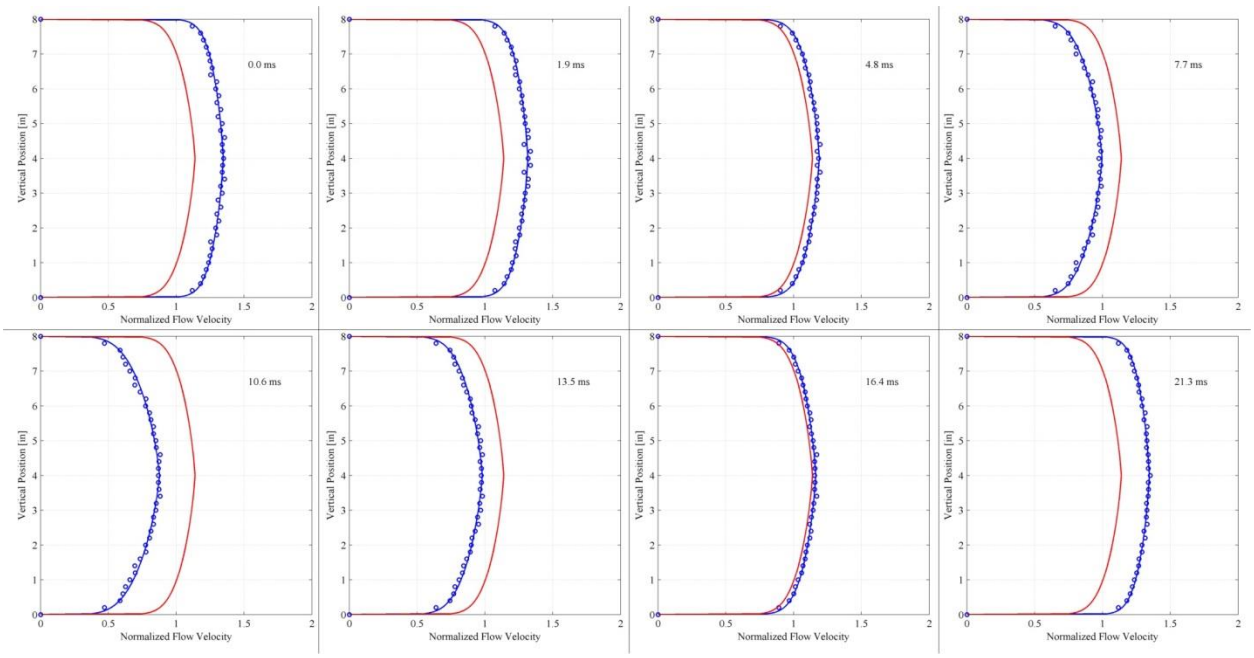

---

200 acfm:

5 Hz

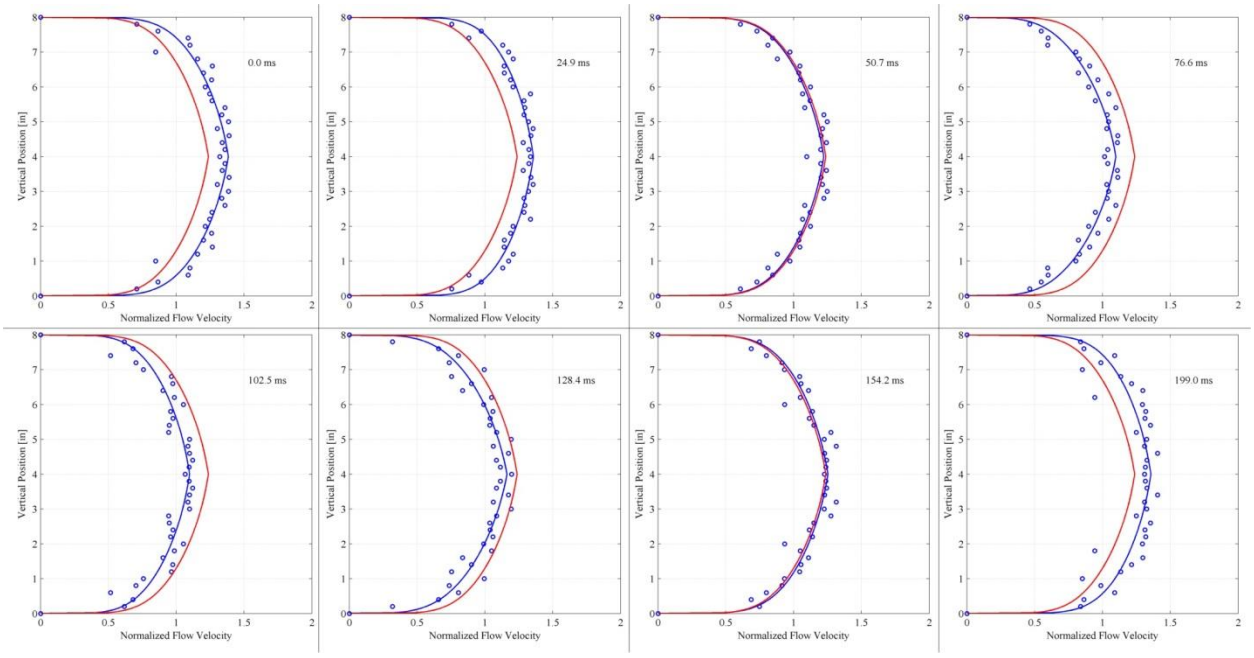

7 Hz

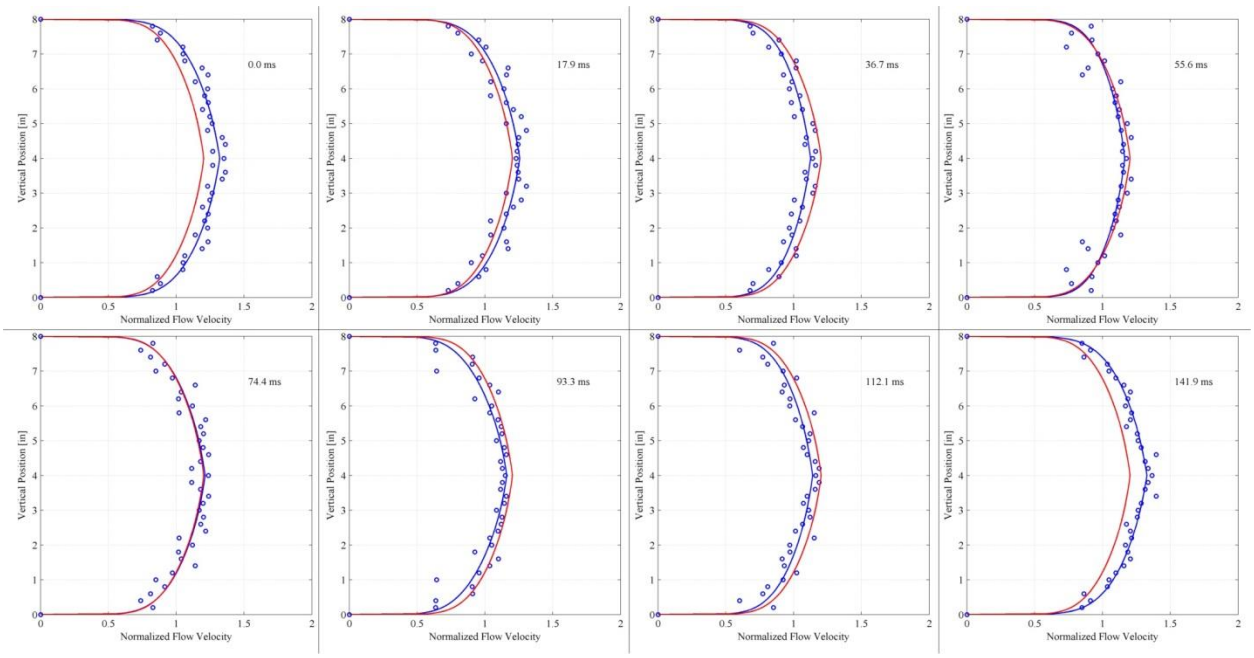

9 Hz

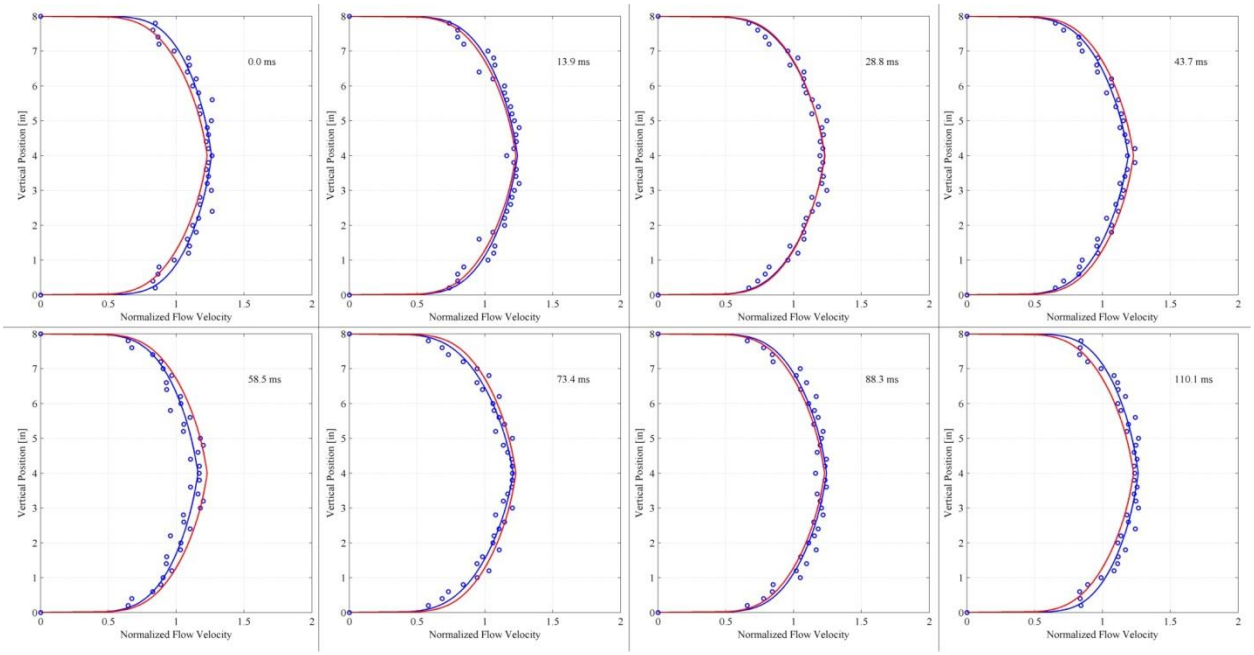

11 Hz

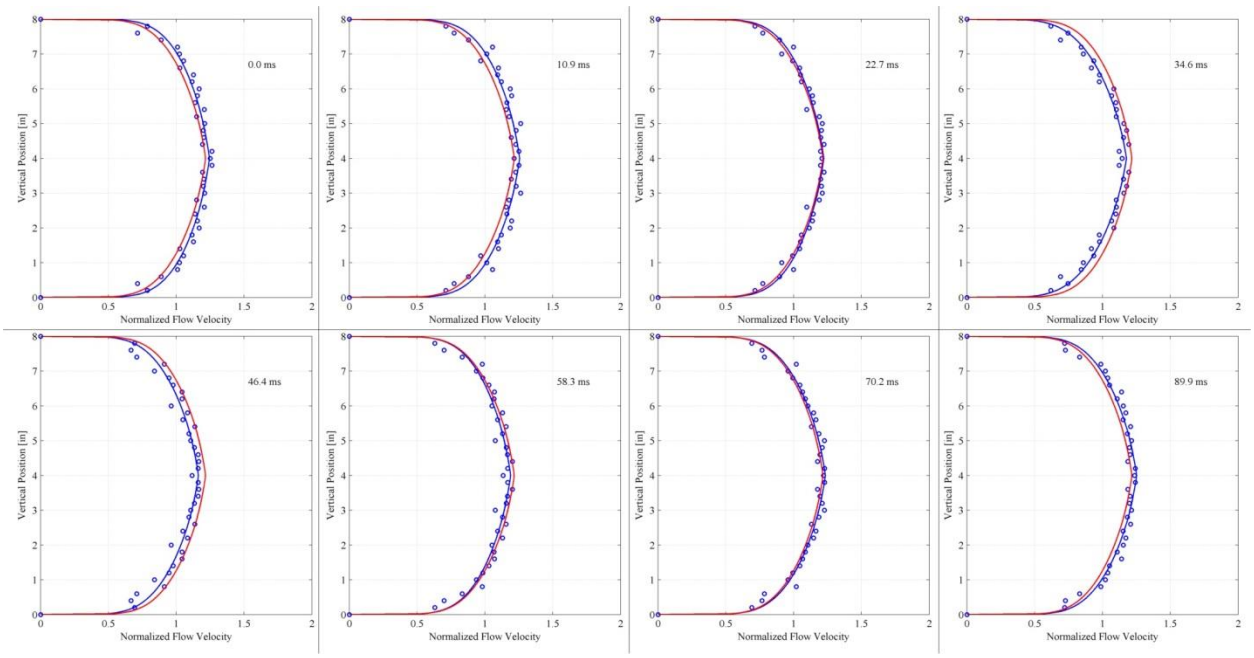

13 Hz

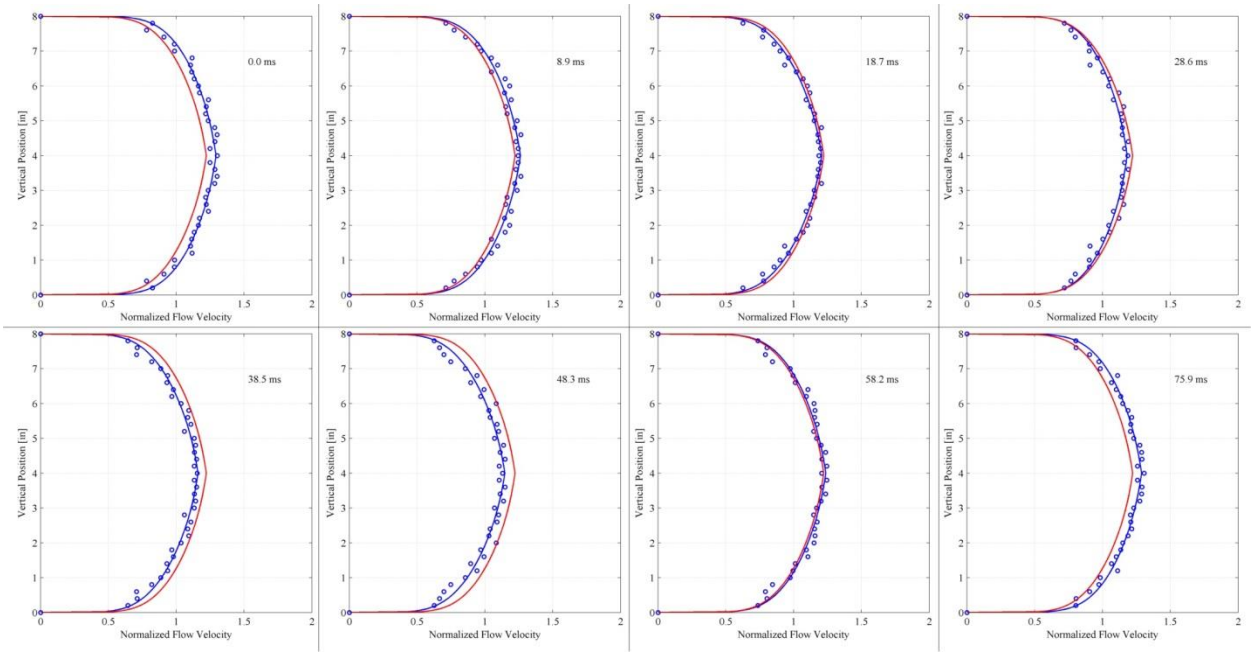

15 Hz

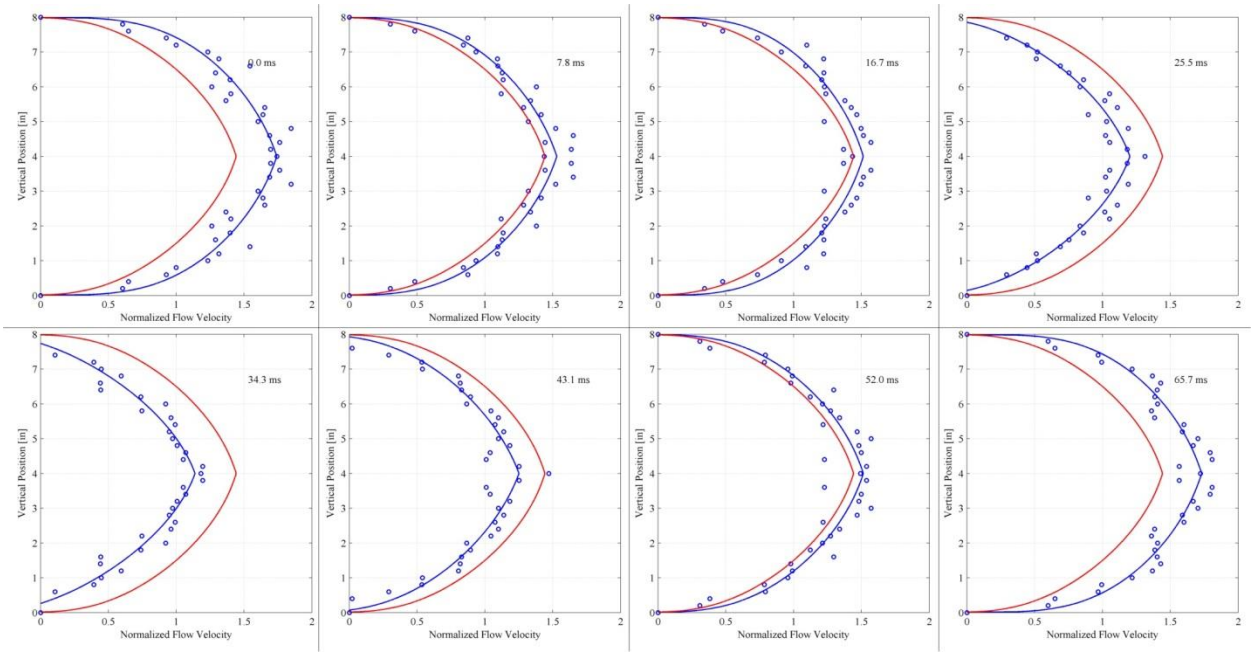

17 Hz

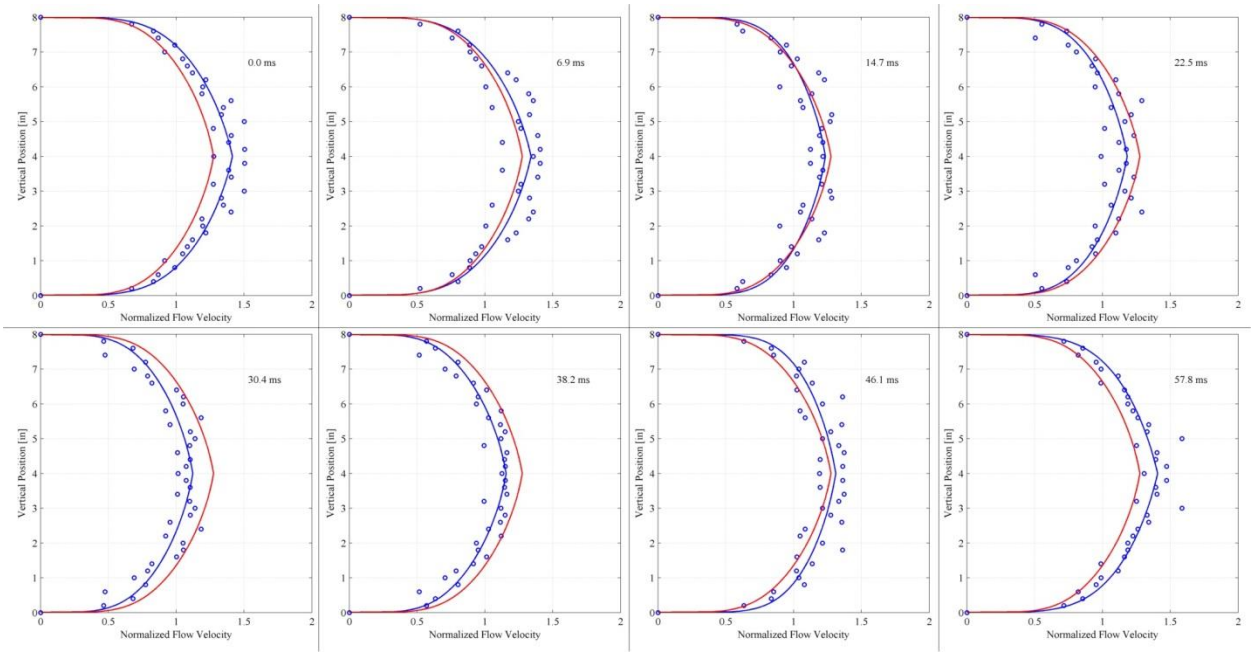

19 Hz

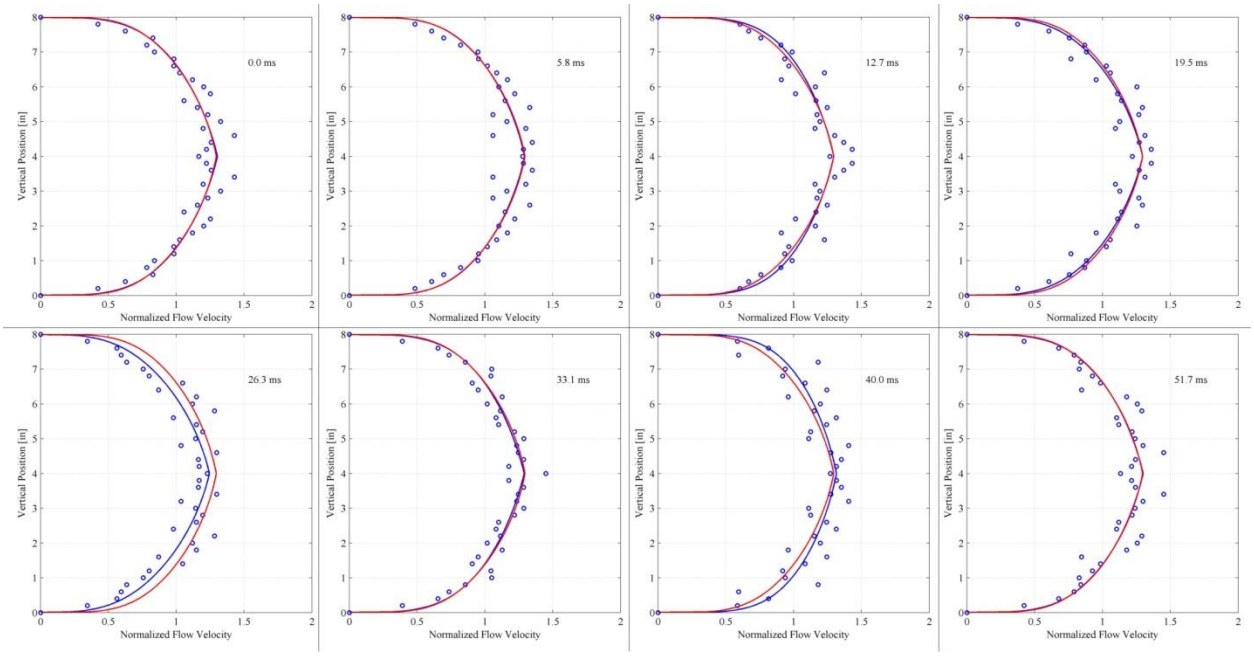

21 Hz

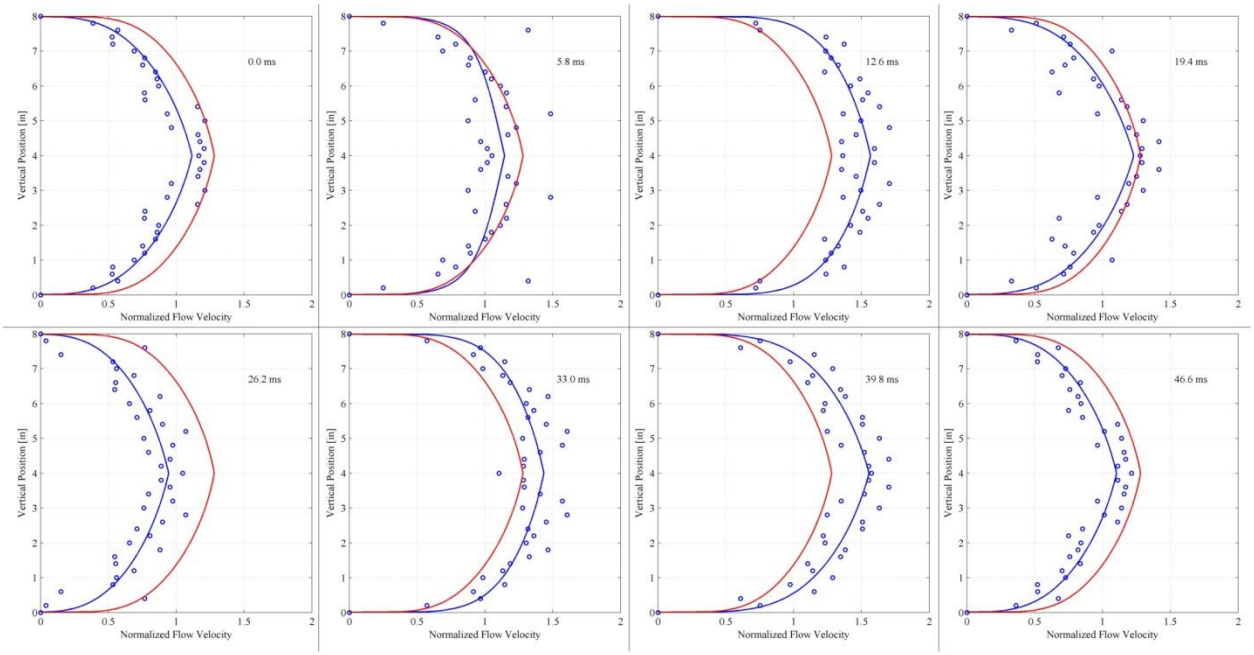

23 Hz

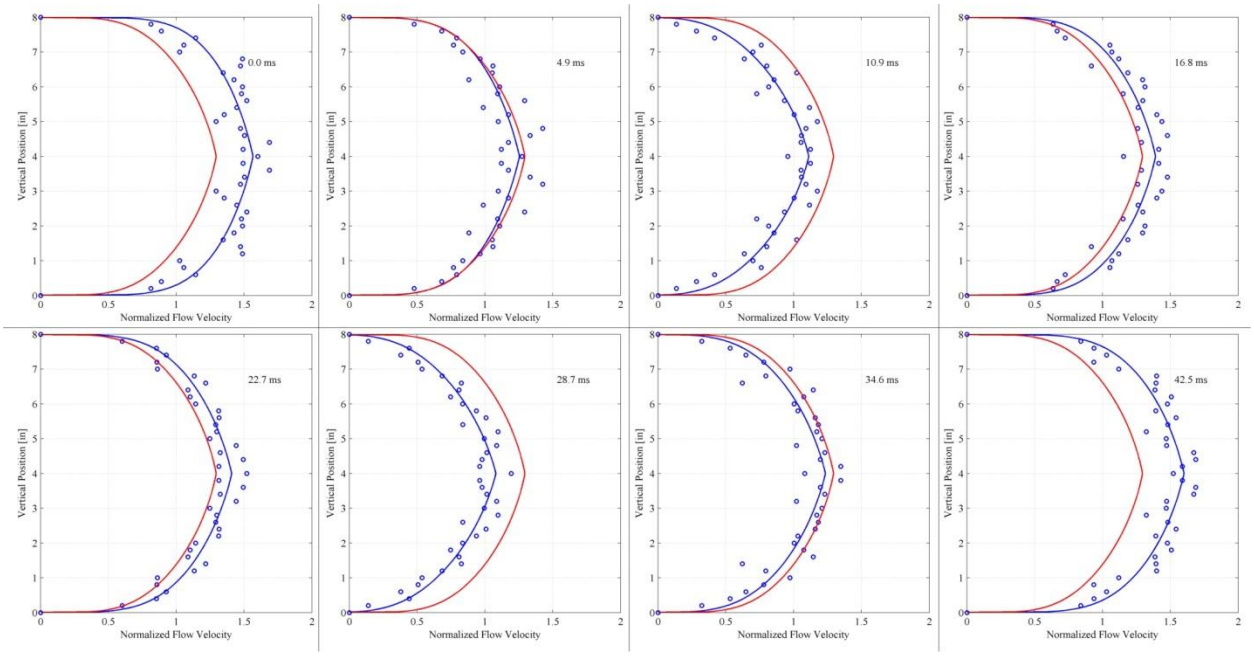

25 Hz

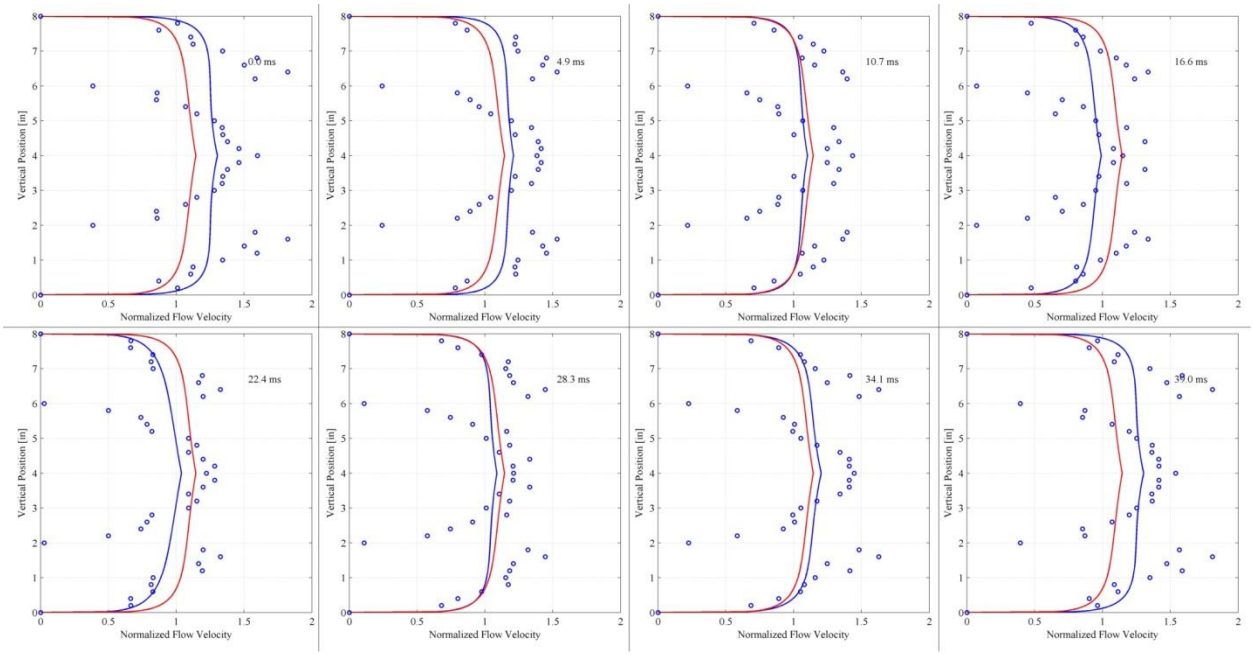

27 Hz

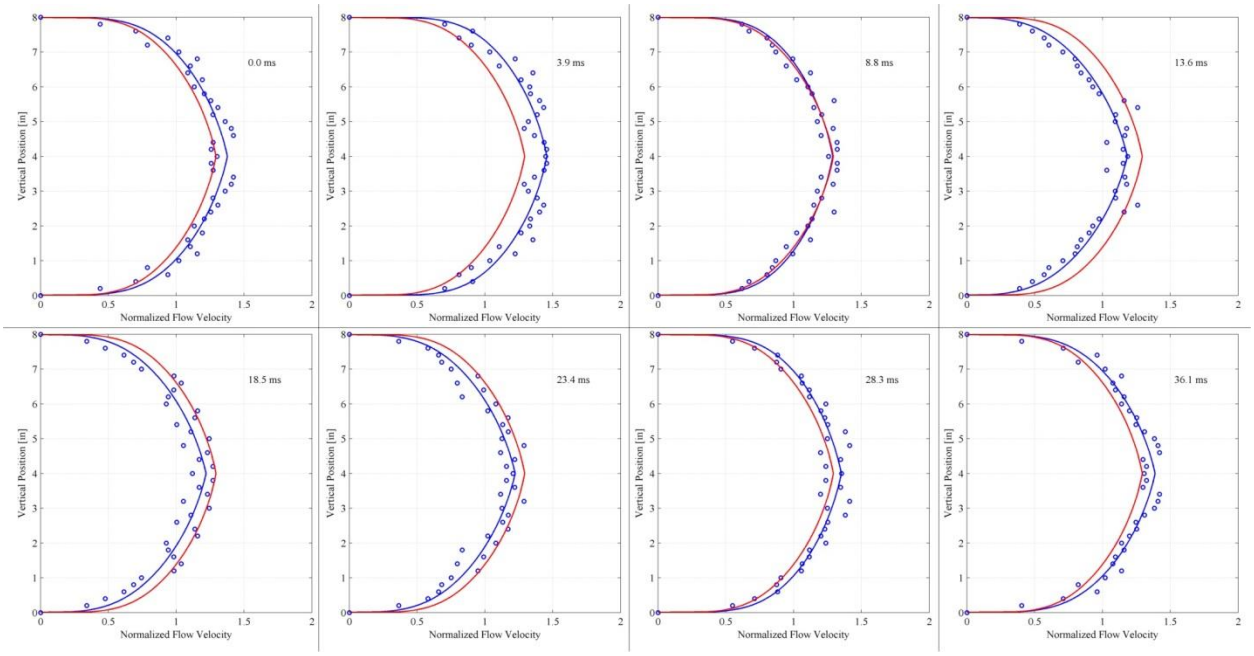

29 Hz

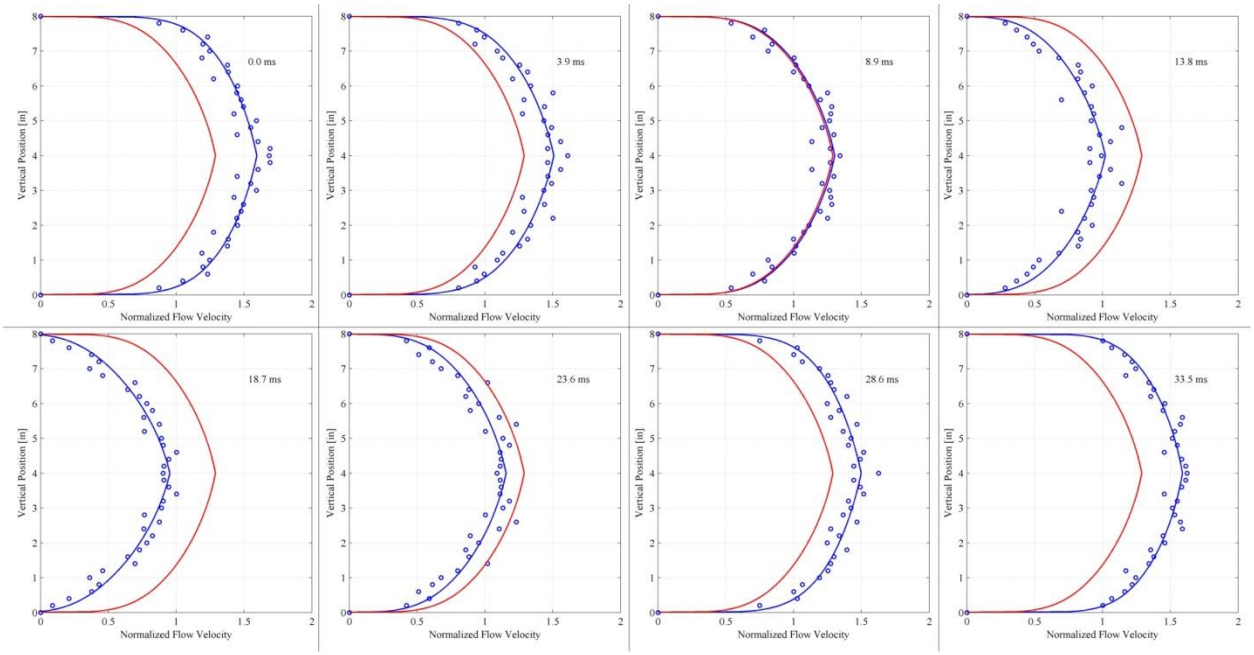

31 Hz

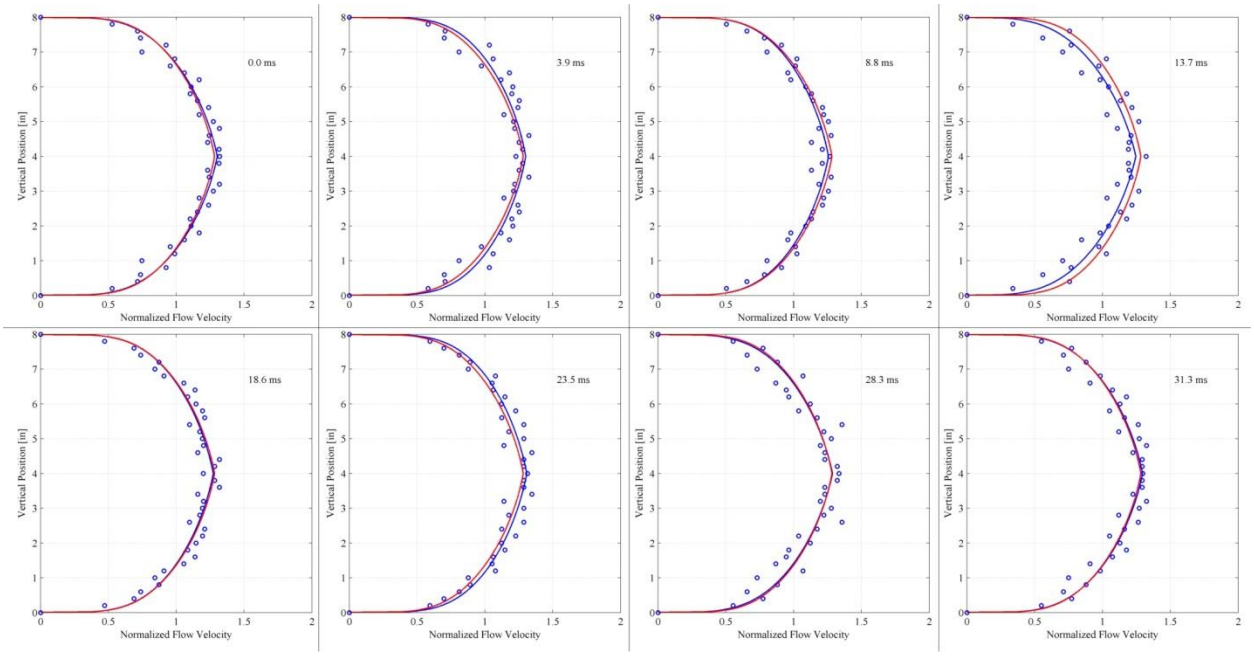

33 Hz

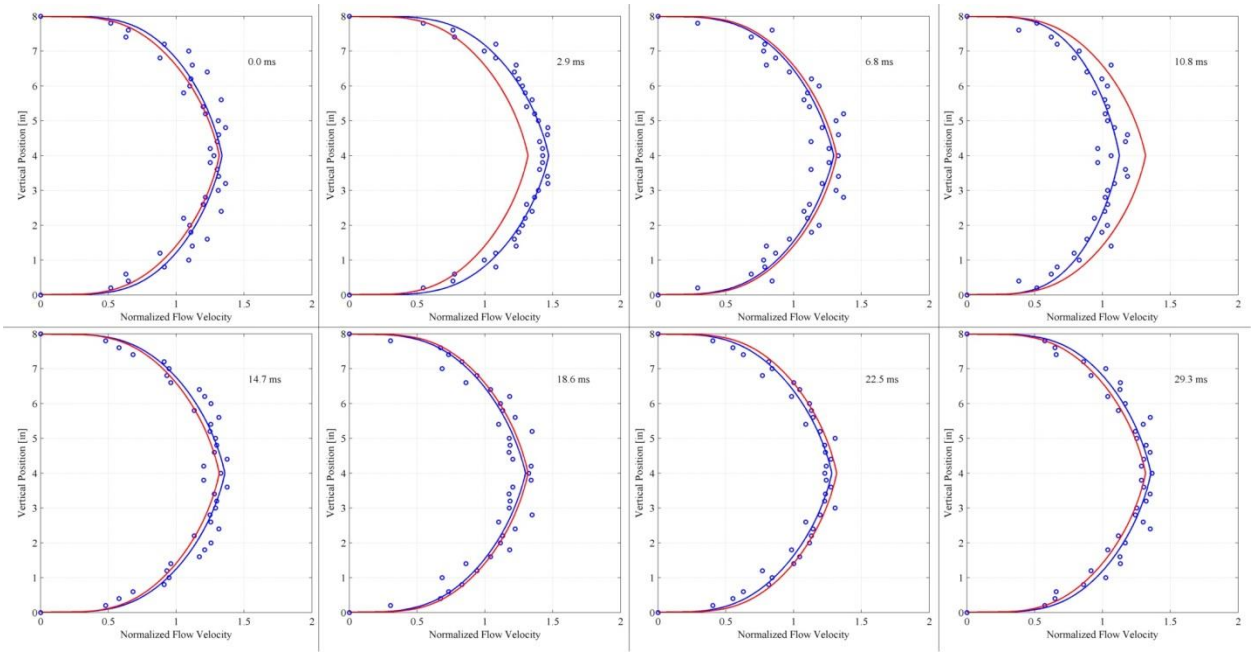

35 Hz

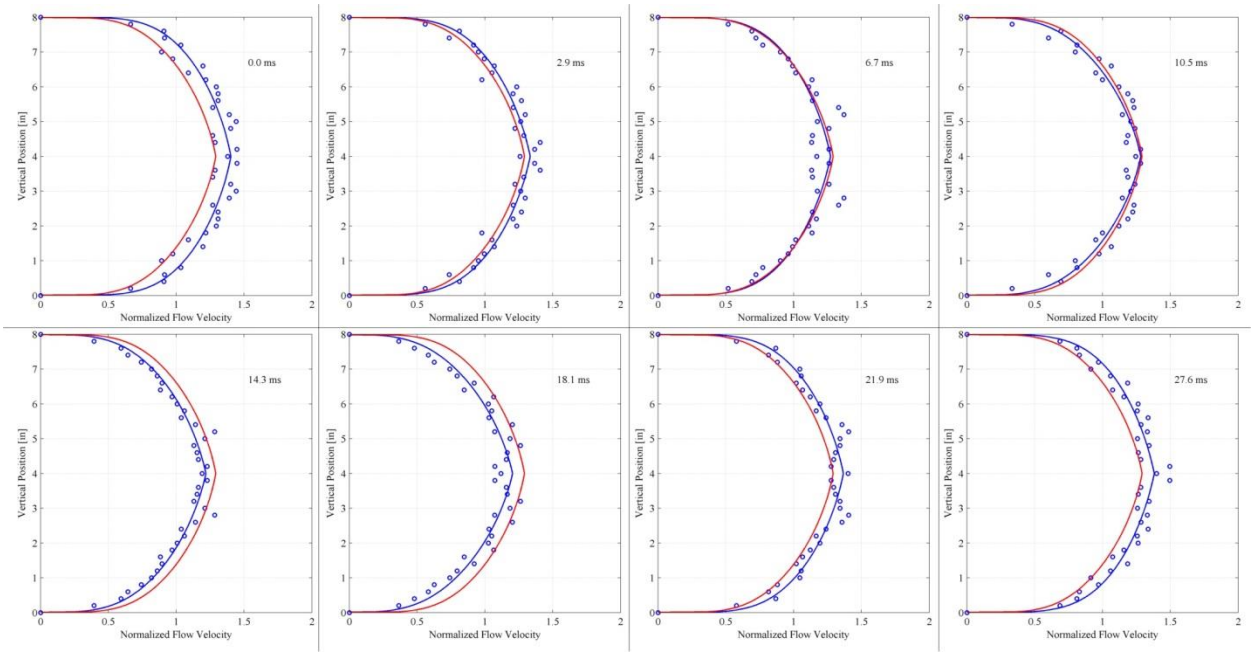

37 Hz

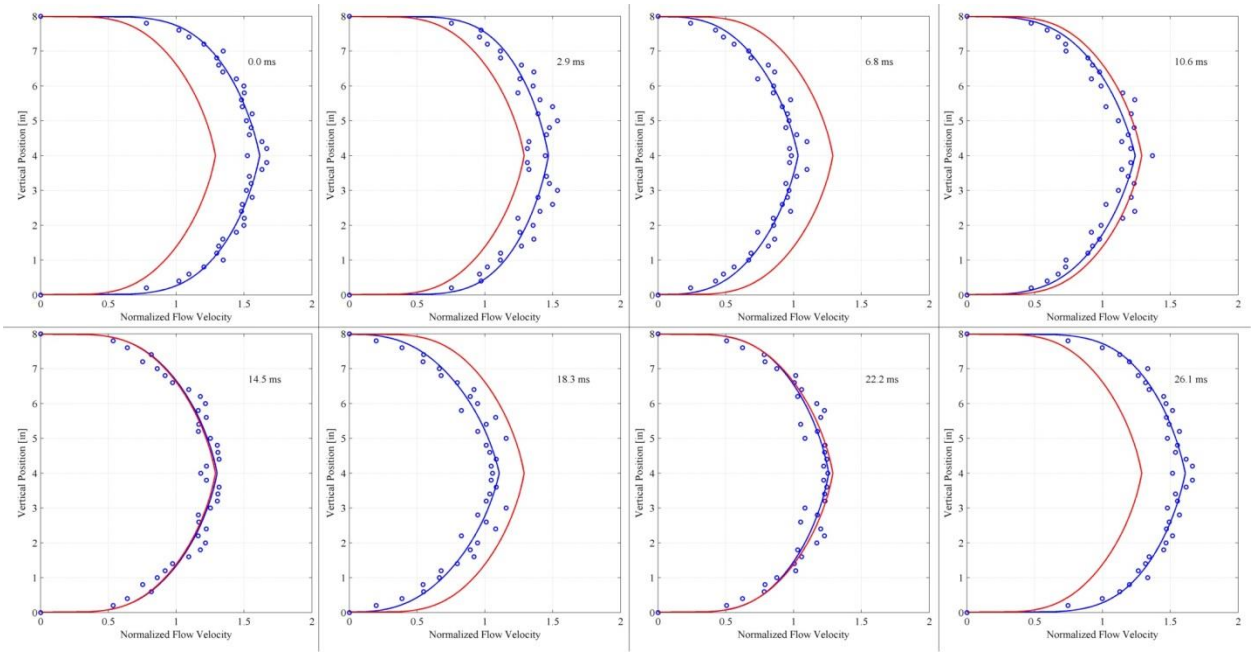

39 Hz

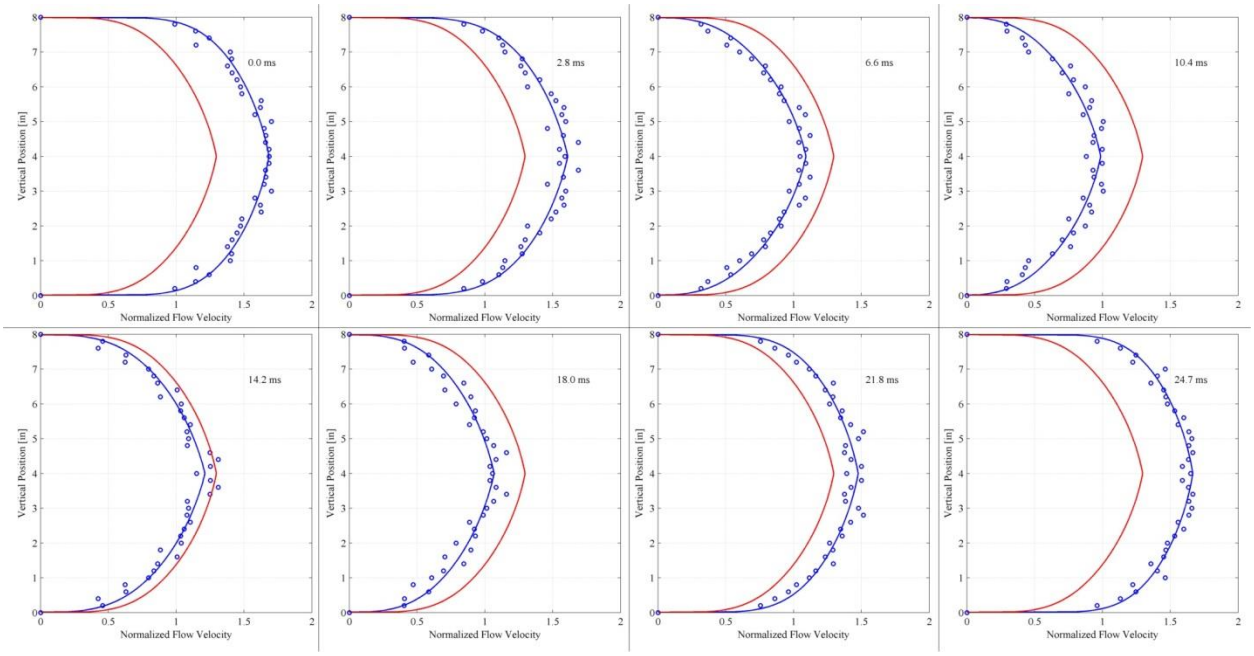

41 Hz

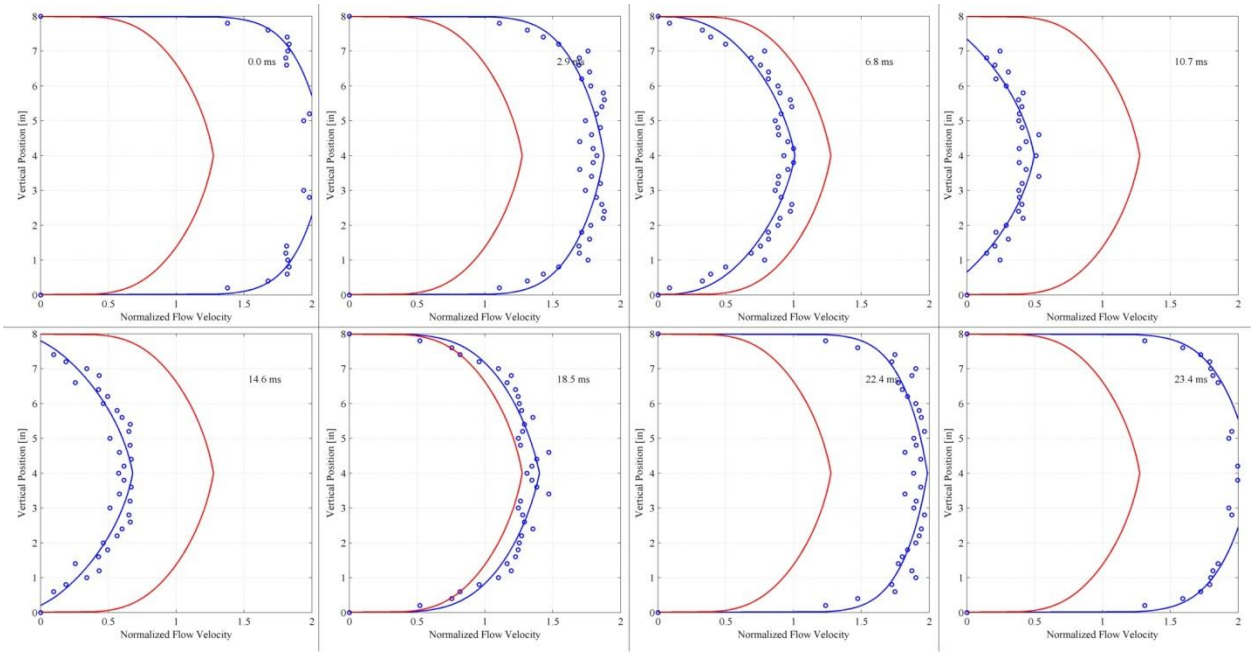

43 Hz

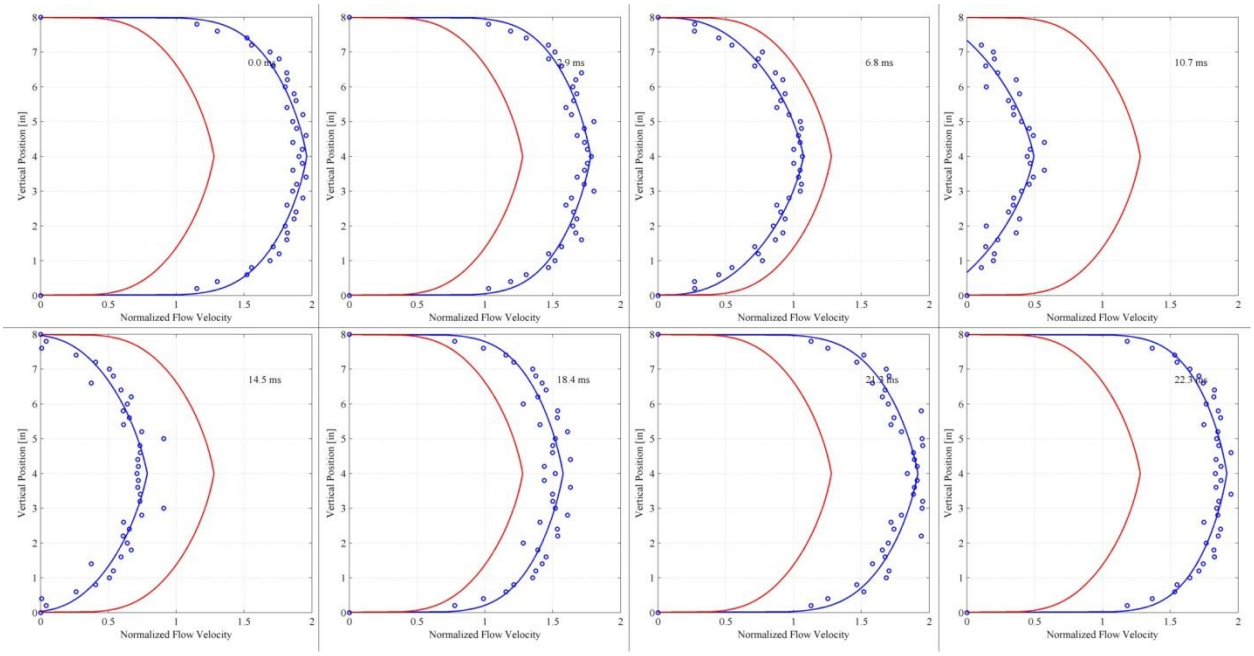

45 Hz

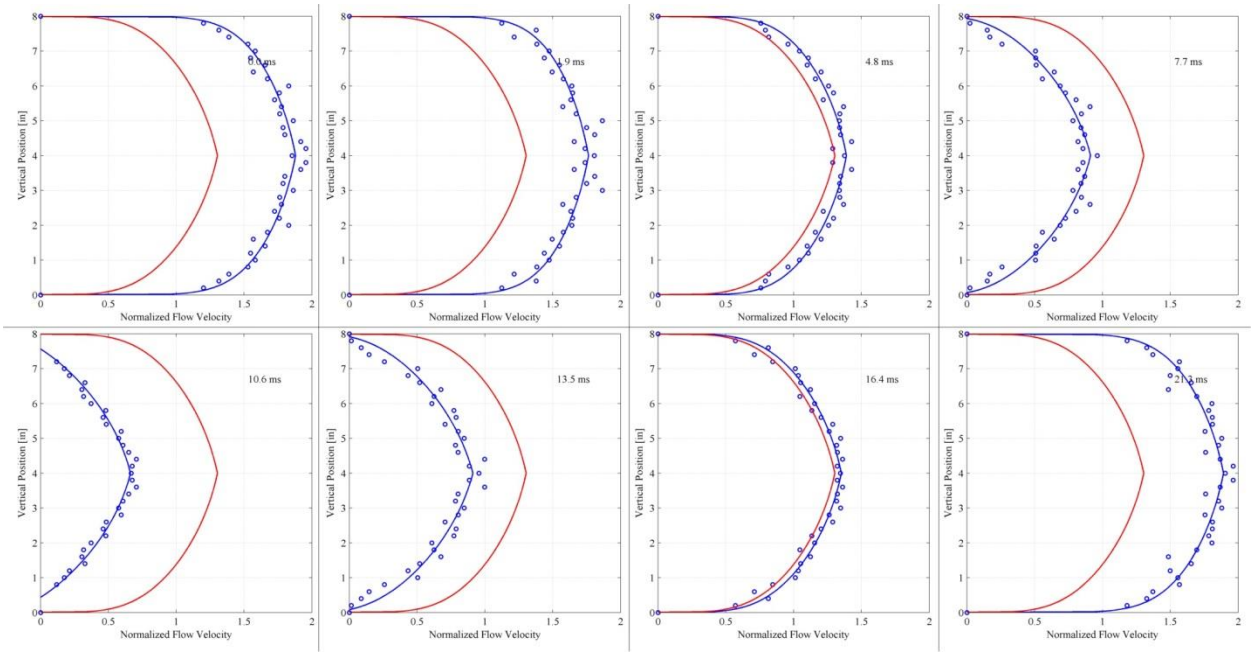

APPENDIX F: VELOCITY PROFILE FIT STATISTICS

700 acfm:

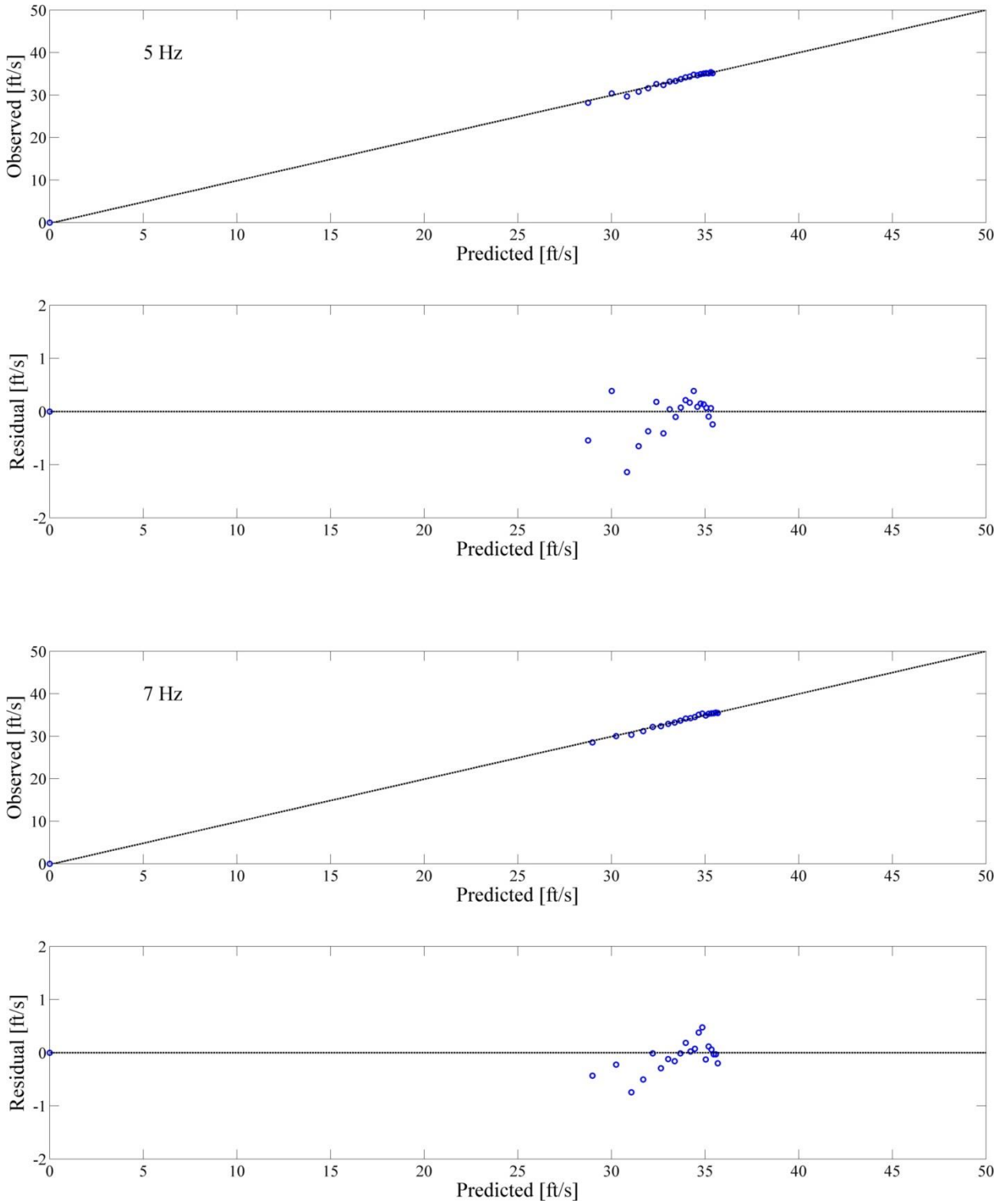

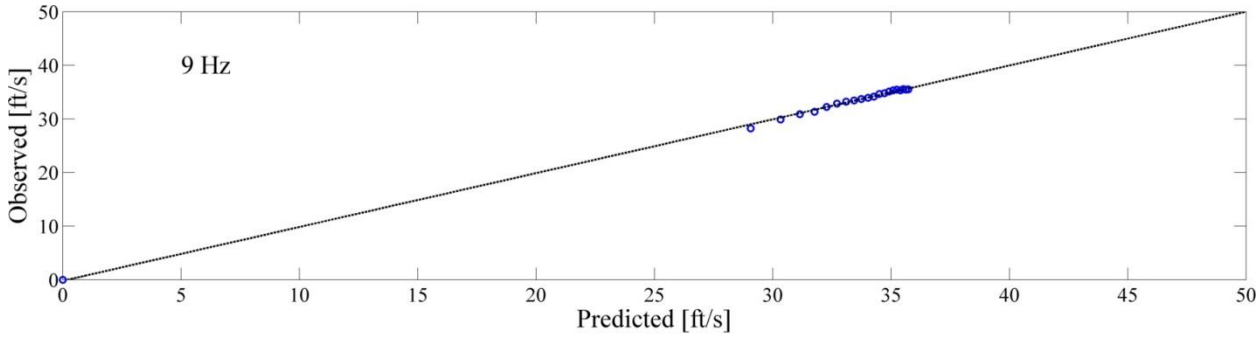

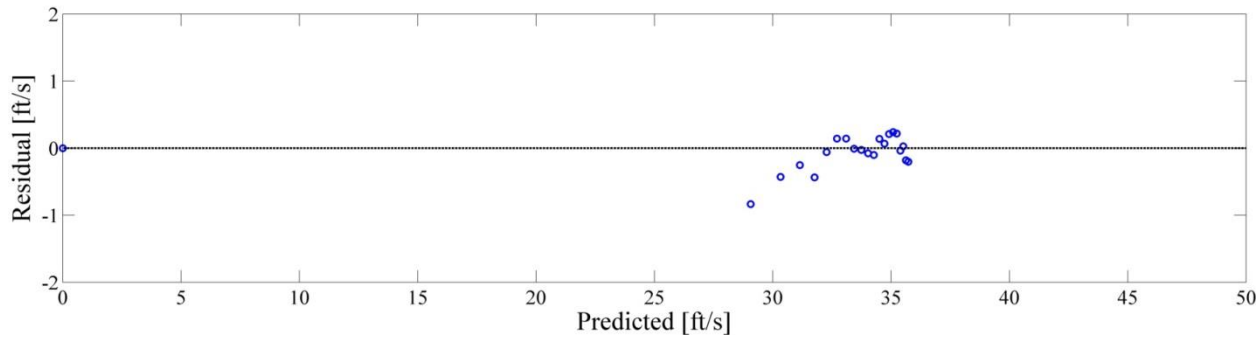

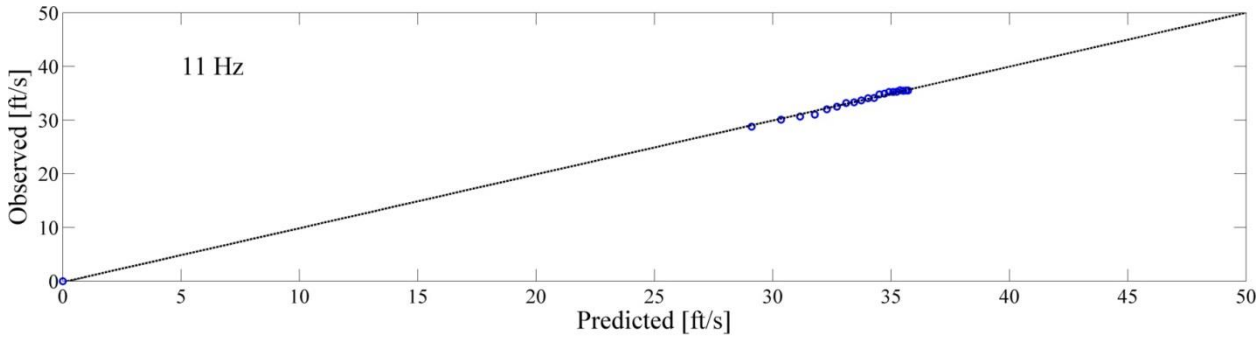

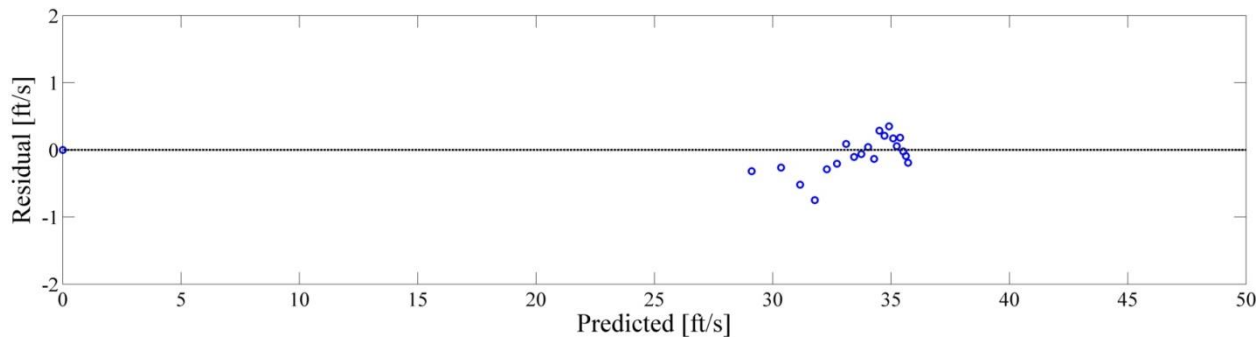

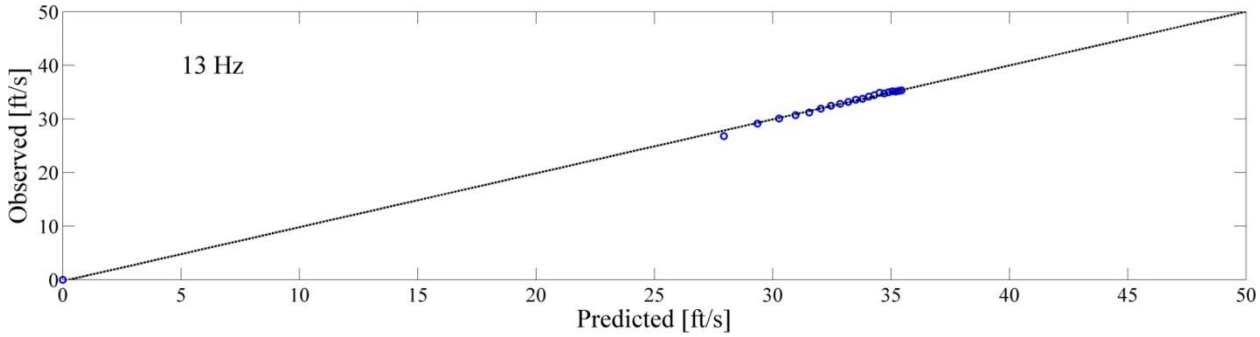

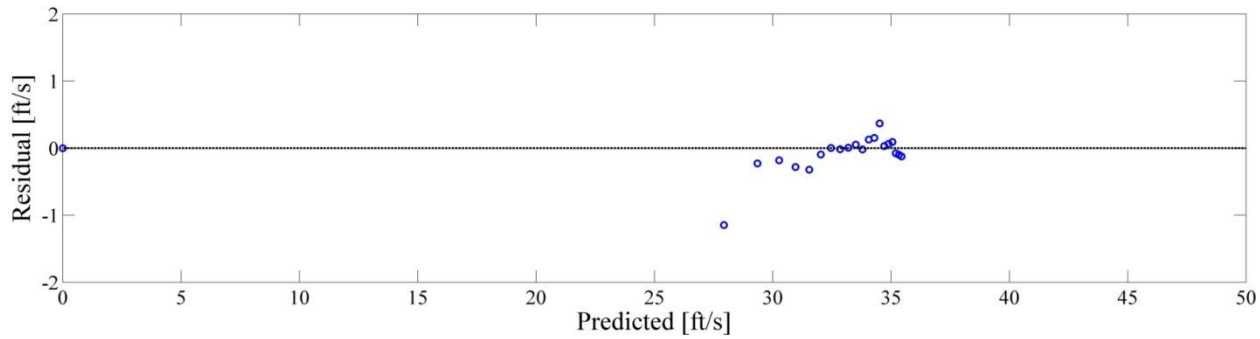

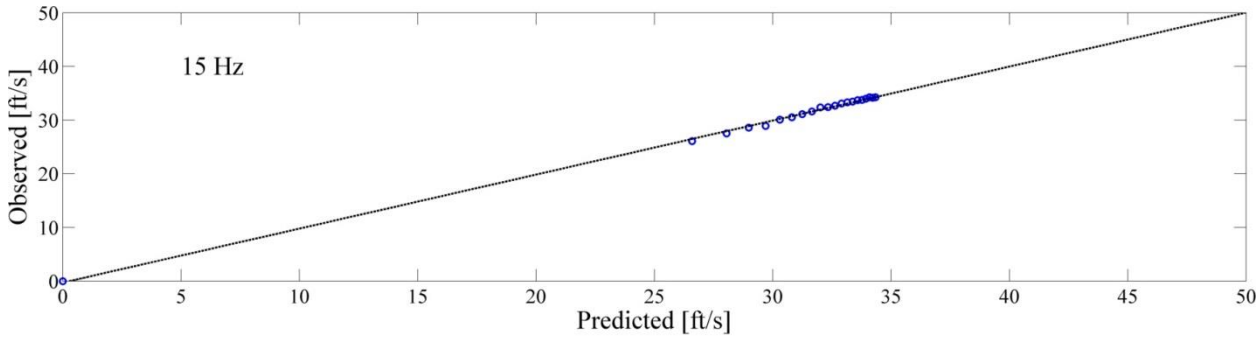

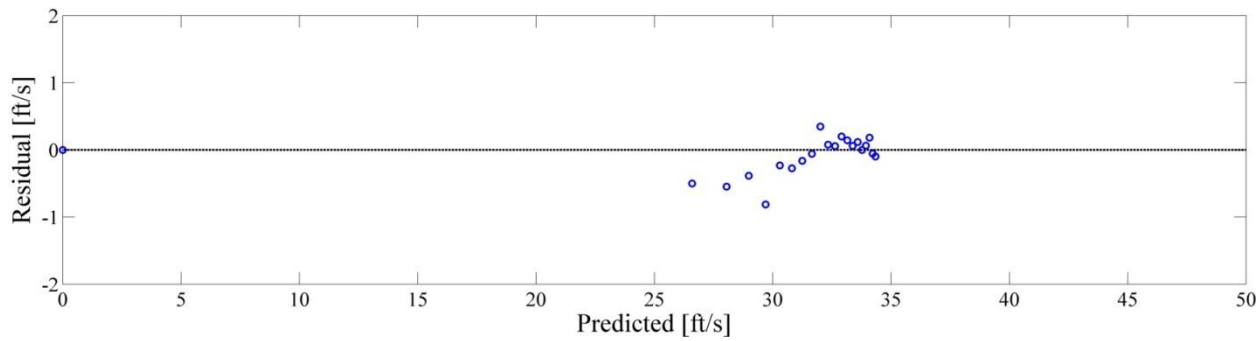

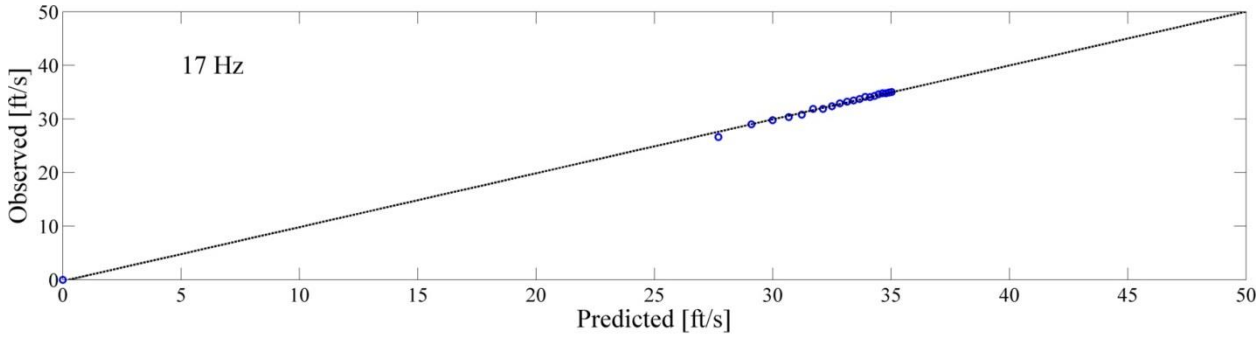

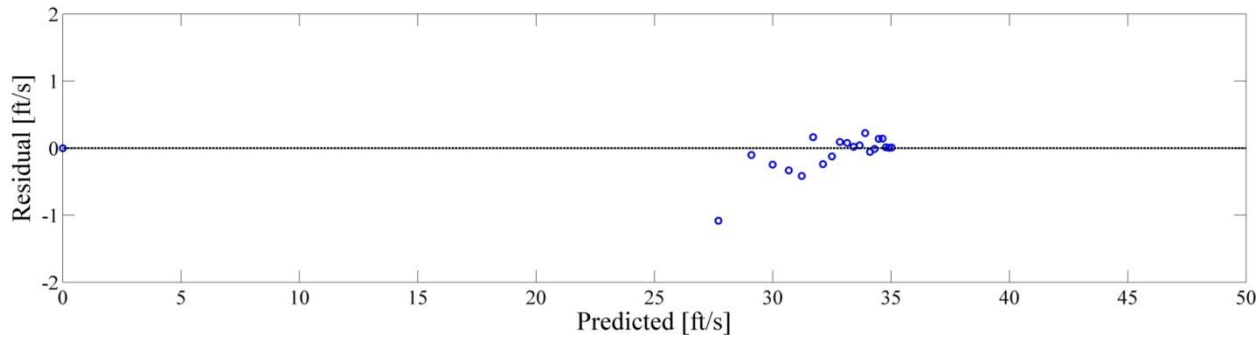

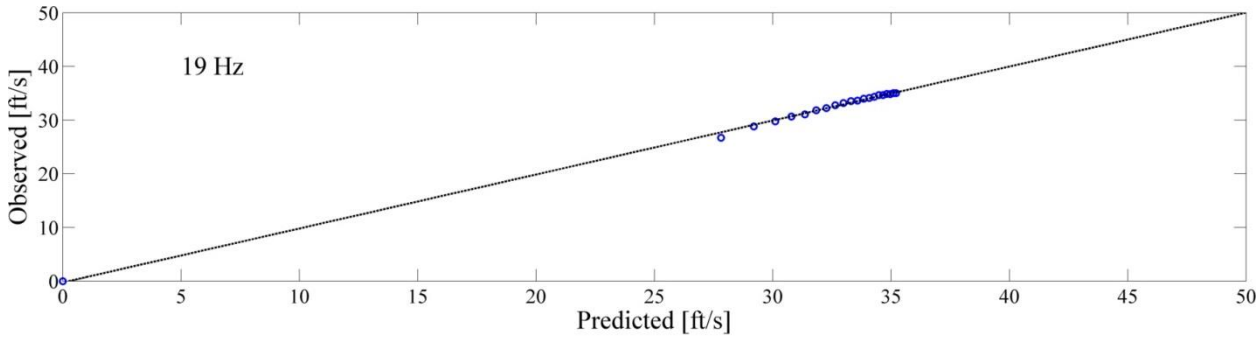

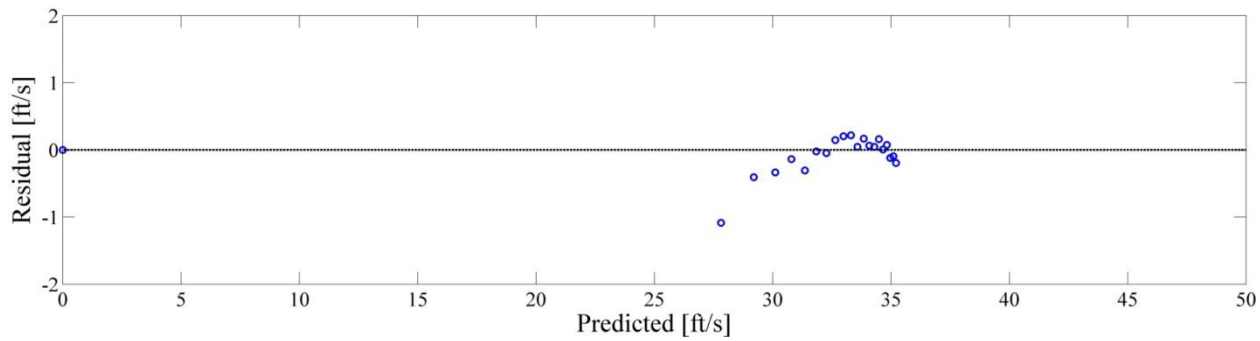

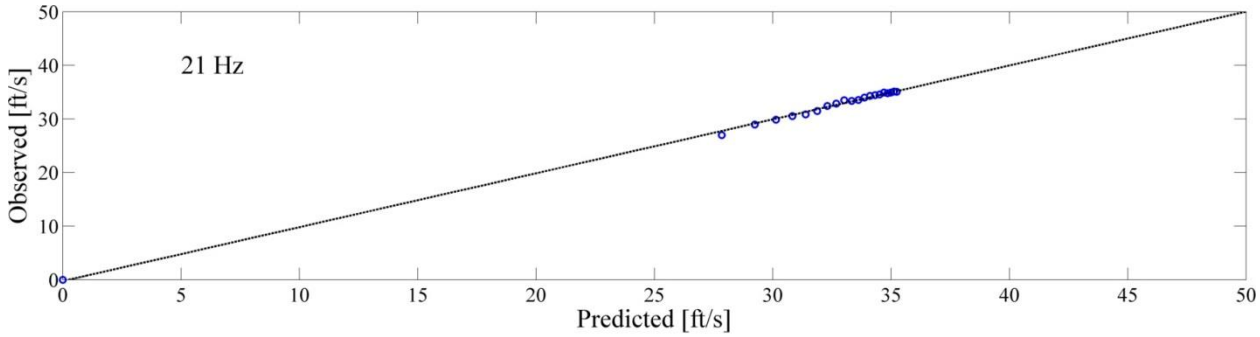

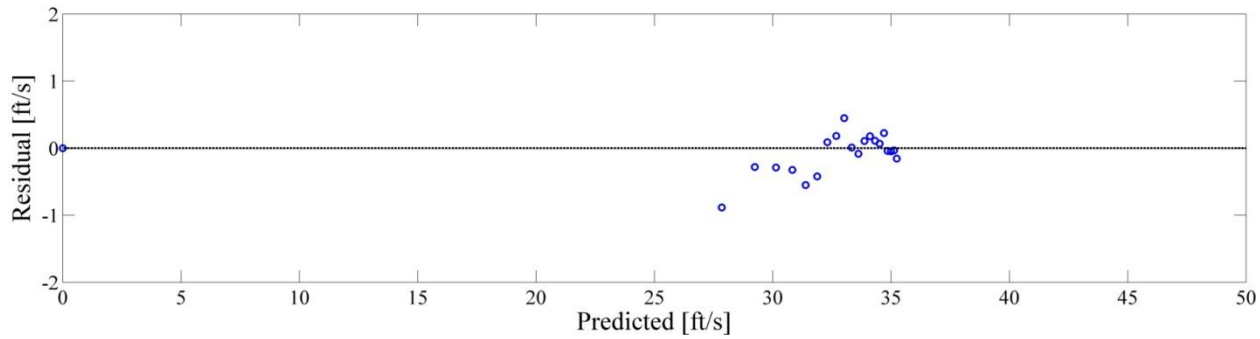

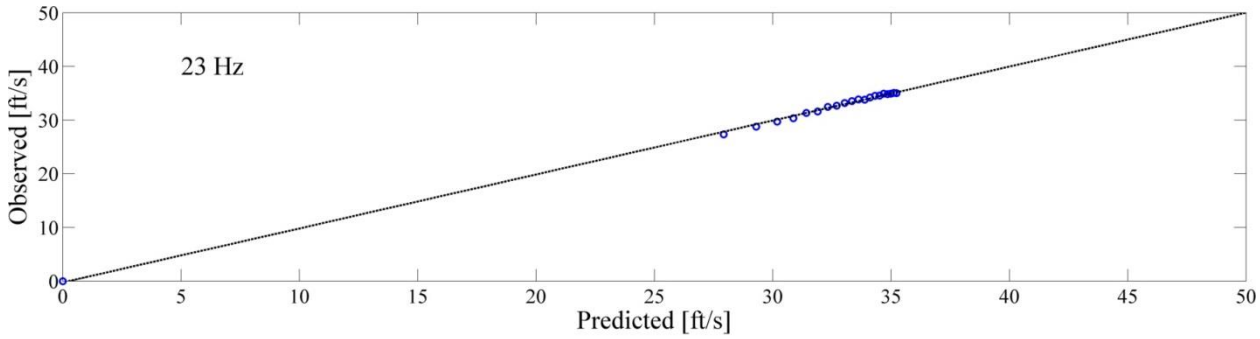

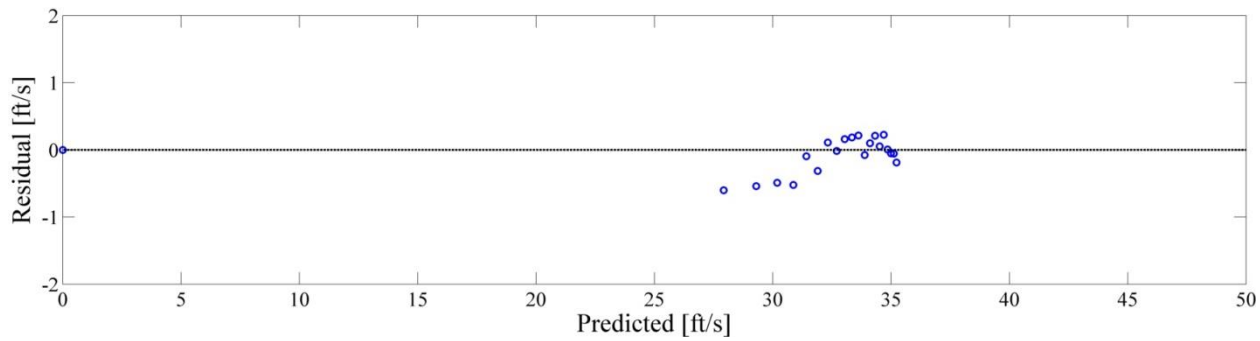

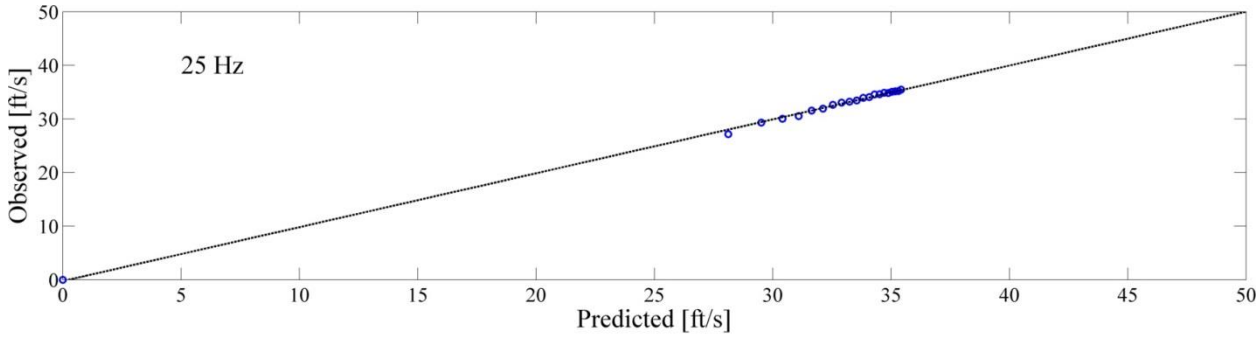

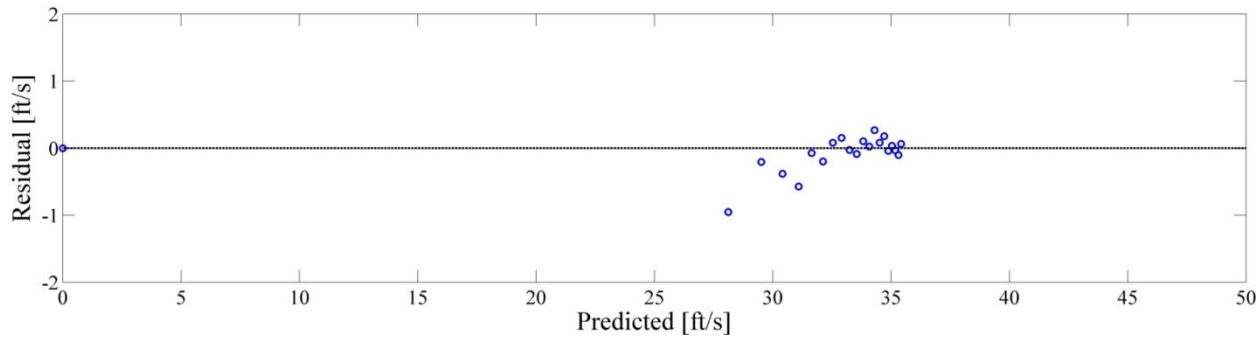

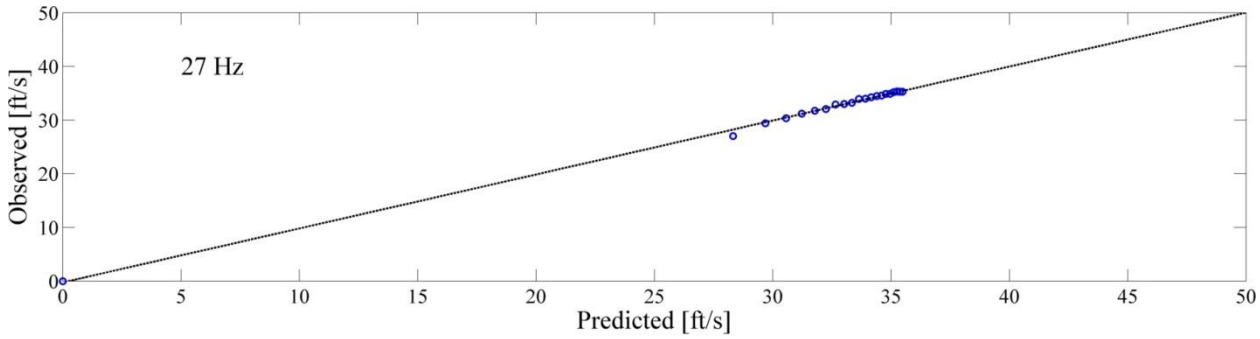

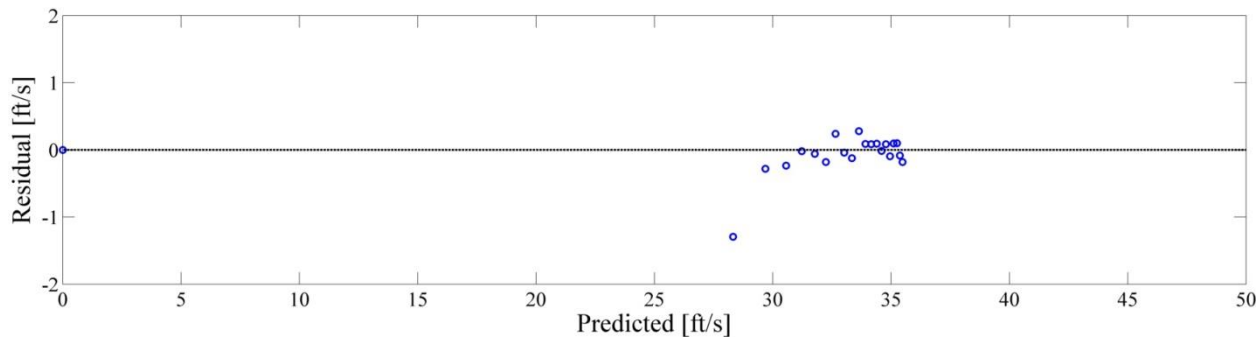

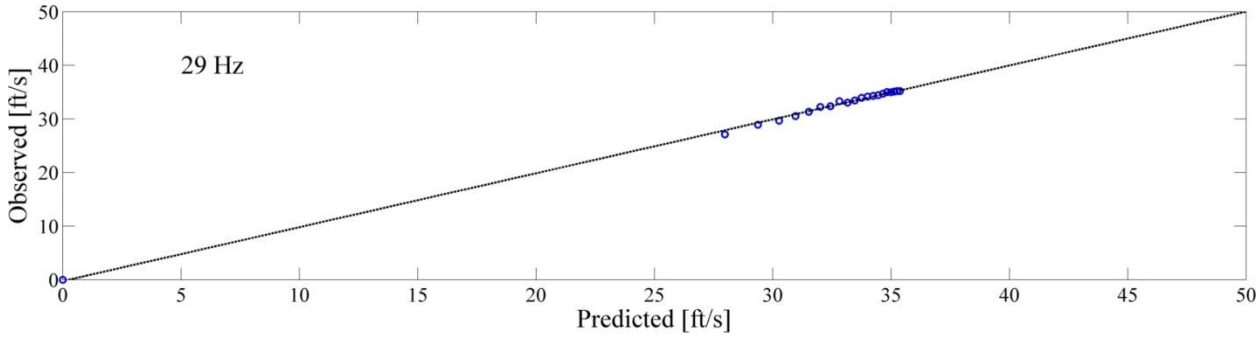

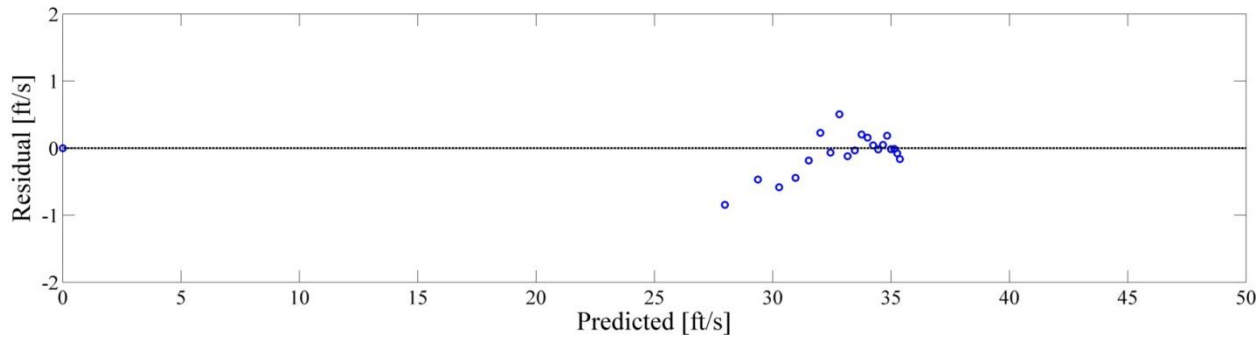

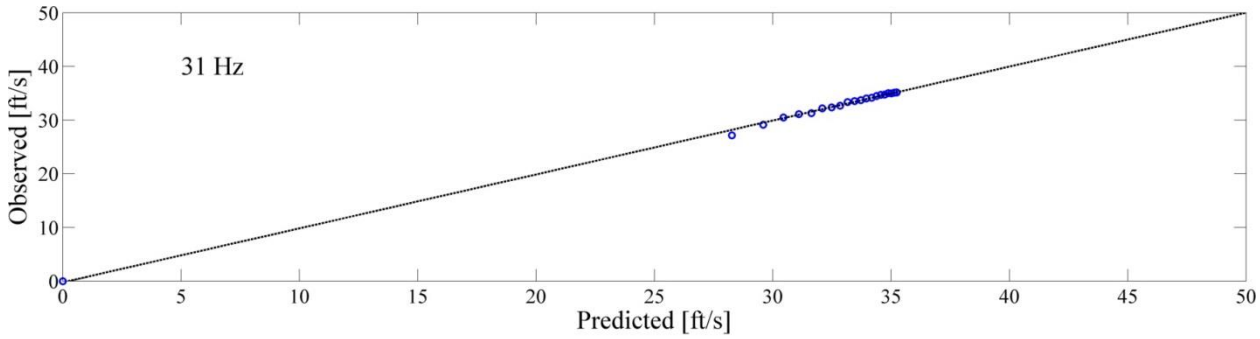

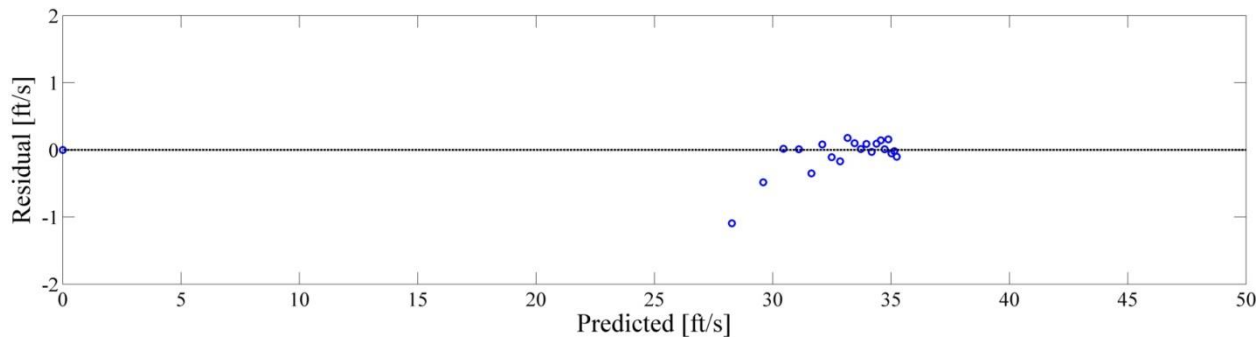

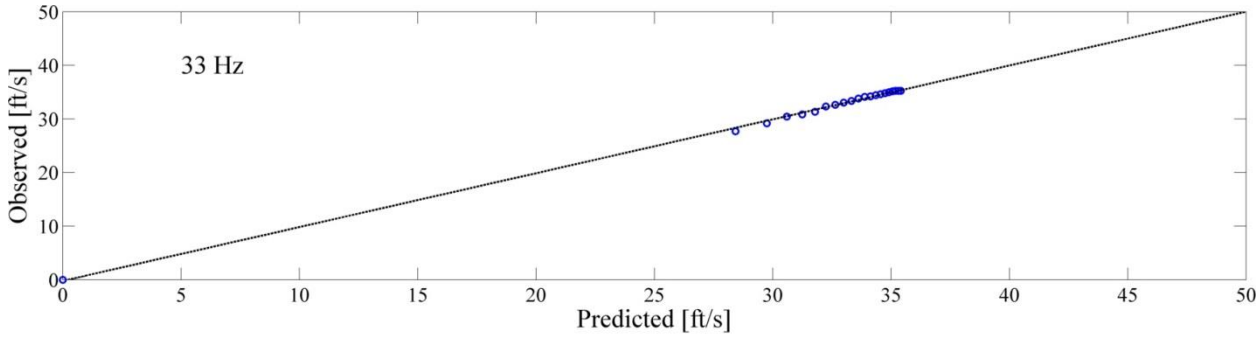

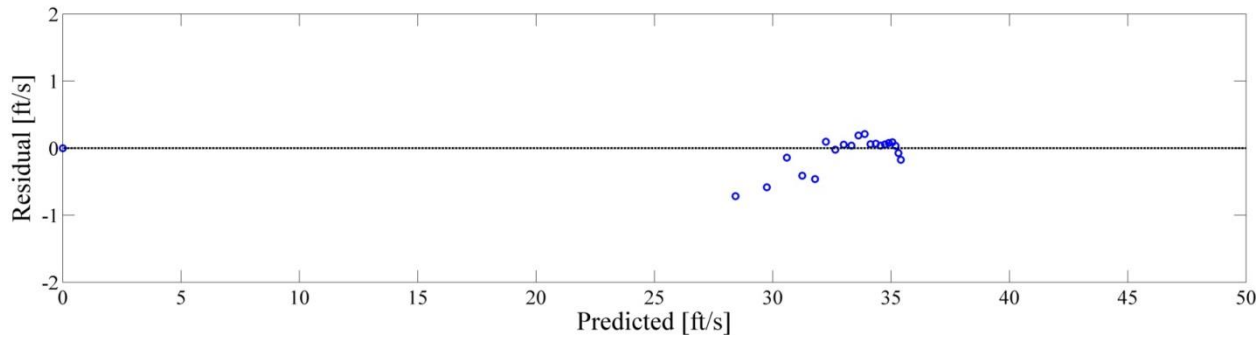

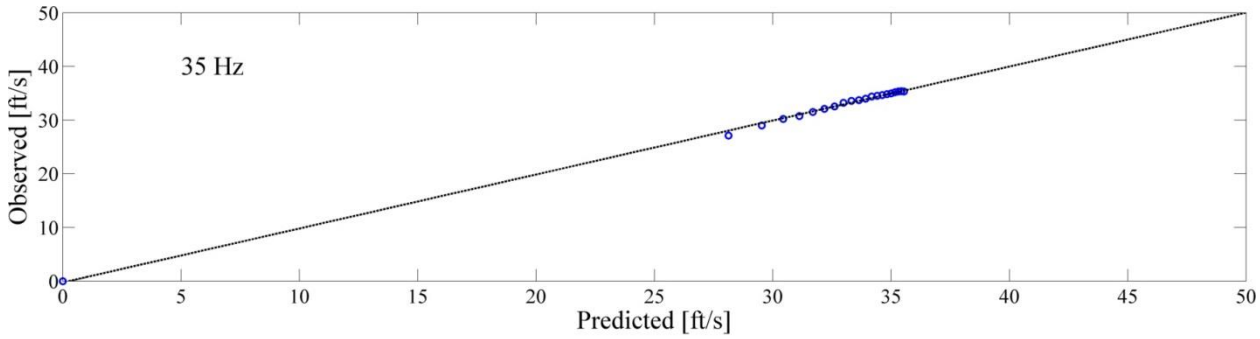

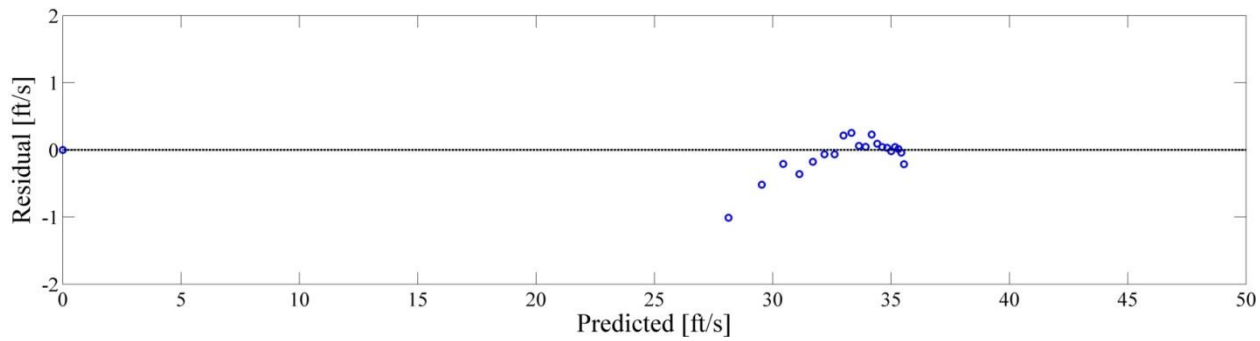

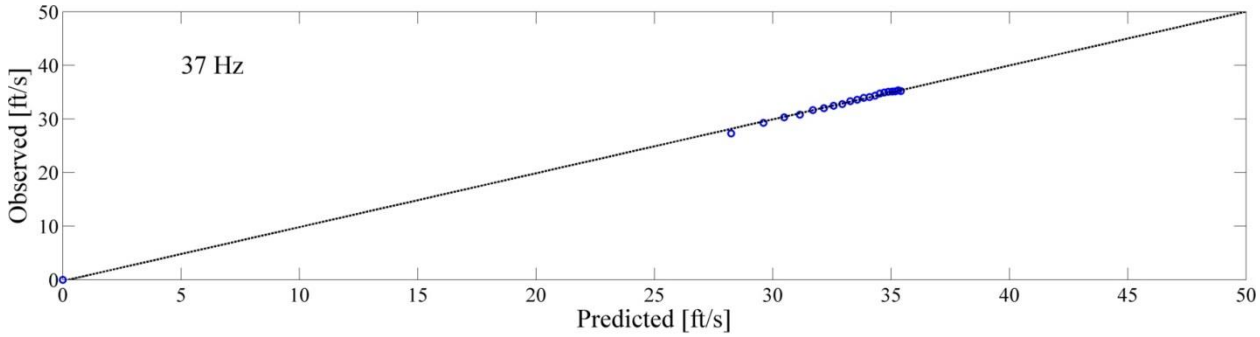

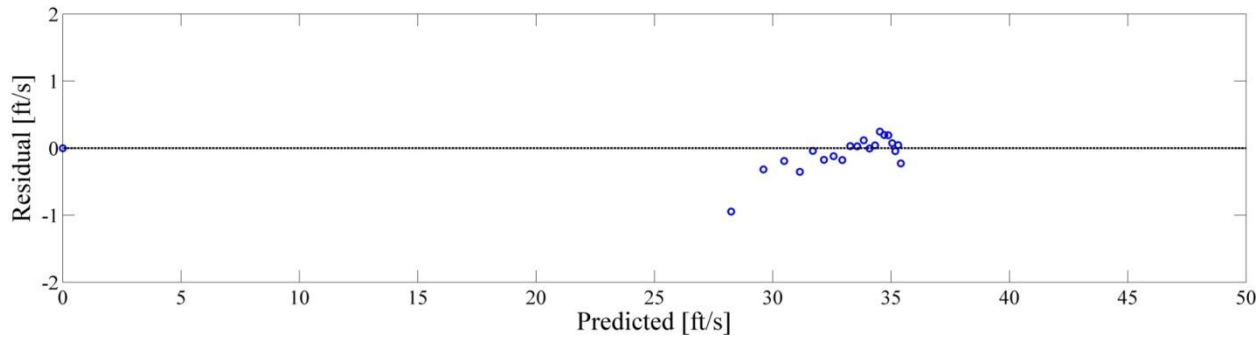

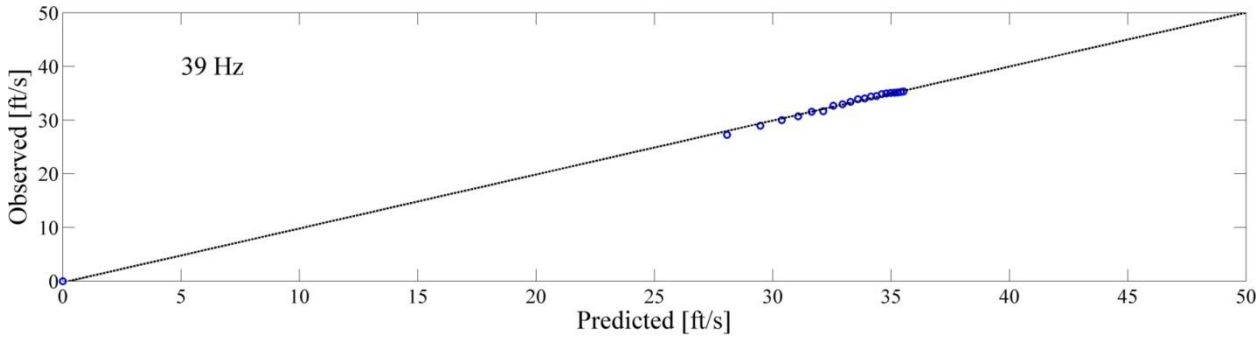

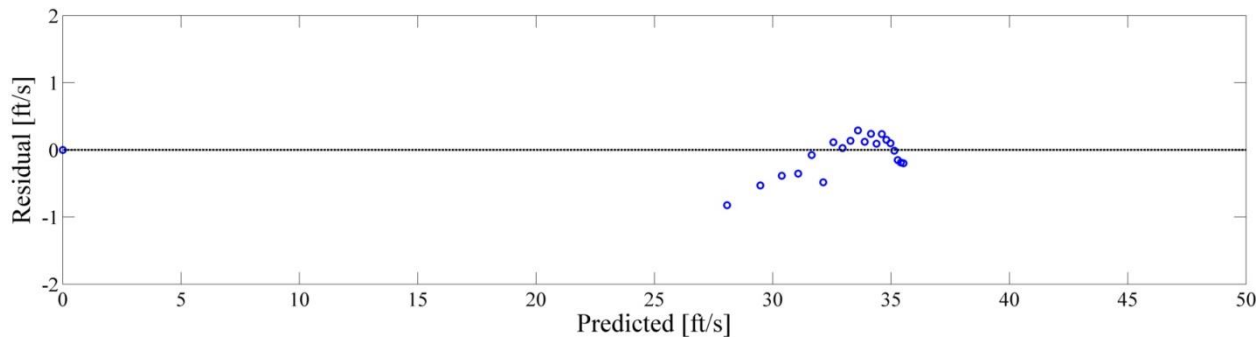

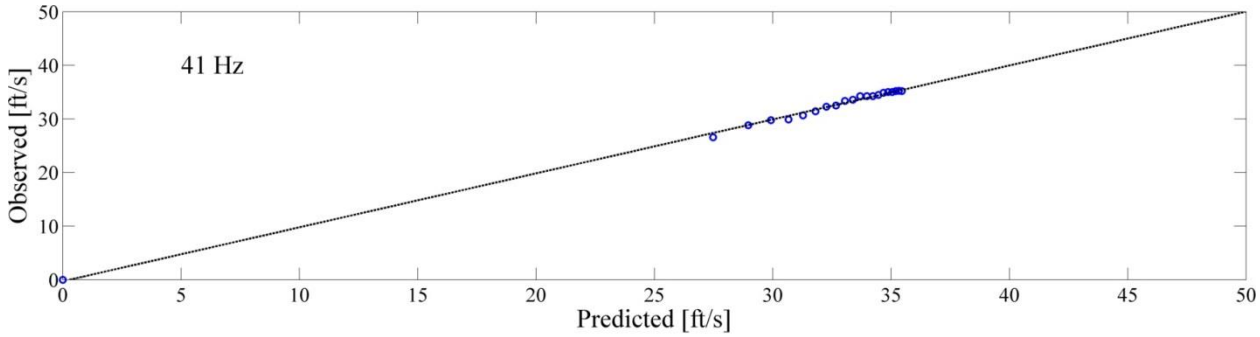

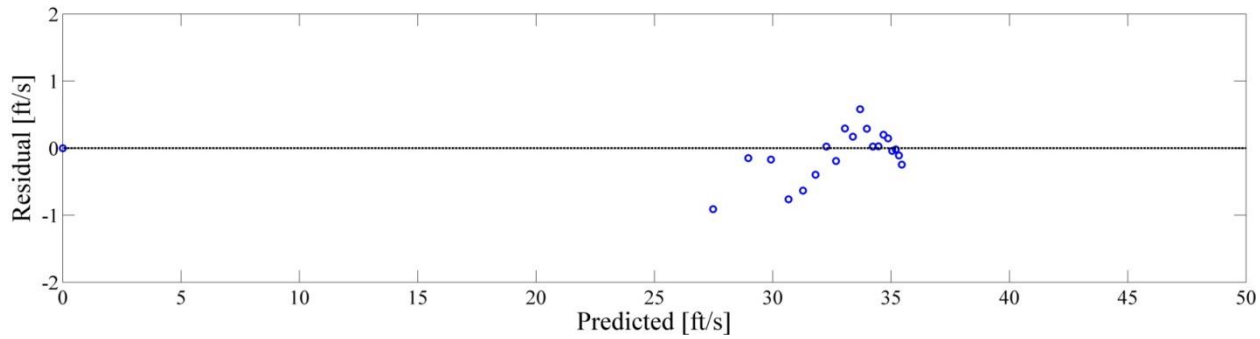

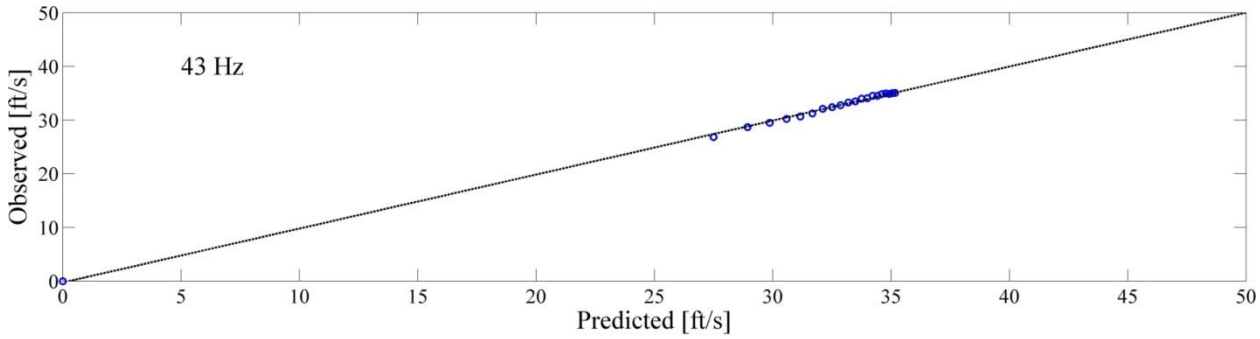

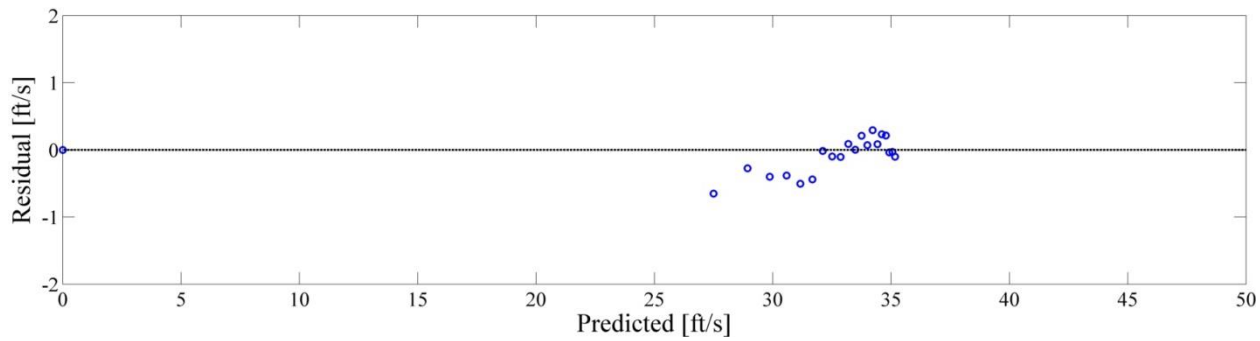

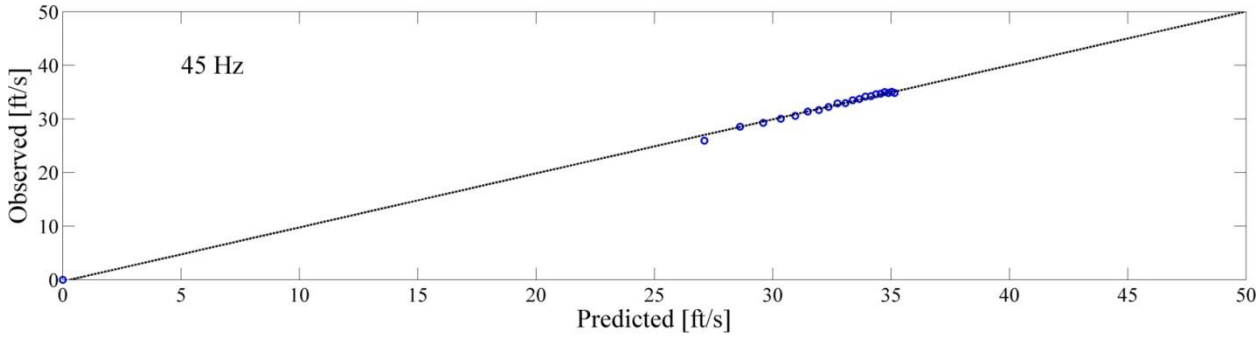

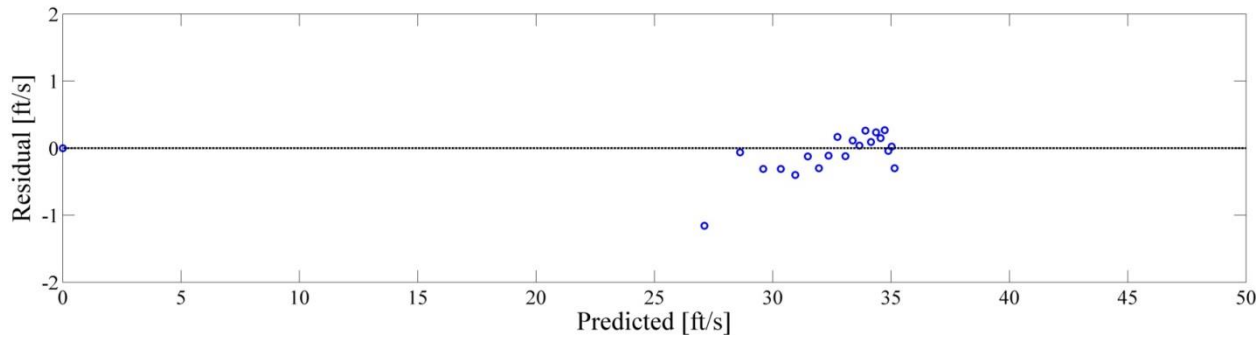

200 acfm:

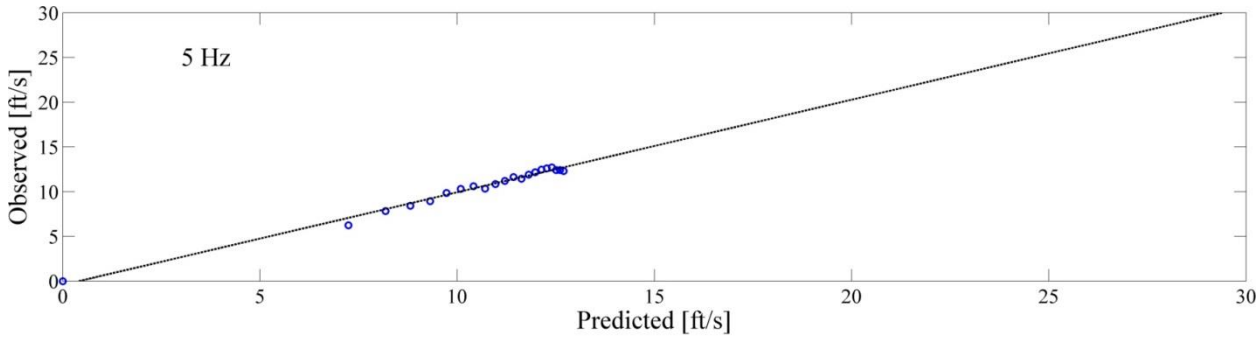

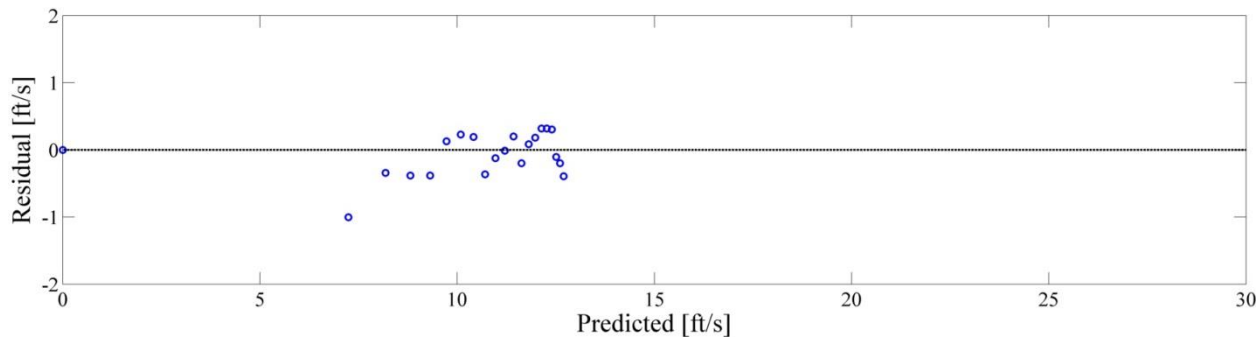

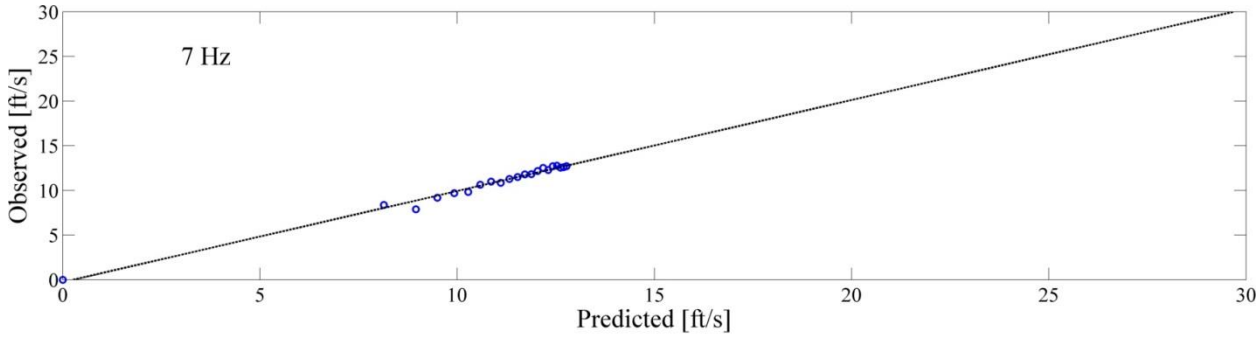

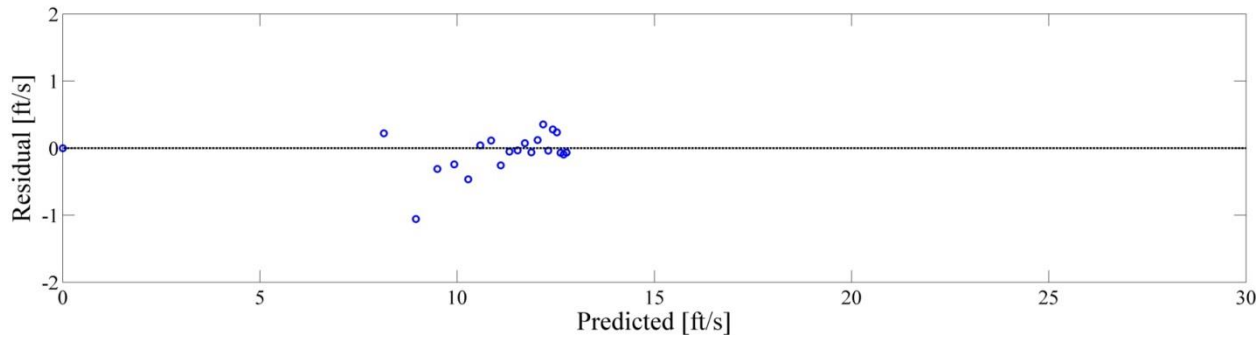

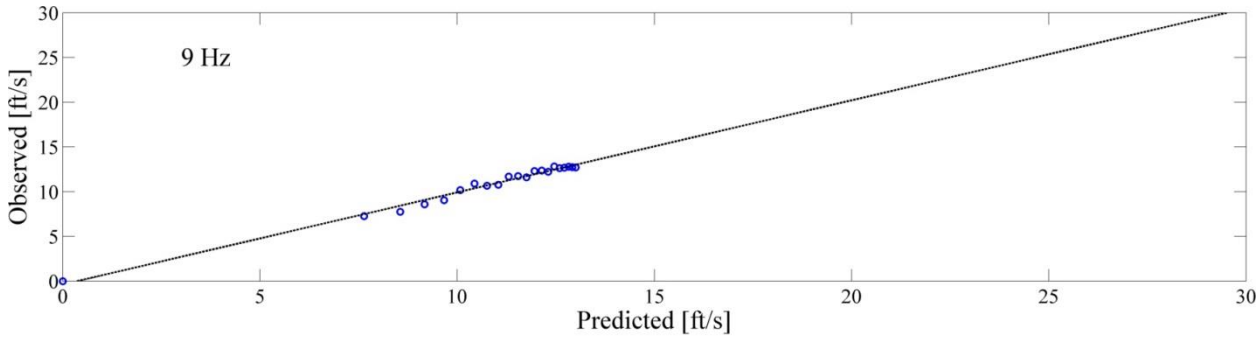

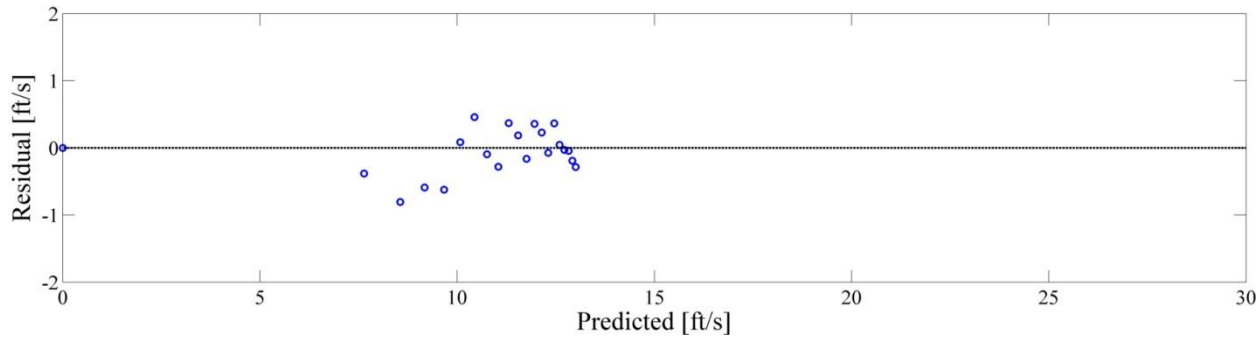

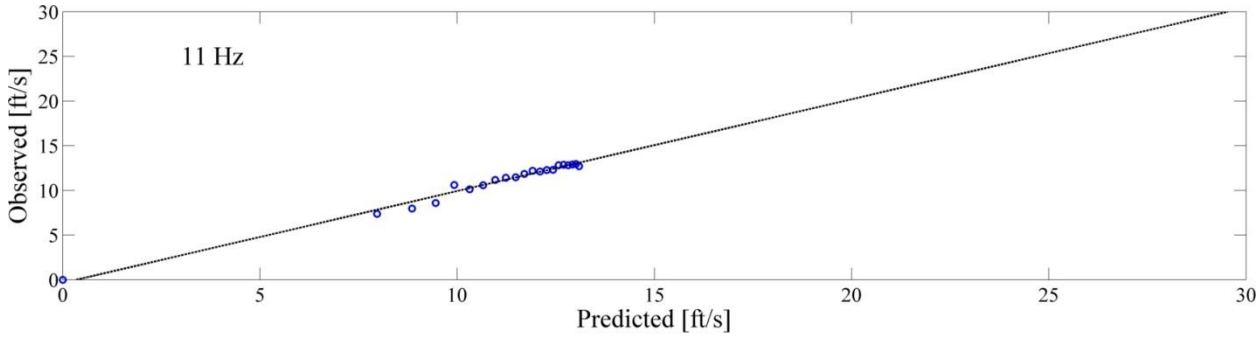

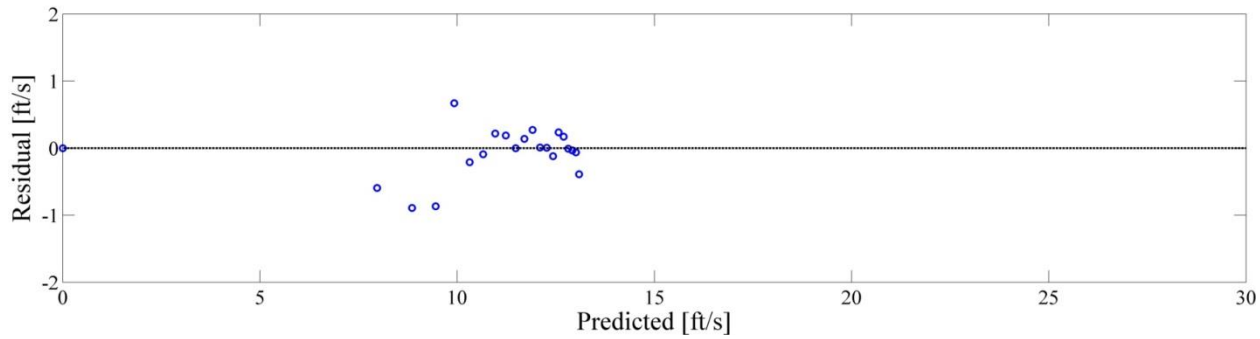

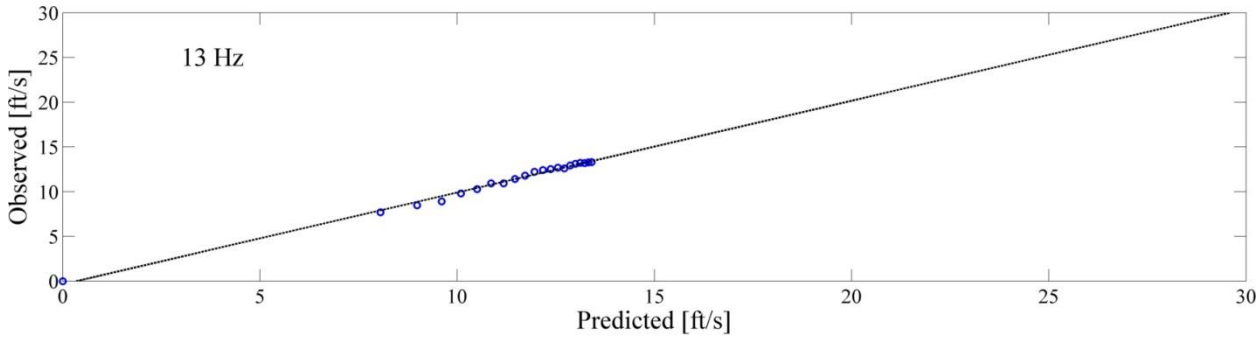

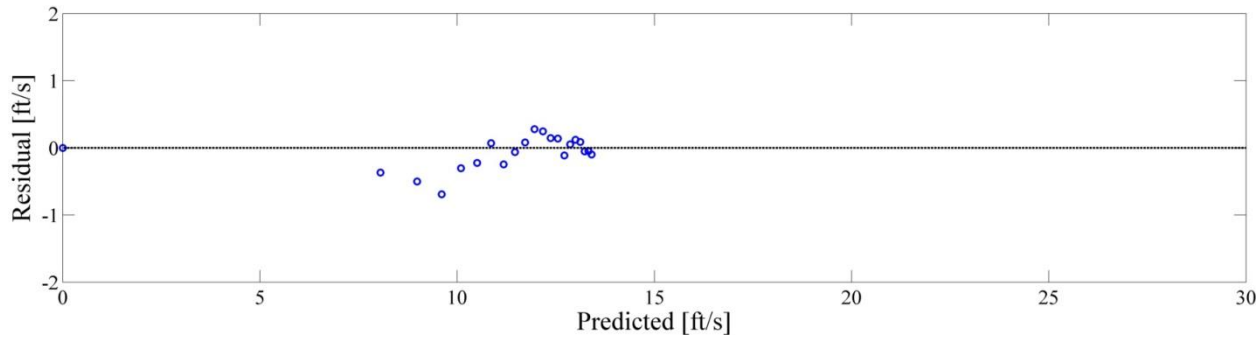

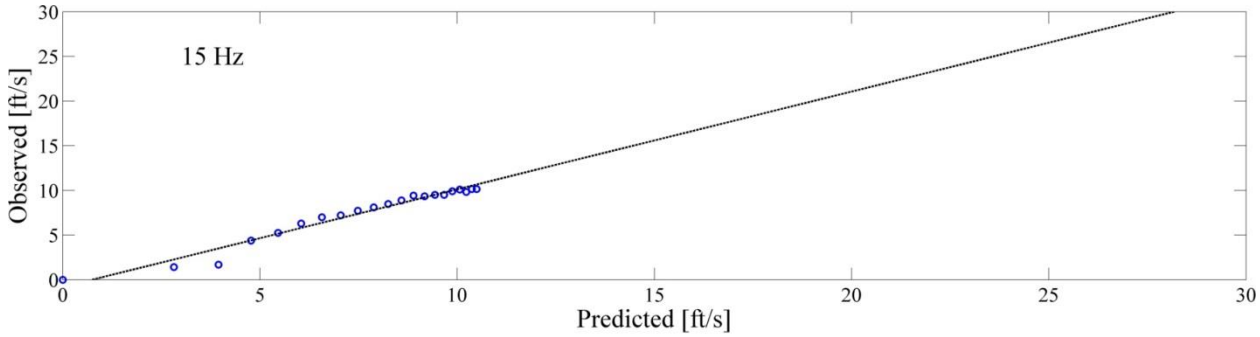

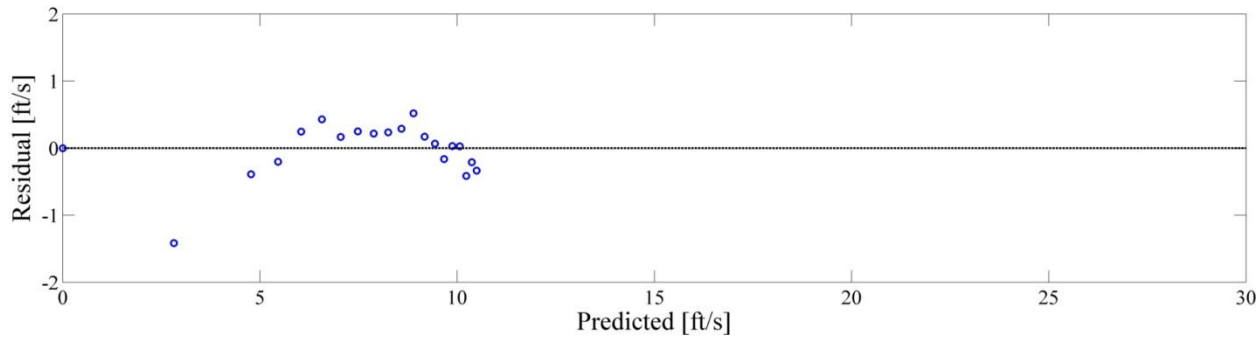

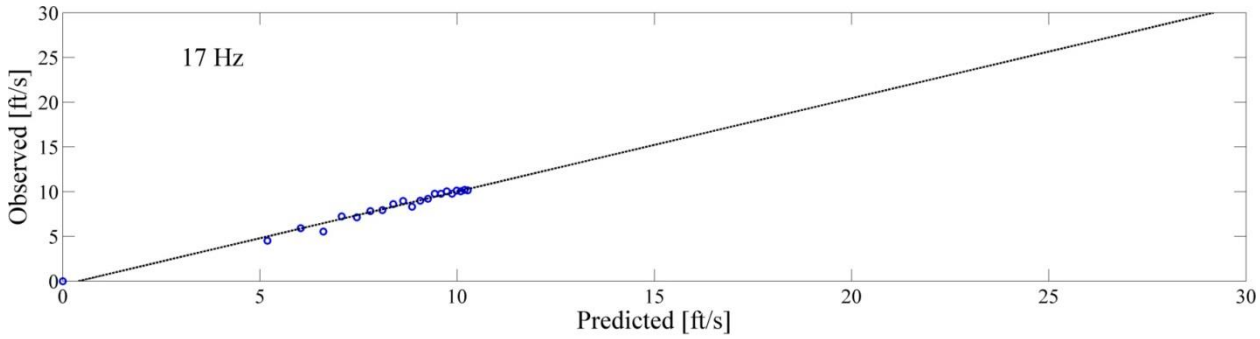

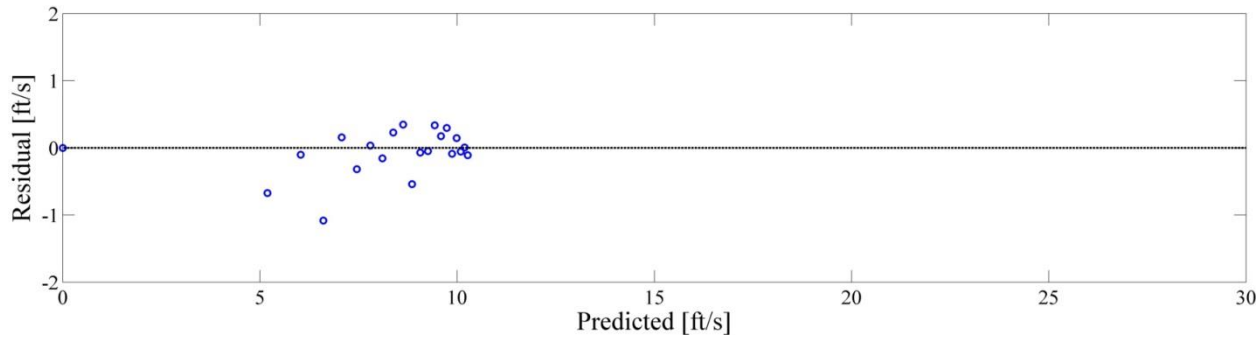

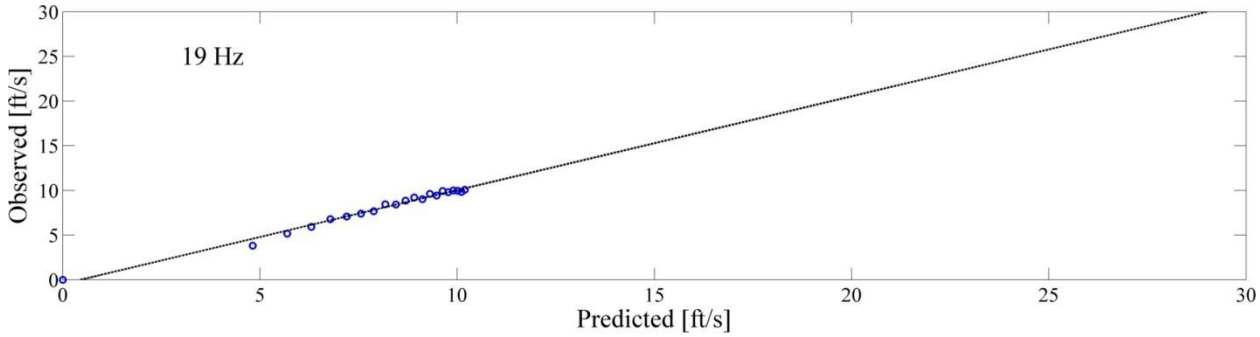

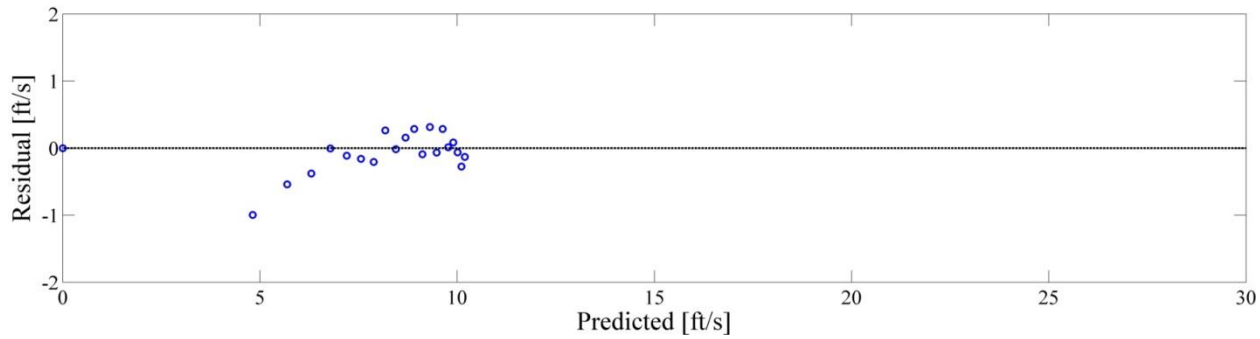

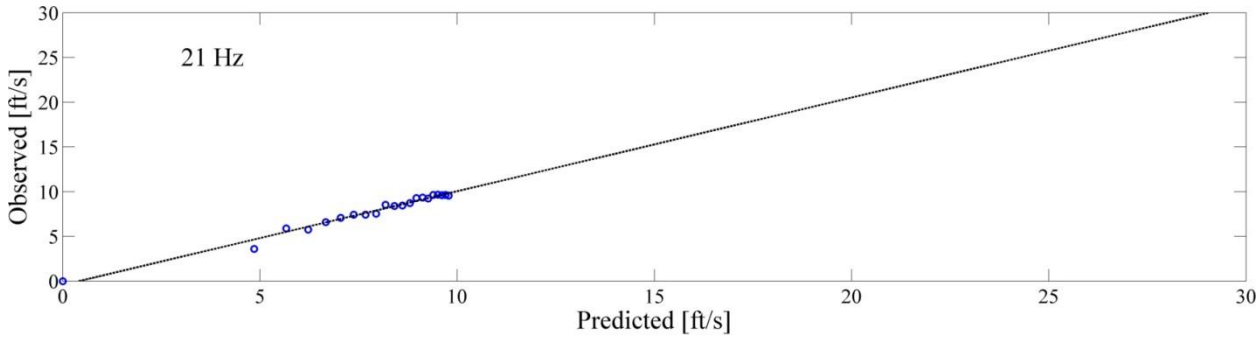

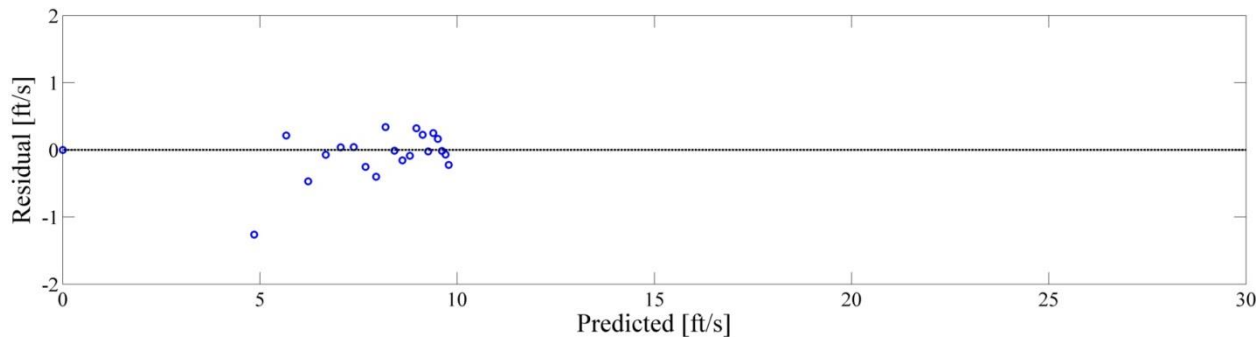

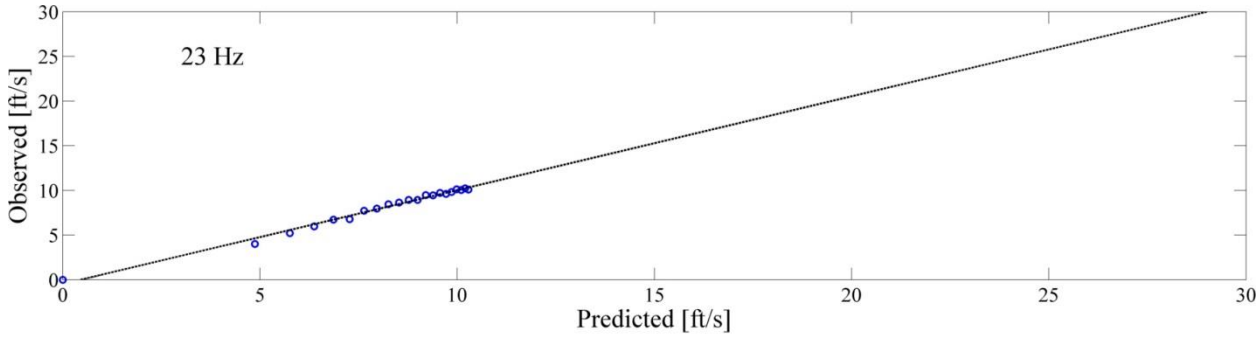

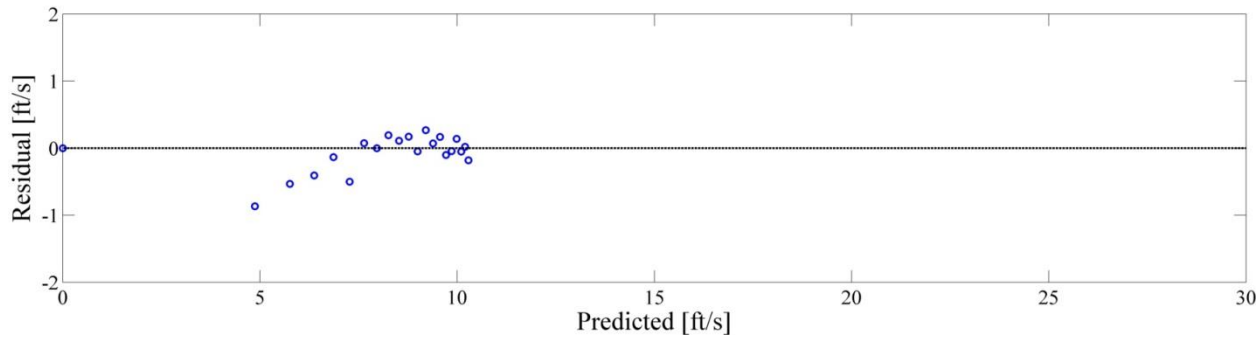

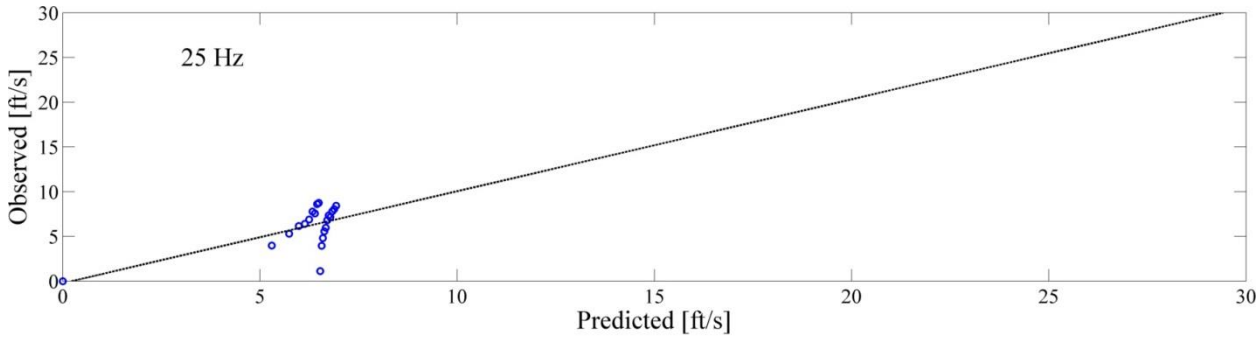

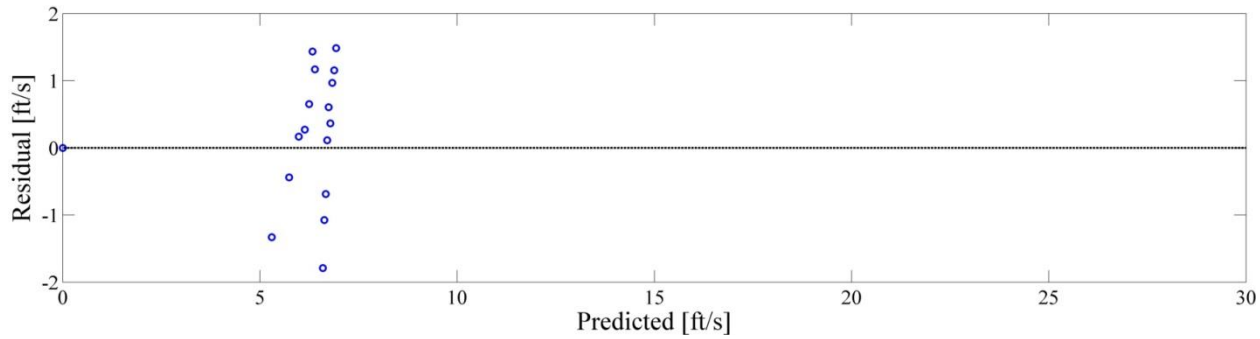

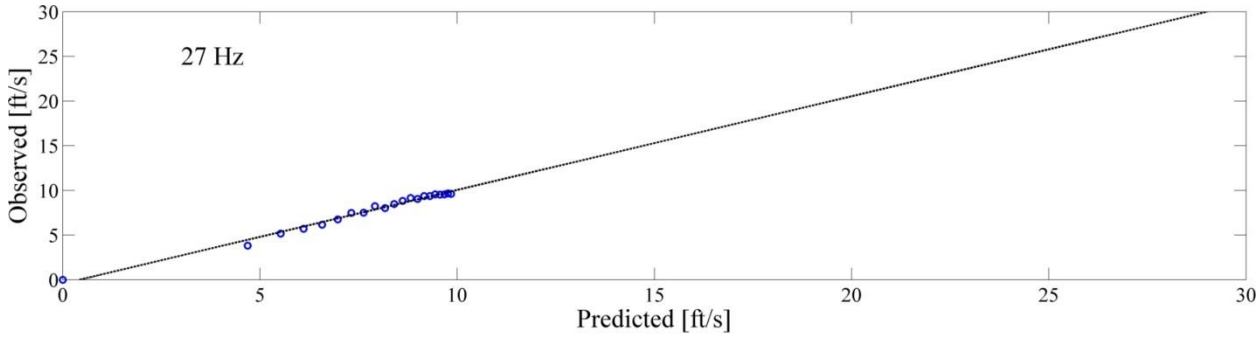

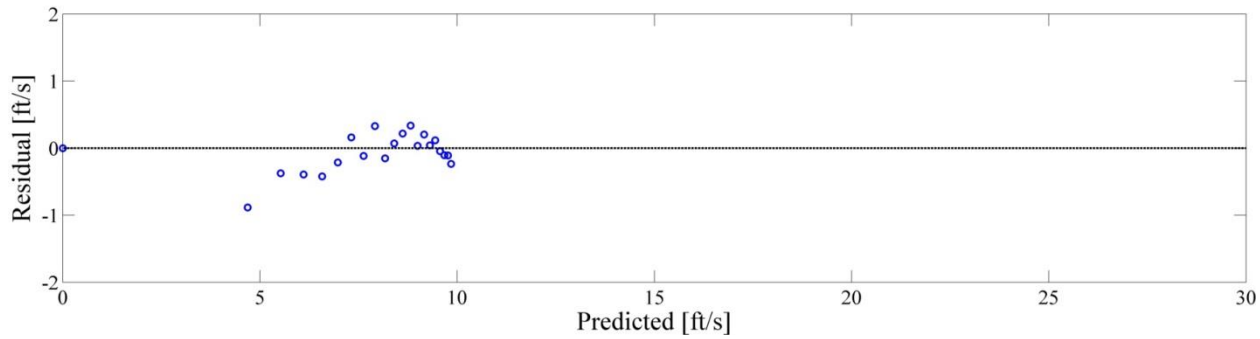

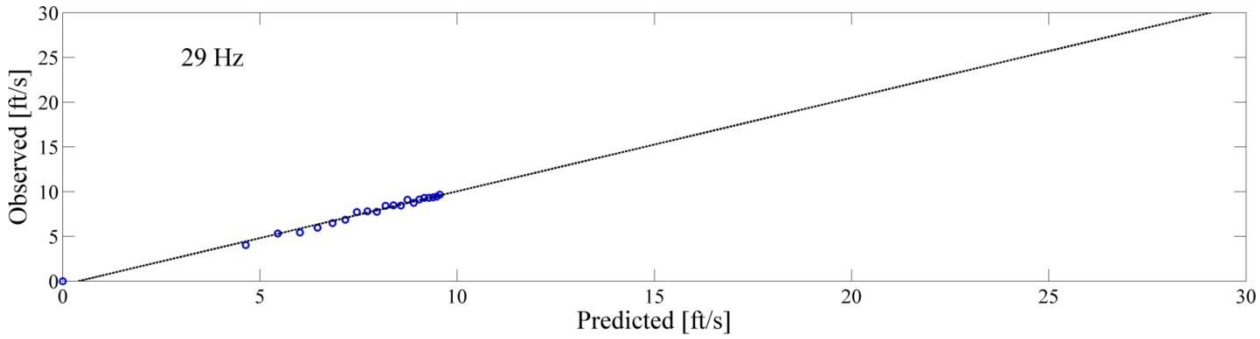

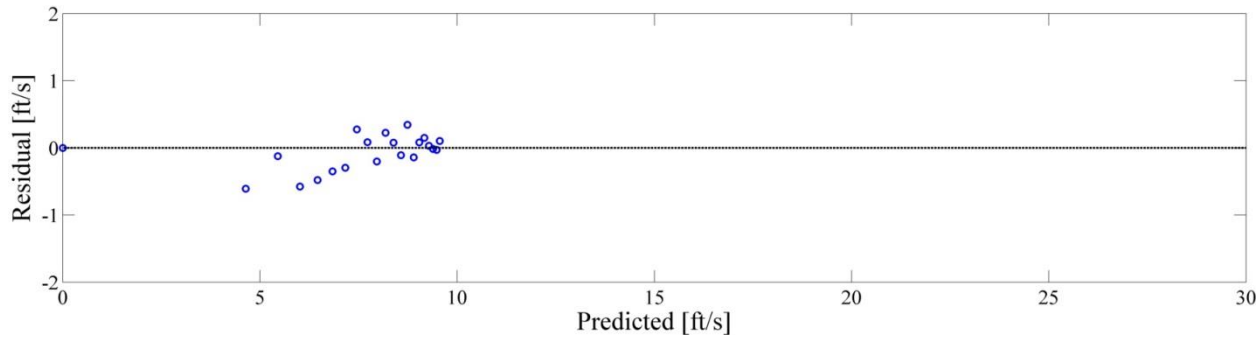

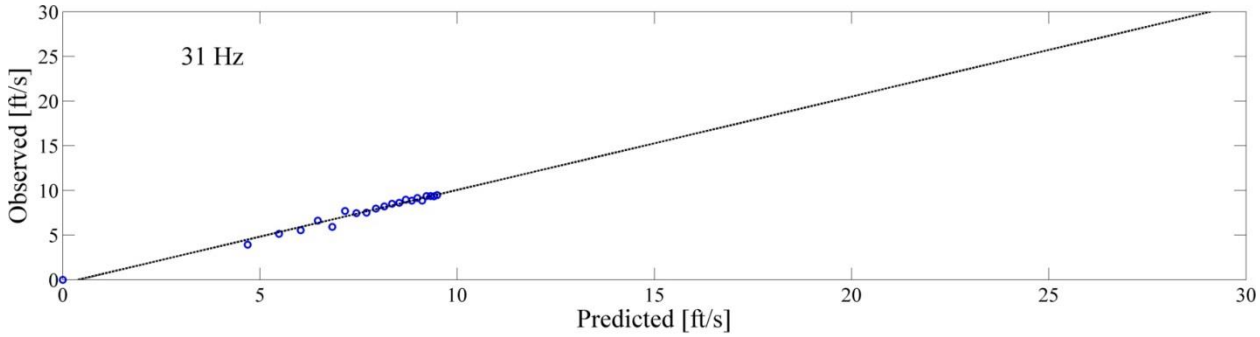

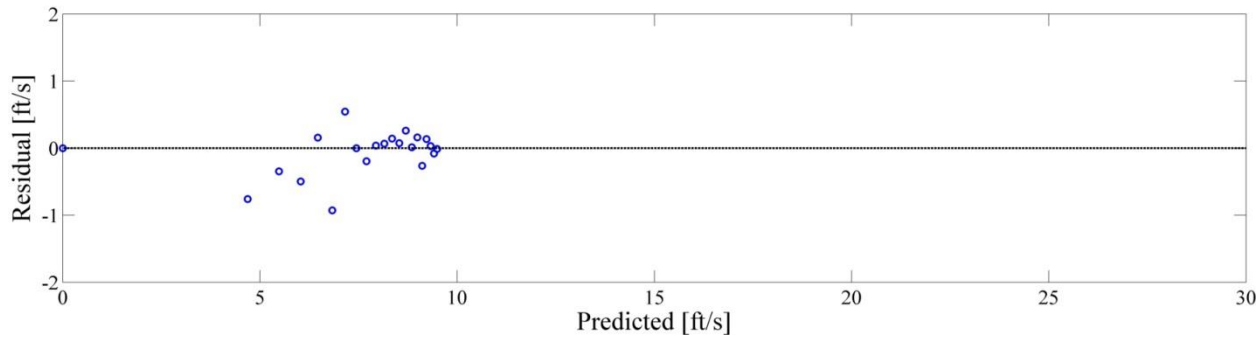

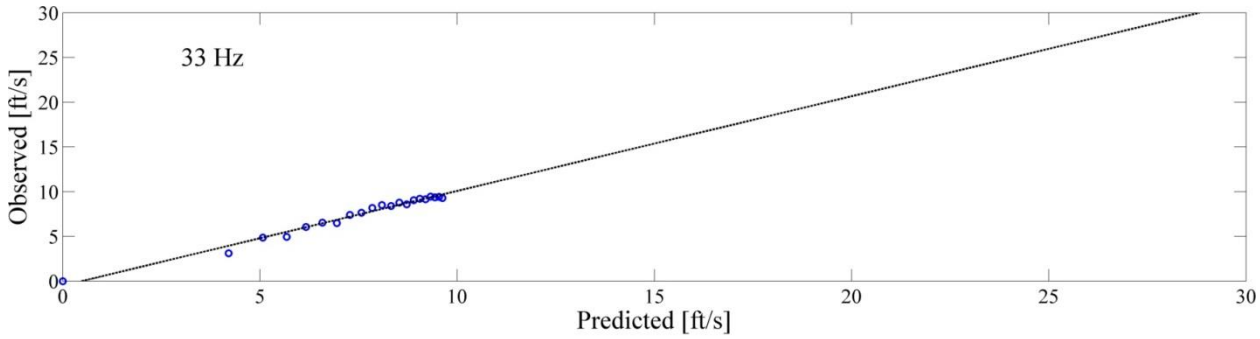

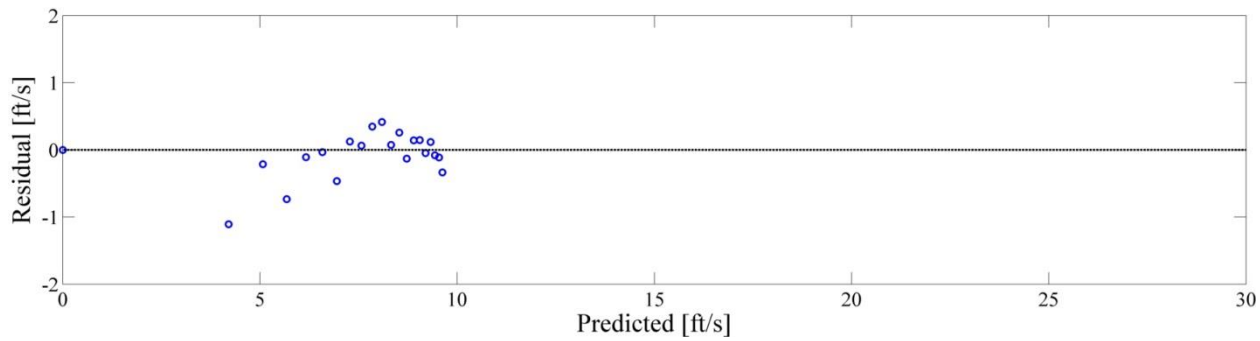

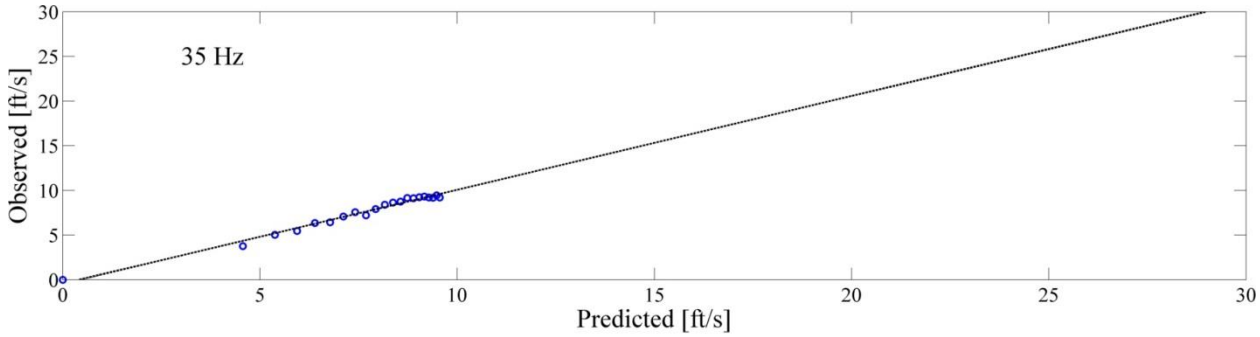

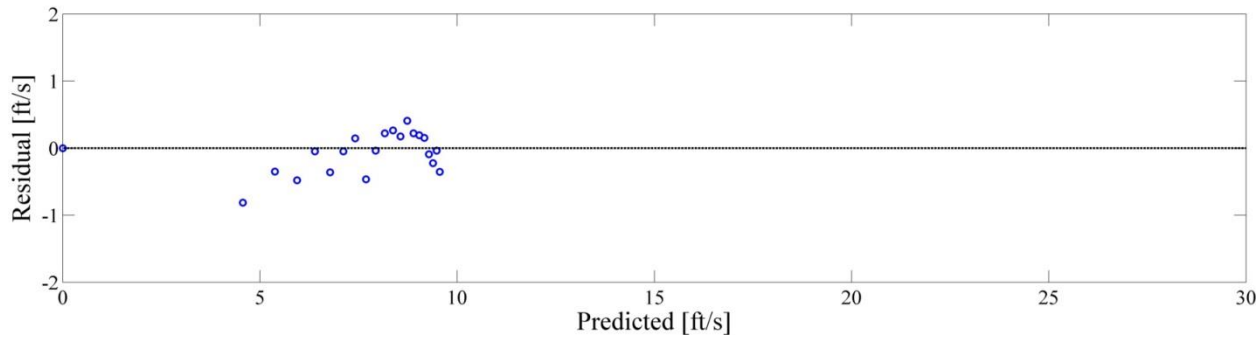

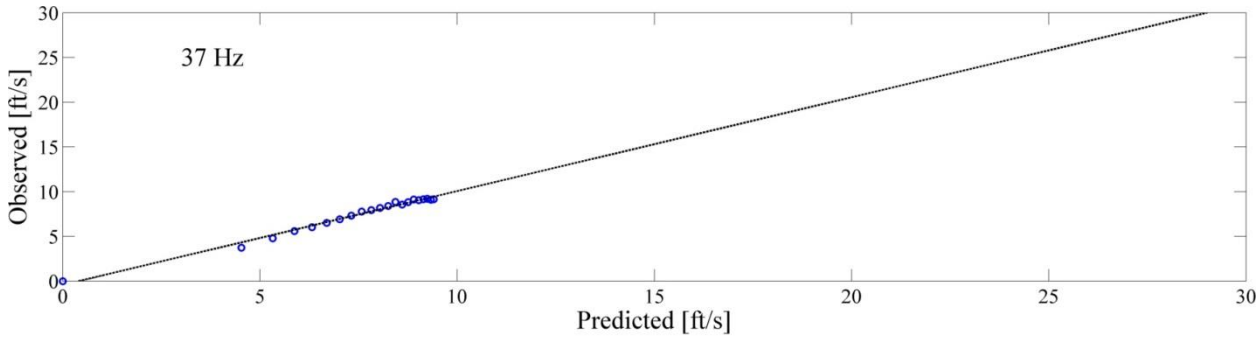

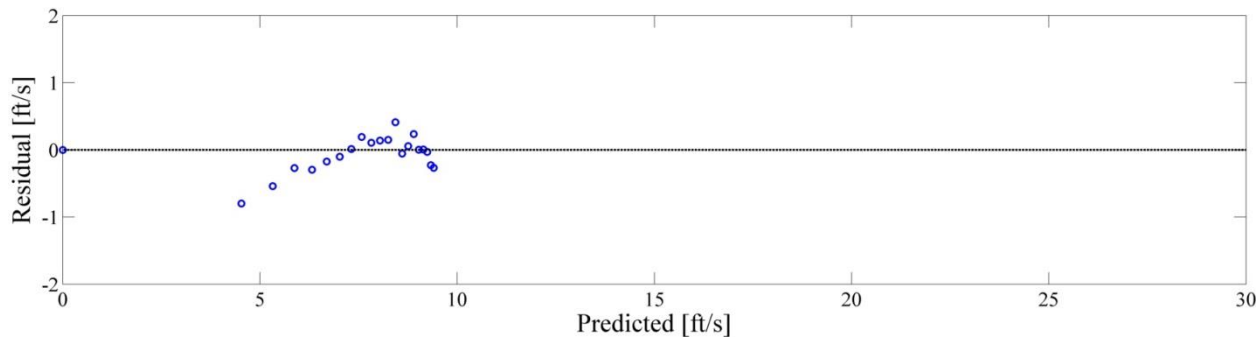

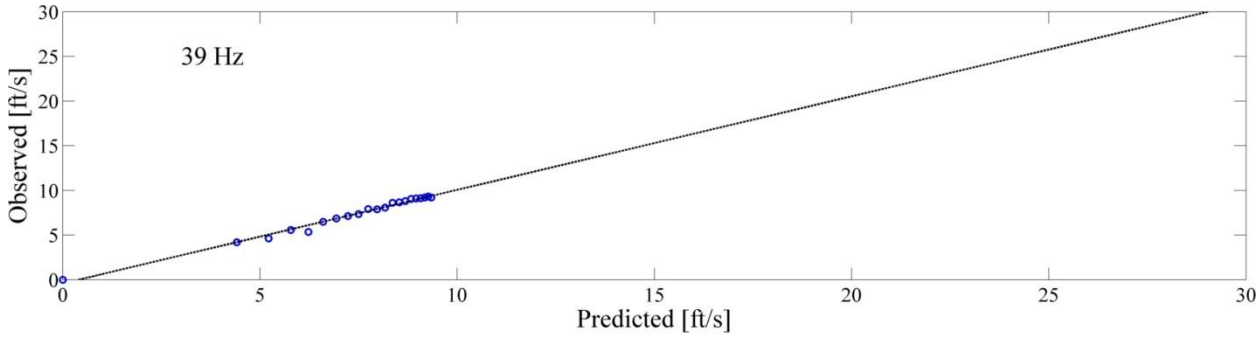

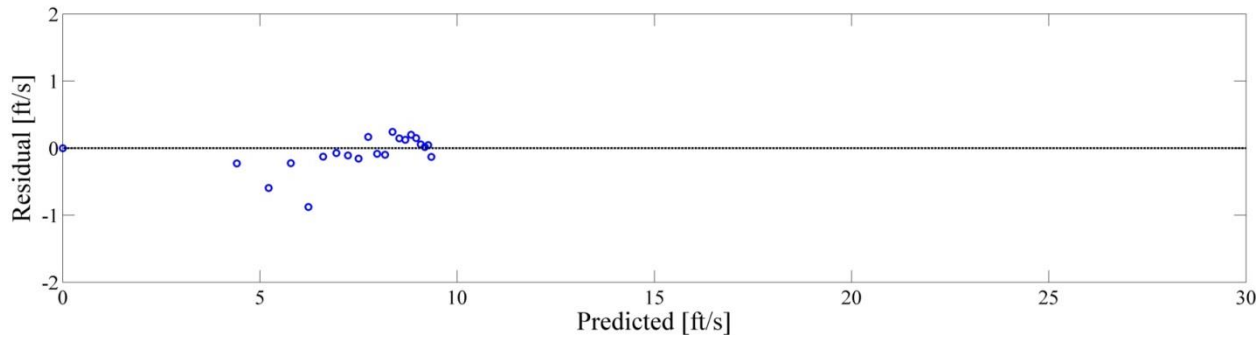

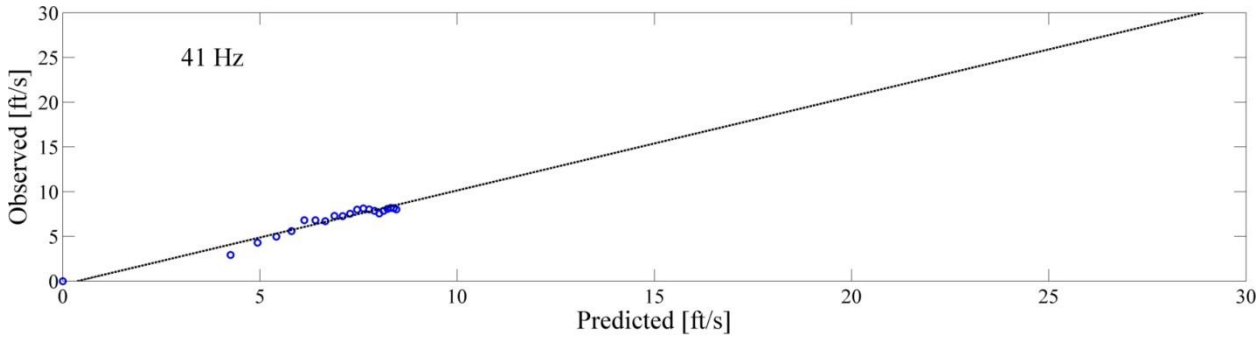

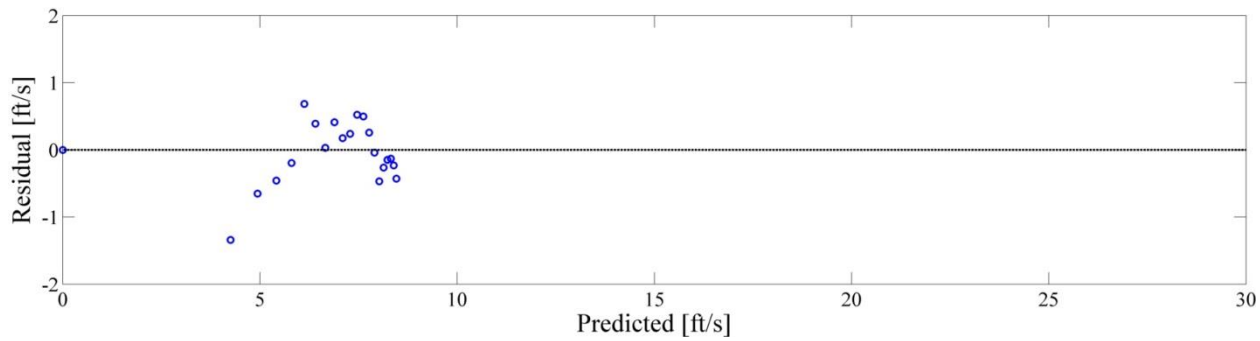

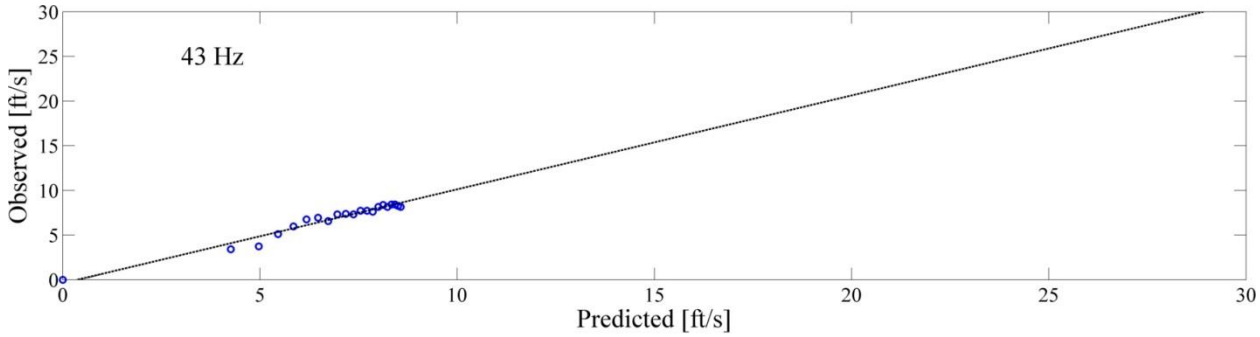

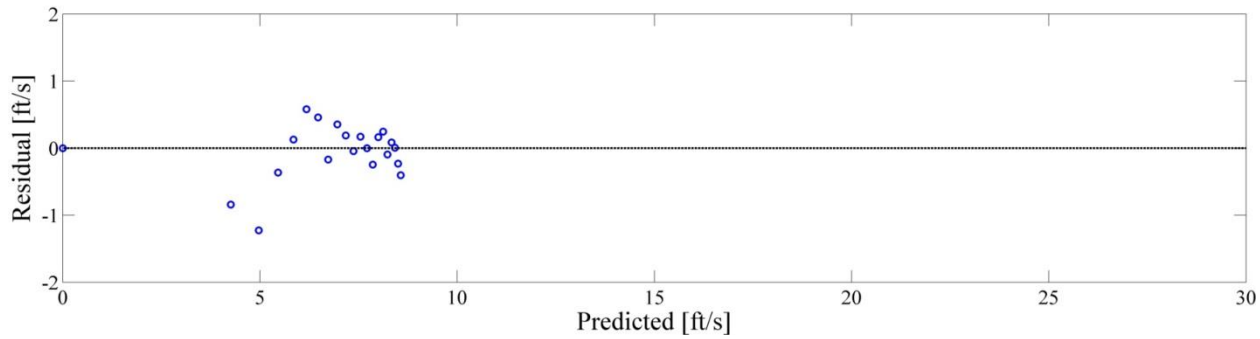

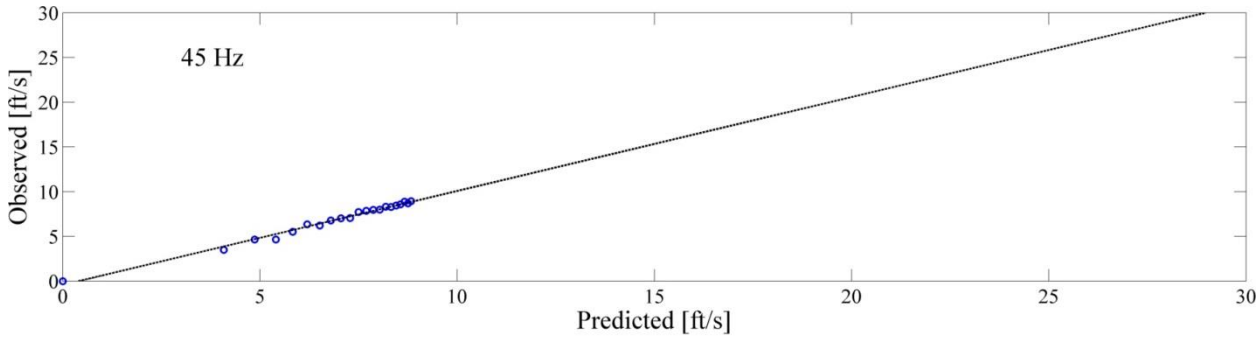

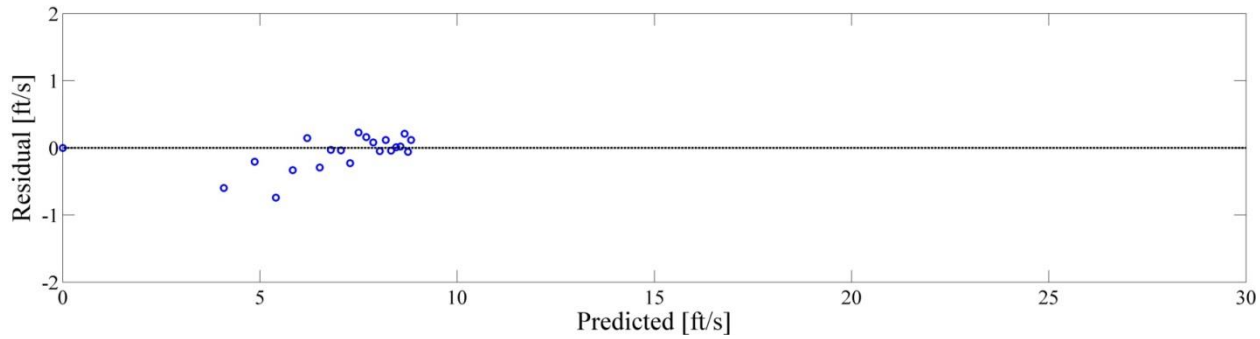

APPENDIX G: REGRESSION ANALYSIS SAS CODE

```
title 'Pulsation Regression Analysis - Christopher Grant';
data hotwire;
       input flowrate freq error maxpp maxvp meterpp metervp wt awt;
cards;
700     5       0.1051  5.6893  5.2747  4.3749  6.8382  1       1
700     7       0.1807  6.9545  2.2749  6.3395  4.2996  1       1
700     9       0.0193  4.5646  1.8013  4.5912  0.1193  1       1
700     11      0.0371  1.7291  1.8815  1.6080  1.0006  1       1
700     13      0.1344  2.9927  3.4446  2.2352  2.5615  1       1
700     15      0.6685  5.5689  8.2345  2.8643  7.3905  1       1
700     17      0.0692  2.9781  3.4301  1.1560  1.9618  1       1
700     19      0.0130  1.2073  0.9570  1.1689  0.6159  1       1
700     21      0.1762  1.8746  2.5751  1.0144  2.1527  1       1
700     23      0.1651  1.9750  2.0398  0.7649  2.0298  1       1
700     25      0.3985  2.8709  3.1132  0.4727  4.0297  1       1
700     27      0.7604  5.3446  3.8596  0.3356  7.2664  1       1
700     29      1.5760  12.8218 5.4738  3.6900  21.1466 0       0
700     31      1.1321  7.9232  0.5728  4.0421  8.4440  1       1
700     33      0.6310  3.9586  2.2968  2.8323  4.5690  1       1
700     35      0.5695  3.6764  3.2383  3.0019  2.7391  1       1
700     37      0.3699  4.1146  4.3133  3.7257  1.6171  1       1
700     39      0.3748  5.1578  7.8197  5.0760  0.9745  1       0
700     41      0.4665  7.8050  10.5416 7.7134  1.8767  1       0
700     43      1.0573  11.6996 16.5974 11.4868 6.7732  1       0
700     45      2.1553  9.4403  16.2764 8.2513  12.0265 1       0
200     5       0.0193  1.0377  2.8086  0.7698  3.6411  1       1
200     7       0.0372  1.7149  1.0533  1.5061  3.9815  1       1
200     9       0.0008  0.9405  1.1430  0.8985  0.0757  1       1
200     11      0.0101  0.2658  1.1042  0.2438  0.5872  1       1
200     13      0.0712  0.5746  1.4503  0.4267  1.0432  1       1
200     15      0.2745  0.9185  5.4504  0.4216  4.9031  1       1
200     17      0.0370  0.4642  2.2517  0.1756  1.0629  1       1
200     19      0.0128  0.2297  0.6787  0.2187  0.1446  1       1
200     21      0.0712  0.2656  1.3027  0.1505  1.0717  1       1
200     23      0.0673  0.2240  0.9230  0.0853  0.9184  1       1
200     25      0.1459  0.3387  1.8511  0.0541  2.3961  1       1
200     27      0.2827  1.1822  1.4960  0.0728  2.7895  1       1
200     29      0.9734  5.6219  5.3350  1.5958  20.6104 0       0
200     31      0.4174  1.4685  0.3351  0.7345  4.9405  1       1
200     33      0.2627  0.8748  0.1058  0.6298  0.2104  1       1
200     35      0.2559  0.8483  1.6670  0.7067  1.4069  1       1
200     37      0.2297  0.8802  2.1430  0.7956  0.8034  1       1
200     39      0.2751  1.1528  4.2650  1.0892  0.3521  1       0
200     41      0.3571  3.1953  11.4034 3.1245  1.8411  1       0
200     43      0.5718  0.4623  10.0749 0.4428  4.1114  1       0
200     45      0.9324  3.0000  8.8339  2.6589  6.5273  1       0
;
run;
* Step one: Basic regression;
proc reg data=hotwire plots(label)=(rstudentbypredicted cooksd dfbetas dffits diagnostics
observedbypredicted);
  model error=flowrate freq maxpp maxvp meterpp metervp/alpha=.05 r p influence collinoint
collin;
  output out=new r=resid  student=sresid p=pred rstudent=rs;
run;
proc corr data=hotwire plots=matrix(histogram);
  var error freq maxpp meterpp metervp;
run;
proc univariate data=new normal;
   var rs;
run;
* Step two: variable selection and transformation;
data hotwire;
       set hotwire;
       sqrterror=sqrt(error);
run;
proc reg data=hotwire;
       model sqrterror=flowrate freq maxpp maxvp meterpp metervp/
```

```
        selection=stepwise slentry=0.25 slstay=0.05 details=all;
        weight wt;
run;
proc reg data=hotwire plots(label)=(rstudentbypredicted cooksd dfbetas dffits diagnostics
observedbypredicted);
  model sqrterror=flowrate freq metervp/alpha=.05 r p clb vif partial influence collinoint
collin;
  weight wt;
  output out=new r=resid  student=sresid p=pred rstudent=rs;
run;
proc corr data=hotwire plots=matrix(histogram);
  var sqrterror freq maxpp meterpp metervp;
run;
proc univariate data=new normal;
   var rs;
run;
* Step three: check for effect of aliasing;
proc reg data=hotwire;
        model sqrterror=flowrate freq maxpp maxvp meterpp metervp/
        selection=stepwise slentry=0.25 slstay=0.05 details=all;
        weight awt;
run;
proc reg data=hotwire plots(label)=(rstudentbypredicted cooksd dfbetas dffits diagnostics
observedbypredicted);
  model sqrterror=freq maxpp metervp/alpha=.05 r p clb partial influence collinoint collin;
  weight awt;
  output out=new r=resid  student=sresid p=pred rstudent=rs;
run;
proc univariate data=new normal;
   var rs;
run;

/*
proc glm data=hotwire;
        class flowrate;
        model sqrterror=flowrate freq metervp/alpha=.05 p;
        weight wt;
run;
*/

quit;
```

APPENDIX H: TURBULENCE INTENSITY ANALYSIS

The output data from the hot-wire anemometer was analyzed for turbulence intensity. Each data set was approximately 5,100 readings, constituting approximately 5.1 seconds of testing. A data set was collected at each of the 21 insertion depths for each frequency and for each flow rate. Turbulence intensity is defined as in Equation [42], where I_t is the turbulence intensity, u_{avg} is the average flow velocity, and u' is the root-mean-square of the turbulent velocity fluctuations. The variable u' is defined in Equation [43] where u_{nt} is the velocity at time nt and nt_{max} is the time at the end of the data set.

$$I_t = \frac{u'}{u_{avg}} \quad [42]$$

$$u' = \sqrt{\frac{1}{nt_{max}}\left(\sum_{nt=1}^{nt_{max}} (u_{nt} - u_{nt+1})^2\right)} \quad [43]$$

The turbulence intensities of each data set are shown in Figures 96 and 97.

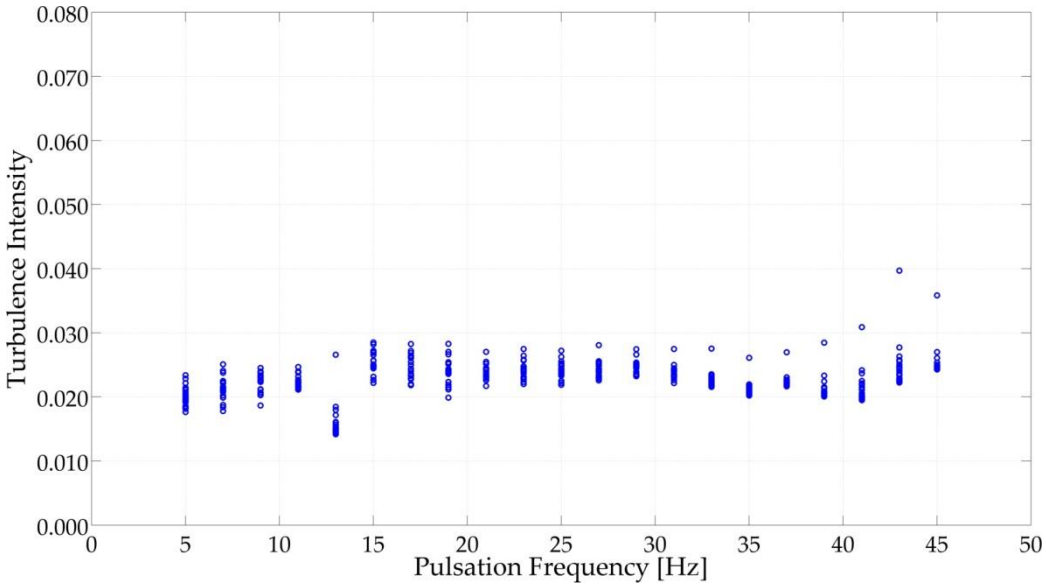

Figure 96. Turbulence intensities for 200 acfm

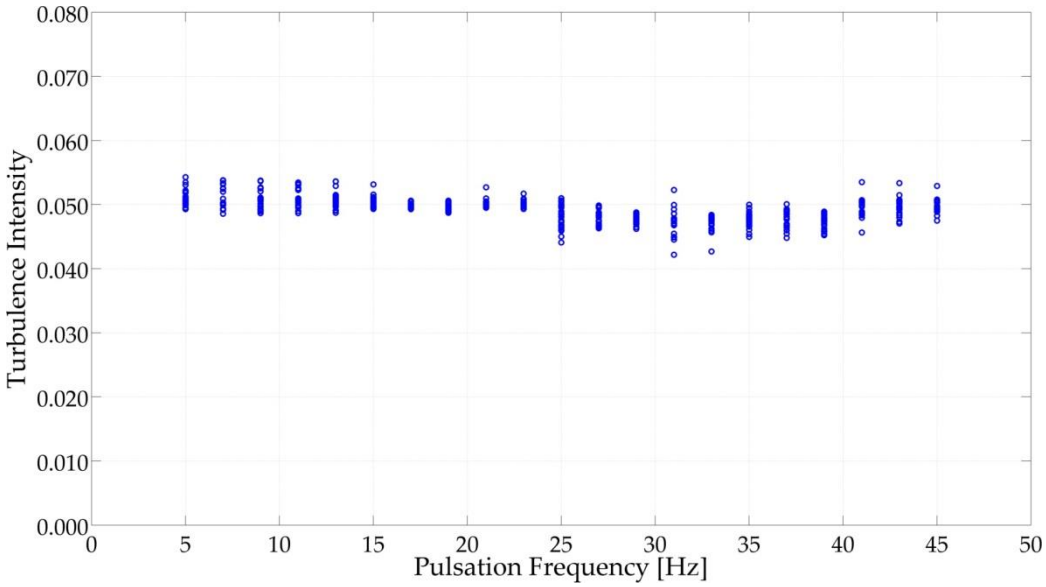

Figure 97. Turbulence intensities for 700 acfm

The average turbulence intensities for each test condition are tabulated in Table 14.

Table 14. Average turbulence intensities for all test conditions

	Flow Rate	
	200 acfm	700 acfm
Pulsation Frequency (Hz)	Turbulence Intensity	
5	0.0509	0.0201
7	0.0509	0.0213
9	0.0507	0.0221
11	0.0509	0.0222
13	0.0507	0.0160
15	0.0505	0.0254
17	0.0499	0.0245
19	0.0496	0.0238
21	0.0503	0.0239
23	0.0501	0.0243
25	0.0488	0.0241
27	0.0479	0.0242
29	0.0476	0.0247
31	0.0473	0.0239
33	0.0473	0.0227
35	0.0477	0.0215
37	0.0478	0.0224
39	0.0472	0.0213
41	0.0496	0.0213
43	0.0497	0.0246
45	0.0500	0.0254

REFERENCES

AGA Report No. 3, *Orifice Metering of Natural Gas and Other Related Hydrocarbon Fluids*, Part 1 – *General Equations and Uncertainty Guidelines*, Fourth Edition, American Petroleum Institute and American Gas Association, 2012.

AGA Report No. 3, *Orifice Metering of Natural Gas and Other Related Hydrocarbon Fluids*, Part 2 – *Specification and Installation Requirements*, Fourth Edition, American Petroleum Institute and American Gas Association, 2000.

AGA Report No. 7, *Measurement of Gas by Turbine Meters*, American Gas Association, Washington, DC, 2009.

AGA Report No. 9, *Measurement of Gas by Multipath Ultrasonic Meters*, Second Edition, American Gas Association, Washington, DC, April 2007.

Allison, T., "Acoustic and Flow Induced Vibration," *Pulsations and Vibrations in Piping Systems Short Course*, Southwest Research Institute, 2013.

API *Manual of Petroleum Measurement Standards*, Chapter 14, Natural Gas Fluids Measurement, Section 1, *Collecting and Handling of Natural Gas Samples for Custody Transfer*, Sixth Edition, American Petroleum Institute, 2006.

Baldwin, R. M., and Simmons, H. R., "Flow-Induced Vibration in Safety Relief Valves," *Journal of Pressure Vessel Technology*, Vol. 109 (1986), pp. 267-272.

Blevins, R. D., *Flow Induced Vibration*, Second Edition, Malabar, Florida: Kreiger Publishing Company, 1990.

Blevins, R. D., Tilden, B. W., and Martens, D. H., "Vortex-Induced Vibration and Damping of Thermowells," *Journal of Fluids and Structures*, Vol. 12 (1998), pp. 427-444.

Brock, J. E., "Stress Analysis of Thermowells," *Calhoun Institutional Archive of the Naval Postgraduate School*, 1974-11-11.

Broerman, E., Gatewood, J., O'Grady, J., Troy, R., Rand, C., and Stroud, G., "Identifying and Mitigating Flow-Induced Vibration in Recycle Loop Gas Piping at a Centrifugal Compressor Station," *Proceedings of the 8th International Pipeline Conference*, 2010.

Bronner, J. W. and McKee, R. J., "Cogen Pulsation Effects on Turbine Metering," *Proceedings of the A.G.A. Operating Section Distribution/Transmission Conference*, Nashville, TN, April-May 1991.

Bruun, H. H., *Hot Wire Anemometry: Principal and Signal Analysis*, Oxford University Press, 1995.

Canada Pipeline Accessories, "Flow Conditioners & Measurement," CPA, http://flowconditioner.com/, 2016

Caro, C. G., Pedley, T. J., Schroter, R. C., and Seed, W. A., *The Mechanics of the Circulation*, Oxford University Press, 1978.

Durke, R. G., Bowles, E. B., George, D. L., and McKee, R. J., "Effects and Control of Pulsation in Gas Measurement," *Proceedings of the 88th International School of Hydrocarbon Measurement*, Oklahoma City, OK, class 1090, May 2012.

Energy Institute, *Guidelines for the Avoidance of Vibration Induced Fatigue Failure in Process Pipework*, Second Edition, 2008.

George, D. L., "Turbine Meters," *Factors in Gas Meter Station Design and Operations*, Southern Gas Association and Southwest Research Institute, 2005.

Graf, H. R., and Ziada, S., "Flow-Induced Acoustic Resonance in Closed Side Branches: An Experimental Determination of the Excitation Source," *Proceedings of the ASME International Symposium on Flow-Induced Vibration and Noise, Vol. 7: Fundamental Aspects of Fluid-Structure Interactions*, AMD-Vol. 51 (1992), pp. 63-80.

Håkansson, E., and Delsing, J., "Effects of Pulsating Flow on an Ultrasonic Gas Flowmeter," *Flow Measurement and Instrumentation*, Vol. 5 (1994), pp. 93-101.

ISO/TR 12765:1998, *Measurement of fluid flow in closed conduits – Methods using transit-time ultrasonic flowmeters*, International Organization for Standardization, 1998.

Jiménez, J., "Turbulence and vortex dynamics," Notes on lectures at the Ecole Polytechnique (France), July 26, 2004.

Jungbauer, D., and Eckhardt, L., "Flow-Induced Turbocompressor and Piping Noise and Vibration Problems—Identification, Diagnosis, and Solution," *Proceedings of the 26th Turbomachinery Symposium*, (1997).

Jungowski, W. M., Bortros, K. K., and Studzinski, W., "Cylindrical Side-Branch as Tone Generator," *Journal of Sound and Vibration*, Vol. 131 (1989), pp. 265-285.

Karnik, U., and Geerligs, J., "Effect of Pulsation on Daniel/Instromet Multi-path Ultrasonic Meters," METCON Technical Report No. 3, NOVA Research and Technology Centre, Calgary, AB, November 2000.

Karnik, U., Geerligs, J., Brett, D., and Given, R., "Effect of Pulsation on a Single Path Daniel Ultrasonic Meter," Technical Report No. 1523, NOVA Research and Technology Centre, Calgary, AB, November 2001.

Karnik, U., Studzinski, W., Geerligs, J., and Rogi, M., "Effect of Flow Conditioners and Pulsation on the Performance of 8-inch Multi-path Ultrasonic Flow Meters," *International Pipeline Conference*, Calgary, Alberta, Canada, ASME IPC Paper No. 98-082, June 1998.

Kurtulu, D. F., "Hot Wire Measurements," *Experimental Aerodynamics AE547-EN*, ocw.metu.edu.tr, 2010.

Lacombe, R., Moussou, P., and Auregan, Y. "Whistling of an Orifice in a Reverberating Duct at Low Mach Number," *Journal of the Acoustical Society of America*, Vol. 130, No. 5 (2011), pp. 2662-2672.

Lansing, J., "How Today's Gas Ultrasonic Meter Handles Compressor Pulsations," *Proceedings of the 2011 AGA Operations Conference*, American Gas Association, Washington, DC, May 2011.

McKee, R. J., "Pulsation Effects on Orifice Metering Considering Primary and Secondary Elements," *1994 Gulf Coast Measurement Short Course*, American School of Gas Measurement Technology, 1994.

McKee, R. J., "Pulsation Effects on Orifice Meters," Southern Gas Association Short Course, *Factors in Gas Meter Station Design and Operations*, Southwest Research Institute, San Antonio, TX, June 2006.

McKee, R. J., "Pulsation Mitigation and its Effects on Metering," *Proceedings of the 2009 Western Gas Measurement Short Course*, Salt Lake City, UT, May 2009.

Miller, R. W., *Flow Measurement Engineering Handbook*, Third Edition, McGraw-Hill, 1996.

Mizushina, D. C., Maruyama, T., and Shiozaki, Y., "Pulsating Turbulent Flow in a Tube," *Journal of Chemical Engineering of Japan*, Vol. 6 (1973), pp. 487-494.

Montgomery, D. C., Peck, E. A., and Vining, G. G., *Introduction to Linear Regression Analysis*, 5th Ed. Hoboken, New Jersey: John Wiley & Sons, Inc., 2012.

Norton, M. and Karczub, D. (2003), *Fundamentals of Noise and Vibration Analysis for Engineers*, 2nd Ed., Cambridge, New York: Cambridge University Press.

PCB Piezotronics, "Model 112M66 Charge Output Dynamic Pressure Sensor Installation and Operating Manual," Document Number 21354, Revision B, PCB Piezotronics, Inc., Depew, New York, USA, February 2005.

Pish, R. H., "Effects and Control of Pulsations in Gas Measurement," Southwest Research Institute, 1991, pp. 37-43.

Richardson, E. G. and Tyler E., "The transverse velocity gradient near the mouths of pipes in which an alternating or continuous flow of air is established," *Proceedings of the Physics Society of London*, Vol. 42, pp. 1-15, 1929.

Rosemount, "Rosemount 3051Pressure Transmitter Product Data Sheet," Document Number 00813-0100-4001, Revision SB, Emerson Electric Co., August 2016.

Rosemount, "Rosemount 3144 Temperature Transmitter Product Data Sheet," Document Number 00813-0100-4021, Revision PA, Emerson Electric Co., September 2016.

Schlichting, H., *Boundary-Layer Theory*, New York: McGraw-Hill, 1968.

Simons, S., "Acoustic and Flow Induced Vibration," *Pulsations and Vibrations in Piping Systems Short Course*, Southwest Research Institute, 2013.

Sparks, C., "A Study of Flow Induced Pulsations at Piping Branches," SGA Project 04-6600-505, 1982.

Stansby, P. K., Pinchbeck, J. N., and Henderson, T., "Spoilers for the Suppression of Vortex-induced Oscillations," *Applied Ocean Research*, Vol. 8 (1986), pp. 169-173.

Studzinski, W., and Geerligs, J., "Effects of Pulsations on 8" Instromet Single Path Ultrasonic Meter and Headers on 8" Multi-Path Instromet Ultrasonic Flow Meter," Technical Report No. 1678, NOVA Research and Technology Centre, Calgary, AB, December 2002.

Studzinski, W., and Geerligs, J., "Effect of Pulsation on 8" Single Path Daniel Ultrasonic Meter and Effect of Swirl on 8" Multi-Path Daniel Ultrasonic Meter," Technical Report No. 1676, NOVA Research and Technology Centre, Calgary, AB, December 2002.

Studzinski, W., and Geerligs, J., "Effect of Pulsations and Swirl on 8-Inch Kongsberg Multi-Path Ultrasonic Flow Meter," Technical Report No. 1679, NOVA Research and Technology Centre, Calgary, AB, December 2002.

Testeud, P., Moussou, P., Hirschberg, A., and Auregan, Y., "Noise Generated by Cavitating a Single-Hole and Multi-Hole Orifices in a Water Pipe," *Journal of Fluids and Structures*, Vol. 23 (2007), pp. 163-189.

TSI, Inc., "Constant Temperature Anemometer Specifications," www.tsi.com, accessed Nov 2016.

Uchida, S. (1956). The Pulsating viscous flow superposed on the steady laminar motion of incompressible fluid in a circular pipe. Zeitschrift fur angewandteMathematik und Physik 7, 403-422. ISBN/ISSN: 1420-9039 OCLC:43807374.

van Bokhorst, E., and Peters, M., "A Test Certificate on the Impact of Piping and Flow Dynamic Effects on Flowmeter Accuracy in Gas and Liquid Flows," *Proceedings of the 5th International Symposium on Fluid Flow Measurement*, Arlington, VA, April 2002.

Wilson, T. A., Beavers, G. S., De Coster, M. A., Holger, D. K., and Regenfuss, D., "Experiments on the Fluid Mechanics of Whistling," *Journal of the Acoustical Society of America*, Vol. 50 (1971), pp. 366-372.

Ziada, S., and Buhlmann, E. T., "Self-Excited Resonances of Two Side-Branches in Close Proximity," *Journal of Fluids and Structures*, Vol. 6 (1992), pp. 583-601.

Ziada, S., and Shine, S., "Strouhal Numbers of Flow-Excited Acoustic Resonance of Closed Side Branches," *Journal of Fluids and Structures*, Vol. 13 (1999), pp. 127-142.

Ziada, S., Buhlmann, E. T., and Bolleter, U., "Flow Impingement as an Excitation Source in Control Valves," *Journal of Fluids and Structures*, Vol. 3 (1989), pp. 529-549.

VITA

Christopher L. Grant was born and raised in Denver, CO. For his undergraduate education, he attended Rose-Hulman Institute of Technology in Terre Haute, IN. He earned separate Bachelor's degrees in Mechanical Engineering and Physics in 2013. He studied fluid dynamics, heat transfer, experimental design, and statistical analysis at The University of Texas at San Antonio and earned a Master's degree in Mechanical Engineering in 2017. Christopher is employed at Southwest Research Institute as a Research Engineer in the Flow Measurement Group. His professional interests include flow measurement, fluid mechanics, surface topology, vibrations and acoustics, controls, statistical design, nanotechnology, and thermal physics. His unprofessional interests include debugging video games, walking rainy forests, telling terrible jokes, and raising lizards. He thinks sometimes about building a house.